

MOISTURE CONTENT DETERMINATION AND TEMPERATURE PROFILE MODELING OF FLEXIBLE PAVEMENT STRUCTURES

Brian K. Diefenderfer

Dissertation submitted to the Faculty of the
Virginia Polytechnic Institute and State University
in partial fulfillment of the requirements for the degree of

Doctor of Philosophy
Civil and Environmental Engineering

Dr. Imad Al-Qadi, chair
Dr. Gerardo Flintsch
Dr. Antonio Trani
Dr. Gary Brown
Dr. Amara Loulizi

April 2002

©Copyright 2002, Brian K. Diefenderfer

Keywords: flexible pavement, time-domain reflectometry, pavement moisture,
pavement temperature, temperature profile

MOISTURE CONTENT DETERMINATION AND TEMPERATURE PROFILE MODELING OF FLEXIBLE PAVEMENT STRUCTURES

Brian K. Diefenderfer

Chair: Dr. Imad Al-Qadi

The Via Department of Civil and Environmental Engineering

ABSTRACT

A majority of the primary roadways in the United States are constructed using hot-mix asphalt (HMA) placed over a granular base material. The strength of this pavement system is strongly influenced by the local environmental conditions. Excessive moisture in a granular base layer can cause that layer to lose its structural contribution by reducing the area over which loading may be distributed. Excessive moisture and fine particles can be transported by hydrostatic pressure to the surface layers, thus reducing the strength of the overlying HMA by contamination. Moisture in the surface HMA layers can cause deterioration through stripping and raveling. In addition, as HMA is a viscoelastic material, it behaves more as a viscous fluid at high temperatures and as an elastic solid at low temperatures. Between these two temperature extremes, a combination of these properties is evident. Thus, understanding the environmental effects on flexible pavements allows better prediction of pavement performance and behavior under different environmental conditions.

As part of the ongoing pavement research at the Virginia Smart Road, instrumentation was embedded during construction to monitor pavement response to loading and environment; moisture content of the granular base layers and temperature of the HMA layers were among the responses monitored. The Virginia Smart Road, constructed in Blacksburg, Virginia, is a pavement test facility is approximately 2.5km in length, of which 1.3km is flexible pavement that is divided into 12 sections of approximately 100m each. Each flexible pavement section is comprised of a multi-layer pavement system and possesses a unique structural configuration. The moisture content of aggregate subbase layers was measured utilizing two types of Time-Domain Reflectometry (TDR) probes that differed in their mode of operation. The temperature profile of the pavement was measured using thermocouples.

Data for the moisture content determination was collected and results from two probe types were evaluated. In addition, the differences in the moisture content within the aggregate subbase layer due to pavement structural configuration and presence of a moisture barrier were investigated. It was shown that the two TDR probe types gave similar results following a calibration procedure. In addition to effects due to pavement structure and subgrade type, the presence of a moisture barrier appeared to reduce the variability in the moisture content caused by precipitation. Temperature profile data was collected on a continuous basis for the purpose of developing a pavement temperature prediction model. A linear relationship was observed between the temperature given by a thermocouple near the ground surface and the pavement temperature at various depths. Following this, multiple-linear regression models were developed to predict the daily maximum or minimum pavement temperature in the HMA layers regardless of binder type or nominal maximum particle size. In addition, the measured ambient temperature and calculated received daily solar radiation were incorporated into an additional set of models to predict daily pavement temperatures at any location. The predicted temperatures from all developed models were found to be in agreement with in-situ measured temperatures.

ACKNOWLEDGEMENT

The author expresses his gratitude to his advisor, Dr. Imad L. Al-Qadi for offering the guidance necessary to undertake such a research project and for his assistance in completing this dissertation. Thanks are also extended to the committee members, Drs. Gerardo Flintsch, Antonio Trani, Gary Brown, and Amara Loulizi for giving their time and expertise to help in the completion of this work. In addition, the assistance of Dr. Sedki Riad of the Electrical Engineering Time Domain Laboratory and Alyaa Zahran and Dr. Donald Jensen of the Statistical Consulting Center is appreciated.

The author extends his heartfelt appreciation to his family for their support and encouragement during his entire education and many years at Virginia Tech. The author also wishes to thank Stacey Reubush for her assistance with the development and analysis of the statistical modeling. The assistance of the author's colleagues: Alex, Kevin, Mohammad, Mostafa, Robin, Samer L., Samer K., Stacey, and Walid from the Roadway Infrastructure Group and Jason Yoho from the Time Domain Laboratory greatly contributed to the author's progress and completion of this research. The author wishes to thank Kenneth, Kevin, and Randy of the Virginia Department of Transportation for their assistance at the Virginia Smart Road.

The author also recognizes and appreciates the support and interest received from the staff of the Via Department of Civil and Environmental Engineering, the Virginia Tech Transportation Institute, and the Virginia Department of Transportation.

TABLE OF CONTENTS

LIST OF FIGURES	ix
------------------------	-----------

LIST OF TABLES	xiv
-----------------------	------------

CHAPTER 1

INTRODUCTION	1
---------------------	----------

1.1 BACKGROUND	2
-----------------------	----------

VIRGINIA SMART ROAD	2
----------------------------	----------

MOISTURE CONTENT DETERMINATION	3
---------------------------------------	----------

PAVEMENT TEMPERATURE PREDICTION	5
--	----------

1.2 PROBLEM STATEMENT	7
------------------------------	----------

MOISTURE CONTENT MONITORING	7
------------------------------------	----------

PAVEMENT TEMPERATURE PREDICTION	7
--	----------

1.3 OBJECTIVES OF RESEARCH	8
-----------------------------------	----------

MOISTURE CONTENT MONITORING	8
------------------------------------	----------

PAVEMENT TEMPERATURE PREDICTION	8
--	----------

1.4 SCOPE OF RESEARCH	9
------------------------------	----------

CHAPTER 2

BACKGROUND	10
-------------------	-----------

2.1 PAVEMENT MOISTURE	10
------------------------------	-----------

2.1.1 MOISTURE RELATED DISTRESSES IN PAVEMENTS	11
---	-----------

2.1.2 DIELECTRIC MATERIALS	12
-----------------------------------	-----------

Development of Polarization Concepts	16
--------------------------------------	----

Material Polarization	17
-----------------------	----

2.1.3 SOIL MOISTURE MEASUREMENT INSTRUMENTS	19
--	-----------

Dielectric Probes	20
-------------------	----

Time Domain Reflectometry	22
---------------------------	----

Sampling Volume	29
-----------------	----

Mixture Theory	37
----------------	----

2.1.4 SOIL PROPERTIES	37
------------------------------	-----------

Solid Phase _____	38
Liquid Phase _____	41
2.2 PAVEMENT TEMPERATURE _____	42
2.2.1 RADIATION THEORY (ENERGY EQUILIBRIUM) _____	44
Solar Radiation _____	45
Radiation Emitted by Pavement Surface _____	48
Conduction Energy _____	49
Convection Energy _____	49
2.2.2 PAVEMENT TEMPERATURE PREDICTION _____	49
Pavement Temperature Prediction models _____	50
2.2.3 APPLICATIONS OF TEMPERATURE PREDICTION _____	64
Considerations on Prediction Accuracy _____	68
CHAPTER 3	
ENVIRONMENTAL MONITORING AT THE VIRGINIA SMART ROAD _____	70
3.1 VIRGINIA SMART ROAD _____	70
3.1.1 INSTRUMENT NOMENCLATURE _____	72
3.2 PAVEMENT MOISTURE _____	73
3.2.1 PROBE TYPES _____	73
CS610 _____	73
CS615 _____	75
3.2.2 CALIBRATION MODEL DEVELOPMENT _____	76
CS610 Calibration _____	77
CS615 Calibration _____	82
3.2.3 TIME-DOMAIN REFLECTOMETRY PROBE PLACEMENT _____	84
3.3 PAVEMENT TEMPERATURE _____	85
3.3.1 THERMOCOUPLE PREPARATION AND CALIBRATION _____	86
3.3.2 THERMOCOUPLE PLACEMENT _____	86
CHAPTER 4	
DATA PRESENTATION AND ANALYSIS _____	88
4.1 PAVEMENT MOISTURE _____	88

4.1.1 MOISTURE DATA COLLECTION AND MANAGEMENT _____	88
4.1.2 ANALYSIS OF RESULTS WITH RESPECT TO PROBE TYPE _____	91
4.1.3 ANALYSIS OF RESULTS WITH RESPECT TO PAVEMENT STRUCTURAL CONFIGURATION _____	92
4.1.4 MODELING TDR PROBE SAMPLING VOLUME _____	93
4.2 PAVEMENT TEMPERATURE _____	98
4.2.1 TEMPERATURE DATA COLLECTION AND MANAGEMENT _____	99
4.2.2 ANALYSIS OF RESULTS WITH RESPECT TO PAVEMENT STRUCTURAL CONFIGURATION _____	101
4.2.3 PAVEMENT TEMPERATURE PREDICTION MODELS _____	102
Linear Modeling for Daily Pavement Temperature Prediction _____	104
Linear Modeling (with Seasonal Component) for Daily Pavement Temperature Prediction _____	106
Linear Modeling (with Seasonal and Depth Components) for Daily Pavement Temperature Prediction _____	109
Thermocouple Reliability _____	111
Model Evaluation _____	112
Hourly Pavement Temperature Prediction Models _____	112
4.2.5 PAVEMENT TEMPERATURE PREDICTION MODELS INCORPORATING CALCULATED SOLAR RADIATION _____	115
Daily Pavement Temperature Prediction Models _____	117
Model Evaluation _____	118
Daily Pavement Temperature Prediction Models Incorporating Ambient Temperature _____	119
Model Evaluation _____	121
Validation of Daily Pavement Temperature Prediction Models Incorporating Ambient Temperature _____	121
Daily Pavement Temperature Prediction Models Incorporating Ambient Temperature from Multiple Locations _____	125
Hourly Pavement Temperature Prediction Models _____	127
Pavement Temperature Prediction Model Selection _____	128

CHAPTER 5

SUMMARY AND CONCLUSIONS _____	129
5.1 FINDINGS _____	130
5.2 CONCLUSIONS _____	131

CHAPTER 6	
RECOMMENDATIONS	135
REFERENCES	136
APPENDIX A	
TDR PROBE CALIBRATION	142
APPENDIX B	
TDR PROBE PLACEMENT AT THE VIRGINIA SMART ROAD	145
APPENDIX C	
THERMOCOUPLE CALIBRATION	148
APPENDIX D	
THERMOCOUPLE PLACEMENT AT THE VIRGINIA SMART ROAD	151
APPENDIX E	
MOISTURE CONTENT MONITORING	154
APPENDIX F	
STATISTICAL ANALYSIS OF THERMOCOUPLE AVERAGING	166
APPENDIX G	
MAXIMUM AND MINIMUM TEMPERATURE TRENDS OVER SEASONAL VARIATION	172

APPENDIX H	
STATISTICAL ANALYSIS OF TEMPERATURE VARIATION ACROSS PAVEMENT SECTIONS	207
APPENDIX I	
PAVEMENT TEMPERATURE PREDICTION MODEL ACROSS PAVEMENT SECTIONS	217
VITAE	299

LIST OF FIGURES

Figure 2.1. External electric field applied to a) vacuum and b) single dipole. _____	15
Figure 2.2. Set of dipoles a) before and b) during application of external electric field.	15
Figure 2.3. Schematic of time-domain reflectometry including a) oscilloscope (showing typical waveform) and b) TDR probe. _____	22
Figure 2.4. a) Coaxial cable and b) end view of connections for three TDR probe configurations. _____	27
Figure 2.5. TDR probe output for a) two-rod transmission line with balancing transformer and b) three-rod transmission line without balancing transformer (after Whalley, 1993). _____	28
Figure 2.6. Analysis of two-rod TDR probe showing a) coordinate axis and b) surfaces S1 and S2 and the region Ω between them. _____	32
Figure 2.7. Dimensions of two-rod TDR probe showing interfocal distance (2a), separation distance (2d), and diameter (2b). _____	35
Figure 2.8. Soil particle size and shape ranges. _____	38
Figure 2.9. Two basic units of clay minerals: a) silica tetrahedron and b) alumina octahedron. _____	39
Figure 2.10. Attraction of polar water molecules to clay particle in diffuse double layer. _____	40
Figure 2.11. Definition of solar and surface angles (from Kreith, 1986). _____	47
Figure 2.12. Temperature profile for Section A showing daily low pavement temperatures at various depths versus daily low surface temperature. ____	53
Figure 2.13. Temperature distribution for Section A - April 10, 2000. _____	54
Figure 3.1. Structural Configuration of Virginia Smart Road. _____	72
Figure 3.2. CS610 TDR probe. _____	73
Figure 3.3. CS615 TDR probe (after Campbell Scientific, 1996). _____	75
Figure 3.4. Gradation of 21B subbase layer aggregate. _____	76

Figure 3.5. Top view of TDR calibration box showing orientation of CS610 and CS615 TDR probes. _____	77
Figure 3.6. Schematic of testing to determine influence of TDR calibration box size using CS610 TDR probe where a) control, b) one probe across from control, and c) one probe beside control. _____	78
Figure 3.7. Typical waveform from a CS610 TDR probe. _____	80
Figure 3.8. Volumetric moisture content for two CS610 TDR probes, the developed calibration model, and results from Topp's Equation (Equation 3.3). ____	81
Figure 3.9. Volumetric moisture content for 22-m wire length and 27-m wire length CS615 TDR probes, developed calibration model (Equation 3.16), and manufacturer equations for three values of soil conductivity (Equations 3.4 through 3.6). _____	83
Figure 4.1. Example of CS615 TDR data from Section K that was shifted after electrical storm showing volumetric moisture content versus date. _____	90
Figure 4.2. End view of a pair of cylindrical conducting cylinders. _____	93
Figure 4.3. Side-view of two dimensional equipotential for a set of infinitely long parallel conducting cylinders having potentials of Φ and $-\Phi$ (from Ramo <i>et al.</i> , 1994). _____	94
Figure 4.4. Plot of equipotential from computer analysis for set of conducting cylinders of geometry similar to CS615 TDR probe. _____	95
Figure 4.5. Surface plot of electric field from computer analysis for set of conducting cylinders of geometry similar to CS615 TDR probe – extents of analysis just beyond surface of conducting cylinders. _____	96
Figure 4.6. Surface plot of electric field from computer analysis for set of conducting cylinders of geometry similar to CS615 TDR probe – extents of analysis 5mm beyond surface of conducting cylinders. _____	97
Figure 4.7. Maximum daily temperature in HMA layers – Section A. _____	100
Figure 4.8. Maximum daily temperature in aggregate base/subbase layers – Section A. _____	101
Figure 4.9. Temperature distribution for Section A - April 10, 2000. _____	103

Figure 4.10. Temperature distribution for Section A - October 10, 2000.	_____	103
Figure 4.11. Section A – daily maximum outside bunker temperature versus daily maximum pavement temperature (0.038m depth) with linear model.	___	105
Figure 4.12. Maximum daily pavement temperature prediction at 0.038m depth showing actual (0.038) versus predicted (0.038 predict).	_____	114
Figure 4.13. Minimum daily pavement temperature prediction at 0.388m depth showing actual (0.038) versus predicted (0.038 predict).	_____	114
Figure 4.14. Temperature distribution over three consecutive days for Section A, showing outside bunker temperature and pavement temperature at depths of 0.038 and 0.188m.	_____	114
Figure 4.15. Maximum daily pavement temperature prediction at 0.038m depth showing actual (0.038) versus predicted (0.038 solar predict).	_____	119
Figure 4.16. Minimum daily pavement temperature prediction at 0.038m depth showing actual (0.038) versus predicted (0.038 solar predict).	_____	120
Figure 4.17. Maximum daily pavement temperature prediction at 0.038m depth showing actual (0.038) versus predicted (0.038 ambient).	_____	122
Figure 4.18. Minimum daily pavement temperature prediction at 0.038m depth showing actual (0.038) versus predicted (0.038 ambient).	_____	122
Figure 4.19. Maximum daily pavement temperature prediction at 0.025m depth showing actual (0.025) versus predicted (0.025 predict) for LTPP site 9-1803 (CT).	_____	124
Figure 4.20. Minimum daily pavement temperature prediction at 0.025m depth showing actual (0.025) versus predicted (0.025 predict) for LTPP site 9-1803 (CT).	_____	124
Figure 4.21. Maximum daily pavement temperature prediction at 0.025m depth showing actual (0.025) versus predicted (0.025 predict) for LTPP site 48-1077 (TX).	_____	125
Figure 4.22. Minimum daily pavement temperature prediction at 0.025m depth showing actual (0.025) versus predicted (0.025 predict) for LTPP site 48-1077 (TX).	_____	125

Figure 4.23. Maximum daily pavement temperature prediction at 0.038m depth showing actual (0.038) versus predicted (0.038 lat). _____ 127

Figure 4.24. Minimum daily pavement temperature prediction at 0.038m depth showing actual (0.038) versus predicted (0.038 lat). _____ 128

LIST OF TABLES

Table 3.1.	Results of testing to determine influence of TDR calibration box size using CS610 TDR probe showing moisture content from control, one probe across from control, and one probe beside control. _____	79
Table 3.2.	Location of CS610 TDR probes at the Virginia Smart Road, showing number of probes by section. _____	85
Table 3.3.	Location of CS615 TDR probes at the Virginia Smart Road, showing number of probes by section. _____	85
Table 3.4.	Location of thermocouples at the Virginia Smart Road, showing number of thermocouples by section. _____	87
Table 4.1.	Average value and variance of moisture content for CS615 and CS610 TDR probes during the Phase 1 study. _____	91
Table 4.2.	Section A - coefficients for linear pavement temperature prediction model. _____	104
Table 4.3.	Section A - coefficients for linear pavement temperature prediction model including seasonal component. _____	107
Table 4.4.	Coefficients for linear pavement temperature prediction model, where A is the outside bunker temperature coefficient, B is the day of year coefficient, C is the depth coefficient, and D is the intercept coefficient. _____	110
Table 4.5.	Coefficients for linear pavement temperatre prediction model, where A is the outside bunker temperature coefficient, B is the day of year coefficient, C is the depth coefficient, and D is the intercept coefficient (A, B, C, and D are held constant). _____	110
Table 4.6.	Daily solar radiation values for three locations in the eastern United States. _____	117

CHAPTER 1

INTRODUCTION

In a time of decreasing highway funds and increasing expectations for performance and quality, it has become more important to understand the effects of environmental conditions on hot-mix asphalt (HMA) pavement performance. Perhaps the two most important environmentally related factors include the temperature profile of the pavement layers and their moisture content. Asphalt binder is a main component of HMA; it is used to hold the aggregate skeletal structure together. However, since asphalt binder is a viscoelastic material, the structural capacity of HMA can vary with temperature. Based on results from the Virginia Smart Road, pavement temperatures for a surface HMA layer can range from approximately -25°C during the winter months to nearly 60°C in midsummer. Regardless of the strength of the HMA surface course, the strength of a pavement system also depends on the strength of its subbase and subgrade. A strong surface layer will undoubtedly fail prematurely if constructed over a weak foundation as the strength of a pavement may fluctuate with changes in moisture content of its sublayers.

The moisture content of civil engineering materials has been monitored utilizing time-domain reflectometry (TDR) techniques since the early 1970's. Although originally developed to measure faults in electrical cables, researchers discovered that an open-ended waveguide could be used to measure the moisture content of soils. The moisture content can be inferred by measuring the travel time of an electromagnetic along stainless steel rods placed in a granular material. Generalized equations were developed by Topp *et al.* in 1980 to determine the moisture content of any soil based on its dielectric properties. It was soon noted, however, that different materials at the same moisture content could give dissimilar results on account of their differing electrical properties. Thus, it should be understood that a generalized equation might introduce inaccuracies in many cases.

Pavement temperature modeling, ongoing since the 1950s, has received renewed attention with the recent introduction of the Superpave (Superior Performing Asphalt Pavements) mix design. Not only does this mix design protocol include new methods of evaluating HMA in the laboratory, but it also includes a new way to specify asphalt

binder based on the temperature experienced at different areas within the United States and Canada. Under the current Superpave protocol, an asphalt binder is specified in terms of the expected minimum air temperature and maximum 7-day average air temperature. With the new thought processes involved in “fitting” an asphalt binder to the project environment, researchers began to give more attention to choosing the proper binder for environmental locations as well as depth within the pavement system. Current pavement temperature research is concentrating on predicting pavement temperatures at different depths from the surface based on location (latitude) and external environmental factors such as ambient temperature, temperature history, solar radiation, and wind speed (Solaimanian and Kennedy, 1993; Bosscher *et al.*, 1998; Hermansson, 2000; Hermansson, 2001; Marshall *et al.*, 2001; Park *et al.*, 2001). However, daily temperature variation through the inclusion of seasonal pavement temperature effects has not been discussed.

Instrumentation to measure the pavement moisture content and temperature profile at the Virginia Smart Road gives a unique opportunity to study some of the problems associated with assessing the interaction of pavements and their environment. To accurately predict the moisture content within the pavement structure; a calibration process must be performed on the material to be analyzed. This accounts for any inaccuracies that may be present when using a generalized moisture equation. In addition, the effects of different pavement structures need analysis to determine the extent to which they influence the moisture content within the pavement structure. To determine the pavement temperature profile, ambient temperature and seasonal changes must be understood such that the effects of heating and cooling trends within the pavement structure can be quantified.

1.1 BACKGROUND

VIRGINIA SMART ROAD

The Virginia Smart Road was constructed as a testing facility for various types of transportation related technology in Blacksburg, Virginia. Included among the various types of conducted research is an instrumented pavement test facility. The pavement test facility is approximately 2.5km in length, of which 1.3km is flexible pavement that is divided into 12 sections of approximately 100m each. Each flexible pavement test

section is comprised of a multi-layer pavement system and possesses a unique structural configuration. Each layer in each section is instrumented to measure quantitative pavement responses to traffic loading and environmental conditions.

The Virginia Smart Road represents a unique opportunity to conduct pavement research at a newly constructed facility and to monitor the changes in pavement response over the life of the pavement. In addition, since more than 500 instruments were installed as the pavement was constructed, the Virginia Smart Road provides a more realistic representation of the in-situ properties than existing pavements that have been “retrofitted” with instruments. Based on previous research (Al-Qadi *et al.*, 2000), time-domain reflectometers and thermocouples were chosen to monitor the moisture content and temperature of the pavement sections, respectively. Two types of TDR probes, manufactured by Campbell Scientific, Inc., were installed: a three-rod TDR probe (CS610) and a recently developed two-rod TDR probe (CS615). In total, 79 TDR probes were installed at different depths in nine of the 12 test sections: 48 CS615s and 31 CS610s. Thermocouples were fabricated in-house and a total of 115 were installed across all 12 sections.

MOISTURE CONTENT DETERMINATION

One of the most influential factors contributing to the deterioration of existing pavements is moisture within the pavement structure. Moisture in pavements may enter the pavement structure in ways such as infiltration through the pavement surface at cracks, joints, and shoulders. Interrupted aquifers, springs, and drainage in cut areas may also add to pavement moisture. Excessive moisture in pavements can cause one or more of the following forms of deterioration: reduction of the shear strength of unbound subgrade and base material, pumping of fines in rigid pavements, movement of unbound fines into flexible pavement base courses, frost heave and reduction of subgrade strength during frost melt, differential swelling in expansive soils, stripping of asphalt in flexible pavements, and durability cracking in rigid pavements (Huang, 1993). The first step to preventing these forms of moisture-induced deterioration is to detect the of moisture before damage occurs. Electromagnetic techniques are attractive for determining soil moisture content because they exploit the large contrast between the dielectric constant of free water and dry paving materials. The dielectric constant of paving materials ranges from three to eight (depending on density and conductivity)

whereas the dielectric constant of free water is given as 81 (depending on frequency and temperature).

Although the measured dielectric properties of paving materials are given for the bulk material, paving materials are actually made up of a host of constituent materials, each with their own physical and dielectric attributes. Paving materials can be considered a mixture of air, water, and mineral and/or organic particles. Water is an electrically complex material due to its dipole structure. The dielectric constant of water can vary from approximately 81, at frequencies below 1 GHz, to 1.75 at optical frequencies (Shen and Kong, 1995). In addition, water can exist in two states: bound and unbound. Bound water consists of molecules that are chemically adsorbed to other particles. Unbound water is free to move within the pavement structure and is more easily polarized than bound water. Mineral particles present in paving materials may consist of many different elements and molecular combinations. Each of these can vary in their dielectric properties due to their chemical and physical makeup. The third component found in paving materials is air. The dielectric constant of this constituent is defined as being equal to one. Changes in the relative amounts of these three constituents, through changes in density or environmental conditions, can alter the perceived moisture content of the mixture. There are several methods currently available to monitor the moisture content of paving materials; these include: gravimetric methods, nuclear methods, electrical resistance (gypsum) blocks, lysimeters, coaxial dielectric probes, and TDR's.

Time domain reflectometers obtain information about the host medium by applying a voltage pulse to an open-ended waveguide and collecting the reflected waveform. In the mid-1970s, TDR techniques were introduced to soil moisture measurements as agricultural researchers adopted this technique to measure the moisture content of soils during irrigation (Davis and Chudobiak, 1975). Civil engineers soon recognized the potential benefits and began their own investigations. However, it was discovered that accurate moisture content measurements of different materials in the field could only be performed after initial laboratory calibration. An empirical relationship (Topp's equation) was developed in 1980 to be used for most granular materials as a "universal" model to determine the moisture content based on the material's dielectric properties (Topp *et al.*, 1980). Many researchers have evaluated the validity of this model finding it to be a reasonable approximation. However, their results include the caveat of calling for a specific calibration process for each material type for increased accuracy (Topp *et al.*,

1982; Topp *et al.*, 1984; Ledieu *et al.*, 1986; Brisco *et al.*, 1992; Whalley, 1993; Rada *et al.*, 1994).

Time-domain reflectometry probes operate as an open-waveguide structure in which multiple stainless steel rods, connected to a coaxial cable, are inserted into the host material and a voltage pulse is applied. This voltage pulse travels along the waveguide until areas of different electrical impedance are encountered. At an interface between materials having different electrical impedances, a portion of the voltage pulse is reflected back towards the source while the remainder continues along the waveguide. Thus, two reflection points exist: one between the cable and the beginning of the waveguide and another at the open end of the waveguide. The dielectric constant of the host material can be found by determining the time it takes for a voltage pulse to travel the distance between these two points. As TDR measurements are based on the dielectric properties of the host material, the amount of moisture present and the moisture status (free or bound) greatly affect the bulk dielectric measurements.

As discussed previously, two types of TDR probes were embedded at the Virginia Smart Road: the CS610 and the CS615. The CS610 TDR probe operates as a traditional TDR instrument. It is a three-rod probe whose response is measured by determining the travel time of an electromagnetic wave between the beginning and end of the probe. The travel time allows the operator to calculate the bulk dielectric constant of the material surrounding the probe, and thus the moisture content can be inferred. The CS615 TDR probe is a two-rod probe that employs active electronics within the probe head that work as a multivibrator. The period of the signal produced by the multivibrator varies with changes in the moisture content of the material surrounding the probe. While the CS610 probe and others of similar operation have been employed elsewhere, the CS615 probe is a recent development and there is no previous experience reported in the general literature.

PAVEMENT TEMPERATURE PREDICTION

Roadways constructed using HMA are difficult to characterize in terms of their in-situ performance due to the nature of the material. Hot-mix asphalt is a viscoelastic material; that is, it exhibits the properties of both a viscous and an elastic material. At low temperatures, HMA acts as an elastic solid in which low amounts of applied strain are recoverable; thus, permanent deformation is not likely to occur until this low strain limit is surpassed. However, at high temperatures, HMA acts as a viscous fluid in which the

material will begin to flow with an applied strain. The temperature within a pavement varies due to several factors, including: latitude, wind speed, and reflectance of the pavement surface.

Barber (1957) was among the first researchers to discuss the calculation of maximum pavement temperatures based on weather reports. A thermal diffusion theory was developed in which the pavement was considered a solid semi-infinite mass in contact with a fluid (air). The total daily radiation was evaluated based on the latitude of the pavement location by considering its effect on the near-surface air temperature. However, this model incorporates a total daily radiation factor instead of a more accurate measure such as hourly radiation. Rumney and Jimenez (1969) developed nomographs from data collected in Tucson, Arizona to predict pavement temperatures at the surface and at a depth of 50mm. The collected data included pavement temperature and hourly solar radiation. Dempsey (1970) developed a simulation model based on the theory of heat transfer and energy balance at the pavement surface. Although significant input was required, the model allowed the user to study the pavement temperature variation over several days.

The next step in pavement monitoring came when the Strategic Highway Research Program (SHRP) established the Long-Term Pavement Performance (LTPP) program in 1987 as a 20-year study to better characterize the in-situ performance of pavements. More than 3,000 sites throughout North America were fitted with instruments to measure the response of pavements due to vehicular loading and environmental conditions (FHWA, 1988). To specifically deal with the challenges of studying climatic conditions, 64 LTPP sites were selected to become part of the Seasonal Monitoring Program (SMP). The 1994 SMP research was also designed to monitor the appropriateness of the Superpave mixture designs by measuring and evaluating the effects of temperature and moisture variations on pavement performance. The SMP sites were chosen to receive testing which includes the following: deflection testing to evaluate effects of temperature variation on structural performance; characterization of climatic conditions by measuring ambient temperature and precipitation; and measurements of subsurface temperature, moisture content, and frost depth (Ali and Lopez, 1996).

As a result of the SMP research, the Superpave mix design protocol can be used to specify an asphalt binder for a particular project in terms of the expected minimum air temperature and maximum seven-day average air temperature. The low air temperature

is considered to be equivalent to the low pavement temperature. The maximum seven-day average air temperature is used to calculate the pavement temperature at a depth of 20mm (Superpave, 1997). From the initial SHRP testing, and the more recent SMP data, pavement temperature models have been developed to assist with the selection of a proper asphalt binder and are given in terms of a PG designation, or performance grade. Asphalt binders can be specified for usage in different climatic regions so that they are able to resist permanent deformation at high temperatures and brittle cracking at low temperatures. For example, in Virginia, a PG 64-22 asphalt binder may be specified. This PG signifies that the pavement temperature is expected to range from a low of -22°C to a high seven-day average of 64°C . Comparing the selected PG and the actual pavement temperature has been studied by Mohseni and Symons, 1998; Lukanen *et al.*, 1998; Bosscher *et al.*, 1998.

1.2 PROBLEM STATEMENT

MOISTURE CONTENT DETERMINATION

Granular materials used as base layers within pavements may retain their initially constructed high strength if infiltrated water is allowed to drain. As the amount of water in a granular material increases from low moisture contents, additional water aids the particles in forming a tightly packed system during the compaction process. However, too much water results in some of the water replacing spaces that were filled by solid particles; thus reducing the dry unit weight and strength of the system. Forsyth *et al.* (1987) stated that over 65% of the estimated \$329 billion spent on road repairs in the United States between 1976 and 1987 could have been saved if pavements were designed with proper drainage. Therefore, it is important to understand the effects of different drainage designs and to develop new strategies for measuring and predicting moisture within the pavement systems.

PAVEMENT TEMPERATURE PREDICTION

Previous research has investigated prediction of pavement temperatures due to changes in air temperature for pavement design purposes. However, the equations predicting pavement temperature from air temperature were based on early studies performed prior to the introduction of the Superpave mix design. Since little field data was available at that time, heat flow models were used to equate air temperature with

pavement temperature, resulting in several erroneous assumptions. The heat flow model assumes that the minimum pavement temperature is equal to the minimum air temperature, the maximum air temperature and the maximum pavement temperature in each layer occur simultaneously, and that the minimum air temperature and the minimum pavement temperature in each layer occur simultaneously.

1.3 OBJECTIVES OF RESEARCH

MOISTURE CONTENT DETERMINATION

Time domain reflectometry has been employed for nearly 30 years to measure the moisture content of soils. During this time several important questions have arisen concerning the usage and theory of operation of these TDR probes. These questions have been posed due to the interdisciplinary nature of TDR probe usage. Therefore, the main objective of this research pertaining to moisture content monitoring is to quantify the effectiveness of TDR in determining the moisture contents in pavements. To achieve this objective, the following must be performed:

- Develop a laboratory based calibration equation for monitoring moisture content in the aggregate subbase layers of the Virginia Smart Road;
- Analyze computer simulations to determine area of measurement around a 2-rod TDR probe and suitability of using TDR probes in coarse aggregate material based on area of measurement;
- Compare response of two types of TDR probes to changes in the moisture content of aggregate subbase layer materials; and
- Analyze response of TDR probes at the Virginia Smart Road due to differences in pavement structural configuration including presence of a moisture barrier within the pavement system.

PAVEMENT TEMPERATURE PREDICTION

The objective of this research pertaining to pavement temperature monitoring involves the development of a relationship between pavement and air temperature. This model should accurately describe the effects of seasonal variation on pavement

temperature and be able to accurately predict temperatures within the HMA layers. To achieve this, the following needs to be accomplished:

- Study the relationship between air temperature and pavement temperature at several depths within the pavement;
- Develop a regression equation to predict temperature at several depths within the pavement based on air temperature;
- Determine the effects of aggregate gradation and binder grade on developed models; and
- Quantify the effects of seasonal variations and pavement location on pavement temperature using parameters such as date or solar radiation to develop a predictive model.

1.4 SCOPE OF RESEARCH

To achieve the objectives of this study, research was performed as part of the ongoing studies at the Virginia Smart Road. Instrumentation was installed which allows for quantitative measurement of the pavement response due to ambient environmental conditions. In addition, a laboratory calibration procedure was established for each instrument type such that the instrument response could be evaluated under in-situ pavement conditions.

Chapter 2 presents a background on pavement moisture, moisture measurement instruments, theory of temperature and radiation influences on a flexible pavement, and previously developed pavement temperature prediction models. Chapter 3 describes the environmental monitoring portion of the research conducted at the Virginia Smart Road. Details of pavement moisture and pavement temperature research are given. Chapter 4 offers the presentation of data and its subsequent analysis. Chapter 5 presents the summary and conclusions of the research described herein and Chapter 6 offers recommendations for further study.

CHAPTER 2

BACKGROUND

2.1 PAVEMENT MOISTURE

One of the most influential factors contributing to the deterioration of existing pavements is moisture within the pavement structure. Moisture in pavements may enter through various points in the pavement structure such as infiltration through the pavement surface, cracks and joints, and shoulders. Interrupted aquifers, springs, and drainage in cut areas may also add to pavement moisture. Excessive moisture in pavements can cause one or more of the following forms of deterioration: reduction of the shear strength of unbound subgrade and base material; pumping of fines in rigid pavements; movement of unbound fines into flexible pavement base courses; frost heave and reduction of strength during frost melt; differential settlement in expansive soils; stripping of asphalt in flexible pavements; and durability cracking in rigid pavements. Electromagnetic techniques are attractive for determining soil moisture content because they exploit the large contrast between the dielectric constant of free water and dry soil. Typically, the dielectric constant of soil ranges from three to eight (depending on the density and conductivity) whereas the dielectric constant of water is given as 81 (depending on frequency and temperature).

Originally developed to measure faults in communication cables and transmission lines, TDR obtains information about the host medium by applying a voltage pulse to a set of parallel metallic rods and collecting the reflected waveform. In the mid-1970's, TDR techniques were introduced to soil moisture measurements. Agricultural researchers adopted this technique to measure the moisture content of soils during irrigation. Civil engineers soon realized the potential benefits and began their own investigations. From this beginning, it was realized that there was a need to correlate laboratory work with moisture content measurements of different soils in the field. An empirical relationship (Topp's equation) was developed in 1980 to be used for most soil types as a "universal" model to determine the moisture content of soils based on the material's dielectric properties. The validity of this model has been evaluated using different soil types by many researchers.

Time-domain reflectometer probes operate as an open-waveguide structure in which multiple-parallel stainless steel rods are inserted into the host material and a voltage pulse is applied. This voltage pulse travels along the waveguide until areas of different electrical impedance are encountered. At an interface between materials having different electrical impedances, a portion of the voltage pulse is reflected back towards the source while the remainder continues along the waveguide. The waveguide structure is terminated as an open circuit. Thus, two reflection points exist: one between the cable and the beginning of the waveguide and another at the open end of the waveguide. The dielectric constant of the host material can be found by determining the time it takes for a voltage pulse to travel the distance between these two points and comparing it to the velocity of this voltage pulse in free space. As TDR measurements are based on the dielectric properties of the host material, the moisture present and the moisture status (free or bound) greatly affect the bulk dielectric measurements. For these reasons, it is seen as advantageous to attempt to relate the bulk dielectric properties to soil moisture content.

2.1.1 MOISTURE RELATED DISTRESSES IN PAVEMENTS

Road builders since the early ages have understood the importance of a properly drained pavement system. In fact, the term *highway* came from the Roman Empire-era road builders who realized that a pavement system elevated above the surrounding countryside would be more durable. Although understood for centuries, these techniques were not always implemented. John McAdam (1820) addressed the London Board of Agriculture in 1820 with the following:

“The roads can never be rendered thus perfectly secure until the following principles be fully understood, admitted, and acted upon: namely that it is the native soil which really supports the weight of traffic; that whilst it is preserved in a dry state it will carry any weight without sinking... that if water pass through a road and fill the native soil, the road whatever may be its thickness loses support and goes to pieces.”

A report containing data from the AASHO Road Test of the early-1960's showed that rates of serviceability loss were 40 to 50 times greater during the spring thaw than during summer months when less or no free water is available in the pavement system (Liddle,

1962). With all of this evidence of the problems associated with moisture in the pavement system, why is it still an issue? Even in the present day, roads tend to be designed with the pavement strength in mind and the accompanying feeling that sufficient strength will give enough support to counter the effects of poor pavement drainage. It has been estimated (Forsyth *et al.*, 1987) that over 65% of the \$329 billion estimated on road repairs in the United States between 1976 and 1987 could be saved if pavements were designed with proper drainage. Therefore, it is important to understand the effects of different drainage designs and their success in removing infiltrated water from the pavement system.

A common occurrence on poorly draining flexible pavements is continued ponding of water on the surface of the pavement. This will eventually lead to stripping of the asphalt from the aggregate. Stripping of the binder will ultimately lead to raveling of the surface of the flexible pavement. Excessive moisture in Portland cement concrete (PCC) pavement base layers can lead to slab faulting. As a heavy vehicle moves from one slab to another, water (along with fines) is pumped from below the slabs. This can ultimately lead to a void below the slab causing a loss of support and finally faulting of the slab. By allowing a pavement to drain the water that infiltrates, the pavement system will retain its strength as the strength of a compacted granular material, such as that used for a pavement base, will vary with moisture content. As the amount of water in a granular material increases from the optimum moisture content, the strength is reduced.

2.1.2 DIELECTRIC MATERIALS

Before discussing specifics of dielectric materials, an introduction to material interaction with electromagnetic fields is presented. Two independent electromagnetic properties describe the interaction of a material with electric and magnetic fields: the complex permittivity, ϵ^* , and the complex (magnetic) permeability, μ^* . These two characterizing properties of materials are used to define materials by the electromagnetic constitutive relations, given as follows:

$$\bar{D} = \epsilon^* \times \bar{E} \quad (2.1)$$

$$\bar{B} = \mu^* \times \bar{H} \quad (2.2)$$

where

\bar{D} = electric flux density (C/m²);

\bar{E} = electric field strength (V/m);

\bar{B} = magnetic flux density (W/m²); and

\bar{H} = magnetic field strength (A/m).

However, most dielectric materials, including most soils and pavement materials, can be described by ϵ^* alone as they are nonmagnetic (therefore, $\mu^* \approx \mu_0 = 4\pi \times 10^{-7}$ H/m). The complex permittivity of a material, ϵ^* , is defined as follows:

$$\epsilon^* = \epsilon' - j\epsilon'' \quad (2.3)$$

where

ϵ' = real part of the complex permittivity;

ϵ'' = imaginary part of the complex permittivity; and

$$j = \sqrt{-1}.$$

By dividing Equation 2.3 by the permittivity of free space, ϵ_0 (8.854×10^{-12} F/m), a relation of dimensionless quantity results and is given as:

$$\frac{\epsilon^*}{\epsilon_0} = \frac{\epsilon'}{\epsilon_0} - j \frac{\epsilon''}{\epsilon_0}$$
$$\epsilon_r^* = \epsilon_r' - j\epsilon_r'' \quad (2.4)$$

where

ϵ_r^* = relative complex permittivity or dielectric constant;

ϵ_r' = real part of the relative complex permittivity; and

ϵ_r'' = imaginary part of the relative complex permittivity.

The real part of the relative complex permittivity indicates a material's ability to store an electric charge, while the imaginary part depicts the loss due to conduction and molecular friction.

Materials that are electrically characterized as *dielectrics* are insulating (non-conducting) materials. In an insulating material, there exists a physical separation between positively and negatively charged entities on an atomic level. These charges are bound by atomic forces and are not free to travel. Ideal dielectrics do not contain any free charges (as do conductors) and are neutrally charged on a molecular level. However, when an external field (e.g., an electric field) is applied, the bound positive and negative entities are able to slightly shift their positions, opposing the binding atomic forces. This shift allows dielectric materials to store energy, like a stretched spring, as potential energy. Common to all dielectric materials is this ability to store energy when an external field is applied; this phenomenon is called *polarization*.

Consider a parallel-plate capacitor with an external electric field. When a vacuum exists between the two plates, equal but opposite charges form on the capacitor plates as shown in Figure 2.1a. A dipole molecule, shown in Figure 2.1b, consists of two point-charges (Q_1 and Q_2) separated by a distance, d . When this dipole is placed between a set of capacitor plates in the presence of an electric field, a force (F) is exerted in the dipole by the electric field and is found to be:

$$F = E \times Q \quad (2.5)$$

Coulomb's Law allows us to resolve the force (F) in a homogeneous medium in terms of the individual dipole charges and their separation distance and is given as:

$$\bar{F} = \frac{Q_1 Q_2}{4\pi d^2 \epsilon_0 \epsilon_r} \bar{r}_{1,2} \quad (2.6)$$

where $\bar{r}_{1,2}$ represents the unit vector pointing from Q_1 to Q_2 .

When a material sample containing dipoles is placed between the capacitor plates, as shown in Figure 2.2a, the dipoles show their natural random orientation. However, when an external electric field is applied, shown in Figure 2.2b, the dipoles orient themselves with the electric field, resisting their natural state of randomization. That is, the dipoles become polarized. The dielectric constant of a material is a measure of the ability of a material to become polarized; the higher the dielectric constant, the more easily a material can become polarized. For example, water and ice possess the same atomic makeup. However, in ice, the molecules are bound in a solid structure, making

polarization of the molecules more difficult. As a result, the dielectric constant for water is approximately twenty times higher than the dielectric constant of ice.

Polar molecules, such as water, possess a permanent dipole moment associated with their asymmetrical charge distribution. Viewing the molecule as a set of point charges, the positive end will attract negative charges, and the negative end will attract positive charges. These charges are randomly oriented when no external energy source is applied. Thus, taking a larger view, the net charge of water is zero. However, when an external energy source (such as an electric field) is applied, the molecules will orient themselves in the direction of the applied field and energy is stored. The total charge in

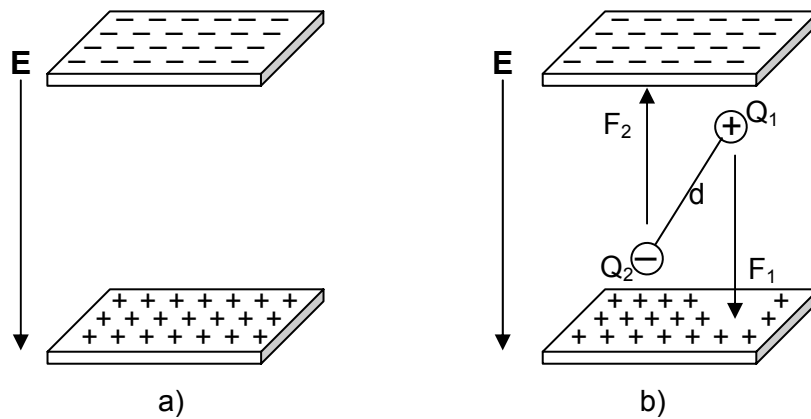


Figure 2.1. External electric field applied to a) vacuum and b) single dipole.

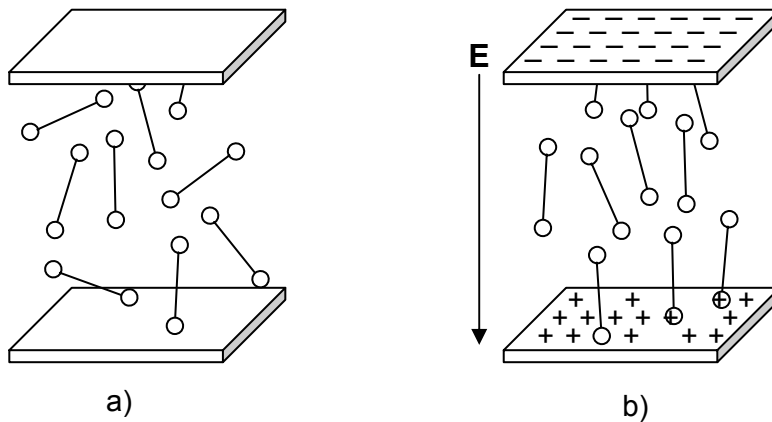


Figure 2.2. Set of dipoles a) before and b) during application of external electric field.

this case is equal to the sum of the vectors of the individual charges. After the field is removed, the molecules will take a finite amount of time to return to their originally randomized state; this is termed the *dielectric relaxation time*.

Development of Polarization Concepts

Electricity has been known as a natural phenomenon since ancient times. However, experimental studies were not performed until the 18th century. In 1745, Caneus and Musschenbroek constructed a condenser consisting of two conducting plates separated by an insulating material. When it was found that this condenser could store large quantities of charge, it became popular for experimental studies under the name of Leyden jar.

Little attention was paid to the insulating material until 1837 when Faraday published the first numerical analysis of the insulating material that he called a *dielectric*. His experiments showed that the capacity of a condenser was dependent on the properties of the insulating material between the two conducting surfaces. Faraday also introduced the term *specific inductive capacity*, defined as the ratio between the capacities of a condenser filled with a dielectric and of the same condenser when empty. This is the same quantity now called the permittivity or dielectric constant.

Summarizing the investigations of electric and magnetic phenomena, Maxwell published his unified theory of electromagnetic phenomena. In this theory, the permittivity is given as the ratio of the electric field intensity and the dielectric displacement. Maxwell also thought that light was a form of electromagnetic radiation. He stated that for most dielectrics, the dielectric constant should be equal to the square of the refractive index, n . The relation, $\epsilon = n^2$, is known as the Maxwell relation (Böttcher, 1973).

In the later part of the nineteenth century and the early part of the 20th century, the dielectric constant was determined for a number of materials, especially to evaluate the validity of the Maxwell relation. The experimental results agreed well with the theoretically obtained values for most solids and even some liquids and gases. However, for many substances, called “associating,” the dielectric constant was measured to be higher than the square of the refractive index over frequencies in the visible region. These same experiments revealed that some substances absorbed energy at frequencies in the visible region and that an anomalous dispersion (or a

decrease in the refractive index with an increase in frequency) always accompanied this energy absorption. Thus, it was possible to extend the validity of Maxwell's relation by determining the dielectric constant using a complex frequency-dependent relation (where the imaginary part measures the absorption of energy) and the refractive index.

It was theorized that the discrepancy between actual measurements and theoretically obtained results was attributable to a permanent electric dipole moment associated with the molecules. However, this theory remained vague and largely qualitative until Debye published his quantitative theory in 1929. Debye (1929) developed an expression for the dielectric constant that depended not only on the molecular polarizability but also the permanent dipole moment of the molecule. Debye later explained the anomalous dispersion of the dielectric constant by pointing out that the orientation process of the permanent dipole moments associated with changes in an applied electric field required a time interval due to the rotational process involved in orienting the molecule. From Debye's assumptions, it was stated that after the removal of an externally applied field, the average dipole orientation decays exponentially with time; this was defined as the relaxation time. Debye concluded that the time lag between the average orientation of the molecules and a change in the electric field became noticeable when the frequency of the field approached the same order as the inverse of the relaxation time. The molecular relaxation time led to the anomalous dispersion of the dielectric constant and subsequent absorption of electromagnetic energy; this process is defined as dielectric relaxation.

Several modifications and additions have been proposed to Debye's theory for the dielectric relaxation time. These have led to the general replacement of a single relaxation time by a set of relaxation times dependent on the description of the macroscopic relaxation process. As an example, the Cole-Cole plot represents a graphical interpretation to distinguish cases of continuous distribution of relaxation time from those of single relaxation times (Cole and Cole, 1941).

Material Polarization

The dielectric constant of many liquids and solids usually depends on the frequency of the measurement. The dependence generally decreases from a static value, ϵ_s , at low frequencies to a smaller limiting value, ϵ_∞ , at high frequencies. Between these frequencies lies a transition region in which an absorption conductivity occurs yielding a

complex dielectric constant, ϵ^* . In an alternating electric field, the orientation of polar molecules is opposed by the effect of the thermal agitation and molecular interaction (Cole and Cole, 1941). Debye (1929) models the second effect as viscous damping, where the molecules are regarded as spheres in a continuous medium. Theoretical analysis of this behavior is presented in the following:

$$\epsilon' = \epsilon_{\infty} + \frac{\epsilon_s - \epsilon_{\infty}}{1 + (\omega\tau_0)^2} \quad (2.7)$$

$$\epsilon'' = \frac{(\epsilon_s - \epsilon_{\infty})\omega\tau_0}{1 + (\omega\tau_0)^2} \quad (2.8)$$

where

ω = angular frequency, $2\pi f$;

ϵ_{∞} = dielectric constant at infinite frequency;

ϵ_s = static dielectric constant;

τ_0 = relaxation time (sec); and

f = frequency.

For a static field, τ_0 ranges from 10^{-6} to 10^{-13} sec. The relaxation time depends on temperature, chemical composition, and structure of the dielectric. In heterogeneous materials, consisting of two or more components having a discrepancy in the conductivity potentials, a dispersion known as the Maxwell-Wagner effect arises. This dispersion can be modeled using Debye's equations after modifying ϵ_s and ϵ_{∞} values.

There are four ways in which substances can be electrically polarized (i.e., polarization due to an electric field): *ionic*, *electronic*, *dipole*, or *heterogeneous*. Ionic (or molecular) polarization occurs in materials that possess positive and negative ions that tend to displace themselves when an external field is applied. Ionic polarization also contributes to the formation of induced dipoles. Ionic polarization is less detectable at microwave frequencies. This is due to a phenomenon known as *anomalous dispersion* and due to ionic bonds that are very strong. Thus, the bonds strongly resist rotational forces induced by an electric field. Sodium chloride (NaCl) is an example of a material that undergoes ionic polarization.

Electronic polarization occurs in materials in which the electron cloud center surrounding the nucleus of the atom is displaced relative to the center of the nucleus when an external field is applied. The magnitude of this type of polarization is dependent upon the strength of the applied field and the attraction forces imposed on the electrons by the nucleus. Additionally, electronic polarization contributes to the formation of induced dipoles.

Dipole (or orientation) polarization occurs in substances composed of polar molecules (e.g., water) that possess permanent dipoles where the molecules are randomly oriented when no external field is applied. However, when an external field is applied, the dipoles align themselves with the applied field. This type of polarization is strongly temperature dependent, because the randomization of the polar molecules is supported by thermal agitation. Rotation of the polar molecules is also affected by the substance's phase. Lattice forces restrict this type of polarization in solid substances. Dipole polarization is easy to detect at both radio and microwave frequencies. This is due to the fact that the forces that hold dipoles together are relatively weak.

Heterogeneous polarization occurs in dielectric materials in which conducting volumes are distributed. A relaxation effect takes place at a critical frequency. Charge carriers can redistribute themselves within the conductive particles, if the applied frequency is less than the critical frequency. This yields an artificially high dielectric constant and low electrical loss associated with a low value of conductivity. However, if the applied frequency of the field is greater than the critical frequency, the charge carriers cannot redistribute fully. This leads to a reduction in dielectric constant and an increase in conductivity.

2.1.3 SOIL MOISTURE MEASUREMENT INSTRUMENTS

Measuring the moisture content of soils has typically relied on gravimetric sampling, resistive (gypsum) blocks, nuclear methods, or dielectric probes. These methods have various drawbacks including, length of time to perform test, deterioration of instrument, and related safety issues. Gravimetric methods may not be preferred since they do not yield instantaneous results of the moisture content. First, a sample must be obtained and then oven dried for a specified period of time (AASHTO specifies 105°C for 24 hrs) so that the associated weight loss can be determined. In addition, this only provides a

“spot” measurement. This technique is only useful where the soil is accessible (either at the surface or through excavation). Nuclear methods require highly trained operators and extensive safety precautions. Again, this method is limited to accessible locations. Additionally, objects considered to be in the background can influence the results. Electrical resistance blocks are relatively inexpensive to install in mass quantities. However, these resistance blocks, made from gypsum, deteriorate with time. Results from non-deteriorating blocks, such as fiberglass, can vary with the soil salinity. Dielectric probes have proved to be useful, however, only for surface measurements.

Time-domain reflectometer probes are relatively inexpensive and allow the user to monitor soil moisture at the location where the probes are installed. Drawbacks to TDR probes include that their results need to be calibrated for a specific soil type to ensure accurate measurements and questions regarding the volume of soil measured still remain. Although these drawbacks may be considered significant, they are common to most of the aforementioned methods. Regardless of which of the above methods are employed, once the measured properties of the soil are determined, they must be related to the moisture content. This can be done by using one of the various formulas derived from dielectric mixture theory or by calibration in which the moisture content is independently determined (e.g., gravimetric determination). Two of the most promising techniques, dielectric probes and TDR, are discussed in further detail.

Dielectric Probes

A dielectric probe consists of an open-ended coaxial cable equipped with multiple tips that are designed to measure the range of dielectric constants found in different soils. This instrument can operate at different frequencies and directly measures the real and imaginary parts of the soil’s dielectric constant based on the reflection coefficient at the end of a coaxial line. The portable dielectric probe has also been used to provide useful information for developing microwave emission and backscattering models to be used in conjunction with radar measurements of soil dielectric properties. Measurements, initialized in air, are calibrated using liquids having known dielectric properties. References are used since the real and imaginary parts of the dielectric constant are determined using a capacitor model involving parameters (a scale factor for the phase and the characteristic impedance of the system) specific to the instrument and probe tip. In this case, liquids are preferred calibration materials since it can be assumed that complete contact with the probe is achieved. The real part of the dielectric constant is

determined by measuring the reflection amplitude while the imaginary part is found from the phase. Following this calibration step using each probe tip, the instrument can be used to measure the dielectric constant of soils. One drawback to the portable dielectric probe is the usage of different probe tips. Each tip is intended for use over a specific dielectric constant range (i.e., the dielectric constant range must be known or assumed prior to measurement to ensure the correct tip is used). In addition, the amount of contact pressure placed on the probe tip when measuring granular materials can affect the results by changing the bulk density of the measurement area. Despite these drawbacks, one advantage of the portable dielectric probe is that it does provide data on both the real and imaginary parts of the test soils dielectric constant.

Development of Methodology and Applications

Jackson (1990) conducted laboratory testing of a portable dielectric probe that operated at a frequency of 1.25 GHz. The probe was used to perform measurements on soil mixed with known quantities of water. A mathematical model was used to calculate the moisture content from these results. The moisture content obtained from the probe was compared with gravimetric moisture content results obtained by oven drying samples. The results obtained from oven drying samples showed good agreement between the values of the real part of the dielectric constant obtained from the portable dielectric probe. However, the portable dielectric probe tended to over estimate the imaginary part of the dielectric constant. Jackson (1990) states that the error is not appreciable for this application, since only the real part of the complex dielectric constant is used in soil moisture measurements. Jackson (1990) also showed that the real part of the dielectric constant obtained with the dielectric probe yielded comparable results to the soil moisture content up to a volumetric moisture content of 30% regardless of soil texture.

Experimental work undertaken by Brisco *et al.* (1992) consisted of evaluating the results from a portable dielectric probe operating at several frequencies (0.45, 1.25, 5.3, and 9.3 GHz) using three different soil types. The results from the portable dielectric probe were compared to the volumetric moisture content (obtained from oven drying samples). The results, using the lowest frequency, were found to be in better agreement with the volumetric moisture content; whereas the other frequencies tended to underestimate the moisture content. According to the authors this is most likely due to the decreasing dielectric constant of water at these high frequencies (the authors stated

that water has a dielectric constant 80 at 0.45 GHz and 63 at 9.3 GHz). Additionally, it was concluded for the portable dielectric probe that textural differences were negligible across all frequencies.

Other researchers (Wang and Schmugge, 1980; Dobson *et al.*, 1984; Dobson *et al.*, 1985) have shown that soil textural effects exist; however, they are more prevalent at lower frequencies. Therefore, their models relating soil properties to the dielectric constant include textural parameters such as percent clay, percent sand, specific surface, and field capacity. The differences in dielectric properties attributable to texture have been suggested to be the result of the differing amounts of free and bound water between soils of different texture. Since the dielectric constant is known to be higher for free water than for bound water, it is suggested (Brisco *et al.*, 1992) that this is only of concern at low volumetric moisture contents (i.e., < 10-15%).

Time Domain Reflectometry

A TDR probe, constructed from parallel rods that form an open parallel transmission line, can be placed within a soil sample to measure its dielectric properties. A short transition duration step-pulse, generated by a pulse generator, travels along the transmission line (made up of a coaxial cable and a probe). At locations where an impedance mismatch occurs, some of the energy from the step-pulse is reflected back to the source and can be viewed on an oscilloscope. When the pulse reaches the discontinuity at the coaxial line/probe interface, part of its energy is reflected back to the source from this discontinuity. This can be seen as the peak of the waveform on the oscilloscope in Figure 2.3a. This corresponds to the pulse reaching location 1 in Figure 2.3b. The remainder of the probe energy continues through the parallel rod structure

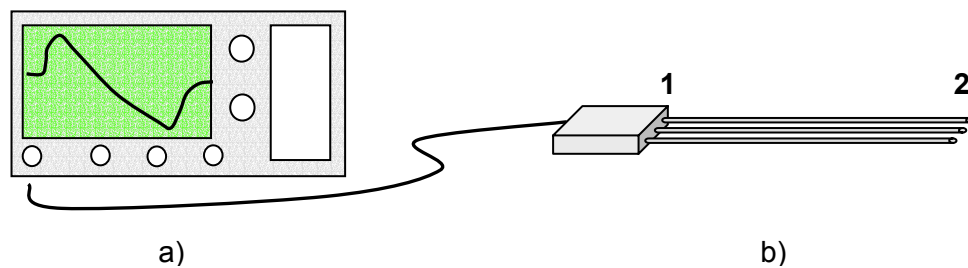


Figure 2.3. Schematic of time-domain reflectometry including a) oscilloscope (showing typical waveform) and b) TDR probe.

and again a reflection occurs at the discontinuity at the end of the waveguide (location 2) and appears as a valley in the waveform in Figure 2.3a. The parallel waveguides act as a transmission line while the soil serves as the dielectric media for the propagation of the electromagnetic wave.

Development of Methodology and Applications

Time-domain reflectometry was applied to measure properties of a dielectric in a precision coaxial line by Fellner-Feldegg (1969). The author states that TDR is useful because the nature of operation in the time-domain allows for characterization over a wide frequency range, eliminating the need for multiple measurements to achieve a wide-band characterization. Davis and Chudobiak (1975) first applied TDR to soil measurements by using a balanced parallel transmission line approximately 0.8m in length. It was found that the material between the two rods had the main influence on the impedance of the line; material found at a distance of greater than twice the rod separation distance had a negligible effect. Several of these TDR probes were placed vertically in soil and the moisture profile with depth was monitored for a 12-month period (Davis and Chudobiak, 1973). The transmission line was comprised of seven sections of alternating rod diameter (9.5 and 12.7mm) so that the moisture content between each section could be determined. In addition, it was reported that over the temperature range of 1 to 40°C, the permittivity of the soil varied by approximately 10%.

Topp *et al.* (1980) took a major step forward by developing an empirical relationship between the volumetric moisture content and the dielectric constant of mineral soils that could be used regardless of soil type, density, texture, or temperature. The dielectric constant of the soil sample was measured using a parallel transmission line (TDR probe). The dielectric constant for each measurement was obtained by finding the travel time along the TDR probe. This dielectric constant of the soil was assumed to be equal to the real part of the complex dielectric constant. This is termed the *apparent dielectric constant* (ϵ_a) and can be found as the following:

$$\epsilon_a = \left(\frac{ct}{l} \right)^2 \quad (2.9)$$

where

c = velocity of an electromagnetic wave in free space (3×10^8 m/s);

t = one-way travel time along the TDR probe (s); and

l = length of the TDR probe electrodes (m).

The term *apparent dielectric constant* arose since it was assumed that the imaginary part of the complex dielectric constant was negligible and therefore only the real part was used. This assumption was made since the material under study (soil) is generally given as a low-loss material. It was noted that some imaginary or loss component of the complex dielectric constant existed, however, its effects were deemed to be negligible when determining the propagation velocity of an electromagnetic wave through the soil. The developed empirical expression relating the apparent dielectric constant to the volumetric moisture content (θ), often referred to as Topp's Equation, is given as follows:

$$\theta = -0.053 + (0.0292 \times \epsilon_a) - (5.5 \times 10^{-4} \times \epsilon_a^2) + (4.3 \times 10^{-6} \times \epsilon_a^3) \quad (2.10)$$

Topp *et al.* (1980) concluded that the dielectric constant of soils was strongly dependent upon the moisture content over the frequency range of 20MHz to 1GHz. It was also reported that the dielectric constant varied weakly upon the soil density (1.14 to 1.44 g/cm³), texture (ranging from sandy loam to clay), salt content, and temperature (from 10 to 36°C). For a volumetric moisture content ranging from 0 to 0.55, the dielectric constant varied from 3 to 40, respectively.

In addition to the universal calibration equation developed by Topp *et al.* (1980), it was shown that little difference exists in the relationship between apparent dielectric constant and moisture content for soils of different texture. It is also stated that temperature over a range of 0-30°C had little effect (within experimental precision, $\pm 5\%$) on measurements of the dielectric constant of a particular soil. Results of testing with variable amounts of dissolved salts also showed that their presence had little effect on the speed of the pulse, however, they did affect the attenuation. This should be expected since the effects of salinity are more evident in the imaginary part of the dielectric constant and TDR, by nature, measures only the real part.

Experimentation published by Topp *et al.* (1982) indicated that the parallel transmission line TDR probe could be used to determine a volumetric moisture content profile of soils at various depths. A 1.05m column of silt loam was compacted in the laboratory and TDR probes consisting of 900mm long rods were installed. Rods were inserted that were both solid and segmented. The segmented rods were divided into

100mm-long sections where each section consisted of a different diameter rod. The different sections were in contact to provide an electrically continuous path. Since each section of the transmission line possessed a different diameter, the impedance varied according to the following:

$$Z = \frac{120}{\sqrt{\epsilon}} \ln\left(\frac{2s}{d}\right) \quad (2.11)$$

where

Z = electrical impedance of the line (ohm);

s = center-to-center spacing of the rods (m); and

d = diameter of the rod (m).

Upon analysis of the collected data, each section was easily distinguishable since an impedance mismatch was created at each section due to the diameter changes. The sectional rods were fabricated using either solid brass rods of different diameter or polystyrene rods painted with a metal paint. Each polystyrene rod was then joined with metallic tape so that they would form an electrically continuous path. In addition, the rods were placed using three methods: soil was added to pre-placed rods, rods were pushed into existing soil, and rods were placed into holes augured into existing soil.

Water was added to the soil columns and allowed to pass each probe section. Also, water was added so that a saturation front was established and its movement along the TDR sections was also monitored. For each set of tests, moisture content values (obtained using the TDR probes) were compared to values obtained from gravimetric samples. These samples (used for both gravimetric and density analysis) were collected using an augur in three different locations: between the TDR probe rods, areas believed to be unaffected by the installation process, and in areas near the TDR probe rods. Results showed that no significant difference (at the 5% level) existed between the densities obtained from the different locations. However, the samples obtained from near the rods that were placed before soil was added consistently showed a lower density than samples obtained where the rods were placed after the soil. Samples obtained from between the rods showed a higher density regardless of insertion method (pushed or augured). The water content obtained by gravimetric analysis showed an opposite trend; higher moisture content in areas close to the rods for those columns where the soil was added after the rods were placed and lower for rods inserted after the

soil was placed. These differences in moisture content were significant at a 5% level. There was no significant difference noted for differences between transmission lines that were solid and segmented.

In 1984, Topp *et al.* again published results of experiments to correlate volumetric moisture contents of soil samples obtained using TDR (Equation 2.10) to gravimetric analysis. Also investigated were the effects of different electrode lengths on a parallel transmission line TDR probe. Two probes were developed (rods of 150 and 300mm length) and were used in conjunction with plastic spacers such that the length of the transmission line in contact with the soil could be varied. Using this method, transmission line lengths of 50, 100, 150, 200, and 300mm were studied in the field to monitor the moisture profile. The probe was fabricated from stainless steel rods held within a Derlin head that served as both a handle and hammering block for insertion.

Measurements were taken at multiple locations containing different soils over approximately four days where the instrument was inserted into an exposed soil face. After each test, the probe was removed and a soil sample for gravimetric analysis was obtained from the area between where the two electrodes had previously resided. Good agreement was shown between volumetric moisture content using the TDR probes having electrodes of different lengths and those values obtained from gravimetric sampling. The only significant difference occurred with electrode lengths of 50mm where these values were indicated to be lower than those obtained by gravimetric sampling. The authors attributed this to the process by which the travel time was obtained. A Polaroid photograph was taken for each measurement and the travel time was manually recorded. The authors noted that this was not an ideal method.

Ledieu *et al.* (1986) developed a parallel-rod TDR probe where the rods were 5mm in diameter and separated by 25mm. This paper states that for this combination, 94% of the electromagnetic energy is contained within a cylinder whose diameter is equal to twice the separation distance. It is also stated that the bulk density does not need to be known in advance of testing. This is based on a determination that a difference of 0.1g/cm^3 causes only a 0.34% change in the volumetric moisture content.

One unique facet of measuring dielectric properties of soils using TDR in the field is the probe orientation. The TDR probe can be used in a horizontal manner to conduct measurements over a larger area, therefore, theoretically providing a more uniform measurement. Brisco *et al.* (1992) stated that TDR is also useful where investigations

require analysis along a vertical profile. By nature of its design, the TDR probe can measure up to a depth from the surface equal to its length. It can also be used for measuring variations in soil properties occurring along its length. Brisco states that the sphere of influence of the TDR probe is usually given as a flattened cylinder whose length is approximately equal to the length of the parallel rods. However, the diameter of this cylinder appears to be open to conjecture but certainly depends on the dielectric properties of the material being measured and the diameter and the spacing of the rods.

Whalley (1993) discusses the differences between two-rod and multi-rod parallel transmission line TDR probes. The coaxial cable, as shown in Figure 2.4a, leading from the cable tester to the instrument is an unbalanced system where the potential of the center conductor varies from +1 to -1 and the outer conductor (shielding) is grounded. In order to use a 2-rod parallel transmission line, an impedance matching transformer is needed to balance the system so that the potential of the rods (in a 2-rod TDR probe) is equal and opposite. Thus, multi-rod parallel transmission line probes have been developed to overcome the need for the transformer. In this situation, multiple rods are situated in a coaxial fashion around an inner rod. The more electrodes, the closer the probe simulates a coaxial line (Knight *at al.*, 1994) and thus the tighter the area of measurement is bound to the area between the inner and outer electrodes. The area of measurement is better defined for a three-electrode TDR probe. However, Knight states that the energy density is greater at the rod surface making the probe sensitive to contact variations between the electrodes and the soil. The inner rod is again connected

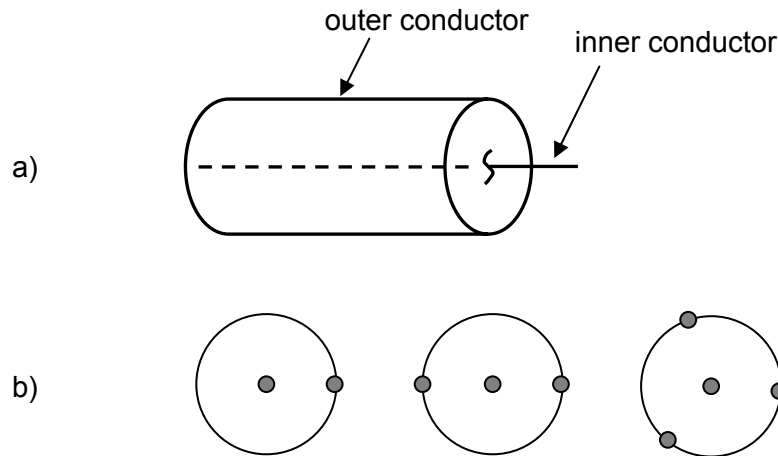


Figure 2.4. a) Coaxial cable and b) end view of connections for three TDR probe configurations.

to the center conductor and the outer rods to the outer conductor. Figure 2.4b shows an end view for a 2, 3, and 4-rod parallel rod TDR probe. Usage of the transformer (2-rod TDR probe) introduces a step in the initial part of the TDR response that can make the initial reflection more difficult to determine during data analysis as seen in Figure 2.5.

In a detailed field study of the operation of TDR probes, the Long-Term Pavement Performance (LTPP) project, within the Strategic Highway Research Program (SHRP) implemented by the Federal Highway Administration (FHWA), began a seasonal monitoring program in 1994. Sixty-four of the nearly 3000 LTPP test sites were chosen to be fitted with instrumentation to monitor environmental conditions and their effects on pavement conditions. The 64 sites were chosen to include a variety of pavement types, pavement thickness, subgrade types, and environmental conditions (Rada *et al.*, 1994). For each site, a 300mm diameter hole was augured approximately 2.1m below the bound pavement layers to allow placement of instrumentation within the pavement structure. Several types of parallel-wire transmission line TDR probes were considered for this undertaking. Two pilot project sites were chosen and instrumented with four types of TDR probes: two and three straight rod TDR probes and 2 and 3 curved rod TDR probes were studied. It was anticipated that the curved rod probes would facilitate placement within the augured hole, however, their placement turned out to be more time consuming. Considering the limitations of the 2-rod probe involving the balancing

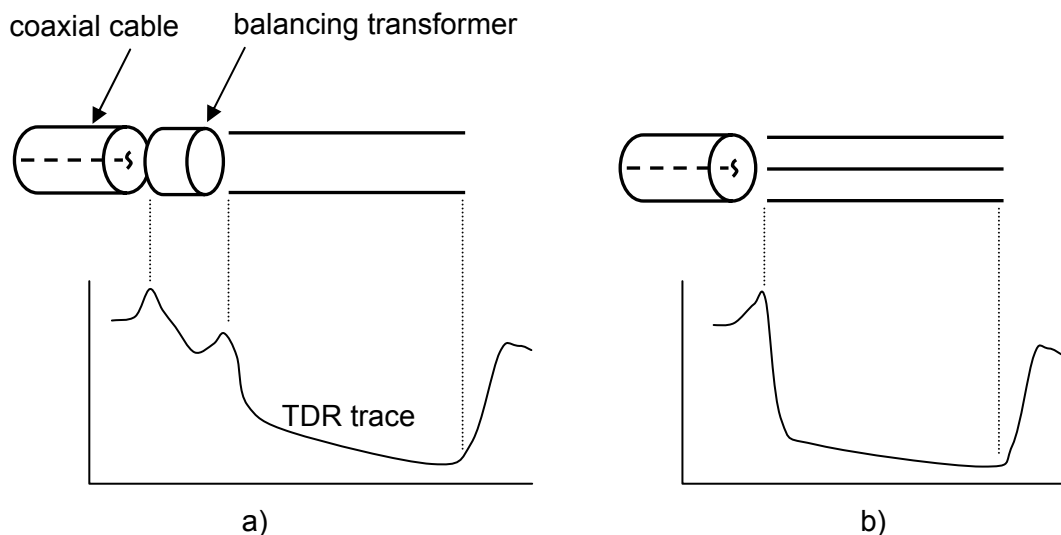


Figure 2.5. TDR probe output for a) two-rod transmission line with balancing transformer and b) three-rod transmission line without balancing transformer (after Whalley, 1993).

transformer, a three-rod probe was chosen.

Personnel affiliated with FHWA manufactured the probes whose three 6.35mm diameter tubular rods were separated by 38.1mm. The spacing between each 250mm long rod was assured to be continuous by a 3.175mm thick piece of Lexan attached to the “open” end of each rod by means of a nylon screw. The dimensions of the probe were chosen based on the diameter of the augured hole and by work undertaken by previous researchers.

Time-domain reflectometry probes were placed at each test site at the following depths: if the uppermost granular base or subbase layer depth was greater than 300mm, the first probe was placed 150mm below the bottom of the lowest stabilized layer, otherwise, the probe was placed at mid-depth of the top granular layer, the next seven probes were placed at 150mm intervals below this and the last two probes placed at 300mm intervals. The material augured from the installation hole was collected at 350mm intervals and replaced in the reverse order from which it was obtained as the instruments were replaced.

Sampling Volume

Zegelin *et al.* (1989) performed an experimental study to determine the effects of employing multi-rod TDR probes to measure the dielectric constant of materials having known values. Instruments discussed in this study included 2, 3, and 4-rod TDR probes (similar to that shown in Figure 2.4) and a coaxial fixture. Assuming that the effects caused by the end and the head of the TDR probe can be ignored, the electric field \mathbf{E} for a TEM wave propagating along a transmission line in the z direction can be written as:

$$\mathbf{E} = \text{Re}\left(\mathbf{E}_0(x,y)e^{i(kz-\omega t)}\right) \quad (2.12)$$

where (x,y,z) represent a point in space, t is time, and Re is the real part of the expression. In a two dimensional (x, y) analysis, \mathbf{E}_0 satisfies the following expression:

$$\nabla \cdot (\varepsilon \mathbf{E}_0) = 0 \quad (2.13)$$

$$\nabla \times \mathbf{E}_0 = 0 \quad (2.14)$$

The electric potential $\varphi(x,y)$ is defined as follows:

$$\mathbf{E}_0 = -\nabla \varphi \quad (2.15)$$

Substituting this expression into Equation 2.13 results in the following:

$$\nabla \cdot (\varepsilon \nabla \varphi) = 0 \quad (2.16)$$

Thus, for a medium with constant dielectric constant (ε), Equation 2.16 reduces to Laplace's equation:

$$\nabla^2 \varphi = 0 \quad (2.17)$$

Senshadri (1971) states that the solution of Laplace's Equation for a two-wire transmission line having wire spacing s and wire diameter d as the following:

$$\Phi(x, y) = \frac{\ln \left[\frac{X^2 + Y^2 + X\sqrt{1-d^2} + \frac{(1-d^2)}{4}}{X^2 + Y^2 - X\sqrt{1-d^2} + \frac{(1-d^2)}{4}} \right]}{2 \ln \left(1 + \frac{\sqrt{1-d^2}}{d} \right)} \quad (2.18)$$

The dimensionless potential $\Phi = (\varphi - \varphi_0)/V$ where φ_0 is an arbitrary constant. Zegelin *et al.* (1989) applied s as a scale such that the dimensionless diameter $D=d/s$, and the dimensionless space coordinates $X=x/s$ and $Y=y/s$. Given that D is much less than unity, Equation 2.18 reduces to the following:

$$\Phi(x, y) \approx \frac{\ln \left[\frac{(X + 1/2)^2 + Y^2}{(X - 1/2)^2 + Y^2} \right]}{2 \ln \left(\frac{2}{D} \right)} \quad (2.19)$$

Equation 2.19 is a good approximation such that $s > 3d$. In the case of multi-rod (more than 2) probes, N rods are located at positions $R_n = (X_n, Y_n)$ where $n = 1, 2, \dots, N$ located on a circle of radius s about the center conductor rod (position 0,0). Thus, the dimensionless potential, given that D is much less than one, is shown as:

$$\Phi(x, y) \approx \frac{\sum_1^N \ln \left(\frac{|R - R_n|}{|R|} \right)}{(1+N) \cdot \ln \left(\frac{2}{D} \right)} \quad (2.20)$$

For a three-rod probe, the conductor rods are located at positions $R_1=(1,0)$ and $R_2=(-1,0)$. For a four-rod probe the conductor rods are located at positions $R_1=(1,0)$, $R_2=\left(-\frac{1}{2}, \frac{\sqrt{3}}{2}\right)$, and $R_3=\left(-\frac{1}{2}, -\frac{\sqrt{3}}{2}\right)$. The simulations following Equation 2.20 yield an increasingly closer approximation to a coaxial fixture, with increasing N , where the electric potential is concentrated within the ring defined by the rods connected to the outer conductor.

Zegelin *et al.* (1989) performed measurements of the dielectric constant of distilled water with the 2-, 3-, and 4-rod TDR probes in addition to a coaxial fixture. While no significant difference occurred in the measurements using these four instruments, the location of the peaks associated with the beginning and the end of the probe were greatly inhibited by the impedance mismatch problems associated with the 2-rod TDR probe. Showing that no difference occurred between the 3 and 4-rod TDR probes when compared to the coaxial fixture, additional testing concerning the rod spacing was performed on the 3-rod TDR probe. Also, the authors suggested that the 3-rod TDR probe is more practical for in-situ usage than the 4-rod TDR probe since it would cause less disturbance of the host material upon insertion of the probe. Several 3-rod TDR probes were manufactured having a total length of 150mm and a rod diameter of 4.7mm. The rod spacing from the center conductor rod to the ring defined by the outer conductor rods varied between 15 and 100mm. Again, no significant difference was noted when measuring the dielectric constant of distilled water. Thus, Zegelin *et al.* (1989) concluded that the 3-rod TDR probe could be used successfully to measure the dielectric constant of a volume of material whose diameter is equal to 200mm. However, this study did not account for lateral variations in the dielectric constant of the material surrounding the probe.

Baker and Lascano (1989) performed work to determine the spatial sensitivity of TDR probes. A 2-rod TDR probe was placed in the middle of a series of glass tubes. The TDR probe was placed horizontally while the glass tubes ran vertically (above and below the probe) and could be individually filled with water. Tubes were filled at varying distances away from the TDR probe. However, employing this method, the top and bottom of the water-filled tube is further away from the TDR probe than the middle of the tube; thus giving rise to inaccuracies. Baker and Lascano determined the 2-dimensional spatial weighting by multiplying the value obtained from water filled tubes for two-

orthogonal distances. However, this incorrectly implies that the weighting function for one of the orthogonal directions is dependent upon the other. Bell *et al.* (1987) and Dean *et al.* (1987) performed similar measurements on a capacitor probe that could measure dielectric properties along its length similar to a TDR probe. However the spatial sensitivity was measured using a small box filled with water that could be moved about the probe.

Knight (1992) proposed the idea that spatial variations of measurements of the water content around TDR probes should be nonuniform. This is stated as being due to the nonuniform distribution of electromagnetic energy density about the TDR probe. Therefore, a weighting function w was used to describe the apparent dielectric constant ε_a at a point $x = (x_1, x_2, x_3)$ in terms of the spatially distributed dielectric constant ε_s as follows:

$$\varepsilon_a(x) = \int_V \varepsilon_s(x'_1, x'_2, x'_3) w(x_1 - x'_1, x_2 - x'_2, x_3 - x'_3) dx'_1 dx'_2 dx'_3 \quad (2.21)$$

Assuming that end effects are negligible and that variations in ε_s along x_3 (as defined in Figure 2.6a) independent of location along the probe axis, Equation 2.21 can be written as follows:

$$\varepsilon_a(x) = \int_A \varepsilon_s(x'_1, x'_2, x'_3) w(x_1 - x'_1, x_2 - x'_2) dx'_1 dx'_2 \quad (2.22)$$

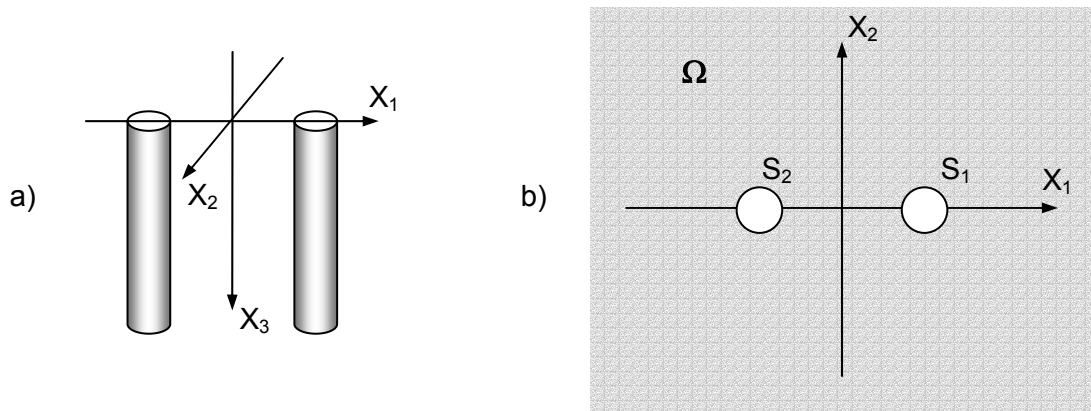


Figure 2.6. Analysis of two-rod TDR probe showing a) coordinate axis and b) surfaces S_1 and S_2 and the region Ω between them.

Electrostatic transmission line theory states that the wave speed is governed by the capacitance of the line. Assuming that we are given a two-dimensional TDR probe, as shown in Figure 6b, let one conductor with surface S_1 have a voltage V_1 and the other conductor with surface S_2 have a voltage of zero. Thus, the capacitance per unit length between surfaces S_1 and S_2 , given that the electric charges per unit length on the two conductors are $\pm Q$:

$$C = \frac{Q}{V_1} \quad (2.23)$$

The total electric energy per unit length along the probe is given as follows:

$$W = \frac{1}{2} QV_1 = \frac{1}{2} CV_1^2 \quad (2.24)$$

Given that dl is an elemental segment of curve S_1 and that $\partial/\partial n$ denotes the derivative in the outward normal direction at S_1 , it can be shown that the charge Q per unit length is given as the following:

$$Q = \epsilon_0 \int_{S_1} \epsilon_S \left(\frac{\partial \Phi}{\partial n} \right) dl \quad (2.25)$$

where $\Phi(x_1, x_2)$ is the static voltage distribution in the region Ω between the two conductors. Following Equations 2.24 and 2.25, the capacitance per unit length is shown as follows:

$$C = \left(\frac{\epsilon_0}{V_1} \right) \int_{S_1} \epsilon_S \left(\frac{\partial \Phi}{\partial n} \right) dl \quad (2.26)$$

Since the voltage Φ satisfies:

$$\nabla \cdot (\epsilon_S \mathbf{E}) = -\nabla \cdot (\epsilon_S \nabla \Phi) = 0$$

Gauss's theorem can be applied to Equation 2.26 resulting in the following:

$$2W = CV_1^2 = \epsilon_0 \iint_{\Omega} \epsilon_S |E|^2 dA \quad (2.27)$$

where the integration occurs in the space Ω between surfaces S_1 and S_2 and dA is an element of area within Ω . Allowing ϵ_s to have the uniform value ϵ_a and considering E_0 and Φ_0 to be the electric field and voltage, respectively, we find the following:

$$E_0 = -\nabla\Phi_0, \nabla^2\Phi_0 = 0$$

and

$$CV_1^2 = \epsilon_0\epsilon_a \iint_{\Omega} |E_0|^2 dA \quad (2.28)$$

By combining Equations 2.27 and 2.28, the apparent uniform dielectric constant ϵ_a that yields the same capacitance as the actual distributed dielectric constant $\epsilon_s(x)$ is found as:

$$\epsilon_a = \frac{\iint_{\Omega} \epsilon_s |E|^2 dA}{\iint_{\Omega} |E_0|^2 dA} \quad (2.29)$$

Comparing Equations 2.22 and 2.29, the two-dimensional weighting function $w(x_1, x_2)$ can be given as:

$$w(x_1, x_2) = \frac{|E(x_1, x_2)|^2}{\iint_{\Omega} |E_0|^2 dA} \quad (2.30)$$

By observing the above expression, the two-dimensional weighting function is seen to depend on E that in turn depends on ϵ_s . However, E or Φ from Equation 2.28 is not affected if ϵ_s is multiplied by an arbitrary constant. Therefore, Knight stated that the weighting function is dependent upon the distribution of ϵ_s but is independent of its value.

Knight also provided analysis for the energy distribution around the rods of a two-rod TDR probe. It is expected that the energy is concentrated close to the rods if the rod diameter is small compared to their spacing. Knight sets up the analysis by using complex variables to describe a bipolar coordinate system from the potential distribution $u(z)$ due to two opposite line charges separated by a distance of $2a$ as seen in Figure 2.7. The separation distance between the two probes, given as $2d$ and $2a$, is the

separation distance between the foci of the bipolar coordinate system. Knight presents the derivation for a normalized weighting function in terms of this bipolar coordinate system that is given as follows:

$$w(r, \varphi) = \frac{a^2}{\pi \cdot \ln \left[\frac{(d+a)}{b} \right] \cdot \left[a^4 - 2a^2 r^2 \cos 2\varphi + r^4 \right]} \quad (2.31)$$

The above expression approaches infinity at $x=\pm a$ and at $y=0$ between the rods. Therefore, when b/d is small most of the energy is concentrated close to the rods. A sensitivity expression can be developed from Equation 2.31 that is valid at all points outside the probe rods. In terms of the (R, φ) plane where $R=r/a$, the sensitivity function is given as follows:

$$G(R, \varphi) = \frac{4}{R^4 - 2R^3 \cos 2\varphi + 1} \quad (2.32)$$

If we let $Z = R \cdot \exp(i\varphi)$ that it can be shown that $|Z^2 - 1|^2$ equals the denominator of Equation 2.32. Therefore an equation of a curve can be written such that $G(R, \varphi) = 4/c^4$ where c is an arbitrary constant as follows:

$$|Z - 1| \cdot |Z + 1| = c^2 \quad (2.33)$$

Equation 2.33 describes a circle with its origin at $(1,0)$ and radius of c^2 . An approximation can be written for the proportion of energy close to the probe rods (for

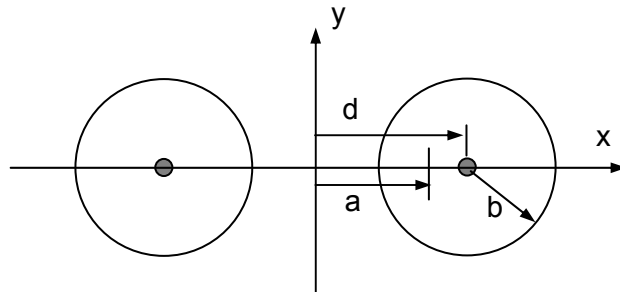


Figure 2.7. Dimensions of two-rod TDR probe showing interfocal distance ($2a$), separation distance ($2d$), and diameter ($2b$).

small b/d). Limiting the discussion to one rod whose center lies at the point $(d,0)$, the proportion of energy that is contained between this surface and a surface of larger diameter f can be estimated. Let the distance between $(d,0)$ and a point (x,y) be s such that: $s^2 = (d-x)^2 + y^2$. Assuming that d and a are approximately equal and for small b/d , the weighting function from Equation 2.31 can be written as the following:

$$w(r, \varphi) \approx \left[4\pi \cdot \ln\left(\frac{2d}{b}\right) s^2 \right]^{-1} \quad (2.34)$$

This is valid for points near $(d,0)$. The proportion of energy between two circles whose radius (given as s) is equal to b and f , respectively can be written as:

$$2\pi \int_b^f w s \, ds = \frac{1}{2} \cdot \frac{\ln(f/b)}{\ln(2d/b)} \quad (2.35)$$

Therefore, the proportion of energy P between two surfaces of diameter b and f is given as:

$$j \approx \frac{\ln(f/b)}{\ln(2d/b)} \quad (2.36)$$

the above is valid given that b/d is small and f is larger than b . For example, if b , d , and f have values of 1, 10, and 2, respectively, then j will be equal to approximately 0.23. Therefore, 23% of the energy will be contained within a surface of radius 2. If b is changed to 5, the resulting j is approximately 0.30. Knight makes the recommendation that the probes be designed such that the ratio b/d is greater than 0.1 to minimize the energy concentrated close to the TDR rods.

For a “far-field” view of the energy concentration, we can take the expression from Equation 2.31 and replace r/a with R and integrating with respect to area the following develops:

$$J(r) = \frac{1}{2\pi \cdot \ln\left(\frac{d+a}{b}\right)} \int_R^\infty \int_0^{2\pi} \left(\frac{2R \, d\varphi \, dR}{R^4 - 2R^2 \cos 2\varphi + 1} \right)$$

which can be rewritten as:

$$J(r) = \frac{\ln\left(\frac{R^2 + 1}{R^2 - 1}\right)}{2 \cdot \ln\left(\frac{d + a}{b}\right)} = \frac{\ln\left(\frac{r^2 + a^2}{r^2 - a^2}\right)}{2 \cdot \ln\left(\frac{d + a}{b}\right)} \quad (2.37)$$

Given that the above expression is dependent upon the probe geometry, it can be expressed in terms of a dimensionless radius $\rho = r/d$ and the shape ratio of $\beta = b/d$ as follows:

$$P(\rho, \beta) = 1 - \frac{\ln\left(\frac{\rho^2 + 1 - \beta^2}{\rho^2 - 1 + \beta^2}\right)}{2 \cdot \ln\left(\beta^{-1} + (\beta^{-2} - 1)^{1/2}\right)} \quad (2.38)$$

Mixture Theory

It is generally understood that the bulk dielectric properties of the soil are not simply a weighted average of the dielectric properties of the soil constituents (soil, air, and water). Rather, these properties are dependent not only on the relative amounts, but also upon the chemical and physical properties of these constituents. In this regard, several mixture theories based on physical soil properties have been presented (Dobson *et al.*, 1985; Roth *et al.*, 1992; Dirksen and Dasberg, 1993). However, these theories require the usage of various material properties (e.g., specific surface of soil, conductivity of water solution) that are most likely not known outside the laboratory setting. Therefore, empirical relationships (Topp *et al.*, 1980; Hallikainen *et al.*, 1985) have been developed to relate the dielectric properties to moisture content. The relationship developed by Topp *et al.* (1980) was developed with the intent of being used as a universal calibration for all mineral soil types. However, it has been shown (Roth *et al.*, 1992; Dirksen and Dasberg, 1993) that this empirical relationship does not correlate well for all soil types.

2.1.4 SOIL PROPERTIES

Soil is the product of mechanical, chemical, and biological weathering of a parent material. It is primarily comprised of four fractions: mineral material, organic matter, water solution, and air. Soils can be complex in nature in terms of their physical appearance, chemical composition, and mechanical properties. The mechanical

properties of soil may change with time and are affected by their loading history; in addition, the soil chemistry, temperature, and available moisture play an important role in this process. Soils can be discussed in terms of their three phases or states of matter: solid, liquid, and gaseous. The solid phase of soil is composed of both mineral and organic matter. The liquid phase of most soil types is comprised of ion-bearing water. The gas phase is comprised of either air or organic gases. As the chemistry of the solid and liquid phases have the potential to exert the greatest influence on dielectric properties, they will be discussed in further detail.

Solid Phase

The solid phase of a soil is primarily comprised of various amounts of crystalline clay and nonclay materials, noncrystalline clay material, organic matter, and precipitated salts. By far, the crystalline materials make up the largest percentage of soils and nonclay materials are more common than clay materials; however, clay materials and organic matter exert an influence that far outweighs their relative proportions. Nearly every element found in the earth's crust can be found in soils; however, oxygen, silicon, hydrogen, and aluminum are by far the most abundant. In addition to these elements, calcium, sodium, potassium, magnesium, and carbon make up over 99 percent of the earth's solid soil mass (Mitchell, 1993).

The size of the solid particles may range from boulder-sized pieces to particles too small to see without magnification. Their shape can vary from thin needles to flat plates to nearly spherical. These properties are primarily determined by the soil mineralogy. Figure 2.8 shows an example of the arbitrary size categorization for soil particles. It is important to note that the term *clay* is used to describe soil both in terms of its size and its mineralogy. In terms of particle size, clay refers to those particles that are smaller

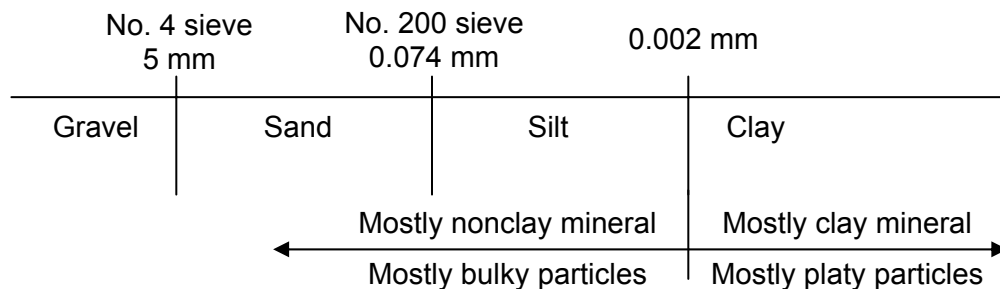


Figure 2.8. Soil particle size and shape ranges.

than 0.002mm. In terms of soil mineralogy, clay primarily refers to aluminum silicates having a small particle size, a net negative charge, and plasticity when mixed with water. Also shown in Figure 2.8 are the approximate ranges for different particle shapes.

The solid phase makes up the skeleton or matrix of the soil; however, this may not always be a solid structure. Soil particles can move with respect to each other or with changes in moisture content depending on the volume of pores. Soil pores are the spaces between the solid soil particles. These cavities are found in various sizes determined by the size and position of the soil particles. Normally, pores form a nearly continuous network throughout the soil space.

Clay minerals

Clay minerals are comprised of two basic units: *silica tetrahedron* and *alumina octahedron* as shown in Figure 2.9. Four oxygen atoms surround an atom of silicon to make a silica tetrahedron unit. *Silica sheets* are formed when these silica tetrahedron units are combined. The alumina octahedron unit is composed of an aluminum atom surrounded by six hydroxyls. Combined alumina octahedron units are called an *octahedral sheet* (also called a *gibbsite sheet*). Sometimes, the aluminum atom is replaced by magnesium. In this situation the octahedral sheet is referred to as a *brucite sheet*.

Particles of clay possess a net negative charge on their surface. This results from a break in the structural continuity at its edges and also from *isomorphous substitution*. This is defined as a substitution of one element for another with no change in crystalline form; such as when aluminum is substituted for silicon in the tetrahedral sheets. Larger

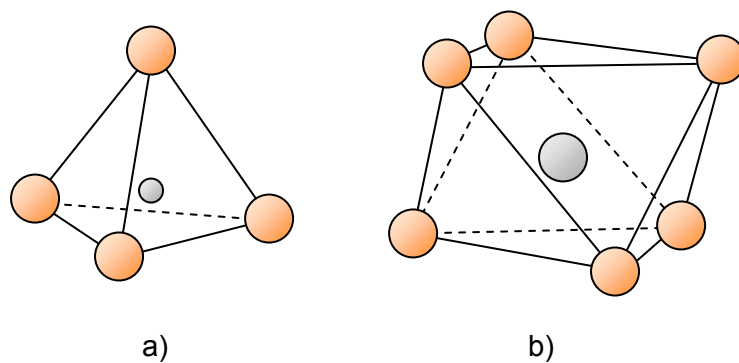


Figure 2.9. Two basic units of clay minerals: a) silica tetrahedron and b) alumina octahedron.

negative charges are found on particles with larger specific surfaces. The specific surface is defined as the surface area per unit of mass (usually m^2g^{-1}). For example, *kaolinite*, formed by repeating layers of silica and gibbsite sheets has a specific surface of approximately $15 \text{ m}^2\text{g}^{-1}$.

When considering dry clay, the negative surface charge is balanced by surrounding exchangeable cations such as Ca^{2+} , Mg^{2+} , Na^+ , and K^+ that are held by electrostatic attraction. However, when water is added to the clay, these cations and a few anions extend out from the surface of the clay sheets as a *diffuse double layer* as shown in Figure 2.10. Their positions are held by the opposing forces of electrostatic attraction and diffusion away from the surface in the direction of decreasing concentration. Water, due to its polar molecular structure, is attracted by both the negatively charged clay particles and the positively charged cations present in the double layer. Water is also attracted to the clay particles through a process known as *hydrogen bonding* where hydrogen atoms from the water molecule are shared with the oxygen atoms at the surface of the clay particle. Also, some partially hydrated cations in the pore water are also attracted to the surface of the clay particles. These cations also attract the polar water molecule. The water held to clay particles by forces of attraction are termed

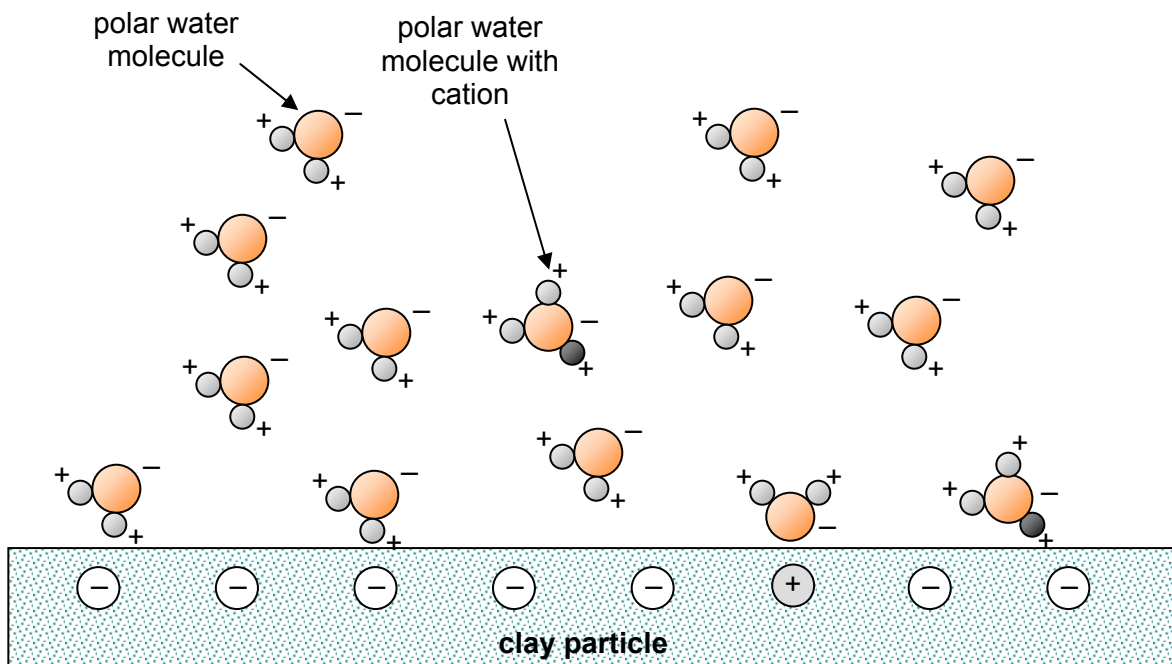


Figure 2.10. Attraction of polar water molecules to clay particle in diffuse double layer.

double-layer water. The innermost layer of the double-layer water is held strongly by the clay and is called *adsorbed water*. The relative percentage of adsorbed water and unbound (free water) can greatly vary the dielectric constant of the bulk material (as discussed in Section 2.1.2).

Liquid Phase

The liquid phase is one of the more interesting and yet understudied components of soil. Both the liquid and the solid particles interact with each other on a physical and chemical basis. The boundary between two materials of different phase is called a surface or phase boundary. Solid particles possess atoms which make up its three dimensional structure. However, unresolved molecular forces exist where this structure is broken, such as the surface. These forces may be resolved through the attraction and adsorption of molecules from the adjacent phase, cohesion with the surface of a mass of the same substance, or through adjustments of the structure beneath the surface. The liquid phase is an aqueous solution containing various ions in solution, including: Na^+ , K^+ , Ca^{2+} , Mg^{2+} , Cl^- , NO_3^- , and SO_4^{2-} , distributed throughout the soil pore system. The soil pore system may be either filled entirely with water (in saturated soils) or partially (in unsaturated soils).

The water molecule (H_2O) contains a V-shaped structure where the angle between the two Hydrogen atoms is approximately 105° . This V-shaped arrangement makes water a polar molecule, as seen in Figure 2.10. Therefore, water molecules are attracted to ions in solution, that is, the ions are hydrated. The presence of ions in water disrupts the normal alternating arrangement of water molecules due to their charge. Those ions that hydrate will attract corners of water molecules of opposite charge. The influence of ions on the structure of water is given as occurring in three zones. The first of which places the water molecule furthest away from the ions and no changes are effected. In the second zone, the structure changes slightly and becomes more random than unaffected water of the first zone. In the third zone, or that which is closest to the ion, the water molecule is strongly oriented in the field of the ion and has little kinetic energy. These three zones of influence on the water molecule will change its ability to be polarized and thus affect its dielectric properties.

Following the review of the general literature and previous research efforts, Time-domain reflectometry instruments were selected to monitor the moisture content of the

pavement layers at the Virginia Smart Road. Details of the testing plan are presented in Chapter 3.

2.2 PAVEMENT TEMPERATURE

Roadways constructed using hot-mix asphalt (HMA) are complex to characterize, in terms of their in-situ performance, due to the nature of the material. Hot-mix asphalt is a viscoelastic material; that is it exhibits the properties of both a viscous and an elastic material. At low temperatures, HMA acts as an elastic solid where low amounts of applied strain are recoverable and thus permanent deformation is not likely to occur until this low strain limit is surpassed. However, at high temperatures, HMA acts as a viscous fluid in which the material will begin to flow with an applied strain. These variations in temperature related performance show why it is important to consider the in-situ properties of HMA during its laboratory evaluation.

The temperature within a section of pavement varies due to several factors. Perhaps most importantly is the ambient temperature. The next most important factor is the solar radiation (especially during the summer months). Following these in lesser significance are wind speed and relative humidity. The ambient temperature will vary with season and location. The solar radiation is an important factor to consider when trying to describe or predict the pavement temperature profile. As the earth revolves about its axis of rotation, different areas of the planet receive differing amounts of radiation. During the summer months, this radiation is greater due to the fact that the surface of the earth at that location is closer to being perpendicular to the sun than during the winter months. In addition, there are seasonal affects that must be considered. During the summer months, the temperature of the ground will tend to increase (even at depths up to 1m) and this heat can be conducted to upper layers following the first law of thermodynamics. Thus, seasonal effects are nearly as important to consider as daily environmental fluctuations.

The prediction of pavement temperatures has advanced significantly since Barber (1957) was among the first researchers to discuss the calculation of maximum pavement temperatures based on weather reports. In this early work, a thermal diffusion theory was developed in which the pavement was considered a semi-infinite mass in contact with the air. The total daily radiation was evaluated, based on the latitude of the

pavement location, by considering its effect on the near-surface air temperature. However, Barber's work employs a total daily radiation instead of a more accurate measure, such as hourly radiation. Rumney and Jimenez (1969) developed nomographs from data collected in Tucson, Arizona to predict pavement temperatures at the surface and at a depth of 50mm. They collected data that included pavement temperature and hourly solar radiation. Dempsey (1970) developed a simulation model based on the theory of heat transfer and an energy balance at the pavement surface. Although significant input is required, the model allowed the user to study the pavement temperature variation over several days.

The Strategic Highway Research Program (SHRP) established the Long-Term Pavement Performance (LTPP) program in 1987 as a twenty-year study to better characterize the in-situ performance of pavements. More than 3,000 sites throughout North America were fitted with instruments to measure the response of pavements due to vehicular loading and environmental conditions (Mohseni, 1988). To specifically deal with the challenges of studying climatic conditions, 64 LTPP sites were selected to become part of the Seasonal Monitoring Program (SMP). The 1994 SMP research was also designed to monitor the appropriateness of the binder specified for the test sections by measuring and evaluating the effects of temperature and moisture variations on pavement performance. The SMP sites were chosen to receive additional testing which included the following: deflection testing to evaluate effects of temperature variation on structural performance; characterization of climatic conditions by measuring ambient temperature and precipitation; measurements of subsurface temperature, moisture content, and frost depth (Ali and Lopez, 1996).

As a result of the SMP research, the Superpave mix design protocol was developed. This procedure is used to specify asphalt binder for a particular project in terms of the expected minimum air temperature and maximum 7-day average air temperature. The low pavement temperature was considered to be equivalent to the low air temperature. The maximum 7-day average air temperature is used to calculate the pavement temperature at a depth of 20mm (Superpave, 1997). These high and low pavement temperatures are the guidelines for choosing a proper asphalt binder and are given in terms of a PG designation, or performance grade. Asphalt binders can be specified for usage in different climatic regions so that they are able to resist permanent deformation at high temperatures and brittle cracking at low temperatures. For example, in Virginia,

a PG 64-22 asphalt binder may be specified. This signifies that the pavement temperature is expected to range from a low of -22°C to a high 7-day average of 64°C . From the initial SHRP testing, and the more recent SMP data, pavement temperature models (presented in the following section on pavement temperature prediction) have been developed to assist with selection of the proper asphalt binder performance grade for usage in a particular location. In addition, several researchers have analyzed the accuracy of these models using data from the LTPP study (and independent studies) to compare actual pavement temperatures to those predicted and used for binder selection (Bosscher *et al.*, 1998; Lukanen *et al.*, 1998; Mohseni and Symons, 1998a and 1998b).

While the models used for binder selection are useful for an indication of a yearly high or low temperature value for a particular pavement, they do not allow a user to predict pavement temperatures for any given day such as might be needed for falling-weight deflectometer (FWD) testing. Recent approaches to this topic by Park *et al.* (2001) and Marshall *et al.* (2001) provide an empirically based method by which the user can estimate the temperature profile within a pavement structure during any portion of the day. Both of these papers relate the importance of this determination by observing the variability of pavement strength during the day using FWD.

2.2.1 RADIATION THEORY (ENERGY EQUILIBRIUM)

This section presents the current theory on heat transfer in a layered pavement system. This constitutes the basis for many of the models discussed in Section 2.2.2 – Pavement Temperature Prediction. Considering the earth as a black body radiator system, the net rate of heat flow in and out of the system, q_{net} , can be expressed as the following:

$$q_{\text{net}} = q_s + q_a + q_t \pm q_c \pm q_k - q_r \quad (2.39)$$

where

q_s = energy absorbed from direct (solar) radiation;

q_a = energy absorbed from diffuse radiation (radiation reflected by the atmosphere);

q_t = energy absorbed from terrestrial radiation;

q_c = energy transferred by convection;

q_k = energy transferred by conduction; and

q_r = energy emitted through outgoing radiation.

The energy absorbed from direct solar radiation and that which is reflected by the atmosphere (q_s and q_a) are positive for the surface of a body such as a pavement on the surface of the earth. The terrestrial radiation component (q_t) can be considered to be zero for a pavement since it is defined as the radiation that is absorbed by a body above the surface of the earth. The energy transferred by convection (q_c) is defined as the transfer of energy from a solid surface to a fluid (in this case the air above the pavement). The convection term is positive if energy is transferred from the pavement to the air in the case that the pavement surface possesses a higher temperature. The convection term will be negative if the air temperature is higher than the pavement surface temperature. Conduction energy will be positive if the heat is transferred from within the pavement to the pavement surface (i.e., when the surface is cooler). A negative sign is used when the pavement surface is warmer than the pavement below the surface. Outgoing radiation from the pavement surface is always given with a negative sign.

Solar Radiation

Due to the high surface temperature of the sun (approximately 6000°K) radiation of high frequency, or shortwave radiation, is emitted. Part of this radiation from the sun can be scattered by clouds or moisture in the atmosphere. Thus, there are two types of shortwave radiation, direct and diffuse. Diffuse shortwave radiation is that which is scattered or diffused by the atmosphere or by particles in the atmosphere. Direct shortwave radiation is that which is not scattered by the atmosphere or by particles in the atmosphere. The relative percentages of direct and diffuse radiation making up the total shortwave radiation are dependent upon the weather and local environmental conditions. On a cloudless day, the percentage of direct shortwave radiation is higher. Bosscher *et al.* (1998) measured the solar radiation using a pyranometer and obtained values in Wisconsin of approximately 500 W/m² (winter) and 1200 W/m² (summer).

The energy received as direct solar radiation, q_s , can be expressed as the following:

$$q_s = \alpha_s \cdot R_i \quad (2.40)$$

where α_s is the solar surface absorptivity and R_i is the incident solar radiation. The surface absorptivity depends upon the wavelength of the radiation received, which is dependent upon the surface temperature of the radiator. Solaimanian and Kennedy (1995) report a typical α_s range as 0.85 to 0.93. The incident solar radiation is defined as the radiation received by a body parallel to the surface of the earth. However, radiation from the sun is not always perpendicular to a specific surface, thus, the incident solar radiation is defined as the following:

$$R_i = R_n \cdot \cos(i) \quad (2.41)$$

where

R_n = radiation received by a body which is placed normal to the direction of the sun; and

i = angle between the normal to the surface and the direction of the sun.

The value of R_n can be calculated from the solar constant, R_o , which is given as 1394 W/m². The solar constant is defined as the solar energy incident upon a surface that is perpendicular to the direction of the sun located at the outer edges of the earth's atmosphere. However, gases, moisture, and suspended particles in the atmosphere together reflect approximately 26% of the incoming solar radiation (insolation) back into space.

The solar energy received at the earth's surface depends upon the time of day, season, and location on the planet. The value of R_n is given as the following:

$$R_n = R_o \cdot \tau_a^m \quad (2.42)$$

where

τ_a = transmission coefficient for a unit air mass;

m = relative air mass, defined as the ratio of the actual path length to the shortest path length $\approx 1/\cos(z)$; and

z = zenith angle (angle between the zenith and the direction of the sun).

The transmission coefficient, according to Kreith (1986), ranges from 0.81 on a clear day to 0.62 on a cloudy day. A value of 0.7 can be used as an average. In addition, the value of the transmission coefficient is higher in the summer than in the winter due to

higher moisture contents. The zenith angle depends on the latitude (ϕ), the time of day, and the solar declination (δ_s). The time is expressed in terms of an hour angle (h) that is defined as the angle through which the earth turns to bring the sun directly overhead a particular location. The hour angle (h) is defined as being zero at local noon. The zenith angle (z) can be found from the following:

$$\cos(z) = \sin(\phi) \cdot \sin(\delta_s) + \cos(\delta_s) \cdot \cos(h) \cdot \cos(\phi) \quad (2.43)$$

For a horizontal surface, $\cos(i) = \cos(z)$, however, if the surface is tilted at an angle ψ (as shown in Figure 2.11), i can be determined from the following:

$$\frac{R_i}{R_n} = \cos(i) = \cos(z - \psi) - \sin(z) \cdot \sin(\psi) + \sin(z) \cdot \cos(\psi) \cdot \sin|A - \beta| \quad (2.44)$$

where

Ψ = angle of tilt from the horizontal;

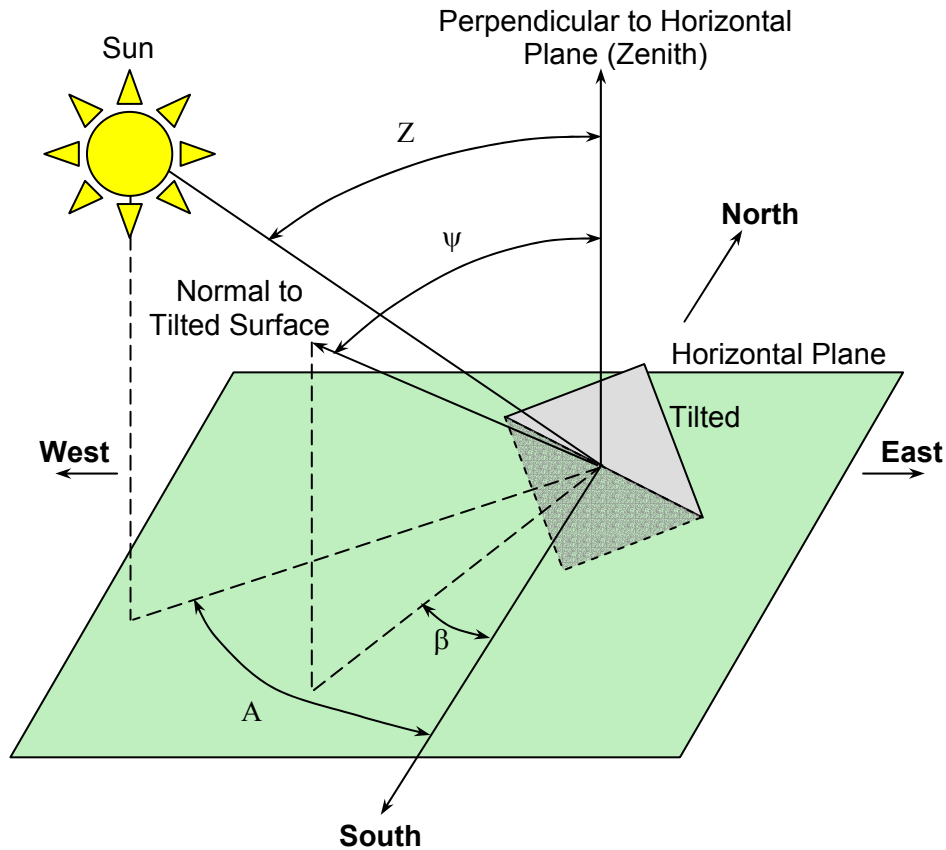


Figure 2.11. Definition of solar and surface angles (from Kreith, 1986).

A = azimuth of the sun; and

β = angle between the south meridian and the normal to the surface measured westward along the horizon.

Solaimanian and Kennedy (1993) report that the zenith angle can be approximated at locations of latitude greater than 22° between the months of May and August (at local noon time) as the following:

$$z = \text{latitude} - 20 \text{ degrees} \quad (2.45)$$

The radiation received by the pavement that is reflected from the atmosphere as longwave radiation, q_a , can be calculated as the following:

$$q_a = \varepsilon_a \sigma T_{\text{air}}^4 \quad (2.46)$$

where

ε_a = atmospheric emissivity, assumed to be 0.7 for a cloudless day,

σ = Stefan-Boltzman constant = $5.68 \times 10^{-8} \left(\frac{\text{W}}{\text{m}^2 \text{K}^4} \right)$; and

T_{air} = the air temperature (°K).

Radiation Emitted by Pavement Surface

Any heat transfer by radiation will involve both emissivity (ability of a surface to emit radiation as compared to a black body) and absorptivity (ability of a surface to absorb radiation) component. It has been reported that the emissivity and the absorptivity to solar radiation for asphaltic materials is identical at approximately 0.93 (Solaimanian and Kennedy, 1993). Solaimanian and Kennedy (1993) state that the outgoing (longwave) radiation, q_r , can be expressed in W/m^2 (using the black body assumption) from the Stefan-Boltzman Law as the following:

$$q_r = \varepsilon_p \sigma T_s^4 \quad (2.47)$$

where

ε_p = pavement emissivity; and

T_s = surface temperature (K).

Conduction Energy

The conduction of thermal energy within the pavement can be expressed as the following:

$$q_k = -k \frac{T_d - T_s}{d} \quad (2.48)$$

where

k = thermal conductivity;

T_s = surface temperature ($^{\circ}\text{C}$);

d = depth (m); and

T_d = temperature at depth = d ($^{\circ}\text{C}$).

Convection Energy

The rate of heat flow by convection to the air surrounding the pavement can be expressed as follows:

$$q_c = h_c (T_s - T_{\text{air}}) \quad (2.49)$$

where h_c is the surface coefficient of heat transfer. The coefficient of heat transfer will depend upon the surface geometry of the pavement, the wind velocity, and physical properties of the air.

2.2.2 PAVEMENT TEMPERATURE PREDICTION

Using results from the LTPP and SMP studies, civil engineers have a higher probability of specifying an asphalt binder that can withstand the effects of vehicular loading at different temperatures regardless of location. More than 3,000 pavement sites throughout North America were fitted with instruments to measure responses of the pavement due to vehicular loading and environmental conditions. The LTPP sites were chosen such that a wide variety of pavement types, structural designs, and environmental factors could be analyzed. As a result of this work, a new method for designing asphalt pavements called Superpave (Superior Performing Asphalt

Pavements) was developed. Not only did this mix design protocol include new methods of evaluating HMA and asphalt binder in the laboratory, but it also included a new way to specify asphalt binder for field projects based on the environmental conditions (temperature) experienced at different areas within the United States and Canada. Under the current Superpave protocol, asphalt binder is specified in terms of the expected minimum air temperature and maximum 7-day average air temperature. These air temperatures are used to estimate the temperature experienced by the pavement. Through the estimation of yearly high and low pavement temperatures, a proper binder can be selected in terms of the performance grade (PG) designation.

Pavement Temperature Prediction Models

Selection of the appropriate binder for different areas of the United States is performed using a set of performance-based equations under the SHRP Superpave Binder PG System. This PG system is intended to ensure that the appropriate binder is used in locations with different environmental conditions. A database was developed in which environmental data from 6092 weather stations in the United States and Canada can be used to determine the seven-day average high air temperature and the one-day low air temperature for any location (Ali and Lopez, 1996). However, the temperature limits used for the PG binder specifications are pavement temperatures and not air temperatures. Thus, expressions were developed to determine the pavement temperature from the air temperature. The current expressions used for the PG grading are given in Equations 2.50 through 2.53 and will be referred herein as the *SHRP models*. Equation 2.50 gives the high pavement temperature for the surface of a pavement as the following:

$$T_{s(\max)} = T_{a(\max)} - 0.00618 * \Phi^2 + 0.2289 * \Phi + 24.4 \quad (2.50)$$

where

$T_{s(\max)}$ = maximum pavement temperature at the surface (°C);

$T_{a(\max)}$ = seven-day average maximum air temperature (°C); and

Φ = latitude of the desired location (degrees).

Equation 2.51 yields the high pavement temperature with depth as the following:

$$T_{pav(max)} = T_{s(max)} \times (1 - 0.063d + 0.007d^2 - 0.0004d^3) \quad (2.51)$$

where

$T_{pav(max)}$ = maximum pavement temperature at depth = d (°F);

$T_{s(max)}$ = maximum pavement temperature at the surface (°F); and

d = depth from surface (in).

The low pavement temperature at the surface is given as being equal to the low air temperature, expressed as the following:

$$T_{s(min)} = T_{a(min)} \quad (2.52)$$

where

$T_{s(min)}$ = minimum pavement temperature at the surface (°C); and

$T_{a(min)}$ = minimum one-day air temperature (°C).

The minimum pavement temperature at any depth is given as the following:

$$T_{pav(min)} = T_{a(min)} + 0.051d - 0.000063d^2 \quad (2.53)$$

where $T_{pav(min)}$ = minimum pavement temperature at depth = d (°C).

Equations 2.50 and 2.52 were based on research performed by Solaimanian and Kennedy (1993).

In addition to the above expressions, updated versions of the SHRP models have been developed (Mohseni, 1998; Mohseni and Symons, 1988a and 1988b) based on current LTPP data, referred herein as the *LTPP models*. Equations 2.54 through 2.57 were developed from additional data obtained after the previously published SHRP work. To determine the maximum pavement temperature at any depth, the following expression is given:

$$T_{d(max)} = (T_{s(max)} + 17.8) \times (1 - 2.48 \times 10^{-3}d + 1.1 \times 10^{-5}d^2 - 2.4 \times 10^{-8}d^3) - 17.8 \quad (2.54)$$

where

$T_{d(\max)}$ = maximum pavement temperature at depth = d ($^{\circ}\text{C}$); and

d = depth (mm).

As an expression for the maximum pavement temperature, at a depth of 20mm, Equation 2.54 simplifies to the following:

$$T_{20(\max)} = 0.955T_{s(\max)} - 0.8 \quad (2.55)$$

The minimum pavement surface temperature is found using the minimum air temperature, shown as the following:

$$T_{s(\min)} = 0.859 \cdot T_{a(\min)} + 1.7 \quad (2.56)$$

To determine the minimum pavement temperature with depth, the following expression is given:

$$T_{d(\min)} = T_{s(\min)} + 5.1 \times 10^{-2}d - 6.3 \times 10^{-5}d^2 \quad (2.57)$$

where $T_{d(\min)}$ is the minimum pavement temperature at depth = d ($^{\circ}\text{C}$).

It is important to keep in mind that these models were developed to calculate annual minimum and maximum pavement temperatures for the purpose of binder specification and not for daily pavement temperature analysis.

Analysis of SHRP Models

Many researchers have investigated the initial SHRP models to determine the appropriateness of these expressions (Ali and Lopez, 1996; Robertson, 1997; Mohseni and Symons, 1988a; Bosscher *et al.*, 1998; Lukanen, *et al.*, 1998). These studies point out that several erroneous assumptions of the physical nature of pavement temperature arise when employing the heat flow model (Equation 2.39). This model assumes that the minimum air temperature is equal to the minimum pavement temperature and the minimum/maximum pavement temperature in each layer and the minimum/maximum air temperature occur simultaneously (the energy equilibrium assumption from Equation 2.39). Figures 2.12 and 2.13, showing the temperature profile for Section A at the Virginia Smart Road, offer evidence that these assumptions are incorrect. Figure 2.12 is a plot of the daily low pavement temperature at different depths versus the daily low air temperature over the four-month period of September to December 2000. Figure 2.12 also includes a line denoting a one-to-one relationship between the pavement

temperature and the air temperature. As seen in this figure, the daily low pavement temperature is as much as 10 to 15°C warmer than the air temperature. Figure 2.13 is a plot of the temperature values for a typical day (April 10, 2000) showing the responses of the thermocouples that were placed at different depths from the surface. As can be seen, the time in which the maximum temperatures occur in each layer vary during the course of the day. Therefore, the qualification of energy equilibrium is inaccurate for the pavement system. By 1995, the initial round (Loop 1) of the Seasonal Monitoring Program (SMP) had collected air and pavement temperature data from 30 test sites located throughout the United States and southern Canada. This data was used to evaluate the initial SHRP pavement temperature models with regard to these erroneous assumptions and to suggest improvements to be incorporated within the Superpave binder selection process.

Mohseni and Symons (1998a and 1998b) presented analysis using the updated data to make comparisons with the initial SHRP models. Their interest was in discussing differences between observed data and the SHRP models. The authors performed statistical analysis on the pavement temperature data in order to determine which physical factors had the most influence on the pavement temperature. They determined

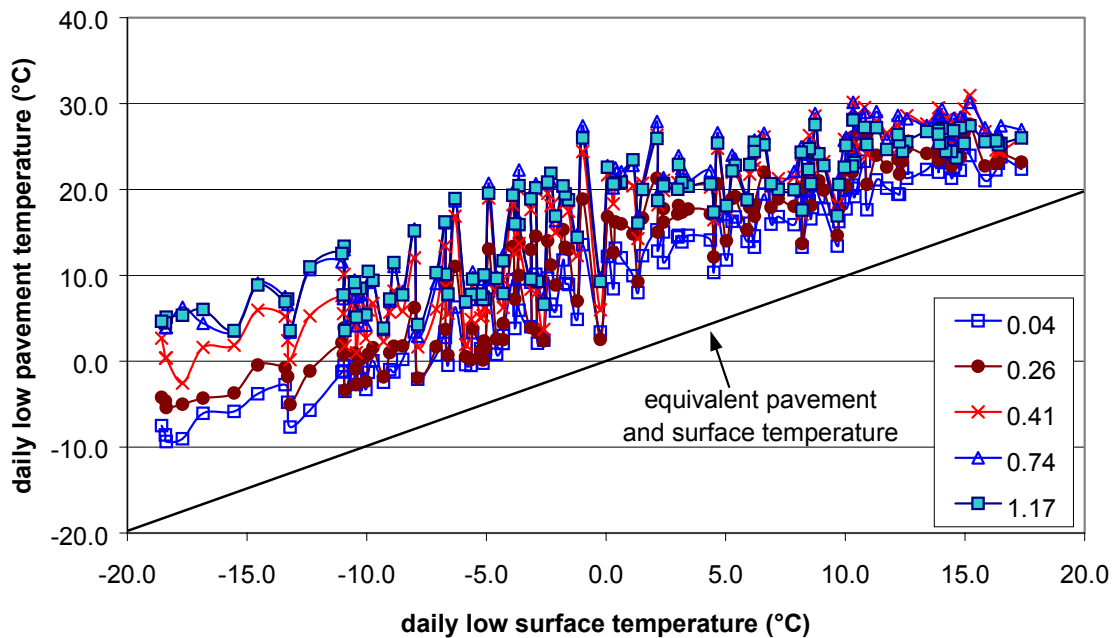


Figure 2.12. Temperature profile for Section A showing daily low pavement temperatures at various depths versus daily low surface temperature.

that the air temperature, latitude, and depth from the surface were the most significant factors. This updated data was used for the development of a revised low-temperature model that consisted of 411 data points. The air and pavement temperatures ranged from 4.6 to -41.5°C and 13 to -33°C, respectively. The location of the sensors ranged from 25.4 to 274mm in depth from the pavement surface. The latitude of the pavement sites varied between approximately 27.0 and 51.9°N. The variables of low air temperature, latitude, and depth were found to have the most influence on the low pavement temperature. The relationship between air and pavement temperatures was found to be linear and it was also found that air temperature was the most influential variable in the model. A latitude variable was found to vary non-linearly with pavement temperature. Through trial and error, the variable latitude-squared was found to be more significant. A third variable, depth from the pavement surface was found to have a weak correlation with the pavement temperature. Therefore, the terms depth-squared and $\log(\text{depth}+25)$ were considered with $\log(\text{depth}+25)$ providing a better fit.

Mohseni and Symmons analyzed SMP data using Equation 2.58 (depth, $d = 25\text{mm}$) and found that the low pavement temperatures were approximately 10°C warmer than the air temperature at a low air temperature of -40°C and approximately 5°C warmer than the air temperature at a low air temperature of -5°C. In light of these differences, it

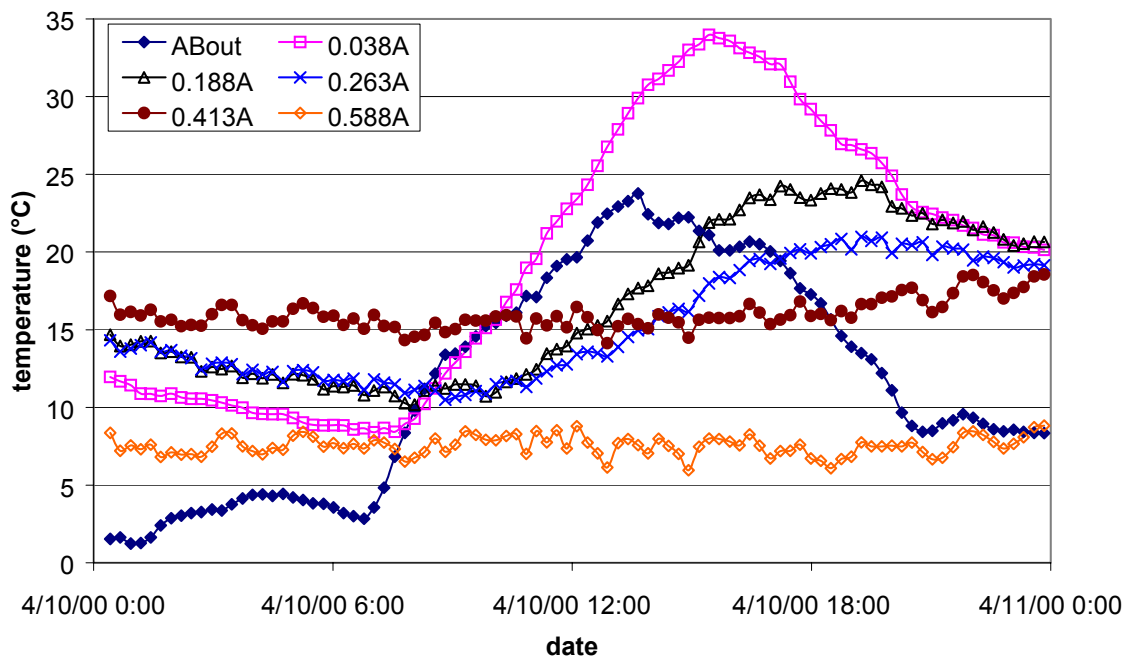


Figure 2.13. Temperature distribution for Section A - April 10, 2000.

was proposed to develop a new model to be able to predict the low pavement temperature at various depths. The variables that were considered to have a significant effect on low pavement temperature are low air temperature, latitude, and depth. It was shown that the relationship between low air temperature and low pavement temperature is of a linear nature; a non-linear relationship exists between low pavement temperature and both latitude and depth.

From this analysis, Mohseni and Symons developed a revised set of temperature prediction equations. These equations termed here the *revised LTPP models*. Equation 2.58 gives the revised LTPP low pavement temperature model as the following:

$$T_{\text{pav}} = -1.56 + 0.72 * T_{\text{air}} - 0.004 * \Phi^2 + 6.26 \log(d + 25) \quad (2.58)$$

where

T_{pav} = Low pavement temperature below the surface (°C);

T_{air} = Low air temperature (°C).

When the residuals (difference between actual pavement temperature and predicted temperature using Equation 2.58) were plotted versus the significant terms, no obvious trend was found and the error appeared to be evenly distributed across the temperature range. A standard error of 2.1°C was reported. Again, this revised model calculates an annual low pavement temperature.

It was reported that in determining the design pavement temperature (such as when using the Superpave binder selection), two types of errors are present: an error based on model prediction, and an error associated with the mean air temperature. To account for these errors, the standard deviation of the mean air temperature and root mean square error (RMSE) of the model is incorporated into Equation 2.58 and thus Equation 2.59 is presented as follows:

$$T_{\text{pav}} = -1.56 + 0.72 * T_{\text{air}} - 0.004 * \Phi^2 + 6.26 \log(d + 25) - z \sqrt{4.4 + 0.52(\sigma_{\text{air}})^2} \quad (2.59)$$

where σ_{air} is the standard deviation of the mean low air temperature (°C), and Z is obtained from the standard normal distribution for the desired area under the normal distribution curve. Equation 2.58 is sufficient to determine the low pavement

temperature having 50% reliability. However, Equation 2.59 allows the calculation of the low pavement temperature with a higher reliability by subtracting the error from the 50% reliability expression. The error portion of Equation 2.59 can be expressed in terms of the standard deviation of the mean air temperature (σ_{air}) and the standard error estimate of the model (σ_{model}). The variability in calculating the low pavement temperature can be written in terms of both of these errors as the following:

$$\sigma_{\text{pav}} = \sqrt{(\sigma_{\text{model}})^2 + (0.72\sigma_{\text{air}})^2} \quad (2.60)$$

Substituting the standard error estimate of the model (2.1°C) into the pavement temperature variability, the error term (Equation 2.60) can be written independently as:

$$\varepsilon = z\sqrt{4.4 + 0.52(\sigma_{\text{air}})^2} \quad (2.61)$$

Mohseni and Symons (1998a) also presented a revised high temperature model. Again, the variables to be included were air temperature, latitude, and depth from the surface. The correlation between pavement temperature and air temperature was again found to be linear and was also the strongest correlation of the three variables. The relationship between latitude and pavement temperature was also found to be strong but was of a non-linear nature. Through trial and error, the term latitude-squared was found to be the most significant variable incorporating latitude. Depth from the surface was also found to have a strong non-linear correlation with pavement temperature. The terms depth-squared and $\log(\text{depth}+25)$ were considered with the second term providing a better fit. The revised high-temperature equation is given as follows:

$$T_{\text{pav}} = 54.32 + 0.78 * T_{\text{air}} - 0.0025 * \Phi^2 + 15.14 \log(d + 25) - z\sqrt{9 + 0.61(\sigma_{\text{air}})^2} \quad (2.62)$$

The standard error was given as 3.0 and an R^2 of 0.76 was reported.

Following this, Mohseni and Symons (1998b) investigated the effects of different estimated pavement temperatures on binder selection using the revised LTPP and the SHRP models. One randomly selected weather station was chosen from each state or province in the United States and Canada and the two models were compared. The randomly selected weather station for Virginia was the Covington Filtration Plant. The original SHRP model indicated that a PG 58-22 and a PG 58-28 binder would be

specified for a 50% and a 98% reliability, respectively. However, using the revised LTPP model, the binder grades were given as 52-16 and 58-22 for 50% and 98% reliability, respectively. For all 62 randomly selected weather stations, it was seen that the revised LTPP model specified binders one or two grades higher than the original SHRP model in estimating the low temperature binder specification. When comparing all 7801 weather stations in the SHRP program, the revised LTPP model specified a higher low temperature binder grade than the original SHRP model for 76% and 85% of the weather station sites for 50% and 98% reliability, respectively. The comparisons between the SHRP data and the LTPP models are discussed in more detail in Mohseni (1998). The low temperature model presented by Mohseni and Symons (Equation 2.59) has recently been incorporated into a revised Superpave standard.

Robertson (1997) developed a model to estimate the low temperature binder specification based on data obtained from Canadian Strategic Highway Research Program (C-SHRP) projects. This study also included a method that allows the user to select the reliability of the estimated pavement temperature. As part of his investigation, Robertson listed some observations about the pavement temperatures under study:

- the maximum and minimum ground temperatures occur sometime after the summer and winter solstices, respectively;
- the pavement temperature range will tend to decrease in coastal areas since the capacity for heat absorption of water is much greater than for land;
- the winter pavement temperatures vary over a smaller range and more slowly than air temperatures;
- the lowest pavement temperature is warmer than the lowest air temperature;
- the difference between low air and low pavement temperatures is larger for areas having lower air temperatures; and
- almost all thermally related cracking occurs in the period of November through February

In addition to the above statements, Robertson (1997) developed a linear relationship between air and pavement temperatures for seven Canadian sites having a pavement thickness greater than 100mm. The model covers an expected minimum air

temperature range from -32 to -48°C. The resulting regression model is given as follows:

$$T_s = 0.749T_a \quad (2.63)$$

where T_s and T_a represent the minimum pavement surface temperature (°C) and the minimum air temperature (°C), respectively. Robertson reports that this model, developed from 653 data points, has a standard error equal to 1.5°C and an R^2 of 0.95. A design equation, allowing the user to specify the desired reliability is presented as follows:

$$T_{\text{design}} = 0.749(T_{\text{air}} - n\sigma_{\text{air}}) - 1.5n \quad (2.64)$$

where

T_{design} = winter pavement (surface) design temperature (°C);

T_{air} = mean of minimum air temperatures at the pavement site (°C);

σ_{air} = standard deviation of the minimum air temperature (°C); and

n = multiplier associated with the desired reliability (1.28 for 99%, 1.00 for 97.5%, 0.76 for 95%, and 0.48 for 90%).

Lukanen *et al.* (1998) presents a summary of comparisons between the initial SHRP temperature model (heat flow model) and three models independently developed by Han (as discussed by Lukanen *et al.*, 1998), Mohseni (1998), and Robertson (1997), using data from the SMP. Han utilized the same data set used by Mohseni to develop the revised LTPP models, however, slightly different results were obtained. Han's model for the maximum pavement temperature is given as follows:

$$T_{d(\text{max})} = 0.52 + 6.225\Phi - 0.15\Phi^2 + 0.0011\Phi^3 + 0.28T_{a(\text{max})} - 8.37\text{LN}(d + 40) \quad (2.65)$$

The standard error for Han's maximum pavement temperature equation was given as 2.2°C using 70 data points. Han's model for the minimum pavement temperature is given as follows:

$$T_{d(\min)} = -0.14 - 1.7\Phi + 0.06\Phi^2 - 0.0007\Phi^3 + 0.69 * T_{a(\min)} + 4.12\text{LN}(d + 100)$$

(2.66)

The standard error for Hans's minimum pavement temperature equation was given as 2.6°C using 71 data points. The standard error for Mohseni's maximum pavement temperature model was given as 3.0°C based on 309 data points. The standard error for Mohseni's minimum pavement temperature model was given as 2.1°C based on 411 data points.

Robertson's work, as discussed earlier, was prompted by previous research at C-SHRP suggesting that the initial minimum temperature prediction model offered by SHRP was too severe (i.e., the pavement temperature was actually warmer than the prediction). Differences between Mohseni's model (and thus Han's also) and Robertson's work may result since although hourly temperature data was available at the time, Robertson's concurrent study did not utilize it since it was suggested that he might not have known of its recent availability. Thus Robertson used only daily minimum temperatures to develop his model (Equation 2.63). Observing the differences between the models, it is seen that Robertson's model does not account for latitude. The latitude variable was seen as less significant with the C-SHRP data since the latitudes for the projects under study are greater than 45°N and thus the air temperature is the predominant factor. If Robertson's model were to be compared with Han's model, it would require a latitude input of approximately 47°N.

In addition, Lukanen *et al.* (1998) present their own maximum and minimum pavement temperature prediction models based on an expanded set of SMP data. At the time this paper was published (1998), data from an additional 15 sites had been added to the SMP first loop (the data used by Mohseni and Han). The models presented by Lukanen *et al.* (1998) were taken from two summer seasons and one winter season. For each test site, only one annual maximum and one annual minimum were used to develop the models. Lukanen's model for predicting maximum pavement temperature's is presented as follows:

$$T_{d(\max)} = 0.47 + 5.717\Phi - 0.1276\Phi^2 + 0.0008121\Phi^3 + 0.3078T_{a(\max)} - 8.602\text{LN}(d + 40)$$

(2.67)

Lukanen *et al.* (1998) reported that the standard error for this model is 2.7°C and is based on 113 data points. Lukanen's model for predicting minimum pavement temperatures is presented as follows:

$$T_{d(\min)} = -0.15 - 1.9\Phi + 0.06\Phi^2 - 0.0007\Phi^3 + 0.59 * T_{a(\min)} + 5.2\text{LN}(d + 100)$$

(2.68)

The standard error for this model is reported to be 2.4°C and is also based on 113 data points. Lukanen also suggested that the temperature profile models could be used to estimate the temperature at different depths within the pavement to determine the appropriate PG binder selection for the asphalt within the base courses of the pavement.

In a study incorporating an independent data set from a field study in Wisconsin, Bosscher *et al.* (1998) described a pavement section instrumented with thermistors to monitor pavement temperature down to a depth of 101.6mm. Models were developed and compared to the original SHRP and the revised LTPP pavement temperature models. Findings presented by Bosscher include that solar radiation values of 500 W/m² and 1200 W/m² were typical for winter and summer, respectively. Conclusions include that during the night, when air temperatures are typically the lowest; the pavement temperature was always found to be higher than the air temperature (probes were installed at a depth of 6.4mm from the surface). The surface layer always experienced the largest temperature fluctuation (compared to the other pavement layers) that coincided with daily changes in air temperature. Also, significant differences exist between the standard deviation of the pavement temperature and the air temperature.

Bosscher developed a model that gave the daily minimum pavement temperature with daily minimum air temperature as the only input. Although, the model correlated well with a linear relationship, the standard error of estimate was reported to be 2.71°C, too high by the authors reasoning. To improve this model, other factors were included to reduce the standard error. The total solar radiation intensity for the previous 24 hours and the average hourly freezing index of the air temperature for the previous three days were included. The total solar radiation (W/m²) was recorded for the 24 hours prior to the time in which the minimum pavement temperature occurred. The hourly freezing index of the air temperature is calculated by summing the hourly air temperatures below 0°C during the 72 hours preceding the minimum pavement temperature and dividing this

total by 72 (total number of hours in three days). The result of these two values when multiplied was taken to the 0.25 power for use in the model equation. This fourth root factor was based on the theory that any blackbody radiator (whose temperature is greater than absolute zero) radiates heat at a rate that is proportional to the fourth power of the absolute temperature (Kreith, 1986). In addition to these factors, the inclusion of the average air temperature of the previous 24-hour period improved the error of the prediction model to between 1.25 and 1.9°C. To further improve pavement temperature prediction, a step approach, employing different models over different air temperature ranges, was incorporated. Two models, predicting the pavement temperature at a depth of 6.4mm, are given as follows:

$$T_{p(\min)6.4} = 0.3768 + 0.687 * T_{a(\min)} \quad (2.69)$$

$$T_{p(\min)6.4} = -1.001 + 0.422 * T_{a(\min)} + 0.359T_{a-01} \quad (2.70)$$

where $T_{a(\min)}$ and T_{a-01} are the minimum air temperature for the day in which the pavement minimum is being predicted and the average air temperature for the 24 hrs preceding the time of the pavement low temperature, respectively.

Bosscher *et al.* (1998) were also interested in determining the pavement temperature as it varied with depth in relationship to the low air temperature. An expression for determining the temperature at depth, d (mm), is given as follows:

$$T_{d(\min)} = T_{p(\min)6.4} - [(0.00123 \times T_{p(\min)6.4}) \times (d - 6.4)] + 0.01416 \times (d - 6.4) \quad (2.71)$$

The authors go on to state that the data used to develop the above expression do not include time as a factor in determining the pavement depth. Thus, it was assumed that the minimum temperature within each layer occurs simultaneously (an assumption incorporated into the heat flow theory used in the original SHRP models). It was also noted that the above expression is only valid for estimating pavement temperatures when the air temperature is less than -5°C.

Since the analysis performed under SHRP assumes that the low temperature occurs at the surface of the pavement, Equations 2.69 and 2.70 can be substituted into Equation 2.71, respectively, to yield:

$$T_{s(\min)} = 0.286 + 0.692 \times T_a \quad (2.72)$$

$$T_{s(\min)} = -1.102 + 0.425 \times T_a + 0.362T_{a-01} \quad (2.73)$$

The authors again state that Equations 2.72 and 2.73 are best suited for air temperatures less than -5°C.

Following this, Bosscher *et al.*, (1998) compared the developed prediction models to the existing SHRP and revised LTPP models. When considering low pavement temperatures, the SHRP models consider the most severe or coldest low pavement temperature to occur at the surface of the pavement. That is, the temperature at this location is equal to the low air temperature at that time. The revised LTPP models incorporate regression analysis that is presented in Mohseni (1998). When comparing the SHRP model, the revised LTPP model, and Equations 2.69 and 2.70 for predicting pavement temperature at a depth of 6.4mm to the actual pavement temperature at 6.4mm, the standard error (in °C) was found to be 2.409, 1.719, 1.655, and 1.226, respectively, for air temperatures less than -5°C. The authors concluded that the developed models (Equations 2.69 and 2.70) and the LTPP models show good agreement between actual pavement temperatures at 6.4mm depth and predicted pavement temperatures at 6.4mm depth. However, according to Bosscher *et al.* (1998), the SHRP models did not show good agreement between actual pavement temperatures at 6.4 mm depth and predicted pavement temperatures at 6.4 mm depth. Bosscher *et al.* (1998) reported that the SHRP models predicted the pavement temperature at 6.4mm depth to be significantly lower than the measured pavement temperature at the same depth. This difference ranged from approximately 3°C to 14°C at measured pavement temperatures of -5°C to -30°C, respectively.

The standard deviation of the pavement temperature versus the standard deviation of the air temperature is also important to consider. The Superpave binder selection protocol assumes that the standard deviations are equal for both the pavement temperature and the air temperature. Bosscher *et al.* (1998) showed that this was not the case for either high or low temperatures. Thus, the assumptions used to determine the reliability of the binder grade selection are erroneous. The standard deviations were calculated from monthly averages of the daily minimum and maximum air and pavement temperatures. Data for the maximum temperature portion were taken from the three hottest months for each summer. It was shown that the standard deviation for the maximum pavement temperature is much higher than the standard deviation of the maximum air temperature. However, at lower temperatures this trend is reversed; the

minimum pavement temperature standard deviation is much lower than the minimum air temperature standard deviation. Equations for determining the standard deviation of the pavement temperatures based on the standard deviation of the air temperatures are given as Equations 2.74 and 2.75 for minimum and maximum temperatures, respectively.

$$SD_{p(\min)} = 1.170 + 0.6422 \times SD_{a(\min)} \quad (2.74)$$

$$SD_{p(\max)} = 1.694 + 1.2733 \times SD_{a(\max)} \quad (2.75)$$

where

SD_p = standard deviation of the pavement temperature; and

SD_a = standard deviation of the air temperatures.

Equations 2.74 and 2.75 are given by Bosscher *et al.* (1998) as valid for pavement surface temperatures below 0°C and above 40°C, respectively.

When predicting maximum pavement temperatures at different pavement sites, Solaimanian and Kennedy (1993) state that latitude is an influential component. For areas in the United States, states of lower latitude in the summertime will receive more direct radiation per hour than states of higher latitude. The greater amount of radiation will manifest itself into a larger difference between maximum air temperature and maximum temperature within the pavement. Solaimanian and Kennedy state that for project sites sharing the same latitude, the difference between maximum air temperature and maximum pavement temperature is nearly constant, varying only upon radiation, conduction, and convection. An expression was developed to yield the difference between air and pavement temperatures as a function of latitude as the following:

$$\Delta T = -0.0062\Phi^2 + 0.2289\Phi + 24.38 \quad (2.76)$$

where

ΔT = difference between maximum air and maximum pavement temperatures (°C); and

Φ = latitude (degrees).

Solaimanian and Kennedy (1993) also state that at lower latitudes, the difference between air and pavement temperatures can be up to approximately 26°C when the air

temperature varies between 24 and 42°C. At a latitude of 60 degrees, the difference can reach approximately 15°C. The authors also discuss prediction of pavement temperature with depth. However, they only state that the form of this equation should be a quadratic where the input variable is the surface temperature. No mention of factors, including a seasonal adjustment, is offered.

2.2.3 APPLICATIONS OF PAVEMENT TEMPERATURE PREDICTION

To this point, the research mentioned previously has focused on maximum or minimum air temperatures to predict the annual maximum or minimum pavement temperatures for the purpose of binder selection. Studying the daily changes in pavement temperature poses a problem of similar nature, however, prediction becomes a more complicated task. Climatologic factors affect the analysis now as much as engineering principles. While the basic theories previously discussed hold true, yearly climatic cycles begin to exert their influence on the pavement temperature. For example, while the air temperature may be identical for two dates, the distribution of temperatures within the pavement may be vastly different supposing the two dates are many months apart. In an effort to model this variance, Hermansson (2000 and 2001) presents a simulation-based prediction model to monitor the diurnal temperature changes in the pavement during the summer months. The models follow the concepts discussed by Salaimanian and Kennedy (1993) and utilize data from LTPP sites in the United States and from sites in Sweden.

Park *et al.* (2001) developed a model that could be used to predict pavement temperatures given the surface temperature and time of day for use with FWD analysis. Huang (1993) lists the pavement temperature and the local climate as significant factors influencing the deflection of the pavement system. The development of Park's model was performed by collecting temperatures using retrofitted (added to the pavement after construction) thermocouples and measuring the temperature of mineral oil in holes of various depths in six flexible pavements in Michigan. A regression-based model was developed using 197 data points and compared with data from SMP sites in seven other states (Colorado, Connecticut, Georgia, Nebraska, Minnesota, South Dakota, and Texas). The developed model is given as follows:

$$T_z = T_{\text{surf}} + \left(-0.3451z - 0.0432z^2 + 0.00196z^3\right) \times \sin(-6.3252t + 5.0967) \quad (2.77)$$

where

T_z = temperature at depth z ($^{\circ}\text{C}$);

T_{surf} = temperature at the surface ($^{\circ}\text{C}$);

z = depth from surface (cm);

\sin = sine function (radians); and

t = time of temperature measurement in fraction of day (i.e., 1:30PM = $13.5/24 = 0.5625$ days).

The model was validated over a surface temperature range of -28.4 to 53.7°C and a depth range of 14 to 27.7cm. An R^2 value better than 90% was reported and a temperature prediction band of $\pm 4^{\circ}\text{C}$ was given. After validating the model with data from SMP sites across the United States, the authors suggested that this model could be adopted for all seasons and other climatic areas.

Marshall *et al.* (2001) present another recent temperature prediction model for use with FWD analysis. Four flexible pavements in Tennessee were instrumented with thermistors during construction or during reconstruction at mid-depth in the asphalt surface and base layers. The data collected from the four sites was used to develop the following regression based model:

$$T_d = 0.95 + 0.892T_s + (\log d - 1.25) \times \left(1.83 \sin\left(\frac{2\pi}{18}A\right) - 0.448T_s + 0.621T_{\text{avg}}\right) + 0.042T_s \sin\left(\frac{2\pi}{18}B\right) \quad (2.78)$$

where

T_d = pavement temperature at mid-layer depth ($^{\circ}\text{C}$);

T_s = surface temperature measured with infrared sensor ($^{\circ}\text{C}$);

T_{avg} = average of high and low temperature of preceding day ($^{\circ}\text{C}$);

a = mid-layer depth (mm); and

A and B are variables defined as

$$A = \begin{cases} t_d + 9.5 & \text{if } 0 \leq t_d < 5 \\ -4.5 & \text{if } 5 \leq t_d < 11 \\ t_d - 15.5 & \text{if } 11 \leq t_d < 24 \end{cases} \quad B = \begin{cases} t_d + 9.5 & \text{if } 0 \leq t_d < 3 \\ -4.5 & \text{if } 3 \leq t_d < 9 \\ t_d - 13.5 & \text{if } 9 \leq t_d < 24 \end{cases}$$

The authors state that the above model gives good agreement between predicted and actual mid-layer temperatures over a range of 5 to 45°C.

Ovik *et al.* (1999) presents an analysis of temperature data from the MnRoad test site in Minnesota. The goal for these researchers was to quantify the relationships between climatic factors and pavement mechanical properties for use in mechanistic-empirical pavement design. A falling weight deflectometer was employed to measure the mechanical response of pavements to load at various times of the year. Data from the instrumented roadway gave the pavement temperature. The measured temperature data was compared with an equation presented in Andersland and Anderson (1978) and is given as follows:

$$T(x,t) = T_{\text{mean}} + Ae^{-x\sqrt{\frac{2\pi}{P\alpha}}} \sin\left(\frac{2\pi}{P} \times t - x\sqrt{\frac{2\pi}{P\alpha}}\right) \quad (2.78)$$

where

$T(x,t)$ = temperature at depth, x and time, t (°C);

x = depth from surface (m);

T_{mean} = average temperature at surface (°C);

A = maximum temperature amplitude = $T_{\text{max}} - T_{\text{mean}}$ (°C);

$$\omega = \frac{2\pi}{P} = \frac{2\pi}{365};$$

P = period or recurrence cycle;

α = thermal diffusivity, assumed to be 0.121 m²/day; and

t = time measured from when the surface temperature passes through T_{mean} (days).

The authors reported that Equation 2.78 gave close approximations to the actual measured temperature at the MnRoad site. In addition, Birgisson *et al.* (2000) utilize data from the MnRoad project to compare predicted pavement temperatures and base course moisture contents using the FHWA Integrated Climatic Model. The authors reported good correlations between predicted and actual values. The model presented by Ovik *et al.* (1999) are given as to be used in predicting a daily pavement temperature and not an hourly distribution as are the models presented by Park *et al.* (2001) and Marshall *et al.* (2001).

FHWA Integrated Climatic Model

An integrated model was developed through research between FHWA and Texas Transportation Institute (TTI) (Lytton *et al.*, 1993) to provide a comprehensive model encompassing all factors to describe the environmental effects on pavements. The climatic model is made up of several components: the Precipitation Model, the Infiltration and Drainage Model, the Climatic-Materials-Structural Model, and the Frost Heave/Thaw Settlement Model. These components are then combined to perform an overall analysis of the pavement and subgrade. The user can add detailed climatic information for specific sites, or employ the provided average data for nine climatic zones in the United States. The model was developed to utilize historical data to give an average expected result of climatic conditions.

The Precipitation Model is a statistical database of precipitation events for various climatic areas of the United States. Through this model, the user may determine the probability of rain occurring during certain time periods and the historically based amount of precipitation that can be expected. The historical data is based from 30 years of observations from National Oceanic and Atmospheric Administration (NOAA) first order weather stations. This model provides input to the Infiltration and Drainage Model. One assumption for this model is that all precipitation occurs in the form of rain. No allowances for snow, sleet, etc. are made. Thus, according to this assumption, at mean monthly temperatures less than -1°C , infiltration of moisture ceases.

The Infiltration and Drainage Model, developed at Texas A&M University, allows for drainage analysis of saturated base courses, design based on an empirical assessment of the drainage characteristics for the base course materials, and analysis of infiltration of moisture into the base course and subgrade moduli from data obtained from the Precipitation Model. The Climatic-Materials-Structural Model, developed at the

University of Illinois, incorporates weather related data to calculate pavement temperature profile, changes in stiffness of asphalt courses, and resilient modulus and Poisson's ratio of base courses. Inputs into this model include percent sunshine, wind speed, air temperature, solar radiation, pavement geometry, and pavement material properties. The Frost Heave/Thaw Settlement Model, developed at the Army Corps of Engineers Cold Region Research and Engineering Laboratory, deals with heat and moisture flow within soils. The soil temperature is derived from the CMS model estimates for pavement temperature, thus estimates of frost depth can also be made.

A study of the effectiveness and sensitivity of the integrated climatic model was performed by Solaimanian and Bolzan (1993). The sensitivity of various parameters was analyzed, including: air temperature, percent sunshine, solar radiation, and pavement emissivity, absorptivity, and thermal conductivity. The effectiveness was analyzed by comparing outputs from the model with measured pavement temperatures from various sites in the United States and Canada during summer and winter conditions. The variables listed above were estimated. The predicted values tended to underestimate the actual pavement temperatures by 4 to 18%. However, below a depth of approximately 50mm the prediction improved. The surface temperature, based on the air temperature, was predicted within 1.1°C. The authors suggested that additional testing needed to be undertaken for better approximations to thermal values (emissivity, absorptivity, and thermal conductivity).

Considerations on Prediction Accuracy

It may be unavoidable to have some discrepancy between predicted and measured pavement temperature values due to the number of variables that could be considered. The number of these input variables will depend upon a balance of the accuracy and the complexity of the model. One important topic that merits discussion (albeit brief in this work) when considering the accuracy of temperature prediction is the measurement of surface temperature. This is not such an arbitrary quantity that a thermometer at ground level can accurately measure it. Many of the aforementioned models utilize air temperature, surface temperature, or both in their prediction. In fact, Geiger (1965) dedicates an entire volume to the treatment of this topic. Factors that can influence the surface temperature include: solar radiation, air temperature, wind speed, cloud cover, time of day, distance from the surface, and physical properties of the material at the surface (Solaimanian and Kennedy, 1993). Not only are there atmospheric effects to

consider, but also the pavement itself presents many variables that can influence the movement of thermal energy. Factors such as color (especially when discussing surface absorptivity), percent voids, moisture content, and orientation to the horizontal may also be important to consider when discussing thermal energy within a pavement structure (Solaimanian and Kennedy, 1993). The research at the Virginia Smart Road made a concentrated effort to account for as many of the variables as practical while still offering data that could be utilized outside the university research setting (e.g., state DOT's).

CHAPTER 3

ENVIRONMENTAL MONITORING AT THE VIRGINIA SMART ROAD

3.1 VIRGINIA SMART ROAD

Construction on the Virginia Smart Road began in 1997 to provide a direct connection between the town of Blacksburg, Virginia and Interstate 81. Through cooperation between Virginia Tech and the Virginia Department of Transportation (VDOT), the Virginia Smart Road also became a test facility incorporating various types of transportation related research. As part of this research, the pavement test facility was constructed. The pavement test facility is approximately 2.5km in length, of which 1.3km is flexible pavement that is divided into 12 sections of approximately 100m each. Each flexible pavement test section is comprised of a multi-layer pavement system and possesses a unique structural configuration. Each layer in each section is instrumented to measure quantitative pavement responses to traffic loading and environmental conditions using instruments such as pressure cells, strain gages, resistivity probes, thermocouples, and TDR probes. One underground bunker, containing a data acquisition system, collects data from all instrument types for every two pavement sections. During instrument installation, all the wires from each instrument in the two sections were brought to their respective bunker and were connected to the data acquisition system. Each of the six data acquisition systems is connected to the Virginia Smart Road control center where the data can be remotely retrieved and stored.

The Virginia Smart Road differs from other types of pavement testing (e.g., LTPP) in that the instruments were placed in the roadbed during the construction process and not “retrofitted” after construction. It is intended that this situation places the instruments within the pavement without disturbing the natural response of the pavement structure. The 12 pavement structural configurations are designated as Sections A through L. Sections A through E are located in a fill area with approximately 1-3.5% longitudinal slope and Sections F through L are located in a cut area having a longitudinal slope of approximately 4-6%.

The structural configurations of the 12 pavement sections are shown in Figure 3.1. Section A has a SM-12.5 (surface HMA with a nominal maximum particle size of 12.5mm) while Sections B through D have a SM-9.5 (surface HMA with a nominal maximum particle size of 9.5mm). Although Sections B through D each have a SM-9.5 for the surface HMA, the asphalt binder employed is somewhat different between the three sections. The surface HMA for Sections B, C, and D is classified as SM-9.5D, SM-9.5E, and a SM-9.5A, respectively. The letter designations with the HMA mixes denote a modified asphalt binder. The letters A, D, and E (as in SM-9.5A) denote a PG 64-22, 70-22, and 76-22 asphalt binder, respectively. The surface layer for Section E is a 38mm-thick SM-9.5D. The 38mm-thick surface layer for Sections H and I is a SM-9.5D and a SM-9.5A, respectively. The surface layer for Section L is a 38mm-thick stone mastic asphalt (SMA) having a nominal maximum particle size of 12.5mm. The surface layer in both Sections F and G is a 38mm-thick layer of SM-9.5D surface HMA. In Section J, a 38mm-thick layer of SM-9.5D surface HMA was placed. In Section K, a 19mm-thick open graded friction course (OGFC) was placed as the surface HMA followed by a 19mm-thick layer of SM-9.5D.

The materials detailed in Figure 3.1 were given layer number designations that are used across all 12 pavement sections. Layer 1 represents all SM surface HMA. Layer 2 represents all BM base HMA. Layer 3 represents all SM mixes placed as a base HMA. Layers 4 and 5 represent all OGD and 21A layers, respectively. And layers 6 and 7 represent the 21B and subgrade, respectively.

As part of the research into new pavement technologies at the Virginia Smart Road, several new technologies were also placed within the pavement during the construction process. A galvanized reinforcing mesh was placed at the interface between layers 2 and 3 in Section I and between layers 2 and 4 in Section L (since there was no SM mix [layer 3] placed as a base). A moisture barrier geocomposite membrane was placed at the interface between layers 4 and 6 in Section J (again, with no 21A in Section J). A stress relieving geocomposite membrane (which also acts as a moisture barrier) was placed at approximately one-third the depth of layer 2 in Section K. In addition, a non-woven geotextile was placed between the 21B aggregate subbase and the subgrade (interface between layers 6 and 7) in Sections B, C, D, E, and G.

3.1.1 INSTRUMENTATION NOMENCLATURE

The individual probes are labeled according to the following format: STL-NP where S indicates the section (A through L), T indicates the type of probe (M indicates TDR probe and T indicates thermocouple), L indicates the layer (1 through 7), N indicates the number or replicate of the probe at that location, and P indicates the position within the layer (T indicates the top of the layer, M the middle, and B the bottom). The CS610 probes also include an extra E on the end of the STL-NP designation to differentiate between the two types of TDR probes. For example, BM6-1M and BM6-1ME indicate a CS615 and a CS610 TDR probe, respectively, at the same location.

Material	Section / Thickness (mm)								
	A-D	E	F	G	H	I	J	K	L
OGFC HMA wearing surface	-	-	-	-	-	-	-	19	-
HMA wearing surface	38	38	38	38	38	38	38	19	38
HMA base	150	225	150	100	100	100	225	244	150
HMA surface (placed as base)	-	-	-	50	50	50	-	-	-
Asphalt Stabilized OGDL	75	-	-	-	75	75	75	-	-
Cement Stabilized OGDL	-	-	-	-	-	-	-	75	75
Cement Stabilized Aggregate Base	150	150	150	150	150	150	-	-	150
21B Aggregate Subbase	175	75	150	150	75	75	75	150	75

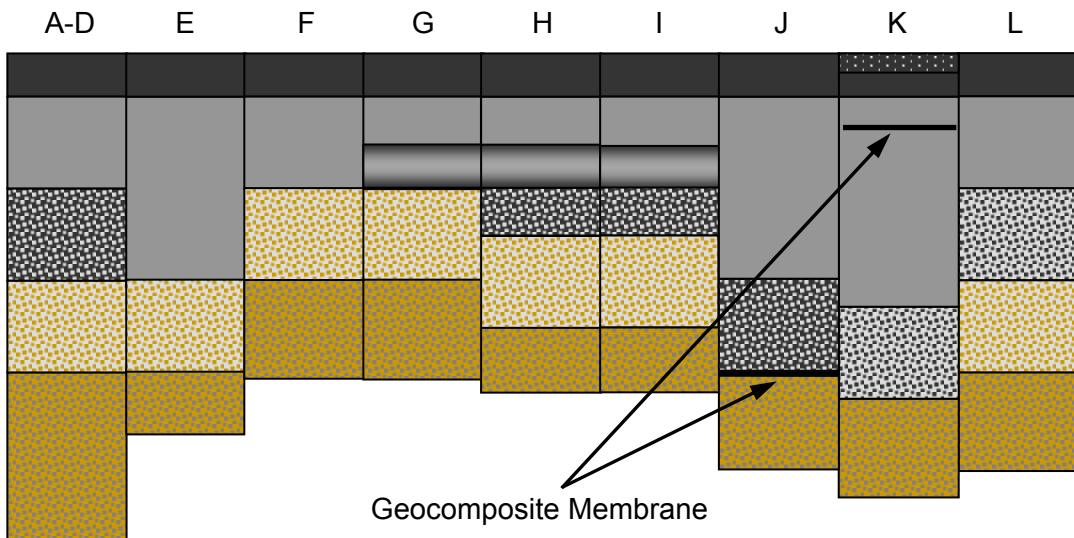


Figure 3.1. Structural configuration of Virginia Smart Road.

3.2 PAVEMENT MOISTURE

At the Virginia Smart Road, two types of TDR probes were used: the CS610 and the CS615. The CS610 and CS615 (a three and a two rod TDR probe, respectively) are both manufactured by Campbell Scientific, Inc., Logan, Utah. The CS610 and similar type probes have been used previously, however the CS615 represents a new development and thus no previous experience with this type of TDR probe was reported in the general literature.

3.2.1 PROBE TYPES

CS610

The CS610 TDR probe, shown in Figure 3.2 is comprised of three parallel conducting rods that are 300mm in length and 5mm in diameter. A distance of 22mm separates the rods. The rods are held rigidly in place on one end by an epoxy head that is 111 mm x 63 mm x 20 mm in size. Output from the CS610 TDR probe is given as a voltage or reflection coefficient versus time. From analysis of the reflected signal, the velocity of the electromagnetic wave along the probe can be determined. When the TDR probe is inserted into a granular material, the travel time of the applied pulse along the probe length is dependent upon the soil water content. Soil moisture content possesses an inverse relationship with velocity of propagation; therefore the relationship is directly related to time. The propagation velocity (v) of an electromagnetic wave traveling along a waveguide in a dielectric material is given as the following:

$$v = \frac{c}{\sqrt{\epsilon'}} \quad (3.1)$$

where,

c = velocity of an electromagnetic wave in free space (3×10^8 m/s); and

ϵ' = real part of the dielectric constant.



Figure 3.2. CS610 TDR probe.

Referring to Davis and Annan (1977), Topp *et al.* (1980) stated that the real part of the dielectric constant of soil did not appear to be strongly frequency dependent over the frequency range of 1 MHz to 1 GHz. Based on this qualification, it was inferred that no relaxation mechanisms exist which impart a temperature dependence to the real part of the dielectric constant for soils. Thus, Topp assumed that the real part of the dielectric constant of soil could be assumed to be equal to the complex dielectric constant. The real part, which Topp called the measured or apparent dielectric constant (ϵ_a), can be found as follows:

$$\epsilon_a = \left(\frac{ct}{l} \right)^2 \quad (3.2)$$

where,

c = velocity of an electromagnetic wave in free space (3×10^8 m/s);

t = the one-way travel time of the electromagnetic wave as measured by the TDR system (sec); and

l = the length of the TDR transmission line (m).

The main result from Topp *et al.* (1980) was the development of a universal empirical relationship to find the volumetric water content (θ_v) in terms of the apparent dielectric constant. This equation, termed universal since it was considered independent of soil density, texture, and salt content, is as follows:

$$\theta_v = -5.3 \times 10^{-2} + 2.92 \times 10^{-2} \epsilon_a - 5.5 \times 10^{-4} \epsilon_a^2 + 4.3 \times 10^{-6} \epsilon_a^3 \quad (3.3)$$

Topp *et al.* (1980) and Rada *et al.* (1994) recommend that if users of Equation 3.3 should require a more accurate determination of moisture content, a series of calibration measurements should be performed. This calibration can be completed by measuring the moisture content as reported using the TDR probe and comparing it to the moisture content received by another method (such as the gravimetric method by oven drying a sample). Topp *et al.* (1980) and Rada *et al.* (1994) cite differences of up to 1.3% for mineral soils and up to 10% for clay subgrades, respectively, between moisture contents from TDR measurements using Topp's equation and gravimetric measurements.

CS615

The CS615 TDR probe, shown in Figure 3.3 is comprised of two parallel conducting rods that are 300mm in length and 2.5mm in diameter. A distance of 32mm separates the rods. The rods are held rigidly in place on one end by an epoxy head that is 110mm x 63mm x 20mm in size. The epoxy head contains electronic components configured as a bistable multivibrator. The oscillation frequency of the multivibrator is dependent upon the dielectric constant of the material surrounding the conducting rods. Circuitry within the probe head scales the multivibrator output in terms of a frequency for measurement with a data acquisition system. The period of the square wave from the multivibrator ranges from 0.7 to 1.6 milliseconds (Campbell Scientific, 1996). Thus, the moisture content given by the CS615 also dependent upon the travel time of a pulse along the conducting rods.

The frequency output from the CS615 TDR probe can be converted into the volumetric moisture content by using the equations provided by the manufacturer (with a manufacturer specified accuracy of $\pm 2\%$). As with the CS610 TDR probe, greater accuracy can be achieved by developing calibration equations from comparisons between moisture contents using the TDR method and gravimetric methods (oven drying). The manufacturer's equations, which vary depending on the soil's conductivity, are expressed as follows:

$$\theta_V(t) = -0.187 + 0.0307t + 0.335t^2 \quad (3.4)$$

$$\theta_V(t) = -0.207 + 0.097t + 0.288t^2 \quad (3.5)$$

$$\theta_V(t) = -0.298 + 0.361t + 0.096t^2 \quad (3.6)$$

where t = the CS615 output expressed as time in milliseconds. According to the manufacturer, Equations 3.4 through 3.6 are to be used for soils with an electrical conductivity of less than 1.0, 1.8, and 3.0 dS/m, respectively.



Figure 3.3. CS615 TDR probe (after Campbell Scientific, 1996).

3.2.2 CALIBRATION MODEL DEVELOPMENT

Calibration measurements were performed on mineral aggregate used as subbase layer material at the Virginia Smart Road. The Virginia Department of Transportation (VDOT) classifies the material as 21B. The gradation of this material is shown in Figure 3.4. The calibration procedure was performed using a wooden calibration box filled with 21B material mixed with known quantities of water to achieve different moisture contents. A wooden calibration box (840mm x 840mm x 450mm) was constructed, using no metallic fasteners, to contain the 21B material and the probes during the calibration process. The calibration box was large enough to allow four probes to be tested simultaneously without adversely affecting the measurements. A schematic of the calibration box is shown in Figure 3.5. To evenly mix water with 21B material, a 0.4m³ concrete mixer was used to mix approximately 40kg of 21B material per batch. This batching procedure was repeated until enough 21B material had been mixed with the desired amount of water to fill the calibration box; approximately 14 batches.

The 21B material was placed in the calibration box in three layers. Each layer, approximately 150-mm-thick, was placed and compacted before the following layer was placed. All four TDR probes were placed within the middle layer, separated by at least 150mm. After the probes were placed, the remainder of the material comprising the

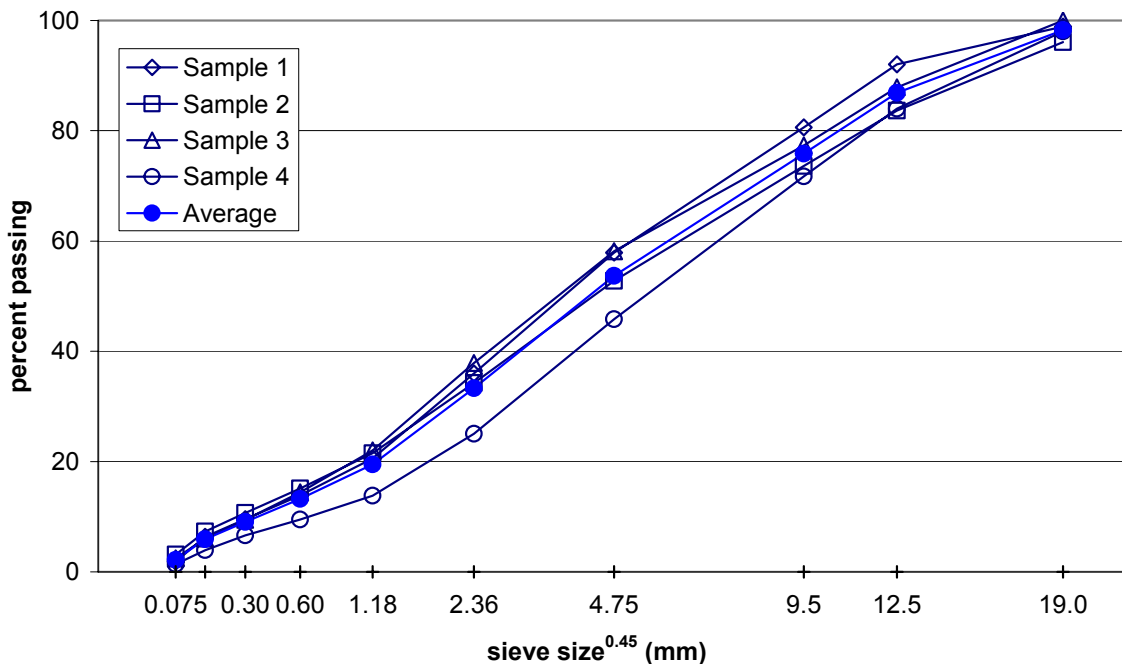


Figure 3.4. Gradation of 21B subbase layer aggregate.

middle layer was placed and compacted. Finally, the third layer was placed and compacted. After readings were obtained with the TDR probes, approximately four kg of 21B material was removed from the center of the middle layer and placed in an oven for 24hrs at 110°C so that the gravimetric moisture content could be determined. To determine the volumetric moisture content, the density of the 21B material was also calculated by weighing a smaller container (approximately 0.014m³) that was filled with 21B and compacted in the same manner as the calibration box.

To ensure that the calibration box was of sufficient size to minimize effects on the measurement of the moisture content, a test was performed using two CS610 TDR probes. One probe was placed in the calibration box, following the installation procedure described above, and the moisture content from this probe was taken as a control (a schematic is shown in Figure 3.6a). After removing the 21B, a second TDR probe was added across from the control probe (Figure 3.6b) according to the installation procedure. Again the moisture content using the control TDR probe was found. The 21B material was removed again and the second TDR probe was placed beside the control probe (Figure 3.6c) following the installation procedure and the moisture content from the control probe was again determined. The results of the calibration box dimension testing are shown in Table 3.1. It was concluded that the differences were well within the anticipated experimental and operational error.

CS610 Calibration

Output data from the CS610 TDR probe was collected using a PC connected to a Tektronix 1502B Metallic Cable Tester. The cable tester was controlled using WinTDR98, a data collection software program developed by Utah State University specifically for the CS610 TDR probe. The software allows the user to window around

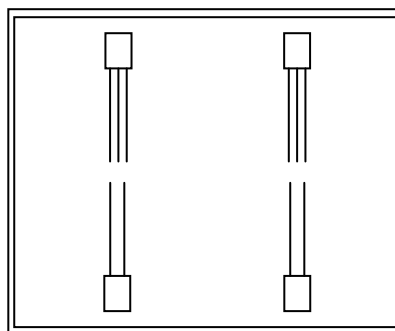


Figure 3.5. Top view of TDR calibration box showing orientation of CS610 and CS615 TDR probes.

the desired area of the reflected waveform and to save 250 points of data within that window. The width of the visible window was set to an effective length of either 1 or 2.5m, depending on the moisture content. The usage of two window sizes was necessary since at volumetric moisture contents near 20%, the effective length of the probe increased beyond the 1m setting within the software.

An independent determination of the moisture content for each trial was performed following ASTM 2216-94, moisture content determination using oven methods. The gravimetric moisture content was determined by collecting approximately four kg from each moisture content trial mixture. The volumetric moisture content was calculated as the product of the soil dry unit weight and the gravimetric moisture content. Calibration equations were determined by correlating the effective length of the CS610 TDR probe with the calculated volumetric moisture content.

The effective length of the TDR probe can be found from the waveform of the reflected response from the CS610 TDR probe using several methods, namely the method of tangents and the method of peaks. However, according to previous research

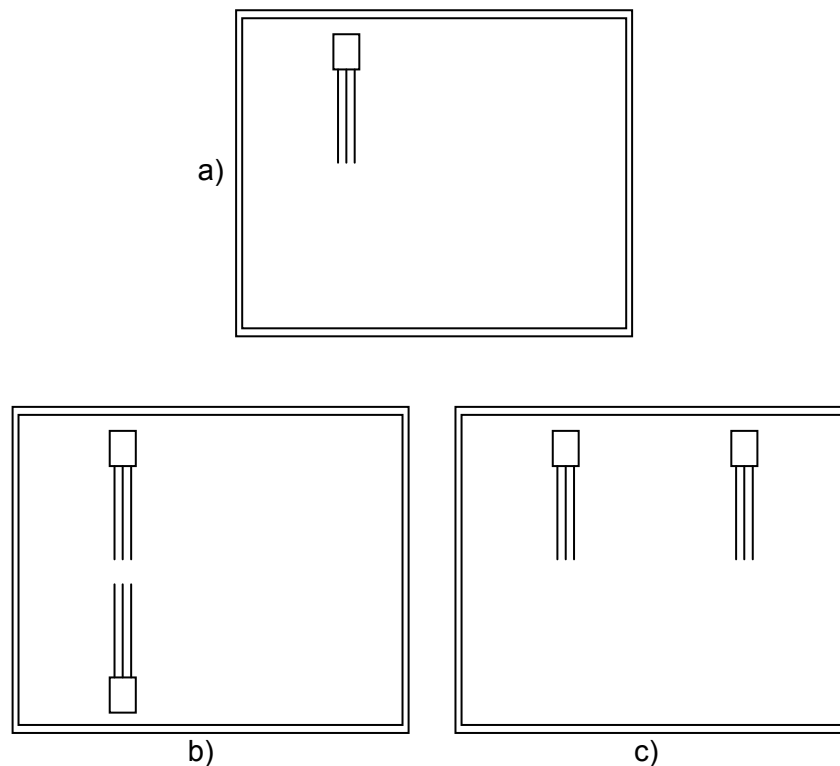


Figure 3.6. Schematic of testing to determine influence of TDR calibration box size using CS610 TDR probe where a) control, b) one probe across from control, and c) one probe beside control.

(Klemunes, 1995; Jiang and Tayabji, 1999), the most accurate is the method of tangents. These two methods differ by the way the maximum and minimum of the reflected TDR response (associated with the coaxial/TDR probe interface and the open end of the TDR probe) are located. Locating the maximum and minimum peaks using the method of tangents is performed by first taking the derivative of the equation describing the waveform of the reflected response. During the calibration procedure, the derivative was performed using the central-difference equation (Applied Numerical Methods, 1985), given as the following:

$$y' = \frac{-y_{i+2} + 8y_{i+1} - 8y_{i-1} + y_{i-2}}{12h} \quad (3.7)$$

where h is the distance between two consecutive data points. According to the method of tangents, the maximum negative derivative following the local maximum associated with the coaxial/TDR probe interface must be located. When the derivative is known, the equation of a tangent line at this point can be found. The intersection of this tangent line with a horizontal at the local maximum marks the initial reflection point (see Figure 3.7). Next, the maximum positive derivative following the local minimum associated with the open end of the TDR probe must be found. Again, when the derivative is known, the equation of a tangent line at this point can be found. The intersection of this tangent line with a horizontal line at the local minimum marks the final reflection point (Figure 3.7). The effective probe length is taken as the difference between the initial and final reflections, as determined using the method of tangents. The dielectric constant can be found according to Equation 3.2.

Calibration of the CS610 TDR probes was performed on 21B material having volumetric moisture contents of approximately 5, 9, 10, 11, 13, and 16%. The TDR probes used during the calibration had different coaxial cable lengths; 25.6 and 26.4 m.

Table 3.1. Results of testing to determine influence of TDR calibration box size using CS610 TDR probe showing moisture content from control, one probe across from control, and one probe beside control.

Test	Volumetric Moisture Content (ω)	% Difference
control	9.0950	-----
beside	9.0930	0.0220
across	9.0980	-0.0330

To see if a difference existed in the response between these two coaxial cable lengths, the probe responses were treated independently. Table A.1 (Appendix A), lists the effective length from each probe using the two procedures for determining the effective length at each calculated volumetric moisture content. Curves plotting the effective length versus volumetric moisture content were used to generate empirically based calibration equations. Three linear equations (one for each probe and one for the average of the two probes) were developed based on the data analysis yielding the volumetric moisture content from measurement of the effective length. The first three calibration curves (Equations 3.8 through 3.10) were developed using the effective length as determined from analysis of the waveform using the method of tangents. The remaining equations were generated using the WinTDR98 software to directly compute the effective length (Equations 3.11 through 3.13). The calibration equations are presented as follows, where ω is the volumetric moisture content and λ represents the effective length in m:

$$\omega = 23.404\lambda - 8.4452 \quad (3.8)$$

$$\omega = 22.378\lambda - 7.8526 \quad (3.9)$$

$$\omega = 22.903\lambda - 8.1623 \quad (3.10)$$

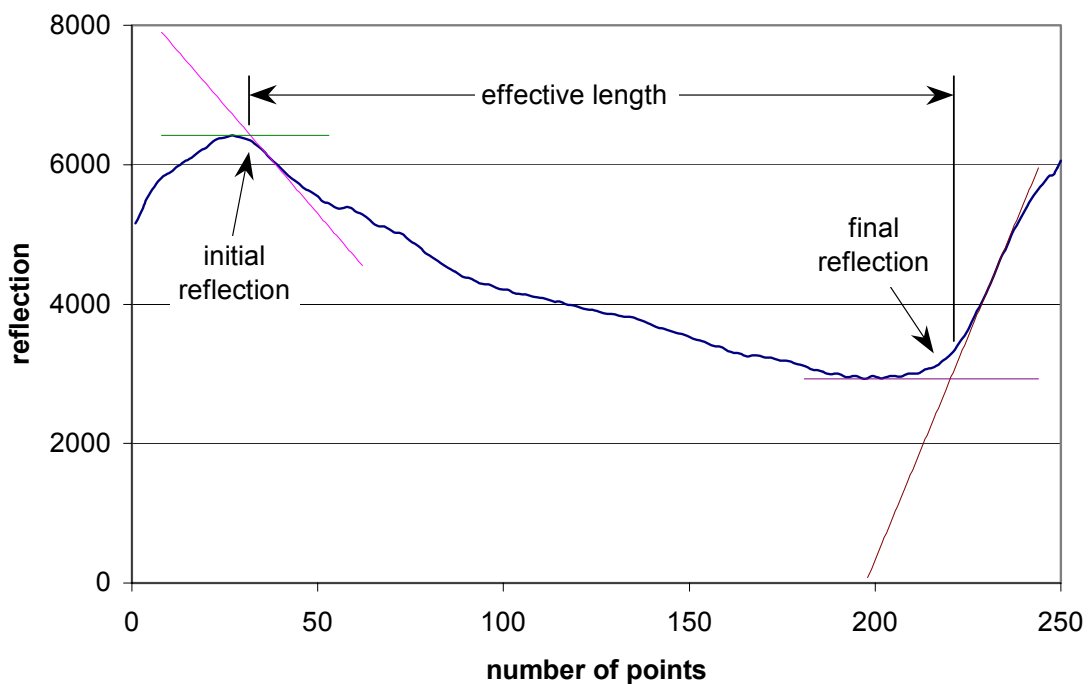


Figure 3.7. Typical waveform from a CS610 TDR probe.

$$\omega = 23.24\lambda - 8.85 \quad (3.11)$$

$$\omega = 21.981\lambda - 8.076 \quad (3.12)$$

$$\omega = 22.709\lambda - 8.5526 \quad (3.13)$$

The moisture content values obtained by Equations 3.8 through 3.13 for each calculated volumetric moisture content are shown in Table A.2, Appendix A. A summary of the errors for the CS610 calibration process is presented in Appendix A, Table A.3. Statistical analysis, through calculation of the root-mean square error (RMSE), shows that the analysis of the waveform (Equation 3.10) is the most representative model. Figure 3.8 shows the effective length versus volumetric moisture content for the two CS610 probes and the calibration model using Equation 3.10. Also shown is the volumetric moisture content calculated from Topp's Equation (Equation 3.3). It can be seen from Figure 3.8 that Topp's Equation does not correlate well with the calibration data and thus was not utilized in further data analysis. Reasons for this high variation may include differences between the 21B material and the finer-grained mineral soils used by Topp to develop Equation 3.3.

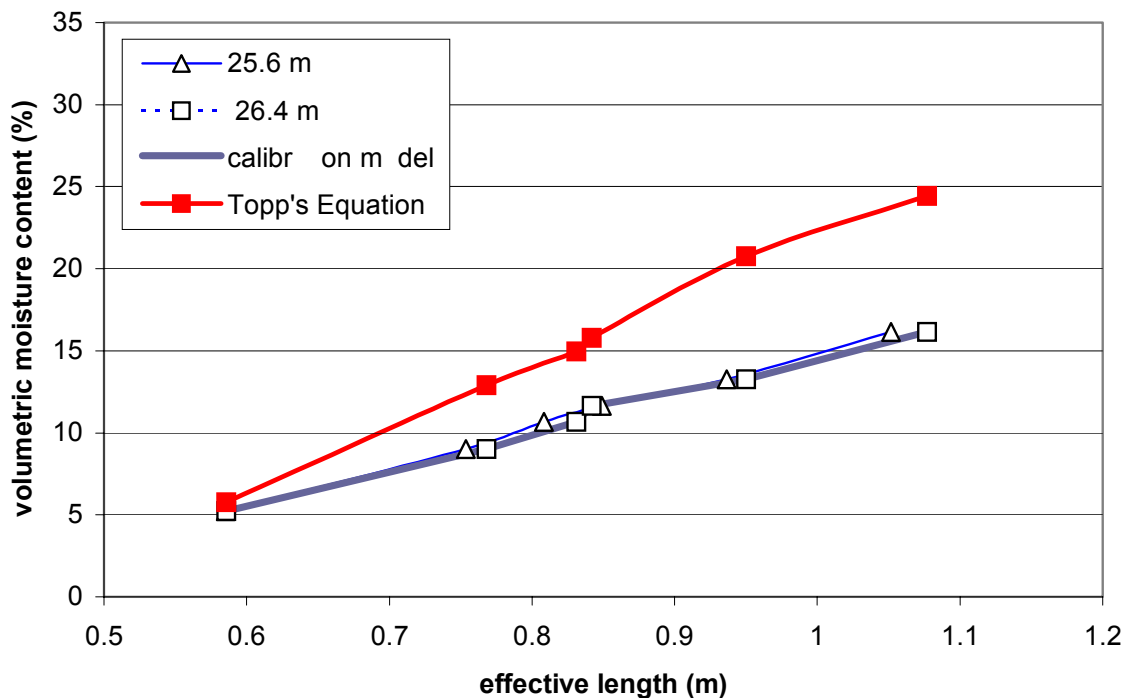


Figure 3.8. Volumetric moisture content for two CS610 TDR probes, the developed calibration model, and results from Topp's Equation (Equation 3.3).

CS615 Calibration

Output data from the CS615 TDR probe was collected using a PC connected to a DaqBook data acquisition system manufactured by IOtech, Inc. Through use of the DaqBook software, the probes collected data at a rate of 1 Hz for 50 readings. The averaged result of these measurements yields a frequency that varies depending on the dielectric constant of the material surrounding the TDR probes. As the moisture content increases, the frequency output decreases. An independent determination of the moisture content for each trial was performed following ASTM 2216-94, moisture content determination using oven methods. The gravimetric moisture content was determined by collecting approximately four kg from each moisture content trial mixture. The volumetric moisture content was calculated as the product of the soil dry unit weight and the gravimetric moisture content. Calibration equations were determined by correlating the period of oscillation (ms) of the CS615 TDR probe with the calculated volumetric moisture content.

The volumetric moisture content of the 21B material during the calibration process using the CS615 TDR probes ranged from approximately 1 to 22%. The probes used in the calibration process had different cable lengths: 22 and 27m. The different cable lengths represented what would be later used at the Virginia Smart Road. Output (frequency and period of oscillation at each moisture content) from the CS615 TDR probes is presented in Table A.4, Appendix A. Results of the calibration showing the period of oscillation versus the calculated volumetric moisture content were graphed to determine empirically based calibration equations. Three second-order (Equations 3.14 through 3.16) and three third-order (Equations 3.17 through 3.19) calibration equations were developed from the data. Each set of three equations shows the results of the 22m probe, the 27m probe, and the average of both CS615 TDR probes. The calibration equations are presented as follows, where ω is the volumetric moisture content and t represents the period of oscillation in ms:

$$\omega = -68.16t^2 + 179.07t - 96.92 \quad (3.14)$$

$$\omega = -64.08t^2 + 169.82t - 92.43 \quad (3.15)$$

$$\omega = -66.38t^2 + 174.90t - 94.89 \quad (3.16)$$

$$\omega = 568.21t^3 - 1726.7t^2 + 1776.7t - 604.95 \quad (3.17)$$

$$\omega = 352.44t^3 - 1136.4t^2 + 1243.4t - 446.2 \quad (3.18)$$

$$\omega = 444.04t^3 - 1389.6t^2 + 1474.6t - 515.72 \quad (3.19)$$

Equations 3.14 through 3.16 represent the second-order trend lines derived from the data for the 22m, 27m, and average of the 22m and 27m probes, respectively. Equations 3.17 through 3.19 represent the third-order trend lines derived from the data for the 22m, 27m, and average of the 22m and 27m probes, respectively. The moisture content values obtained by Equations 3.14 through 3.19 for each calculated volumetric moisture content are shown in Table A.5, Appendix A. A summary of error for the above equations can be found in Table A.6, Appendix A. It appears from the analyses presented in Table A.6 that no significant effect results from the difference in the cable length and Equation 3.16 is the most representative model. Figure 3.9 shows the period of oscillation versus volumetric moisture content for the two CS615 TDR probes and the

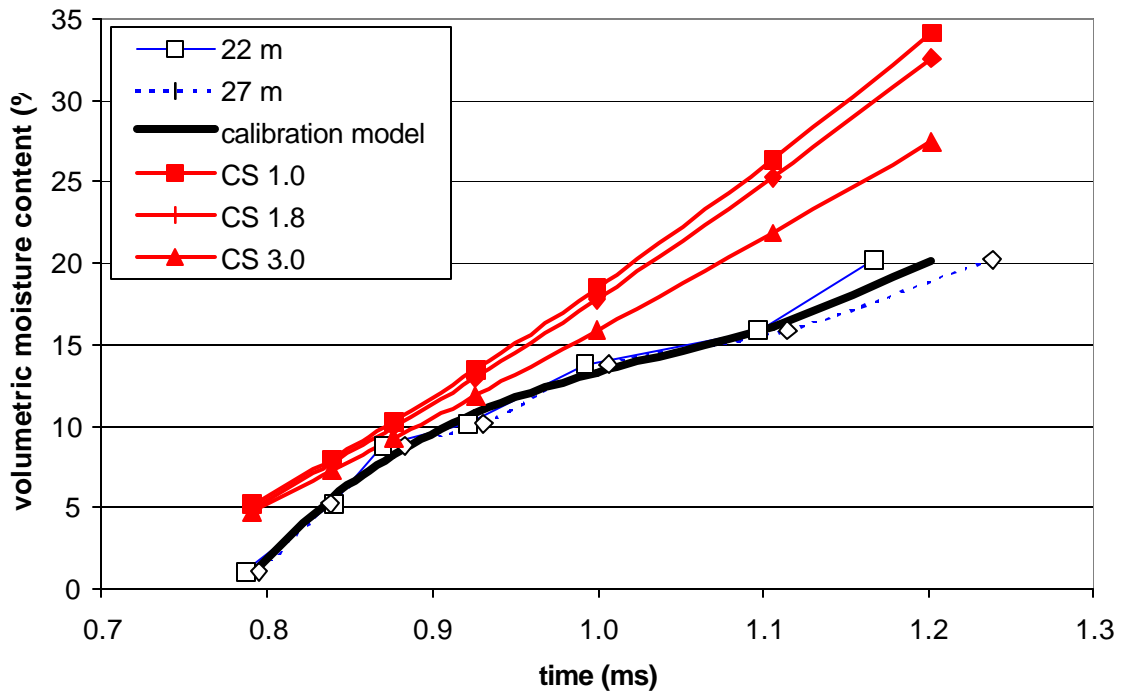


Figure 3.9. Volumetric moisture content for 22-m wire length and 27-m wire length CS615 TDR probes, developed calibration model (Equation 3.16), and manufacturer equations for three values of soil conductivity (Equations 3.4 through 3.6).

calibration model from Equation 3.16. Also shown, are the volumetric moisture contents for soils of varying conductivity (≤ 1.0 , 1.8, and 3.0 dS/m) determined using equations provided by the probe manufacturer (Equations 3.4 through 3.6). It can be seen in Figure 3.9 that the equations provided by the manufacturer do not correlate well with the calibration data. Thus, the developed calibration model was used in predicting the volumetric moisture content in future analysis. Again, it is postulated that the differences can be attributed to differences in particle sizes between the 21B and finer-grained mineral soils that were likely used to develop the manufacturer equations.

3.2.3 TIME-DOMAIN REFLECTOMETRY PROBE PLACEMENT

Time-domain reflectometry (TDR) probes were placed at the Virginia Smart Road to determine if differences exist in the moisture content due to the pavement structural configuration and inclusion of a geocomposite moisture barrier. As with the other instruments, the TDR probes were placed as each layer was constructed. The instrument locations were established through survey. From this location, a small trench was dug in the pavement material toward an underground bunker where the data acquisition system was located. The depth of the trench was just enough to allow the wires from the instruments to be slightly below the surface of the layer in which the instruments were placed. The small trenches containing wires from each instrument were connected into a slightly larger main trench containing all the wires from each instrument in that particular section and layer. Wires in the smaller trenches were wrapped in an asphalt-impregnated geosynthetic to protect them when the overlying material was placed. Once all the wires reached the main trench, they were all wrapped in the same geosynthetic, as a group, all the way to the data acquisition bunker. The epoxy head of the TDR probe was surrounded with Ottawa sand to protect it from puncture; care was taken to ensure that only the TDR probe head was surrounded with sand and not the TDR probe rods.

The locations of the CS610 and CS615 TDR probes are shown in Tables 3.2 and 3.3, respectively. A more detailed description (showing locations of the individual TDR probes) is given in Table B.1, Appendix B. In total, 79 TDR probes were installed; 31 CS610 TDR probes and 48 CS615 TDR probes.

3.3 PAVEMENT TEMPERATURE

The temperature within the pavement at the Virginia Smart Road is monitored using T-type thermocouples. As opposed to thermistors, that report a temperature change, the output from the thermocouples can be directly computed as actual temperature values.

Table 3.2. Location of CS610 TDR probes at the Virginia Smart Road, showing number of probes by section.

Layer	Depth from Surface (m)	Section											
		A	B	C	D	E	F	G	H	I	J	K	L
4	0.263		1						1	1			1
	0.338										1		
	0.356											1	
5	0.413		1			1				1			
6	0.488					1	1	1	1	2	2		2
	0.506										2		
	0.588		1										
7	0.638							2					
	0.993		1										
	0.994	1											
	0.996						1						
	1.02		1										
	1.147	1											
1.238							2						

Table 3.3. Location of CS615 TDR probes at the Virginia Smart Road, showing number of probes by section.

Layer	Depth from Surface (m)	Section											
		A	B	C	D	E	F	G	H	I	J	K	L
4	0.263	2	2		2				2	2			2
	0.338										2		
	0.356											2	
5	0.413		2			2				2			
6	0.488					2	2	1	2		2		2
	0.506										2		
	0.588		2										
7	0.638							2					
	0.738		2										
	0.918	1											
	0.945	1					1						
	0.996						1						
	1.096		1										
1.121		1											
1.238							1						

3.3.1 THERMOCOUPLE PREPARATION AND CALIBRATION

The thermocouples used at the Virginia Smart Road were fabricated in-house from T-type thermocouple wire. The T-type thermocouple wire consists of a stranded constantan and copper wire pair. After the wire pair was twisted and soldered, it was inserted into a 6.4mm inside diameter copper tube. The copper tubing was connected to the T-type thermocouple wire using heat shrink tubing. Type TFM Inner Mount-Melt Heat Shrinkable Teflon Tubing was chosen due to its maximum service temperature of 230°C. Epoxy (3M DP-270 electrical grade) was used to surround and protect the thermocouple wire within the copper tubing. The thermocouple wire was not spliced as each was cut to the full in-service length. After fabrication, the response from the thermocouples was checked at two reference temperatures using an ice-water bath and a container of boiling water. The response from each thermocouple was recorded and is presented in Table C.1, Appendix C. From this procedure it was determined that the thermocouples yielded results that were within expected operational ranges (the largest difference between measured and actual temperature was 2°C) and thus no calibration procedures for individual thermocouples were necessary. A 95% confidence interval was established and was calculated to be $\pm 1.23^{\circ}\text{C}$.

3.3.2 THERMOCOUPLE PLACEMENT

Thermocouples were placed at the Virginia Smart Road to determine the temperature at various depths from the surface of the pavement. As with the other instruments, the thermocouples were placed as each layer was constructed. The same procedure of wire protection and connection to the underground bunker, described for the TDR probes, was adopted for the thermocouples. Locations of the thermocouples are shown in Table 3.4. A more detailed description (showing locations of the individual thermocouples) is presented in Table D.1, Appendix D. In total, 115 thermocouples were installed at the Virginia Smart Road.

Table 3.4. Location of thermocouples at the Virginia Smart Road, showing number of thermocouples by section.

Layer	Depth from Surface (m)	Section											
		A	B	C	D	E	F	G	H	I	J	K	L
1 - Bottom	0.038	3	2	2	2	2	2	2	2	2	2		2
	0.149											2	
2 - Top	0.063	2	2	2	2	2	2		2	2	2		2
	0.065							2				2	
	0.118											2	
2 - Bottom	0.138							2	2	2			
	0.188	2	2	2	2	2	2						2
	0.263										2		
	0.281											2	
3 - Bottom	0.188							2	2	2			
4 - Bottom	0.263	2								2			2
	0.338										2		
5 - Bottom	0.388							2					
	0.413	2								2			2
6 - Bottom	0.488					2	2			2	2		2
	0.588	2											
7 - Top	0.638							2					
	0.74	2											
7 - Middle	0.994	1											
	1.172	1											
	1.238							2					

CHAPTER 4

DATA PRESENTATION AND ANALYSIS

4.1 PAVEMENT MOISTURE

The data pertaining to pavement moisture was collected as part of two studies, designated herein as Phase 1 and Phase 2. Data from Phase 1 consists of measurements from both the CS610 and CS615 TDR probes. Data from the Phase 1 study, obtained at the Virginia Smart Road during the period of March 1999 to May 2000, was used in making comparisons between the two types of TDR probes. The data from the Phase 2 study, collected from approximately March 2000 to May 2001 at the Virginia Smart Road, was used to make comparisons between the different pavement sections. Since a calibration procedure was only performed for the materials used in Layer 6, the analysis presented in this chapter will only involve the TDR probes from that layer. Details of the instrumentation were presented in Section 3.2.

4.1.1 MOISTURE DATA COLLECTION AND MANAGEMENT

During the Phase 1 study, the moisture content from each probe type was measured every seven to 10 days. The data from all CS615 TDR probes was collected using a computer controlled data acquisition system. The moisture content using the CS610 TDR probes was collected by manually connecting an oscilloscope (such as the Tektronix 1502B) to each individual probe. During the Phase 2 study, the moisture content from the CS615 TDR probes was continuously monitored by the computer controlled data acquisition system with one reading taken every hour. The Phase 2 data was saved as a tab-delimited text file and run through a processing program. The processing program organizes the data by section, instrument type, and also checks for compliance with a pre-determined output range. While the data acquisition system was used to control all the CS615 TDR probes, this option was not considered for the CS610 TDR probes since it would involve purchasing additional specialized equipment for the task. As a result, it became impractical to attempt a continuous data collection schedule using the CS610 TDR probes. Thus, only the CS615 TDR probes were utilized in the Phase 2 study.

Data from the Phase 2 study was used to make comparisons between the moisture content of different sections at the Virginia Smart Road. Figures E.1 through E.6, Appendix E, show the full-range of data collected for each section where CS615 TDR probes are located. The moisture content for each section was compared with precipitation to determine the effects of the pavement structural configuration on the moisture content in the 21B aggregate subbase layer. The precipitation data was collected at the National Weather Service office in Blacksburg, VA. The location of this weather station is approximately 2km from the western portion of the Virginia Smart Road. The precipitation values were obtained from the website of a local TV station (<http://www.wdbj7.com/climate/climate.htm>) where a daily summary of high and low temperature and precipitation from the National Weather Service is presented.

Phase 2, continuous monitoring of the moisture in the 21B aggregate subbase, began in March 2000, approximately five months after construction was completed on all sections. The continuous data collection continued uneventfully until two severe electrical storms in June 2000 damaged components of the data acquisition system through an electrical spike when lightning struck a nearby power transformer. Upon restarting the continuous data collection in July 2000, it appeared that the data from some of the CS615 TDR probes did not match data from before the electrical storms. Upon contacting the manufacturer, it was related that static discharge from electrical storms could cause a shift in the frequency value obtained from the CS615 TDR probes by affecting the electrical components in the probe head. This shift in the frequency caused a subsequent shift in the determined moisture content. The probes continued to react to changes in the moisture content; however the moisture content for several probes was reported as being significantly higher than the expected void content of approximately 14% by volume. Following this, it was deemed necessary to apply a shift factor to correct the values obtained by the CS615 probes that appeared to be affected by the electrical storms.

To correctly apply the shift factor, it was necessary to view the moisture content in terms of the raw probe output. The output from the CS615 probe is given in terms of a frequency value and is related to the volumetric moisture content by use of a calibration equation, described in Chapter 3.2.2. By determining a reference frequency value from the initial stages of continuous data collection, a shift factor could be calculated to return responses to “pre-electrical storm” values. An example showing results of shifted data is presented in Figure 4.1. This figure shows the responses from the two CS615 TDR

probes in the 21B aggregate subbase layer in Section K. Shift factors were determined for CS615 probes in Sections B, J, and K.

Figures E.1 through E.6, Appendix E, show the volumetric moisture content and precipitation versus date for the CS615 TDR probes in Sections B, E, H, J, and K, respectively. Although it can be seen that the moisture content varies throughout the time shown in each figure there was not any readily apparent agreement between amount of received precipitation and change in the moisture content. For each figure, the results from July 2000 throughout the remainder of the figure were scaled according to the values obtained during the period of March/April 2000. This scaling procedure was not performed for Section E where the erratic behavior of the probes did not provide enough information to establish an initial trend and thus only data for the first few months is presented. In addition, the results for only one probe are shown for Section H as one probe (HM6-1M) suddenly began to give unexplainable readings within the first few days of operation. No shift factor was determined for Section L as the probes did not appear to move beyond the range of values seen in the initial portion of the figure.

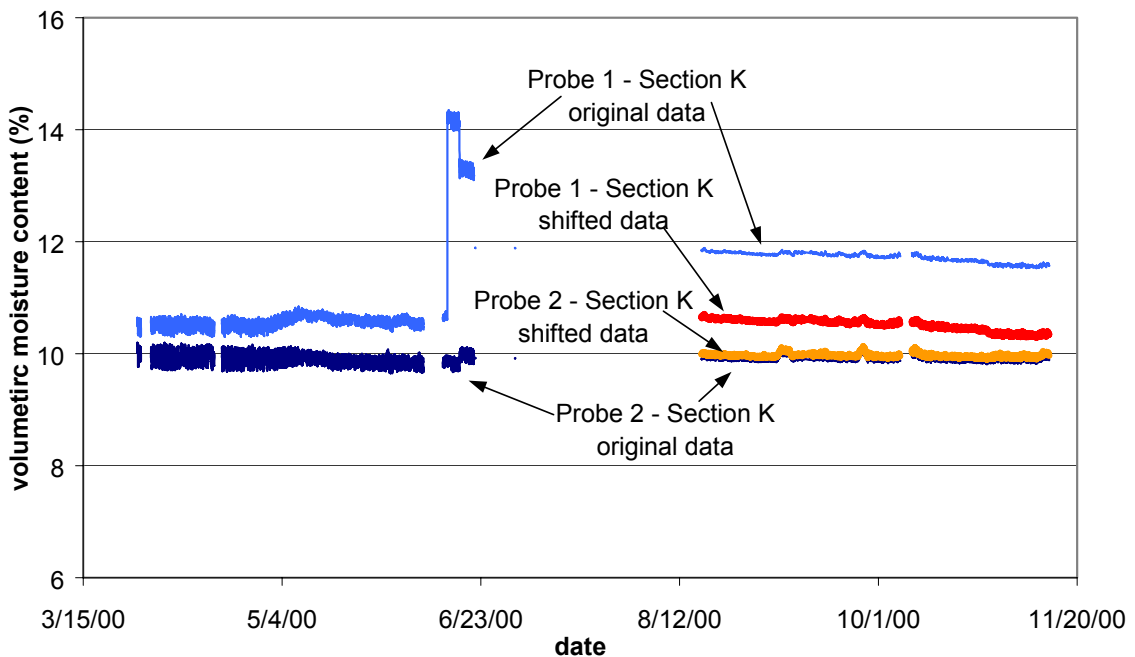


Figure 4.1. Example of CS615 TDR data from Section K that was shifted after an electrical storm showing volumetric moisture content versus date.

4.1.2 ANALYSIS OF RESULTS WITH RESPECT TO PROBE TYPE

A statistical analysis of the difference in moisture content as reported by the two types of TDR probes was performed using data obtained during the Phase 1 study. A paired t-test ($\alpha = 0.05$) assuming unequal variances showed that the two probe types across all sections were unequal. During this test, each probe of type CS610 was contrasted to each probe of type CS615 within each section. This contrast was performed only for dates where measurements were taken using both probe types (between 18 and 28 readings per section). In all cases, the probability that the means were equal was less than 0.002 except for BM6-2M versus BM6-1ME ($P = 0.51$) and EM6-1M versus EM6-1ME ($P = 0.49$). However, observation of the mean values in Table 4.1 shows that for Sections B, E, and J that the difference between the moisture contents from the different probe types is likely within the accuracy of the TDR method employed.

When considering the moisture content of all probes across all sections, the results using the CS610 TDR probe for sections H, K, and L are significantly lower than the results from the CS615 TDR probes in the same sections as seen in Table 4.1. From

Table 4.1. Average value and variance of moisture content for CS615 and CS610 TDR probes during the Phase 1 study.

Probe Name	615		610	
	Average	Standard Deviation	Average	Standard Deviation
BM6-1M	9.90	2.31		
BM6-2M	12.82	2.56		
BM6-1ME			13.28	2.65
EM6-1M	15.26	0.61		
EM6-2M	16.51	0.95		
EM6-1ME			15.36	0.36
HM6-2M	14.26	0.34		
HM6-1ME			8.93	1.23
JM6-1M	9.92	0.30		
JM6-2M	11.74	0.35		
JM6-1ME			8.60	0.73
JM6-2ME			8.48	0.54
KM6-1M	10.12	0.48		
KM6-2M	10.88	0.62		
KM6-2ME			6.81	0.86
LM6-1M	10.83	0.51		
LM6-2M	11.20	0.45		
LM6-1ME			8.20	0.50
LM6-2ME			7.48	0.97

analysis of the void content of the 21B material it can be expected that the moisture content should be at least 10-12% assuming that the 21B material is at approximately 75% saturated (for additional details, see Marienfeld and Baker, 1999). Thus, it appears that the moisture content for Sections H, K, and L as reported by the CS610 TDR probe is too low considering the percentage of voids and the degree of saturation expected. As a result, it was decided that the recently developed CS615 TDR probe gives acceptable moisture content values for all sections and could be used in place of the CS610 TDR probe for continuous monitoring purposes. Tables E.1 and E.2, Appendix E, show the actual moisture contents used to determine the values shown in Table 4.1. The data for Sections B through H dates earlier than for Sections I through L due to the sequence of construction. The completion of the construction of Layer 6 for Sections B through H preceded completion of the remainder of the sections by approximately four months.

4.1.3 ANALYSIS OF RESULTS WITH RESPECT TO PAVEMENT STRUCTURAL CONFIGURATION

The Phase 2 data of continuously monitoring the moisture content in Layer 6 using the CS615 TDR probes was studied to determine effects due to the pavement structural configuration. The first and perhaps most noticeable trend is the variation in moisture content due to precipitation. During the initial stages of data collection it appeared that the precipitation had a noticeable effect on the moisture content (especially for Section B during April 2000) as seen in Figure E.1, Appendix E. However, it soon became apparent that there was no discernible pattern as to a particular amount of precipitation that would cause a change in the moisture content for any section; nor was a similar reaction to precipitation evident. For example in Section B, a sharp increase in the moisture content is seen during April 2000 apparently in response to the precipitation of April 17 (46mm). However, the 45mm of precipitation received on March 29, 2001 appears to have a negligible effect on the moisture content. In addition, the 48mm of precipitation received on August 27, 2000 appears to have affected the moisture content as measured by probe BM6-2M and not BM6-1M whereas the precipitation of April 17, 2000 shows an increase in the moisture content as measured by both probes. Also, the sudden increase in the reported moisture content in Section H (Figure E.2, Appendix E) starting in January 2001 may be a result of movement of moisture within the pavement

rather than an increase in moisture due to precipitation. On the other hand, what does appear more evident is the difference in moisture content variability between the pavement sections containing the moisture barrier (Sections J and K) and those with no moisture barrier (Sections B, E, H, and L). To a lesser degree, a difference in moisture contents between the cut (e.g., Section L) and fill (e.g., Section B) areas for sections that do not contain a moisture barrier can be seen.

4.1.4 MODELING TDR PROBE SAMPLING VOLUME

The sampling volume of a TDR probe of specified geometry (diameter and separation distance between rods) is important to consider when applying TDR technology to monitor the moisture content of inhomogeneous coarse-grained materials (e.g., pavement base layers). If a significant portion of the energy of the electric field decays within a sufficiently close distance from the probe rods, the assumption of measuring the dielectric constant within a homogeneous medium is no longer valid. Before presenting the specific solution, consider the end view of a set of parallel conducting cylinders having voltage $V_0/2$ and $-V_0/2$ as shown in Figure 4.2. Ramo *et al.* (1994) gives the electrostatic potential at any point (x,y) for a set of parallel conducting cylinders as the following:

$$\Phi = \frac{V_0}{4 \cosh^{-1}(d/R)} \ln \left[\frac{(x-a)^2 + y^2}{(x+a)^2 + y^2} \right] \quad (4.1)$$

where

V_0 = voltage applied to the cylindrical conductors (v);

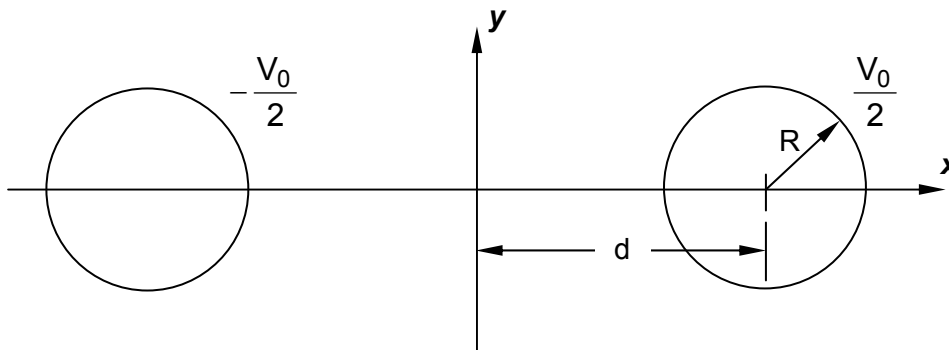


Figure 4.2. End view of a pair of cylindrical conducting cylinders.

d = distance from the origin to the center of a conducting cylinder (m);

R = radius of conducting cylinder (m); and

$$a = \pm \sqrt{d^2 - R^2} .$$

Equation 4.1 is valid for $\Phi > 0$, $x > 0$, and for $R \ll d$. Although Equation 4.1 actually only describes the cylinder centered at $(d, 0)$ with voltage $V_0/2$, due to symmetry, the same analysis can be applied to the other cylinder having a center of $(-d, 0)$ and voltage $-V_0/2$. Figure 4.3 shows the analytical solution of Equation 4.1 as a two dimensional equipotential plot for a set of infinitely long, parallel conducting cylinders having potentials of Φ and $-\Phi$. The spaces between the sets of vertical dashed lines in Figure 4.3 represent the diameters of the conducting cylinders. The equation describing the electric field (V/m) can be expressed as the following:

$$E = -\nabla\Phi \tag{4.2}$$

After performing the above operation on Equation 4.1, a computer program (Mathematica) was used to simplify the resulting expression. This simplified form of the

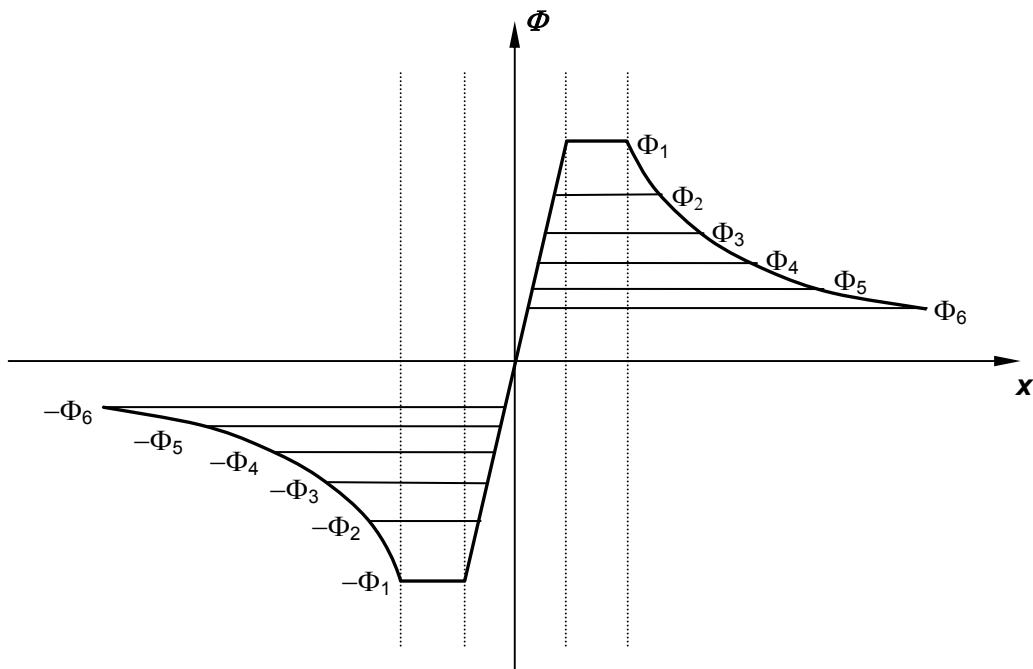


Figure 4.3. Side-view of two dimensional equipotential for a set of infinitely long parallel conducting cylinders having potentials of Φ and $-\Phi$ (from Ramo *et al.*, 1994).

electric field about a pair of cylindrical conductors is presented as follows:

$$E = \frac{a * V_0 * (a^2 - x^2 - 2xy + y^2)}{\cosh^{-1}(d/R) * [(a+x)^2 + y^2] * [(a-x)^2 + y^2]} \quad (4.3)$$

Equation 4.3 was applied to determine the shape of the sampling volume for the TDR probes used at the Virginia Smart Road. Since Equation 4.3 covers only the two-cylinder application, analysis could only be applied to the CS615 TDR probe; there is no general solution for more than two conductors. A solution for Equation 4.3 was found (using Matlab) for a two rod TDR probe having a cylinder radius (R) of 1.61mm and a separation distance (2d) of 27mm, the dimensions of the CS615 TDR probe. Figure 4.4 shows the side view of a three dimensional surface plot of the electrostatic potential for a set of conducting cylinders with the above dimensions. It should be noted that Equation

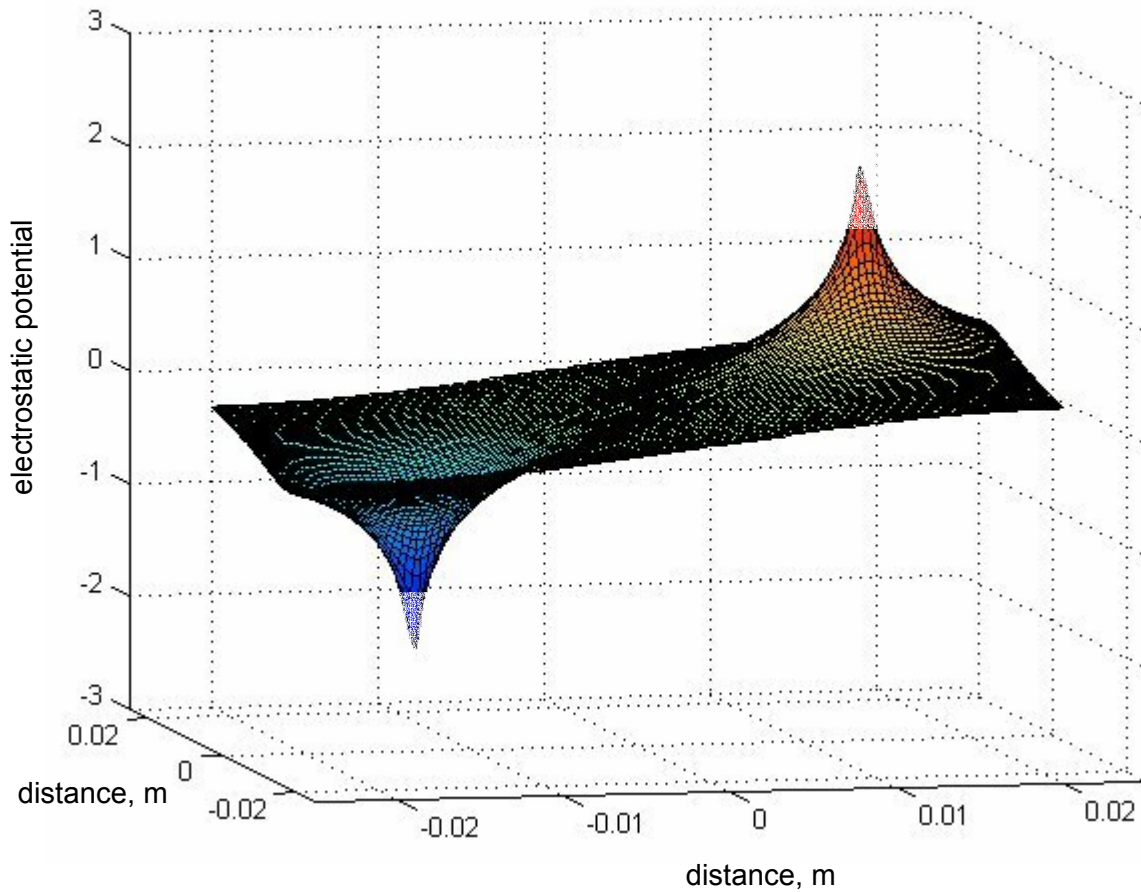


Figure 4.4. Plot of equipotential from computer analysis for set of conducting cylinders of geometry similar to CS615 TDR probe.

4.1 includes the potential within the volume of the cylinders; however, the expression only has physical meaning outside the volume of the cylinders. The potential shown to be within the volume of the cylinders in Figure 4.4 has been partially shaded to match the analytical diagram of Figure 4.3. As seen in Figure 4.4, a voltage (V_0) of 2.5 volts was used in the analysis, following specifications found in Campbell Scientific (1998).

Figure 4.5 shows a three-dimensional surface plot of the electric field for the aforementioned probe geometry. In Figure 4.5, the analysis is carried out to a distance of 15.5mm from the center point between the two conducting rods. This allows for an indication of the strength of the electric field just beyond the surface of the conducting cylinders (since the radius of the cylinders is given as 1.61mm and the distance between the center of the cylinders is 27mm). From Figure 4.5, the electric field at the extents of the analysis in the same plane as the center of the probe rods is approximately 240 V/m. The electric field at the extents of the analysis at the midpoint between the probe rods is approximately 35 V/m. Figure 4.6 shows the same view; however the analysis is carried

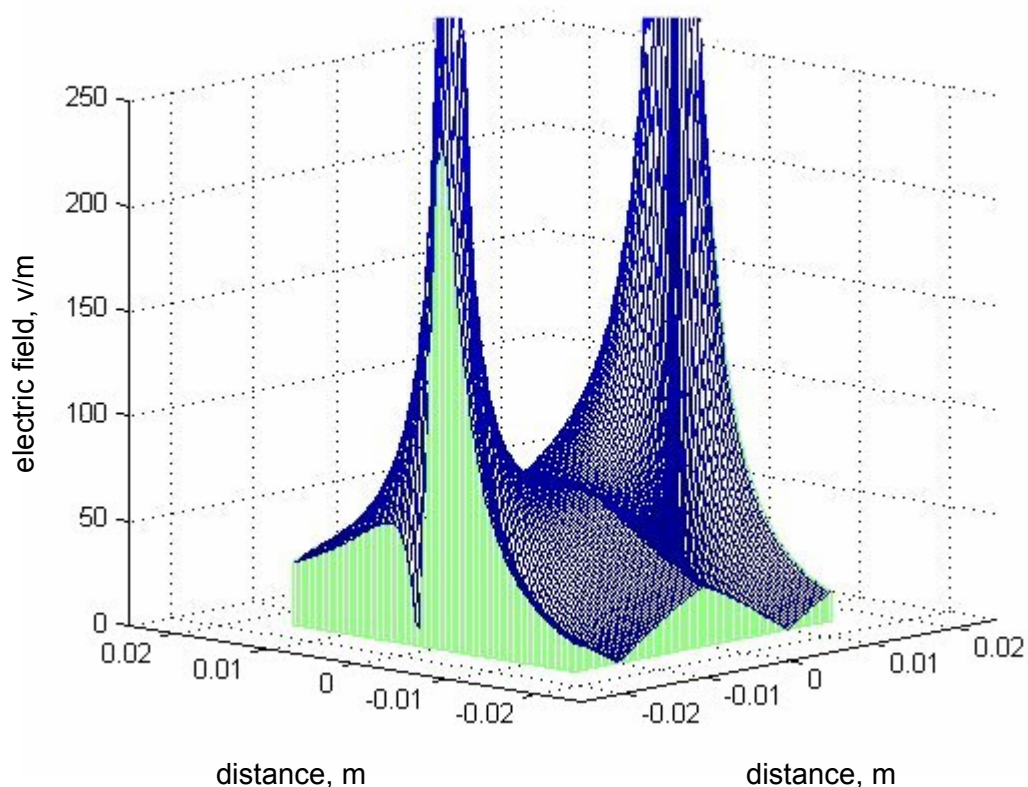


Figure 4.5. Surface plot of electric field from computer analysis for set of conducting cylinders of geometry similar to CS615 TDR probe – extents of analysis just beyond surface of conducting cylinders.

out to a distance of 21mm, 5.5mm beyond Figure 4.5. It is seen in Figure 4.6 that the electric field at the extents in the same plane as the center of the probe rods is approximately 60 V/m. The electric field at the extents of the analysis at the midpoint between the probe rods is approximately 20 V/m.

The solutions show that the electric field decays rapidly from the edge of the conducting cylinders in the same plane as the center of the probe rods. The electric field at a distance of approximately 5mm from the edge of the cylinder along the same plane as the center of the probe rods appears to decay to less than 20% of the value close to the cylinder edge. The electric field is approximately the same at the extents of the analysis on a line at the midpoint between the probe rods. Although the CS615 TDR probe employs active electronics operating as a multivibrator where a square wave is output from the probe rods, it was assumed for this solution that the static potential for this oscillating system still follows the general form of Equations 4.1 and 4.3.

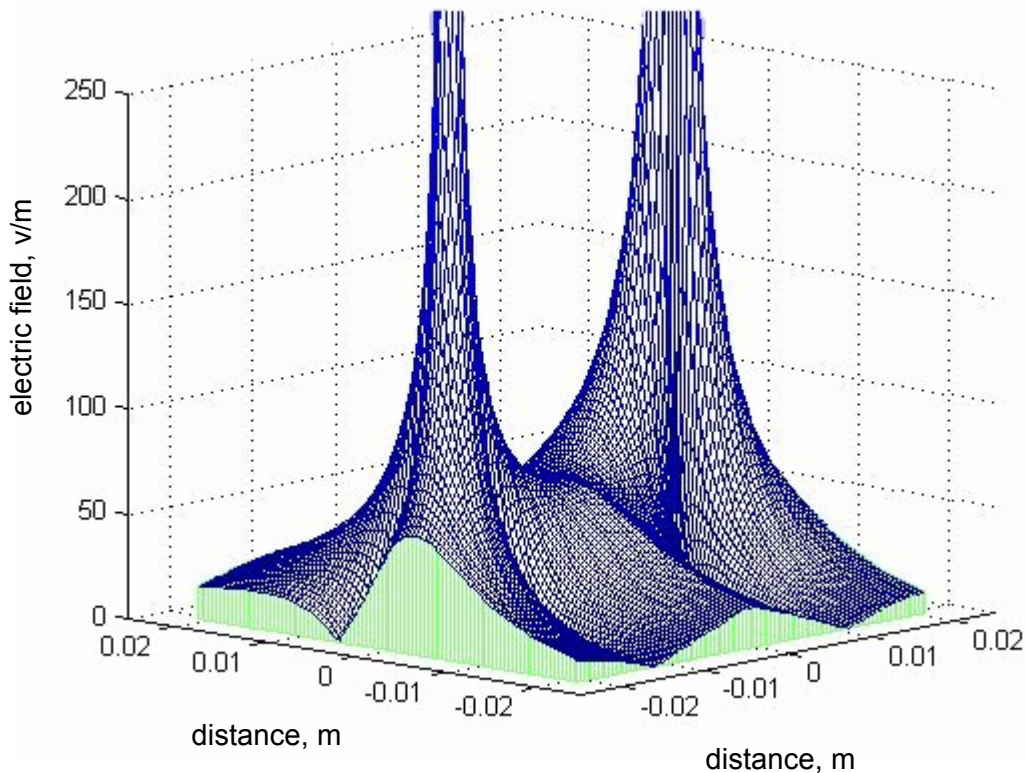


Figure 4.6. Surface plot of electric field from computer analysis for set of conducting cylinders of geometry similar to CS615 TDR probe – extents of analysis 5mm beyond surface of conducting cylinders.

The results of this analysis can be applied to the data from the Virginia Smart Road. It can be seen from Figures 4.5 and 4.6, that the electric field is not evenly distributed around the TDR probe. In addition, the decay of the electric field with increasing distance from the probe rods depends upon the orientation of the probe. These two effects may influence the results from a 2-rod TDR probe. For instance, if a small pocket of moisture were to migrate close to the probe rods, it could greatly exaggerate the perceived moisture content in the area around the TDR probe depending on the location with respect to the axis of the probe rods. In addition, if the pavement was not properly compacted around the TDR probe during installation, an increased percentage of air voids might exist close to the TDR probe rods resulting in a reported moisture content that is much less than expected. This may help to explain what is seen in Figure E.1 (Appendix E) where the moisture content varies significantly between the two TDR probes present and gives values much greater than expected for one probe (BM6-1M) and not for the other (BM6-2M). In light of this analysis, the two-rod CS615 TDR probe may provide a qualitative indication of a change in moisture content rather than a quantitative measure provided that the compaction around the probe rods is identical to the compaction of the rest of the pavement layer.

4.2 PAVEMENT TEMPERATURE

As HMA is a viscoelastic material, its mechanical properties vary with temperature. Thus, to study the difference in strength characteristics of various pavement designs, it is imperative to know the temperature distribution within the pavement cross-section. The falling-weight deflectometer (FWD) is a typical device used to determine the structural capacity of pavements. The temperature of the pavement during FWD testing is most often either estimated from the surface temperature or taken at various depths from an oil bath in a hole that is drilled into the pavement. Although many researchers have studied the area of pavement temperature (as discussed in Chapter 3), this previous work has primarily focused on determining yearly maximum and minimum pavement temperatures for the purpose of binder selection with very few discussing daily pavement temperature prediction. It is the goal of this study to develop an accepted approach to determine the daily high and low pavement temperatures at various depths within the pavement system and to develop a predictive model to determine the daily temperature distribution within a pavement section given the data

obtained at the Virginia Smart Road. For this purpose, pavement temperature data was collected continuously at the Virginia Smart Road from late February 2000 to May 2001. Details of the instrumentation were presented in Section 3.3.2.

4.2.1 TEMPERATURE DATA COLLECTION AND MANAGEMENT

At the Virginia Smart Road, data from 115 thermocouples in twelve pavement sections was collected using a computer controlled data acquisition system. The temperature from each thermocouple was continuously recorded with a time interval of 15 minutes between successive measurements. The data was saved as a tab-delimited text file and run through a processing program. The processing program organized the data by section, instrument type, and also checked for compliance with a pre-determined output range. For the data analysis herein, the temperatures from each location were averaged and given as one reading. For example, the three thermocouples at the bottom of Layer 1 in Section A (AT1-1B, AT1-2B, and AT1-3B) were averaged and reported as the temperature at A1B (Section A, Layer 1, Bottom).

To ensure that this averaging process is statistically valid, an analysis procedure was performed to check that the differences between the readings from each thermocouple were within the accuracy as seen in the thermocouple calibration procedure. For one randomly chosen date (October 10, 2000), the differences between all thermocouples at the same location were analyzed for repeatability. The mean of the differences between the readings for each thermocouple pair (93 readings) were analyzed for compliance with what was found during the thermocouple calibration ($\pm 2^{\circ}\text{C}$). It was found that the averaging process is statistically valid. For all comparisons, the mean difference was less than 2.6°C and only in three comparisons out of 166 did the mean of the differences exceed 2°C . A 95% confidence interval was calculated as $\pm 1.23^{\circ}\text{C}$ during the calibration procedure. The results of the mean difference analysis (including the standard deviation and standard error) are presented in Appendix F.

Prior to discussing the temperature data analysis, a brief summary of the temperature data set is presented. Figures 4.7 and 4.8 show an example of the high pavement temperature distribution in Section A from February 2000 through May 2001. Each figure gives the averaged temperature output at each depth and the temperature output of a thermocouple placed just above ground level between every two sections (at

each bunker location). The temperature from the thermocouple at the ground level was given the designation *near surface temperature* due to its location. Use of this term is intended to differentiate the temperature from the ambient temperature and the surface temperature. Since the thermocouple is unprotected from solar radiation and is located close to ground level (approximately 100mm above the surface), it is not an accurate measure of the ambient temperature. In addition the *near surface temperature* is not an indication of the pavement surface temperature since it is not actually located at the pavement, rather it is approximately 1m from the pavement edge. This term is seen in Figures 4.7 and 4.8 as the *ABnear* temperature (near surface temperature between Sections A and B).

Figure 4.7 offers an example of the daily maximum temperature at Section A from the near surface thermocouple and the daily maximum pavement temperature at depths of 0.038, 0.063, and 0.188m from the surface. Figure 4.8 shows an example of the daily maximum temperature from the near surface thermocouple and the daily maximum pavement temperature at depths of 0.263, 0.413, and 0.588m from the surface. Figure 4.8 represents the temperature distribution of the aggregate base and subbase layers in Section A.

Appendix G presents figures showing both the high and low temperature distribution

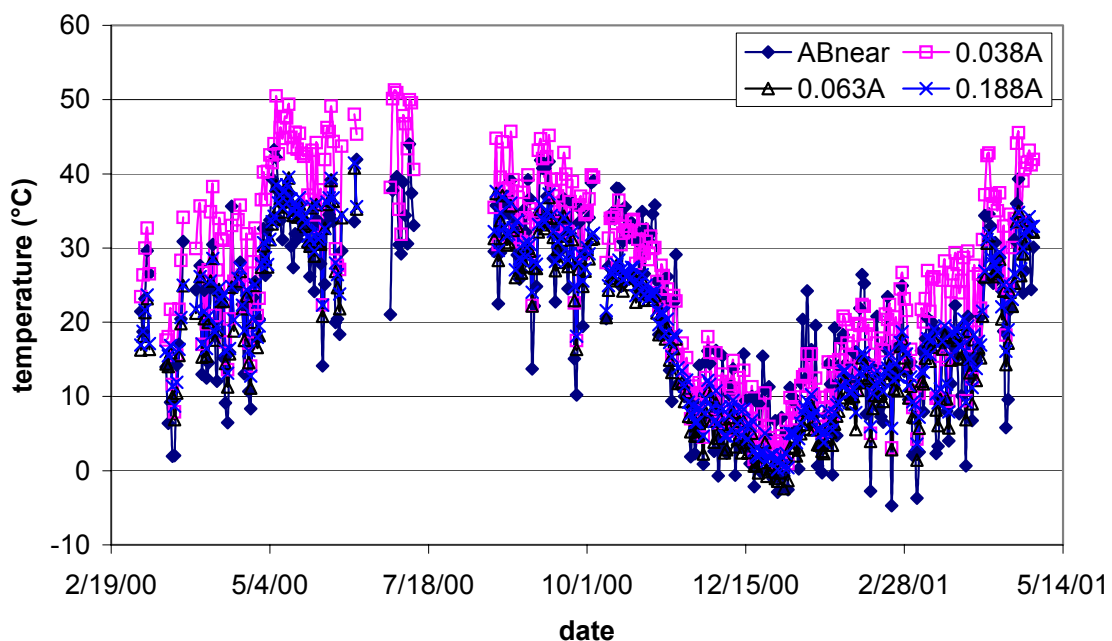


Figure 4.7. Maximum daily temperature in HMA layers – Section A.

for the remaining sections. For each section, the high and low pavement temperatures are presented and are divided into HMA layers and aggregate base/subbase layers (where applicable). The figures for Section A are divided into three parts: the HMA layers, the aggregate base/subbase layers, and the subgrade layers. The aggregate base/subbase figure for Section G also includes the subgrade temperature.

4.2.2 ANALYSIS OF RESULTS WITH RESPECT TO PAVEMENT STRUCTURAL CONFIGURATION

To compare the effect of pavement structural configuration on the pavement temperature at given depths from the surface, the temperatures were divided into daily high and daily low values. The daily maximum temperatures were analyzed from May 1, 2000 to September 30, 2000 and the daily minimum temperatures were analyzed from November 1, 2000 to March 31, 2001. These dates were chosen since they are when the maximum and minimum temperatures would have their strongest effect on the pavement. For the daily high and low temperatures, the difference in daily temperature was taken for all thermocouples at the same depth from the surface (0.038, 0.063, 0.138, 0.188, 0.263, 0.413, and 0.588m). Tables H.3 through H.22, Appendix H, provide the complete analysis including the mean, standard deviation, and the standard error for

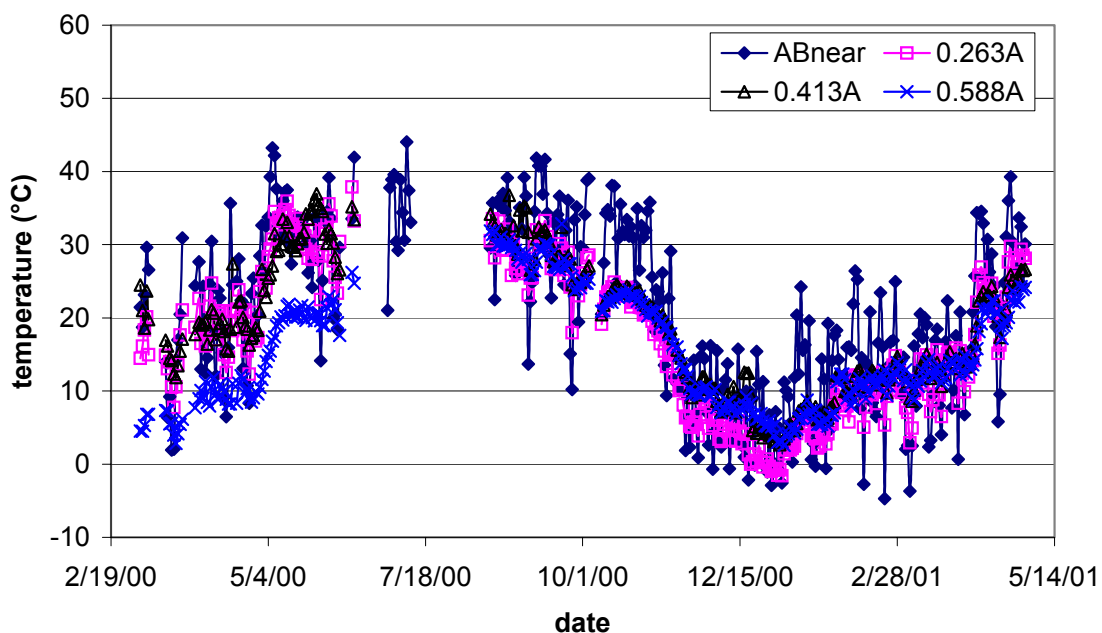


Figure 4.8. Maximum daily temperature in aggregate base/subbase layers – Section A.

the differences. Although in some cases, differences of greater than 4°C were found, there was no discernible trend with regard to material property or position of the section within the overall layout of the Virginia Smart Road. The differences noted are most likely due to variations in thermocouple placement (i.e., depth from the surface).

4.2.3 PAVEMENT TEMPERATURE PREDICTION MODELS

Development of temperature prediction models using data from the Virginia Smart Road began by finding daily high and daily low temperatures within each layer. For simplicity, it was assumed that the minimum temperature occurred between 12midnight and 12noon at each layer and that the maximum temperature occurred between 9:00AM and 12midnight within each layer. For most days, the minimum temperature at the surface occurs just before sunrise and the maximum temperature at the surface occurs between 2:00PM and 4:00PM, with the respective minimum or maximum temperatures in each layer occurring with a time lag that increases with increasing depth.

Initially, the daily temperature prediction portion of this study was intended to model the distribution of temperature within a pavement on a year-round basis. Previous work in predicting pavement temperatures (Bosscher *et al.*, 1998; Lukanen *et al.*, 1998; Mohseni and Symons, 1998) has offered prediction equations yielding the annual maximum or minimum pavement temperature with depth based on the annual maximum or minimum ambient air temperature. However, these models do not consider seasonal effects that would allow them to accurately predict daily pavement temperature changes across a full year.

An example of seasonal variations seen in pavement temperatures is shown in Figures 4.9 and 4.10. These figures show the temperature profile (pavement temperature at depths of 0.038, 0.188, 0.263, 0.413, and 0.588m from the surface) for Section A at the Virginia Smart Road for the 10th day of April and the 10th day of October 2000, respectively. The near surface temperature, given as “ABnear” in the two figures is similar. However, the maximum pavement temperature at a depth of 0.038m varies by approximately 6°C between the two dates. An even larger difference exists between pavement temperatures depths greater than 0.5m over the two time periods. The models offered from previous research (Mohseni, 1998) would state that the distribution of temperatures is equal for these two examples since the ambient conditions are

similar. However, these two figures clearly show that seasonal effects exist and need to be considered to accurately model the temperature distribution. To determine the effects of seasonal trends in pavement temperature prediction, several forms of daily temperature models were developed and are discussed in the following sections.

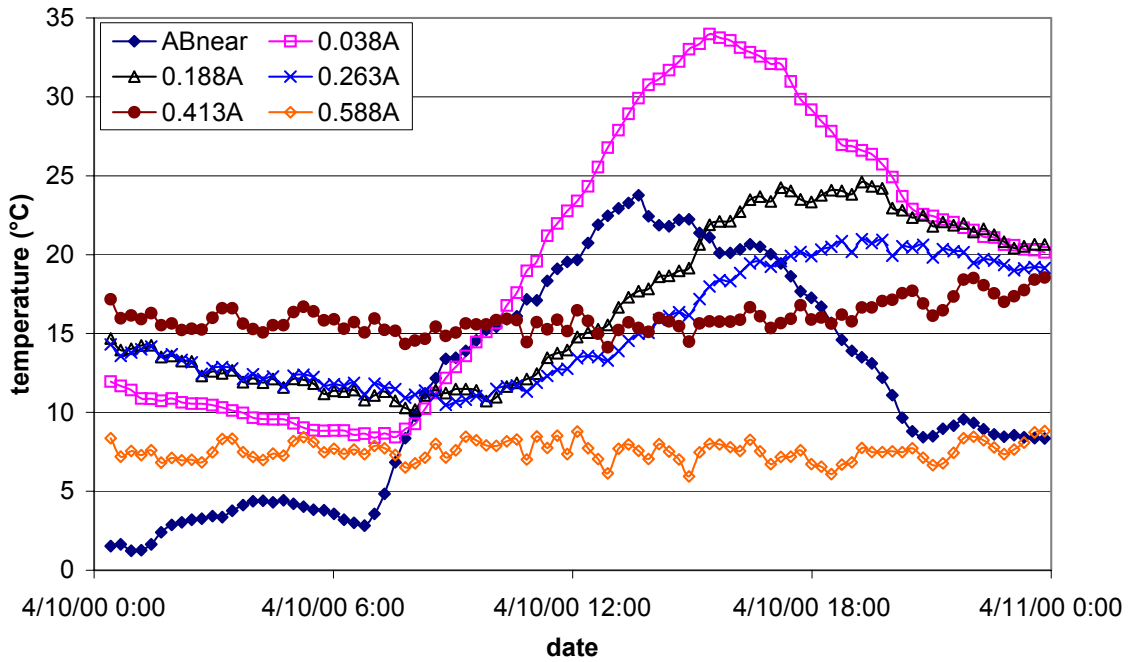


Figure 4.9. Temperature distribution for Section A - April 10, 2000.

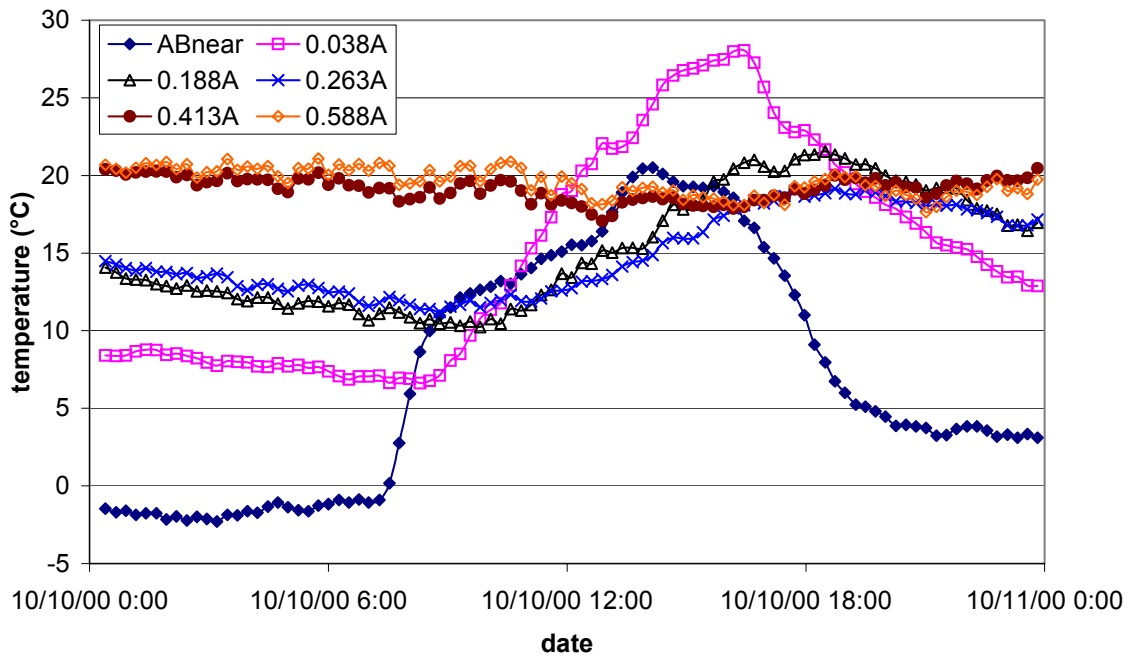


Figure 4.10. Temperature distribution for Section A - October 10, 2000.

Linear Modeling for Daily Pavement Temperature Prediction

The first model type to predict daily maximum or minimum pavement temperatures is a single linear regression relationship between the near surface temperature and the pavement temperature at different depths from the surface. This trend is of the following form:

$$y = Ax + B \quad (4.4)$$

where

y = predicted pavement temperature ($^{\circ}\text{C}$);

A = near surface temperature coefficient;

x = near surface temperature ($^{\circ}\text{C}$); and

B = intercept coefficient.

Table 4.2 presents the coefficients for the linear prediction models developed for each depth in Section A. Included with the model coefficients are the root-mean squared error (RMSE) and the adjusted R^2 . Tables of coefficients for the linear pavement temperature

Table 4.2. Section A - coefficients for linear pavement temperature prediction model.

Daily Maximum Temperature				
depth, m	A	B	RMSE	Adjusted R ²
0.038	1.0111	4.8988	5.0616	0.8508
0.063	0.8500	1.4274	4.7322	0.8133
0.188	0.8075	3.4388	4.6309	0.8093
0.263	0.7548	1.7713	4.8164	0.7741
0.413	0.6081	6.3616	5.3185	0.6457
0.588	0.4646	5.9334	5.4737	0.5008
0.74	0.4409	7.7700	5.2986	0.4908
0.994	0.4433	5.7432	5.8035	0.4481
1.172	0.3885	7.1195	5.5294	0.4070
Daily Minimum Temperature				
depth, m	A	B	RMSE	Adjusted R ²
0.038	1.0264	9.1801	2.7832	0.9127
0.063	1.0180	8.4302	3.4086	0.8663
0.188	0.9838	10.9246	3.3888	0.8596
0.263	0.9853	10.8678	3.7453	0.8340
0.413	0.8749	14.4247	4.2273	0.7566
0.588	0.7510	11.4557	5.2536	0.5970
0.74	0.6525	14.0522	5.0470	0.5478
0.994	0.6201	11.0919	5.0238	0.5247
1.172	0.5652	12.7255	5.2465	0.4565

prediction model (Equation 4.4) for the remaining sections are presented in Tables I.1 through I.12, Appendix I. Tables I.13 through I.19 group the same information by layer.

A graphical example of the linear relationship developed for Section A is shown in Figure 4.11 where the relationship between the daily maximum temperature at the temperature at the bottom of the HMA surface layer (0.038m) in Section A is shown versus the daily maximum near surface temperature between Sections A and B. Figures I.1 through I.106, Appendix I, graphically present data for the remaining sections and the remaining depths. The figures are presented by section where the daily maximum near surface temperatures versus the daily maximum pavement temperatures for each depth are followed by the daily minimum near surface temperatures versus the daily minimum pavement temperatures.

The tables and figures in Appendix I show that the agreement between the pavement temperature and the near surface temperature in terms of a linear relationship decreases with increasing depth from the surface. As the depth from the surface increases, the slope of the line describing the relationship between the near surface temperature and pavement temperature decreases. That is, as the surface temperature varies, less of an effect is seen with increasing depth. It is also noted that the

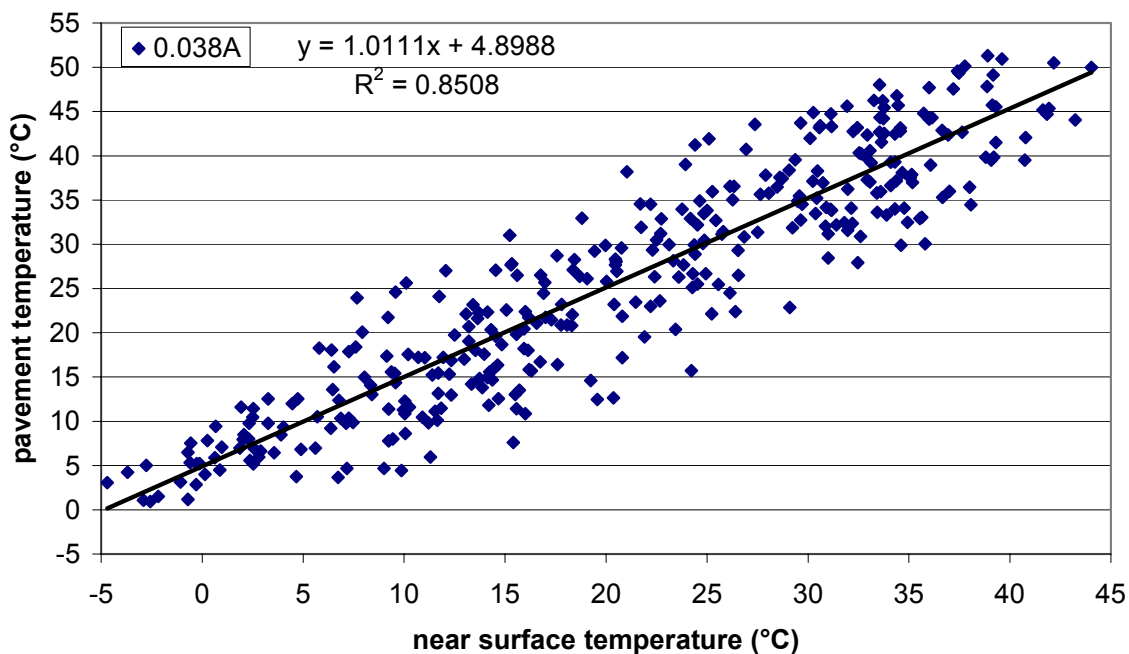


Figure 4.11. Section A – daily maximum near surface temperature vs. daily maximum pavement temperature (0.038m depth) with linear model.

agreement between the predicted and measured values is generally better for the daily minimum temperatures than the daily maximum temperatures. This may be caused by additional parameters (e.g., solar radiation) that are not measured at the Virginia Smart Road.

Upon evaluation of the regression data obtained from Equation 4.4, it can be seen that only small differences exist between the values of the near surface temperature coefficient (A) within the HMA layers (Layers 1 through 3) for the different sections. Physically, this signifies that for each depth within the HMA layers, the sections can be potentially modeled with an equation containing identical near surface temperature coefficients and differ only in their intercept coefficient that may vary upon the pavement properties. To this regard, additional analysis was performed on the data from Equation 4.4 to determine a unique intercept coefficient for each section at each depth while holding the near surface temperature coefficient constant. As the structural properties of the aggregate base layers vary little with temperature, the additional analysis was only performed for Layers 1 through 3 (0.038, 0.063, and 0.188m from the surface). Tables I.20 and I.21, Appendix I, present the developed coefficients for the daily maximum and minimum temperature models, respectively, from Equation 4.4 for all sections at depths of 0.038, 0.063, and 0.188m from the surface. Tables I.22 and I.23, Appendix I, present the revised coefficients for the daily maximum and minimum temperature models, respectively, from Equation 4.4 for all sections at depths of 0.038, 0.063, and 0.188m from the surface where the coefficient for the near surface temperature was held constant. When comparing Tables I.20 and I.21 to Tables I.22 and I.23, it can be seen that when the near surface temperature coefficient is held constant, little or no reduction in the model fit occurs for both maximum and minimum temperatures.

Linear Modeling (with Seasonal Component) for Daily Pavement Temperature Prediction

The second model type to predict daily maximum or minimum pavement temperatures is a multiple linear regression relationship that incorporates a seasonal component. The seasonal component variable is simply the day of the year ranging from 1 to 183 (for use on days from January 1 to July 2) and 182 back to 1 (for use on days from July 3 to December 31). The linear prediction model including the seasonal component is of the following form:

$$y = Ax_1 + Bx_2 + C \tag{4.5}$$

where

y = predicted pavement temperature ($^{\circ}\text{C}$);

A = near surface temperature coefficient;

x_1 = near surface temperature ($^{\circ}\text{C}$);

B = day of year coefficient;

x_2 = day of year value (1 to 183); and

C = intercept coefficient.

Table 4.3 presents the coefficients developed for the linear pavement temperature prediction model including the seasonal parameter. Included with the model coefficients are the root-mean squared error (RMSE) and the adjusted R^2 . As seen in Table 4.3, the agreement with the linear model decreases (increasing RMSE and decreasing adjusted R^2) with depth for both the daily maximum and the daily minimum temperatures. It is also noted that the addition of the day of the year coefficient improves the agreement of

Table 4.3. Section A - coefficients for linear pavement temperature prediction model including seasonal component.

Daily Maximum Temperature					
depth, m	A	B	C	RMSE	Adjusted R ²
0.038	0.7095	0.1154	1.7786	3.3451	0.9348
0.063	0.5405	0.1286	-2.2970	2.5412	0.9476
0.188	0.5023	0.1268	-0.2339	2.4388	0.9471
0.263	0.4301	0.1349	-2.1345	2.3799	0.9448
0.413	0.2865	0.1336	2.4917	3.3307	0.8611
0.588	0.3020	0.0676	3.9767	5.0632	0.5729
0.74	0.2826	0.0658	5.8648	4.8961	0.5652
0.994	0.2843	0.0661	3.8298	5.4371	0.5156
1.172	0.2681	0.0500	5.6710	5.3033	0.4538
Daily Minimum Temperature					
depth, m	A	B	C	RMSE	Adjusted R ²
0.038	1.0511	-0.0376	-6.6718	2.4758	0.9203
0.063	0.9853	-0.0332	-5.7302	3.0546	0.8716
0.188	1.0002	-0.0303	-8.5649	3.1442	0.8639
0.263	0.9621	-0.0279	-8.2671	3.4382	0.8373
0.413	0.7698	0.0220	-12.6571	4.1887	0.7585
0.588	0.4254	0.0981	-12.1688	4.6406	0.7036
0.74	0.3995	0.1084	-13.6891	4.7811	0.6854
0.994	0.3836	0.1128	-12.6542	4.8239	0.6797
1.172	0.3364	0.1229	-13.4483	4.8818	0.6720

the daily maximum temperature portion much more than the daily minimum temperature portion. This would seem to suggest that the linear model including the seasonal component accounts for some of the parameters missing from the daily maximum temperature portion of the simple linear model. In fact, Solaimanian and Kennedy (1993) present a figure showing a concave downward curve estimating the solar radiation based on the day of the year and the latitude. According to this figure, the maximum solar radiation occurs approximately on day 175 with the minimum approximately on day 355. From the agreement shown in Table 4.3, it may be possible to simply include the day of the year and forgo the measurement of solar radiation if merely the prediction of daily maximum pavement temperature is sought; however, this approximation was found to be too simplified for hourly temperature estimation (to be discussed in the following section). Tables of coefficients for the linear pavement temperature prediction model incorporating the seasonal component from the remaining sections are presented in Tables I.24 through I.34, Appendix I. Tables I.35 through I.42 group the same information by layer.

Again, additional analysis was performed on the linear model that included the seasonal parameter. Few differences were noted between the values of the near surface temperature coefficients for each section and the day of year coefficients for each section. This would again suggest that all sections could be potentially modeled with an expression holding the values of the near surface temperature coefficients and the day of year coefficients constant and only varying the intercept coefficient. To this regard, additional analysis was performed on data obtained from Equation 4.5 where a unique intercept coefficient for each section is determined while holding constant the values of the near surface temperature coefficients and the day of year coefficients. Tables I.43 and I.44, Appendix I, present the developed coefficients for the daily maximum and minimum temperature models, respectively, from Equation 4.5 for all sections at depths of 0.038, 0.063, and 0.188m from the surface. Tables I.45 and I.46, Appendix I, present the revised coefficients for the daily maximum and minimum temperature models, respectively, from Equation 4.5 for all sections at depths of 0.038, 0.063, and 0.188m from the surface where the coefficients for the near surface temperature and the day of year variables were held constant. When comparing Tables I.43 and I.44 to Tables I.45 and I.46, it can be seen that when the near surface temperature and day of year coefficients are held constant that little or no reduction in the model fit occurs for both maximum and minimum temperatures.

Linear Modeling (with Seasonal and Depth Components) for Daily Pavement Temperature Prediction

A third model type to predict daily maximum or minimum pavement temperatures using a multiple linear regression relationship is presented in Equation 4.6. This expression incorporates a depth component to the linear model with seasonal component given in Equation 4.5. The linear prediction model including both seasonal and depth components is of the following form:

$$y = Ax_1 + Bx_2 + Cx_3 + D \quad (4.6)$$

where

y = predicted pavement temperature ($^{\circ}\text{C}$);

A = near surface temperature coefficient;

x_1 = near surface temperature ($^{\circ}\text{C}$);

B = day of year coefficient;

x_2 = day of year value (1 to 183);

C = depth coefficient;

x_3 = depth from the surface (m); and

D = intercept coefficient.

Table 4.4 presents the coefficients developed for the linear pavement temperature prediction model including the seasonal and depth parameters. Included with the model coefficients are the root-mean squared error (RMSE) and the adjusted R^2 . It can be seen that the agreement with the linear model decreases (increasing RMSE and decreasing adjusted R^2) with depth for both the daily maximum and the daily minimum temperatures.

Additional analysis showed that it was possible to develop an expression where the near surface temperature, day of year, and depth parameters are held constant and the intercept coefficient is allowed to vary. Table 4.5 presents the revised linear pavement temperature prediction model including the seasonal and depth parameters for all sections at depths of 0.038, 0.063, and 0.188m from the surface where the coefficients for the near surface temperature, day of year, and depth parameters are held constant.

Table 4.4. Coefficients for linear pavement temperature prediction model, where A is the near surface temperature coefficient, B is the day of year coefficient, C is the depth coefficient, and D is the intercept coefficient.

Daily Maximum Temperature						
Section	A	B	C	D	RMSE	Adjusted R ²
A	0.5822	0.1263	-21.5730	1.6984	3.8531	0.8984
B	0.5689	0.1122	-25.9824	3.3894	2.9570	0.9361
C	0.7132	0.0893	-26.3771	2.8406	2.6491	0.9494
D	0.6798	0.0971	-17.9335	1.3558	2.6892	0.9460
F	0.6454	0.1030	-29.2511	2.8864	3.6190	0.8974
H	0.7027	0.0992	-47.6713	6.8033	2.9681	0.9466
I	0.6910	0.0913	-33.4771	4.0045	3.8493	0.9049
L	0.6953	0.0912	-19.5590	2.7507	3.8787	0.9054
Daily Minimum Temperature						
Section	A	B	C	D	RMSE	Adjusted R ²
A	0.6779	0.0827	14.6229	1.8044	2.4120	0.9329
B	0.6680	0.0777	9.2851	3.4538	2.8430	0.9118
C	0.7618	0.0723	11.3894	2.3245	2.6794	0.9189
D	0.7469	0.0768	7.4692	2.6671	2.5312	0.9265
F	0.6591	0.0913	3.6746	0.7973	2.8150	0.9167
H	0.7309	0.0687	0.2563	3.9253	2.3906	0.9377
I	0.7077	0.0705	6.1508	0.7624	2.4591	0.9284
L	0.7354	0.0724	4.0348	1.6592	2.2600	0.9445

Table 4.5. Coefficients for linear pavement temperature prediction model, where A is the near surface temperature coefficient, B is the day of year coefficient, C is the depth coefficient, and D is the intercept coefficient (A, B, and C are held constant).

Daily Maximum Temperature						
Section	A	B	C	D	RMSE	R ²
A	0.6470	0.1040	-27.8095	2.7312	3.9331	0.8941
B	0.6470	0.1040	-27.8095	2.5920	3.0430	0.9323
C	0.6470	0.1040	-27.8095	3.2440	2.6899	0.9478
D	0.6470	0.1040	-27.8095	2.4720	2.7722	0.9426
F	0.6470	0.1040	-27.8095	2.6310	3.6154	0.8976
H	0.6470	0.1040	-27.8095	5.5224	3.2730	0.9350
I	0.6470	0.1040	-27.8095	3.3224	3.8770	0.9035
L	0.6470	0.1040	-27.8095	3.5484	3.9242	0.9032
Daily Minimum Temperature						
Section	A	B	C	D	RMSE	R ²
A	0.7072	0.0770	7.2498	2.9399	2.4612	0.9301
B	0.7072	0.0770	7.2498	3.6596	2.8604	0.9107
C	0.7072	0.0770	7.2498	2.4961	2.7075	0.9172
D	0.7072	0.0770	7.2498	2.7704	2.5476	0.9255
F	0.7072	0.0770	7.2498	1.3344	2.8510	0.9146
H	0.7072	0.0770	7.2498	2.6323	2.4439	0.9348
I	0.7072	0.0770	7.2498	0.1712	2.4734	0.9276
L	0.7072	0.0770	7.2498	1.1303	2.2688	0.9440

After reviewing Tables 4.4 and 4.5 it was proposed that even the intercept coefficient could be held constant. Thus, it was postulated that a simplified model could be developed which needed no section specific slope (intercept) coefficient. Such a model was developed for both the daily maximum and daily minimum pavement temperatures. The section independent model for maximum daily pavement temperatures is presented as follows:

$$y = 0.6356x_1 + 0.1061x_2 - 27.7975x_3 + 3.2935 \quad (4.7)$$

where

y = predicted pavement temperature ($^{\circ}\text{C}$);

x_1 = daily maximum near surface temperature ($^{\circ}\text{C}$);

x_2 = day of year value (1 to 183); and

x_3 = depth from the surface (m).

The RMSE and adjusted R^2 for this model were calculated to be 3.5386 and 0.9136, respectively. The section independent model for minimum daily pavement temperatures is presented as follows.

$$y = 0.6504x_1 + 0.0861x_2 + 7.2385x_3 + 1.6472 \quad (4.8)$$

where

y = predicted pavement temperature ($^{\circ}\text{C}$);

x_1 = daily minimum near surface temperature ($^{\circ}\text{C}$);

x_2 = day of year value (1 to 183); and

x_3 = depth from the surface (m).

The RMSE and adjusted R^2 for this model were calculated to be 2.7896 and 0.9141, respectively. Upon observation of the errors for these models, it can be seen that the prediction of the minimum daily temperatures is slightly more accurate than the prediction of the maximum daily temperatures.

Thermocouple Reliability

As discussed in Chapter 3.3.1, the thermocouple calibration process indicated that the thermocouples possessed a statistical deviation in measurement from the actual temperature. The standard deviation for the thermocouple calibration process was

calculated to be 0.630°C. Thus, if one is interested in introducing this reliability into the pavement temperature prediction model, an error term (ε) can be added as follows:

$$\varepsilon = Z \times \sigma$$

where

z = statistic from standard normal table; and

σ = standard deviation.

Given the standard deviation of 0.630 and an example confidence of 95% ($z=1.96$) the error term would be found as follows:

$$\varepsilon = 1.96 \times 0.63 = 1.23$$

Therefore, any of the models described herein may be adjusted for the thermocouple reliability as follows:

$$y = 0.6356x_1 + 0.1061x_2 - 27.7975x_3 + 3.2935 \pm \varepsilon \quad (4.7)$$

Model Evaluation

The models presented in Equations 4.7 and 4.8 were evaluated using temperature data from the Virginia Smart Road for the dates of July 1, 2001 through December 31, 2001. This time period offers temperature data that is outside the original data set used to create the models in Equations 4.7 and 4.8. The RMSE and adjusted R^2 values were calculated as 3.7596 and 0.9025, respectively, for the maximum daily pavement temperature model. The RMSE and adjusted R^2 values for the minimum daily pavement temperature model were calculated as 3.1493 and 0.8995, respectively. Figure 4.12 presents the actual maximum daily pavement temperature and the predicted maximum daily pavement temperature at a depth of 0.038m for this model validation time period. Figure 4.13 presents the actual minimum daily pavement temperature and the predicted minimum daily pavement temperature at a depth of 0.038m for this model validation time period. The RMSE and correlation coefficient values show that Equations 4.7 and 4.8 can accurately predict the pavement temperature using data outside the original dataset.

Hourly Temperature Prediction Models

One of the goals of this research was to develop a model to predict the pavement temperature distribution during any day (hourly prediction) with a minimum number of inputs. In addition, the inputs required should be readily available. In this regard,

attempts were made to simply model the daily temperature distribution in one layer. The simplest model would be a linear relation between the day of year, time of day, and the near surface temperature. However, this type of model was found to be too simplistic to

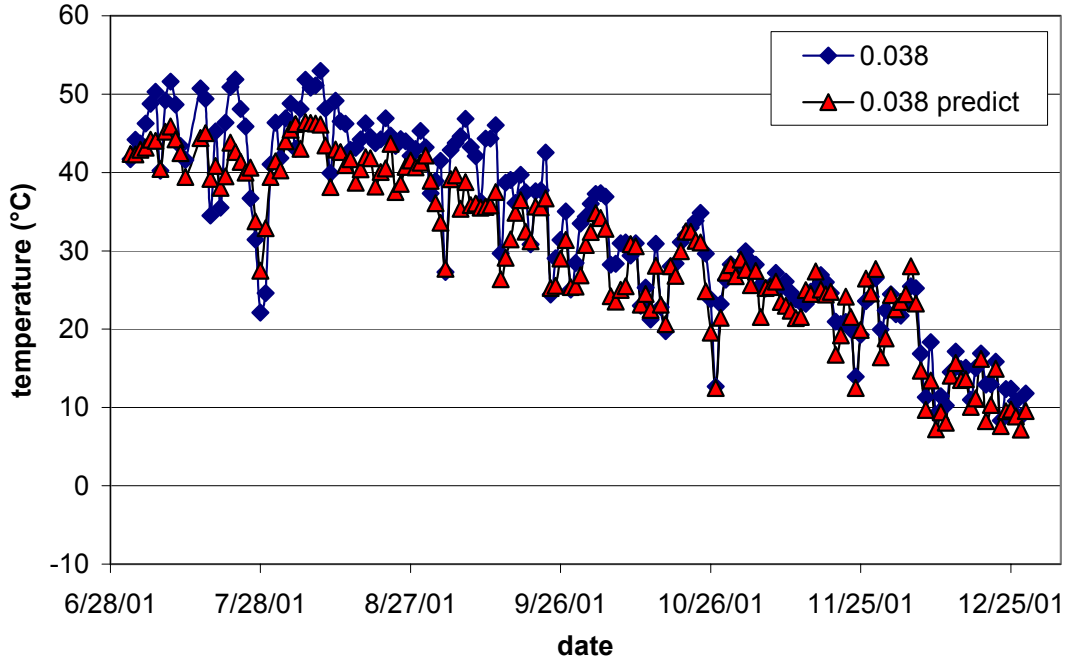


Figure 4.12. Maximum daily pavement temperature at 0.038m depth showing actual (0.038) versus predicted (0.038 predict).

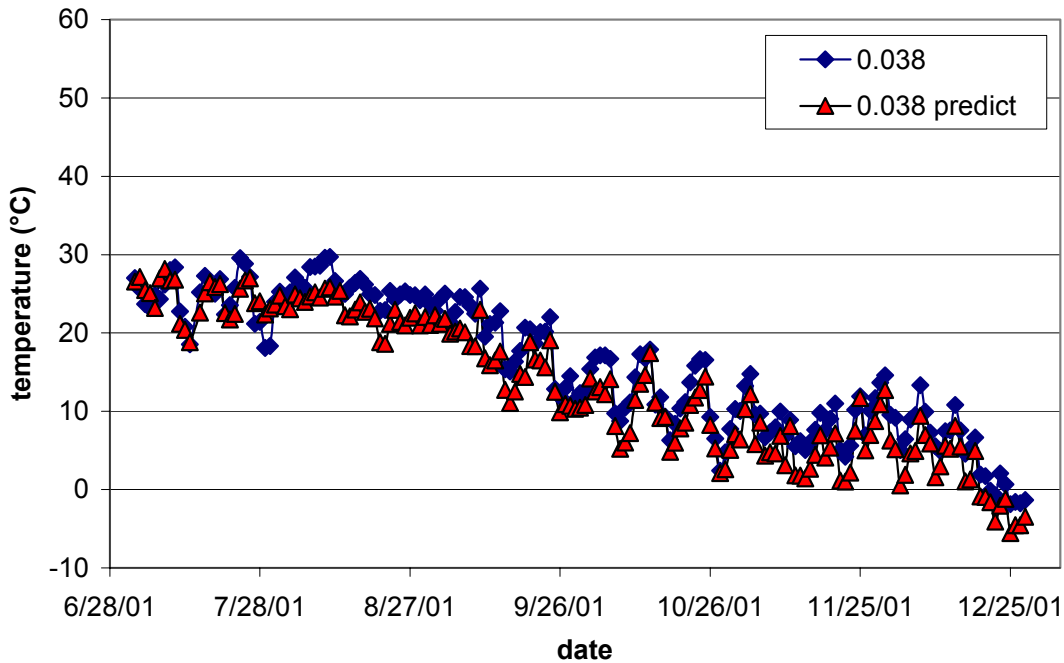


Figure 4.13. Minimum daily pavement temperature at 0.038m depth showing actual (0.038) versus predicted (0.038 predict).

provide an accurate prediction of the pavement temperature on an hourly level. Another attempted method was to fit a sinusoidal curve to the near surface temperature and then use a shift factor (in terms of both the temperature and the time lag) to predict the pavement temperature at different depths. However, this too proved to be too simplistic. Figure 4.14 is a good example of the difficulties encountered when trying to predict pavement temperatures using this method.

Figure 4.14 shows the near surface temperature between Sections A and B and the temperature of the pavement in Section A at depths of 0.038 and 0.188m for the 14th through the 16th of May 2001. Difficulties in accurately predicting the pavement temperature from the near surface temperature can be seen for the first two days of the figure. While the near surface temperature is nearly the same for these two dates, the temperature at a depth of 0.038 and 0.188m differs by approximately 10°C and 7°C, respectively. In addition, the time lag between the maximum near surface temperature and the maximum pavement temperature at each depth is not equal across these first two days. Reasons for these trends may include a difference in solar radiation that would tend to increase the temperature of the pavement surface (in turn heating the

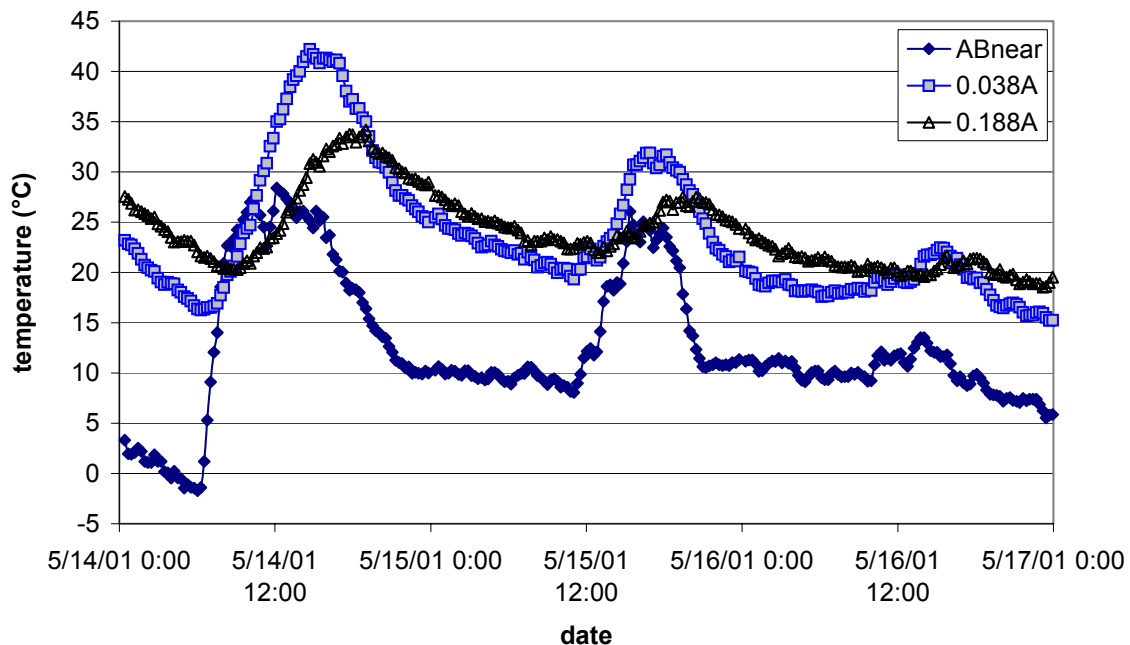


Figure 4.14. Temperature distribution over three consecutive days for Section A, showing the near surface temperature and pavement temperature at depths of 0.038 and 0.188m.

pavement below) while the near surface temperature would be nearly constant. Another cause could be an increase in wind speed that would tend to cool the pavement surface (and thus cool the pavement below) while the near surface temperature would be approximately the same. During the third day of Figure 4.14, the effect of precipitation throughout the day can be seen in that the magnitude of temperature change between daily maximum and daily minimum temperature was much lower than the previous two days. Thus, it can be seen that simply employing a sinusoidal curve to predict the pavement temperature without considering other parameters causes a significant reduction in prediction accuracy. Following this process, several recently developed models (Park *et al.*, 2001; Marshall *et al.*, 2001; and Hermansson, 2000 and 2001) were considered for the purpose of hourly pavement temperature prediction at the Virginia Smart Road; however, they were unable to be used due to the specific input parameters for each model that were not part of the collected data at the Virginia Smart Road.

4.2.5 PAVEMENT TEMPERATURE PREDICTION MODELS INCORPORATING CALCULATED SOLAR RADIATION

It has been shown that the models presented in Equations 4.7 and 4.8 can accurately predict the daily maximum and minimum pavement temperature at the Virginia Smart Road. However, these models cannot accurately predict the pavement temperatures at other locations as the incoming solar radiation varies with location (with respect to the latitude). One reason for this variation is that as the earth traverses its orbit around the sun, different locations on the planet receive varying amounts of solar radiation due to the tilt of the North/South Axis with respect to the orbital plane. This tilt is termed the *solar declination*. The declination is given as a positive value when the sun is in the northern latitudes and as a negative value when the sun is in the southern latitudes. At the vernal and autumnal equinoxes, the declination is zero (Anderson, 1983). In addition, there are seasonal variations on the incoming solar radiation since the earth's orbit follows an elliptical path. This changing distance between the sun and the earth causes a variation in the solar radiation received at the earth's surface. An *eccentricity factor* expresses this variation in distance in terms of one astronomical unit (AU). One AU is equal to the mean distance between the earth and sun (1.496×10^8 km). In order to model the pavement temperature at other locations (designated by their respective latitude), these parameters must be calculated.

The daily amount of solar radiation at any location on the earth can be determined by knowing the latitude and day of the year. From these variables, the solar declination and eccentricity factor can be calculated and then used to determine the daily solar radiation (Iqbal, 1983). The eccentricity factor is given as:

$$E_0 = 1.000110 + 0.034221 \cos \Gamma + 0.001280 \sin \Gamma + 0.000719 \cos 2\Gamma + 0.000077 \sin 2\Gamma \quad (4.9)$$

where

E_0 = eccentricity factor; and

Γ = day angle (rad), given as the following:

$$\Gamma = \frac{2\pi(d_n - 1)}{365} \quad (4.10)$$

where d_n is the day number of the year ranging from 1 to 365.

The solar declination can be calculated using the following:

$$\delta = \left(\begin{array}{l} 0.006918 - 0.399912 \cos \Gamma + 0.070257 \sin \Gamma - 0.006758 \cos 2\Gamma \\ + 0.000907 \sin 2\Gamma - 0.002697 \cos 3\Gamma + 0.00148 \sin 3\Gamma \end{array} \right) \times \left(\frac{180}{\pi} \right) \quad (4.11)$$

where δ is the solar declination (degrees).

The final term used to calculate the daily solar radiation at a particular location is the *sunrise hour angle*. The hour angle is the angle between the sun's highest point each day (where the hour angle is zero) and the location of the sun at sunrise or sunset. At sunrise the hour angle is positive and at sunset the hour angle is negative. The sunrise hour angle is given as the following:

$$\omega_s = \cos^{-1}(-\tan \phi \tan \delta) \quad (4.12)$$

where

ω_s = sunrise hour angle (degrees); and

ϕ = latitude (degrees).

From Equations 4.9 through 4.12, the daily solar radiation on a horizontal surface can be given as the following:

$$H_0 = \left(\frac{24}{\pi}\right) \times I_{sc} \times E_0 \times \sin(\phi) \sin(\delta) \times \left[\frac{\omega_s \times \pi}{180} - \tan(\omega_s)\right] \quad (4.13)$$

where

H_0 = daily solar radiation on a horizontal surface (kJ/m²day); and

I_{sc} = solar constant = 4871 kJ/m²h.

Table 4.6 gives an example of the difference in solar radiation values for three locations in the eastern United States at different times of the year.

Daily Pavement Temperature Prediction Models

A set of linear daily pavement temperature prediction models utilizing the calculated daily solar radiation (latitude = 37.19°N for Blacksburg, VA) in place of the day of year variable was developed following the same procedures described in Section 4.2.3. These models utilize the same near surface temperature and depth within the pavement values as were used to develop Equations 4.7 and 4.8. The model to calculate the daily maximum pavement temperature incorporating the calculated daily solar radiation is given as follows:

$$y = 0.7178x_1 + 4.5870 \times 10^{-4}x_2 - 27.8587x_3 - 2.5932 \quad (4.14)$$

where

y = predicted pavement temperature (°C);

x_1 = daily maximum near surface temperature (°C);

x_2 = calculated daily solar radiation (kJ/m²day); and

x_3 = depth from the surface (m).

The RMSE and adjusted R^2 for this model were calculated to be 3.7586 and 0.9025, respectively. The model to calculate the daily minimum pavement temperature

Table 4.6. Daily solar radiation values for four locations in the eastern United States.

Location	Latitude, °N	H_0 , kJ/m ² day		
		January 1	May 1	September 1
Caribou, ME	46.87	9580	36095	31820
Washington, DC	38.95	14461	37661	34214
Blacksburg, VA	37.19	15554	37927	34664
Tampa, FL	27.97	21207	38801	36505

incorporating the calculated daily solar radiation is given as follows.

$$y = 0.7941x_1 + 3.0337 \times 10^{-4}x_2 + 7.1988x_3 - 0.2984 \quad (4.15)$$

where

y = predicted pavement temperature ($^{\circ}\text{C}$);

x_1 = daily minimum near surface temperature ($^{\circ}\text{C}$);

x_2 = calculated daily solar radiation ($\text{kJ}/\text{m}^2\text{day}$); and

x_3 = depth from the surface (m).

The RMSE and adjusted R^2 for this model were calculated to be 3.1493 and 0.8905, respectively. These models show that little difference exists in the accuracy of calculating the pavement temperature utilizing the calculated daily solar radiation in place of the day of year coefficient. The RMSE for the models utilizing the calculated daily solar radiation in place of the day of year increased by only 0.22 and 0.35 for maximum and minimum pavement temperatures, respectively. Based on the accuracy obtained with Equations 4.14 and 4.15 for predicting the pavement temperature at one location (Blacksburg, VA), it is anticipated that similar models could be developed for other locations.

Model Evaluation

The models presented in Equations 4.14 and 4.15 were evaluated using pavement temperature data from the Virginia Smart Road for the dates of July 1, 2001 through December 31, 2001. This time period offers temperature data that is outside the original data set used to create the models in Equations 4.9 and 4.10. The RMSE and adjusted R^2 values were calculated as 3.0540 and 0.9302, respectively, for the maximum daily pavement temperature model incorporating the solar radiation calculation during this evaluation period. The RMSE and adjusted R^2 values for the minimum daily pavement temperature model incorporating the solar radiation calculation were found to be 3.8886 and 0.8043, respectively during the evaluation period. Figure 4.15 presents the actual maximum daily pavement temperature and the predicted maximum daily pavement temperature using the day of year integer and solar radiation calculation (0.038 solar predict) at a depth of 0.038m for the evaluation period. Figure 4.16 presents the actual minimum daily pavement temperature and the predicted minimum daily pavement temperature using the day of year integer and the solar radiation calculation (0.038 solar

predict) at a depth of 0.038m for the evaluation period. It is seen that the usage of the calculated solar radiation in place of the day of year integer to develop these models offers a similarly accurate method to calculate the daily maximum and minimum pavement temperature.

Daily Pavement Temperature Prediction Models Incorporating Ambient Temperature

The dataset used in developing the models presented in Equations 4.14 and 4.15 were evaluated utilizing the daily maximum (Equation 4.14) and daily minimum (Equation 4.15) near surface temperature value. However, as many researchers do not incorporate this quantity into their studies, usage of the ambient temperature would make these models more applicable to other data sets. The daily ambient temperature dataset was downloaded from the National Virtual Climatic Data section within the National Oceanographic and Atmospheric Administration (NOAA) website for the Blacksburg Municipal Airport (BCB). The Blacksburg Municipal Airport is a second order weather station, approximately 1.7km from the Virginia Smart Road, and thus only daily ambient temperatures are available from this station. The model to calculate the daily

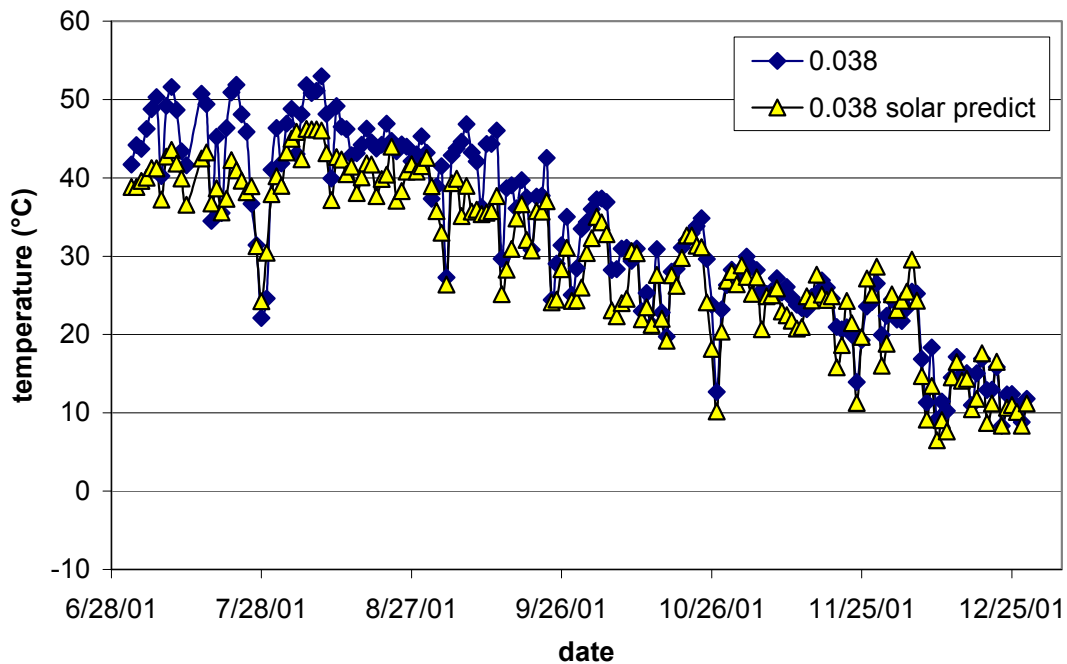


Figure 4.15. Maximum daily pavement temperature at 0.038m depth showing actual (0.038) versus predicted (0.038 solar predict).

maximum pavement temperature incorporating the calculated daily solar radiation and ambient temperature is given as follows:

$$y = 0.6861x_1 + 5.6736 \times 10^{-4}x_2 - 27.8739x_3 + 2.78752 \quad (4.16)$$

where

y = predicted pavement temperature (°C);

x_1 = daily maximum ambient temperature (°C);

x_2 = calculated daily solar radiation (kJ/m²day); and

x_3 = depth from the surface (m).

The RMSE and adjusted R² for this model were calculated to be 5.7643 and 0.7707, respectively. The model to calculate the daily minimum pavement temperature incorporating the calculated daily solar radiation and ambient temperature is given as follows.

$$y = 0.6754x_1 + 3.7642 \times 10^{-4}x_2 + 7.2043x_3 - 1.2097 \quad (4.17)$$

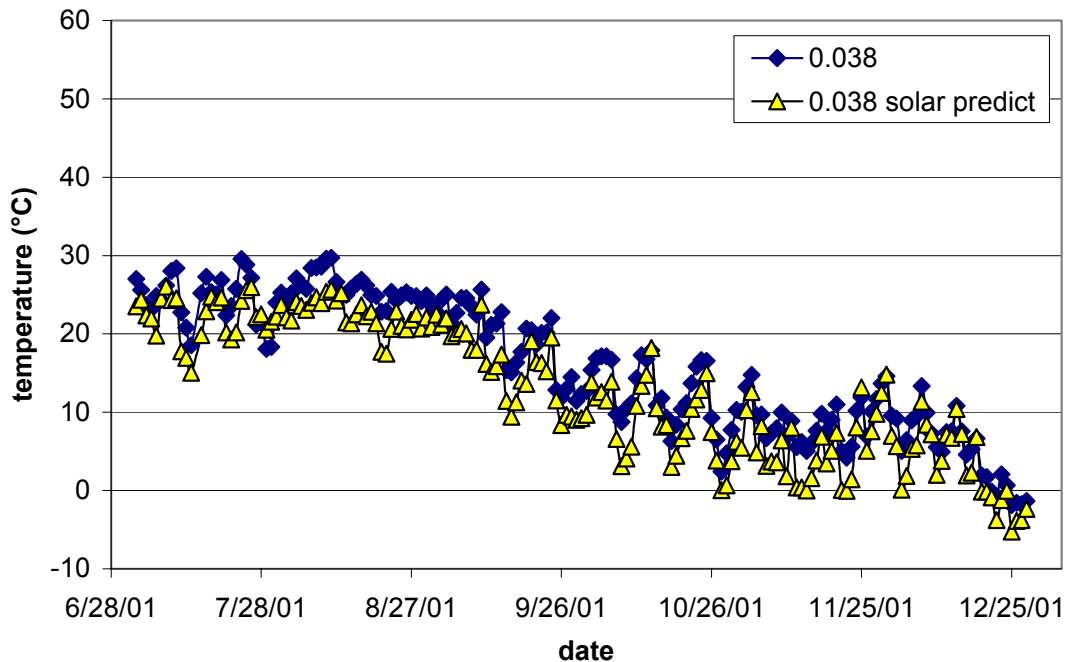


Figure 4.16. Minimum daily pavement temperature at 0.038m depth showing actual (0.038) versus predicted (0.038 solar predict).

where

y = predicted pavement temperature ($^{\circ}\text{C}$);

x_1 = daily minimum ambient temperature ($^{\circ}\text{C}$);

x_2 = calculated daily solar radiation ($\text{kJ}/\text{m}^2\text{day}$); and

x_3 = depth from the surface (m).

The RMSE and adjusted R^2 for this model were calculated to be 4.2787 and 0.7979, respectively.

Model Evaluation

The models presented in Equations 4.16 and 4.17 were evaluated using a different data set, pavement temperature data from the Virginia Smart Road from July 1, 2001 through December 31, 2001. This is the same data set used to evaluate Equations 4.14 and 4.15; the only difference being that the ambient temperature measured at the Blacksburg Municipal Airport was included in place of the near surface temperature measured at the Virginia Smart Road. The RMSE and adjusted R^2 values were calculated as 4.1452 and 0.8714, respectively, for the maximum daily pavement temperature model incorporating both the calculated solar radiation and ambient temperatures. The evaluation of the maximum pavement temperature model at a depth of 0.038m and the actual pavement temperature at a depth of 0.038m are presented in Figure 4.17. The RMSE and adjusted R^2 values for the minimum daily pavement temperature model incorporating both the calculated solar radiation and ambient temperatures were calculated as 4.6127 and 0.7246, respectively. The evaluation of the minimum temperature model at a depth of 0.038m and the actual pavement temperature at a depth of 0.038m are presented in Figure 4.18.

Validation of Daily Pavement Temperature Prediction Models Incorporating Ambient Temperature

Daily pavement and ambient temperature data is readily available from LTPP studies for numerous test sites in the United States and portions of Canada. Two LTPP sites were randomly selected for inclusion in this study to validate the daily pavement temperature models that incorporate the ambient temperature measurements. As ambient temperature (and not near surface temperature) is a measured quantity by LTPP, this is the only model developed in this study that can be validated in this manner.

The two selected LTPP test locations are test sites 9-1803 and 48-1077. LTPP test site 9-1803 is located in New London, CT at latitude 41.39°N. The pavement is comprised of

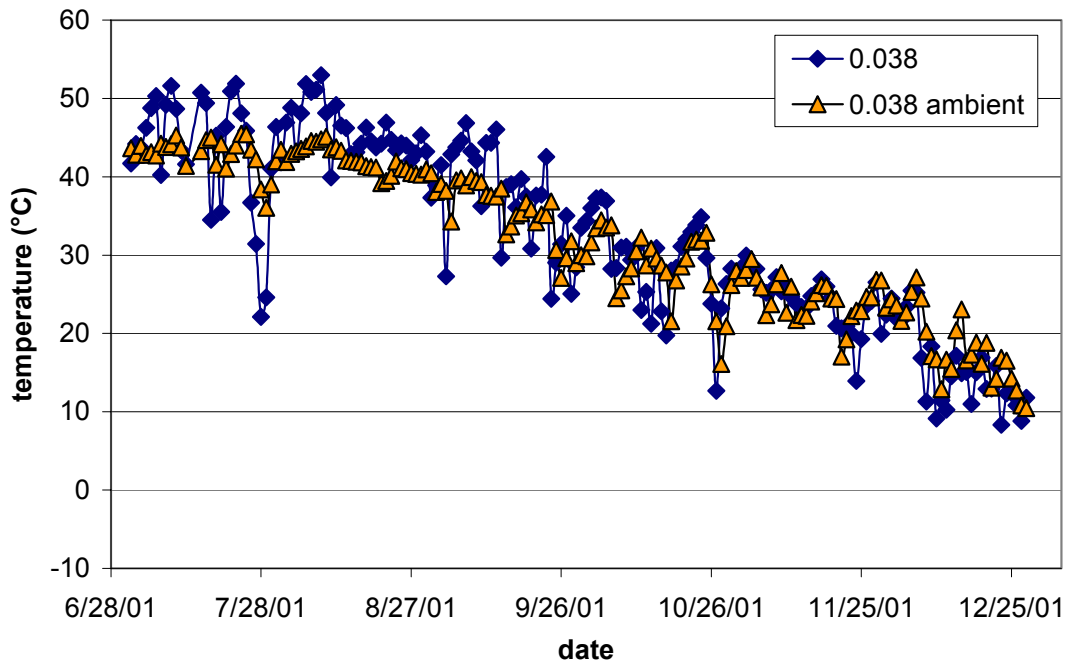


Figure 4.17. Maximum daily pavement temperature at 0.038m depth showing actual (0.038) versus predicted (0.038 ambient).

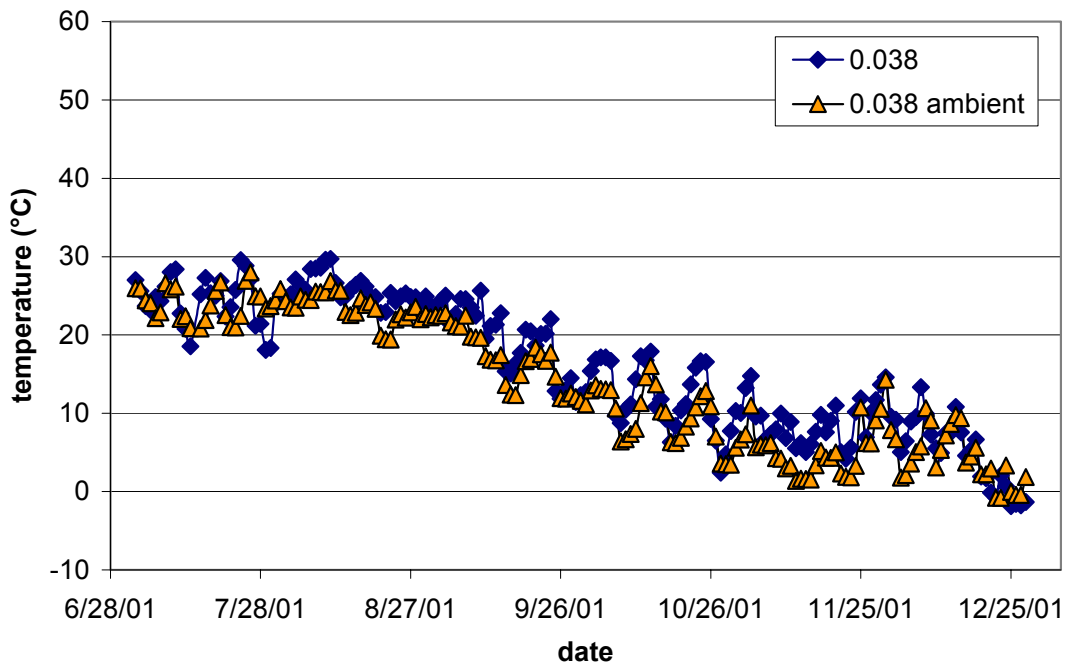


Figure 4.18. Minimum daily pavement temperature at 0.038m depth showing actual (0.038) versus predicted (0.038 ambient).

a 0.079m thick layer of surface HMA, a 0.109m thick layer of base HMA, and a third layer of compacted gravel. LTPP test site 48-1077 is located in Hall, TX at latitude 34.53°N. The pavement is comprised of a 0.037m thick layer of surface HMA, a 0.040m thick layer of base HMA, and a layer of crushed stone. The models presented in Equations 4.16 and 4.17 were evaluated incorporating the data from these LTPP test sites in an effort to validate the applicability of these models to multiple locations. Input data used to validate the models includes the latitude of the LTPP test site, date, and maximum/minimum daily ambient and pavement temperatures.

Instrumentation to measure the pavement temperature at LTPP site 9-1803 in Connecticut was placed at depths of 0.025, 0.089, and 0.153m below the surface of the pavement. These three depths are located within the HMA layers of the pavement structure. The input data covered a period of January 21, 1994 through June 21, 1995. Analysis of the maximum daily pavement temperatures at LTPP site 9-1803 using Equation 4.16 yielded an adjusted R^2 and a RMSE of 0.8239 and 5.2521, respectively. A 95% confidence interval was calculated as being $\pm 10.3^\circ\text{C}$ for the maximum daily temperature prediction. Analysis of the minimum daily pavement temperatures at LTPP site 9-1803 using Equation 4.17 yielded an adjusted R^2 of 0.8928 and a RMSE of 3.0354, respectively. A 95% confidence interval was calculated as being $\pm 5.6^\circ\text{C}$ for the minimum daily temperature prediction. The actual pavement temperature at a depth of 0.025m versus the predicted temperature is shown in Figures 4.19 and 4.20 for maximum and minimum temperatures, respectively.

Instrumentation to measure the pavement temperature at LTPP site 48-1077 in Texas was placed at depths of 0.025, 0.065, 0.105, and 0.182m below the pavement surface; placing all four locations within the HMA layers. The input data for this test section covered a period of January 1, 1994 through June 27, 1994. Analysis of the maximum daily pavement temperatures using Equation 4.16 yielded an adjusted R^2 and a RMSE of 0.9041 and 4.1168, respectively. A 95% confidence interval was calculated as being $\pm 8.1^\circ\text{C}$ for the maximum daily temperature prediction. Analysis of the minimum daily pavement temperatures using Equation 4.17 yielded an adjusted R^2 and a RMSE of 0.9296 and 2.9429, respectively. A 95% confidence interval was calculated as being $\pm 5.7^\circ\text{C}$ for the minimum daily temperature prediction. The actual pavement temperature at a depth of 0.025m versus the predicted temperature is shown in Figures 4.21 and 4.22 for maximum and minimum temperatures, respectively.

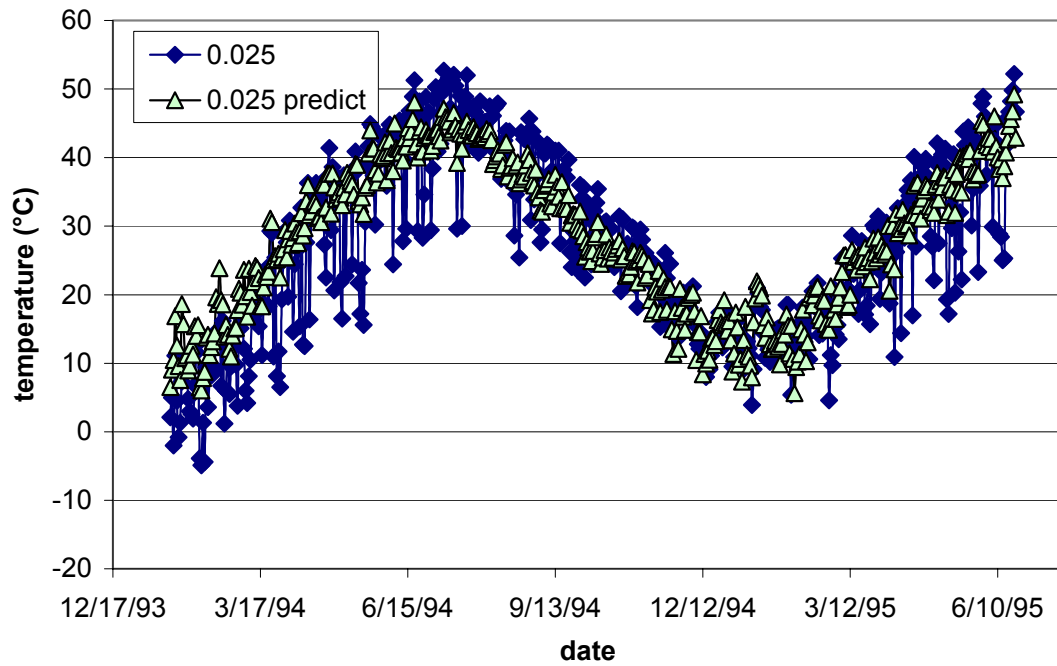


Figure 4.19. Maximum daily pavement temperature at 0.025m depth showing actual (0.025) versus predicted (0.025 predict) for LTPP site 9-1803 (CT).

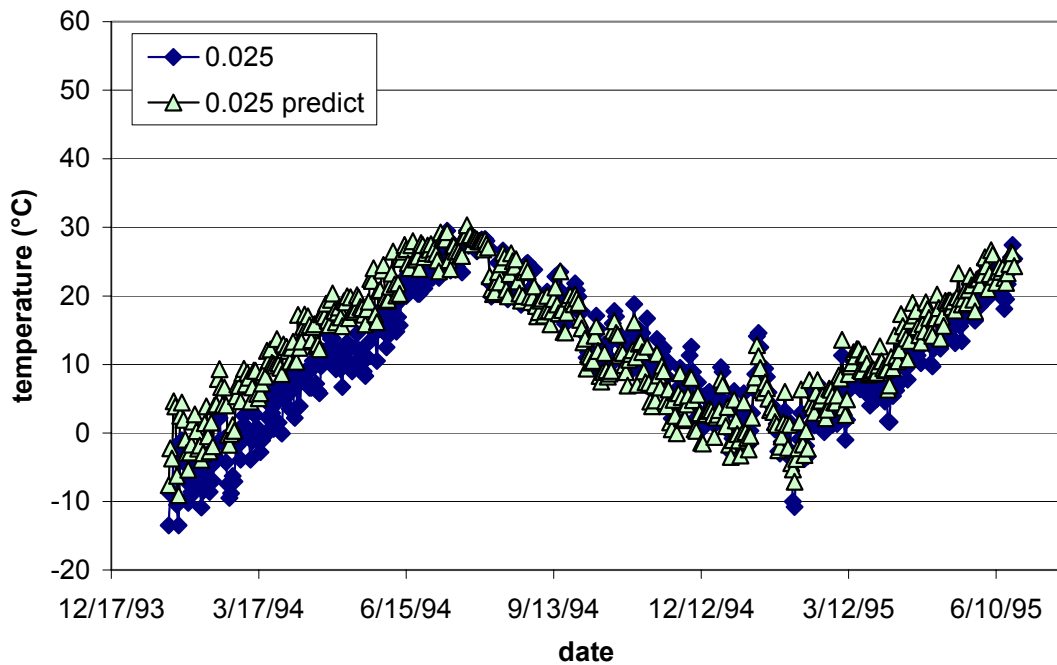


Figure 4.20. Minimum daily pavement temperature at 0.025m depth showing actual (0.025) versus predicted (0.025 predict) for LTPP site 9-1803 (CT).

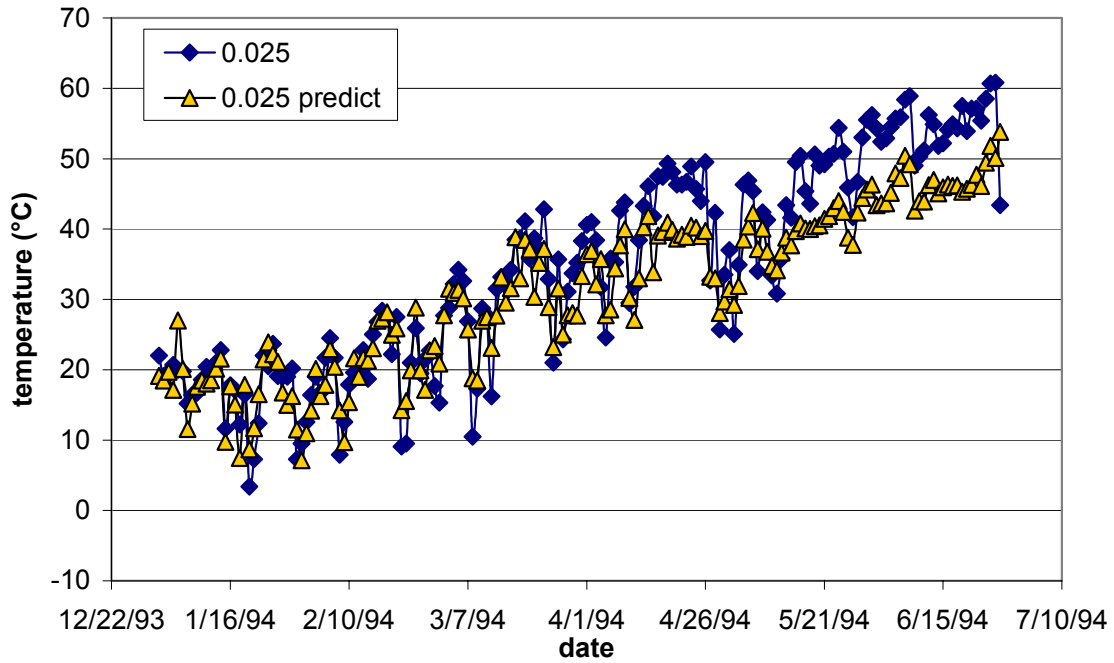


Figure 4.21. Maximum daily pavement temperature at 0.025m depth showing actual (0.025) versus predicted (0.025 predict) for LTPP site 48-1077 (TX).

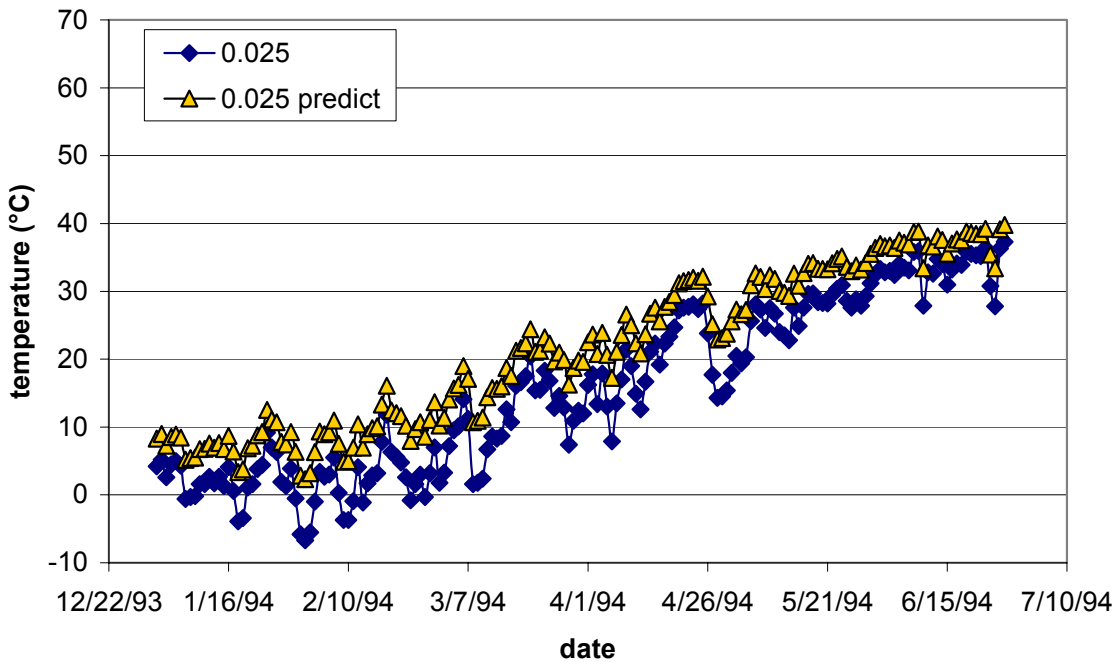


Figure 4.22. Minimum daily pavement temperature at 0.025m depth showing actual (0.025) versus predicted (0.025 predict) for LTPP site 48-1077 (TX).

Daily Pavement Temperature Prediction Models Incorporating Ambient Temperature from Multiple Locations

By incorporating data from the Smart Road and the two LTPP test locations (Connecticut and Texas) a set of models was developed which incorporate the day of year and latitude rather than the calculated solar radiation. It is intended that these models will provide a simplified means of predicting the daily maximum or daily minimum pavement temperature. The model to calculate the daily maximum pavement temperature based on the day of year and latitude is given as follows:

$$y = 1.1265x_1 + 0.001820x_2 + 0.0839x_3 - 53.5247x_4 + 6.0775 \quad (4.18)$$

where

y = predicted pavement temperature ($^{\circ}\text{C}$);

x_1 = daily maximum ambient temperature ($^{\circ}\text{C}$);

x_2 = day of year (1 to 365);

x_3 = latitude (degrees); and

x_4 = depth from surface (m).

The RMSE and adjusted R^2 for this model were calculated to be 5.8787 and 0.7936, respectively. A 95% confidence interval of $\pm 11.53^{\circ}$ was also calculated. Figure 4.23 presents the actual pavement temperature at 0.038m depth from the Virginia Smart Road and the predicted temperature from Equation 4.18. The model to calculate the daily minimum pavement temperature based on the day of year and latitude is given as follows:

$$y = 0.9608x_1 + 0.0641x_2 - 0.5616x_3 + 9.4893x_4 + 27.5986 \quad (4.19)$$

where

y = predicted pavement temperature ($^{\circ}\text{C}$);

x_1 = daily minimum ambient temperature ($^{\circ}\text{C}$);

x_2 = day of year (1 to 365);

x_3 = latitude (degrees); and

x_4 = depth from surface (m).

The RMSE and adjusted R^2 for this model were calculated to be 3.5922 and 0.8663, respectively. A 95% confidence interval of $\pm 7.05^\circ$ was also calculated. Figure 4.24 presents the actual pavement temperature at 0.038m depth from the Virginia Smart Road and the predicted temperature from Equation 4.19.

Hourly Pavement Temperature Prediction Models

A set of models was developed to predict the hourly pavement temperature following the form of Equations 4.16 and 4.17 (ambient temperature and calculated daily solar radiation). A single model was developed based on the hourly ambient temperature from the nearby Blacksburg Municipal Airport, an accumulated hourly solar radiation (a cumulative solar radiation calculated hourly for each ambient measurement), and depth within the pavement. Although inclusion of the ambient temperature does not accurately predict the pavement temperature trend or magnitude, a RMSE and correlation coefficient of 5.58 and 0.74, respectively, were found. Due to the inaccuracies of the prediction model including ambient temperature, further investigation of hourly pavement temperature prediction, given the inputs used in this study, is not recommended.

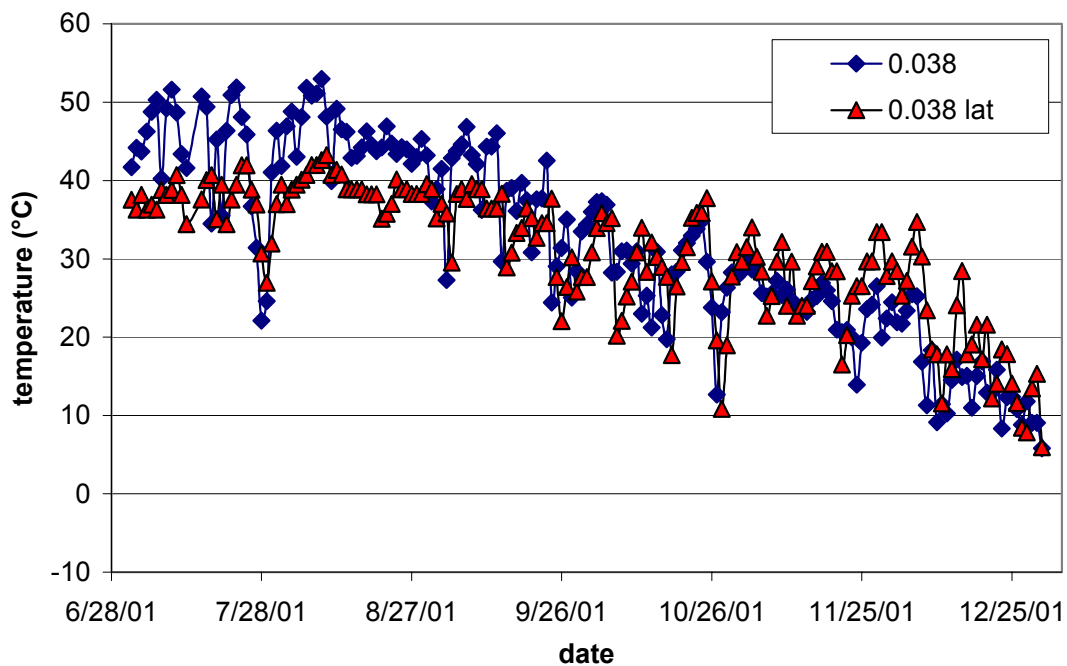


Figure 4.23. Maximum daily pavement temperature at 0.038m depth showing actual (0.038) versus predicted (0.038 lat).

Pavement Temperature Prediction Model Selection

Equations 4.14 and 4.15 have been shown to be accurate models for predicting the maximum and minimum daily pavement temperatures, respectively, at the Virginia Smart Road. However, these models were developed to incorporate the near surface temperature, a quantity that is most likely not available to most users and has not been used in previous studies. Therefore, Equations 4.16 through 4.19 were developed to incorporate the maximum or minimum daily ambient temperature, respectively, such that these models can be more readily used for locations beyond those incorporated in this study. In addition, Equations 4.16 through 4.19 incorporate the calculated daily solar radiation such that these models can be evaluated using pavement temperature data within the HMA layers from other studies in any location given a maximum or minimum ambient temperature, date, and latitude. Using data from two test locations from the LTPP study, the daily pavement temperature prediction models presented in Equations 4.16 through 4.19 have been shown to be applicable to predicting the pavement temperature in multiple locations. The maximum or minimum daily pavement temperature prediction is calculated by incorporating the day of the year, the latitude of the location in question (such that the daily solar radiation for that location can be calculated), and the daily ambient maximum or minimum temperature.

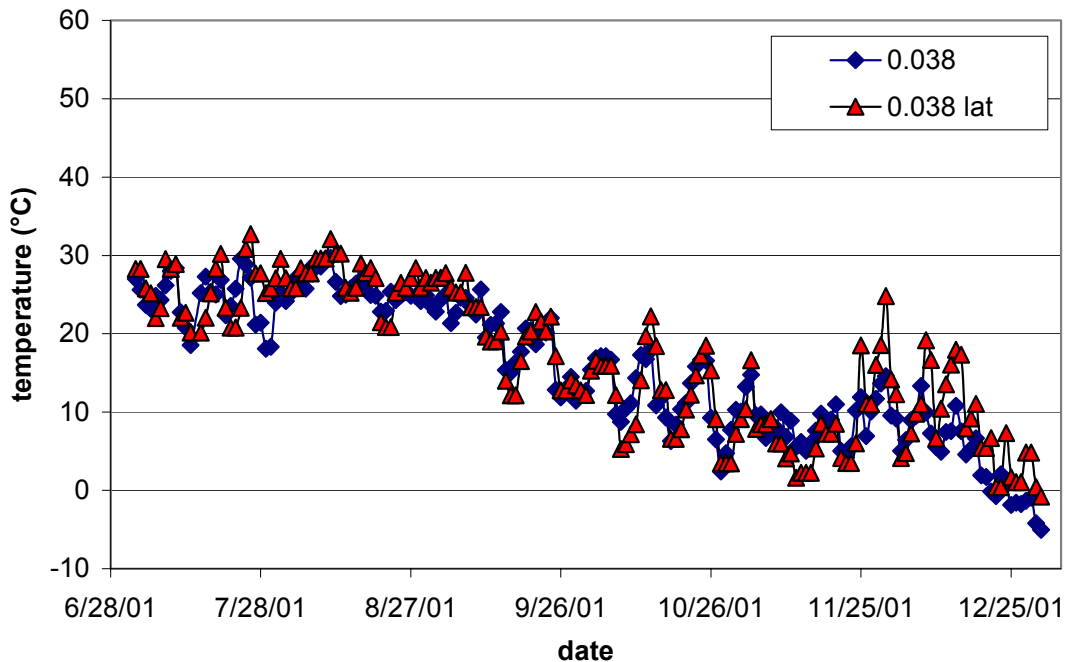


Figure 4.24. Minimum daily pavement temperature at 0.038m depth showing actual (0.038) versus predicted (0.038 lat).

CHAPTER 5

SUMMARY AND CONCLUSIONS

The Virginia Smart Road was constructed in Blacksburg, Virginia as a testing facility for various types of transportation-related technology. Included among the various types of conducted research is an instrumented pavement test facility. The pavement test facility is approximately 2.5km in length, of which 1.3km is flexible pavement that is divided into 12 sections of approximately 100m each. Each flexible pavement section is comprised of a multi-layer pavement system and possesses a unique structural configuration. Each layer within each section is instrumented to measure quantitative pavement responses to traffic loading and environmental conditions. This study focuses on assessing the effects of environment on flexible pavements and is divided into two sections: moisture content determination and temperature profile modeling.

The data pertaining to moisture content determination was collected in two portions, designated herein as Phase 1 and Phase 2. Data from Phase 1 consisted of measurements from two types of time domain reflectometers: CS610 and CS615 TDR probes. Data from the Phase 1 study, obtained at the Virginia Smart Road during the period of March 1999 to May 2000, was used to make comparisons between the two types of TDR probes. The data from the Phase 2 study, collected from approximately March 2000 to May 2001, was used to make comparisons between the different pavement sections. A calibration model was developed for both the CS610 and the CS615 TDR probes utilizing material from the 21B aggregate subbase layer (Layer 6). The moisture content was analyzed across probe type and across the different sections through measurements of the moisture content in Layer 6. In addition, a software simulation was used to qualitatively determine the sampling volume from which the moisture content is determined for the CS615 TDR probe.

The data pertaining to temperature profile monitoring was analyzed to develop a model that is capable of accurately predicting the pavement temperature distribution given limited input variables. The pavement temperatures were compared across similar layers and for different layer-materials at the same depth. A set of models was developed which allows for the determination of daily maximum or minimum pavement temperatures within the HMA layers at the Virginia Smart Road. In addition, another set of models was developed to allow calculation of the daily maximum and minimum HMA

pavement temperatures at other locations based on the variation of solar radiation with respect to latitude.

5.1 FINDINGS

The following findings were noted during this study:

- The differences between the methods of data collection for the two TDR probe types used in this study would necessitate the use of the CS615 TDR probe for large scale studies where the moisture content would be remotely monitored at small time intervals.
- Utilization of the CS615 TDR probe in a coarse-grained material (such as an aggregate base layer) may be questionable due to the limited distribution distance of the electric field about the probe rods.
- The electric field surrounding a two-rod TDR probe (as determined by computer modeling) does not appear to be evenly distributed about the probe. It was seen that the decay in the strength of the electric field (as given by computer modeling) varies with respect to the probe orientation.
- It was found that static discharge from electrical storms may cause a change in the moisture content as derived from the CS615 TDR probe output. Probes in several pavement sections were affected as determined by a sudden increase in the reported moisture content that was well beyond the physical possibility.
- A calibration procedure is essential for accurate moisture content measurements using the CS610 TDR probe. The universal calibration equation given by Topp *et al.* (1980) may not prove accurate in all situations.
- This study showed that a calibration procedure can be performed for the CS610 TDR probe to improve the accuracy of the moisture content measurements obtained using this TDR probe.
- A difference in the variability of the moisture content was noted between sections incorporating a geocomposite moisture barrier and those sections that did not contain the geocomposite moisture barrier. The variability in moisture content is not dependent upon the location of the moisture barrier given the two depths in

this study, but on the presence or absence of the moisture barrier within the pavement system.

- The maximum pavement temperature at a depth of 0.038m is generally much higher than the maximum near surface temperature and the maximum air temperature (measured off-site) during the summer months. The same phenomenon is observed to a lesser degree in the winter months.
- The minimum pavement temperature at a depth of 0.038m is generally slightly higher than the minimum near surface temperature and the minimum air temperature (measured off-site) during the summer months. The same phenomenon is observed to a lesser degree in the winter months.
- The difference between the maximum pavement temperature at a depth of 0.038m and the maximum near surface temperature is greatest during the summer months when the solar radiation is at its highest.
- The maximum (or minimum) temperature in each layer occurs at different times than the maximum (or minimum) near surface temperature with a time lag that increases with increasing depth from the surface.
- A linear relationship exists between the daily maximum (and minimum) near surface temperature and the daily maximum (and minimum) pavement temperature at each depth.
- Daily max or min pavement temp can be predicted from local ambient temp and solar radiation for any location. In addition, if the solar radiation measurement is not available it may be calculated from the latitude and day of the year.
- Incorporating the ambient temperature and a calculated daily solar radiation into a model to predict the daily maximum or minimum pavement temperatures allows for prediction in multiple locations using data from previous studies.

5.2 CONCLUSIONS

The moisture content was measured using two types of TDR probes placed across multiple flexible pavement sections having different structural configurations at the

Virginia Smart Road. The following conclusions are presented from this portion of the study:

- The moisture content as given by the CS610 and the CS615 TDR probes is approximately equal following a calibration procedure for each.
- A calibration model has been developed to give the moisture content for the CS610 and CS615 TDR probe in a typical aggregate base layer (VDOT 21B) based on their respective outputs.

- The moisture content can be calculated using the CS610 TDR probe from the following:

$$\omega = 22.903\lambda - 8.1623$$

where ω is the volumetric moisture content and λ represents the effective length in m.

- The moisture content can be calculated using the CS615 TDR probe from the following:

$$\omega = -66.38t^2 + 174.90t - 94.89$$

where ω is the volumetric moisture content and t represents the period of oscillation in ms.

- It was seen that the presence of a geocomposite material acting as a moisture barrier reduces the variability of the moisture content within the subbase material.

The temperature profile was measured and modeled using thermocouples placed at different depths across multiple flexible pavement sections having different structural configurations at the Virginia Smart Road. The following conclusions are presented from this portion of the study:

- An accurate model has been developed to predict the daily maximum or minimum pavement temperature for surface HMA mixes independent of different asphalt binders and gradations.

- An accurate model has been developed to predict the daily maximum and minimum pavement temperature at various locations by calculating the daily solar radiation or latitude and day of year.
- The maximum daily pavement temperature (°C) for any location can be calculated from either of the following:

$$y = 0.6861x_1 + 5.6736 \times 10^{-4}x_2 - 27.8739x_3 + 2.78752$$

where

y = predicted pavement temperature (°C);

x_1 = daily minimum ambient temperature (°C);

x_2 = calculated daily solar radiation (kJ/m²day); and

x_3 = depth from the surface (m).

or

$$y = 1.1265x_1 + 0.001820x_2 + 0.0839x_3 - 53.5247x_4 + 6.0775$$

where

y = predicted pavement temperature (°C);

x_1 = daily maximum ambient temperature (°C);

x_2 = day of year (1 to 365);

x_3 = latitude (degrees); and

x_4 = depth from surface (m).

- The minimum daily pavement temperature (°C) for any location can be calculated from either of the following:

$$y = 0.6754x_1 + 3.7642 \times 10^{-4}x_2 + 7.2043x_3 - 1.2097$$

where

y = predicted pavement temperature (°C);

x_1 = daily minimum ambient temperature (°C);

x_2 = calculated daily solar radiation (kJ/m²day); and

x_3 = depth from the surface (m).

or

$$y = 0.9608x_1 + 0.0641x_2 - 0.5616x_3 + 9.4893x_4 + 27.5986$$

where

y = predicted pavement temperature ($^{\circ}\text{C}$);

x_1 = daily minimum ambient temperature ($^{\circ}\text{C}$);

x_2 = day of year (1 to 365);

x_3 = latitude (degrees); and

x_4 = depth from surface (m).

CHAPTER 6

RECOMMENDATIONS

Based on this study, the following recommendations are made:

- Further study of the electric field distribution about the CS615 TDR probe needs consideration to determine the suitability of using this probe in a coarse grained material for quantitative moisture content measurements.
- It is suggested for future study, that the TDR probe geometry be investigated to determine if an optimum configuration exists to maximize the interaction between the electric field and the material surrounding the TDR probe.
- The data set used to develop the model covered a period of 14 months. Incorporating data from a longer period of time is suggested to improve the accuracy of the developed models.
- If the prediction of pavement temperatures was desired on an hourly or some other sub-day time interval, a study involving “real-time” measurement of solar radiation at the location where the pavement temperature is measured could prove beneficial in terms of increased accuracy over calculated solar radiation values.

REFERENCES

- Al-Qadi, I. L., W. M. Nassar, A. Loulizi, G. W. Flintsch, and T. Freeman (2000) "Flexible Pavement Instrumentation at the Virginia Smart Road." Presented at 79th Transportation Research Board Annual Meeting, Washington, DC, Jan.
- Ali, H. and A. Lopez (1996) "Statistical Analysis of Temperature and Moisture Effects on Pavement Structural Properties Based on Seasonal Monitoring Data." Transportation Research Record, No. 1540, 48-55.
- Andersland, O. B. and D. M. Anderson (1978) *Geotechnical Engineering for Cold Regions*. McGraw-Hill Co., New York, NY, 566p.
- Anderson, E. E. (1983) *Fundamentals of Solar Energy Conversion*. Addison-Wesley Publishing Co., Reading, MA, 636p.
- Applied Numerical Methods for Digital Computation. (1985) 3rd ed., Eds. M. L. James, G. M. Smith, and J. C. Wolford, Harper and Row Publishers, New York, NY, 753p.
- Baker, J. M. and R. J. Lascano (1989) "The Spatial Sensitivity of Time-Domain Reflectometry." *Soil Science*, Vol. 147, No. 5, May, 378-384.
- Barber, E. S. (1957) "Calculation of Maximum Pavement Temperatures from Weather Reports." Bulletin 168, Highway Research Board, National Research Council, 1-8.
- Bell, J. P., T. J. Dean, and M. G. Hodnett (1987) "Soil Moisture Measurement by an Improved Capacitance Technique, Part II. Field Techniques, Evaluation, and Calibration." *Journal of Hydrology*, Vol. 93, 79-90.
- Birgisson, B., J. Ovik, and D. E. Newcomb (2000) "Analytical Predictions of Seasonal Variations in Flexible Pavements at the MnRoad Site." Transportation Research Record No. 1730, Transportation Research Board, 81-90.
- Bosscher, P. J., H. U. Bahia, S. Thomas, and J. S. Russell (1998) "Relationship Between Pavement Temperature and Weather Data: Wisconsin Field Study to Verify SuperPave Algorithm." Transportation Research Record No. 1609, Transportation Research Board, 1-11.
- Böttcher, C. J. F. (1973) *Theory of Electric Polarization*. Elsevier Publishing Co., New York, NY.

- Brisco, B., T. J. Pultz, R. J. Brown, S. C. Topp, M. A. Hares, and W. D. Zebchuk (1992) "Soil Moisture Measurement Using Portable Dielectric Probes and Time Domain Reflectometry." *Water Resources Research*, Vol. 28, No. 5, May, 1339-1346.
- Campbell Scientific (1996) *CS615 Water Content Reflectometer Instruction Manual*. Version 8221-07, Campbell Scientific, Inc., Logan, UT, 12p.
- Cole, K. S. and R. H. Cole (1941) "Dispersion and Absorption in Dielectrics; I. Alternating Current Characteristics." *Journal of Chemical Physics*, Vol. 9, 341-351.
- Davis, J. L. and W. J. Chudobiak (1975) "In-Situ Meter for Measuring Relative Permittivity of Soils." Geological Survey of Canada, Paper 75-1, Part A, 75-79.
- Dean, T. J., J. P. Bell, and A. J. B. Baty (1987) "Soil Moisture Measurement by and Improved Capacitance Technique, Part I. Sensor Design and Performance." *Journal of Hydrology*, Vol. 93, 67-78.
- Debye, P. (1929) *Polar Molecules*. Chemical Catalog Co., New York, NY, 172p.
- Dempsey, B. J. (1970) "A Heat Transfer Model for Evaluating Frost Action and Temperature Related Effects in Multilayered Pavement Systems." *Highway Research Record No. 342*, National Research Council, 39-56.
- Dirksen, C. and S. Dasberg (1993) "Improved Calibration of Time Domain Reflectometry Soil Water Content Measurements." *Soil Science Society of America Journal*, Vol. 57, 660-667.
- Dobson, M. C., F. Kouyate, and F. T. Ulaby (1984) "A Reexamination of Soil Textural Effects on Microwave Emission and Backscattering." *IEEE Transactions on Geoscience and Remote Sensing*, Vol. 22, 530-535.
- Dobson, M. C., F. T. Ulaby, M. T. Hallikainen, and M. A. El-Rayes (1985) "Microwave Dielectric Behavior of Wet Soil – Part II: Dielectric Mixing Models." *IEEE Transactions on Geoscience and Remote Sensing*, Vol. GE-23, Jan, 35-46.
- Fellner-Feldegg, H. (1969) "The Measurement of Dielectric in Time Domain." *Journal of Physical Chemistry*, Vol. 73, No. 3, 616-623.
- Forsyth, R. A., G. K. Wells, and J. H. Woodstrom (1987) "Economic Impact of Pavement Subsurface Drainage" *Transportation Research Record No. 1121*, Transportation Research Board, 77-85.

- Geiger, R. (1965) *The Climate Near the Ground*. Harvard University Press, Cambridge, MA, 611p.
- Hallikainen, M. T., F. T. Ulaby, M. C. Dobson, M. A. El-Rayes, and L. Wu (1985) "Microwave Dielectric Behavior of Wet Soil – Part I: Empirical Models and Experimental Observations from 1.4 to 18 GHz." *IEEE Transactions on Geoscience and Remote Sensing*, Vol. 23, Jan, 25-34.
- Hermansson, A. (2000) "Simulation Model for Calculating Pavement Temperatures, Including Maximum Temperature." *Transportation Research Record No. 1699*, Transportation Research Board, 134-141.
- Hermansson, A. (2001) "A Mathematical Model for Calculating Pavement Temperatures, Comparisons Between Calculated and Measured Temperatures." Presented at Transportation Research Board 80th Annual Meeting, Washington, DC, Jan.
- Huang, Y. H. (1993) *Pavement Analysis and Design*. Prentice Hall, Englewood Cliffs, NJ, 805p.
- Iqbal, M. (1983) *An Introduction to Solar Radiation*. Academic Press, New York, NY, 390p.
- Jackson, T. J. (1980) "Laboratory Evaluation of a Field-Portable Dielectric/Soil-Moisture Probe." *IEEE Transactions on Geoscience and Remote Sensing*, Vol. 28, No. 2, Mar, 241-245.
- Jiang, Y. J. and S. D. Tayabji (1999) "Evaluation of In-Situ Moisture Content at LTPP Seasonal Monitoring Program Sites." Presented at Transportation Research Board 78th Annual Meeting, Washington, D. C., Jan.
- Klemunes, Jr., J. A. (1995) "Determining Soil Volumetric Moisture Content Using Time Domain Reflectometry." Master of Science Thesis, University of Maryland, College Park, MD, 329p.
- Knight, J. H. (1992) "Sensitivity of Time Domain Reflectometry Measurements to Lateral Variations in Soil Water Content." *Water Resources Research*, Vol. 28, No. 9, Sept, 2345-2352.
- Knight, J. H., I. White, and S. J. Zegelin (1994) "Sampling Volume of TDR Probes Used for Water Content Monitoring." *Proceedings, Symposium on TDR in Environmental, Infrastructure, and Mining Applications*, Northwestern University, Evanston, IL,

Special Publication, SP 19-94, US Department of the Interior, Bureau of Mines, Sept, 93-104.

Kreith, F. (1986) *Principles of Heat Transfer*. 4th ed., Harper and Row, New York, NY, 700p.

Liddle, W. J. (1962) "Application of AASHO Road Test Results to the Design of Flexible Pavement Structures." Proceedings of the International Conference on the Structure Design of Asphalt Pavements, University of Michigan, Ann Arbor, MI.

Ledieu, J., P. De Ridder, P. De Clerck, and S. Dautrebande (1986) "A Method of Measuring Soil Moisture by Time Domain Reflectometry." *Journal of Hydrology*, Vol. 88, 319-328.

Lukanen, E. O., C. Han, and E. L. Skok, Jr. (1998) "Probabilistic Method of Asphalt Binder Selection Based on Pavement Temperature." *Transportation Research Record No. 1609*, Transportation Research Board, 12-20.

Lytton, R. L., D. E. Pufahl, C. H. Michalak, H. S. Liang, and B. J. Dempsey (1993) "An Integrated Model of the Climatic Effects on Pavements." FHWA Report RD-90-033, Federal Highway Administration, Washington DC, 304p.

Marienfild, M. L. and T. L. Baker (1999) "Paving Fabric Interlayer as a Pavement Moisture Barrier." *Transportation Research Circular No. E-C006*, Transportation Research Board, Mar.

Marshall, C., Meier, R. W., and M. Welsh (2001) "Seasonal Temperature Effects on Flexible Pavements in Tennessee." Presented at Transportation Research Board 80th Annual Meeting, Washington, DC, Jan.

McAdam, J. (1820) *Report to the London Board of Agriculture*.

Mitchell, J. K. (1993) *Fundamentals of Soil Behavior*, 2nd ed., John Wiley and Sons, New York, NY, 437p.

Mohseni, A. (1998) *LTPP Seasonal Asphalt Concrete Pavement Temperature Models*, Publication No. FHWA-RD-97-103, Federal Highway Administration, Washington, DC, 65p.

Mohseni, A and M. Symons (1998a) "Improved AC Pavement Temperature Models from LTPP Seasonal Data." Presented at Transportation Research Board 77th Annual Meeting, Washington, DC, Jan.

- Mohseni, A and M. Symons (1998b) "Effect of Improved LTPP AC Pavement Temperature Models on SuperPave Performance Grades." Presented at Transportation Research Board 77th Annual Meeting, Washington, DC, Jan.
- Ovik, J. M., B. Birgisson, D. E. Newcomb (1999) "Characterizing Seasonal Variations in Flexible Pavement Material Properties." Transportation Research Record No. 1684, Transportation Research Board, 1-7.
- Park, D., N. Buch, K. Chatti (2001) "Development of Effective Layer Temperature Prediction Model and Temperature Correction Using FWD Deflections." Presented at Transportation Research Board 80th Annual Meeting, Washington, DC, Jan.
- Rada, G. R., G. E. Elkins, A. Lopez, C. A. Richter, and B. Henderson (1994) "LTPP Seasonal Monitoring Program: Instrumentation Selection and Installation." Transportation Research Record No. 1432, Transportation Research Board, 32-43.
- Ramo, S., J. R. Whinnery, and T. Van Duzer (1994) *Fields and Waves in Communication Electronics*. 3rd ed., John Wiley and Sons, New York, NY, 844p.
- Roberston, W. D. (1997) "Determining the Winter Design Temperature for Asphalt Pavements." Association of Asphalt Paving Technologists, Vol. 66, 312-343.
- Roth, C. H., M. A. Malicki, and R. Plagge (1992) "Empirical Evaluation of the Relationship Between Soil Dielectric Constant and Volumetric Water Content as the Basis for Calibrating Soil Moisture Measurements by TDR." Journal of Soil Science, Vol. 43, Mar, 1-13.
- Rumney, T. N. and R. A. Jimenez (1969) "Pavement Temperatures in the Southwest." Highway Research Record No. 361, National Research Council, 1-13.
- Solaimanian, M. and P. Bolzan (1993) *Analysis of the Integrated Model of Climatic Effects on Pavements*. SHRP Report A-637, Strategic Highway Research Program, National Research Council, Washington, DC, 158p.
- Solaimanian, M. and T. W. Kennedy (1993) "Predicting Maximum Pavement Surface Temperature Using Maximum Air Temperature and Hourly Solar Radiation." Transportation Research Record No. 1417, Transportation Research Board, 1-11.
- Shen, L. C. and J. A. Kong (1995) *Applied Electromagnetism*. PWS Publishing Co., Boston, MA, 606p.

- Topp, G. C., J. L. Davis, and A. P. Annan (1980) "Electromagnetic Determination of Soil Water Content: Measurements in Coaxial Transmission Lines." *Water Resources Research*, Vol. 16, 574-582.
- Topp, G. C., J. L. Davis, and A. P. Annan (1982) "Electromagnetic Determination of Soil Water Content Using TDR: II – Evaluation of Installation and Configuration of Parallel Transmission Lines." *Soil Science Society of America Journal*, Vol. 46, 678-684.
- Topp, G. C., J. L. Davis, W. G. Bailey, and W. D. Zebchuck (1984) "The Measurement of Soil Water Content Using a Portable TDR Hand Probe." *Canadian Journal of Soil Science*, Vol. 64, 313-321.
- Wang, J. R. and T. J. Schmugge (1980) "An Empirical Model for the Complex Dielectric Permittivity of Soils as a Function of Water Content." *IEEE Transactions on Geoscience and Remote Sensing*, Vol. 18, No. 4, Oct, 288-295.
- Whalley, W. R. (1993) "Considerations on the Use of Time-Domain Reflectometry (TDR) for Measuring Soil Water Content." *Journal of Soil Science*, Vol. 44, 1-9.
- Zegelin, S. J., I. White, and D. R. Jenkins (1989) "Improved Field Probes for Soil Water Content and Electrical Conductivity Measurement Using Time Domain Reflectometry." *Water Resources Research*, Vol. 25, No. 11, Nov, 2367-2376.

APPENDIX A

TDR PROBE CALIBRATION

Table A.1. Output from CS610 probes for each calculated volumetric moisture content.

θ	Effective length - waveform		Effective length - wintdr98	
	25.6m	26.4m	25.6m	26.4m
5.2175	0.5855	0.5859	0.6070	0.5959
9.0066	0.7536	0.7681	0.7786	0.8092
10.6863	0.8084	0.8312	0.8218	0.8672
11.6405	0.8488	0.8420	0.8739	0.8564
13.2783	0.9364	0.9501	0.9820	0.9901
16.1545	1.0517	1.0768	1.0610	1.0875

Table A.2. Volumetric moisture contents obtained using CS610 TDR probe showing calculated moisture content and results from each calibration equation.

θ	Equation 3.8	Equation 3.9	Equation 3.10	Equation 3.11	Equation 3.12	Equation 3.13
5.2175	5.2578	5.2577	5.2515	5.2557	5.0228	5.1054
9.0066	9.1930	9.3357	9.2638	9.2436	9.7111	9.4756
10.6863	10.4745	10.7476	10.6133	10.2479	10.9861	10.6249
11.6405	11.4211	10.9903	11.2007	11.4601	10.7487	11.0945
13.2783	13.4701	13.4091	13.4410	13.9709	13.6864	13.8387
16.1545	16.1694	16.2447	16.2129	15.8076	15.8288	15.8428

Table A.3. Summary of error for CS610 TDR probe (Topp's equation and developed trend lines).

Equation	Description	SSE	RMSE	R-squared
3.3	Topp's Equation	175.9	5.9313	-----
3.8	waveform - 25.6m	0.4305	0.4913	0.9976
3.9	waveform - 26.4m	0.5617	0.3352	0.9919
3.10	Average from waveform	0.7055	0.3756	0.9958
3.11	wintdr98 software - 25.6m	1.9238	0.6203	0.9873
3.12	wintdr98 software - 26.4m	2.4488	0.6998	0.9757
3.13	Average from software	1.6399	0.5727	0.9864

Table A.4. Output from CS615 probes for each calculated volumetric moisture content.

ω	22m		27m	
	Frequency, Hz	Period, ms	Frequency, Hz	Period, ms
1.0648	1270.6520	0.7870	1257.9410	0.7949
5.2337	1190.4708	0.8400	1192.8184	0.8384
8.7846	1149.4990	0.8699	1132.0010	0.8834
10.1206	1084.7940	0.9218	1074.2070	0.9309
13.7839	1007.6865	0.9924	993.6861	1.0064
15.8698	911.5828	1.0970	896.8631	1.1150
20.2137	856.6634	1.1673	807.3552	1.2386

Table A.5. Volumetric moisture contents obtained using CS615 TDR probe showing calculated moisture content and results from each calibration equation.

ω	Equation 3.14	Equation 3.15	Equation 3.16	Equation 3.17	Equation 3.18	Equation 3.19
1.0648	1.7917	2.0733	1.9200	0.8184	1.1515	0.9987
5.2337	5.4054	4.9012	5.1360	5.8991	5.1716	5.5604
8.7846	7.2772	7.5808	7.4201	8.0043	8.3502	8.2154
10.1206	10.2320	10.1263	10.1665	10.6706	10.8177	10.8042
13.7839	13.6599	13.5721	13.6011	13.0454	13.4143	13.3011
15.8698	17.4952	17.2534	17.3488	16.2799	15.9409	16.1178
20.2137	19.2347	19.6021	19.4323	19.9770	20.1877	20.1883

Table A.6. Summary of error for CS615 TDR probe (manufacturer equations and developed trend lines).

Equation	Description	SSE	RMSE	R-squared
3.4	≤ 1.0 dS/m	2340.5	19.57	-----
3.5	1.8 dS/m	2136.5	18.87	-----
3.6	3.0 dS/m	1583.6	16.246	-----
3.14	2nd degree - 22m	6.458×10^{-4}	1.0374×10^{-2}	0.9745
3.15	2nd degree - 27m	4.9101×10^{-4}	9.0462×10^{-3}	0.9806
3.16	Average - 2nd degree	5.4363×10^{-4}	9.5186×10^{-3}	0.9786
3.17	3rd degree - 22m	2.1844×10^{-4}	6.0337×10^{-3}	0.9915
3.18	3rd degree - 27m	8.2836×10^{-5}	3.7156×10^{-3}	0.9967
3.19	Average - 3rd degree	1.1976×10^{-4}	4.4676×10^{-3}	0.9953

APPENDIX B

TDR PROBE PLACEMENT AT VIRGINIA SMART ROAD

Table B.1a. Location of TDR probes (CS610 and CS615) at the Virginia Smart Road.

Layer	Material Description	Depth from Surface (m)	Section					
			A	B	C	D	E	F
4	Open-Graded Drainage Layer	0.263	AM4-1B AM4-2B	BM4-1ME BM4-1M BM4-2M		DM4-1M DM4-2M		
		0.338						
		0.356						
5	21A Cement Treated Aggregate Base Layer	0.413		BM5-1ME BM5-1M BM5-2M			EM4-1ME EM4-1M EM4-2M	
6	21B Aggregate Base Layer	0.488					EM6-1ME EM6-1M EM6-2M	FM6-2ME FM6-1M FM6-2M
		0.506						
		0.588		BM6-1ME BM6-1ME BM6-2M				
7	Original Subgrade	0.638						
		0.738		BM7-1T BM7-2T				
		0.918	AM7-1M					
		0.945					FM7-1M	
		0.969	AM7-2M					
		0.993		BM7-2ME				
		0.994	AM7-1ME					
		0.996					FM7-2M FM7-1ME	
		1.02		BM7-1ME				
		1.096		BM7-1M				
		1.147	AM7-2ME					
		1.121		BM7-2M				
1.238								

Table B.1b. Location of TDR probes (CS610 and CS615) at the Virginia Smart Road.

Layer	Material Description	Depth from Surface (m)	Section					
			G	H	I	J	K	L
4	Open-Graded Drainage Layer	0.263		HM4-1ME HM4-1M HM4-2M	IM4-1ME IM4-1M IM4-2M			LM4-1ME LM4-1M LM4-2M
		0.338			JM4-1ME JM4-1M JM4-2M			
		0.356						KM4-1ME KM4-1M KM4-2M
5	21A Cement Treated Aggregate Base Layer	0.413			IM5-1ME IM5-1M IM5-2M			
6	21B Aggregate Base Layer	0.488	GM6-1ME GM6-1M	HM6-1ME HM6-1M HM6-2M	IM6-2ME IM6-2ME	JM6-1ME JM6-2ME JM6-1M JM6-2M		LM6-1ME LM6-2ME LM6-1M LM6-2M
		0.506						KM6-1ME KM6-2ME KM6-1M KM6-2M
		0.588						
7	Original Subgrade	0.638	GM7-1TE GM7-2TE GM7-1T GM7-2T					
		0.738						
		0.918						
		0.945						
		0.969						
		0.993						
		0.994						
		0.996						
		1.02						
		1.096						
		1.147						
1.121								
1.238		GM7-1ME GM7-2ME GM7-1M						

APPENDIX C

THERMOCOUPLE CALIBRATION

Table C.1a. Thermocouple calibration showing actual temperature value with value obtained from thermocouple.

Thermocouple	Total Wire Length, m	High Temperature, °C			Low Temperature, °C		
		Actual Value	Thermocouple Value	Difference	Actual Value	Thermocouple Value	Difference
AT1-1B	22.82	98.0	97.3	0.7	0.4	1.1	-0.7
AT1-2B	23.32	97.8	97.5	0.3	0.2	0.2	0.0
AT1-3B	23.82	98.0	96.6	1.4	0.4	0.6	-0.2
AT2-1B	26.55	98.0	97.2	0.8	0.4	0.5	-0.1
AT2-1T	26.32	98.0	97.3	0.7	0.2	0.3	-0.1
AT2-2B	27.05	97.6	97.0	0.6	0.4	0.8	-0.4
AT2-2T	26.82	97.8	96.9	0.9	0.2	0.6	-0.4
AT2-3B	27.55	98.0	96.0	2.0	0.2	1.0	-0.8
AT2-3T	27.32	98.0	97.5	0.5	0.6	1.0	-0.4
AT4-1B	24.63	98.2	97.5	0.7	0.2	0.4	-0.2
AT4-2B	25.13	98.2	97.6	0.6	0.0	0.2	-0.2
AT6-1B	23.88	98.2	97.9	0.3	0.6	0.5	0.1
AT6-2B	24.38	98.2	97.9	0.3	0.4	0.5	-0.1
AT7-1B	28.58	98.0	97.6	0.4	0.6	0.5	0.1
AT7-1M	27.18	98.0	97.6	0.4	1.0	0.6	0.4
AT7-7T	26.73	98.0	97.8	0.2	0.2	0.5	-0.3
AT7-2B	29.08	98.2	97.6	0.6	0.4	0.3	0.1
AT7-2M	27.68	98.0	97.3	0.7	0.6	0.5	0.1
AT7-2T	27.23	98.0	97.6	0.4	0.4	0.7	-0.3
CT7-1B	29.54	98.2	97.5	0.7	0.0	0.1	-0.1
CT7-1M	25.84	98.0	96.9	1.1	0.4	0.6	-0.2
CT7-2B	30.04	98.2	97.5	0.7	0.2	0.5	-0.3
CT7-2M	26.34	98.0	97.6	0.4	0.0	0.2	-0.2
ET2-1B	17.51	98.6	98.2	0.4	0.2	0.6	-0.4
ET2-2B	17.81	98.6	97.8	0.8	0.2	0.8	-0.6
ET2-3B	18.11	98.6	97.6	1.0	0.2	1.4	-1.2
GT1-1B	20.08	98.4	97.8	0.6	0.6	0.4	0.2
GT1-2B	20.58	98.4	97.5	0.9	0.4	0.4	0.0
GT1-3B	21.08	98.8	98.2	0.6	1.2	0.7	0.5
GT2-1T	23.68	98.6	98.5	0.1	0.4	0.7	-0.3
GT2-2B	24.29	98.4	97.5	0.9	0.6	1.0	-0.4
GT2-2T	24.18	98.6	98.1	0.5	0.0	0.7	-0.7
GT2-3B	24.79	98.6	98.1	0.5	0.2	0.7	-0.5
GT2-3T	24.68	98.8	98.2	0.6	0.4	0.8	-0.4
GT3-1B	26.34	98.4	97.6	0.8	0.6	1.0	-0.4
GT3-2B	26.84	98.6	97.6	1.0	0.4	0.4	0.0
GT3-3B	27.34	98.4	97.8	0.6	0.6	0.7	-0.1
GT5-1B	19.26	98.8	98.1	0.7	1.4	1.3	0.1
GT5-2B	19.76	99.0	98.1	0.9	1.0	0.5	0.5
GT5-3B	20.26	98.8	98.1	0.7	0.8	0.5	0.3
GT7-1B	22.64	98.8	98.1	0.7	1.4	1.3	0.1
GT7-1M	21.24	98.8	98.2	0.6	0.4	1.0	-0.6
GT7-1T	20.79	98.6	98.1	0.5	0.4	0.6	-0.2
GT7-2B	23.14	98.6	98.1	0.5	0.2	0.4	-0.2
GT7-2M	21.74	98.6	97.2	1.4	0.6	0.8	-0.2
GT7-2T	21.29	98.8	97.9	0.9	0.6	1.1	-0.5

Table C.1b. Thermocouple calibration showing actual temperature value with value obtained from thermocouple.

Thermocouple	Total Wire Length, m	High Temperature, °C			Low Temperature, °C		
		Actual Value	Thermocouple Value	Difference	Actual Value	Thermocouple Value	Difference
IT1-3B	21.98	98.6	98.3	0.3	2.0	2.0	0.0
IT2-1B	24.69	99.0	98.0	1.0	0.4	1.3	-0.9
IT2-1T	24.58	97.2	97.0	0.2	0.0	0.9	-0.9
IT2-2B	25.19	98.4	98.2	0.2	0.8	1.1	-0.3
IT2-2T	25.08	98.8	98.1	0.7	0.2	0.5	-0.3
IT2-3B	25.69	99.0	98.2	0.8	1.0	1.5	-0.5
IT2-3T	25.58	99.2	97.5	1.7	1.4	2.0	-0.6
IT3-1B	21.14	98.2	98.1	0.1	0.6	0.5	0.1
IT3-2B	21.64	98.2	97.8	0.4	0.4	0.4	0.0
IT3-3B	22.14	99.0	98.1	0.9	1.4	2.5	-1.1
IT4-1B	22.71	98.2	97.7	0.5	0.4	0.4	0.0
IT4-2B	23.21	99.0	97.6	1.4	0.4	0.2	0.2
IT4-3B	23.71	98.0	97.6	0.4	0.4	0.6	-0.2
IT5-1B	20.44	98.2	97.6	0.6	0.2	0.3	-0.1
IT5-2B	20.94	98.4	97.3	1.1	0.4	0.9	-0.5
IT5-3B	21.44	98.4	97.7	0.7	0.2	0.4	-0.2
IT6-1B	23.14	98.2	97.3	0.9	0.6	0.8	-0.2
IT6-2B	23.64	98.2	97.7	0.5	0.4	0.5	-0.1
IT6-3B	24.14	97.8	96.7	1.1	0.4	1.0	-0.6
JT1-1B	18.98	99.2	98.2	1.0	0.2	1.1	-0.9
JT1-2B	19.48	98.8	98.0	0.8	0.2	0.5	-0.3
JT1-3B	19.98	98.4	98.2	0.2	0.2	0.3	-0.1
JT2-1B	21.71	98.6	96.6	2.0	0.2	1.2	-1.0
JT2-1T	21.48	98.6	98.0	0.6	0.2	0.5	-0.3
JT2-2B	22.21	98.8	97.7	1.1	0.2	0.6	-0.4
JT2-2T	21.98	98.6	98.0	0.6	0.2	0.5	-0.3
JT2-3B	22.71	98.6	97.9	0.7	0.2	1.6	-1.4
JT2-3T	22.48	98.6	97.4	1.2	0.2	0.9	-0.7
JT4-1B	22.29	98.8	98.1	0.7	0.2	1.3	-1.1
JT4-2B	22.79	99.0	98.4	0.6	0.2	1.3	-1.1
JT4-3B	23.29	98.8	98.1	0.7	0.4	0.7	-0.3
JT6-1B	22.04	98.8	98.5	0.3	0.2	0.8	-0.6
JT6-2B	22.54	98.6	97.8	0.8	0.0	0.5	-0.5
JT6-3B	23.04	98.6	97.9	0.7	0.2	0.8	-0.6
JT1-1B	22.58	98.8	97.9	0.9	0.4	0.8	-0.4
JT1-2B	23.08	98.8	98.1	0.7	0.4	0.5	-0.1
JT1-3B	23.58	98.8	98.0	0.8	0.2	0.3	-0.1
JT2-1B	27.14	98.6	97.9	0.7	1.2	1.7	-0.5
JT2-2B	27.64	98.8	98.0	0.8	0.4	1.1	-0.7
JT2-2T	27.64	98.2	97.1	1.1	0.4	0.4	0.0
JT2-3B	28.14	98.8	98.1	0.7	0.6	0.7	-0.1
JT2-3T	28.14	98.4	97.4	1.0	0.4	0.5	-0.1
JT4-1B	21.31	98.8	98.3	0.5	0.4	0.7	-0.3
JT4-2B	21.81	98.6	97.6	1.0	0.4	1.0	-0.6
JT4-3B	22.31	98.8	98.0	0.8	0.4	0.7	-0.3
JT5-1B	24.94	98.4	98.0	0.4	0.4	0.4	0.0
JT5-2B	25.44	98.6	97.7	0.9	0.2	0.6	-0.4
JT6-1B	27.64	98.6	97.9	0.7	0.2	0.3	-0.1

APPENDIX D

THERMOCOUPLE PLACEMENT AT THE VIRGINIA SMART ROAD

Table D.1a. Location of thermocouples at the Virginia Smart Road.

Layer	Material Description	Depth from Surface (m)	Section					
			A	B	C	D	E	F
1 - Bottom	Surface HMA	0.038	AT1-1B AT1-2B AT1-3B	BT1-1B BT1-2B	CT1-1B CT1-2B	DT1-1B DT1-2B	ET1-1B ET1-2B	FT1-1B FT1-2B
		0.149						
2 - Top	Base HMA	0.063	AT2-1T AT2-2T	BT2-1T BT2-2T	CT2-1T CT2-2T	DT2-1T DT2-2T	ET2-1T ET2-2T ET2-3T	FT2-1T FT2-2T
		0.065						
		0.118						
2 - Bottom	Base HMA	0.138						
		0.188	AT2-1B AT2-2B	BT2-2B	CT2-1B CT2-2B	DT2-1B DT2-2B		FT2-1B FT2-2B
		0.263					ET2-1B ET2-2B	
		0.281						
3 - Bottom	Surface HMA placed as base	0.188						
4 - Bottom	Open-Graded Drainage Layer	0.263	AT4-1B AT4-2B					
		0.338						
5 - Bottom	21A Cement Treated Aggregate Base Layer	0.388						
		0.413	AT5-1B AT5-2B					
6 - Bottom	21B Aggregate Base Layer	0.588	AT6-1B AT6-2B					
7 - Top	Natural Subgrade	0.638						
		0.74	AT7-1T AT7-2T					
7 - Middle	Natural Subgrade	0.994	AT7-2M					
		1.172	AT7-1M					
		1.238						

Table D.1b. Location of thermocouples at the Virginia Smart Road.

Layer	Material Description	Depth from Surface (m)	Section					
			G	H	I	J	K	L
1 - Bottom	Surface HMA	0.038	GT1-1B GT1-2B	HT1-1B HT1-2B	IT1-1B IT1-2B	JT1-1B JT1-2B		LT1-1B LT1-2B
		0.12					KT1-1B KT1-2B	
2 - Top	Base HMA	0.063		HT2-1T HT2-2T	IT2-1T IT2-2T	JT2-1T JT2-2T		LT2-1T LT2-2T
		0.065	GT2-1T GT2-2T					
		0.118					KT2-1T KT2-2T	
2 - Bottom	Base HMA	0.138	GT2-1B GT2-2B	HT2-1B HT2-2B	IT2-1B IT2-2B			
		0.188						LT2-1B LT2-2B
		0.263				JT2-1B JT2-2B		
		0.281					KT2-1B KT2-2B	
3 - Bottom	Surface HMA placed as base	0.188	GT3-1B GT3-2B	HT3-1B HT3-2B	IT3-1B IT3-2B			
4 - Bottom	Open-Graded Drainage Layer	0.263			IT4-1B IT4-2B		LT4-1B LT4-2B	
		0.338				JT4-1B JT4-2B		
5 - Bottom	21A Cement Treated Aggregate Base Layer	0.388	GT5-1B GT5-2B					
		0.413			IT5-1B IT5-2B		LT5-1B LT5-2B	
6 - Bottom	21B Aggregate Base Layer	0.588			IT6-1B IT6-2B	JT6-1B JT6-2B	LT6-1B LT6-2B	
7 - Top	Natural Subgrade	0.638	GT7-1T GT7-2T					
		0.74						
7 - Middle	Natural Subgrade	0.994						
		1.172						
		1.238	GT7-1M GT7-2M					

APPENDIX E

MOISTURE CONTENT MONITORING

Table E.1a. Moisture content values obtained from CS610 TDR probe during Phase 1 studies (comparisons between probe types).

DATE	CS610										
	BM6-1ME	EM6-1ME	HM6-1ME	IM6-1ME	IM6-2ME	JM6-1ME	JM6-2ME	KM6-1ME	KM6-2ME	LM6-1ME	LM6-2ME
5/26/99	18.22	15.86	8.63								
6/11/99	16.46	15.83	9.33								
6/18/99	12.83	15.46									
6/25/99	13.51	15.49									
6/30/99	12.82	15.39									
7/1/99	12.60	15.58									
7/7/99	12.14	15.42									
7/9/99	14.88	15.49									
7/16/99	15.11	15.18									
7/21/99	15.11	15.51									
7/22/99	15.10	15.41									
7/28/99	12.92	15.28									
8/3/99	14.88	15.23									
8/10/99				7.53	6.07	7.17	0.32				
8/17/99	15.09	15.22	7.64	7.33	7.53	8.17	7.88		5.52	7.47	5.71
8/27/99	15.11	15.12	5.22	9.52	9.08	9.17	9.07				
9/3/99	14.65	15.25		6.61	5.71	8.63	8.92		5.43	6.81	5.25
9/8/99	14.88	15.05		11.66	12.14	8.81	8.70		6.44	8.27	6.53

Table E.1b. Moisture content values obtained from CS610 TDR probe during Phase 1 studies (comparisons between probe types).

DATE	CS610										
	BM6-1ME	EM6-1ME	HM6-1ME	IM6-1ME	IM6-2ME	JM6-1ME	JM6-2ME	KM6-1ME	KM6-2ME	LM6-1ME	LM6-2ME
9/22/99	15.11	15.01		10.19	11.36	8.35	8.57	5.43	6.62	7.72	6.62
10/1/99	16.40	14.88	8.98	11.65	12.43	9.03	8.59		7.27	8.45	7.91
10/11/99	15.99	14.99	8.95	11.76	12.48	9.25	8.50		8.02	8.34	7.79
10/22/99	11.84	14.98	9.07	11.63	11.63	9.12	8.68	5.14	7.56	8.52	7.90
10/29/99	9.99	15.09	8.71	10.45	11.40	9.09	8.79		7.16	8.17	7.49
11/8/99		15.17									
11/15/99	9.19	15.03	8.68	10.53	11.39	9.09	7.88		7.40	8.22	7.69
11/29/99	7.24	15.06	8.70	10.09	11.17	8.84	8.31		6.89	8.16	7.43
12/8/99	6.74	15.21	8.74	10.62	11.13	8.96	7.56		5.99	8.21	7.73
12/30/99	13.72	15.46									
1/25/00	9.76			10.70	10.96	8.77	8.42				
2/9/00			9.76	10.67	10.97	8.48	9.47	6.12	6.50	8.49	8.10
2/16/00	15.93	15.60	8.16	10.82	11.40	6.51	8.73	6.28	7.05	8.36	7.95
2/22/00		15.50									
3/1/00	15.03	15.44	9.62						5.00	8.84	8.53
3/8/00	13.20	16.43	9.88	10.59	10.26	9.18	8.18				
3/15/00	11.87	15.31	9.34	9.99	9.83			6.50	6.14	8.91	8.61
3/22/00	12.06	15.35	10.07	13.35	13.84			5.94			
3/29/00	12.35	15.96	9.52	11.39	11.40	7.39	9.05			8.44	8.21
4/4/00	12.14	14.91	9.94	11.28	11.70	8.73	8.92		7.92	8.66	8.41
4/27/00	16.79	15.56	10.03	10.75	10.60	9.13	8.58		7.87	8.91	8.77
5/3/00	16.49	16.22	9.98	8.97	11.45	8.69	7.46		5.82	8.48	8.04

Table E.2a. Moisture content values obtained from CS615 TDR probe during Phase 1 studies (comparisons between probe types).

DATE	CS615										
	BM6-1M	BM6-2M	EM6-1M	EM6-2M	HM6-2M	JM6-1M	JM6-2M	KM6-1M	KM6-2M	LM6-1M	LM6-2M
3/31/99			7.59	7.06							
4/5/99	5.60	6.64									
4/7/99											
4/8/99					13.82						
4/9/99	15.16	19.01									
4/13/99											
4/14/99			14.98		13.57						
4/17/99	14.74	17.61									
4/19/99			13.34	13.34							
4/20/99			13.06	13.06	13.99						
4/22/99	14.77	17.49			14.00						
5/18/99	16.40	18.34									
5/20/99											
5/25/99					14.38						
5/31/99			15.57	16.37							
6/1/99			15.59	16.43							
6/9/99	12.45	16.28	15.86	16.96	14.41						
6/11/99	11.75	15.09	15.96	17.15	14.43						

Table E.2b. Moisture content values obtained from CS615 TDR probe during Phase 1 studies (comparisons between probe types).

DATE	CS615										
	BM6-1M	BM6-2M	EM6-1M	EM6-2M	HM6-2M	JM6-1M	JM6-2M	KM6-1M	KM6-2M	LM6-1M	LM6-2M
6/18/99	12.82	12.29	15.47	16.53	14.72						
6/23/99	13.08	12.76	15.51	16.62	14.89						
6/24/99	12.90	12.90	15.65	16.83	14.82						
6/30/99	10.68	12.42	15.82	17.13	14.68						
7/1/99	10.42	12.32	15.81	17.14	14.65						
7/7/99	9.60	11.83	16.19	17.85	14.69						
7/9/99	9.98	13.01	16.18	17.88	14.66						
7/21/99	15.05	17.25	15.89	17.46	14.59						
7/28/99	11.83	14.11	16.09	17.91	14.64						
8/3/99	12.75	16.76	16.06	17.95	14.64						
8/17/99	9.21	13.97	15.98	17.95	14.66	9.12	11.06	10.03	11.18	9.70	10.41
8/27/99	8.81	15.46	15.50	17.08	14.52			10.63	12.42		
9/3/99	8.76	13.12	15.62	17.30	14.57			9.55	10.24	9.49	9.92
9/8/99	10.62	16.59			14.61	10.42	12.21	10.17	11.42	10.83	11.04
9/22/99	9.10	14.89	15.10	16.36	14.54	9.99	11.94	11.23	12.07	10.73	11.06
10/1/99	9.92	15.59			14.57	10.18	12.20				
10/4/99	10.41	15.15	15.09	16.30	14.66						
10/11/99	9.51	13.66	14.85	15.92	14.55	10.12	12.30	10.94	11.63	11.02	11.38
10/22/99	8.20	11.32	14.61	15.56	14.43	10.29	12.18	10.71	11.78	11.16	11.43
10/29/99	7.72	10.30	14.56	15.45	14.42	10.05	11.81	10.23	11.10	10.92	11.32

Table E.2c. Moisture content values obtained from CS615 TDR probe during Phase 1 studies (comparisons between probe types).

DATE	CS615										
	BM6-1M	BM6-2M	EM6-1M	EM6-2M	HM6-2M	JM6-1M	JM6-2M	KM6-1M	KM6-2M	LM6-1M	LM6-2M
11/1/99						9.97	11.74	10.12	10.97	10.78	11.23
11/8/99			14.64	15.57	14.40	9.90	11.67				
11/10/99								10.04	10.83	10.86	11.27
11/11/99	7.21	9.09									
11/15/99	7.40	9.41	14.69	15.63	14.38	9.85	11.61	10.00	10.73	10.77	11.21
11/18/99	7.35	9.26	14.51	15.38	14.25	9.85	11.60	10.00	10.66	10.85	11.25
11/23/99	7.17	8.97									
11/29/99	7.09	8.69	14.57	15.46	14.54	9.81	11.56	9.96	10.61	10.90	11.29
12/8/99	7.04	8.59	14.45	15.27	14.26	9.81	11.55	9.96	10.55	10.88	11.28
12/17/99	13.08	15.10	14.38	15.17	14.16	9.81	11.55	9.96	10.50	10.96	11.32
2/9/00					13.75	9.95	11.69	9.77	10.19	11.13	11.40
2/16/00						9.78	11.45	9.64	10.17	11.08	11.36
2/22/00	8.55	11.28	14.47	15.25							
3/1/00			14.77	15.66							
3/8/00	8.09	10.61	14.92	15.91							
3/15/00	7.94	10.18	14.81	15.77							
3/22/00	8.02	10.39			14.36	9.50	11.29				
3/29/00	7.98	10.46			13.80	9.97	11.67	9.88	10.32	11.04	11.43
4/4/00	8.03	10.11	15.00	16.08	13.71	9.92	11.69	9.87	10.41	11.11	11.52
4/27/00	14.52	15.31	14.87	15.91	14.17	9.69	11.45	10.00	10.60	11.47	11.81
5/3/00	14.26	15.16	15.24	16.51	13.73	9.70	11.45	9.76	10.46	11.03	11.38

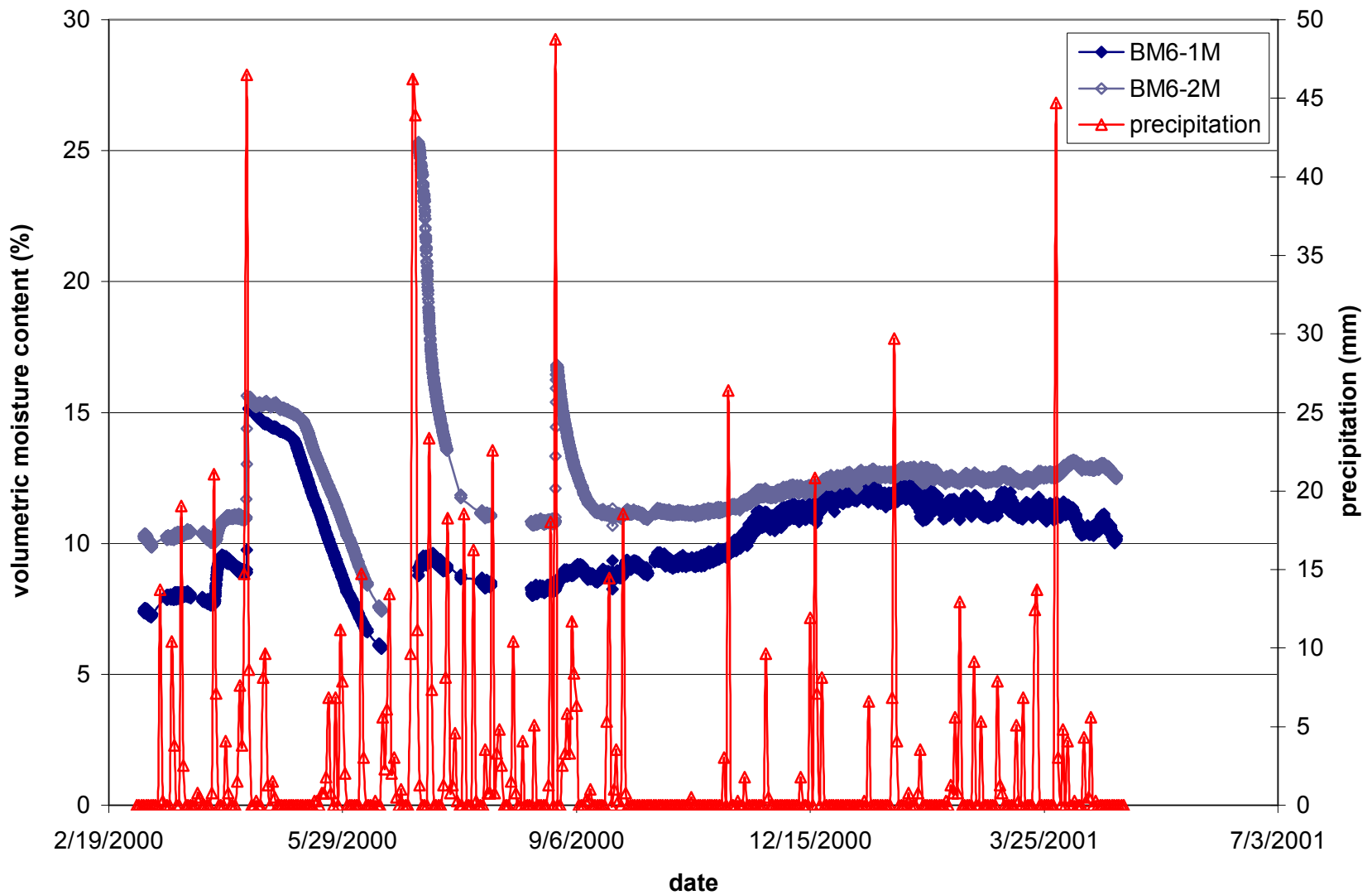


Figure E.1. Moisture content as measured by time-domain reflectometers in Section B with precipitation versus date.

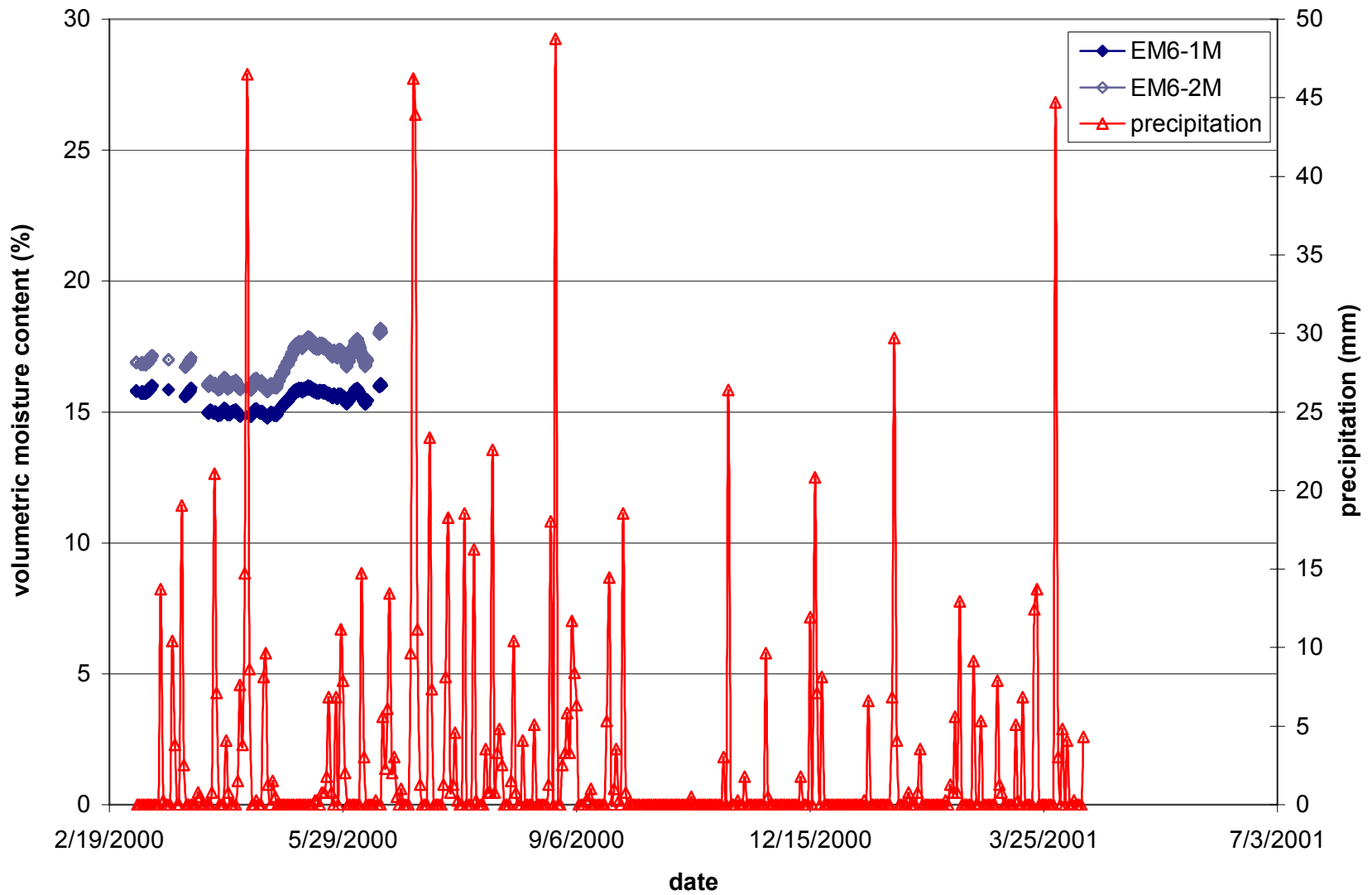


Figure E.2. Moisture content as measured by time-domain reflectometers in Section E with precipitation versus date.

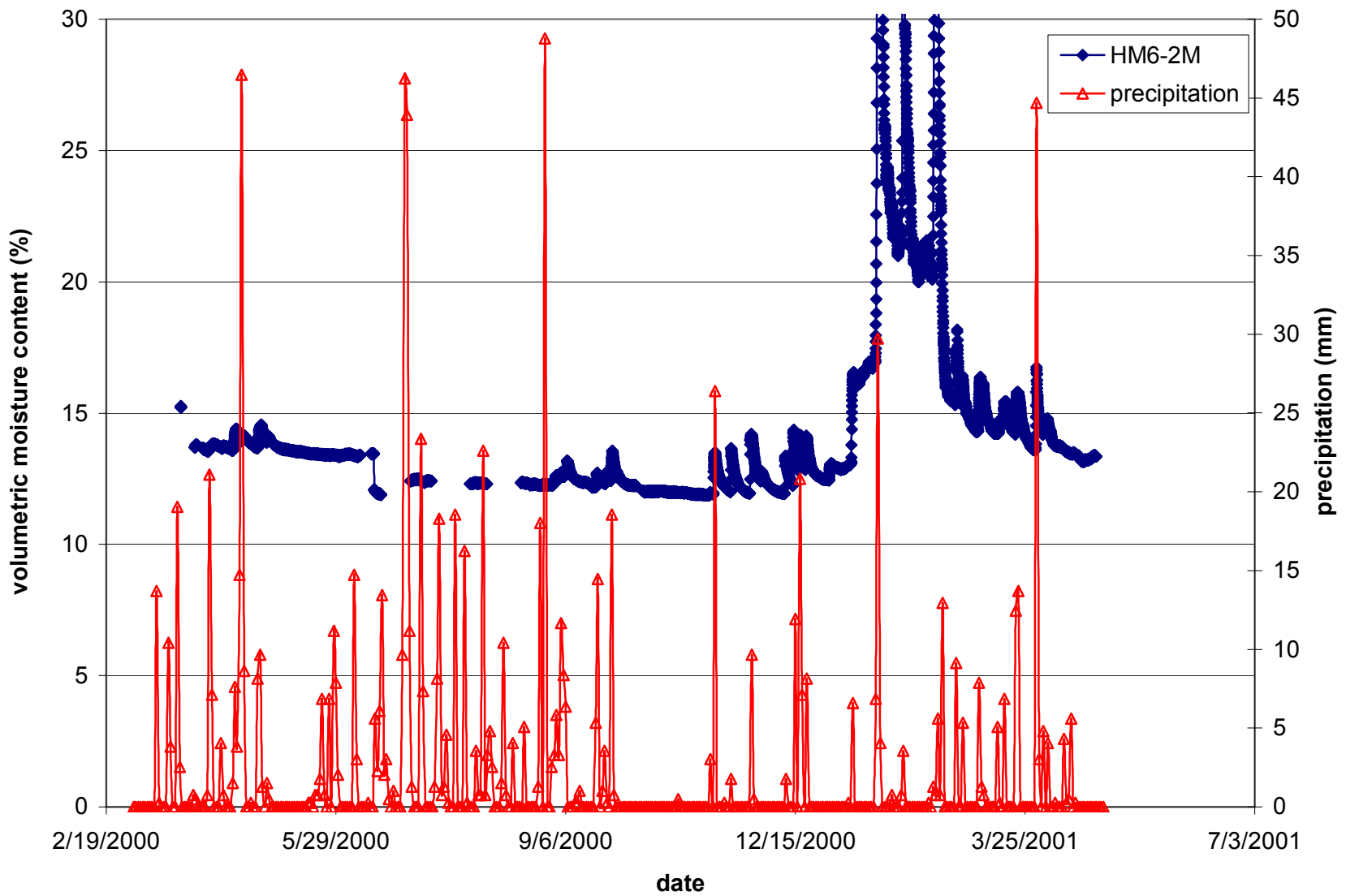


Figure E.3. Moisture content as measured by time-domain reflectometers in Section H with precipitation versus date.

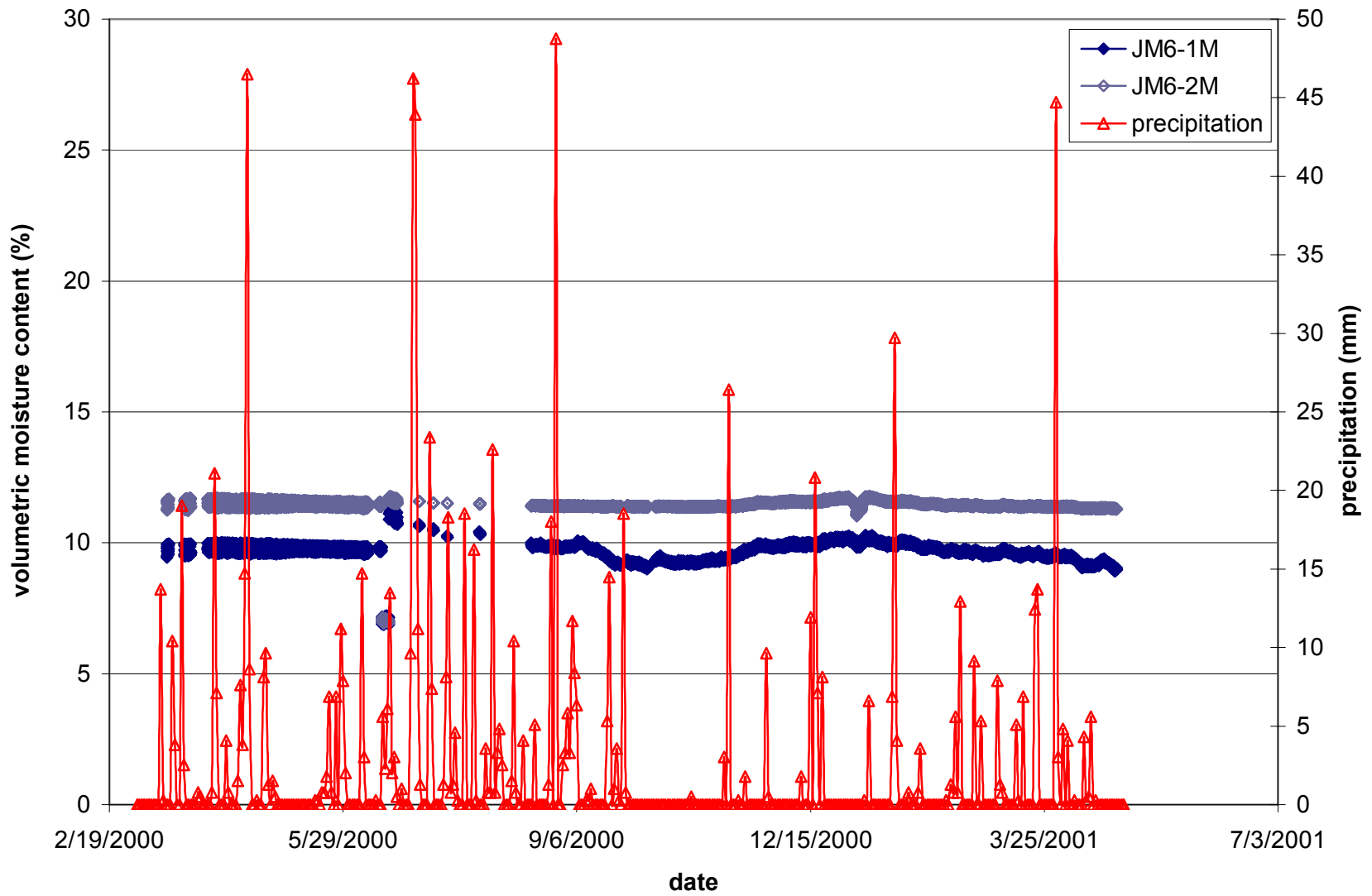


Figure E.4. Moisture content as measured by time-domain reflectometers in Section J with precipitation versus date.

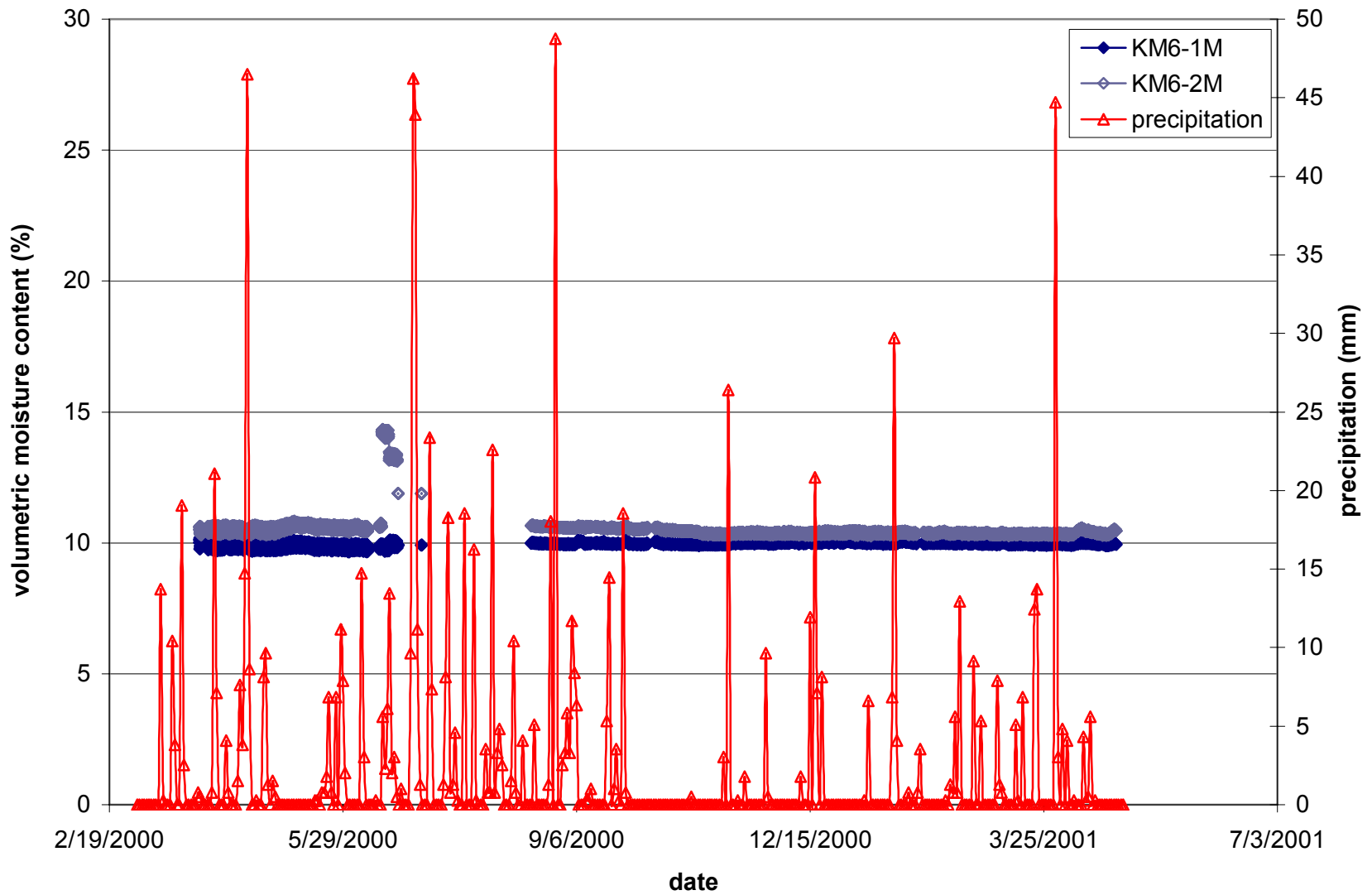


Figure E.5. Moisture content as measured by time-domain reflectometers in Section K with precipitation versus date.

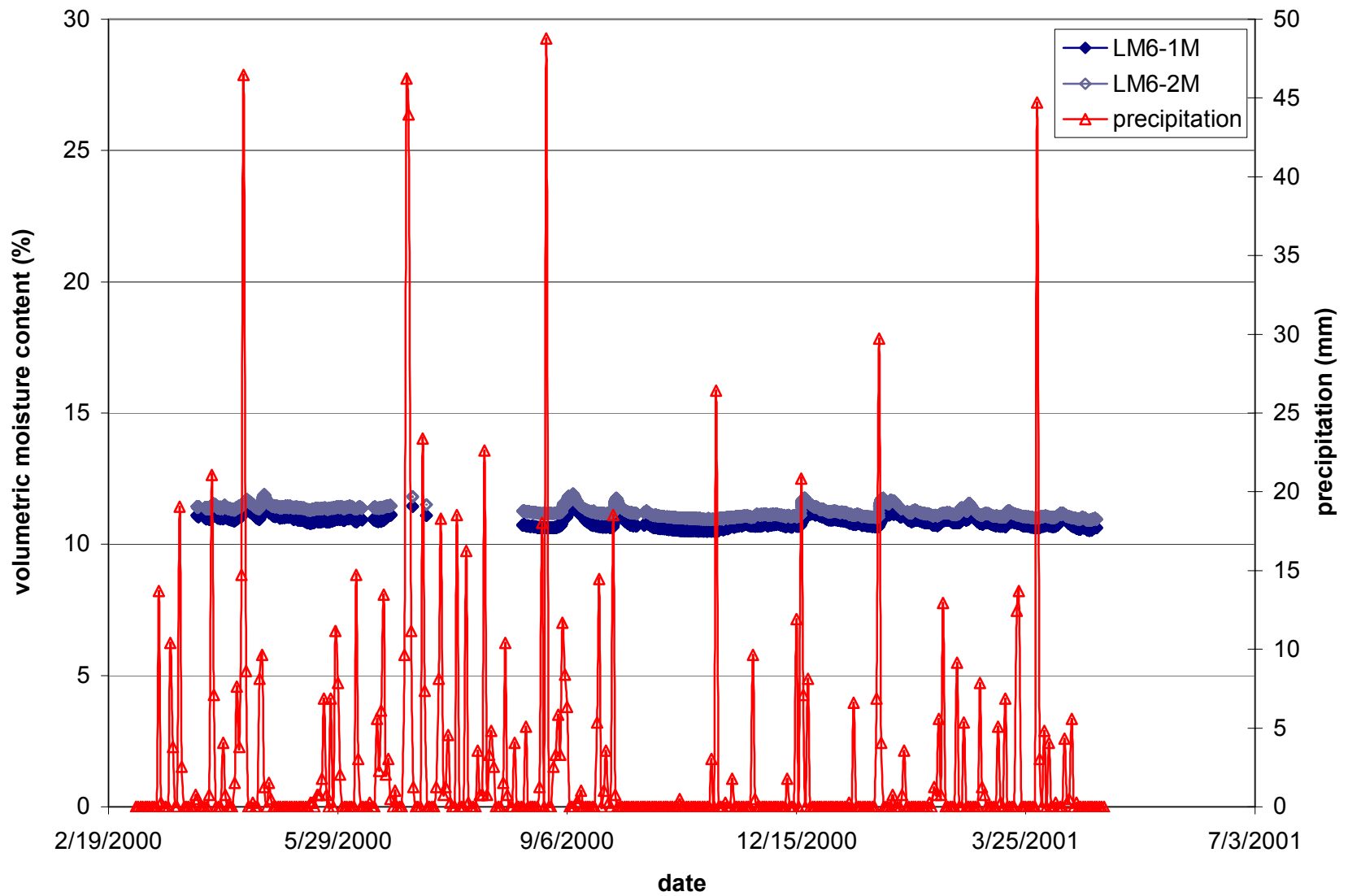


Figure E.6. Moisture content as measured by time-domain reflectometers in Section L with precipitation versus date.

APPENDIX F

STATISTICAL ANALYSIS OF THERMOCOUPLE AVERAGING

Table F.1. Comparison of thermocouple probe replicates for averaging procedure in Section A.

Difference	Mean	Std Dev	Std Error
ab_out-ab_outavg	0.0001	0.5311	0.0551
a1b1-a1b2	0.6957	0.5447	0.0565
a1b1-a1b3	-0.1817	0.7258	0.0753
a1b1-a1b3	-0.8774	0.6207	0.0644
a1b1-a1bavg	0.1680	0.7094	0.0736
a1b2-a1bavg	-0.5277	0.6597	0.0684
a1b3-a1bavg	0.3497	0.6110	0.0634
a2t1-a2t2	1.2516	0.5338	0.0553
a2t1-a2tavg	0.6192	1.0116	0.1049
a2t2-a2tavg	-0.6324	1.1487	0.1191
a2b1-a2b2	0.6774	0.5259	0.0545
a2b1-a2bavg	0.3346	0.6226	0.0646
a2b2-a2bavg	-0.3428	0.7953	0.0825
a4b1-a4b2	1.3247	0.6045	0.0627
a4b1-a4bavg	0.6629	0.4864	0.0504
a4b2-a4bavg	-0.6618	0.4726	0.0490
a5b1-a5b2	0.9527	0.4942	0.0512
a5b1-a5bavg	0.4740	0.8387	0.0870
a5b2-a5bavg	-0.4787	0.8103	0.0840
a6b1-a6b2	1.4151	0.5209	0.0540
a6b1-a6bavg	0.7038	1.2621	0.1309
a6b2-a6bavg	-0.7112	1.1510	0.1194
a7t1-a7t2	0.7742	0.4339	0.0450
a7t1-a7tavg	0.3812	1.1185	0.1160
a7t2-a7tavg	-0.3930	1.1634	0.1206
a7m2-a7m2avg	-0.0074	1.2269	0.1272
a7m1-a7m1avg	-0.0059	0.6972	0.0723

Table F.2. Comparison of thermocouple probe replicates for averaging procedure in Section B.

Difference	Mean	Std Dev	Std Error
ab_out-ab_outavg	0.0001	0.5311	0.0551
b1b1-b1b2	-0.7946	0.7957	0.0825
b1b1-b1bavg	-0.4041	0.6491	0.0673
b1b2-b1bavg	0.3905	0.5361	0.0556
b2t1-b2t2	0.2505	0.5164	0.0535
b2t1-b2tavg	0.1254	0.8326	0.0863
b2t2-b2tavg	-0.1251	0.7634	0.0792
b2b2-b2bavg	-0.0002	0.7304	0.0757

Table F.3. Comparison of thermocouple probe replicates for averaging procedure in Section C.

Difference	Mean	Std Dev	Std Error
cd_out-cd_outavg	0.0082	0.8098	0.0840
c1b1-c1b2	0.7774	0.6085	0.0631
c1b1-c1bavg	0.3926	0.5078	0.0527
c1b2-c1bavg	-0.3848	0.5058	0.0525
c2t1-c2t2	0.4710	0.6109	0.0633
c2t1-c2tavg	0.2413	0.6952	0.0721
c2t2-c2tavg	-0.2296	0.7345	0.0762
c2b1-c2b2	0.6968	0.8978	0.0931
c2b1-c2bavg	0.3499	0.5997	0.0622
c2b2-c2bavg	-0.3469	0.8951	0.0928

Table F.4. Comparison of thermocouple probe replicates for averaging procedure in Section D.

Difference	Mean	Std Dev	Std Error
cd_out-cd_outavg	0.0082	0.8098	0.0840
d1b1-d1b2	0.4968	0.5220	0.0541
d1b1-d1bavg	0.2532	0.5367	0.0556
d1b2-d1bavg	-0.2435	0.5931	0.0615
d2t1-d2t2	0.6505	0.6355	0.0659
d2t1-d2tavg	0.3311	0.6523	0.0676
d2t2-d2tavg	-0.3195	0.5538	0.0574
d2b1-d2b2	0.9591	0.5123	0.0531
d2b1-d2bavg	0.4866	0.7141	0.0740
d2b2-d2bavg	-0.4726	0.7587	0.0787

Table F.5. Comparison of thermocouple probe replicates for averaging procedure in Section E.

Difference	Mean	Std Dev	Std Error
ef_out-ef_outavg	-0.0023	0.5479	0.0568
e1b1-e1b2	1.1430	0.4264	0.0442
e1b1-e1bavg	0.5645	0.7280	0.0755
e1b2-e1bavg	-0.5786	0.6913	0.0717
e2t1-e2t2	0.4839	0.3734	0.0387
e2t1-e2tavg	0.2378	0.6771	0.0702
e2t2-e2tavg	-0.2460	0.6966	0.0722
e2b1-e2b2	0.8258	0.4242	0.0440
e2b1-e2bavg	0.4081	0.6910	0.0717
e2b2-e2bavg	-0.4177	0.6646	0.0689
e3t1-e3t2	0.9032	6.5138	0.6755
e3t1-e3tavg	0.4456	3.3276	0.3451
e3t2-e3tavg	-0.4576	3.3066	0.3429

Table F.6. Comparison of thermocouple probe replicates for averaging procedure in Section F.

Difference	Mean	Std Dev	Std Error
ef_out-ef_outavg	-0.0023	0.5479	0.0568
f1b1-f1b2	1.3280	0.7101	0.0736
f1b1-f1bavg	0.6609	0.6458	0.0670
f1b2-f1bavg	-0.6670	0.4919	0.0510
f2t1-f2t2	0.5409	0.3757	0.0390
f2t1-f2tavg	0.2654	0.6822	0.0707
f2t2-f2tavg	-0.2754	0.6460	0.0670
f2b1-f2b2	0.9054	0.3262	0.0338
f2b1-f2bavg	0.4484	0.6310	0.0654
f2b2-f2bavg	-0.4570	0.6043	0.0627

Table F.7. Comparison of thermocouple probe replicates for averaging procedure in Section G.

Difference	Mean	Std Dev	Std Error
gh_out-gh_outavg	-0.0030	0.4727	0.0490
g1b1-g1b2	1.8237	0.5828	0.0604
g1b1-g1bavg	0.9074	0.7438	0.0771
g1b2-g1bavg	-0.9163	0.6919	0.0717
g2t1-g2t2	0.9032	0.7543	0.0782
g2t1-g2tavg	0.4570	0.8014	0.0831
g2t2-g2tavg	-0.4463	0.8715	0.0904
g2b1-g2b2	-0.1839	0.6752	0.0700
g2b1-g2bavg	-0.0852	0.6662	0.0691
g2b2-g2bavg	0.0987	0.8059	0.0836
g3b1-g3b2	0.6882	0.7849	0.0814
g3b1-g3bavg	0.3503	0.7609	0.0789
g3b2-g3bavg	-0.3379	0.6557	0.0680
g5b1-g5b2	1.6677	0.5859	0.0608
g5b1-g5bavg	0.8415	0.8839	0.0917
g5b2-g5bavg	-0.8263	0.7900	0.0819
g7t1-g7t2	0.9495	0.6657	0.0690
g7t1-g7tavg	0.4834	0.9197	0.0954
g7t2-g7tavg	-0.4660	0.9122	0.0946
g7m1-g7m2	0.7054	0.5963	0.0618
g7m1-g7mavg	0.3585	0.6507	0.0675
g7m2-g7mavg	-0.3469	0.7772	0.0806

Table F.8. Comparison of thermocouple probe replicates for averaging procedure in Section H.

Difference	Mean	Std Dev	Std Error
gh_out-gh_outavg	-0.0030	0.4727	0.0490
h1b1-h1b2	1.6430	0.5085	0.0527
h1b1-h1bavg	0.8207	0.5773	0.0599
h1b2-h1bavg	-0.8223	0.4968	0.0515
h2t1-h2t2	-0.0301	0.5069	0.0526
h2t1-h2tavg	-0.0207	0.8020	0.0832
h2t2-h2tavg	0.0094	0.7950	0.0824
h2b1-h2b2	1.0387	0.5257	0.0545
h2b1-h2bavg	0.5178	0.5008	0.0519
h2b2-h2bavg	-0.5209	0.6270	0.0650
h3b1-h3b2	0.6699	0.8218	0.0852
h3b1-h3bavg	0.3406	0.5970	0.0619
h3b2-h3bavg	-0.3293	0.7017	0.0728

Table F.9. Comparison of thermocouple probe replicates for averaging procedure in Section I.

Difference	Mean	Std Dev	Std Error
ij_out-ij_outavg	0.0051	0.6094	0.0632
i1b1-i1b2	-0.2097	1.1577	0.1200
i1b1-i1bavg	-0.1068	0.7875	0.0817
i1b2-i1bavg	0.1029	0.7562	0.0784
i2t1-i2t2	0.4355	1.2631	0.1310
i2t1-i2tavg	0.2165	0.7935	0.0823
i2t2-i2tavg	-0.2189	0.8373	0.0868
i2b1-i2b2	1.7452	1.3736	0.1424
i2b1-i2bavg	0.8653	1.1077	0.1149
i2b2-i2bavg	-0.8799	1.1523	0.1195
i3t1-i3t2	1.5505	1.2693	0.1316
i3t1-i3tavg	0.7696	0.8472	0.0879
i3t2-i3tavg	-0.7809	1.1782	0.1222
i4t1-i4t2	2.4613	1.1601	0.1203
i4t1-i4tavg	1.2306	0.5801	0.0601
i4t2-i4tavg	-1.2306	0.5801	0.0601
i5b1-i5b2	-1.3153	1.6660	0.1728
i5b1-i5bavg	-0.8185	1.8705	0.1940
i5b2-i5bavg	0.4968	1.2175	0.1262
i6b1-i6b2	-1.3897	1.2597	0.1306
i6b1-i6bavg	-0.1596	1.4704	0.1525
i6b2-i6bavg	1.2301	1.0486	0.1087

Table F.10. Comparison of thermocouple probe replicates for averaging procedure in Section J.

Difference	Mean	Std Dev	Std Error
ij_out-ij_outavg	0.0051	0.6094	0.0632
j1b1-j1b2	1.9505	0.6885	0.0714
j1b1-j1bavg	0.9737	0.6279	0.0651
j1b2-j1bavg	-0.9768	0.5893	0.0611
j2t1-j2t2	0.2129	1.0002	0.1037
j2t1-j2tavg	0.1021	0.7728	0.0801
j2t2-j2tavg	-0.1108	0.6525	0.0677
j2b1-j2b2	2.4398	0.7422	0.0770
j2b1-j2bavg	1.2117	0.7169	0.0743
j2b2-j2bavg	-1.2281	0.6158	0.0639
j4b2-j4bavg	-0.0048	1.0495	0.1088
j6b2-j6bavg	-0.0023	1.2915	0.1339

Table F.11. Comparison of thermocouple probe replicates for averaging procedure in Section L.

Difference	Mean	Std Dev	Std Error
kl_out-kl_outavg	-0.0093	0.9400	0.0975
l1b1-l1b2	0.9215	1.0585	0.1098
l1b1-l1bavg	0.4592	1.0156	0.1053
l1b2-l1bavg	-0.4623	0.8087	0.0839
l2t1-l2t2	1.4344	1.1987	0.1243
l2t1-l2tavg	0.7224	1.0319	0.1070
l2t2-l2tavg	-0.7120	1.1730	0.1216
l2b1-l2b2	0.2409	0.9978	0.1035
l2b1-l2bavg	0.1198	0.8753	0.0908
l2b2-l2bavg	-0.1211	0.9508	0.0986
l4b1-l4b2	1.5871	1.4378	0.1491
l4b1-l4bavg	0.7943	1.0498	0.1089
l4b2-l4bavg	-0.7928	1.0522	0.1091
l5b1-l5b2	0.9785	1.0346	0.1073
l5b1-l5bavg	0.4898	1.0155	0.1053
l5b2-l5bavg	-0.4887	0.8434	0.0875
l6b1-l6b2	2.5043	1.1436	0.1186
l6b1-l6bavg	1.2554	1.1445	0.1187
l6b2-l6bavg	-1.2489	1.1069	0.1148

APPENDIX G

MAXIMUM AND MINIMUM TEMPERATURE TRENDS OVER SEASONAL VARIATION

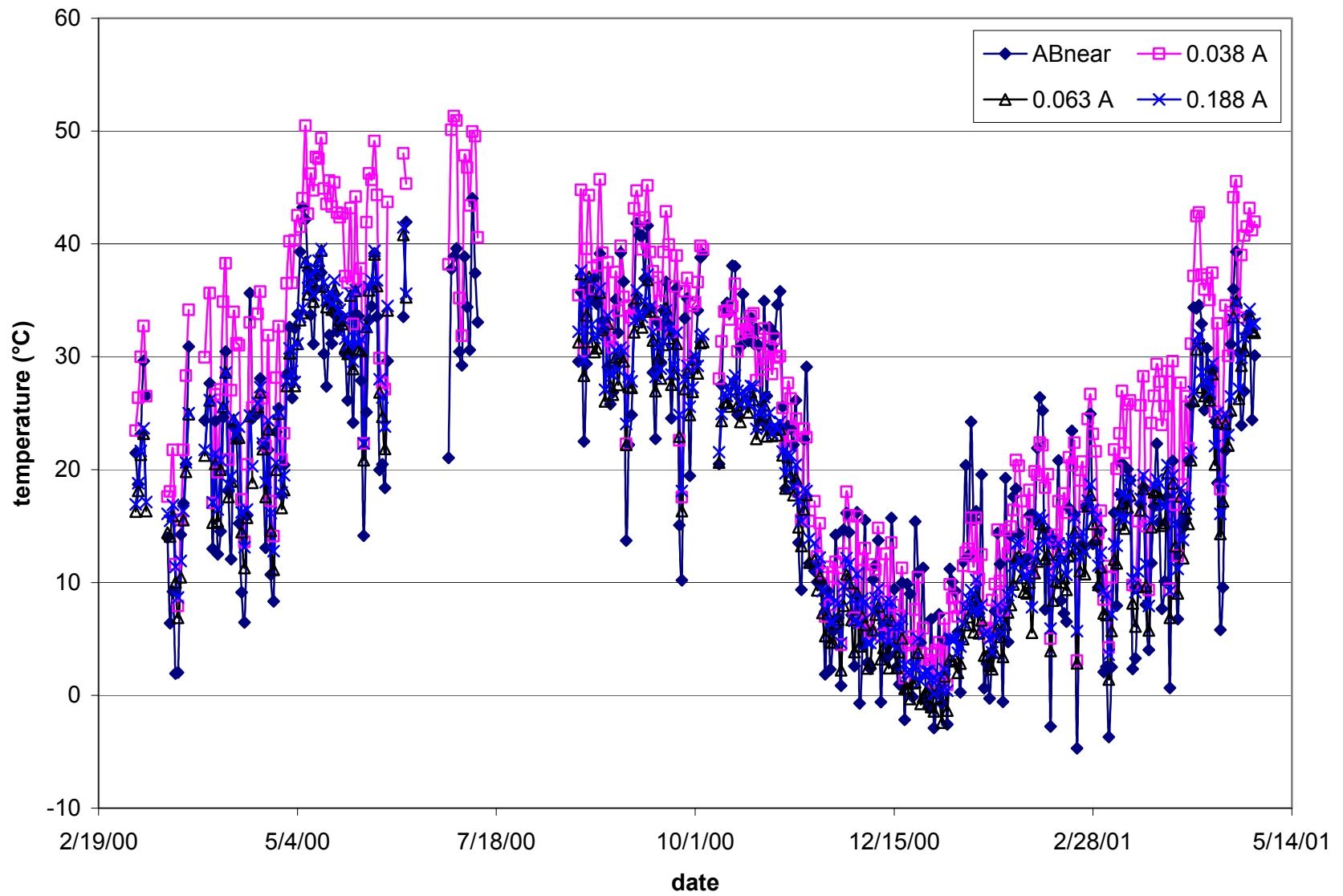


Figure G.1. Maximum daily temperature in HMA layers – Section A.

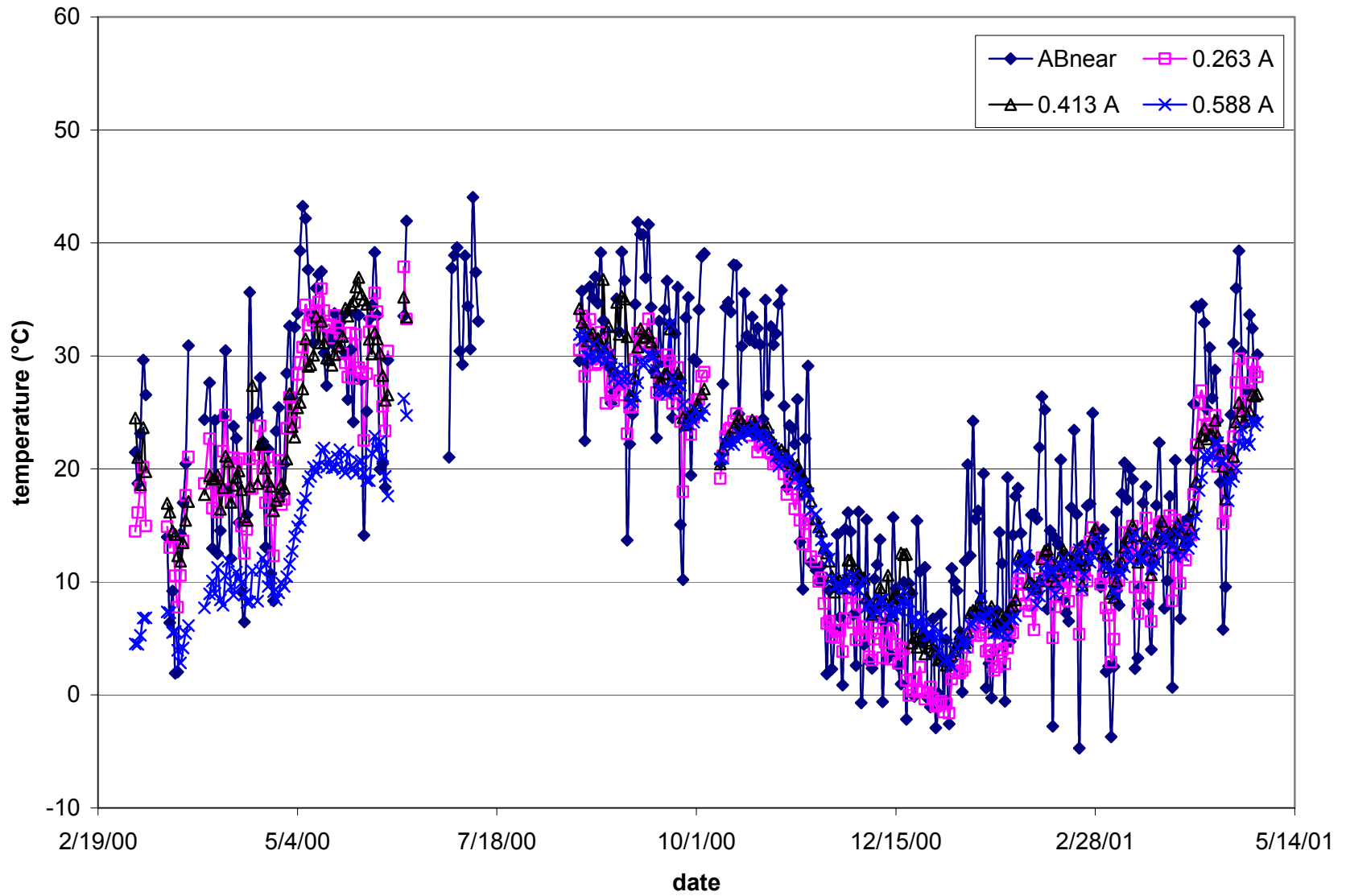


Figure G.2. Maximum daily temperature in aggregate base/subbase layers – Section A.

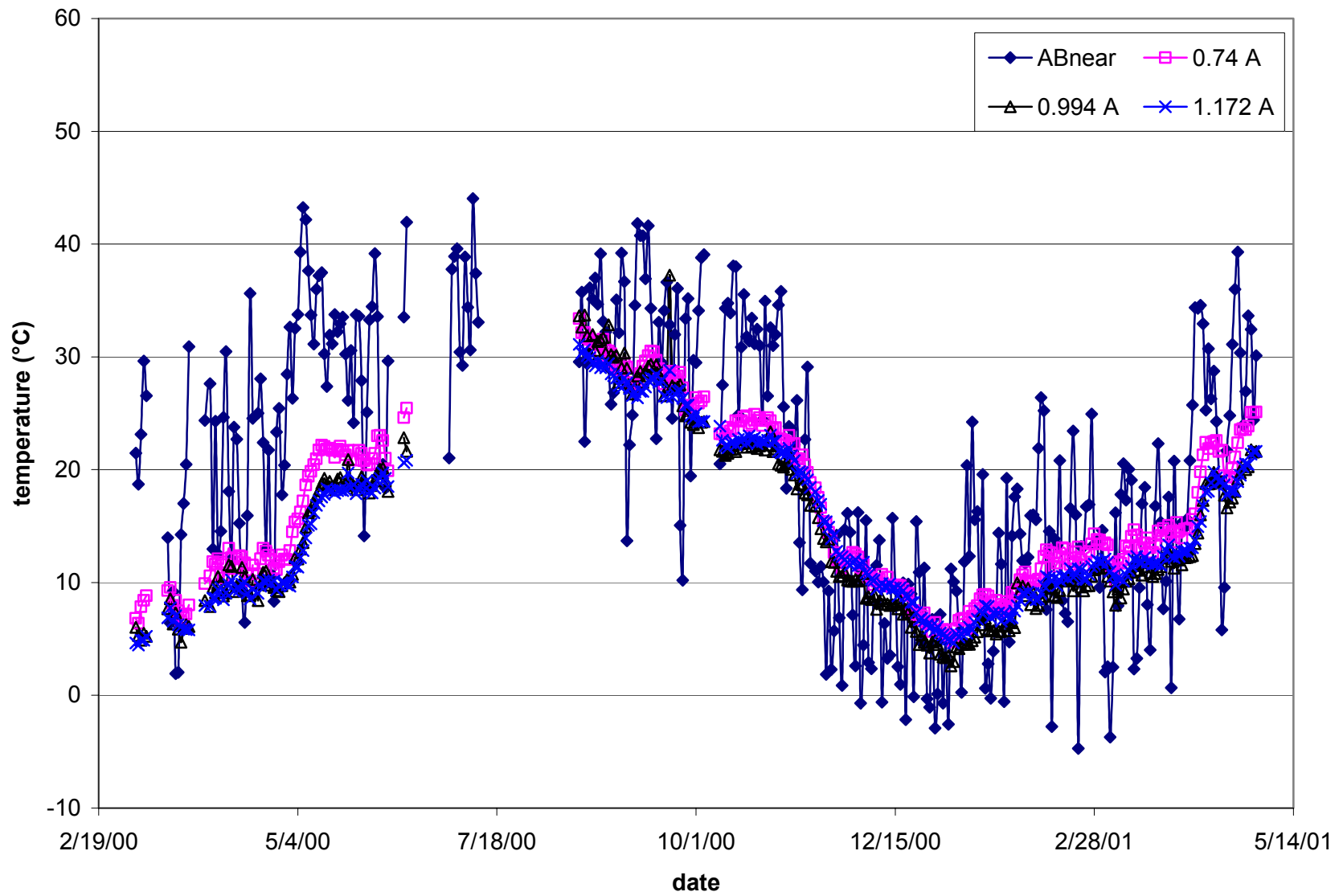


Figure G.3. Maximum daily temperature in subgrade – Section A.

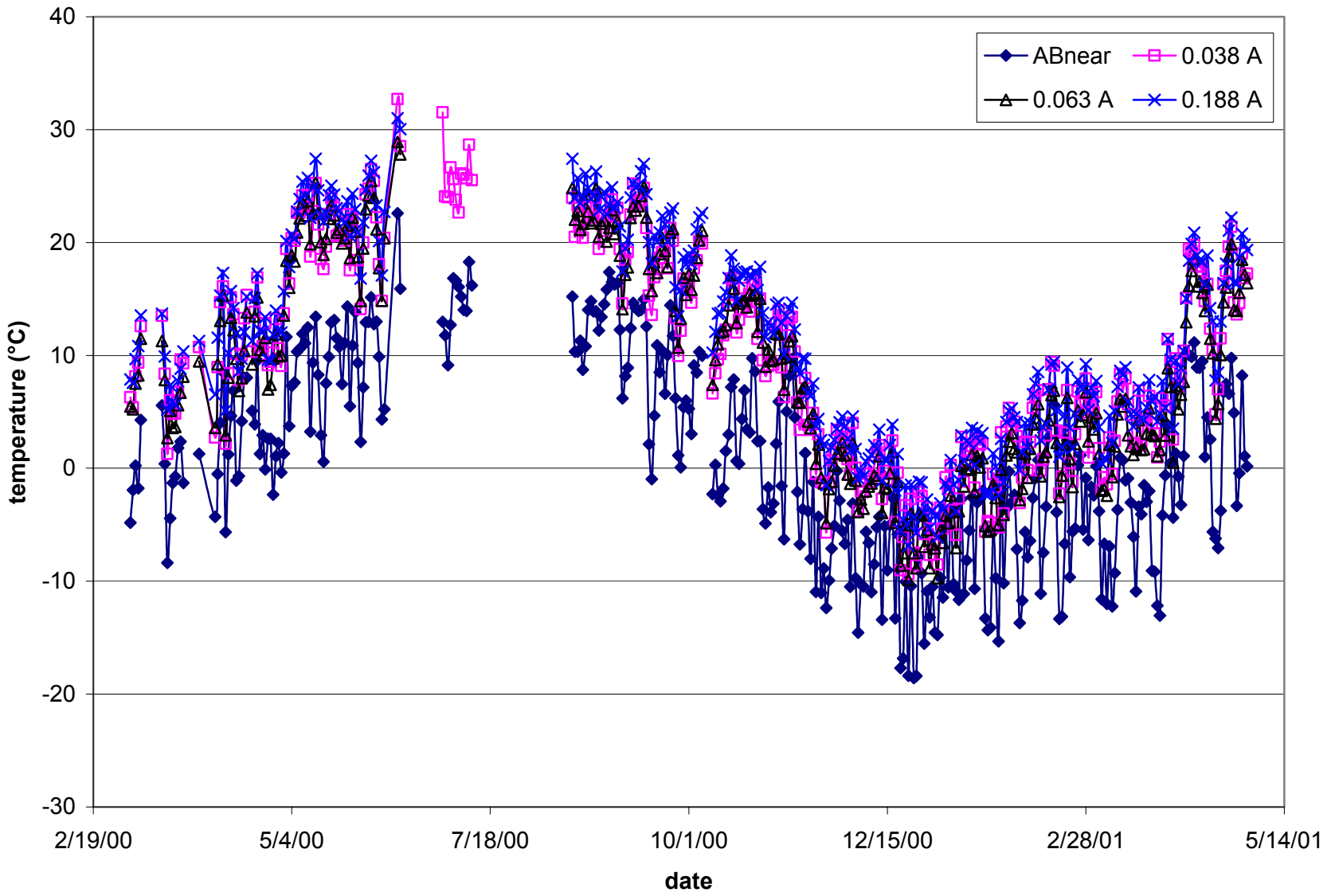


Figure G.4. Minimum daily temperature in HMA layers – Section A.

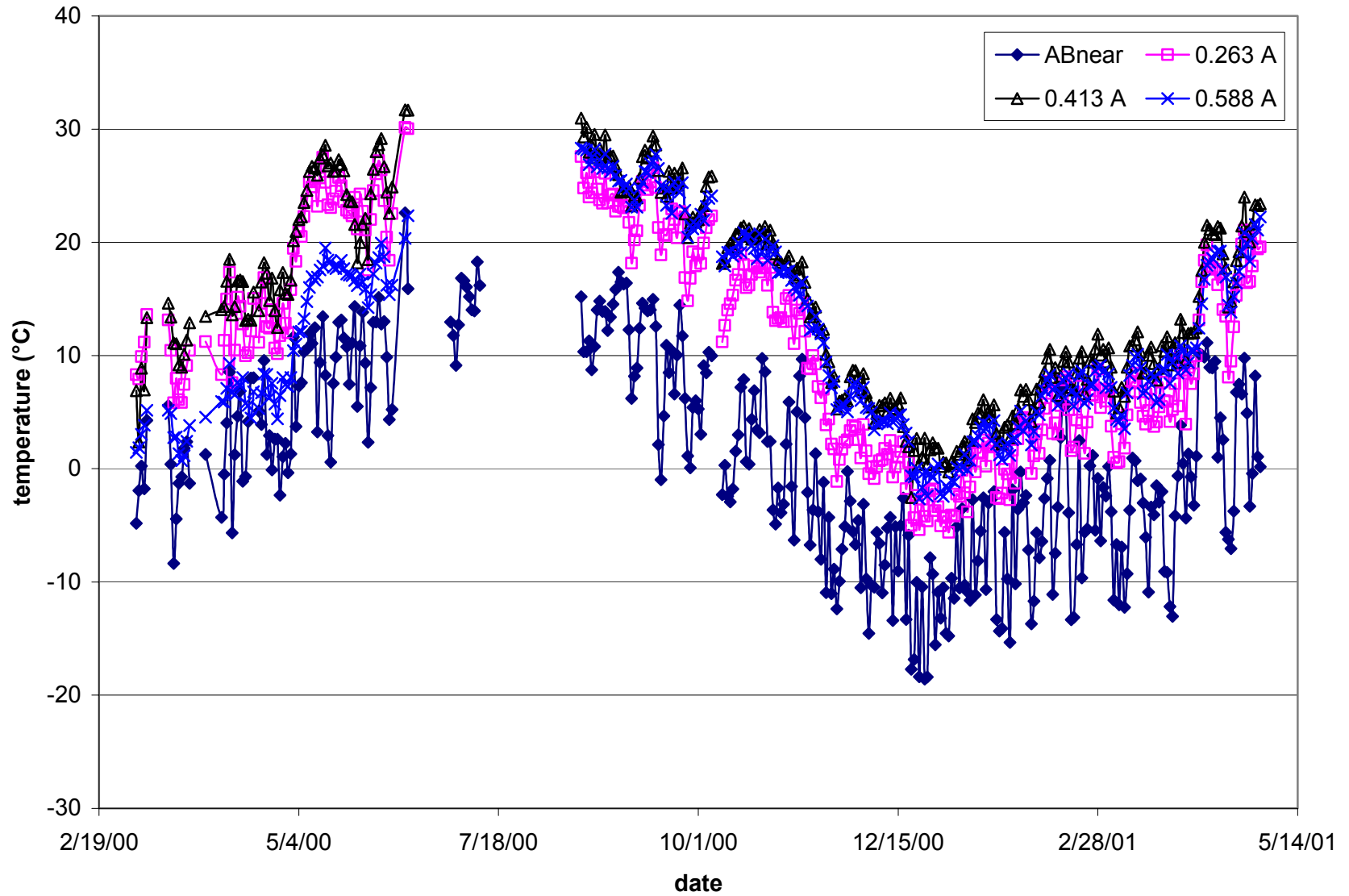


Figure G.5. Minimum daily temperature in aggregate base/subbase layers – Section A.

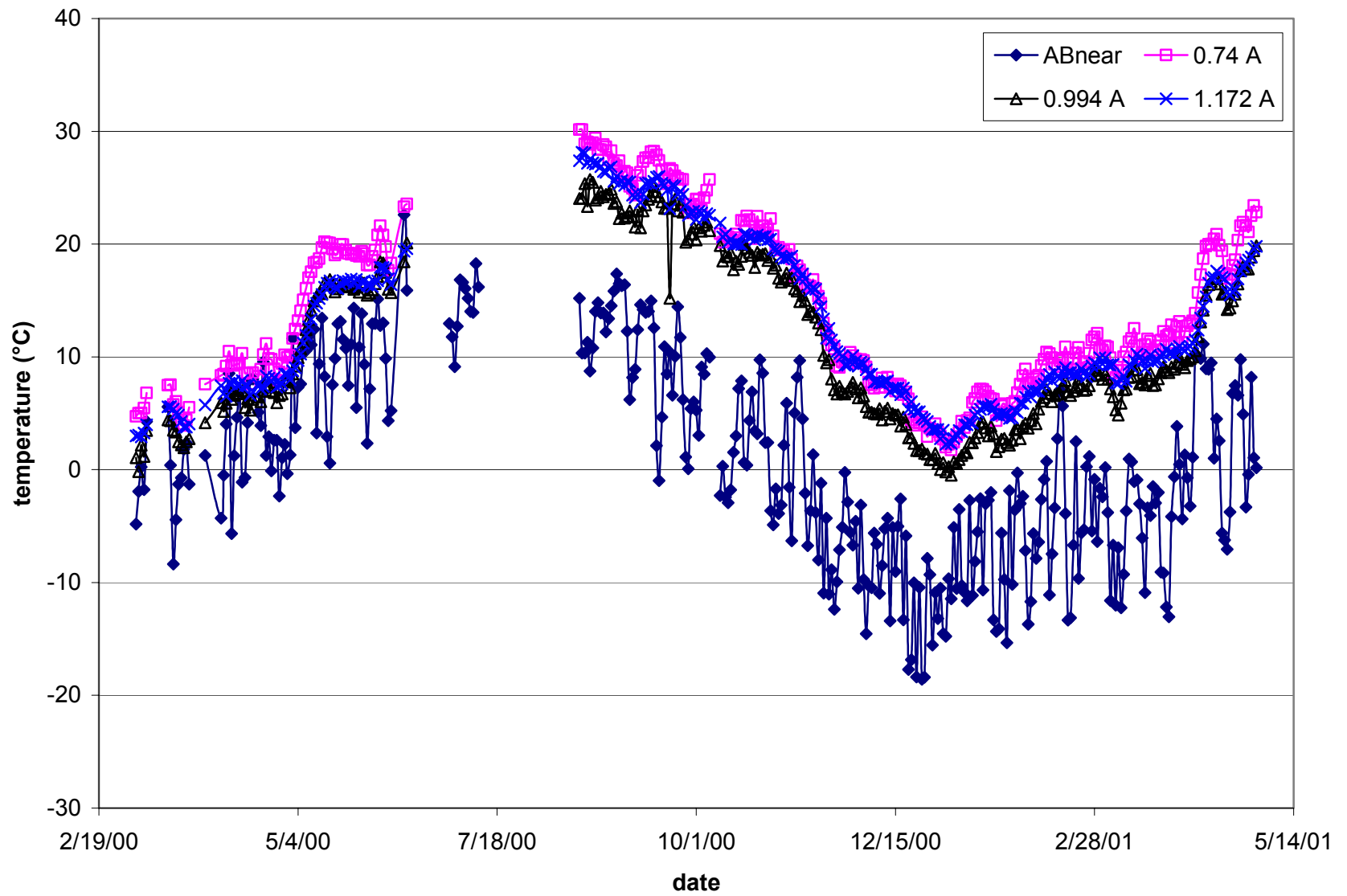


Figure G.6. Minimum daily temperature in subgrade – Section A.

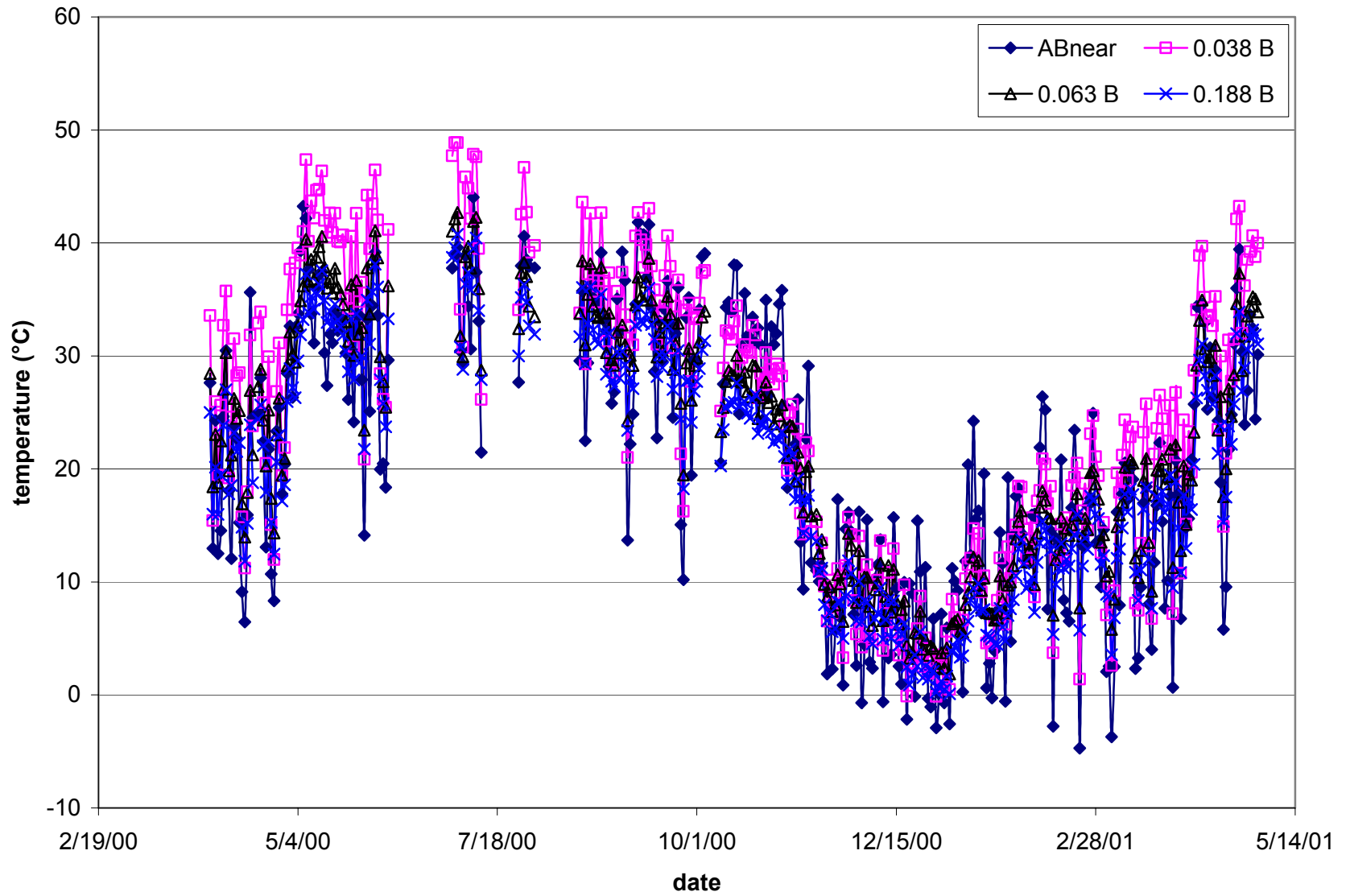


Figure G.7. Maximum daily temperature in HMA layers – Section B.

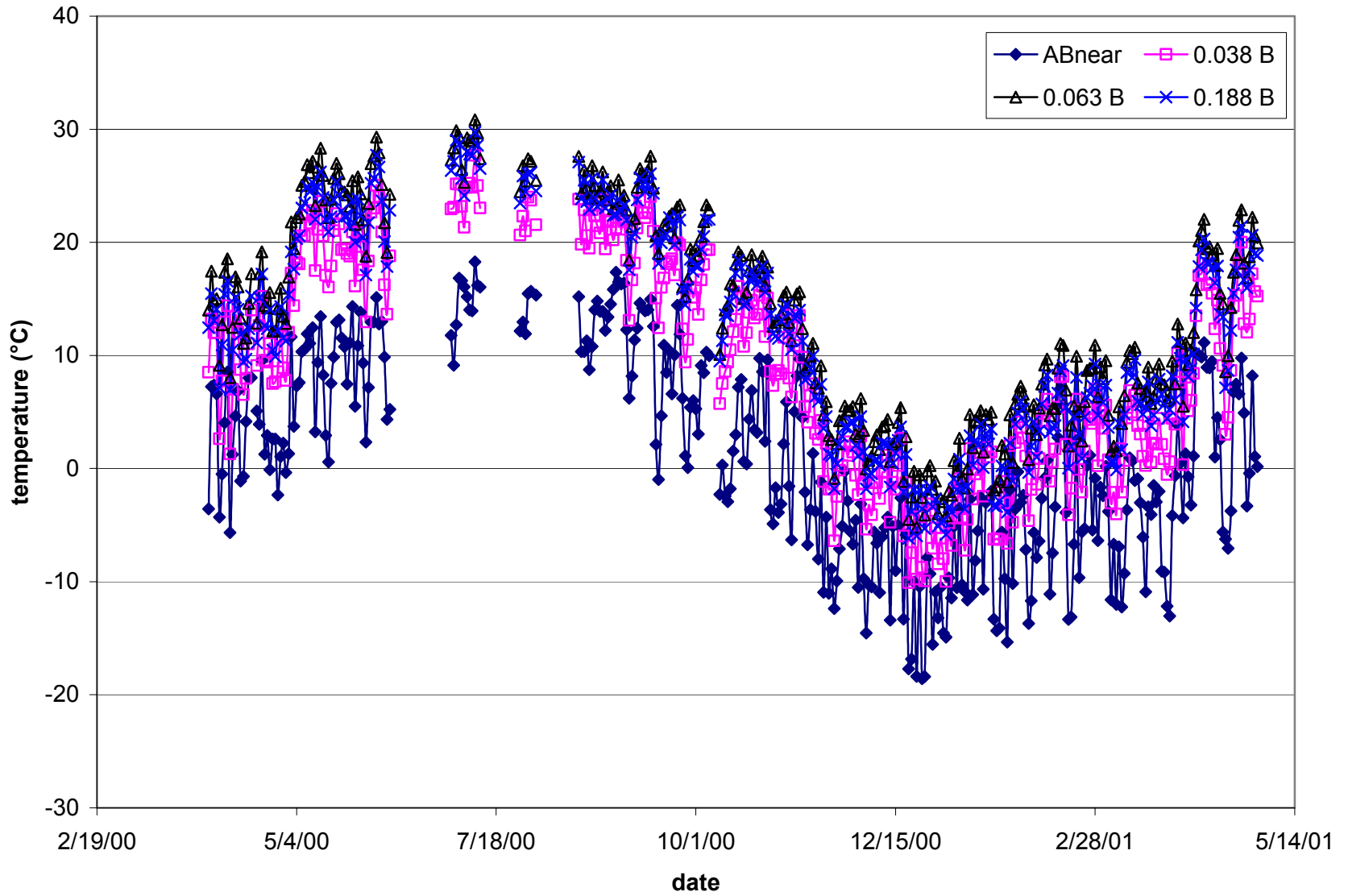


Figure G.8. Minimum daily temperature in HMA layers – Section B.

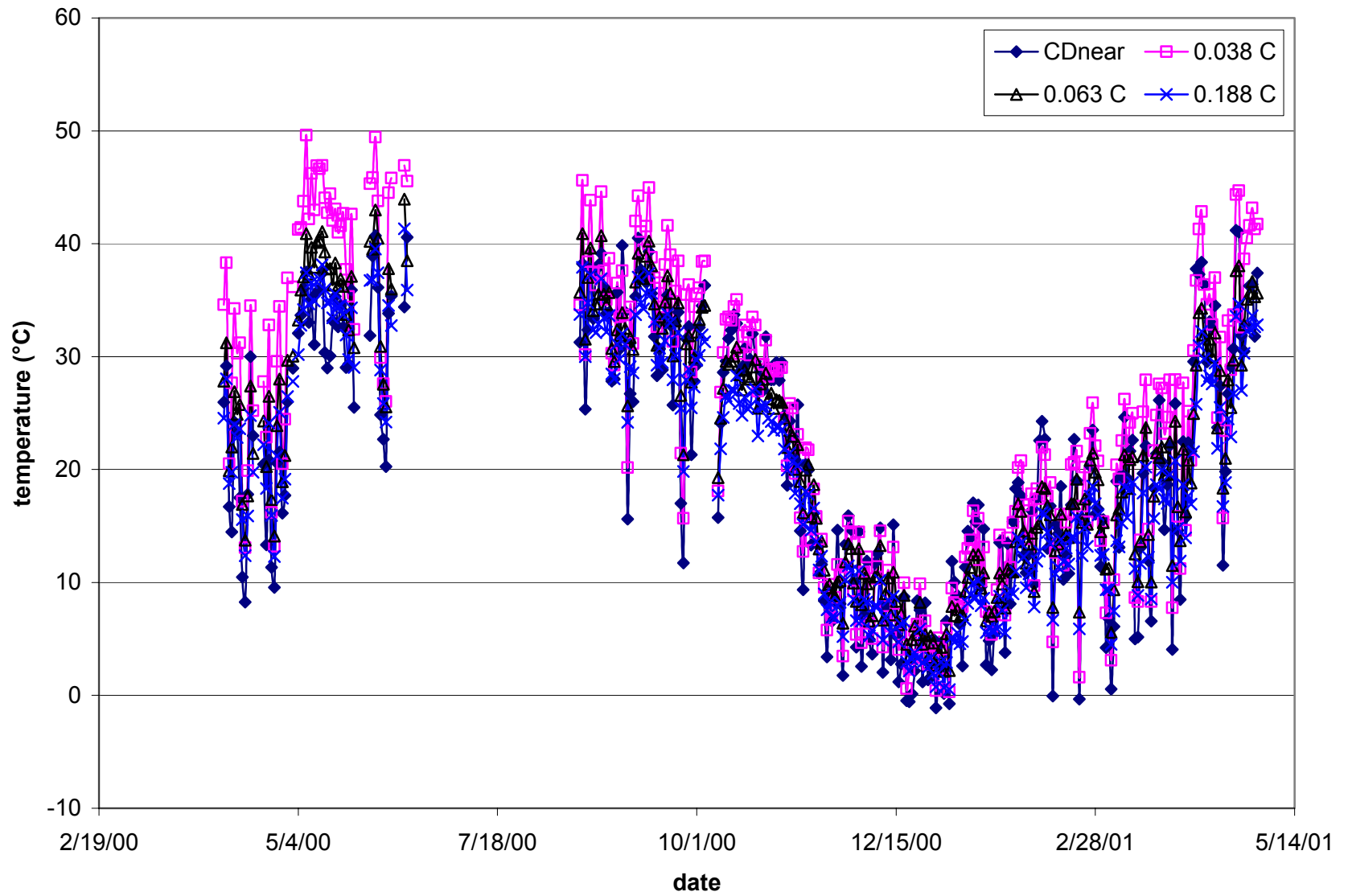


Figure G.9. Maximum daily temperature in HMA layers – Section C.

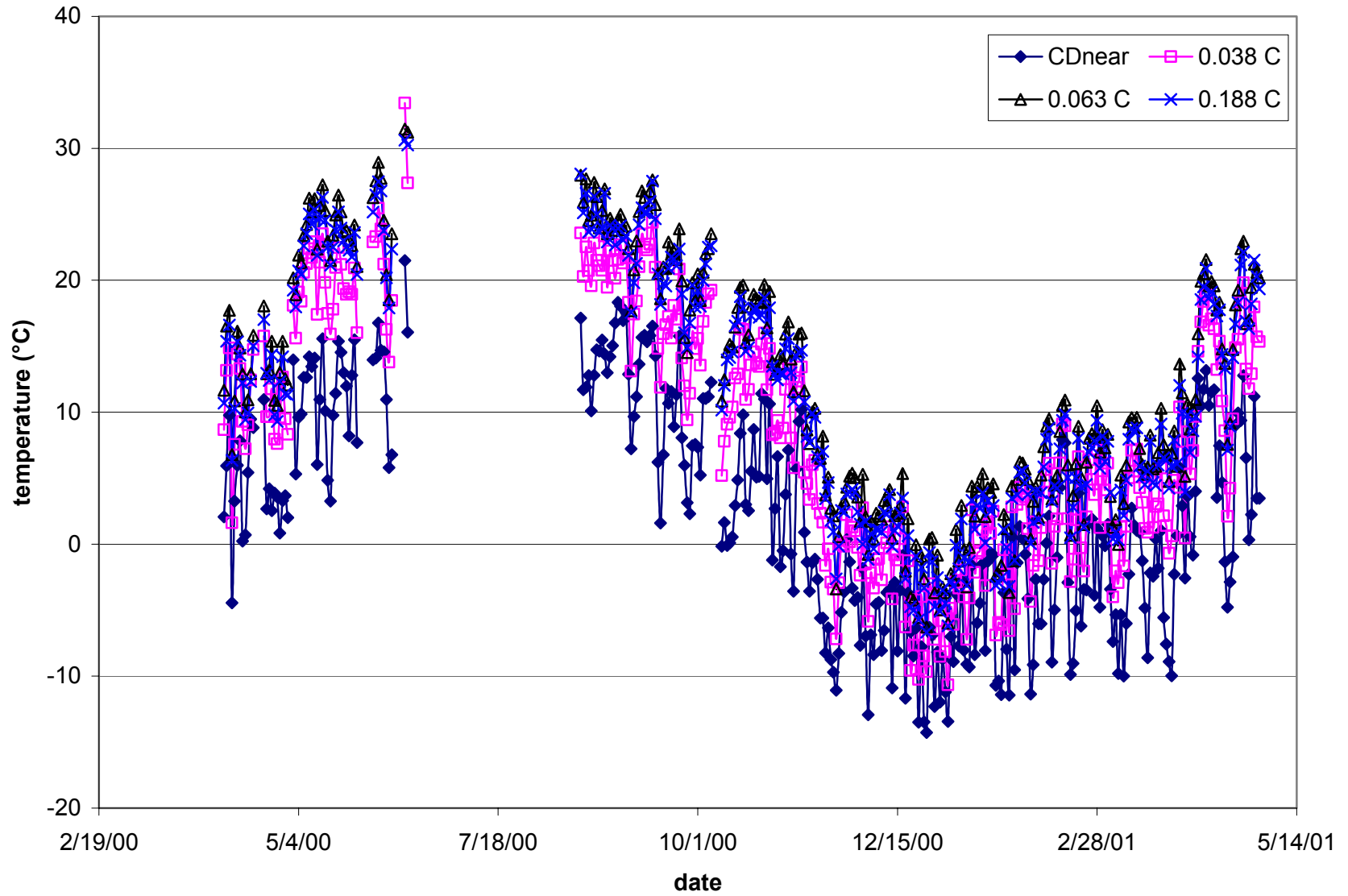


Figure G.10. Minimum daily temperature in HMA layers – Section C.

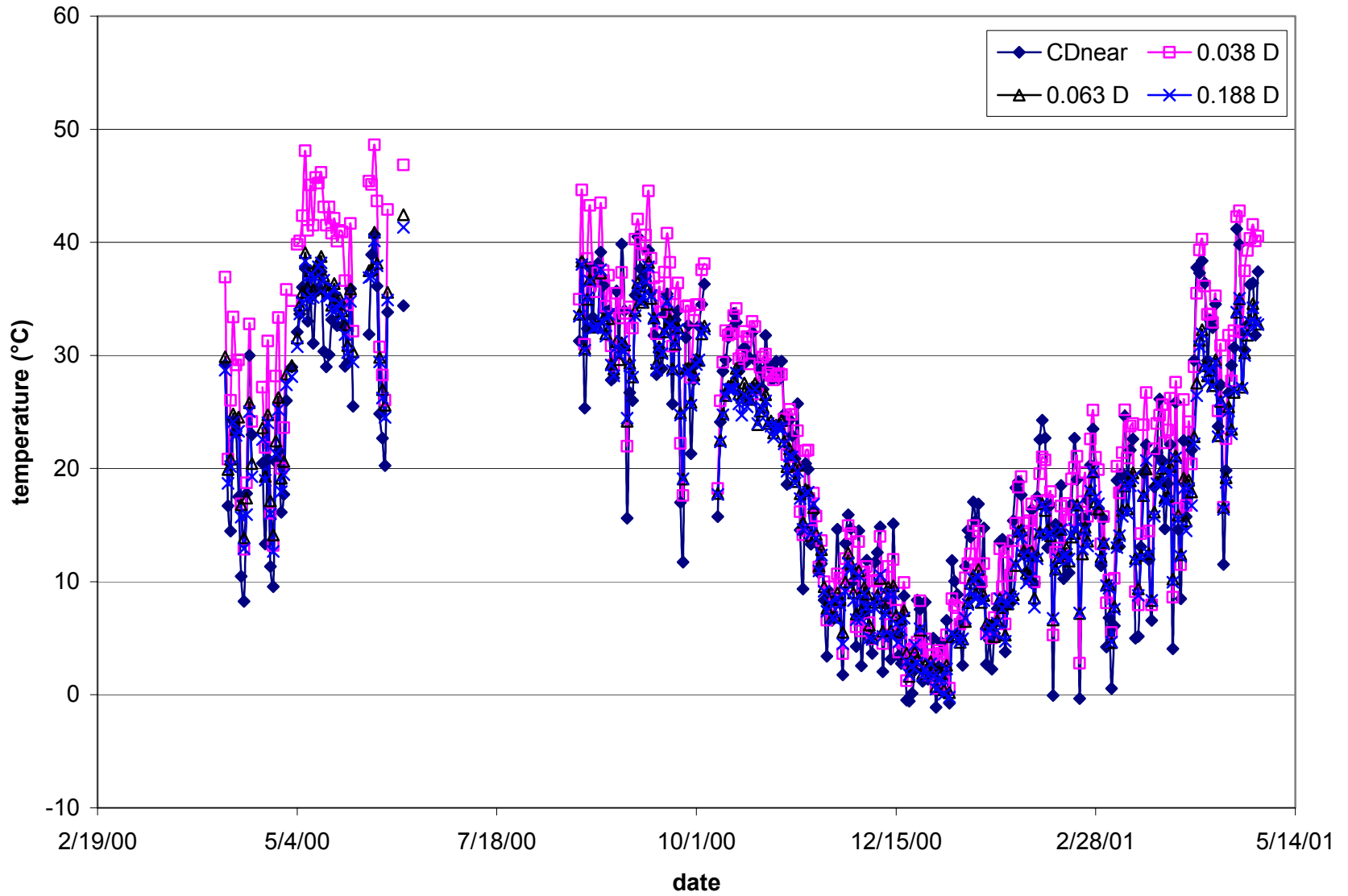


Figure G.11. Maximum daily temperature in HMA layers – Section D.

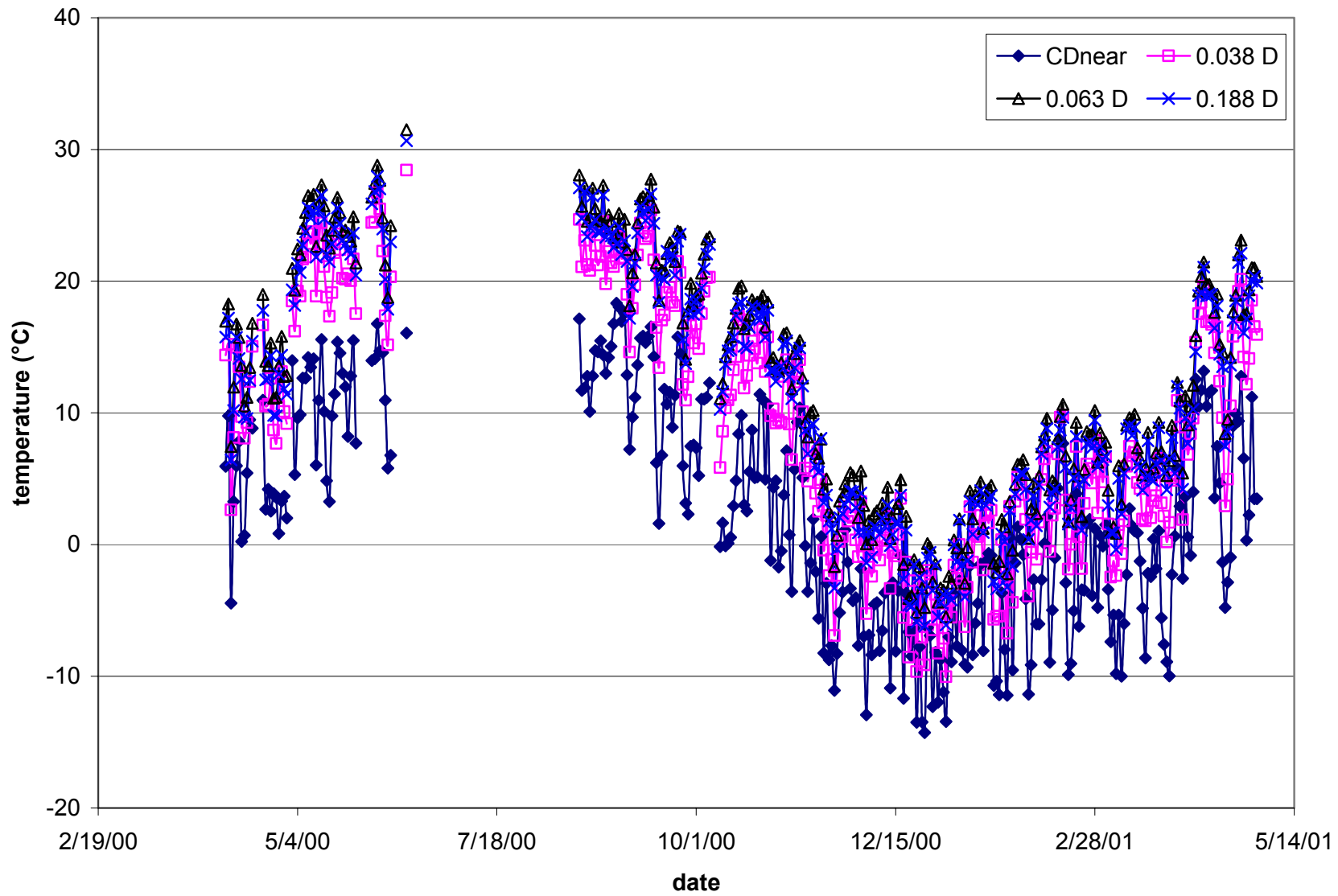


Figure G.12. Minimum daily temperature in HMA layers – Section D.

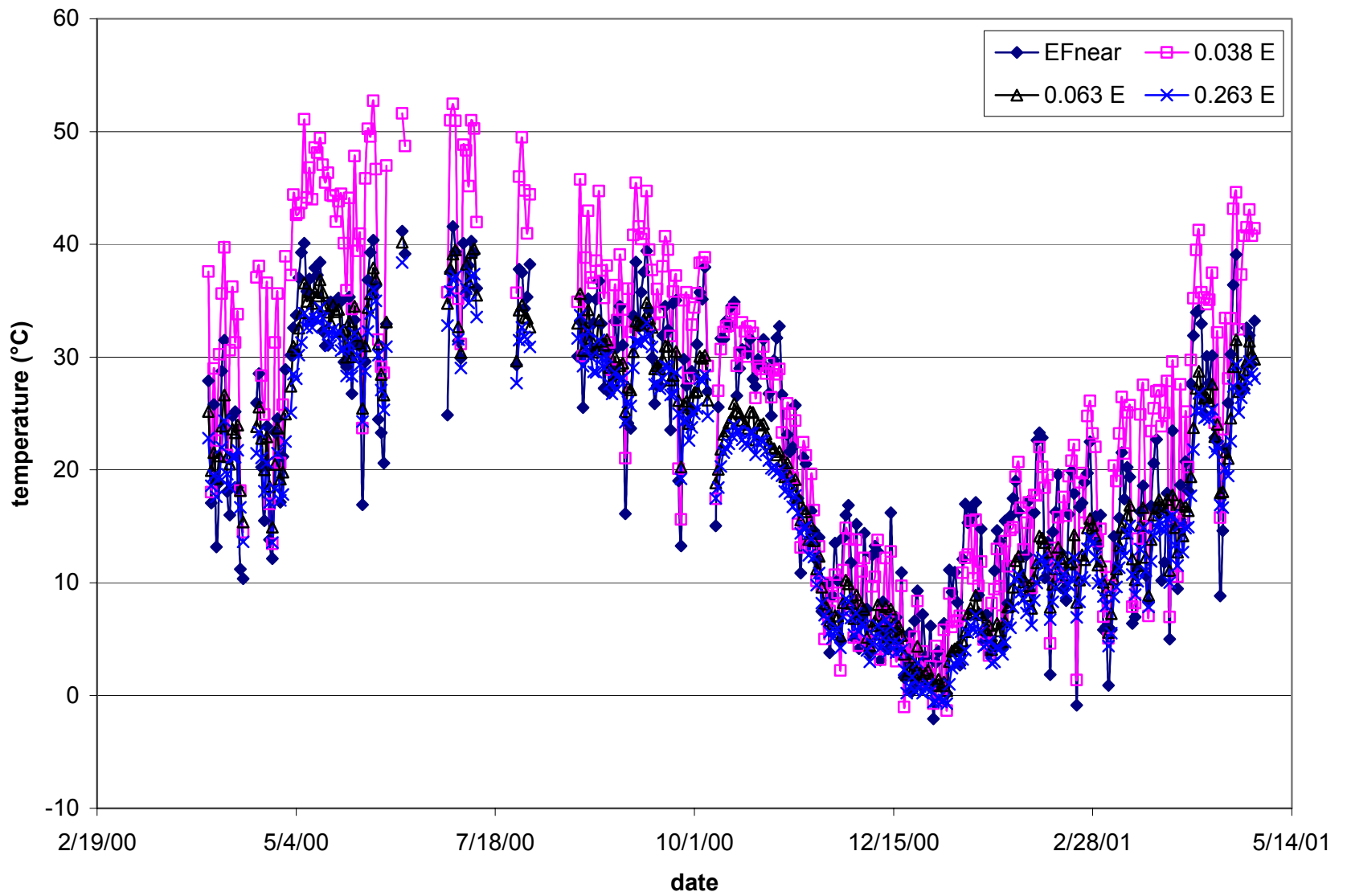


Figure G.13. Maximum daily temperature in HMA layers – Section E.

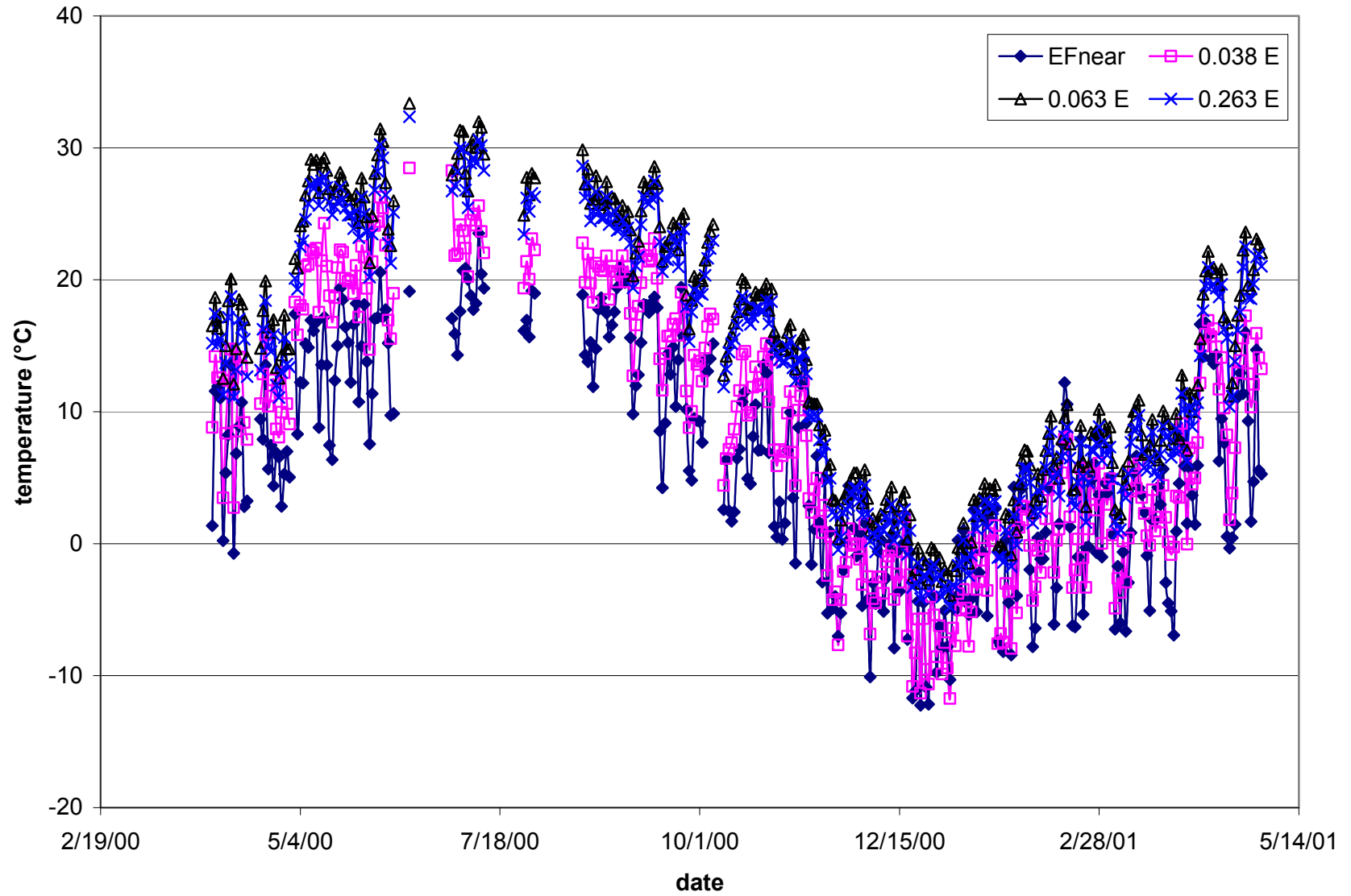


Figure G.14. Minimum daily temperature in HMA layers – Section E.

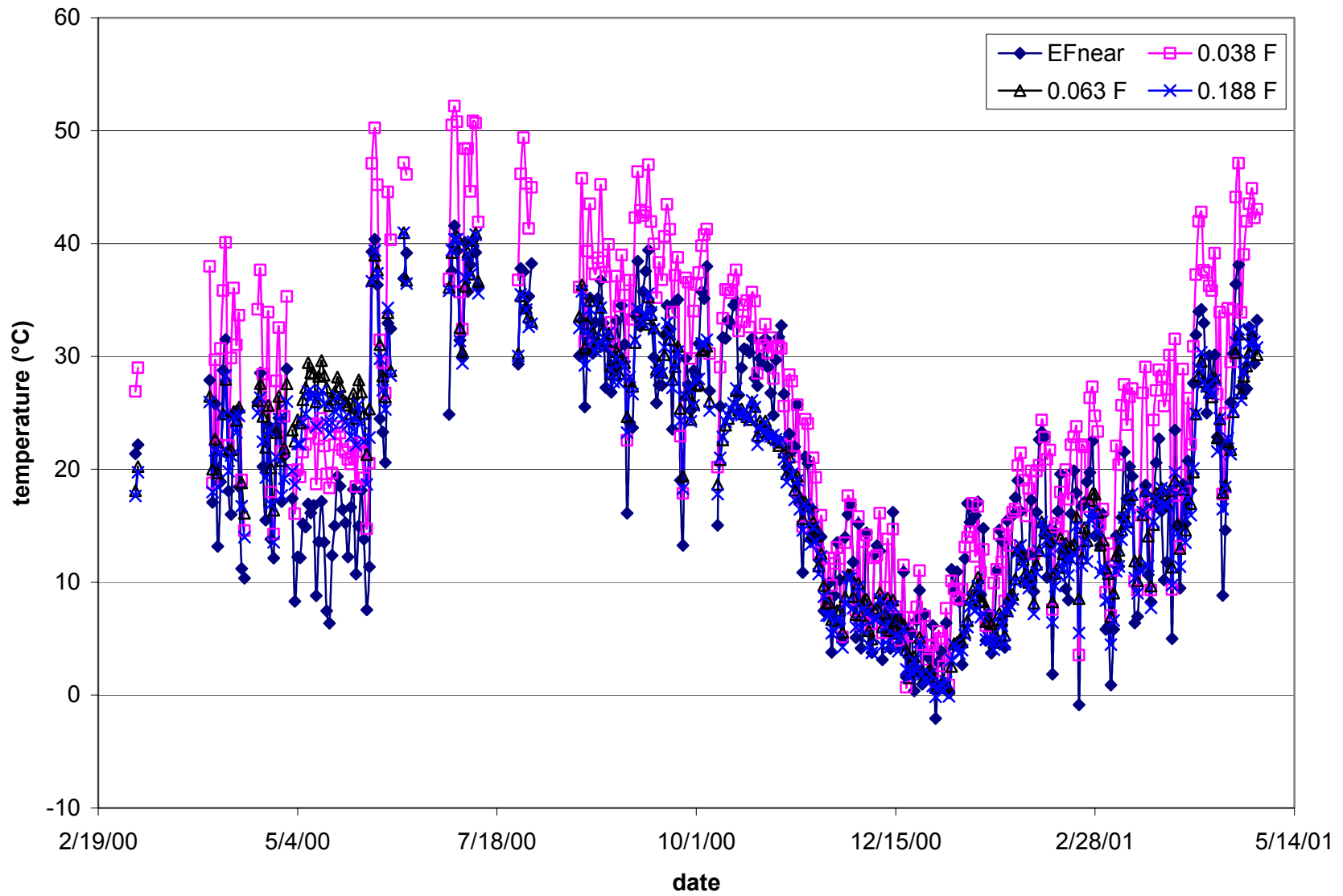


Figure G.15. Maximum daily temperature in HMA layers – Section F.

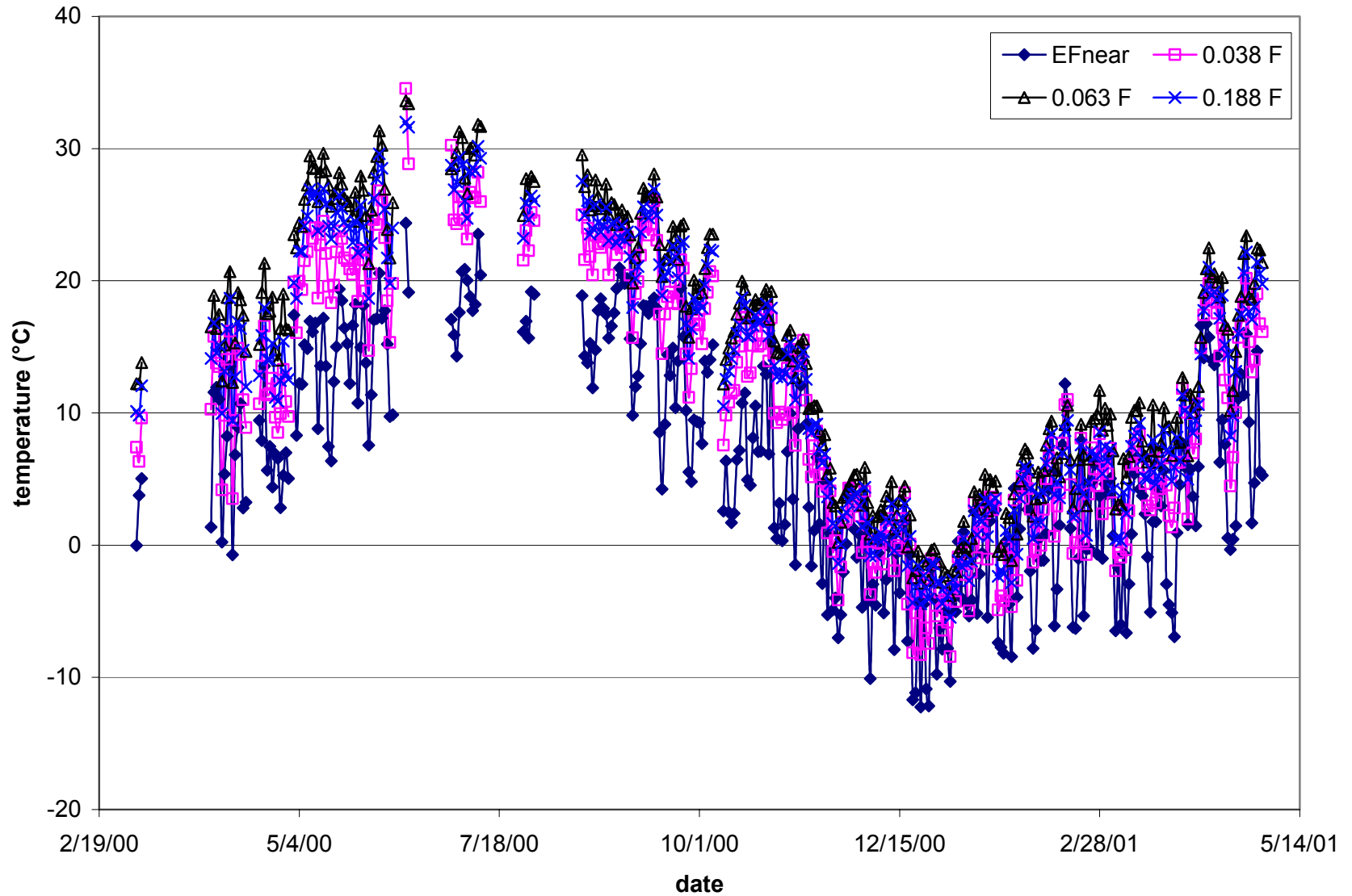


Figure G.16. Minimum daily temperature in HMA layers – Section F.

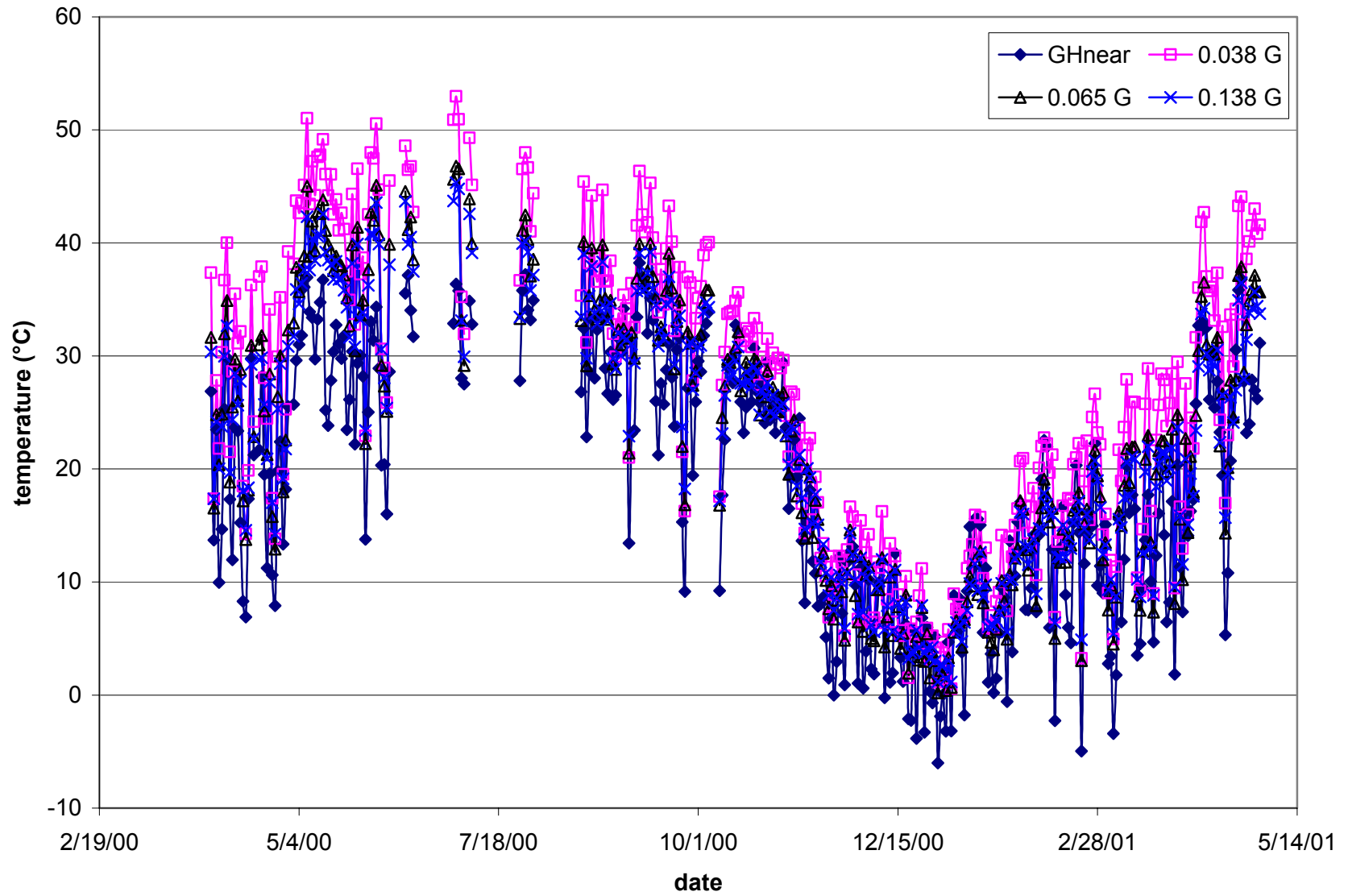


Figure G.17. Maximum daily temperature in HMA layers – Section G.

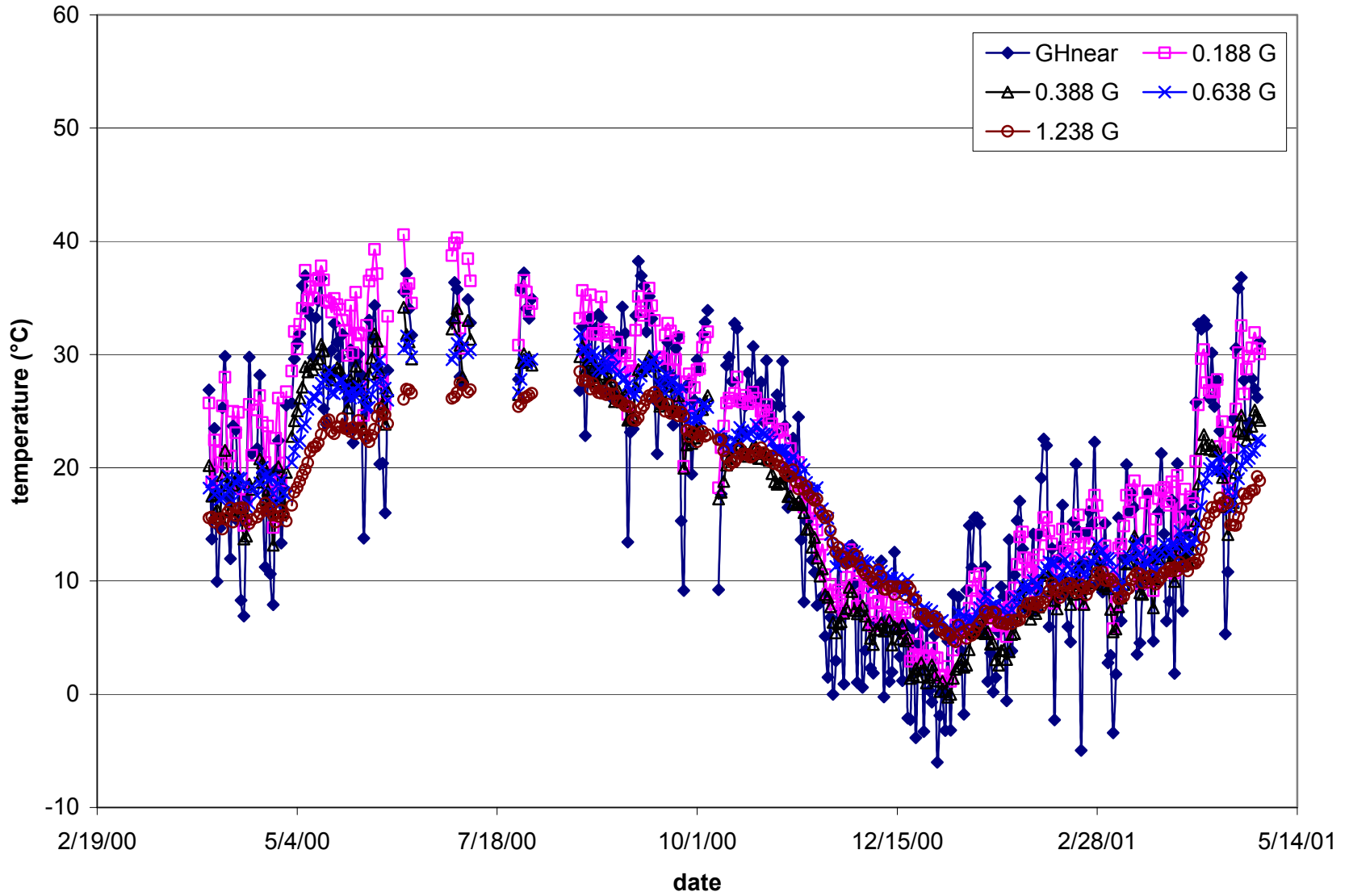


Figure G.18. Maximum daily temperature in aggregate base/subbase and subgrade layers – Section G.

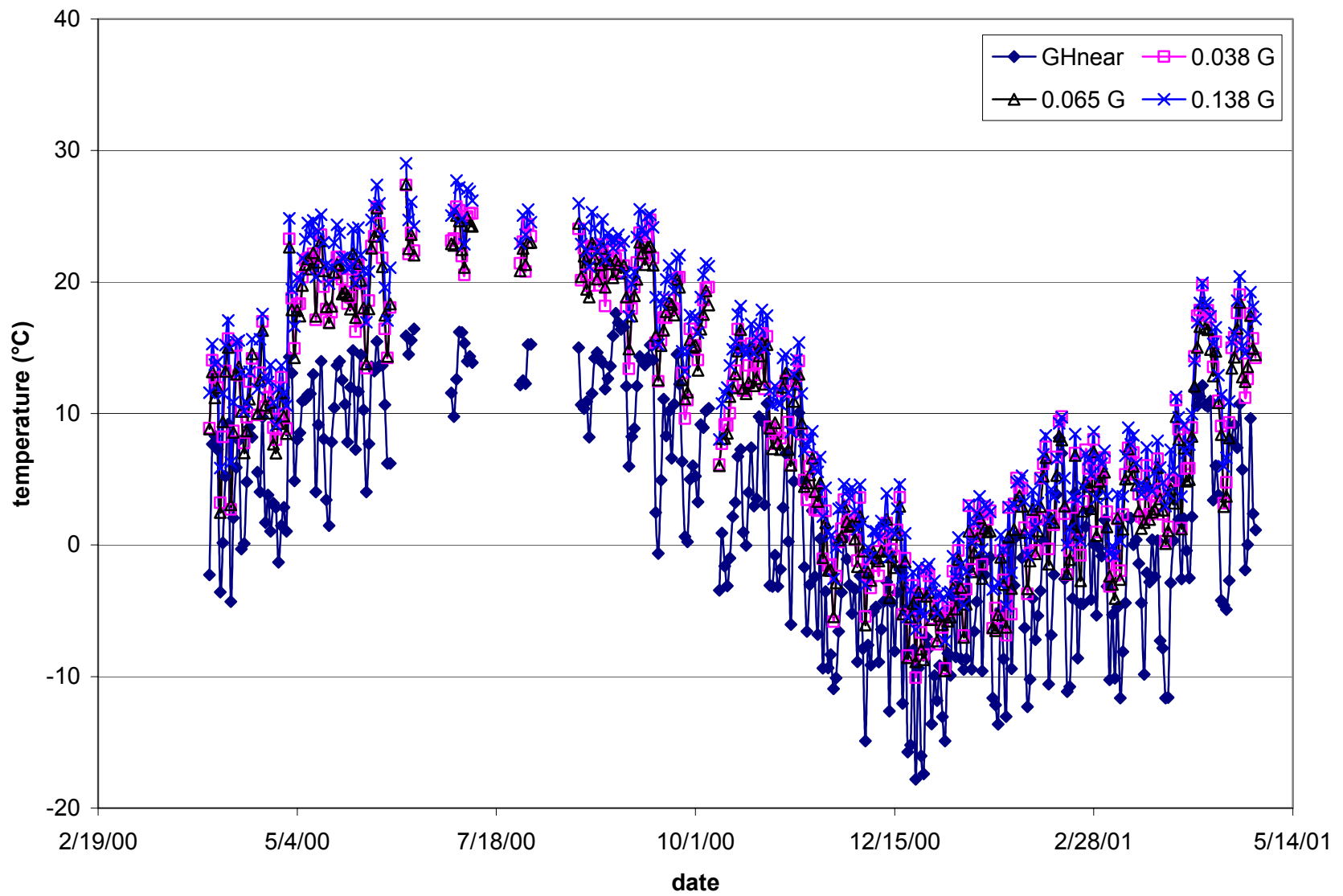


Figure G.19. Minimum daily temperature in HMA layers – Section G.

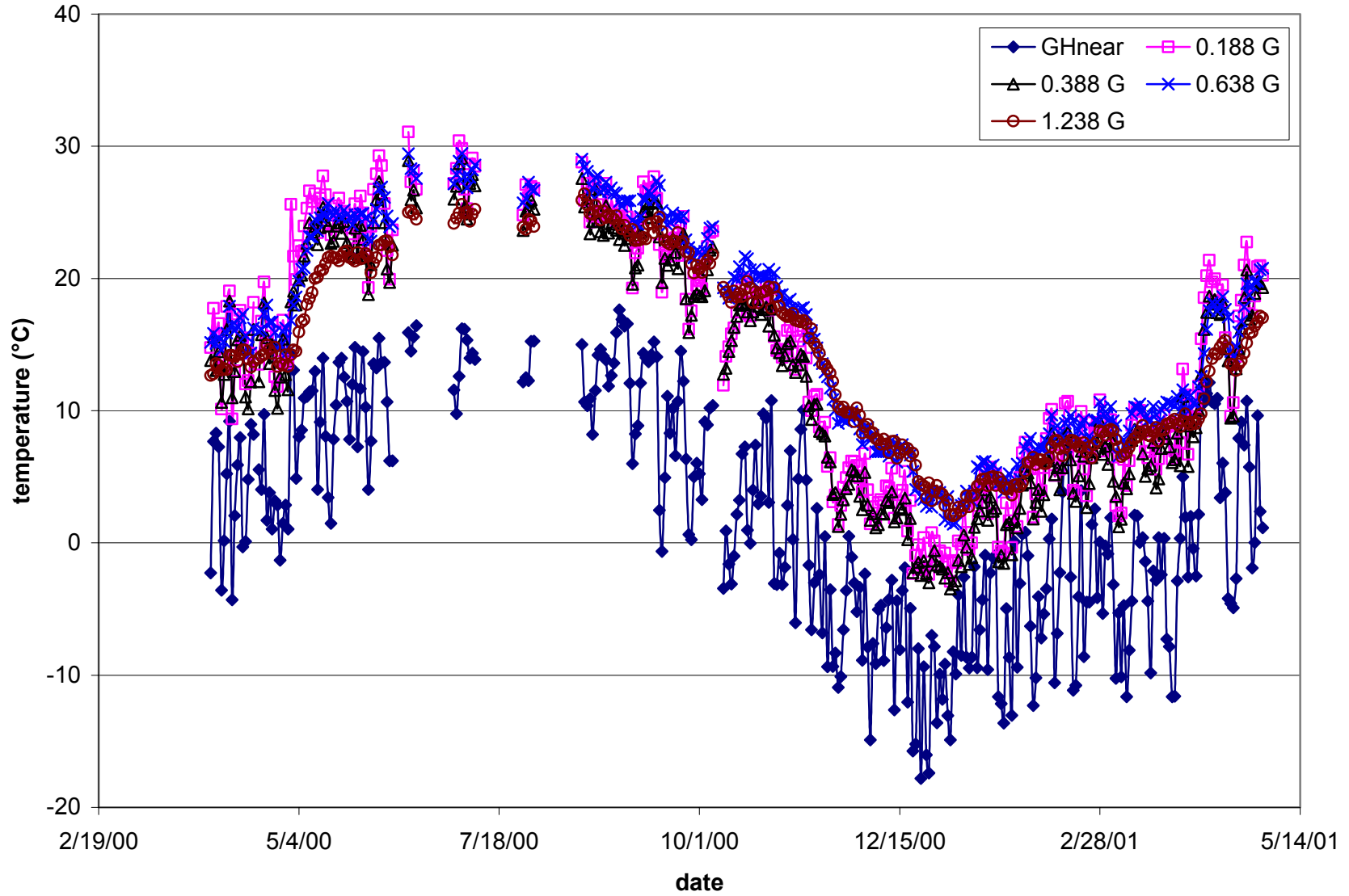


Figure G.20. Minimum daily temperature in aggregate base/subbase and subgrade layers – Section G.

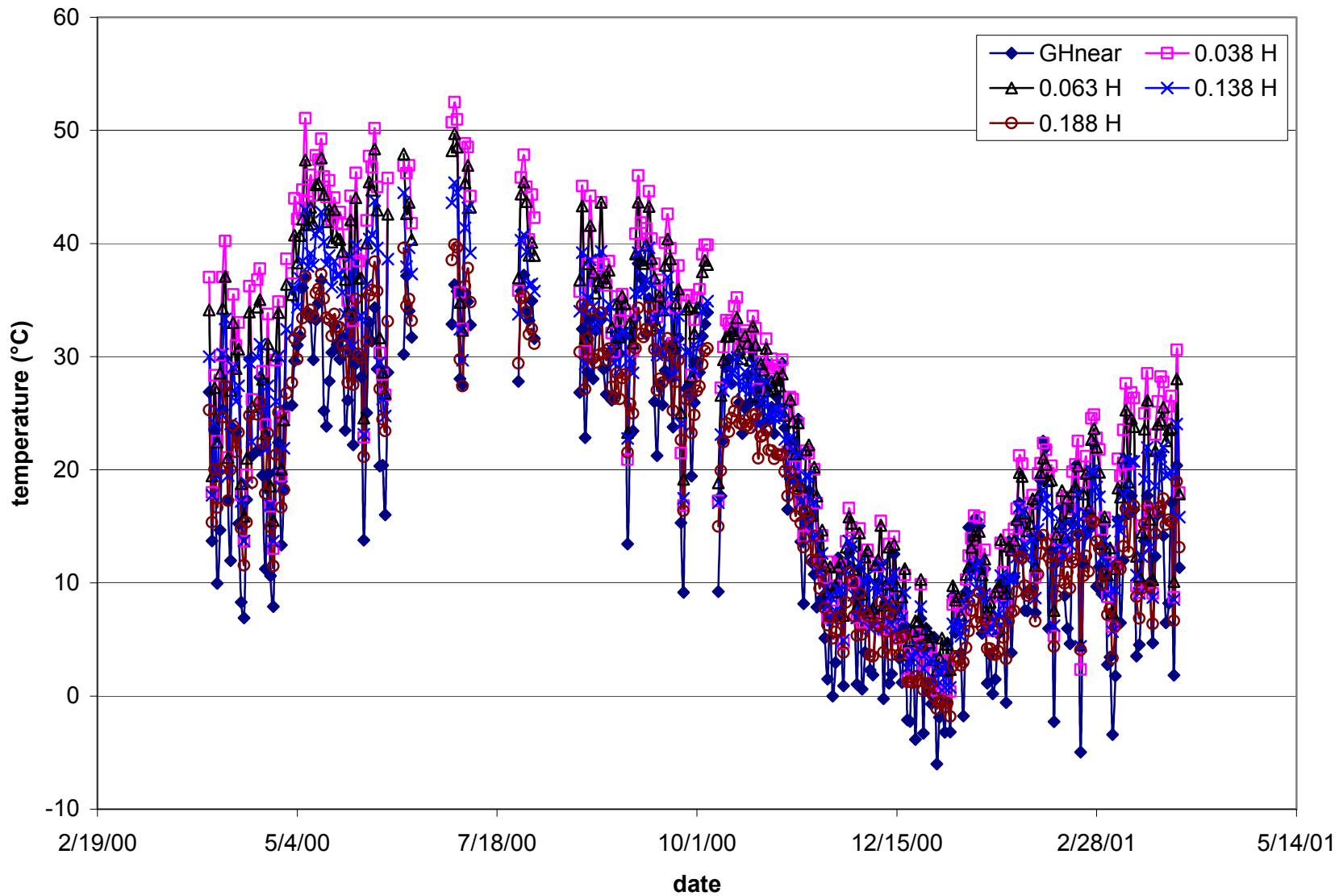


Figure G.21. Maximum daily temperature in HMA layers – Section H.

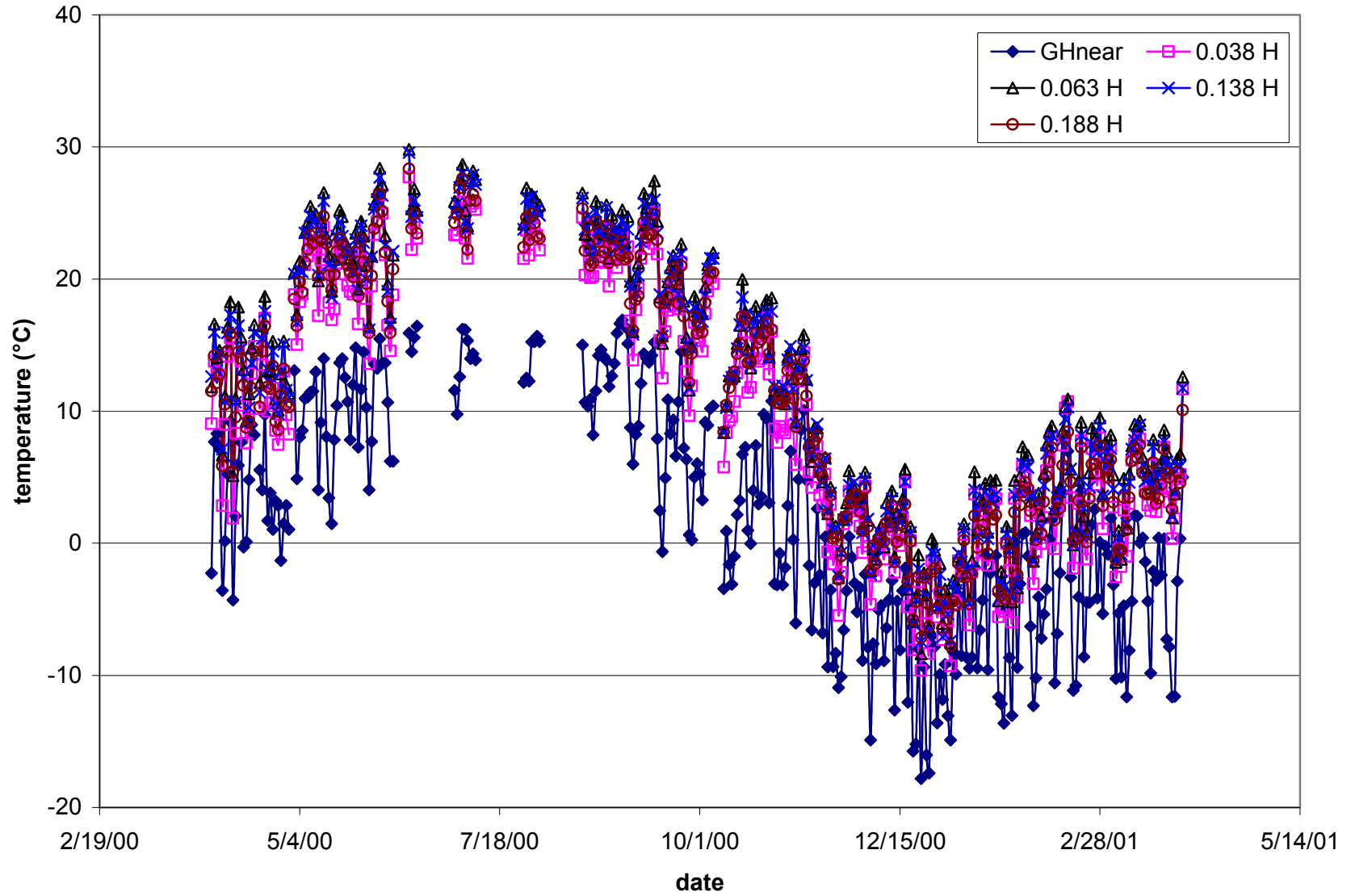


Figure G.22. Minimum daily temperature in HMA layers – Section H.

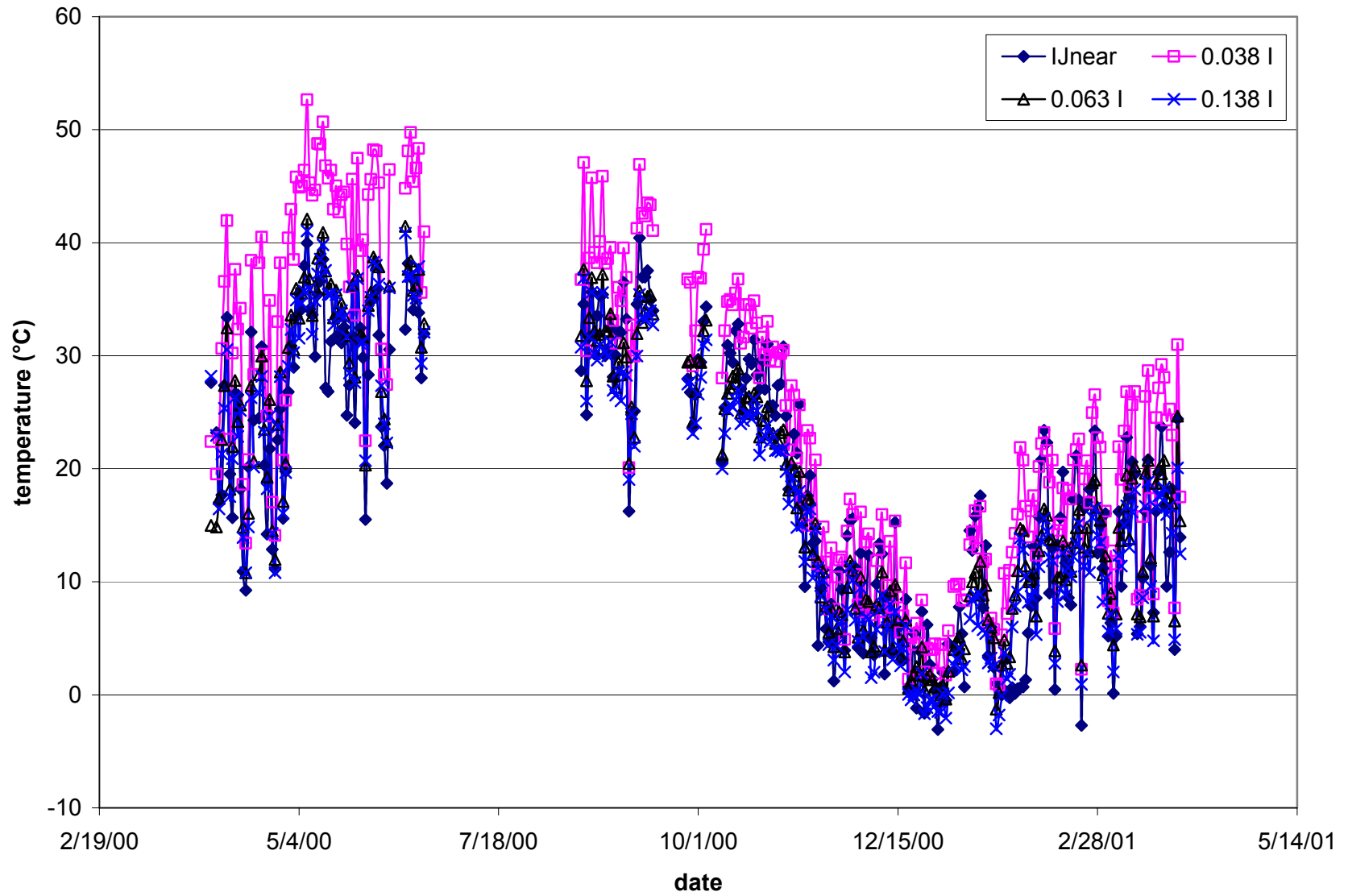


Figure G.23. Maximum daily temperature in HMA layers – Section I.

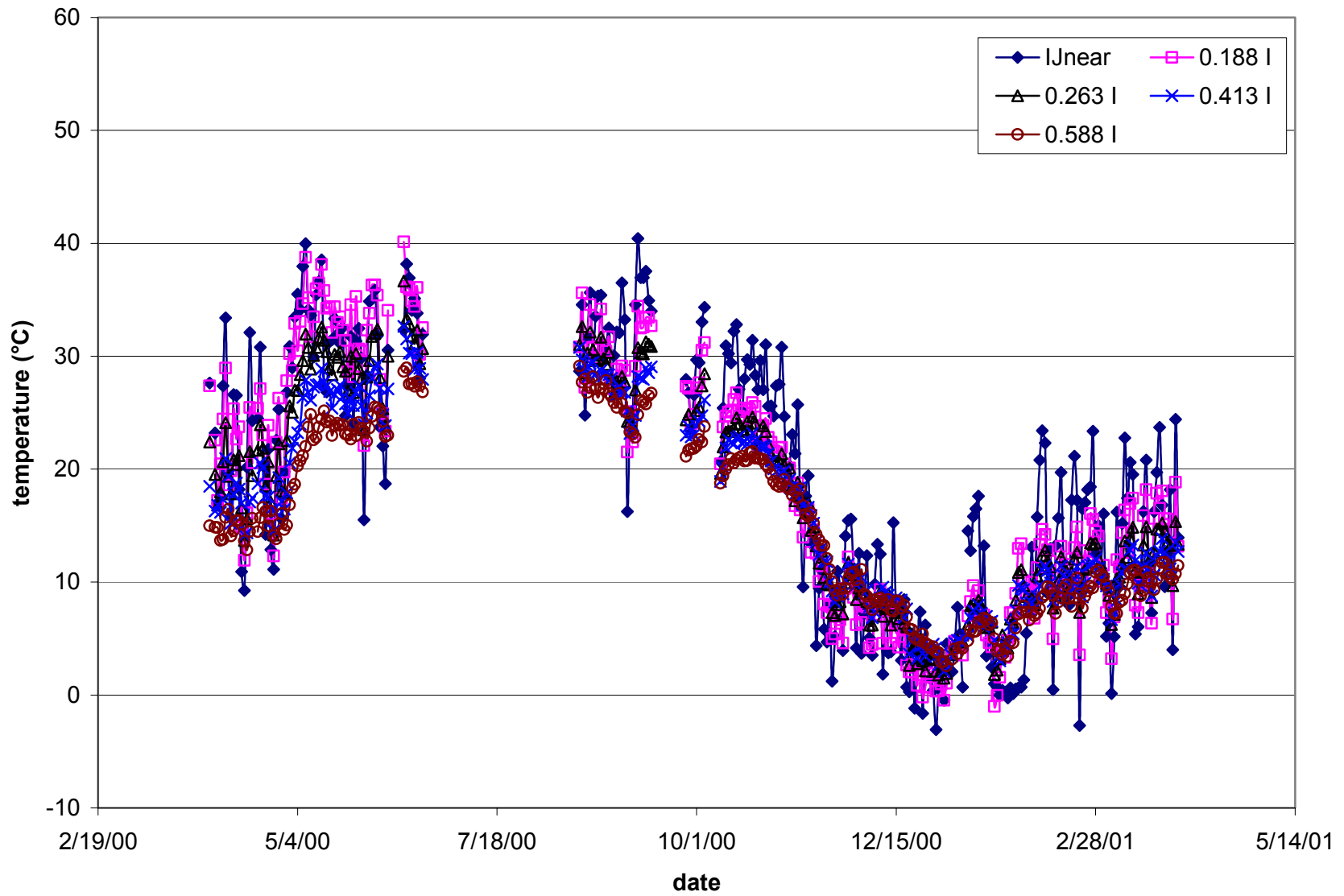


Figure G.24. Maximum daily temperature in aggregate base/subbase layers – Section I.

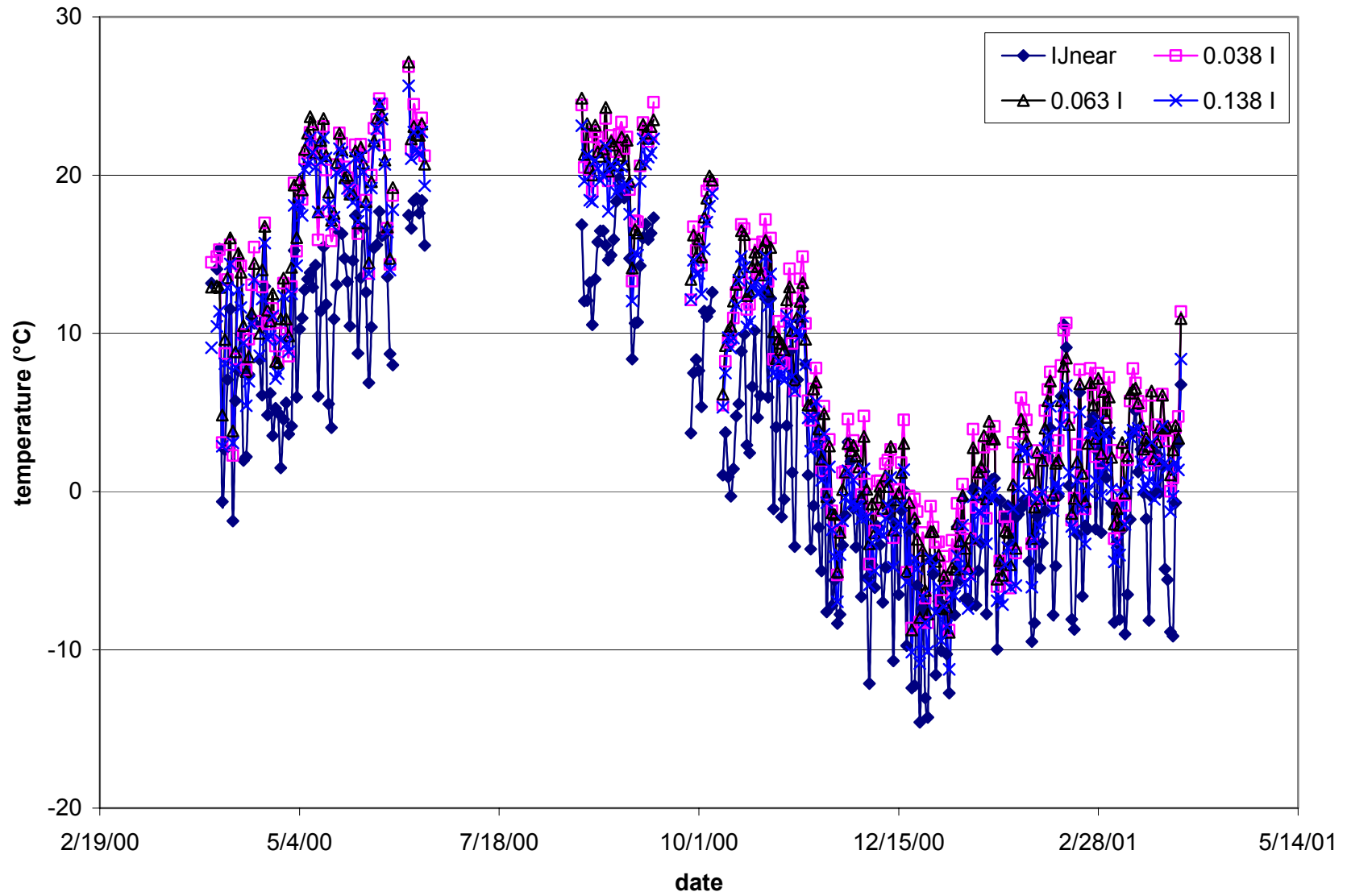


Figure G.25. Minimum daily temperature in HMA layers – Section I.

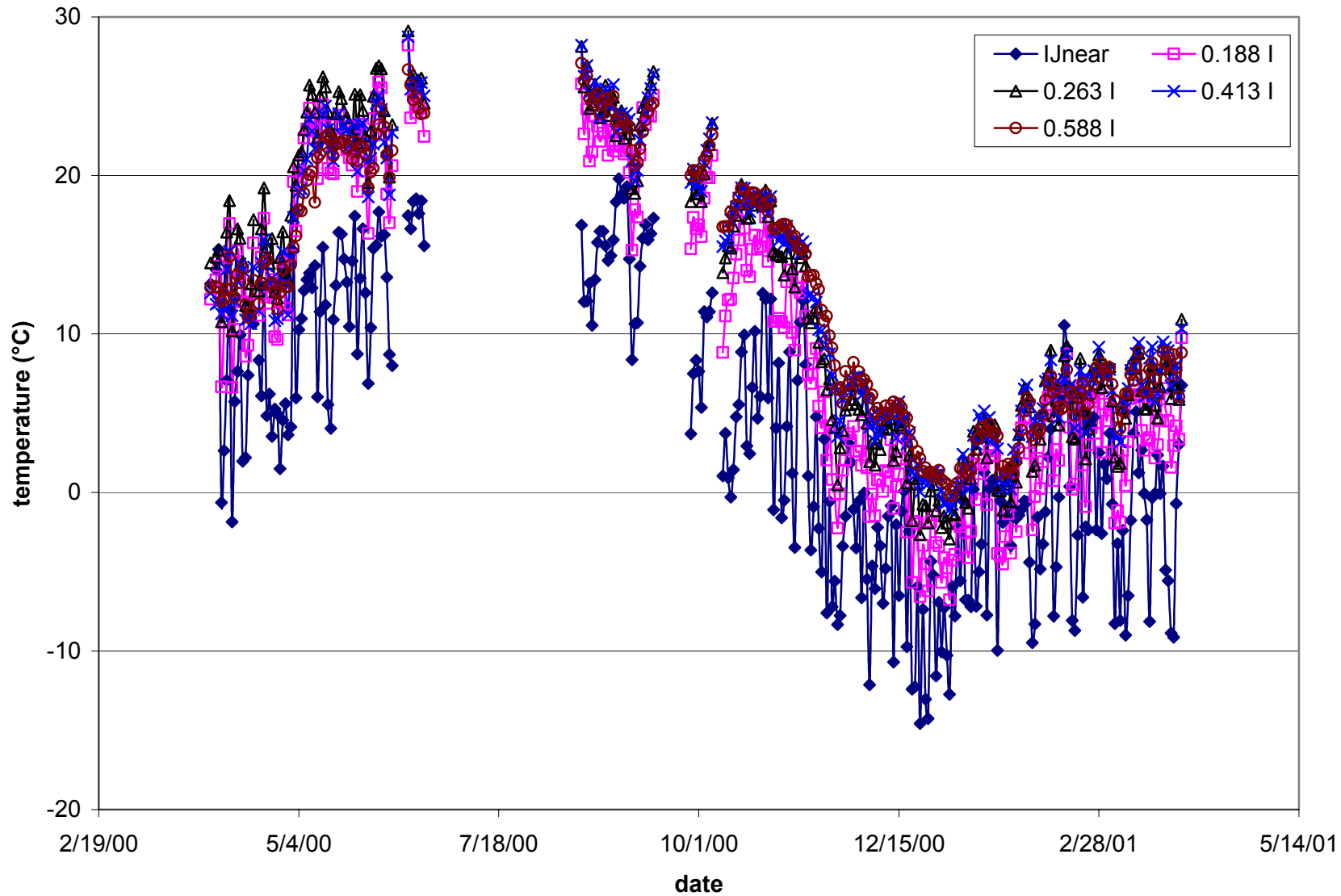


Figure G.26. Minimum daily temperature in aggregate base/subbase layers – Section I.

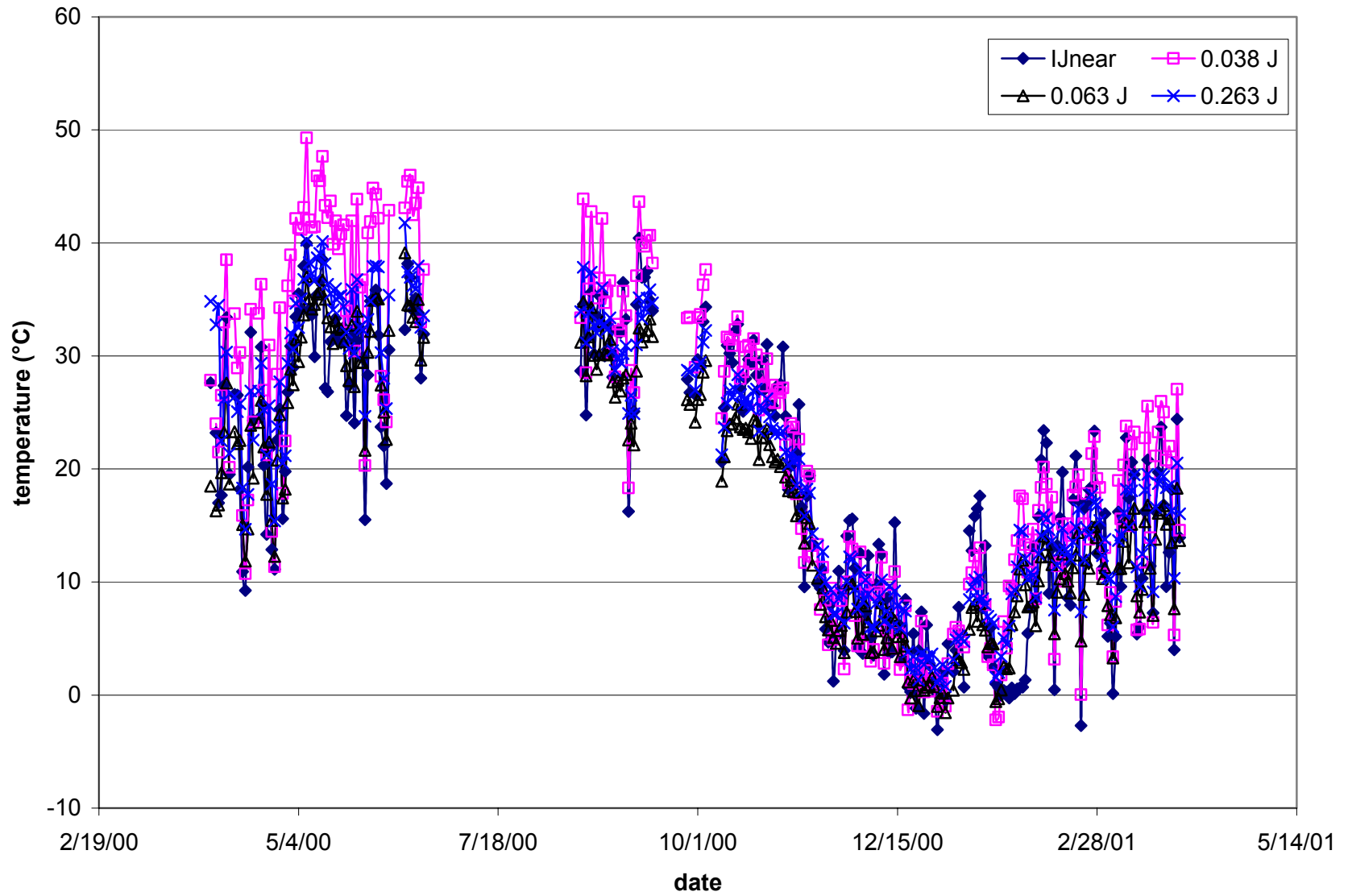


Figure G.27. Maximum daily temperature in HMA layers – Section J

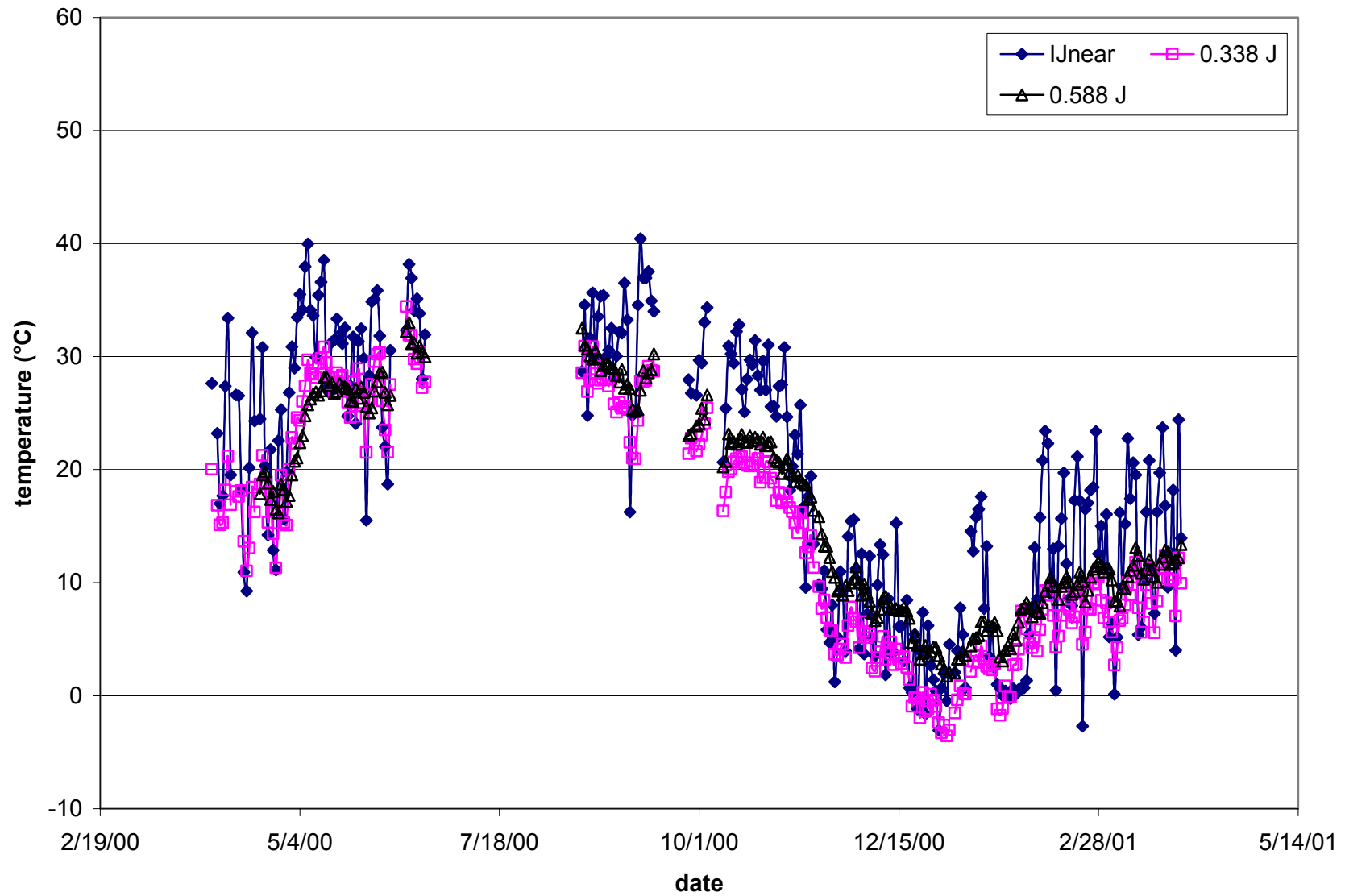


Figure G.28. Maximum daily temperature in aggregate base/subbase layers – Section J.

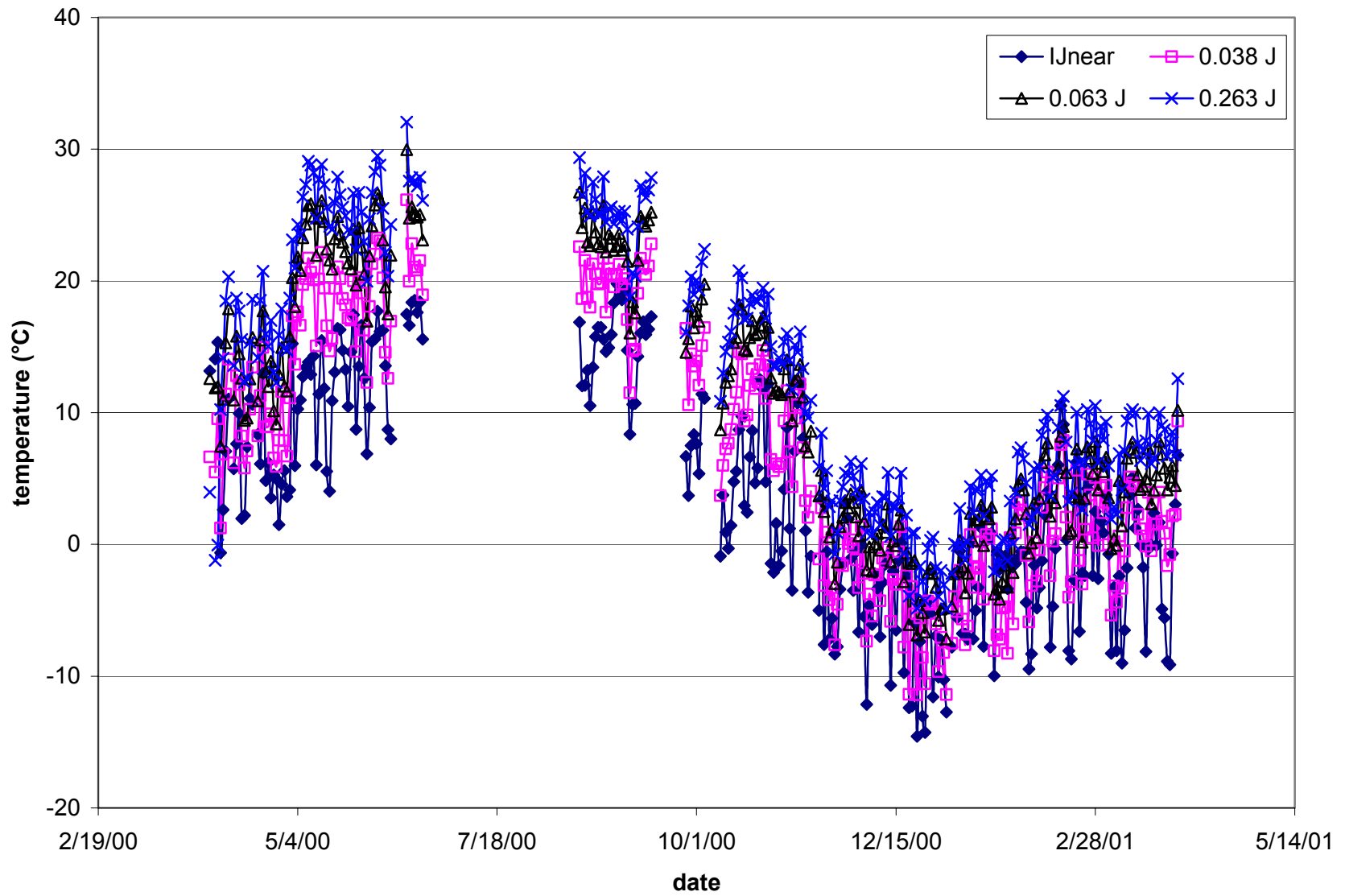


Figure G.29. Minimum daily temperature in HMA layers – Section J

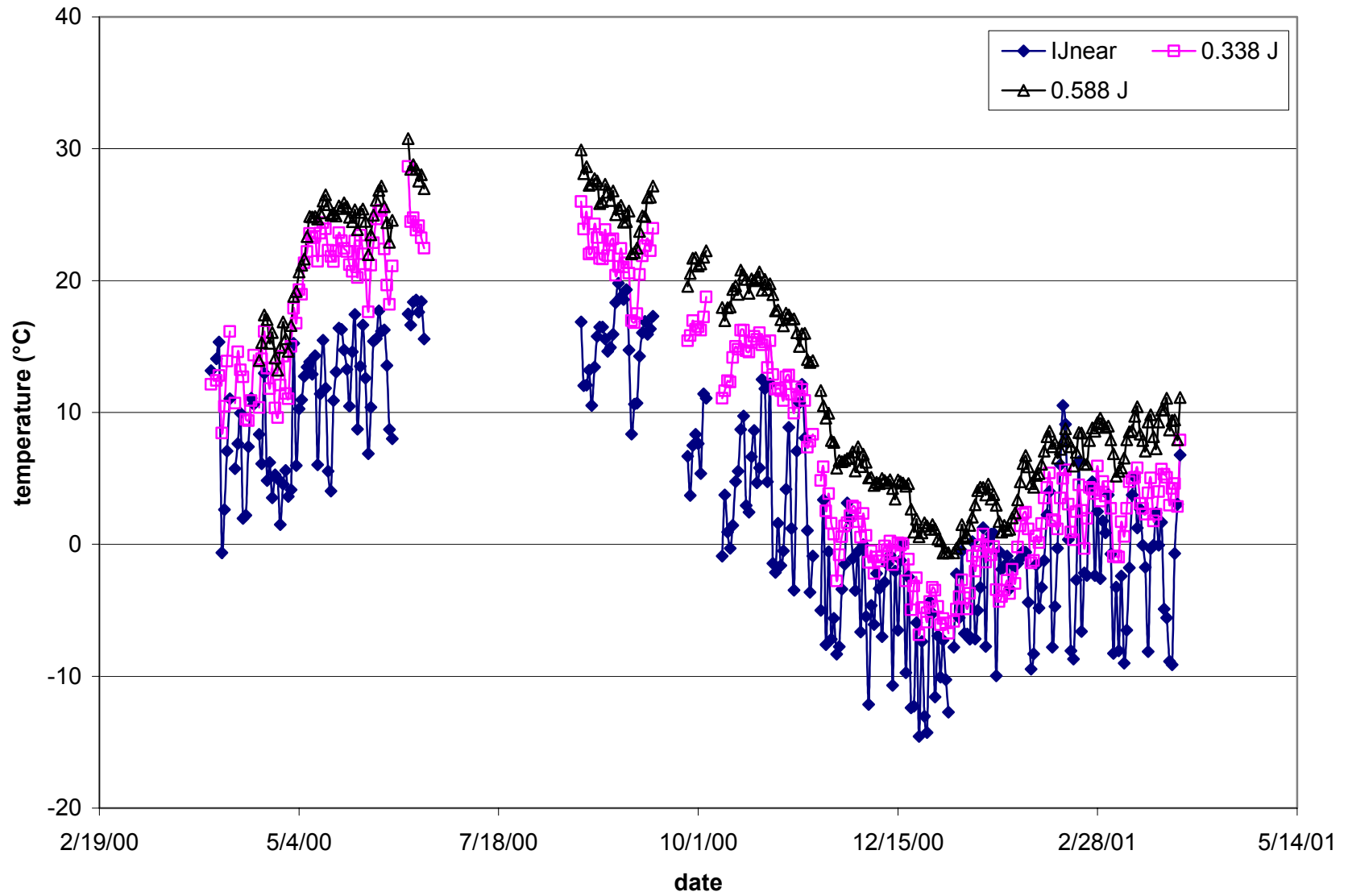


Figure G.30. Minimum daily temperature in aggregate base/subbase layers – Section J.

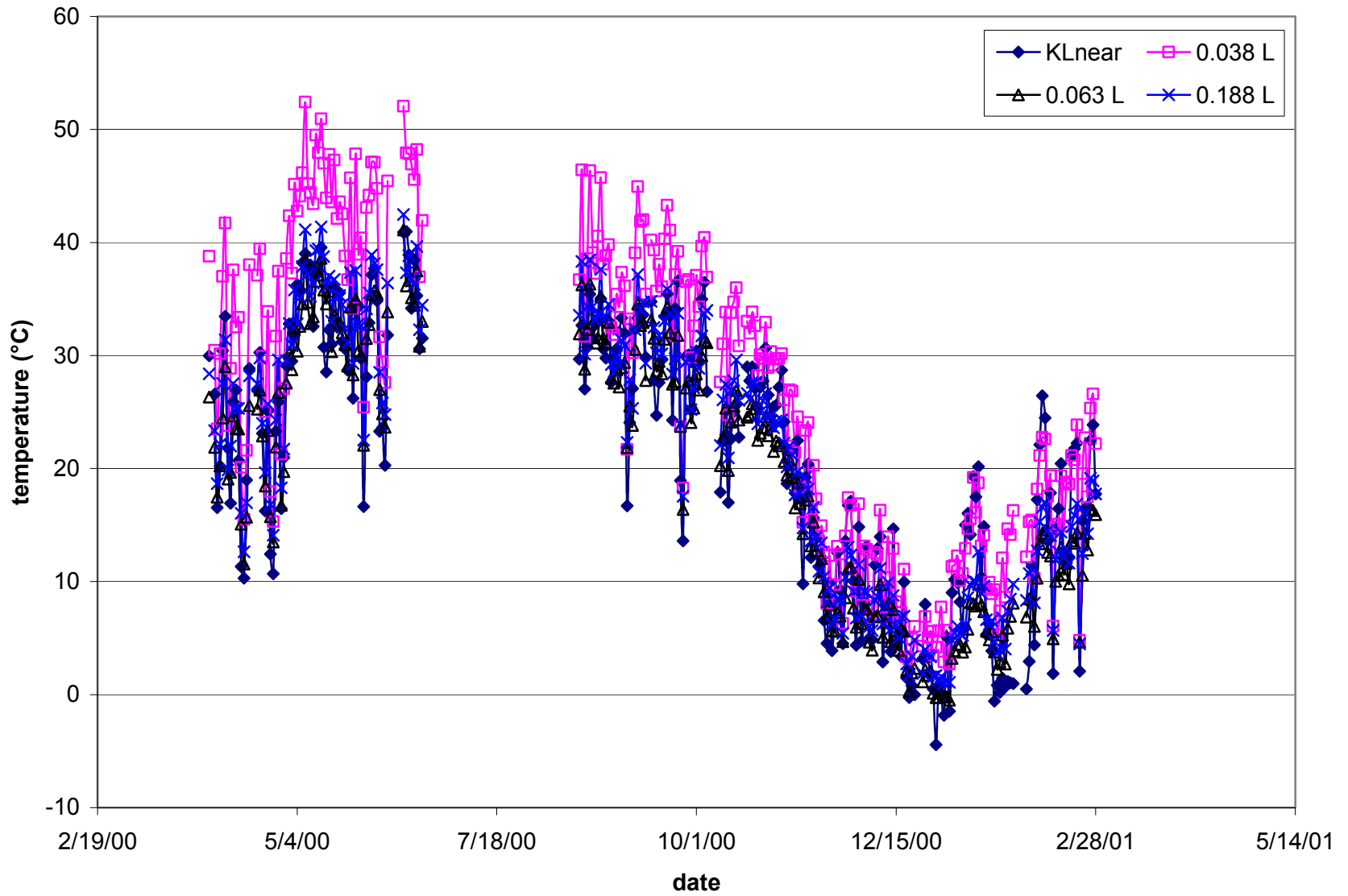


Figure G.31. Maximum daily temperature in HMA layers – Section L.

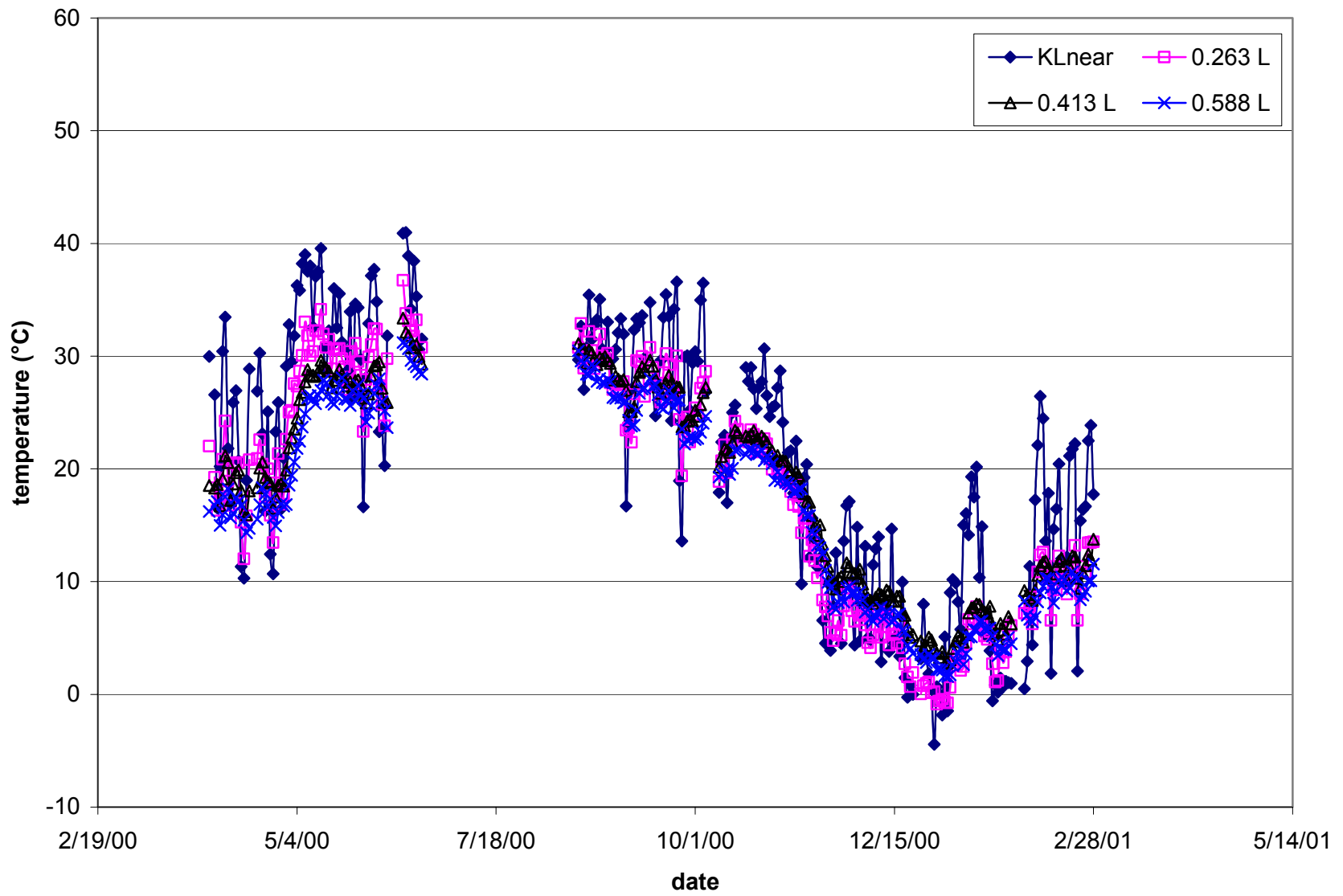


Figure G.32. Maximum daily temperature in aggregate base/subbase layers – Section L.

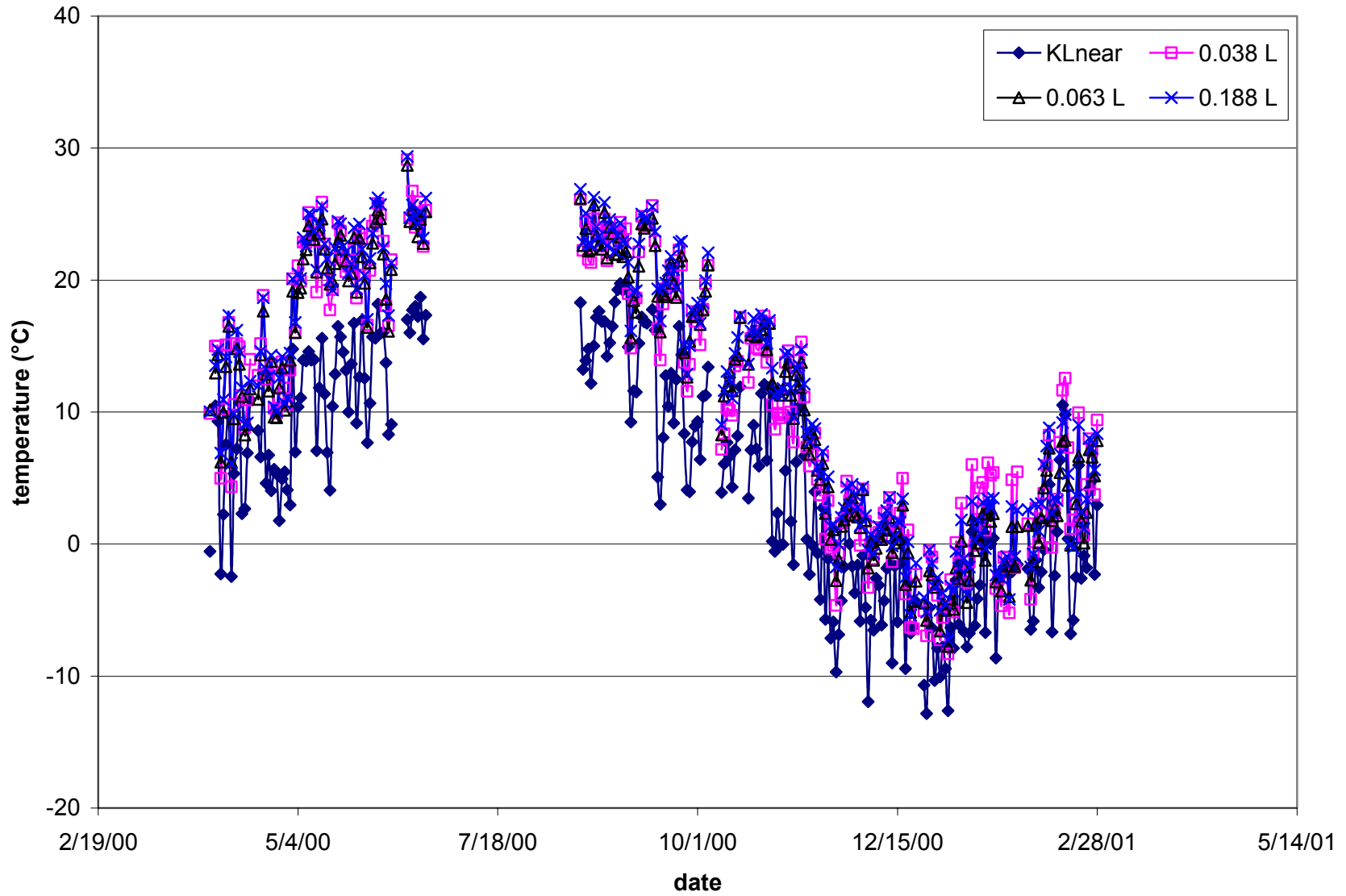


Figure G.33. Minimum daily temperature in HMA layers – Section L.

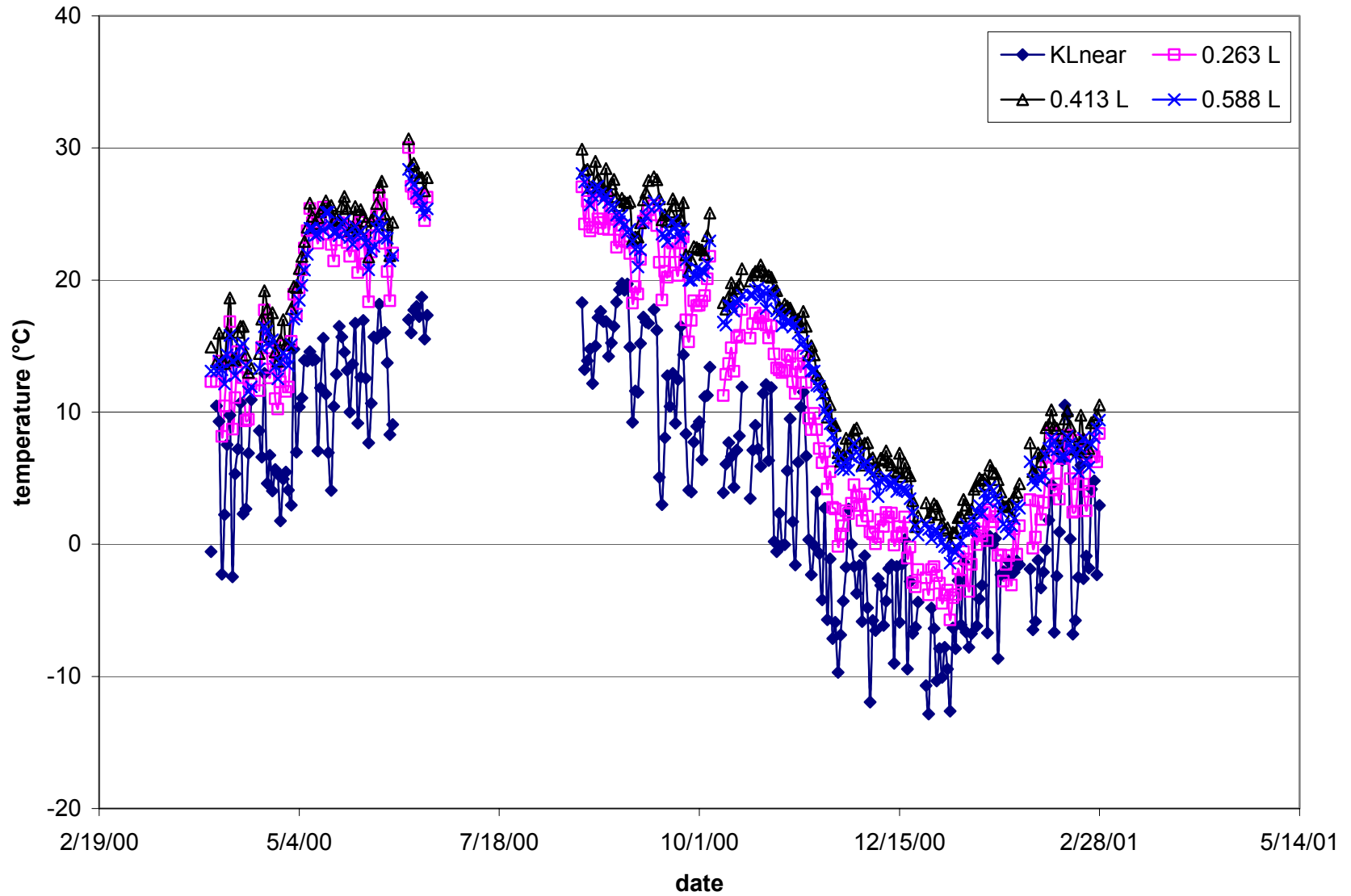


Figure G.34. Minimum daily temperature in aggregate base/subbase layers – Section L.

APPENDIX H

STATISTICAL ANALYSIS OF TEMPERATURE VARIATION ACROSS PAVEMENT SECTIONS

Table H.1. Maximum temperature mean difference analysis at depth of 0.038m.

Difference	Mean	Std Dev	Std Error	Difference	Mean	Std Dev	Std Error
a-b	2.2454	0.8335	0.1067	d-e	-1.7694	1.4378	0.1841
a-c	0.6732	0.8736	0.1119	d-f	6.7680	10.9568	1.4029
a-d	1.3747	1.0400	0.1332	d-g	-1.4276	1.3205	0.1691
a-e	-0.3947	1.5127	0.1937	d-h	-1.2478	1.2196	0.1562
a-f	8.1427	11.4664	1.4681	d-i	-2.2254	1.7632	0.2258
a-g	-0.0529	1.4541	0.1862	d-j	0.9629	1.7188	0.2201
a-h	0.1269	1.3012	0.1666	d-l	-1.8437	1.9056	0.2440
a-i	-0.8507	1.6781	0.2149	e-f	8.5374	11.8689	1.5197
a-j	2.3375	1.7115	0.2191	e-g	0.3418	1.2731	0.1630
a-l	-0.4690	1.9669	0.2518	e-h	0.5216	1.1287	0.1445
b-c	-1.5722	0.9903	0.1268	e-i	-0.4560	1.6779	0.2148
b-d	-0.8708	1.0256	0.1313	e-j	2.7323	1.8469	0.2365
b-e	-2.6402	1.9045	0.2439	e-l	-0.0743	1.9969	0.2557
b-f	5.8972	10.9661	1.4041	f-g	-8.1956	11.6252	1.4885
b-g	-2.2984	1.6936	0.2168	f-h	-8.0158	11.6783	1.4953
b-h	-2.1186	1.5562	0.1992	f-i	-8.9934	11.7811	1.5084
b-i	-3.0961	1.7843	0.2285	f-j	-5.8051	11.6623	1.4932
b-j	0.0921	1.7203	0.2203	f-l	-8.6117	11.8939	1.5229
b-l	-2.7145	1.9516	0.2499	g-h	0.1798	0.6988	0.0895
c-d	0.7015	0.8051	0.1031	g-i	-0.7978	1.4616	0.1871
c-e	-1.0679	1.2611	0.1615	g-j	2.3904	1.5055	0.1928
c-f	7.4695	11.2778	1.4440	g-l	-0.4161	1.7524	0.2244
c-g	-0.7261	1.0803	0.1383	h-i	-0.9776	1.1549	0.1479
c-h	-0.5463	0.9478	0.1214	h-j	2.2107	1.2248	0.1568
c-i	-1.5239	1.4105	0.1806	h-l	-0.5959	1.5114	0.1935
c-j	1.6643	1.4777	0.1892	i-j	3.1882	0.5832	0.0747
c-l	-1.1422	1.7861	0.2287	i-l	0.3817	1.3866	0.1775
				j-l	-2.8066	1.3376	0.1713

Table H.2. Maximum temperature mean difference analysis at depth of 0.063m.

Difference	Mean	Std Dev	Std Error	Difference	Mean	Std Dev	Std Error
a-b	-1.9284	0.8749	0.1120	d-e	1.5609	1.1425	0.1463
a-c	-3.3003	1.1200	0.1434	d-f	4.0377	3.9394	0.5044
a-d	-1.3371	1.0147	0.1299	d-h	-4.8517	1.9925	0.2551
a-e	0.2237	1.7653	0.2260	d-i	0.7422	1.6154	0.2068
a-f	2.7006	4.5418	0.5815	d-j	2.9521	1.0597	0.1357
a-h	-6.1889	1.7145	0.2195	d-l	2.0297	1.4045	0.1798
a-i	-0.5949	1.5369	0.1968	e-f	2.4768	3.7790	0.4838
a-j	1.6150	1.4015	0.1794	e-h	-6.4126	2.8243	0.3616
a-l	0.6926	1.5771	0.2019	e-i	-0.8186	2.2868	0.2928
b-c	-1.3719	1.0555	0.1351	e-j	1.3913	1.1300	0.1447
b-d	0.5913	0.8143	0.1043	e-l	0.4689	1.6668	0.2134
b-e	2.1521	1.4338	0.1836	f-h	-8.8894	5.5556	0.7113
b-f	4.6290	4.0612	0.5200	f-l	-3.2955	4.9474	0.6334
b-h	-4.2604	2.0304	0.2600	f-j	-1.0856	4.1831	0.5356
b-i	1.3335	1.5828	0.2027	f-l	-2.0080	4.2874	0.5489
b-j	3.5434	1.1758	0.1506	h-i	5.5940	1.4749	0.1888
b-l	2.6210	1.4006	0.1793	h-j	7.8039	2.2826	0.2923
c-d	1.9632	0.6946	0.0889	h-l	6.8815	2.2589	0.2892
c-e	3.5240	1.6876	0.2161	i-j	2.2099	1.4125	0.1809
c-f	6.0009	4.0308	0.5161	i-l	1.2875	1.4385	0.1842
c-h	-2.8886	1.8530	0.2373	j-l	-0.9224	1.1113	0.1423
c-i	2.7054	1.6370	0.2096				
c-j	4.9153	1.4390	0.1842				
c-l	3.9929	1.6552	0.2119				

Table H.3. Maximum temperature mean difference analysis at depth of 0.138m.

Difference	Mean	Std Dev	Std Error
g-h	0.0507	0.6383	0.0747
g-i	3.2389	1.2732	0.1490
h-i	3.1882	1.1144	0.1304

Table H.4. Maximum temperature mean difference analysis at depth of 0.188m –

Difference	Mean	Std Dev	Std Error
a-b	1.1623	0.7842	0.0792
a-c	-0.0420	0.8961	0.0905
a-d	-0.1945	0.8229	0.0831
a-f	3.2622	4.3142	0.4358
a-l	-0.5267	1.4645	0.1479
b-c	-1.2042	0.7675	0.0775
b-d	-1.3568	0.7563	0.0764
b-f	2.0999	3.8271	0.3866
b-l	-1.6890	1.5730	0.1589
c-d	-0.1526	0.4819	0.0487
c-f	3.3042	3.8571	0.3896
c-l	-0.4847	1.5821	0.1598
d-f	3.4567	3.9766	0.4017
d-l	-0.3322	1.5588	0.1575
f-l	-3.7889	4.7175	0.4765

Table H.5. Maximum temperature mean difference analysis at depth of 0.188m –

Difference	Mean	Std Dev	Std Error
g-h	1.6535	0.7903	0.0925
g-i	1.2050	1.2818	0.1500
h-i	-0.4484	0.8423	0.0986

Table H.6. Maximum temperature mean difference analysis at depth of 0.263m –

Difference	Mean	Std Dev	Std Error
e-j	-3.2418	1.5640	0.1897

Table H.7. Maximum temperature mean difference analysis at depth of 0.263m –

Difference	Mean	Std Dev	Std Error
a-i	0.9056	1.5089	0.1791
a-j	0.8594	1.4293	0.1696
i-j	-0.0462	0.8791	0.1043

Table H.8. Maximum temperature mean difference analysis at depth of 0.413m.

Difference	Mean	Std Dev	Std Error
a-i	4.0889	2.6771	0.3200
a-l	2.9419	2.5670	0.3068
i-l	-1.1470	0.7120	0.0851

Table H.9. Maximum temperature mean difference analysis at depth of 0.588m.

Difference	Mean	Std Dev	Std Error
a-i	-0.8644	3.4119	0.4078
a-j	-3.6478	3.7267	0.4454
a-l	-2.6596	4.0911	0.4890
i-j	-2.7834	0.6773	0.0809
i-l	-1.7952	0.9977	0.1192
j-l	0.9882	0.6913	0.0826

Table H.10. Maximum temperature mean difference analysis at depth of 0.188m across multiple sections.

Difference	Mean	Std Dev	Std Error
a-g	-2.0288	0.6011	-0.6000
a-h	1.0241	0.5078	2.1330
a-i	1.0158	0.8906	4.0830
b-g	-2.2761	0.6100	-0.8170
b-h	0.7768	0.5328	2.1500
b-i	0.7685	0.8437	3.5670
c-g	-2.0018	0.8645	-0.2330
c-h	1.0511	0.7510	2.5340
c-i	1.0428	1.0919	4.0840
d-g	-1.9940	0.8260	-0.1830
d-h	1.0589	0.6657	2.6330
d-i	1.0506	1.0146	3.6340
f-g	-1.9636	0.4227	-1.0500
f-h	1.0893	0.5552	2.3330
f-i	1.0810	0.8400	3.8830
l-g	-2.3253	0.7904	-0.4840
l-h	0.7276	0.5969	2.0330
l-i	0.7193	0.7306	2.4000

Table H.11. Maximum temperature mean difference analysis at depth of 0.288 across multiple sections.

Difference	Mean	Std Dev	Std Error
e-a	0.7168	0.4474	1.9840
e-i	-1.2655	0.8795	0.7840
e-l	0.4964	0.6242	2.5500
j-a	1.7967	0.9252	5.1500
j-i	-0.1856	1.1119	2.8500
j-l	1.5763	1.0740	4.0500

Table H.12. Minimum temperature mean difference analysis at depth of 0.038m.

Difference	Mean	Std Dev	Std Error	Difference	Mean	Std Dev	Std Error
a-b	1.0604	0.4945	0.0467	d-e	1.9628	0.5570	0.0526
a-c	1.0588	0.7427	0.0702	d-f	-0.8993	0.5992	0.0566
a-d	0.2103	0.5671	0.0536	d-g	0.1002	0.5761	0.0544
a-e	2.1731	0.6193	0.0585	d-h	-0.4364	0.5159	0.0487
a-f	-0.6890	0.5991	0.0566	d-i	-0.5537	0.9388	0.0887
a-g	0.3106	0.6309	0.0596	d-j	2.0307	0.9117	0.0861
a-h	-0.2261	0.5976	0.0565	d-l	-1.4853	1.0388	0.0982
a-i	-0.3434	0.9688	0.0915	e-f	-2.8621	0.4859	0.0459
a-j	2.2410	0.9339	0.0882	e-g	-1.8626	0.6440	0.0609
a-l	-1.2750	1.1226	0.1061	e-h	-2.3993	0.5710	0.0540
b-c	-0.0016	0.7732	0.0731	e-i	-2.5165	0.9240	0.0873
b-d	-0.8501	0.5318	0.0503	e-j	0.0678	0.8765	0.0828
b-e	1.1127	0.6191	0.0585	e-l	-3.4481	0.9983	0.0943
b-f	-1.7494	0.5806	0.0549	f-g	0.9996	0.6598	0.0623
b-g	-0.7499	0.6669	0.0630	f-h	0.4629	0.5707	0.0539
b-h	-1.2866	0.6359	0.0601	f-i	0.3456	0.9114	0.0861
b-i	-1.4039	1.0086	0.0953	f-j	2.9300	0.8584	0.0811
b-j	1.1805	0.9471	0.0895	f-l	-0.5860	1.0651	0.1006
b-l	-2.3354	1.1221	0.1060	g-h	-0.5367	0.4241	0.0401
c-d	-0.8485	0.6334	0.0599	g-i	-0.6540	0.8334	0.0787
c-e	1.1143	0.6768	0.0639	g-j	1.9304	0.7829	0.0740
c-f	-1.7478	0.7959	0.0752	g-l	-1.5855	1.0834	0.1024
c-g	-0.7483	0.6682	0.0631	h-i	-0.1173	0.7542	0.0713
c-h	-1.2849	0.7313	0.0691	h-j	2.4671	0.7757	0.0733
c-i	-1.4022	1.0745	0.1015	h-l	-1.0488	0.9681	0.0915
c-j	1.1822	1.0379	0.0981	i-j	2.5844	0.4576	0.0432
c-l	-2.3338	1.1913	0.1126	i-l	-0.9315	1.1517	0.1088
				j-l	-3.5159	1.1382	0.1076

Table H.13. Minimum temperature mean difference analysis at depth of 0.063m.

Difference	Mean	Std Dev	Std Error	Difference	Mean	Std Dev	Std Error
a-b	-4.1218	-2.8340	0.0556	d-e	-0.5990	1.0170	0.0700
a-c	-3.6966	-1.3500	0.0693	d-f	-0.6780	1.1170	0.0633
a-d	-3.7284	-2.3500	0.0487	d-h	0.9086	3.2670	0.0914
a-e	-4.3273	-2.4500	0.0821	d-i	2.7757	5.0000	0.0980
a-f	-4.4064	-2.6340	0.0753	d-j	1.7853	4.7000	0.0708
a-h	-2.8197	-0.3660	0.0896	d-l	2.1061	4.2000	0.0742
a-i	-0.9526	1.5000	0.0980	e-f	-0.0790	1.2330	0.0403
a-j	-1.9431	1.3670	0.0801	e-h	1.5076	4.4670	0.1384
a-l	-1.6223	1.0670	0.0844	e-i	3.3747	6.1830	0.1338
b-c	0.4252	2.5000	0.0695	e-j	2.3842	5.0500	0.0811
b-d	0.3934	1.5000	0.0490	e-l	2.7050	5.0660	0.0815
b-e	-0.2055	1.4830	0.0823	f-h	1.5866	4.7840	0.1271
b-f	-0.2846	1.9340	0.0731	f-l	3.4537	6.5330	0.1236
b-h	1.3021	3.9160	0.0877	f-j	2.4633	5.2000	0.0780
b-i	3.1692	5.5330	0.0916	f-l	2.7841	5.0670	0.0803
b-j	2.1787	4.8330	0.0740	h-i	1.8671	4.3340	0.0848
b-l	2.4995	4.9170	0.0823	h-j	0.8766	4.0670	0.1073
c-d	-0.0317	1.1830	0.0541	h-l	1.1975	3.8170	0.1177
c-e	-0.6307	1.4500	0.1046	i-j	-0.9905	2.3170	0.0819
c-f	-0.7097	1.6000	0.0964	i-l	-0.6696	2.6500	0.1055
c-h	0.8769	3.1330	0.0828	j-l	0.3208	2.9000	0.0724
c-i	2.7440	4.9830	0.1030				
c-j	1.7535	5.0330	0.0954				
c-l	2.0744	4.5830	0.1010				

Table H.14. Minimum temperature mean difference analysis at depth of 0.138m.

Difference	Mean	Std Dev	Std Error
g-h	-0.0625	0.6759	0.0550
g-i	3.5370	0.7869	0.0640
h-i	3.5994	0.7236	0.0589

Table H.15. Minimum temperature mean difference analysis at depth of 0.188m – layer 2.

Difference	Mean	Std Dev	Std Error
a-b	0.2473	0.5243	0.0489
a-c	-0.0270	0.7048	0.0657
a-d	-0.0348	0.6325	0.0590
a-f	-0.0652	0.5544	0.0517
a-l	0.2965	0.7212	0.0673
b-c	-0.2743	0.7391	0.0689
b-d	-0.2821	0.6596	0.0615
b-f	-0.3125	0.5632	0.0525
b-l	0.0492	0.7950	0.0741
c-d	-0.0078	0.6505	0.0607
c-f	-0.0382	0.7826	0.0730
c-l	0.3235	0.9104	0.0849
d-f	-0.0304	0.6975	0.0650
d-l	0.3313	0.8918	0.0832
f-l	0.3617	0.7909	0.0738

Table H.16. Minimum temperature mean difference analysis at depth of 0.188m – layer 3.

Difference	Mean	Std Dev	Std Error
g-h	3.0824	0.5506	0.0448
g-i	3.2019	0.7799	0.0635
h-i	0.1195	0.6491	0.0528

Table H.17. Minimum temperature mean difference analysis at depth of 0.263m – layer 2.

Difference	Mean	Std Dev	Std Error
e-j	-1.0641	0.9400	0.0775

Table H.18. Minimum temperature mean difference analysis at depth of 0.263m – layer 4.

Difference	Mean	Std Dev	Std Error
a-i	-2.0025	0.8759	0.0817
a-j	-0.2106	0.6406	0.0597
i-j	1.7919	0.7953	0.0742

Table H.19. Minimum temperature mean difference analysis at depth of 0.413m.

Difference	Mean	Std Dev	Std Error
a-i	1.2603	1.0438	0.0973
a-l	-0.3263	1.0648	0.0993
i-l	-1.5866	0.7043	0.0657

Table H.20. Minimum temperature mean difference analysis at depth of 0.588m.

Difference	Mean	Std Dev	Std Error
a-i	-0.4100	1.2382	0.1170
a-j	-0.5182	0.9020	0.0852
a-l	-0.3068	0.9427	0.0891
i-j	-0.1082	0.9127	0.0862
i-l	0.1031	0.8468	0.0800
j-l	0.2113	0.5710	0.0540

Table H.21. Minimum temperature mean difference analysis at depth of 0.188m across multiple sections.

Difference	Mean	Std Dev	Std Error
a-g	-2.0288	0.6011	-0.6000
a-h	1.0241	0.5078	2.1330
a-i	1.0158	0.8906	4.0830
b-g	-2.2761	0.6100	-0.8170
b-h	0.7768	0.5328	2.1500
b-i	0.7685	0.8437	3.5670
c-g	-2.0018	0.8645	-0.2330
c-h	1.0511	0.7510	2.5340
c-i	1.0428	1.0919	4.0840
d-g	-1.9940	0.8260	-0.1830
d-h	1.0589	0.6657	2.6330
d-i	1.0506	1.0146	3.6340
f-g	-1.9636	0.4227	-1.0500
f-h	1.0893	0.5552	2.3330
f-i	1.0810	0.8400	3.8830
l-g	-2.3253	0.7904	-0.4840
l-h	0.7276	0.5969	2.0330
l-i	0.7193	0.7306	2.4000

Table H.22. Minimum temperature mean difference analysis at depth of 0.263m across different sections.

Difference	Mean	Std Dev	Std Error
e-a	0.7168	0.4474	1.9840
e-i	-1.2655	0.8795	0.7840
e-l	0.4964	0.6242	2.5500
j-a	1.7967	0.9252	5.1500
j-i	-0.1856	1.1119	2.8500
j-l	1.5763	1.0740	4.0500

APPENDIX I

PAVEMENT TEMPERATURE PREDICTION MODELS ACROSS SEASONAL VARIATION

Table I.1. Section A - coefficients for linear pavement temperature prediction model.

Daily Maximum Temperature				
depth, m	A	B	RMSE	Adjusted R ²
0.038	1.0111	4.8988	5.0616	0.8508
0.063	0.8500	1.4274	4.7322	0.8133
0.188	0.8075	3.4388	4.6309	0.8093
0.263	0.7548	1.7713	4.8164	0.7741
0.413	0.6081	6.3616	5.3185	0.6457
0.588	0.4646	5.9334	5.4737	0.5008
0.74	0.4409	7.7700	5.2986	0.4908
0.994	0.4433	5.7432	5.8035	0.4481
1.172	0.3885	7.1195	5.5294	0.4070
Daily Minimum Temperature				
depth, m	A	B	RMSE	Adjusted R ²
0.038	1.0264	9.1801	2.7832	0.9127
0.063	1.0180	8.4302	3.4086	0.8663
0.188	0.9838	10.9246	3.3888	0.8596
0.263	0.9853	10.8678	3.7453	0.8340
0.413	0.8749	14.4247	4.2273	0.7566
0.588	0.7510	11.4557	5.2536	0.5970
0.74	0.6525	14.0522	5.0470	0.5478
0.994	0.6201	11.0919	5.0238	0.5247
1.172	0.5652	12.7255	5.2465	0.4565

Table I.2. Section B - coefficients for linear pavement temperature prediction model.

Daily Maximum Temperature				
depth, m	A	B	RMSE	Adjusted R ²
0.038	0.9993	3.1881	4.7781	0.8647
0.063	0.8188	4.9502	4.4665	0.8307
0.188	0.8046	2.8854	4.5079	0.8231
Daily Minimum Temperature				
depth, m	A	B	RMSE	Adjusted R ²
0.038	1.0208	7.9223	2.6966	0.9194
0.063	0.9768	12.2678	3.2642	0.8770
0.188	0.9869	10.8329	3.3909	0.8709

Table I.3. Section C - coefficients for linear pavement temperature prediction model.

Daily Maximum Temperature				
depth, m	A	B	RMSE	Adjusted R ²
0.038	1.1064	1.0935	3.4130	0.9318
0.063	0.9215	2.7711	3.2975	0.9104
0.188	0.8887	1.1349	3.3956	0.8991
Daily Minimum Temperature				
depth, m	A	B	RMSE	Adjusted R ²
0.038	1.0834	5.9226	2.3929	0.9339
0.063	1.0527	9.8109	3.0808	0.8895
0.188	1.0454	9.0031	3.1879	0.8812

Table I.4. Section D - coefficients for linear pavement temperature prediction model.

Daily Maximum Temperature				
depth, m	A	B	RMSE	Adjusted R ²
0.038	1.0779	1.0641	3.3562	0.9300
0.063	0.8992	1.3691	3.5100	0.8943
0.188	0.8998	0.9993	3.4416	0.8981
Daily Minimum Temperature				
depth, m	A	B	RMSE	Adjusted R ²
0.038	1.0857	6.6747	2.5112	0.9270
0.063	1.0520	9.8264	3.1688	0.8822
0.188	1.0503	8.9271	3.2247	0.8782

Table I.5. Section E - coefficients for linear pavement temperature prediction model.

Daily Maximum Temperature				
depth, m	A	B	RMSE	Adjusted R ²
0.038	1.2136	-0.5408	4.2589	0.9086
0.063	0.9024	0.3155	4.0139	0.8597
0.263	0.8843	-0.9673	4.0483	0.8526
Daily Minimum Temperature				
depth, m	A	B	RMSE	Adjusted R ²
0.038	1.1162	1.6849	2.9783	0.9086
0.063	1.0792	7.8544	4.0128	0.8365
0.263	1.0716	6.7190	4.0704	0.8306

Table I.6. Section F - coefficients for linear pavement temperature prediction model.

Daily Maximum Temperature				
depth, m	A	B	RMSE	Adjusted R ²
0.038	1.1218	2.8029	3.7386	0.9091
0.063	0.8195	3.5644	5.2480	0.7301
0.188	0.8653	1.8914	4.8245	0.7811
Daily Minimum Temperature				
depth, m	A	B	RMSE	Adjusted R ²
0.038	1.0780	4.2928	2.7723	0.9145
0.063	1.0666	7.9311	3.8831	0.8421
0.188	1.0678	6.1704	3.6923	0.8553

Table I.7. Section G - coefficients for linear pavement temperature prediction model.

Daily Maximum Temperature				
depth, m	A	B	RMSE	Adjusted R ²
0.038	1.1168	5.3232	4.3463	0.8940
0.065	1.0183	3.7999	3.9820	0.8930
0.138	0.9585	4.5655	3.8838	0.8861
0.188	0.8566	4.7647	3.8701	0.8622
0.388	0.7328	3.0552	4.1818	0.7967
0.638	0.5534	7.8537	4.5261	0.6559
1.238	0.4779	7.2706	4.4365	0.5967
Daily Minimum Temperature				
depth, m	A	B	RMSE	Adjusted R ²
0.038	1.0362	7.5937	2.6622	0.9167
0.065	1.0336	7.1517	2.8893	0.9029
0.138	1.0230	9.4841	3.1340	0.8856
0.188	0.9905	11.9831	3.5028	0.8531
0.388	0.9486	10.8340	3.9230	0.8094
0.638	0.7900	14.0946	4.1774	0.7219
1.238	0.6698	12.7741	4.1758	0.6512

Table I.8. Section H - coefficients for linear pavement temperature prediction model.

Daily Maximum Temperature				
depth, m	A	B	RMSE	Adjusted R ²
0.038	1.1275	4.9169	4.3482	0.8979
0.063	1.0359	5.9976	4.0800	0.8939
0.138	0.9821	4.1173	3.9250	0.8911
0.188	0.9147	1.8547	3.8159	0.8825
Daily Minimum Temperature				
depth, m	A	B	RMSE	Adjusted R ²
0.038	1.0472	7.9556	2.5425	0.9276
0.063	1.0701	9.9440	2.9123	0.9107
0.138	1.0541	9.5457	3.0781	0.8985
0.188	1.0209	8.7793	3.2429	0.8821

Table I.9. Section I - coefficients for linear pavement temperature prediction model.

Daily Maximum Temperature				
depth, m	A	B	RMSE	Adjusted R ²
0.038	1.1126	4.0430	4.4743	0.8935
0.063	0.9365	1.4266	3.7401	0.8949
0.138	0.9549	-0.2084	3.8817	0.8915
0.188	0.8850	1.4560	3.5961	0.8916
0.263	0.7478	3.1746	3.4755	0.8628
0.413	0.6478	4.0728	3.6010	0.8146
0.588	0.5647	4.3167	3.8048	0.7494
Daily Minimum Temperature				
depth, m	A	B	RMSE	Adjusted R ²
0.038	1.0254	5.3055	2.6503	0.9150
0.063	1.0157	5.2361	3.1452	0.8824
0.138	1.0535	3.3651	3.3712	0.8753
0.188	1.0204	6.1523	3.4585	0.8622
0.263	0.9568	8.8311	3.7453	0.8243
0.413	0.8485	9.4091	3.9053	0.7724
0.588	0.7890	9.6032	4.0684	0.7299

Table I.10. Section J - coefficients for linear pavement temperature prediction model.

Daily Maximum Temperature				
depth, m	A	B	RMSE	Adjusted R ²
0.038	1.1154	0.7314	4.3208	0.9010
0.063	0.8773	0.5850	3.7474	0.8822
0.263	0.8927	3.0926	4.0227	0.8706
0.338	0.8054	-1.0799	3.8430	0.8571
0.588	0.6716	3.7478	4.1780	0.7847
Daily Minimum Temperature				
depth, m	A	B	RMSE	Adjusted R ²
0.038	1.0490	3.0500	3.1272	0.8902
0.063	1.0355	6.6871	3.7886	0.8432
0.263	1.0626	9.1754	3.7367	0.8526
0.338	1.0228	5.7414	4.2158	0.8090
0.588	0.9327	10.5985	4.3598	0.7712

Table I.11. Section L - coefficients for linear pavement temperature prediction model.

Daily Maximum Temperature				
depth, m	A	B	RMSE	Adjusted R ²
0.038	1.1279	3.1688	3.7768	0.9227
0.063	0.9366	0.0377	3.4913	0.9060
0.188	0.9660	1.1821	3.4277	0.9141
0.263	0.8481	0.1490	3.7129	0.8748
0.413	0.6774	4.3805	4.0627	0.7882
0.588	0.6614	3.0476	4.3904	0.7522
Daily Minimum Temperature				
depth, m	A	B	RMSE	Adjusted R ²
0.038	1.1053	5.8255	2.5354	0.9299
0.063	1.0893	5.6274	3.1285	0.8943
0.188	1.0921	6.3582	2.9741	0.9039
0.263	1.0846	6.8226	3.5530	0.8667
0.413	0.9528	11.0607	3.8036	0.8140
0.588	0.9352	9.6805	4.0126	0.7912

Table I.12. Layer 1 (bottom) - coefficients for linear pavement temperature prediction model.

Daily Maximum Temperature					
Section	depth, m	A	B	RMSE	Adjusted R ²
A	0.038	1.0111	4.8988	5.0616	0.8508
B	0.038	0.9993	3.1881	4.7781	0.8647
C	0.038	1.1064	1.0935	3.4130	0.9318
D	0.038	1.0779	1.0641	3.3562	0.9300
E	0.038	1.2136	-0.5408	4.2589	0.9086
F	0.038	1.1218	2.8029	3.7386	0.9091
G	0.038	1.1168	5.3232	4.3463	0.8940
H	0.038	1.1275	4.9169	4.3482	0.8979
I	0.038	1.1126	4.0430	4.4743	0.8935
J	0.038	1.1154	0.7314	4.3208	0.9010
L	0.038	1.1279	3.1688	3.7768	0.9227
Daily Minimum Temperature					
Section	depth, m	A	B	RMSE	Adjusted R ²
A	0.038	1.0264	9.1801	2.7832	0.9127
B	0.038	1.0208	7.9223	2.6966	0.9194
C	0.038	1.0834	5.9226	2.3929	0.9339
D	0.038	1.0857	6.6747	2.5112	0.9270
E	0.038	1.1162	1.6849	2.9783	0.9086
F	0.038	1.0780	4.2928	2.7723	0.9145
G	0.038	1.0362	7.5937	2.6622	0.9167
H	0.038	1.0472	7.9556	2.5425	0.9276
I	0.038	1.0254	5.3055	2.6503	0.9150
J	0.038	1.0490	3.0500	3.1272	0.8902
L	0.038	1.1053	5.8255	2.5354	0.9299

Table I.13. Layer 2 (top) - coefficients for linear pavement temperature prediction model.

Daily Maximum Temperature					
Section	depth, m	A	B	RMSE	Adjusted R ²
A	0.063	0.8500	1.4274	4.7322	0.8133
B	0.063	0.8188	4.9502	4.4665	0.8307
C	0.063	0.9215	2.7711	3.2975	0.9104
D	0.063	0.8992	1.3691	3.5100	0.8943
E	0.063	0.9024	0.3155	4.0139	0.8597
F	0.063	0.8195	3.5644	5.2480	0.7301
G	0.065	1.0183	3.7999	3.9820	0.8930
H	0.063	1.0359	5.9976	4.0800	0.8939
I	0.063	0.9365	1.4266	3.7401	0.8949
J	0.063	0.8773	0.5850	3.7474	0.8822
L	0.063	0.9366	0.0377	3.4913	0.9060
Daily Minimum Temperature					
Section	depth, m	A	B	RMSE	Adjusted R ²
A	0.063	1.0180	8.4302	3.4086	0.8663
B	0.063	0.9768	12.2678	3.2642	0.8770
C	0.063	1.0527	9.8109	3.0808	0.8895
D	0.063	1.0520	9.8264	3.1688	0.8822
E	0.063	1.0792	7.8544	4.0128	0.8365
F	0.063	1.0666	7.9311	3.8831	0.8421
G	0.065	1.0336	7.1517	2.8893	0.9029
H	0.063	1.0701	9.9440	2.9123	0.9107
I	0.063	1.0157	5.2361	3.1452	0.8824
J	0.063	1.0355	6.6871	3.7886	0.8432
L	0.063	1.0893	5.6274	3.1285	0.8943

Table I.14. Layer 2 (bottom) - coefficients for linear pavement temperature prediction model.

Daily Maximum Temperature					
Section	depth, m	A	B	RMSE	Adjusted R ²
G	0.138	0.9585	4.5655	3.8838	0.8861
H	0.138	0.9821	4.1173	3.9250	0.8911
I	0.138	0.9549	-0.2084	3.8817	0.8915
Daily Minimum Temperature					
Section	depth, m	A	B	RMSE	Adjusted R ²
G	0.138	1.0230	9.4841	3.1340	0.8856
H	0.138	1.0541	9.5457	3.0781	0.8985
I	0.138	1.0535	3.3651	3.3712	0.8753

Table I.15. Layer 3 (bottom) - coefficients for linear pavement temperature prediction model.

Daily Maximum Temperature					
Section	depth, m	A	B	RMSE	Adjusted R ²
A	0.188	0.8075	3.4388	4.6309	0.8093
B	0.188	0.8046	2.8854	4.5079	0.8231
C	0.188	0.8887	1.1349	3.3956	0.8991
D	0.188	0.8998	0.9993	3.4416	0.8981
F	0.188	0.8653	1.8914	4.8245	0.7811
G	0.188	0.8566	4.7647	3.8701	0.8622
H	0.188	0.9147	1.8547	3.8159	0.8825
I	0.188	0.8850	1.4560	3.5961	0.8916
L	0.188	0.9660	1.1821	3.4277	0.9141
Daily Minimum Temperature					
Section	depth, m	A	B	RMSE	Adjusted R ²
A	0.188	0.9838	10.9246	3.3888	0.8596
B	0.188	0.9869	10.8329	3.3909	0.8709
C	0.188	1.0454	9.0031	3.1879	0.8812
D	0.188	1.0503	8.9271	3.2247	0.8782
F	0.188	1.0678	6.1704	3.6923	0.8553
G	0.188	0.9905	11.9831	3.5028	0.8531
H	0.188	1.0209	8.7793	3.2429	0.8821
I	0.188	1.0204	6.1523	3.4585	0.8622
L	0.188	1.0921	6.3582	2.9741	0.9039

Table I.16. Layer 2 (bottom) for Sections A and E and Layer 4 (bottom) for Sections I and J - coefficients for linear pavement temperature prediction model.

Daily Maximum Temperature					
Section	depth, m	A	B	RMSE	Adjusted R ²
A	0.263	0.7548	1.7713	4.8164	0.7741
E	0.263	0.8843	-0.9673	4.0483	0.8526
I	0.263	0.7478	3.1746	3.4755	0.8628
J	0.263	0.8927	3.0926	4.0227	0.8706
Daily Minimum Temperature					
Section	depth, m	A	B	RMSE	Adjusted R ²
A	0.263	0.9853	10.8678	3.7453	0.8340
E	0.263	1.0716	6.7190	4.0704	0.8306
I	0.263	0.9568	8.8311	3.7453	0.8243
J	0.263	1.0626	9.1754	3.7367	0.8526

Table I.17. Layer 4 (bottom) - coefficients for linear pavement temperature prediction model.

Daily Maximum Temperature					
Section	depth, m	A	B	RMSE	Adjusted R ²
G	0.388	0.7328	3.0552	4.1818	0.7967
J	0.338	0.8054	-1.0799	3.8430	0.8571
Daily Minimum Temperature					
Section	depth, m	A	B	RMSE	Adjusted R ²
G	0.388	0.9486	10.8340	3.9230	0.8094
J	0.338	1.0228	5.7414	4.2158	0.8090

Table I.18. Layer 5 (bottom) - coefficients for linear pavement temperature prediction model.

Daily Maximum Temperature					
Section	depth, m	A	B	RMSE	Adjusted R ²
A	0.413	0.6081	6.3616	5.3185	0.6457
I	0.413	0.6478	4.0728	3.6010	0.8146
L	0.413	0.6774	4.3805	4.0627	0.7882
Daily Minimum Temperature					
Section	depth, m	A	B	RMSE	Adjusted R ²
A	0.413	0.8749	14.4247	4.2273	0.7566
I	0.413	0.8485	9.4091	3.9053	0.7724
L	0.413	0.9528	11.0607	3.8036	0.8140

Table I.19. Layer 6 (bottom) - coefficients for linear pavement temperature prediction model.

Daily Maximum Temperature					
Section	depth, m	A	B	RMSE	Adjusted R ²
A	0.588	0.4646	5.9334	5.4737	0.5008
I	0.588	0.5647	4.3167	3.8048	0.7494
J	0.588	0.6716	3.7478	4.1780	0.7847
L	0.588	0.6614	3.0476	4.3904	0.7522
Daily Minimum Temperature					
Section	depth, m	A	B	RMSE	Adjusted R ²
A	0.588	0.7510	11.4557	5.2536	0.5970
I	0.588	0.7890	9.6032	4.0684	0.7299
J	0.588	0.9327	10.5985	4.3598	0.7712
L	0.588	0.9352	9.6805	4.0126	0.7912

Table I.20. Coefficients for linear pavement temperature prediction model, where A is the near surface temperature coefficient and B is the intercept coefficient.

Daily Maximum Temperature					
Section	depth, m	A	B	RMSE	Adjusted R ²
A	0.038	1.0111	4.8988	5.0616	0.8508
B	0.038	0.9993	3.1881	4.7781	0.8647
C	0.038	1.1064	1.0935	3.4130	0.9318
D	0.038	1.0779	1.0641	3.3562	0.9300
E	0.038	1.2136	-0.5408	4.2589	0.9085
F	0.038	1.1218	2.8029	3.7386	0.9091
G	0.038	1.1168	5.3232	4.3463	0.8940
H	0.038	1.1275	4.9169	4.3482	0.8979
I	0.038	1.1126	4.0430	4.4743	0.8935
J	0.038	1.1154	0.7314	4.3208	0.9010
L	0.038	1.1279	3.1688	3.7768	0.9227
Daily Maximum Temperature					
Section	depth, m	A	B	RMSE	Adjusted R ²
A	0.063	0.8500	1.4274	4.7322	0.8133
B	0.063	0.8188	4.9502	4.4665	0.8307
C	0.063	0.9215	2.7711	3.2975	0.9104
D	0.063	0.8992	1.3691	3.5100	0.8943
E	0.063	0.9024	0.3155	4.0139	0.8597
F	0.063	0.8195	3.5644	5.2480	0.7301
H	0.063	1.0359	5.9976	4.0800	0.8939
I	0.063	0.9365	1.4266	3.7401	0.8949
J	0.063	0.8773	0.5850	3.7474	0.8822
L	0.063	0.9366	0.0377	3.4913	0.9060
Daily Maximum Temperature					
Section	depth, m	A	B	RMSE	Adjusted R ²
A	0.188	0.8075	3.4388	4.6309	0.8093
B	0.188	0.8046	2.8854	4.5079	0.8231
C	0.188	0.8887	1.1349	3.3956	0.8991
D	0.188	0.8998	0.9993	3.4416	0.8981
F	0.188	0.8653	1.8914	4.8245	0.7811
G	0.188	0.8566	4.7647	3.8701	0.8622
H	0.188	0.9147	1.8547	3.8159	0.8825
I	0.188	0.8850	1.4560	3.5961	0.8916
L	0.188	0.9660	1.1821	3.4277	0.9141

Table I.21. Coefficients for linear pavement temperature prediction model, where A is the near surface temperature coefficient and B is the intercept coefficient.

Daily Minimum Temperature					
Section	depth, m	A	B	RMSE	Adjusted R ²
A	0.038	1.0264	9.1801	2.7832	0.9127
B	0.038	1.0208	7.9223	2.6966	0.9194
C	0.038	1.0834	5.9226	2.3929	0.9339
D	0.038	1.0857	6.6747	2.5112	0.9270
E	0.038	1.1162	1.6849	2.9783	0.9086
F	0.038	1.0780	4.2928	2.7723	0.9145
G	0.038	1.0362	7.5937	2.6622	0.9167
H	0.038	1.0472	7.9556	2.5425	0.9276
I	0.038	1.0254	5.3055	2.6503	0.9150
J	0.038	1.0490	3.0500	3.1272	0.8902
L	0.038	1.1053	5.8255	2.5354	0.9299
Daily Minimum Temperature					
Section	depth, m	A	B	RMSE	Adjusted R ²
A	0.063	1.0180	8.4302	3.4086	0.8663
B	0.063	0.9768	12.2678	3.2642	0.8770
C	0.063	1.0527	9.8109	3.0808	0.8895
D	0.063	1.0520	9.8264	3.1688	0.8822
E	0.063	1.0792	7.8544	4.0128	0.8365
F	0.063	1.0666	7.9311	3.8831	0.8421
H	0.063	1.0701	9.9440	2.9123	0.9107
I	0.063	1.0157	5.2361	3.1452	0.8824
J	0.063	1.0355	6.6871	3.7886	0.8432
L	0.063	1.0893	5.6274	3.1285	0.8943
Daily Minimum Temperature					
Section	depth, m	A	B	RMSE	Adjusted R ²
A	0.188	0.9092	10.5860	4.4315	0.7592
B	0.188	0.9838	10.9246	3.3888	0.8596
C	0.188	1.0454	9.0031	3.1879	0.8812
D	0.188	1.0503	8.9271	3.2247	0.8782
F	0.188	1.0678	6.1704	3.6923	0.8553
G	0.188	0.9905	11.9831	3.5028	0.8531
H	0.188	1.0209	8.7793	3.2429	0.8821
I	0.188	1.0204	6.1523	3.4585	0.8622
L	0.188	1.0921	6.3582	2.9741	0.9039

Table I.22. Coefficients for linear pavement temperature prediction model, where A is the near surface temperature coefficient that is held constant and B is the intercept coefficient.

Daily Maximum Temperature					
Section	depth, m	A	B	RMSE	R ²
A	0.038	1.0987	3.0857	5.1616	0.8448
B	0.038	1.0987	1.0931	4.9201	0.8565
C	0.038	1.0987	1.2537	3.4085	0.9320
D	0.038	1.0987	0.6314	3.3590	0.9299
E	0.038	1.0987	1.9523	4.4386	0.9008
F	0.038	1.0987	3.2653	3.7410	0.9089
G	0.038	1.0987	5.6604	4.3446	0.8940
H	0.038	1.0987	5.4394	4.3535	0.8976
I	0.038	1.0987	4.3044	4.4692	0.8938
J	0.038	1.0987	1.0471	4.3174	0.9012
L	0.038	1.0987	3.7727	3.7845	0.9224
Daily Maximum Temperature					
Section	depth, m	A	B	RMSE	R ²
A	0.063	0.8971	0.4768	4.7576	0.8163
B	0.063	0.8971	3.2999	4.5593	0.8236
C	0.063	0.8971	3.2816	3.3036	0.9101
D	0.063	0.8971	1.4121	3.5043	0.8946
E	0.063	0.8971	0.4300	4.0082	0.8601
F	0.063	0.8971	2.0130	5.3037	0.7243
H	0.063	0.8971	8.5197	4.3714	0.8782
I	0.063	0.8971	2.1685	3.7612	0.8937
J	0.063	0.8971	0.2118	3.7474	0.8822
L	0.063	0.8971	0.8541	3.5141	0.9048
Daily Maximum Temperature					
Section	depth, m	A	B	RMSE	R ²
A	0.188	0.8719	2.1384	4.6860	0.8047
B	0.188	0.8719	1.4678	4.5740	0.8179
C	0.188	0.8719	1.4858	3.3954	0.8991
D	0.188	0.8719	1.5806	3.4506	0.8975
F	0.188	0.8719	1.7588	4.8177	0.7817
G	0.188	0.8719	4.4796	3.8682	0.8623
H	0.188	0.8719	2.6321	3.8410	0.8810
I	0.188	0.8719	1.7030	3.5927	0.8918
L	0.188	0.8719	3.1253	3.5899	0.9057

Table I.23. Coefficients for linear pavement temperature prediction model, where A is the near surface temperature coefficient that is held constant and B is the intercept coefficient.

Daily Minimum Temperature					
Section	depth, m	A	B	RMSE	R ²
A	0.038	1.0594	9.1487	2.7943	0.9120
B	0.038	1.0594	7.8746	2.7151	0.9183
C	0.038	1.0594	5.9776	2.3974	0.9337
D	0.038	1.0594	6.7362	2.5162	0.9268
E	0.038	1.0594	2.0427	3.0138	0.9064
F	0.038	1.0594	4.4064	2.7730	0.9144
G	0.038	1.0594	7.5459	2.6655	0.9165
H	0.038	1.0594	7.9333	2.5403	0.9277
I	0.038	1.0594	5.1844	2.6611	0.9143
J	0.038	1.0594	3.0135	3.1223	0.8905
L	0.038	1.0594	6.0497	2.5595	0.9286
Daily Minimum Temperature					
Section	depth, m	A	B	RMSE	R ²
A	0.063	1.0438	8.4182	3.4108	0.8661
B	0.063	1.0438	12.1852	3.3139	0.8732
C	0.063	1.0438	9.8313	3.0766	0.8898
D	0.063	1.0438	9.8452	3.1641	0.8826
E	0.063	1.0438	8.0715	4.0183	0.8360
F	0.063	1.0438	8.0702	3.8824	0.8422
H	0.063	1.0438	9.9948	2.9175	0.9104
I	0.063	1.0438	5.1362	3.1485	0.8821
J	0.063	1.0438	6.6577	3.7823	0.8438
L	0.063	1.0438	5.8490	3.1456	0.8931
Daily Minimum Temperature					
Section	depth, m	A	B	RMSE	R ²
A	0.188	1.0257	10.9050	3.4024	0.8584
B	0.188	1.0257	10.7852	3.4037	0.8699
C	0.188	1.0257	9.0485	3.1869	0.8812
D	0.188	1.0257	8.9846	3.2259	0.8781
F	0.188	1.0257	6.4285	3.7040	0.8544
G	0.188	1.0257	11.9106	3.5105	0.8525
H	0.188	1.0257	8.7710	3.2380	0.8825
I	0.188	1.0257	6.1334	3.4526	0.8627
L	0.188	1.0257	6.6821	3.0201	0.9009

Table I.24. Section A - coefficients for linear pavement temperature prediction model including seasonal component.

Daily Maximum Temperature					
depth, m	A	B	C	RMSE	Adjusted R ²
0.038	0.7095	0.1154	1.7786	3.3451	0.9348
0.063	0.5405	0.1286	-2.2970	2.5412	0.9476
0.188	0.5023	0.1268	-0.2339	2.4388	0.9471
0.263	0.4301	0.1349	-2.1345	2.3799	0.9448
0.413	0.2865	0.1336	2.4917	3.3307	0.8611
0.588	0.3020	0.0676	3.9767	5.0632	0.5729
0.74	0.2826	0.0658	5.8648	4.8961	0.5652
0.994	0.2843	0.0661	3.8298	5.4371	0.5156
1.172	0.2681	0.0500	5.6710	5.3033	0.4538
Daily Minimum Temperature					
depth, m	A	B	C	RMSE	Adjusted R ²
0.038	1.0511	-0.0376	-6.6718	2.4758	0.9203
0.063	0.9853	-0.0332	-5.7302	3.0546	0.8716
0.188	1.0002	-0.0303	-8.5649	3.1442	0.8639
0.263	0.9621	-0.0279	-8.2671	3.4382	0.8373
0.413	0.7698	0.0220	-12.6571	4.1887	0.7585
0.588	0.4254	0.0981	-12.1688	4.6406	0.7036
0.74	0.3995	0.1084	-13.6891	4.7811	0.6854
0.994	0.3836	0.1128	-12.6542	4.8239	0.6797
1.172	0.3364	0.1229	-13.4483	4.8818	0.6720

Table I.25. Section B - coefficients for linear pavement temperature prediction model including seasonal component.

Daily Maximum Temperature					
depth, m	A	B	C	RMSE	Adjusted R ²
0.038	1.1185	-0.0826	0.7461	3.9704	0.8921
0.063	1.4808	-0.1224	-1.7434	4.2142	0.8785
0.188	1.5344	-0.1316	1.4519	4.2659	0.8755
Daily Minimum Temperature					
depth, m	A	B	C	RMSE	Adjusted R ²
0.038	1.0359	-0.0313	-5.6999	2.4404	0.9252
0.063	1.0894	-0.0423	-9.9624	3.0196	0.8856
0.188	1.0353	-0.0343	-8.4157	3.1356	0.8766

Table I.26. Section C - coefficients for linear pavement temperature prediction model including seasonal component.

Daily Maximum Temperature					
depth, m	A	B	C	RMSE	Adjusted R ²
0.038	0.9745	-0.0474	0.8983	2.7850	0.9404
0.063	1.2677	-0.0815	-0.8342	2.9924	0.9312
0.188	1.3276	-0.0886	1.4663	3.1811	0.9222
Daily Minimum Temperature					
depth, m	A	B	C	RMSE	Adjusted R ²
0.038	1.0021	-0.0348	-3.4777	2.0107	0.9414
0.063	0.9529	-0.0264	-7.3427	2.7132	0.8933
0.188	0.9548	-0.0272	-6.5184	2.8163	0.8850

Table I.27. Section D - coefficients for linear pavement temperature prediction model including seasonal component.

Daily Maximum Temperature					
depth, m	A	B	C	RMSE	Adjusted R ²
0.038	1.0493	-0.0646	1.0288	2.6636	0.9450
0.063	1.3563	-0.1028	1.3224	3.1356	0.9237
0.188	1.3329	-0.0955	1.7174	3.1196	0.9245
Daily Minimum Temperature					
depth, m	A	B	C	RMSE	Adjusted R ²
0.038	0.9973	-0.0358	-4.1319	2.1014	0.9351
0.063	0.9916	-0.0372	-7.0243	2.7400	0.8896
0.188	0.9695	-0.0325	-6.2311	2.8102	0.8839

Table I.28. Section E - coefficients for linear pavement temperature prediction model including seasonal component.

Daily Maximum Temperature					
depth, m	A	B	C	RMSE	Adjusted R ²
0.038	0.8760	-0.0439	2.7195	3.1914	0.9169
0.063	1.4219	-0.1172	3.0256	3.5411	0.8966
0.263	1.4243	-0.1131	5.0204	3.7076	0.8867
Daily Minimum Temperature					
depth, m	A	B	C	RMSE	Adjusted R ²
0.038	1.0237	-0.0487	1.3975	2.3495	0.9220
0.063	0.9204	-0.0333	-4.4452	3.3493	0.8415
0.263	0.9035	-0.0293	-3.4596	3.4240	0.8343

Table I.29. Section F - coefficients for linear pavement temperature prediction model including seasonal component.

Daily Maximum Temperature					
depth, m	A	B	C	RMSE	Adjusted R ²
0.038	0.9101	-0.0356	-0.0368	2.9765	0.9202
0.063	1.6368	-0.1772	1.9386	4.1969	0.8414
0.188	1.4926	-0.1470	3.4633	3.7019	0.8766
Daily Minimum Temperature					
depth, m	A	B	C	RMSE	Adjusted R ²
0.038	0.9882	-0.0319	-2.0216	2.3645	0.9210
0.063	0.9862	-0.0444	-4.4914	3.2496	0.8507
0.188	0.9634	-0.0368	-3.0970	3.1252	0.8619

Table I.30. Section G - coefficients for linear pavement temperature prediction model including seasonal component.

Daily Maximum Temperature					
depth, m	A	B	C	RMSE	Adjusted R ²
0.038	0.9192	-0.0401	-2.1191	3.5608	0.9007
0.065	1.0931	-0.0651	-0.9505	3.4082	0.9091
0.138	1.2087	-0.0799	-1.9542	3.4239	0.9082
0.188	1.4084	-0.1004	-2.3683	3.7142	0.8920
0.388	1.4282	-0.0749	0.8806	4.9095	0.8113
0.638	0.8591	0.0633	-2.1270	6.4801	0.6713
1.238	0.7097	0.0997	-0.9742	6.6974	0.6489
Daily Minimum Temperature					
depth, m	A	B	C	RMSE	Adjusted R ²
0.038	1.0317	-0.0330	-5.2580	2.3543	0.9237
0.065	1.0276	-0.0346	-4.6343	2.5555	0.9101
0.138	1.0199	-0.0343	-6.9399	2.7980	0.8923
0.188	0.9875	-0.0275	-9.5287	3.2246	0.8569
0.388	0.8914	-0.0080	-8.6757	3.7239	0.8092
0.638	0.6806	0.0453	-12.3650	4.3900	0.7348
1.238	0.5411	0.0788	-12.0756	4.6215	0.7061

Table I.31. Section H - coefficients for linear pavement temperature prediction model including seasonal component.

Daily Maximum Temperature					
depth, m	A	B	C	RMSE	Adjusted R ²
0.038	0.9348	-0.0451	-1.9739	3.5011	0.9063
0.063	1.0892	-0.0667	-3.5406	3.4229	0.9104
0.138	1.1994	-0.0809	-1.7120	3.3598	0.9137
0.188	1.3414	-0.0966	1.0963	3.3975	0.9118
Daily Minimum Temperature					
depth, m	A	B	C	RMSE	Adjusted R ²
0.038	0.9994	-0.0250	-6.0272	2.2757	0.9314
0.063	0.9760	-0.0281	-7.5315	2.5320	0.9151
0.138	0.9805	-0.0284	-7.1406	2.7090	0.9029
0.188	0.9779	-0.0245	-6.6097	2.9461	0.8851

Table I.32. Section I - coefficients for linear pavement temperature prediction model including seasonal component.

Daily Maximum Temperature					
depth, m	A	B	C	RMSE	Adjusted R ²
0.038	0.8572	-0.0186	-1.1834	3.7840	0.8946
0.063	1.1323	-0.0499	1.0336	3.6301	0.9030
0.138	1.1420	-0.0596	3.0589	3.6388	0.9026
0.188	1.2799	-0.0717	1.0809	3.5594	0.9068
0.263	1.4702	-0.0708	-1.1647	4.1031	0.8761
0.413	1.3464	-0.0178	-1.7228	5.0151	0.8149
0.588	1.1054	0.0422	-0.9000	5.7669	0.7553
Daily Minimum Temperature					
depth, m	A	B	C	RMSE	Adjusted R ²
0.038	0.9654	-0.0164	-3.8489	2.4495	0.9166
0.063	0.9503	-0.0181	-3.4836	2.8890	0.8840
0.138	0.9300	-0.0227	-1.3407	2.9635	0.8779
0.188	0.9157	-0.0158	-4.2064	3.1369	0.8632
0.263	0.8804	-0.0039	-6.9194	3.5608	0.8238
0.413	0.7405	0.0345	-8.2475	3.9813	0.7797
0.588	0.6489	0.0542	-8.5843	4.2367	0.7505

Table I.33. Section J - coefficients for linear pavement temperature prediction model including seasonal component.

Daily Maximum Temperature					
depth, m	A	B	C	RMSE	Adjusted R ²
0.038	0.8922	-0.0288	1.6214	3.6241	0.9039
0.063	1.3270	-0.0834	2.4512	3.6793	0.9010
0.263	1.2629	-0.0763	-0.5157	3.9453	0.8861
0.338	1.4060	-0.0819	5.2317	4.1546	0.8737
0.588	1.1527	0.0036	-0.3661	5.5233	0.7839
Daily Minimum Temperature					
depth, m	A	B	C	RMSE	Adjusted R ²
0.038	0.9099	-0.0140	-1.5519	2.8019	0.8910
0.063	0.8823	-0.0154	-4.4332	3.3536	0.8439
0.263	0.9045	-0.0233	-6.4071	3.2238	0.8548
0.338	0.8220	-0.0069	-3.6387	3.7138	0.8086
0.588	0.7076	0.0255	-8.2853	4.0851	0.7737

Table I.34. Section L - coefficients for linear pavement temperature prediction model including seasonal component.

Daily Maximum Temperature					
depth, m	A	B	C	RMSE	Adjusted R ²
0.038	0.9086	-0.0286	-1.1648	3.1601	0.9255
0.063	1.2403	-0.0701	2.0698	3.2927	0.9191
0.188	1.1821	-0.0626	0.5445	3.1655	0.9252
0.263	1.3462	-0.0735	2.5942	3.8898	0.8870
0.413	1.1005	0.0127	-0.5547	5.3325	0.7877
0.588	0.8957	0.0484	1.9189	5.6978	0.7576
Daily Minimum Temperature					
depth, m	A	B	C	RMSE	Adjusted R ²
0.038	0.9164	-0.0163	-4.1288	2.1912	0.9312
0.063	0.8875	-0.0143	-3.7191	2.7085	0.8949
0.188	0.8979	-0.0151	-4.4379	2.5784	0.9048
0.263	0.8381	-0.0083	-4.6240	3.0529	0.8668
0.413	0.6806	0.0348	-8.5254	3.5441	0.8201
0.588	0.6073	0.0476	-7.4858	3.7053	0.8034

Table I.35. Layer 1 (bottom) - coefficients for linear pavement temperature prediction model including seasonal component.

Daily Maximum Temperature						
Section	depth, m	A	B	C	RMSE	Adjusted R ²
A	0.038	0.7095	0.1154	1.7786	3.3451	0.9348
B	0.038	1.1185	-0.0826	0.7461	3.9704	0.8921
C	0.038	0.9745	-0.0474	0.8983	2.7850	0.9404
D	0.038	1.0493	-0.0646	1.0288	2.6636	0.9450
E	0.038	0.8760	-0.0439	2.7195	3.1914	0.9169
F	0.038	0.9101	-0.0356	-0.0368	2.9765	0.9202
G	0.038	0.9192	-0.0401	-2.1191	3.5608	0.9007
H	0.038	0.9348	-0.0451	-1.9739	3.5011	0.9063
I	0.038	0.8572	-0.0186	-1.1834	3.7840	0.8946
J	0.038	0.8922	-0.0288	1.6214	3.6241	0.9039
L	0.038	0.9086	-0.0286	-1.1648	3.1601	0.9255
Daily Minimum Temperature						
Section	depth, m	A	B	C	RMSE	Adjusted R ²
A	0.038	1.0511	-0.0376	-6.6718	2.4758	0.9203
B	0.038	1.0359	-0.0313	-5.6999	2.4404	0.9252
C	0.038	1.0021	-0.0348	-3.4777	2.0107	0.9414
D	0.038	0.9973	-0.0358	-4.1319	2.1014	0.9351
E	0.038	1.0237	-0.0487	1.3975	2.3495	0.9220
F	0.038	0.9882	-0.0319	-2.0216	2.3645	0.9210
G	0.038	1.0317	-0.0330	-5.2580	2.3543	0.9237
H	0.038	0.9994	-0.0250	-6.0272	2.2757	0.9314
I	0.038	0.9654	-0.0164	-3.8489	2.4495	0.9166
J	0.038	0.9099	-0.0140	-1.5519	2.8019	0.8910
L	0.038	0.9164	-0.0163	-4.1288	2.1912	0.9312

Table I.36. Layer 2 (top) - coefficients for linear pavement temperature prediction model including seasonal component.

Daily Maximum Temperature						
Section	depth, m	A	B	C	RMSE	Adjusted R ²
A	0.063	0.5405	0.1286	-2.2970	2.5412	0.9476
B	0.063	1.4808	-0.1224	-1.7434	4.2142	0.8785
C	0.063	1.2677	-0.0815	-0.8342	2.9924	0.9312
D	0.063	1.3563	-0.1028	1.3224	3.1356	0.9237
E	0.063	1.4219	-0.1172	3.0256	3.5411	0.8966
F	0.063	1.6368	-0.1772	1.9386	4.1969	0.8414
G	0.065	1.0931	-0.0651	-0.9505	3.4082	0.9091
H	0.063	1.0892	-0.0667	-3.5406	3.4229	0.9104
I	0.063	1.1323	-0.0499	1.0336	3.6301	0.9030
J	0.063	1.3270	-0.0834	2.4512	3.6793	0.9010
L	0.063	1.2403	-0.0701	2.0698	3.2927	0.9191
Daily Minimum Temperature						
Section	depth, m	A	B	C	RMSE	Adjusted R ²
A	0.063	0.9853	-0.0332	-5.7302	3.0546	0.8716
B	0.063	1.0894	-0.0423	-9.9624	3.0196	0.8856
C	0.063	0.9529	-0.0264	-7.3427	2.7132	0.8933
D	0.063	0.9916	-0.0372	-7.0243	2.7400	0.8896
E	0.063	0.9204	-0.0333	-4.4452	3.3493	0.8415
F	0.063	0.9862	-0.0444	-4.4914	3.2496	0.8507
G	0.065	1.0276	-0.0346	-4.6343	2.5555	0.9101
H	0.063	0.9760	-0.0281	-7.5315	2.5320	0.9151
I	0.063	0.9503	-0.0181	-3.4836	2.8890	0.8840
J	0.063	0.8823	-0.0154	-4.4332	3.3536	0.8439
L	0.063	0.8875	-0.0143	-3.7191	2.7085	0.8949

Table I.37. Layer 2 (bottom) - coefficients for linear pavement temperature prediction model including seasonal component.

Daily Maximum Temperature						
Section	depth, m	A	B	C	RMSE	Adjusted R ²
G	0.138	1.2087	-0.0799	-1.9542	3.4239	0.9082
H	0.138	1.1994	-0.0809	-1.7120	3.3598	0.9137
I	0.138	1.1420	-0.0596	3.0589	3.6388	0.9026
Daily Minimum Temperature						
Section	depth, m	A	B	C	RMSE	Adjusted R ²
G	0.138	1.0199	-0.0343	-6.9399	2.7980	0.8923
H	0.138	0.9805	-0.0284	-7.1406	2.7090	0.9029
I	0.138	0.9300	-0.0227	-1.3407	2.9635	0.8779

Table I.38. Layer 3 (bottom) - coefficients for linear pavement temperature prediction model including seasonal component.

Daily Maximum Temperature						
Section	depth, m	A	B	C	RMSE	Adjusted R ²
A	0.188	0.5023	0.1268	-0.2339	2.4388	0.9471
B	0.188	1.5344	-0.1316	1.4519	4.2659	0.8755
C	0.188	1.3276	-0.0886	1.4663	3.1811	0.9222
D	0.188	1.3329	-0.0955	1.7174	3.1196	0.9245
F	0.188	1.4926	-0.1470	3.4633	3.7019	0.8766
G	0.188	1.4084	-0.1004	-2.3683	3.7142	0.8920
H	0.188	1.3414	-0.0966	1.0963	3.3975	0.9118
I	0.188	1.2799	-0.0717	1.0809	3.5594	0.9068
L	0.188	1.1821	-0.0626	0.5445	3.1655	0.9252
Daily Minimum Temperature						
Section	depth, m	A	B	C	RMSE	Adjusted R ²
A	0.188	1.0002	-0.0303	-8.5649	3.1442	0.8639
B	0.188	1.0353	-0.0343	-8.4157	3.1356	0.8766
C	0.188	0.9548	-0.0272	-6.5184	2.8163	0.8850
D	0.188	0.9695	-0.0325	-6.2311	2.8102	0.8839
F	0.188	0.9634	-0.0368	-3.0970	3.1252	0.8619
G	0.188	0.9875	-0.0275	-9.5287	3.2246	0.8569
H	0.188	0.9779	-0.0245	-6.6097	2.9461	0.8851
I	0.188	0.9157	-0.0158	-4.2064	3.1369	0.8632
L	0.188	0.8979	-0.0151	-4.4379	2.5784	0.9048

Table I.39. Layer 2 (bottom) for Sections A and E and Layer 4 (bottom) for Sections I and J - coefficients for linear pavement temperature prediction model including seasonal component.

Daily Maximum Temperature						
Section	depth, m	A	B	C	RMSE	Adjusted R ²
A	0.263	0.4301	0.1349	-2.1345	2.3799	0.9448
E	0.263	1.4243	-0.1131	5.0204	3.7076	0.8867
I	0.263	1.4702	-0.0708	-1.1647	4.1031	0.8761
J	0.263	1.2629	-0.0763	-0.5157	3.9453	0.8861
Daily Minimum Temperature						
Section	depth, m	A	B	C	RMSE	Adjusted R ²
A	0.263	0.9621	-0.0279	-8.2671	3.4382	0.8373
E	0.263	0.9035	-0.0293	-3.4596	3.4240	0.8343
I	0.263	0.8804	-0.0039	-6.9194	3.5608	0.8238
J	0.263	0.9045	-0.0233	-6.4071	3.2238	0.8548

Table I.40. Layer 5 (bottom) - coefficients for linear pavement temperature prediction model including seasonal component.

Daily Maximum Temperature						
Section	depth, m	A	B	C	RMSE	Adjusted R ²
G	0.388	1.4282	-0.0749	0.8806	4.9095	0.8113
J	0.338	1.4060	-0.0819	5.2317	4.1546	0.8737
Daily Minimum Temperature						
Section	depth, m	A	B	C	RMSE	Adjusted R ²
G	0.388	0.8914	-0.0080	-8.6757	3.7239	0.8092
J	0.338	0.8220	-0.0069	-3.6387	3.7138	0.8086

Table I.41. Layer 5 (bottom) - coefficients for linear pavement temperature prediction model including seasonal component.

Daily Maximum Temperature						
Section	depth, m	A	B	C	RMSE	Adjusted R ²
A	0.413	0.2865	0.1336	2.4917	3.3307	0.8611
I	0.413	1.3464	-0.0178	-1.7228	5.0151	0.8149
L	0.413	1.1005	0.0127	-0.5547	5.3325	0.7877
Daily Minimum Temperature						
Section	depth, m	A	B	C	RMSE	Adjusted R ²
A	0.413	0.7698	0.0220	-12.6571	4.1887	0.7585
I	0.413	0.7405	0.0345	-8.2475	3.9813	0.7797
L	0.413	0.6806	0.0348	-8.5254	3.5441	0.8201

Table I.42. Layer 6 (bottom) - coefficients for linear pavement temperature prediction model including seasonal component.

Daily Maximum Temperature						
Section	depth, m	A	B	C	RMSE	Adjusted R ²
A	0.588	0.3020	0.0676	3.9767	5.0632	0.5729
I	0.588	1.1054	0.0422	-0.9000	5.7669	0.7553
J	0.588	1.1527	0.0036	-0.3661	5.5233	0.7839
L	0.588	0.8957	0.0484	1.9189	5.6978	0.7576
Daily Minimum Temperature						
Section	depth, m	A	B	C	RMSE	Adjusted R ²
A	0.588	0.4254	0.0981	-12.1688	4.6406	0.7036
I	0.588	0.6489	0.0542	-8.5843	4.2367	0.7505
J	0.588	0.7076	0.0255	-8.2853	4.0851	0.7737
L	0.588	0.6073	0.0476	-7.4858	3.7053	0.8034

Table I.43. Coefficients for linear pavement temperature prediction model, where A is the near surface temperature coefficient, B is the day of year coefficient, and C is the intercept coefficient.

Daily Maximum Temperature						
Section	depth, m	A	B	C	RMSE	Adjusted R ²
A	0.038	0.7095	0.1154	1.7786	3.3451	0.9348
B	0.038	1.1185	-0.0826	0.7461	3.9704	0.8921
C	0.038	0.9745	-0.0474	0.8983	2.7850	0.9404
D	0.038	1.0493	-0.0646	1.0288	2.6636	0.9450
E	0.038	0.8760	-0.0439	2.7195	3.1914	0.9169
F	0.038	0.9101	-0.0356	-0.0368	2.9765	0.9202
G	0.038	0.9192	-0.0401	-2.1191	3.5608	0.9007
H	0.038	0.9348	-0.0451	-1.9739	3.5011	0.9063
I	0.038	0.8572	-0.0186	-1.1834	3.7840	0.8946
J	0.038	0.8922	-0.0288	1.6214	3.6241	0.9039
L	0.038	0.9086	-0.0286	-1.1648	3.1601	0.9255
Daily Maximum Temperature						
Section	depth, m	A	B	C	RMSE	Adjusted R ²
A	0.063	0.5405	0.1286	-2.2970	2.5412	0.9476
B	0.063	1.4808	-0.1224	-1.7434	4.2142	0.8785
C	0.063	1.2677	-0.0815	-0.8342	2.9924	0.9312
D	0.063	1.3563	-0.1028	1.3224	3.1356	0.9237
E	0.063	1.4219	-0.1172	3.0256	3.5412	0.8966
F	0.063	1.6368	-0.1772	1.9386	4.1969	0.8414
H	0.063	1.0892	-0.0667	-3.5406	3.4229	0.9104
I	0.063	1.1323	-0.0499	1.0336	3.6301	0.9030
J	0.063	1.3270	-0.0834	2.4512	3.6793	0.9010
L	0.063	1.2403	-0.0701	2.0698	3.2927	0.9191
Daily Maximum Temperature						
Section	depth, m	A	B	C	RMSE	Adjusted R ²
A	0.188	0.1268	-0.2339	-0.2339	2.4388	0.9471
B	0.188	1.5344	-0.1316	1.4519	4.2659	0.8755
C	0.188	1.3276	-0.0886	1.4663	3.1811	0.9222
D	0.188	1.3329	-0.0955	1.7174	3.1196	0.9245
F	0.188	1.4926	-0.1470	3.4633	3.7019	0.8766
G	0.188	1.4084	-0.1004	-2.3683	3.7142	0.8920
H	0.188	1.3414	-0.0966	1.0963	3.3975	0.9118
I	0.188	1.2799	-0.0717	1.0809	3.5594	0.9068
L	0.188	1.1821	-0.0626	0.5445	3.1655	0.9252

Table I.44. Coefficients for linear pavement temperature prediction model, where A is the near surface temperature coefficient, B is the day of year coefficient, and C is the intercept coefficient.

Daily Minimum Temperature						
Section	depth, m	A	B	C	RMSE	Adjusted R ²
A	0.038	1.0511	-0.0376	-6.6718	2.4758	0.9203
B	0.038	1.0359	-0.0313	-5.6999	2.4404	0.9252
C	0.038	1.0021	-0.0348	-3.4777	2.0107	0.9414
D	0.038	0.9973	-0.0358	-4.1319	2.1014	0.9351
E	0.038	1.0237	-0.0487	1.3975	2.3495	0.9220
F	0.038	0.9882	-0.0319	-2.0216	2.3645	0.9210
G	0.038	1.0317	-0.0330	-5.2580	2.3543	0.9237
H	0.038	0.9994	-0.0250	-6.0272	2.2757	0.9314
I	0.038	0.9654	-0.0164	-3.8489	2.4495	0.9166
J	0.038	0.9099	-0.0140	-1.5519	2.8019	0.8910
L	0.038	0.9164	-0.0163	-4.1288	2.1912	0.9312
Daily Minimum Temperature						
Section	depth, m	A	B	C	RMSE	Adjusted R ²
A	0.063	0.9853	-0.0332	-5.7302	3.0546	0.8716
B	0.063	1.0894	-0.0423	-9.9624	3.0196	0.8856
C	0.063	0.9529	-0.0264	-7.3427	2.7132	0.8933
D	0.063	0.9916	-0.0372	-7.0243	2.7400	0.8896
E	0.063	0.9204	-0.0333	-4.4452	3.3493	0.8415
F	0.063	0.9862	-0.0444	-4.4914	3.2496	0.8507
H	0.063	0.9760	-0.0281	-7.5315	2.5320	0.9151
I	0.063	0.9503	-0.0181	-3.4836	2.8890	0.8840
J	0.063	0.8823	-0.0154	-4.4332	3.3536	0.8439
L	0.063	0.8875	-0.0143	-3.7191	2.7085	0.8949
Daily Minimum Temperature						
Section	depth, m	A	B	C	RMSE	Adjusted R ²
A	0.188	1.0002	-0.0303	-8.5649	3.1442	0.8639
B	0.188	1.0353	-0.0343	-8.4157	3.1356	0.8766
C	0.188	0.9548	-0.0272	-6.5184	2.8163	0.8850
D	0.188	0.9695	-0.0325	-6.2311	2.8102	0.8839
F	0.188	0.9634	-0.0368	-3.0970	3.1252	0.8619
G	0.188	0.9875	-0.0275	-9.5287	3.2246	0.8569
H	0.188	0.9779	-0.0245	-6.6097	2.9461	0.8851
I	0.188	0.9157	-0.0158	-4.2064	3.1369	0.8632
L	0.188	0.8979	-0.0151	-4.4379	2.5784	0.9048

Table I.45. Coefficients for linear pavement temperature prediction model, where A is the near surface temperature coefficient, B is the day of year coefficient, and C is the intercept coefficient (A and B are held constant).

Daily Maximum Temperature						
Section	depth, m	A	B	C	RMSE	R ²
A	0.038	0.8225	0.0916	1.3720	3.4794	0.9295
B	0.038	0.8225	0.0916	-0.6180	3.3078	0.9351
C	0.038	0.8225	0.0916	0.0694	2.6594	0.9586
D	0.038	0.8225	0.0916	-0.5296	2.3592	0.9654
E	0.038	0.8225	0.0916	0.4058	3.3637	0.9430
F	0.038	0.8225	0.0916	1.2389	3.2786	0.9301
G	0.038	0.8225	0.0916	3.3366	3.3683	0.9363
H	0.038	0.8225	0.0916	3.1470	3.2657	0.9424
I	0.038	0.8225	0.0916	2.5514	3.7236	0.9263
J	0.038	0.8225	0.0916	-0.6926	3.4822	0.9357
L	0.038	0.8225	0.0916	2.3471	3.0386	0.9500
Daily Maximum Temperature						
Section	depth, m	A	B	C	RMSE	R ²
A	0.063	0.5666	0.1109	-1.4540	2.5993	0.9452
B	0.063	0.5666	0.1109	1.1439	2.5449	0.9450
C	0.063	0.5666	0.1109	1.7640	2.2382	0.9587
D	0.063	0.5666	0.1109	-0.0768	2.0949	0.9623
E	0.063	0.5666	0.1109	-1.5053	2.1636	0.9592
F	0.063	0.5666	0.1109	-0.5208	2.3972	0.9437
H	0.063	0.5666	0.1109	5.6713	3.0389	0.9412
I	0.063	0.5666	0.1109	-0.0294	2.8162	0.9404
J	0.063	0.5666	0.1109	-1.9700	2.4158	0.9510
L	0.063	0.5666	0.1109	-0.9545	2.3132	0.9587
Daily Maximum Temperature						
Section	depth, m	A	B	C	RMSE	R ²
A	0.188	0.5515	0.1088	0.1685	2.4958	0.9446
B	0.188	0.5515	0.1088	-0.7261	2.4706	0.9469
C	0.188	0.5515	0.1088	-0.0820	2.1875	0.9581
D	0.188	0.5515	0.1088	0.0415	2.1605	0.9598
F	0.188	0.5515	0.1088	-0.8018	2.2316	0.9532
G	0.188	0.5515	0.1088	1.5765	2.2955	0.9515
H	0.188	0.5515	0.1088	-0.2300	2.2359	0.9597
I	0.188	0.5515	0.1088	-0.5236	2.4290	0.9506
L	0.188	0.5515	0.1088	1.2733	2.4119	0.9574

Table I.46. Coefficients for linear pavement temperature prediction model, where A is the near surface temperature coefficient, B is the day of year coefficient, and C is the intercept coefficient (A and B are held constant).

Daily Minimum Temperature						
Section	depth, m	A	B	C	RMSE	R ²
A	0.038	0.7763	0.0644	4.1969	2.0578	0.9523
B	0.038	0.7763	0.0644	2.9234	2.0978	0.9512
C	0.038	0.7763	0.0644	1.7250	1.8646	0.9599
D	0.038	0.7763	0.0644	2.5153	1.9424	0.9564
E	0.038	0.7763	0.0644	-1.5587	2.1662	0.9517
F	0.038	0.7763	0.0644	0.8503	2.0972	0.9511
G	0.038	0.7763	0.0644	2.8328	2.0256	0.9518
H	0.038	0.7763	0.0644	3.2799	2.0324	0.9537
I	0.038	0.7763	0.0644	1.3329	2.2302	0.9398
J	0.038	0.7763	0.0644	-0.8732	2.5198	0.9287
L	0.038	0.7763	0.0644	2.4102	2.0558	0.9539
Daily Minimum Temperature						
Section	depth, m	A	B	C	RMSE	R ²
A	0.063	0.6602	0.0878	1.7860	2.5548	0.9249
B	0.063	0.6602	0.0878	5.4306	2.3179	0.9380
C	0.063	0.6602	0.0878	4.0265	2.4108	0.9323
D	0.063	0.6602	0.0878	4.0841	2.3221	0.9368
E	0.063	0.6602	0.0878	3.1959	2.7354	0.9240
F	0.063	0.6602	0.0878	3.2060	2.5427	0.9323
H	0.063	0.6602	0.0878	3.6453	2.2733	0.9456
I	0.063	0.6602	0.0878	-0.1246	2.5038	0.9254
J	0.063	0.6602	0.0878	1.3493	2.7685	0.9163
L	0.063	0.6602	0.0878	0.8746	2.3704	0.9393
Daily Minimum Temperature						
Section	depth, m	A	B	C	RMSE	R ²
A	0.188	0.6564	0.0850	4.4817	2.5570	0.9200
B	0.188	0.6564	0.0850	4.2416	2.4432	0.9330
C	0.188	0.6564	0.0850	3.4225	2.4476	0.9299
D	0.188	0.6564	0.0850	3.4008	2.4207	0.9314
F	0.188	0.6564	0.0850	1.7046	2.5436	0.9314
G	0.188	0.6564	0.0850	5.6777	2.5385	0.9229
H	0.188	0.6564	0.0850	2.6181	2.4168	0.9345
I	0.188	0.6564	0.0850	1.0314	2.6377	0.9199
L	0.188	0.6564	0.0850	1.8544	2.3062	0.9422

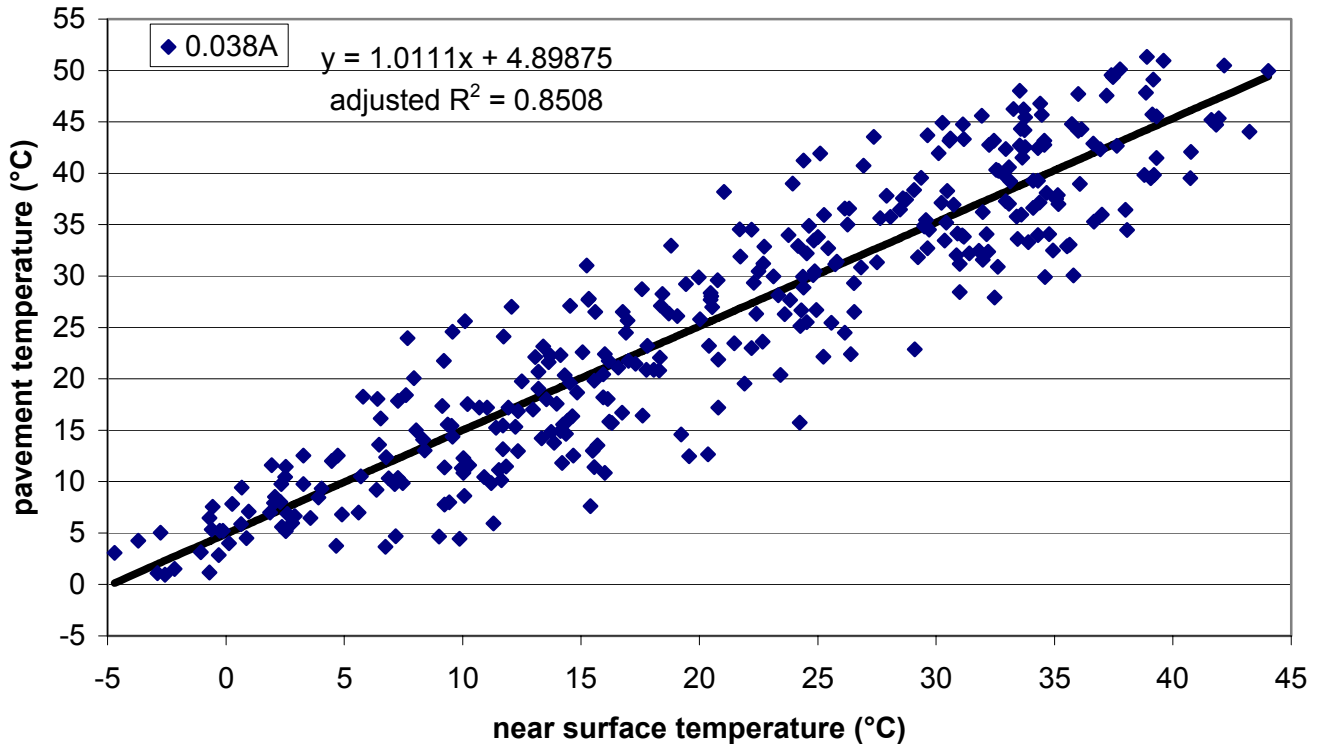


Figure I.1. Section A – daily maximum near surface temperature vs. daily maximum pavement temperature (0.038m depth) with linear model.

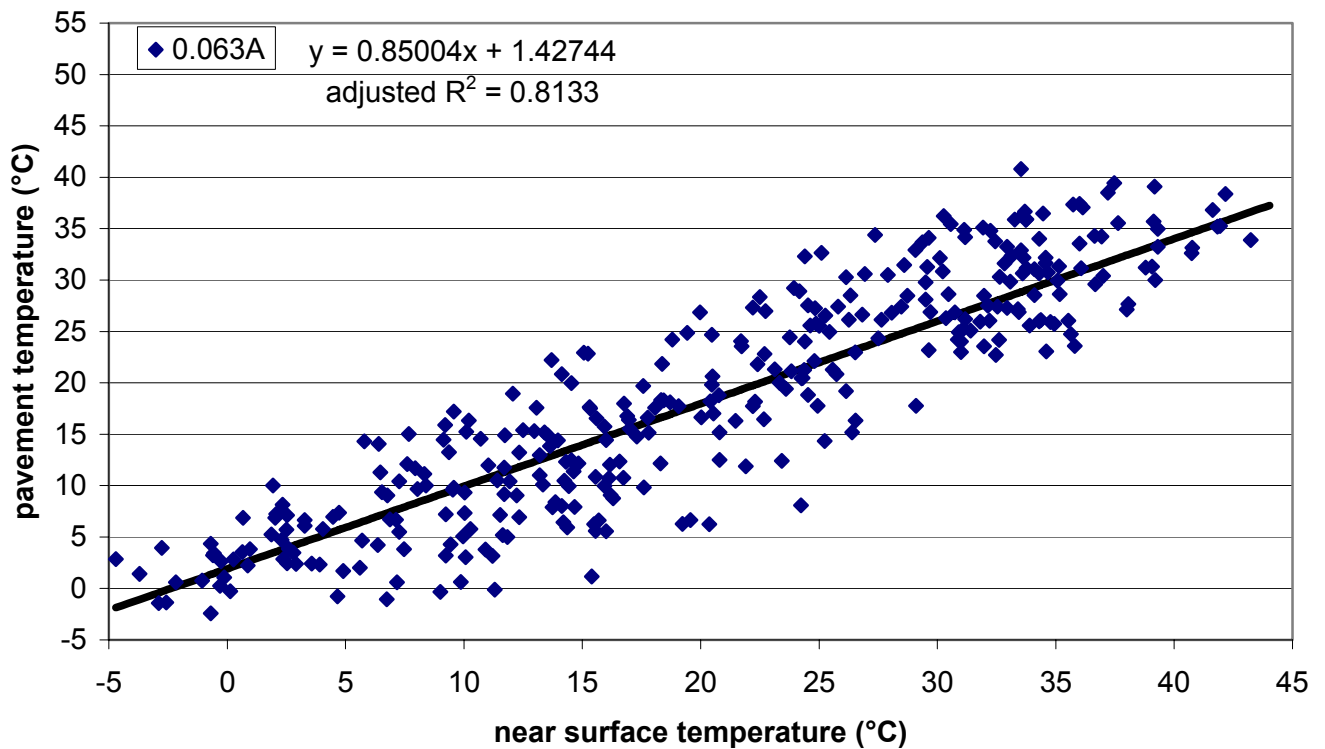


Figure I.2. Section A – daily maximum near surface temperature vs. daily maximum pavement temperature (0.063m depth) with linear model.

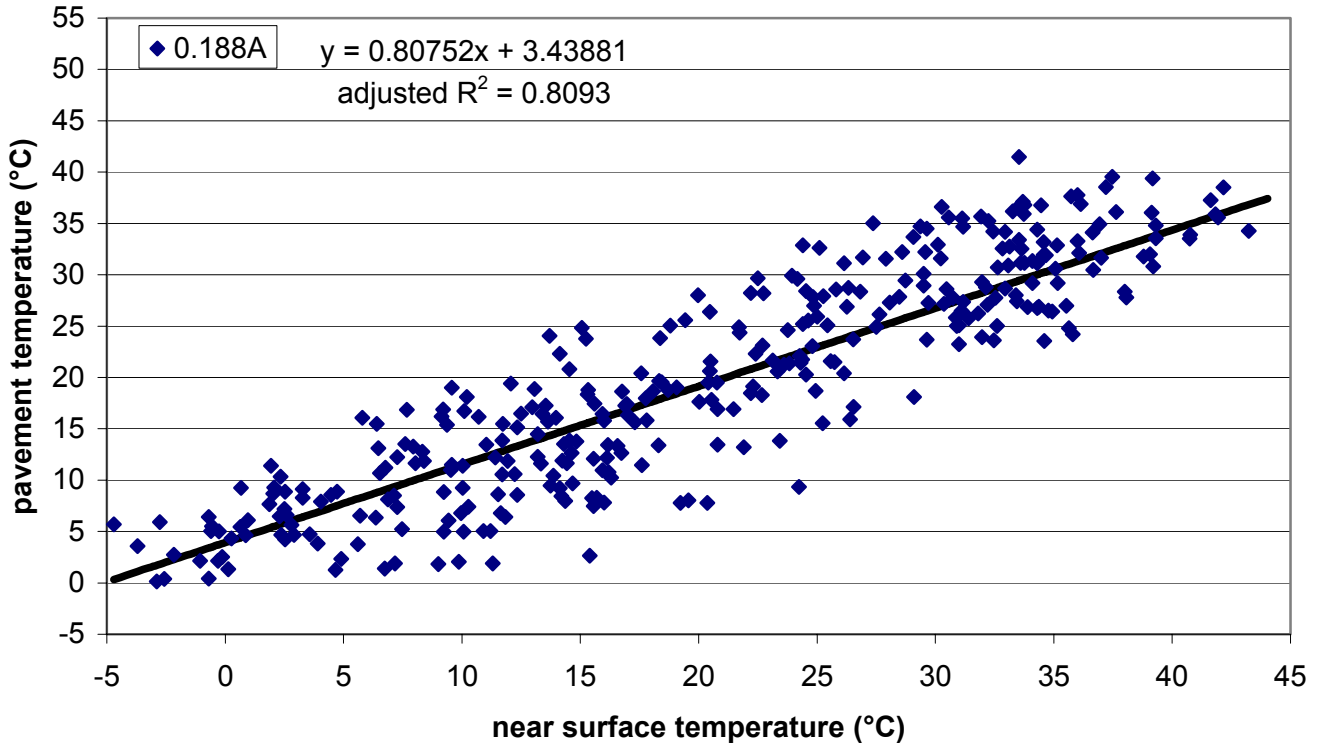


Figure I.3. Section A – daily maximum near surface temperature vs. daily maximum pavement temperature (0.188m depth) with linear model.

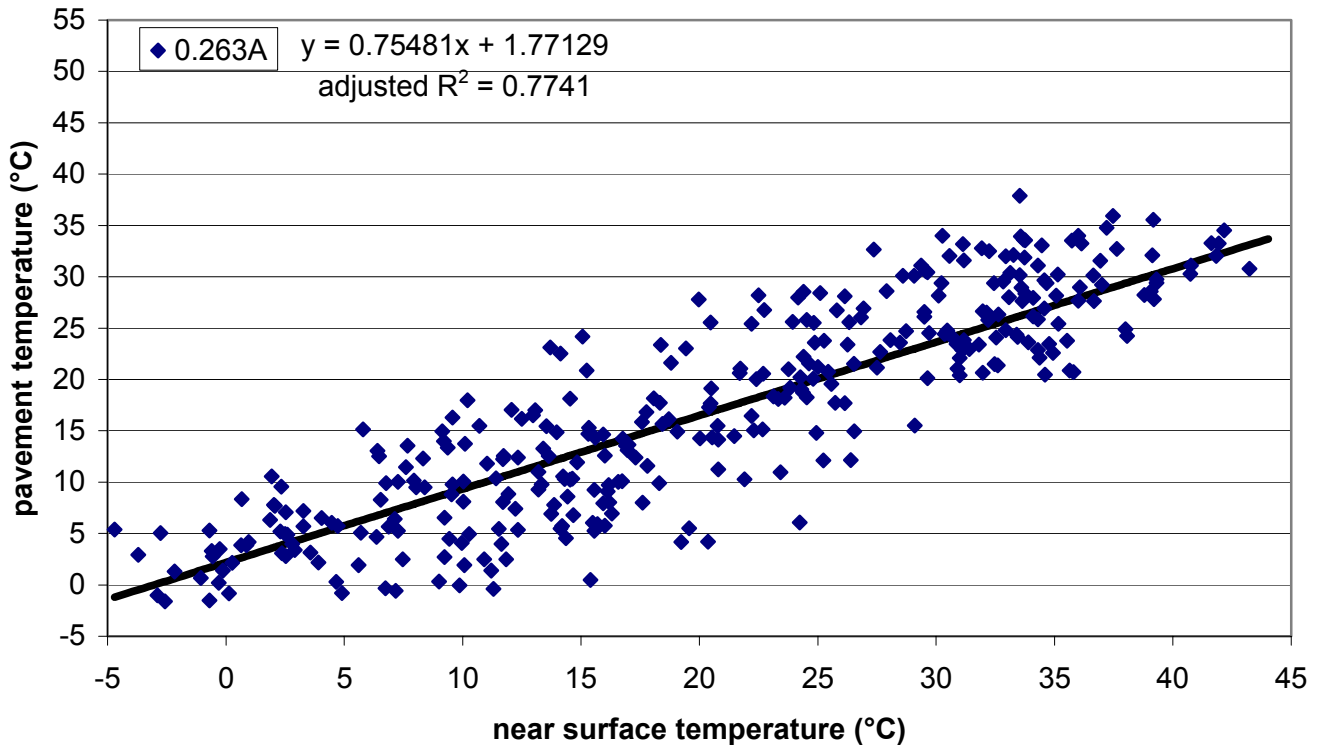


Figure I.4. Section A – daily maximum near surface temperature vs. daily maximum pavement temperature (0.263m depth) with linear model.

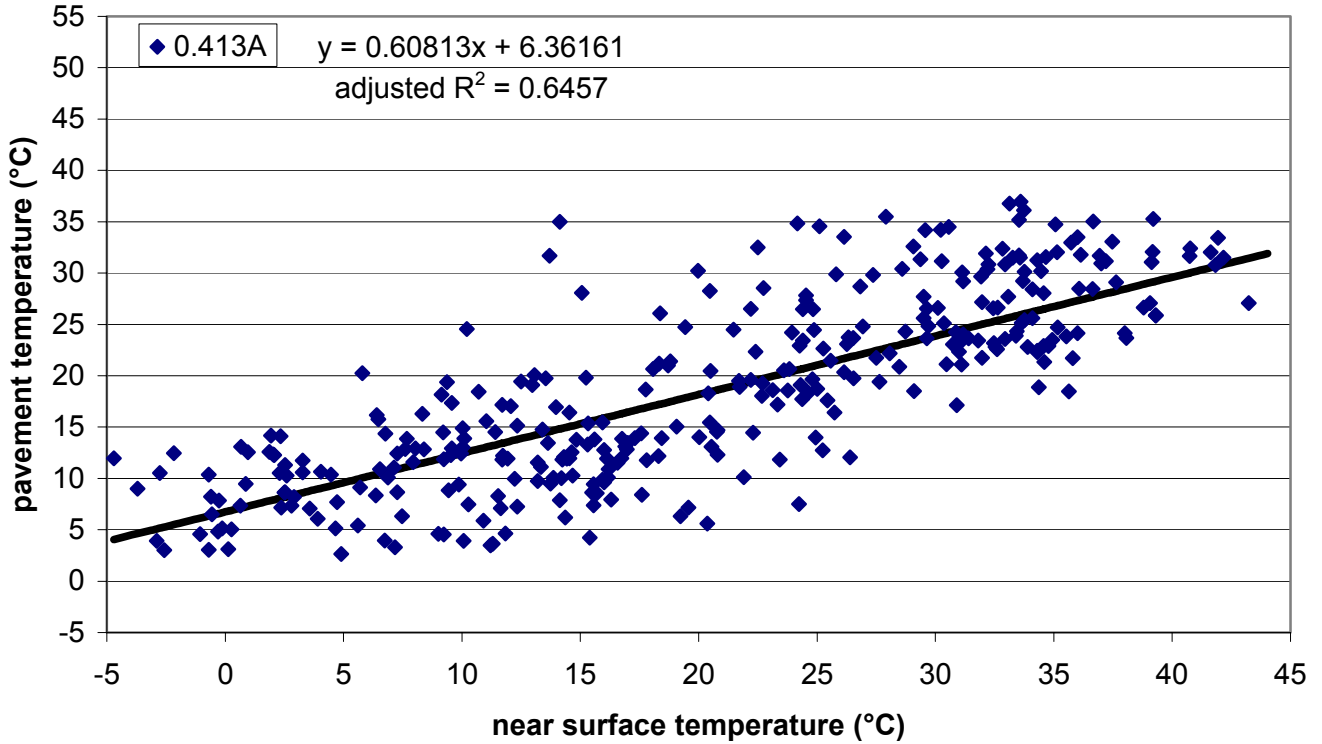


Figure I.5. Section A – daily maximum near surface temperature vs. daily maximum pavement temperature (0.413m depth) with linear model.

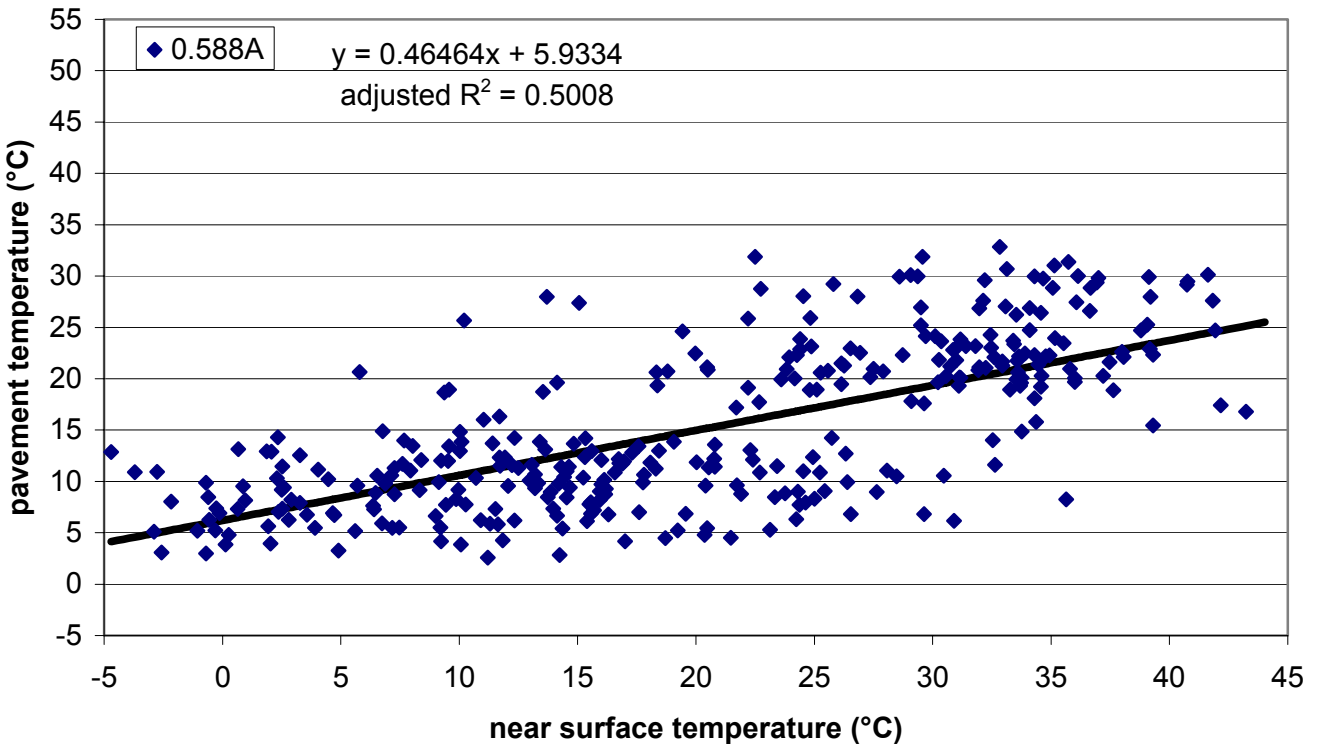


Figure I.6. Section A – daily maximum near surface temperature vs. daily maximum pavement temperature (0.588m depth) with linear model.

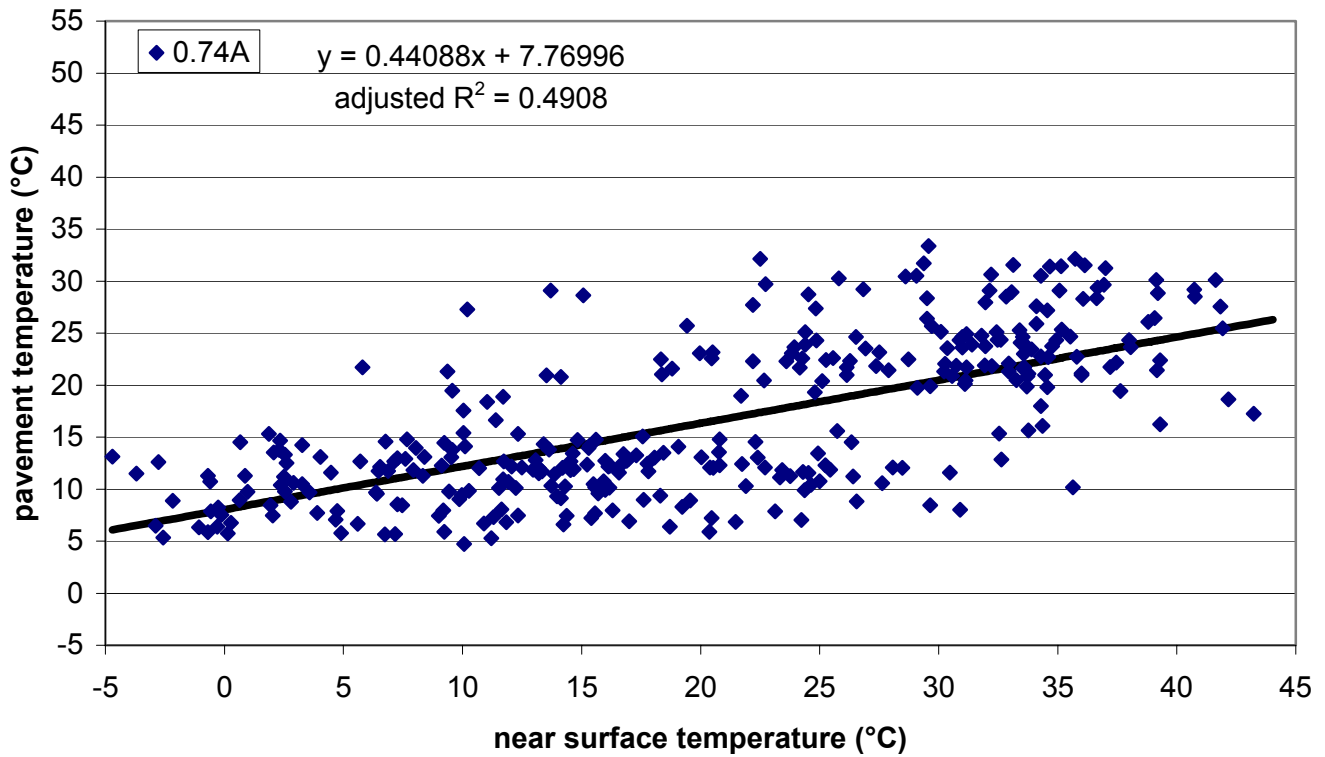


Figure I.7. Section A – daily maximum near surface temperature vs. daily maximum pavement temperature (0.74m depth) with linear model.

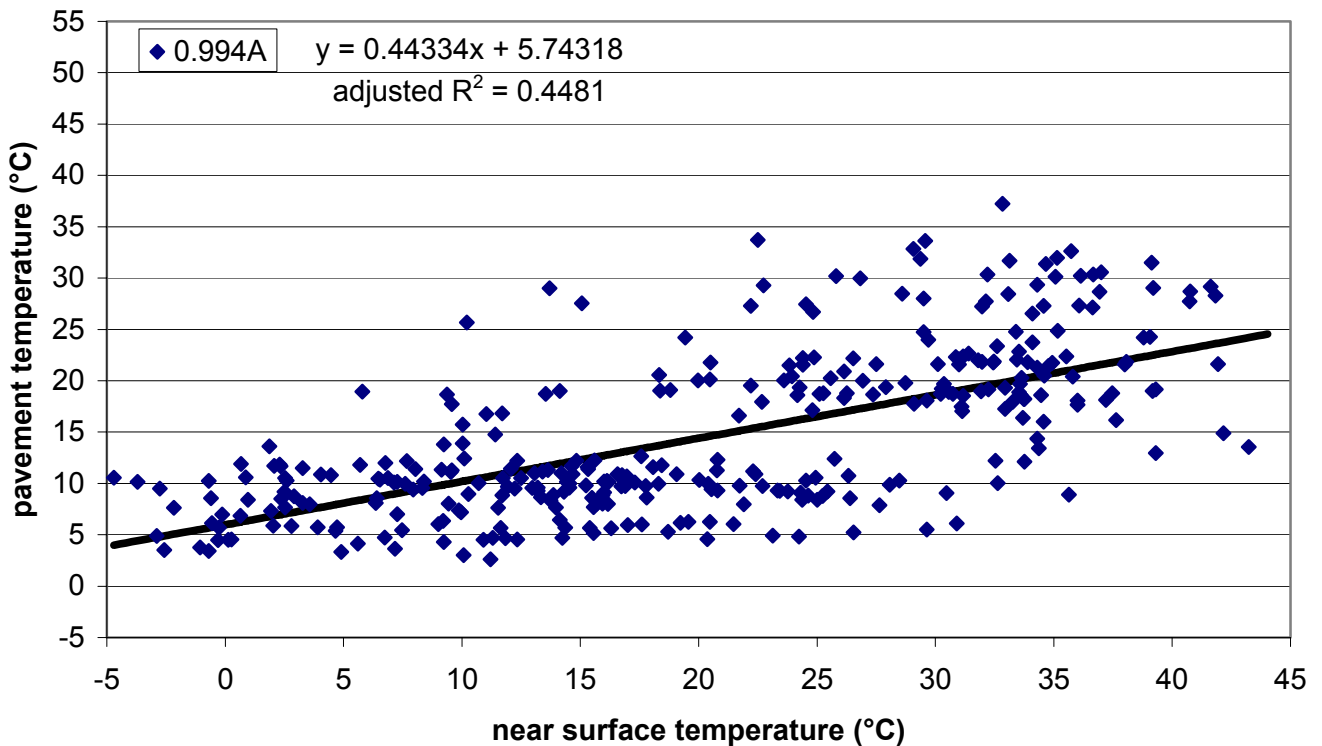


Figure I.8. Section A – daily maximum near surface temperature vs. daily maximum pavement temperature (0.994m depth) with linear model.

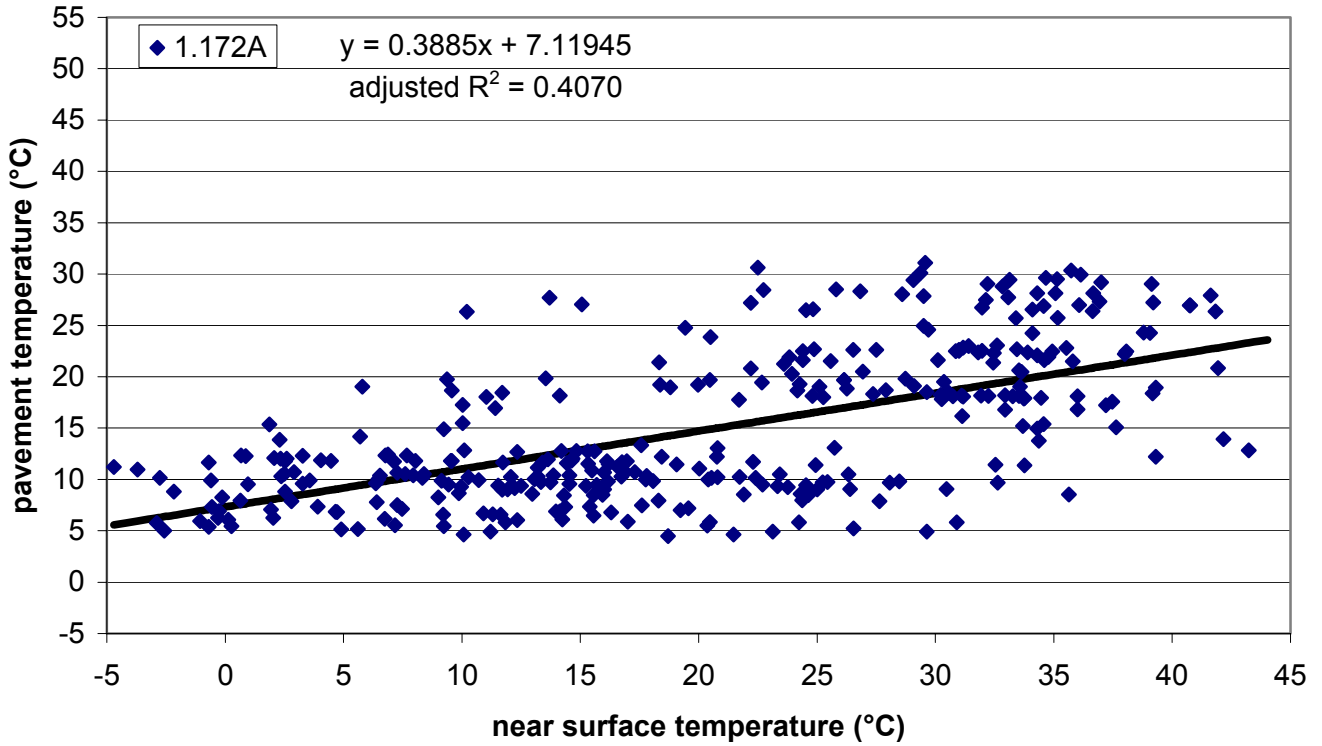


Figure I.9. Section A – daily maximum near surface temperature vs. daily maximum pavement temperature (1.172m depth) with linear model.

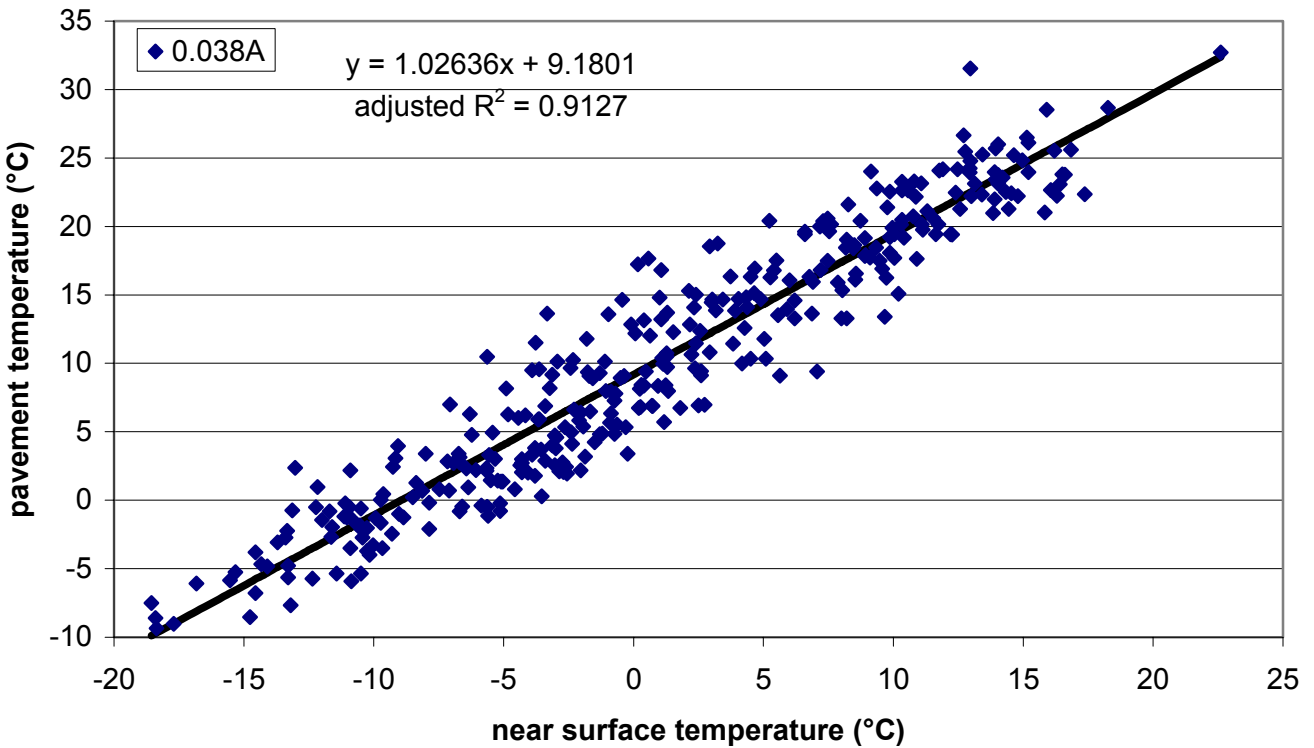


Figure I.10. Section A – daily minimum near surface temperature vs. daily minimum pavement temperature (0.038m depth) with linear model.

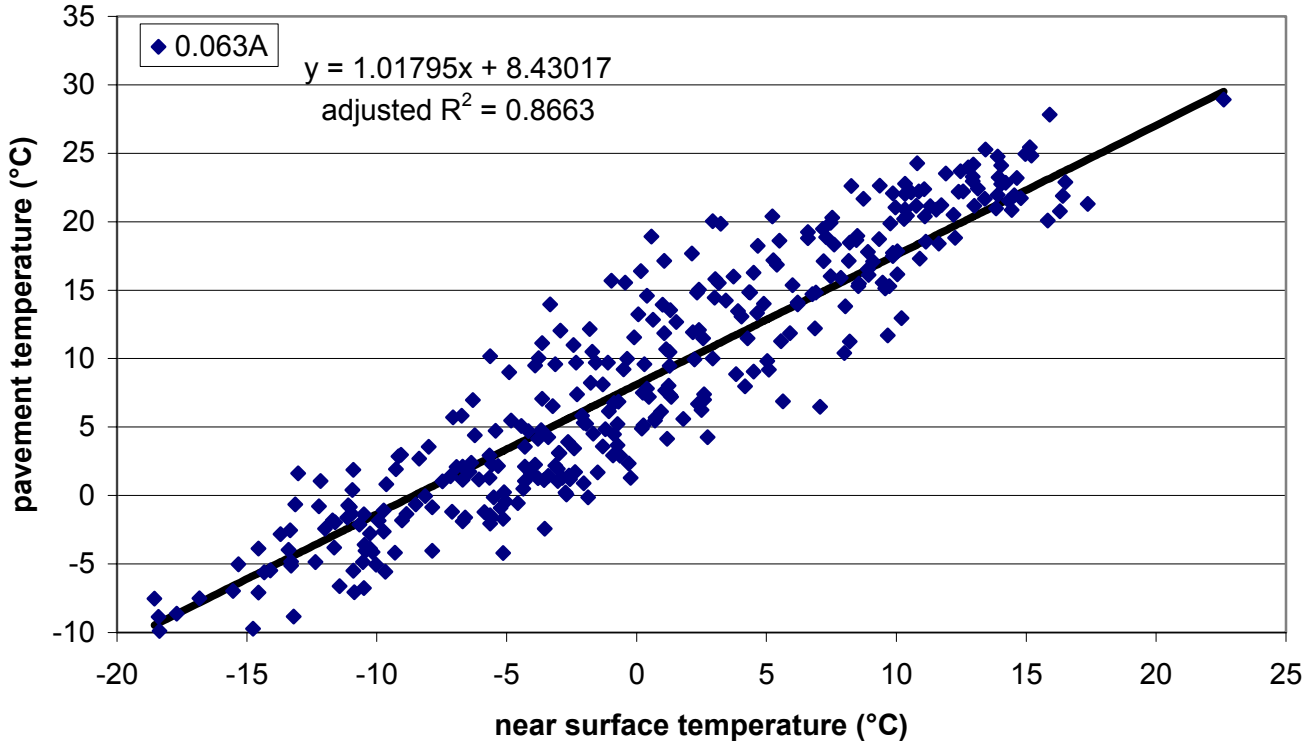


Figure I.11. Section A – daily minimum near surface temperature vs. daily minimum pavement temperature (0.063m depth) with linear model.

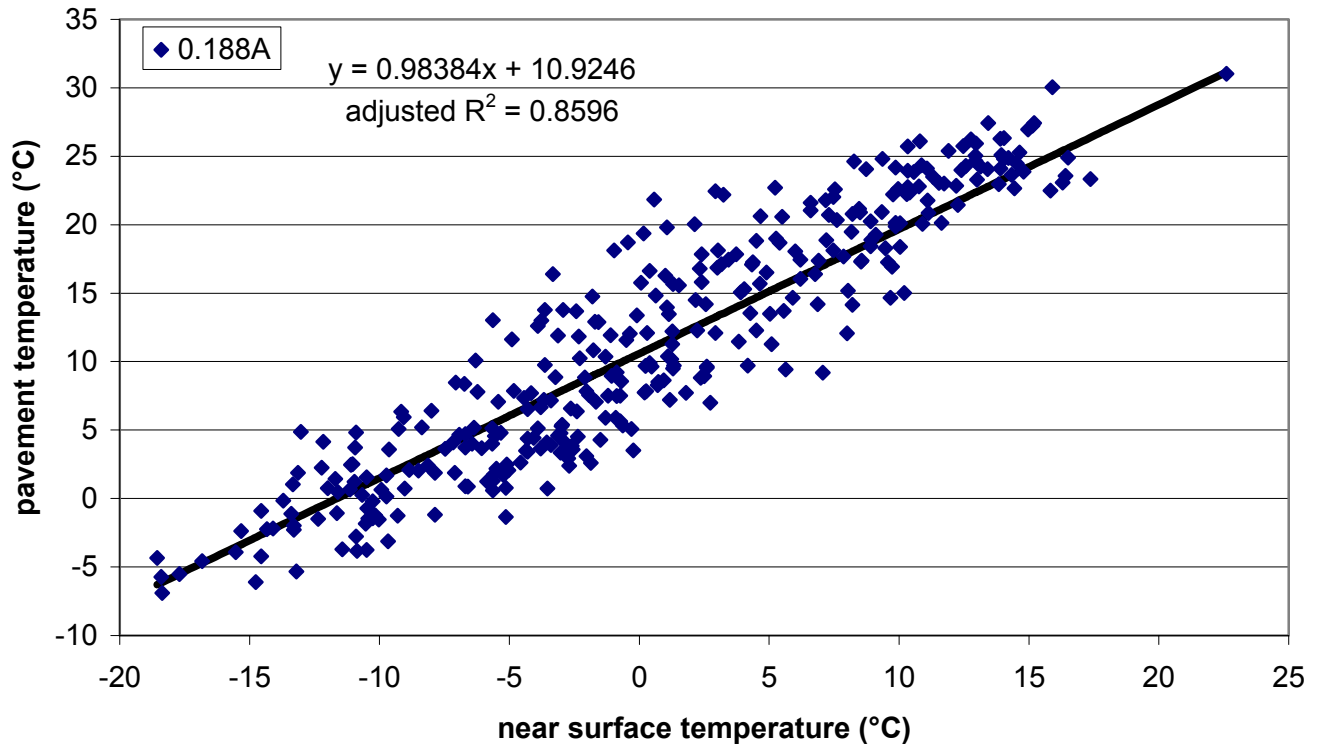


Figure I.12. Section A – daily minimum near surface temperature vs. daily minimum pavement temperature (0.188m depth) with linear model.

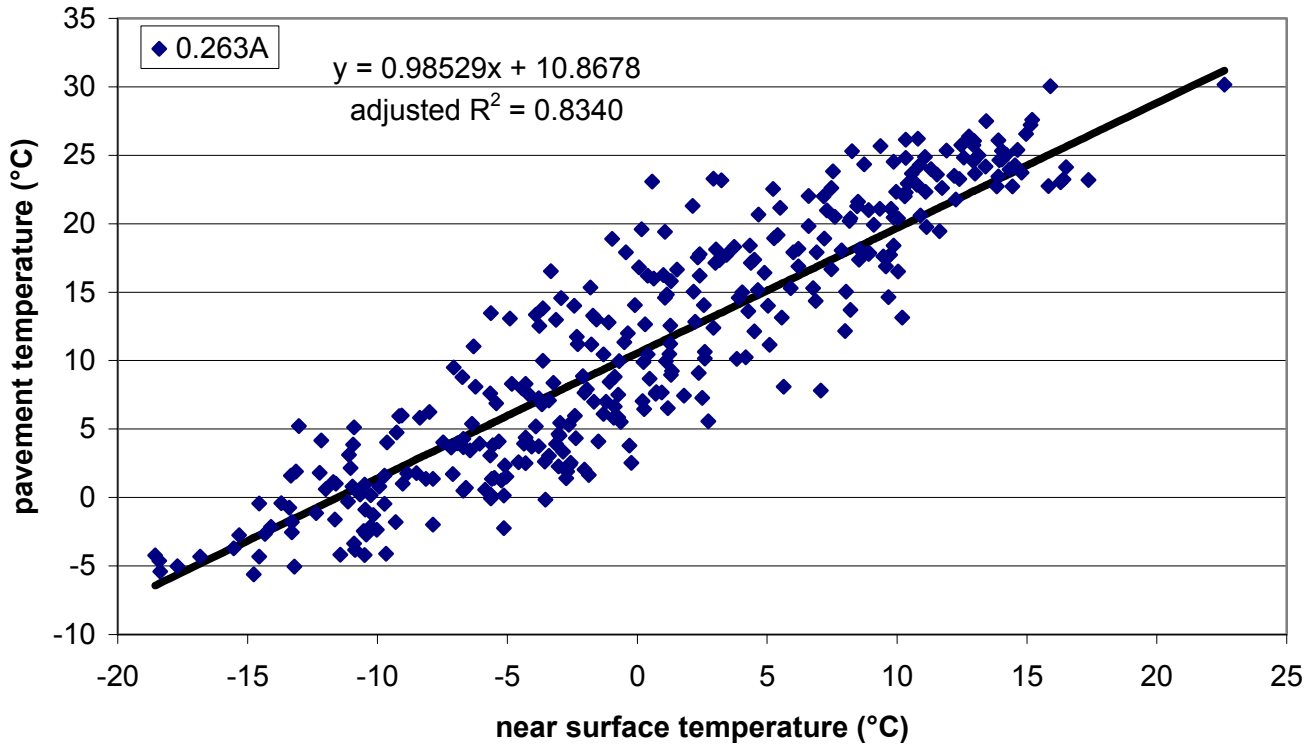


Figure I.13. Section A – daily minimum near surface temperature vs. daily minimum pavement temperature (0.263m depth) with linear model.

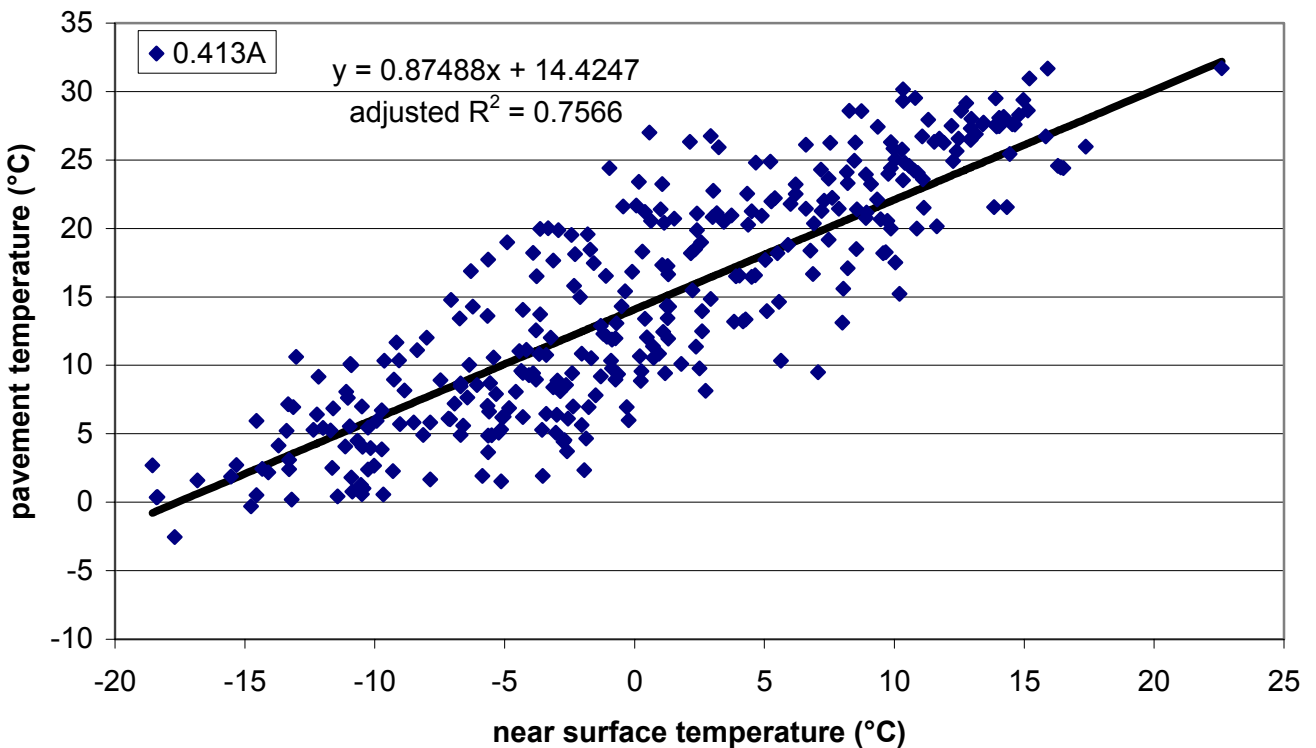


Figure I.14. Section A – daily minimum near surface temperature vs. daily minimum pavement temperature (0.413m depth) with linear model.

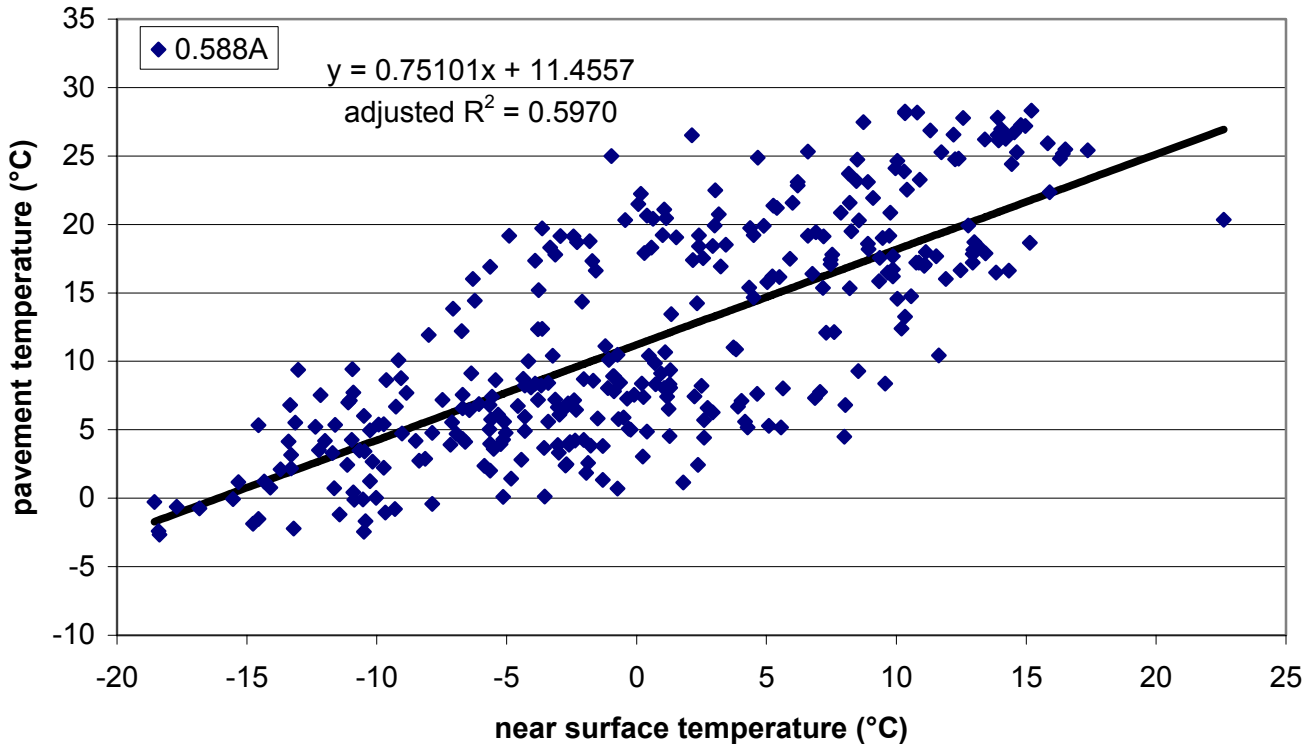


Figure I.15. Section A – daily minimum near surface temperature vs. daily minimum pavement temperature (0.588m depth) with linear model.

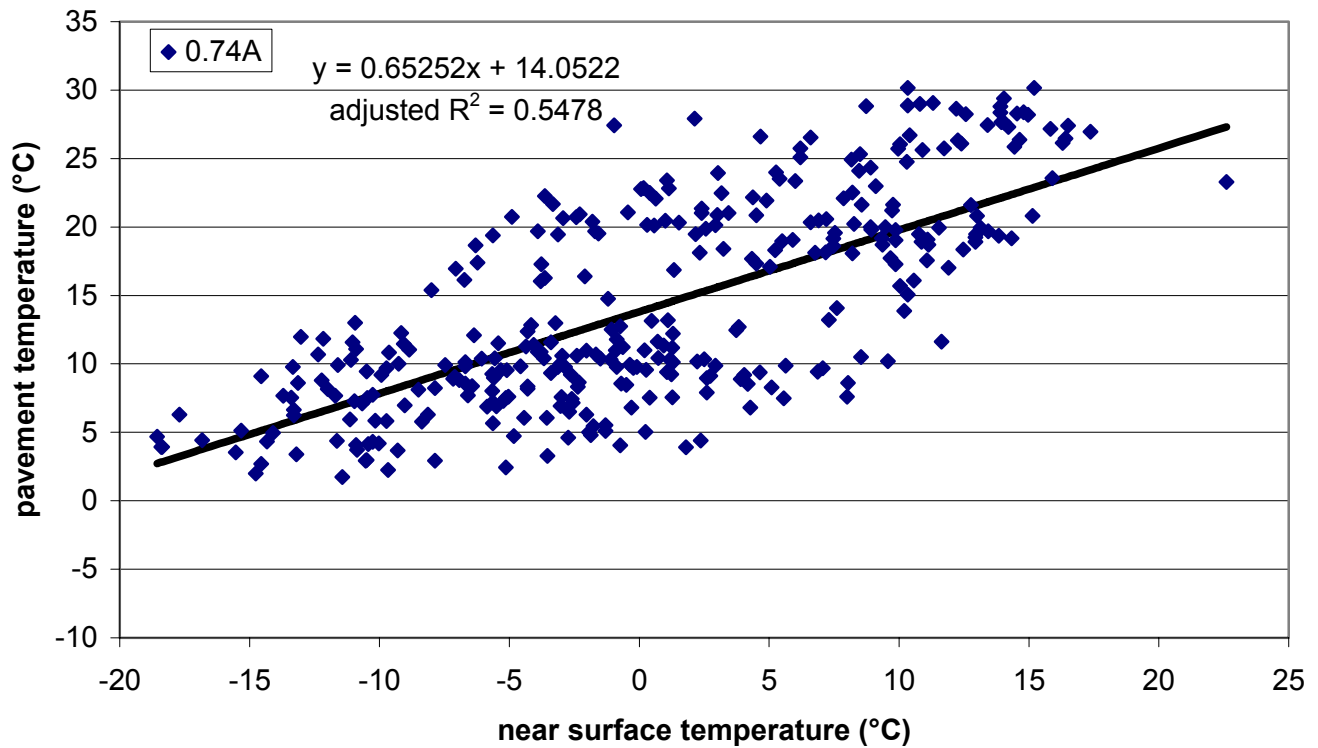


Figure I.16. Section A – daily minimum near surface temperature vs. daily minimum pavement temperature (0.74m depth) with linear model.

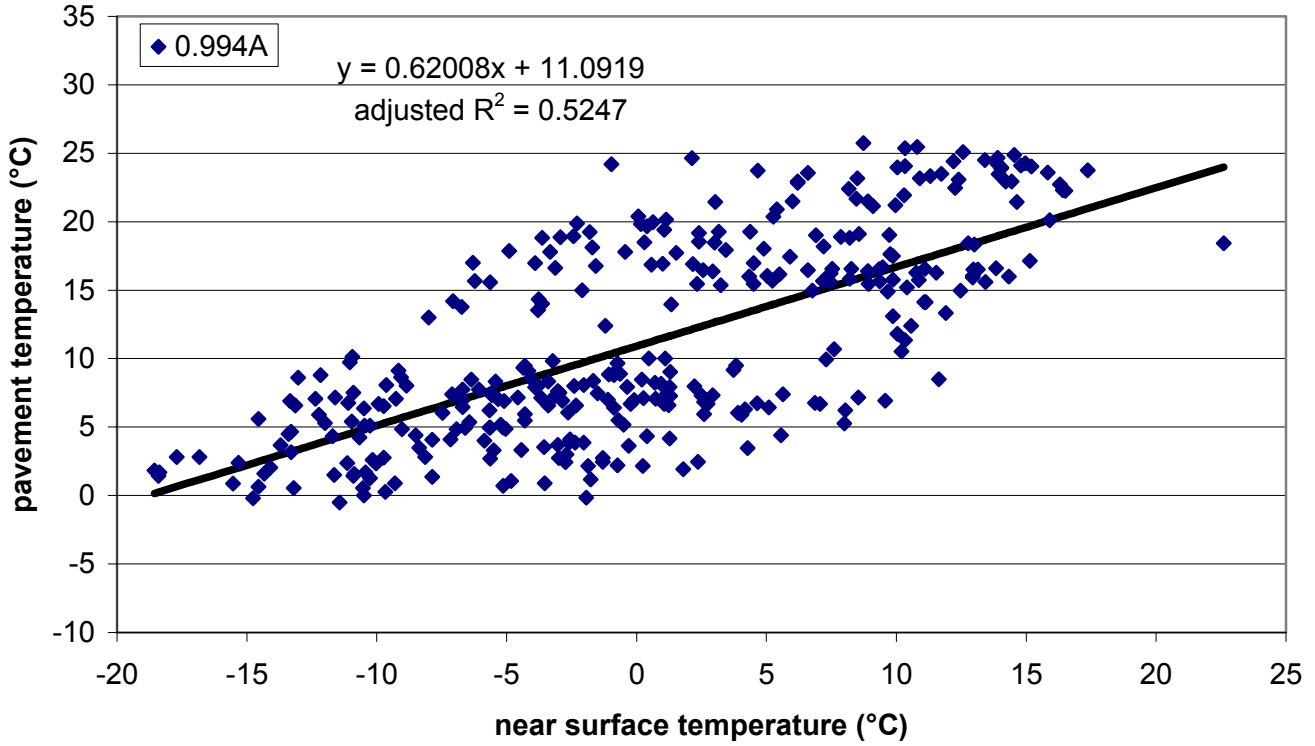


Figure I.17. Section A – daily minimum near surface temperature vs. daily minimum pavement temperature (0.994m depth) with linear model.

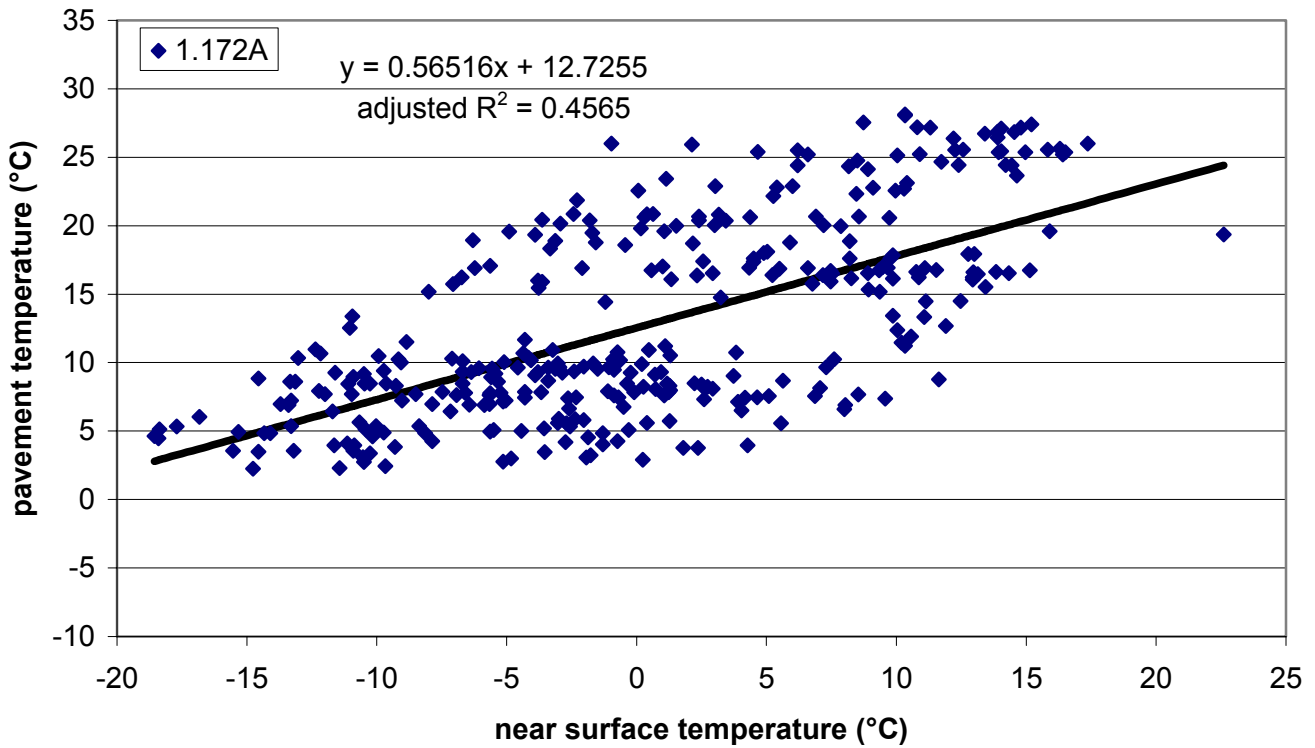


Figure I.18. Section A – daily minimum near surface temperature vs. daily minimum pavement temperature (1.172m depth) with linear model.

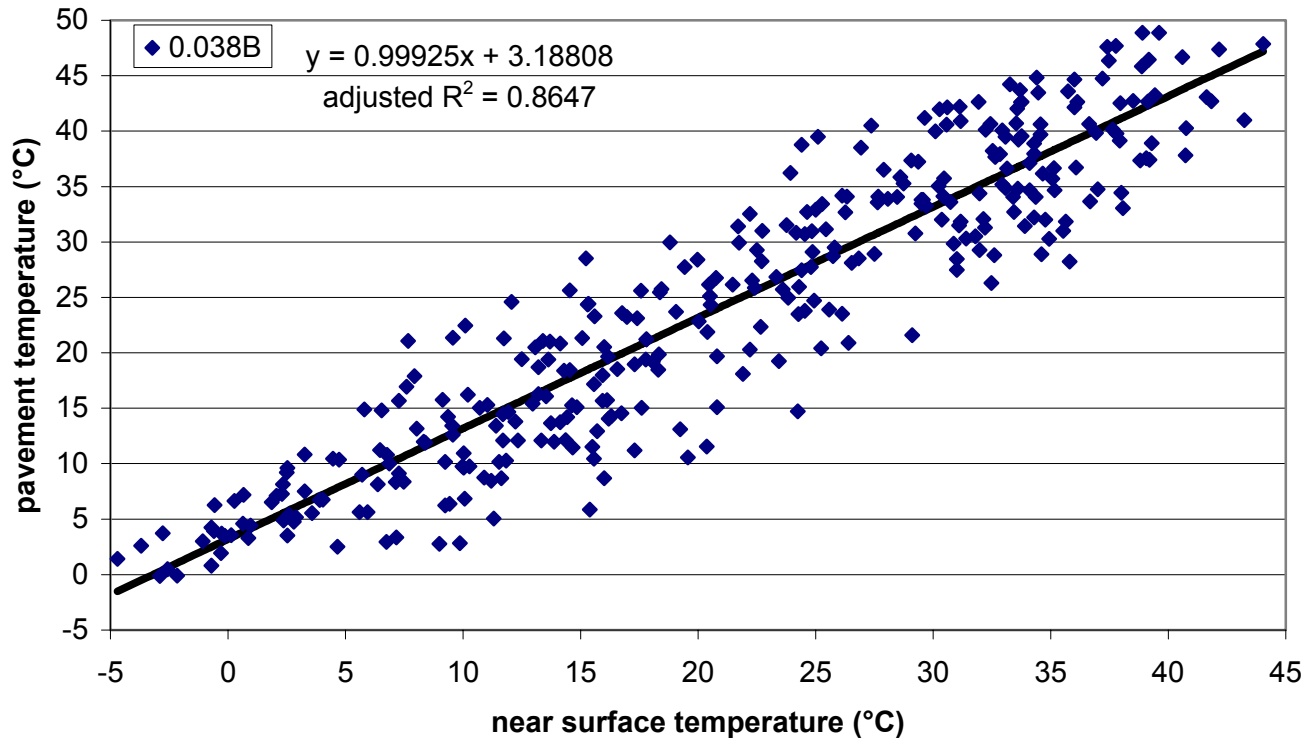


Figure I.19. Section B – daily maximum near surface temperature vs. daily maximum pavement temperature (0.038m depth) with linear model.

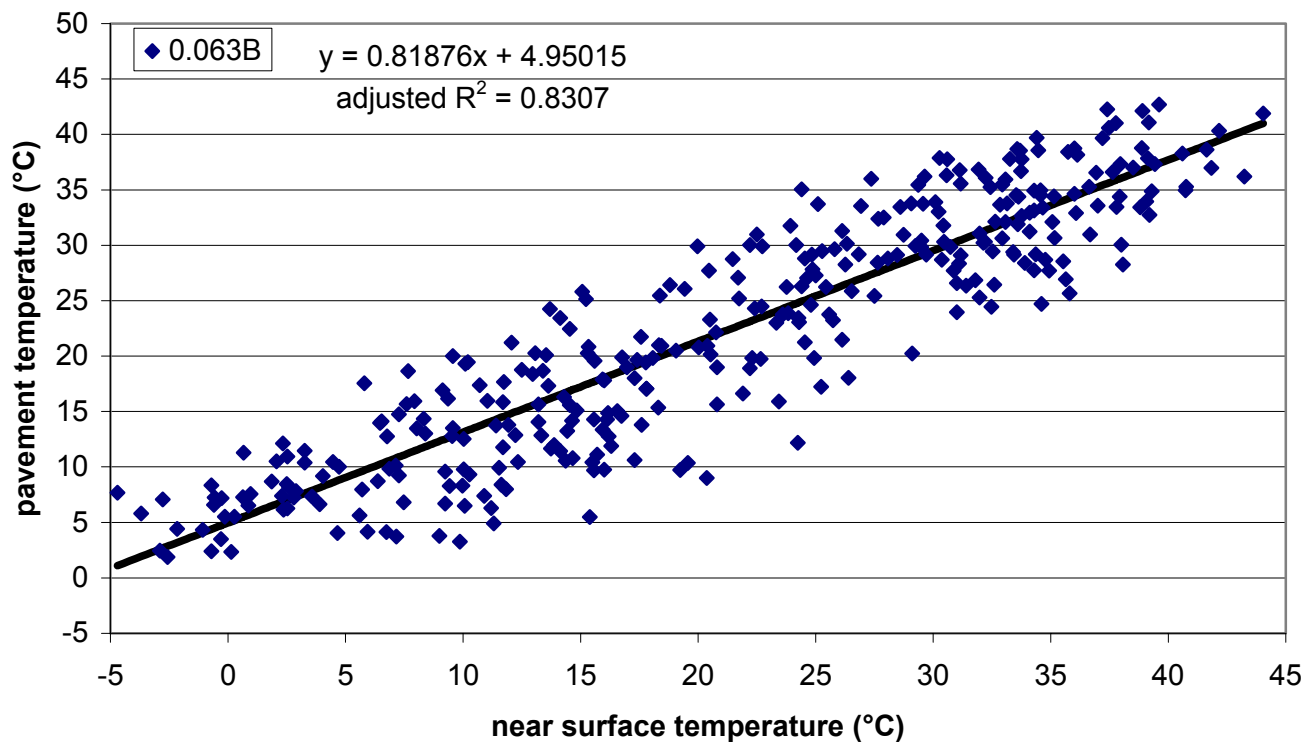


Figure I.20. Section B – daily maximum near surface temperature vs. daily maximum pavement temperature (0.063m depth) with linear model.

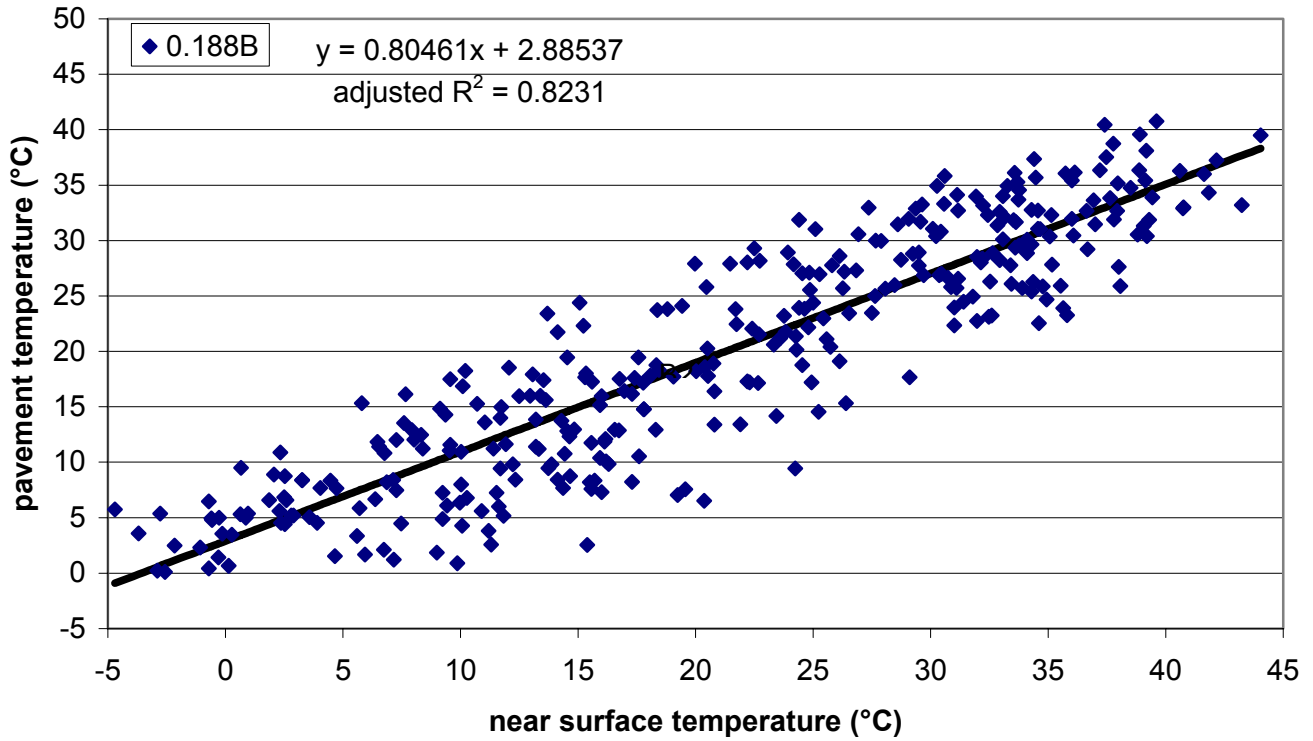


Figure I.21. Section B – daily maximum near surface temperature vs. daily maximum pavement temperature (0.188m depth) with linear model.

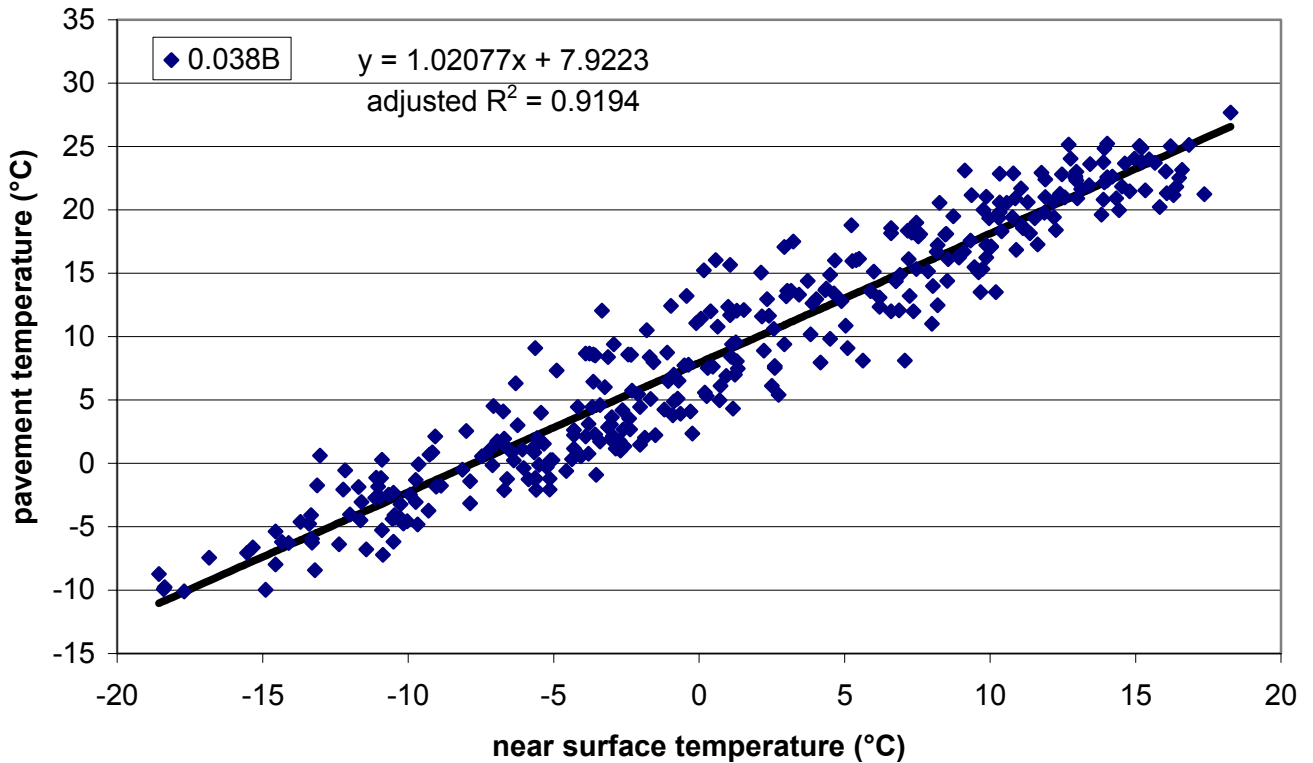


Figure I.22. Section B – daily minimum near surface temperature vs. daily minimum pavement temperature (0.038m depth) with linear model.

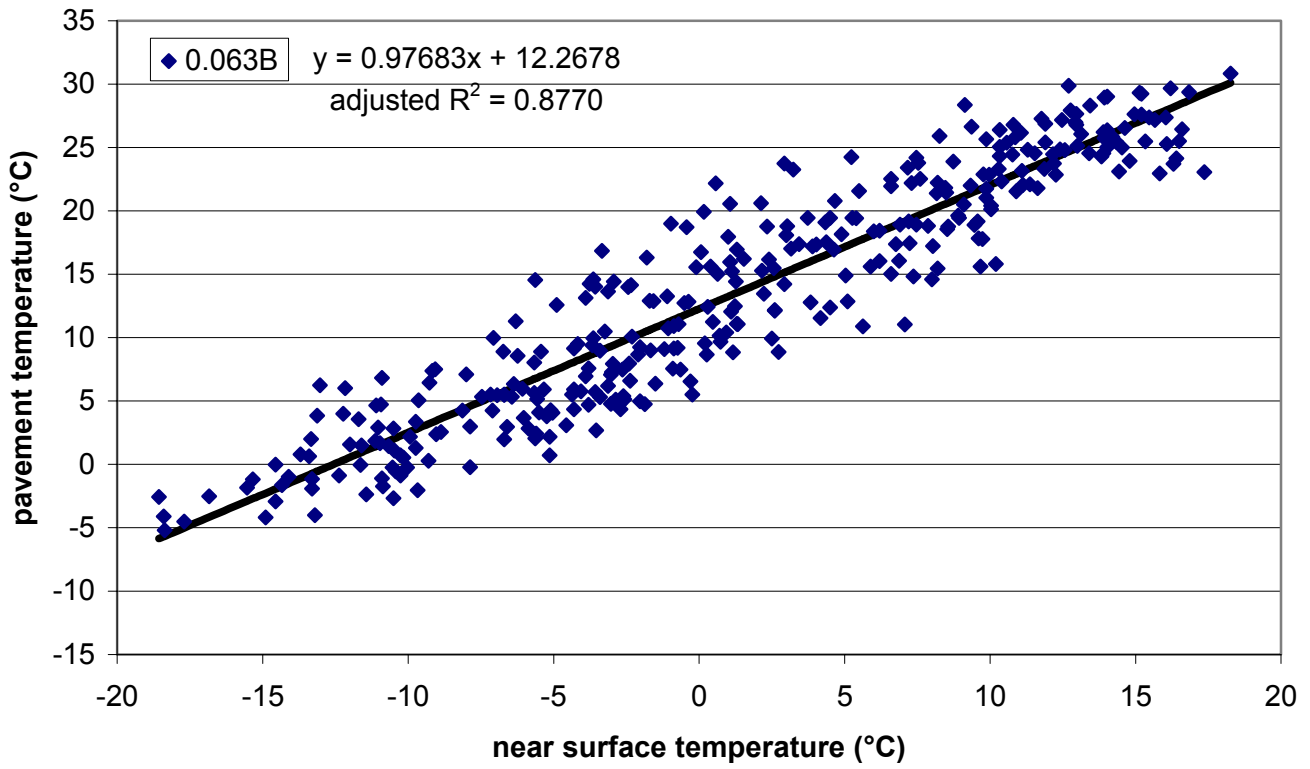


Figure I.23. Section B – daily minimum near surface temperature vs. daily minimum pavement temperature (0.063m depth) with linear model.

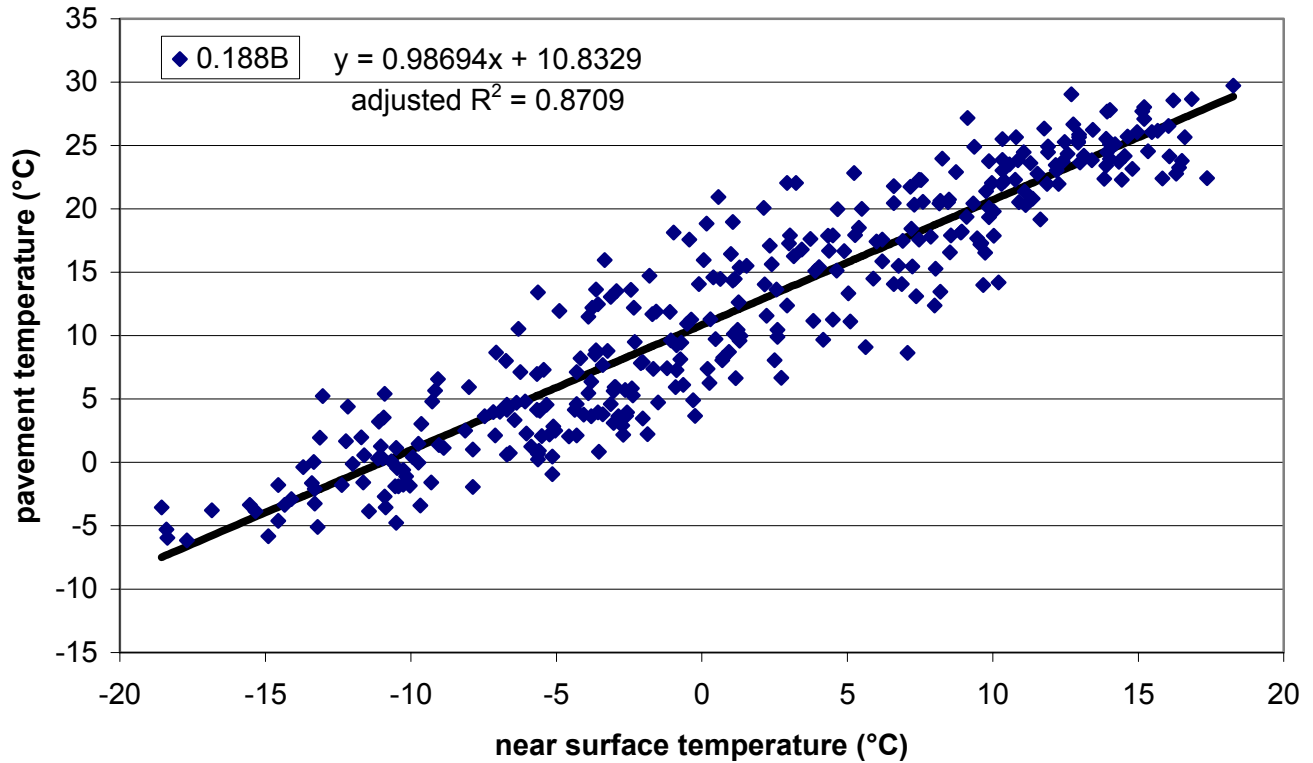


Figure I.24. Section B – daily minimum near surface temperature vs. daily minimum pavement temperature (0.188m depth) with linear model.

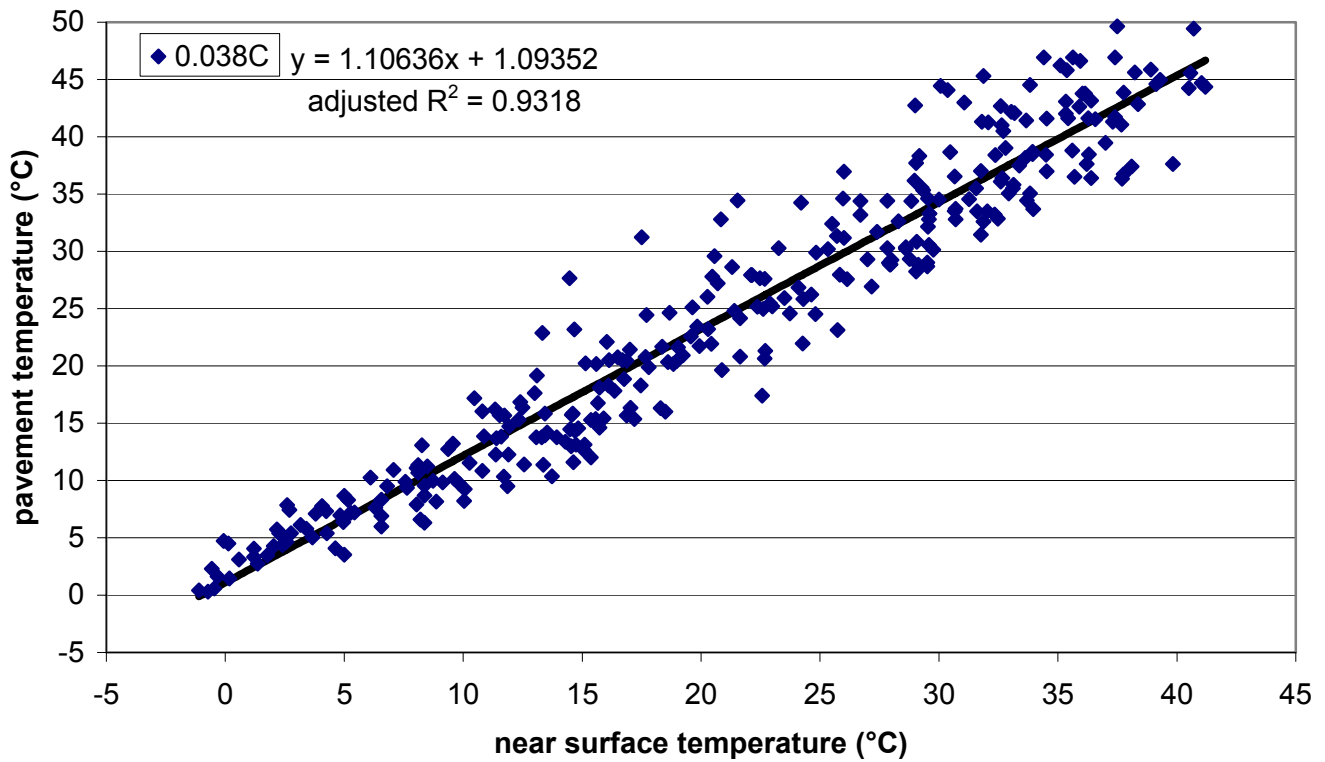


Figure I.25. Section C – daily maximum near surface temperature vs. daily maximum pavement temperature (0.038m depth) with linear model.

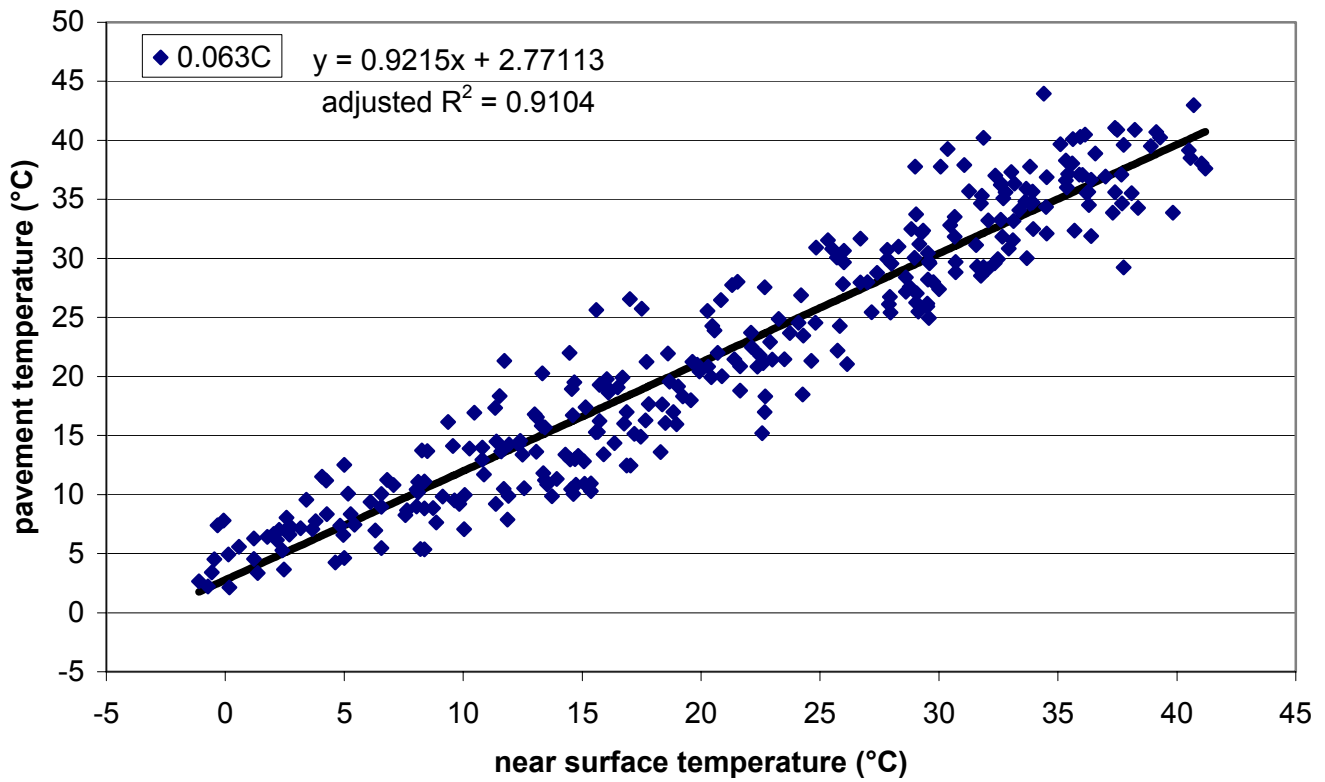


Figure I.26. Section C – daily maximum near surface temperature vs. daily maximum pavement temperature (0.063m depth) with linear model.

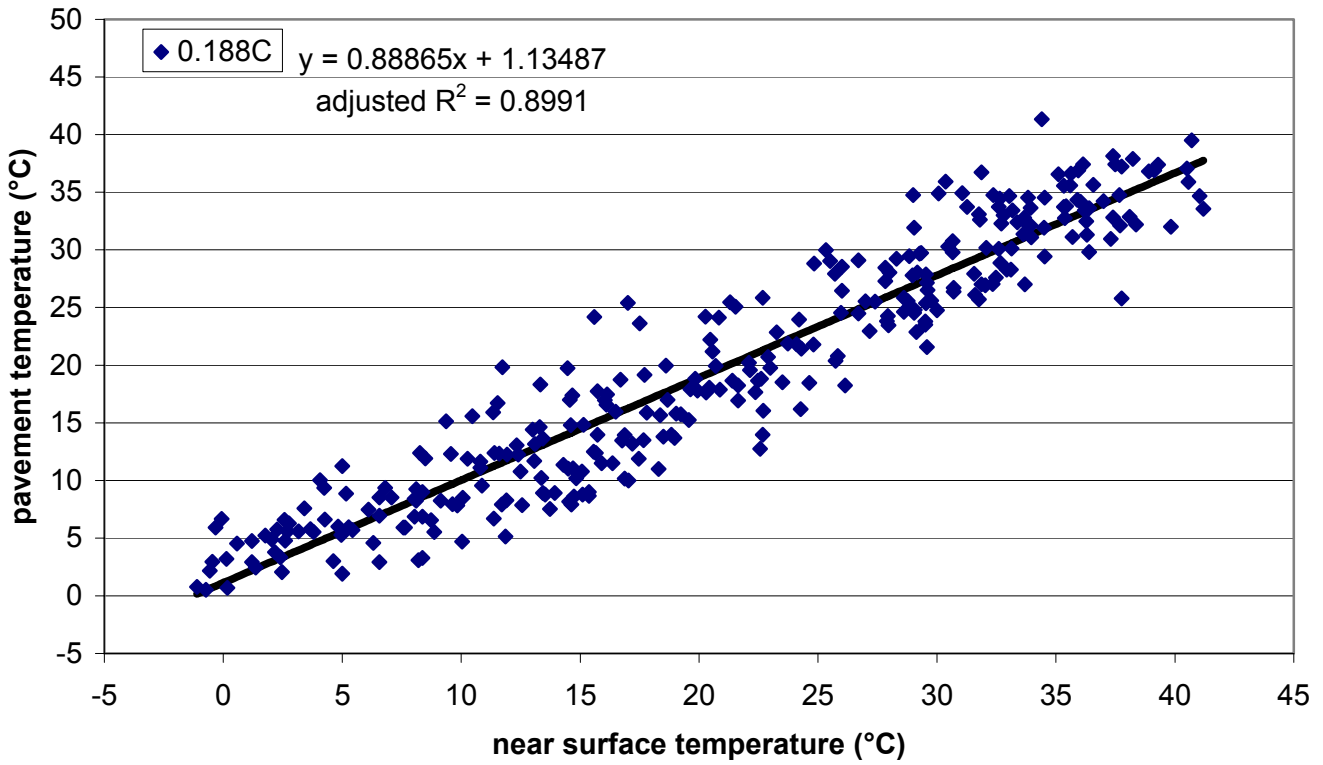


Figure I.27. Section C – daily maximum near surface temperature vs. daily maximum pavement temperature (0.188m depth) with linear model.

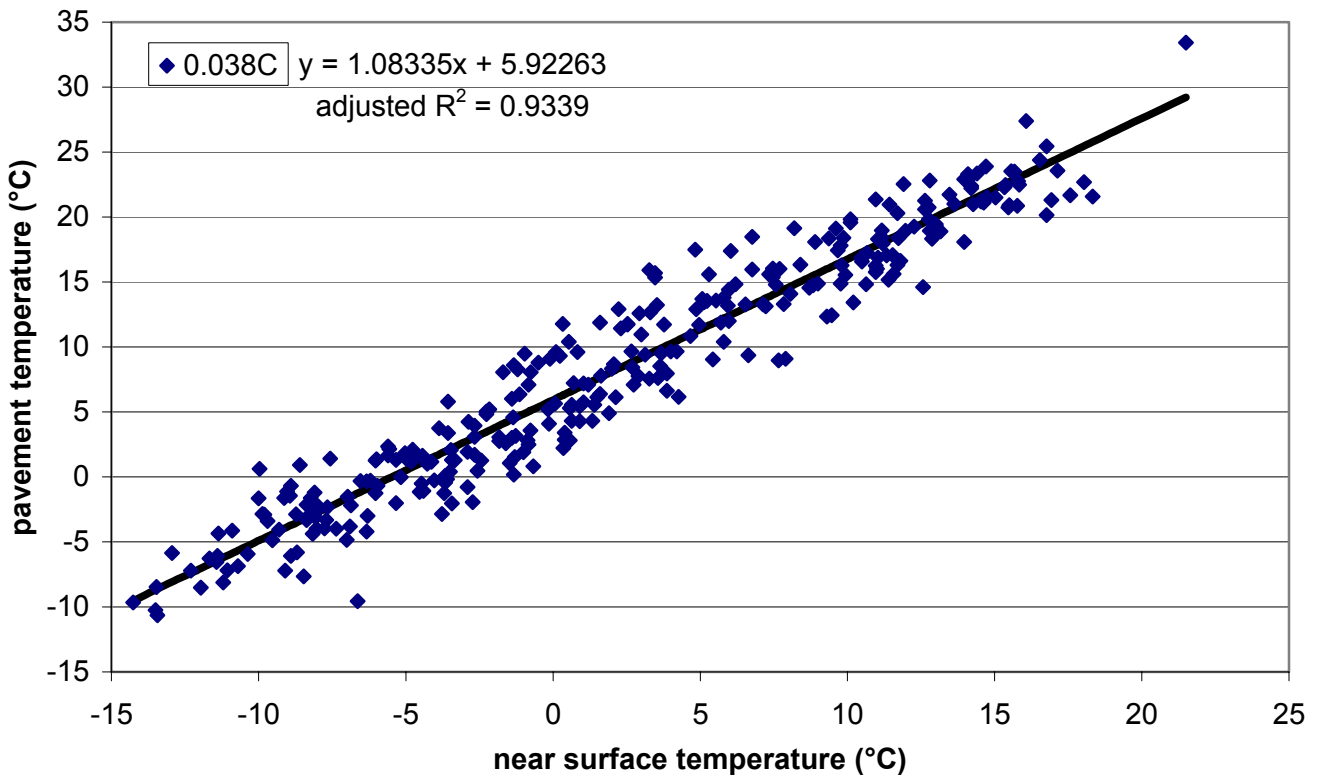


Figure I.28. Section C – daily minimum near surface temperature vs. daily minimum pavement temperature (0.038m depth) with linear model.

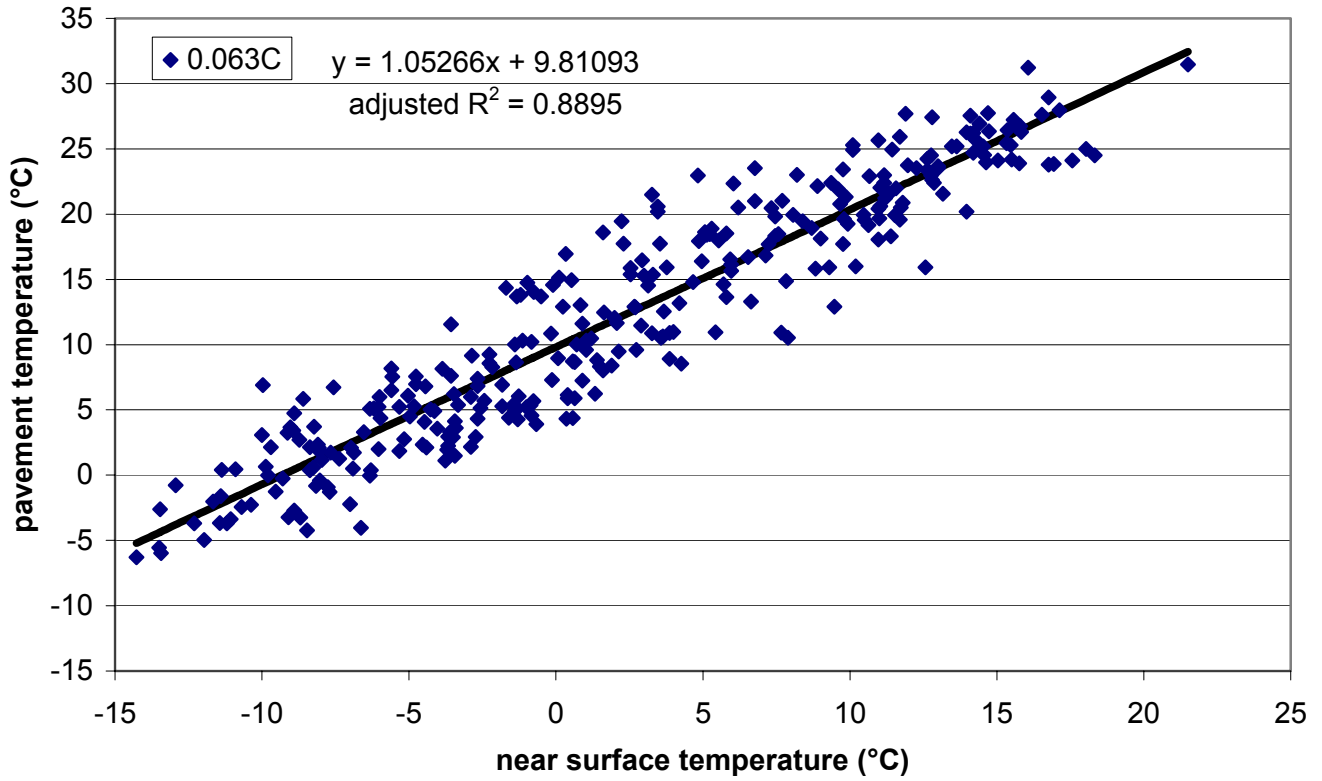


Figure I.29. Section C – daily minimum near surface temperature vs. daily minimum pavement temperature (0.063m depth) with linear model.

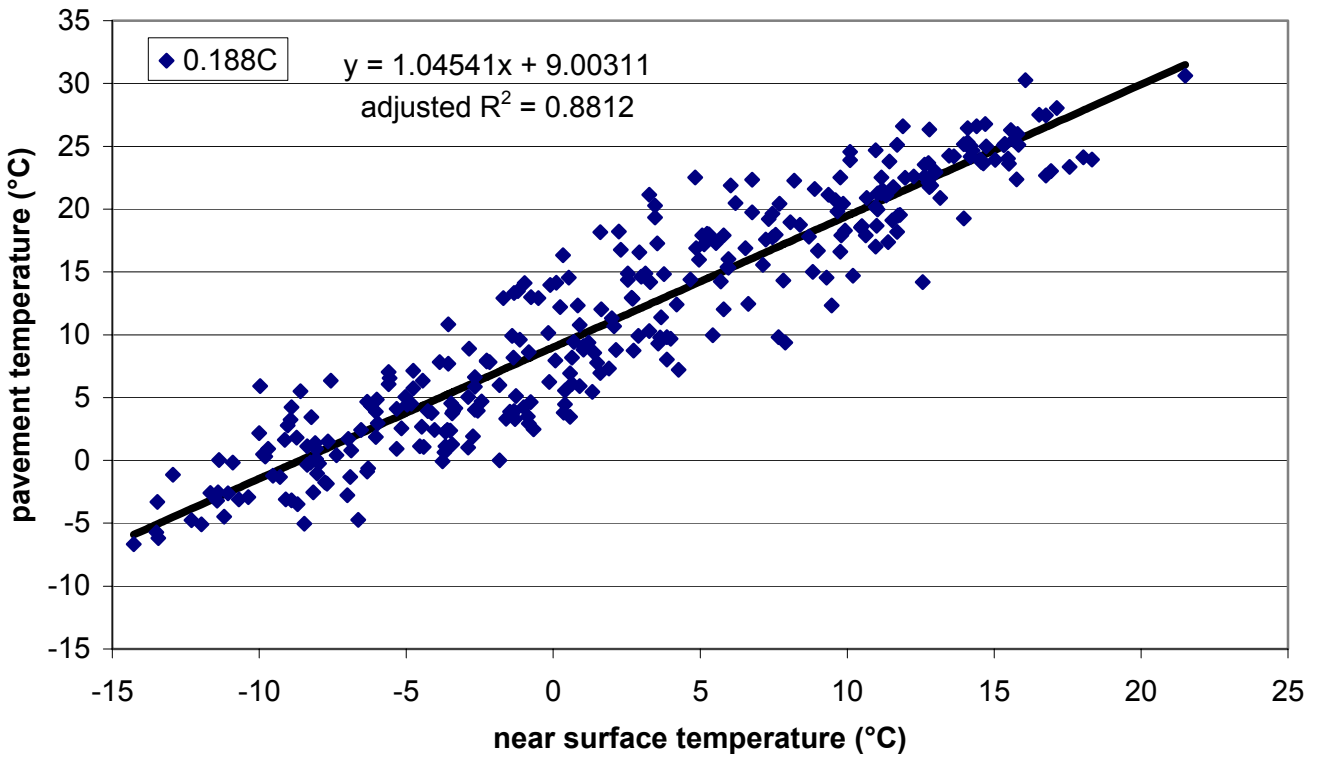


Figure I.30. Section C – daily minimum near surface temperature vs. daily minimum pavement temperature (0.188m depth) with linear model.

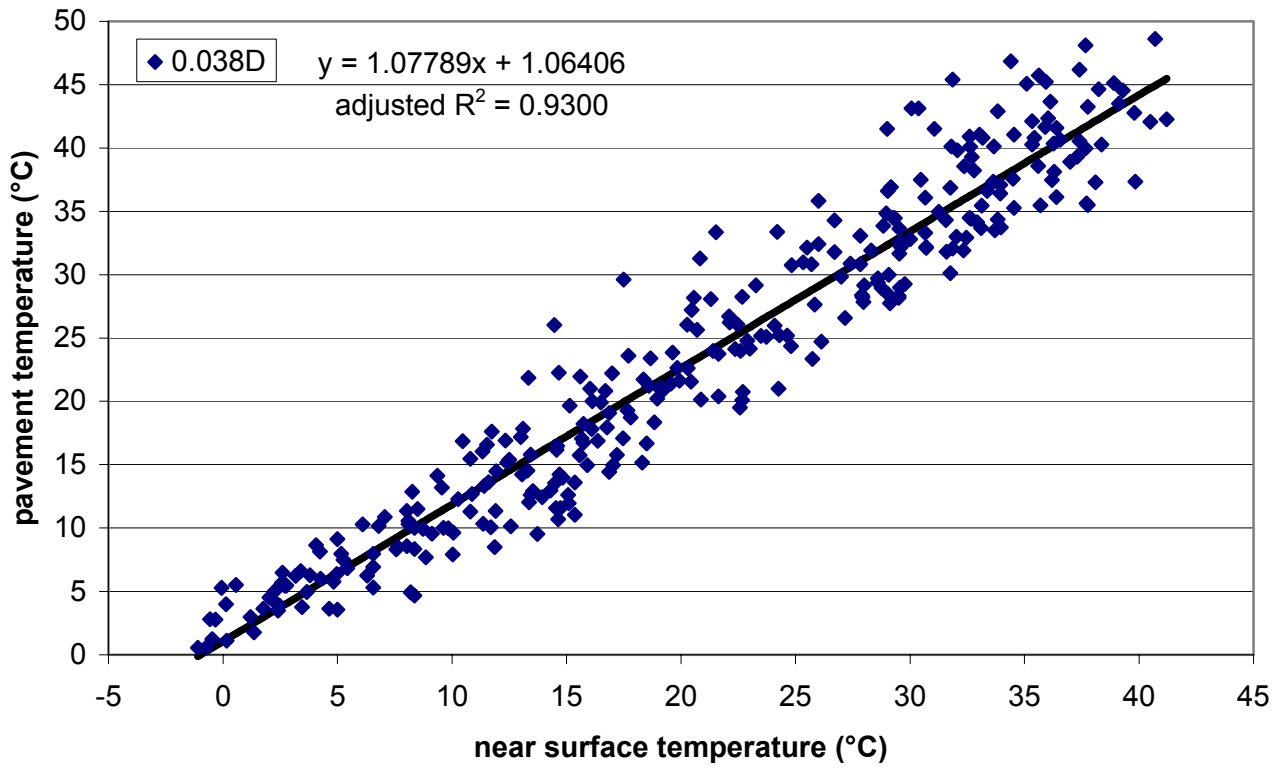


Figure I.31. Section D – daily maximum near surface temperature vs. daily maximum pavement temperature (0.038m depth) with linear model.

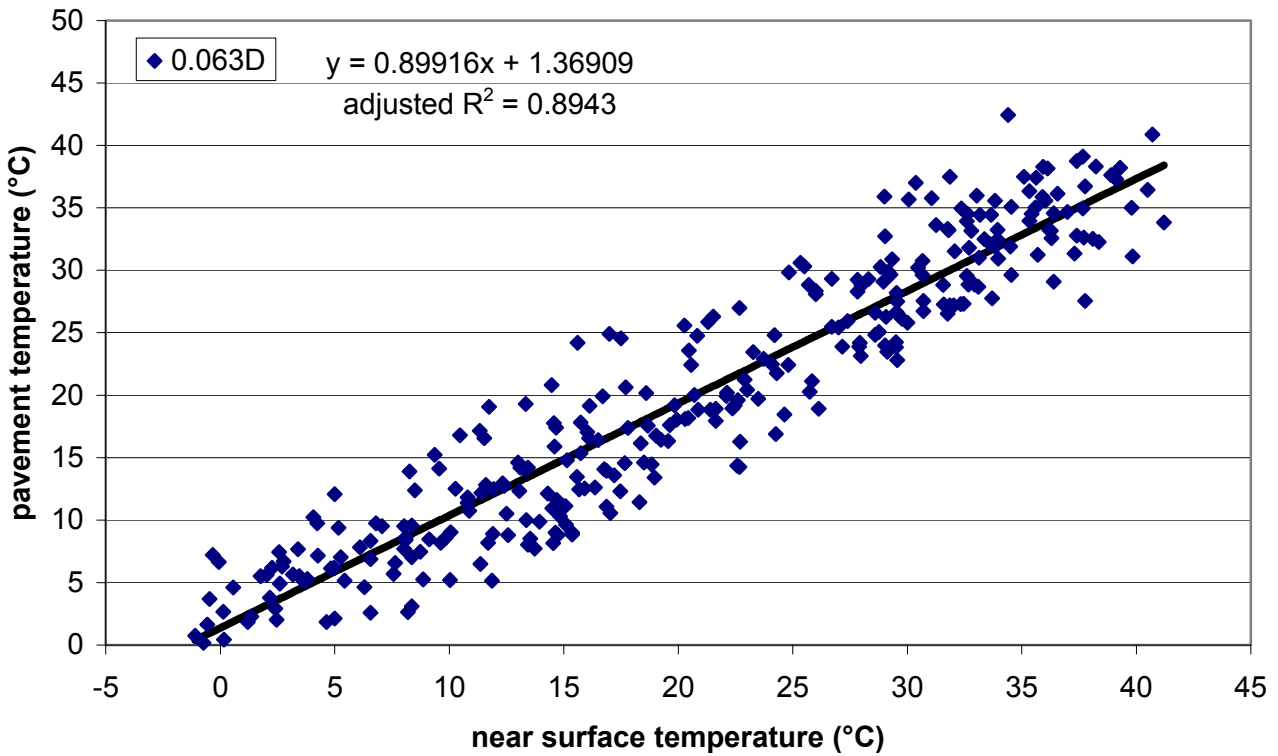


Figure I.32. Section D – daily maximum near surface temperature vs. daily maximum pavement temperature (0.063m depth) with linear model.

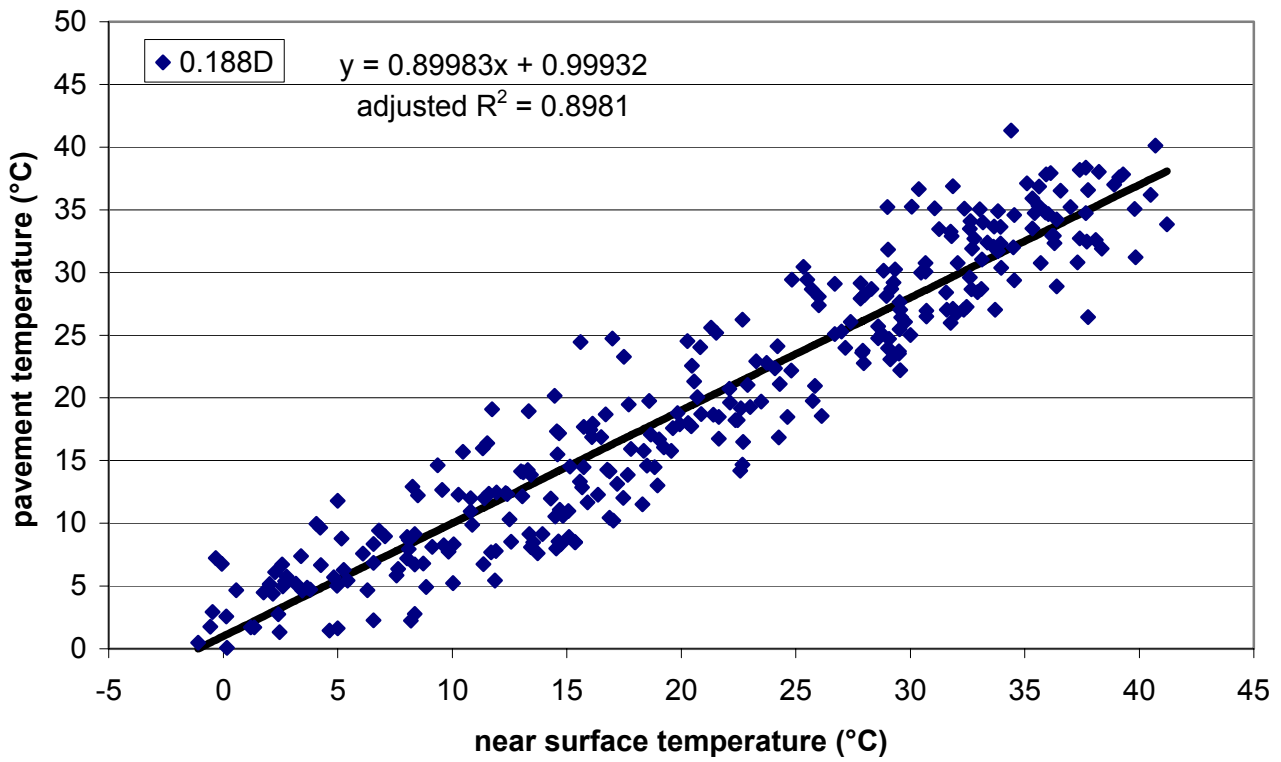


Figure I.33. Section D – daily maximum near surface temperature vs. daily maximum pavement temperature (0.188m depth) with linear model.

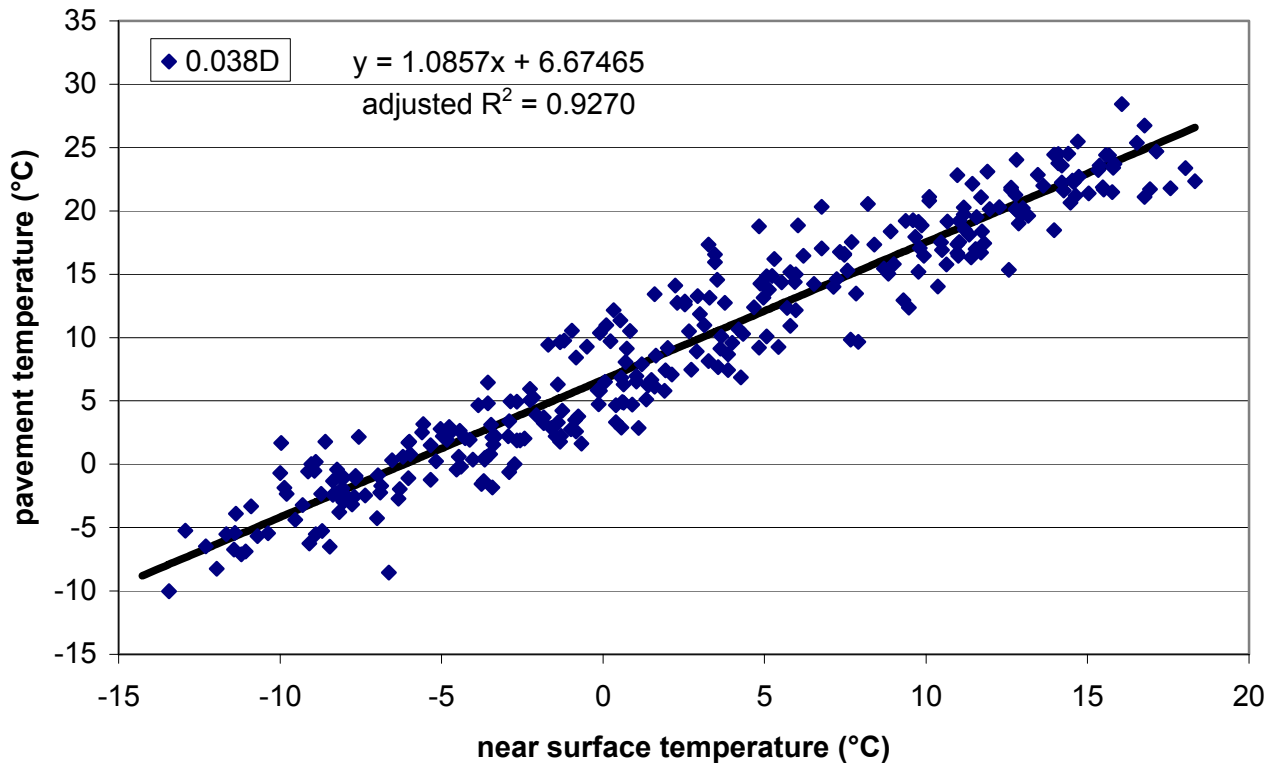


Figure I.34. Section D – daily minimum near surface temperature vs. daily minimum pavement temperature (0.038m depth) with linear model.

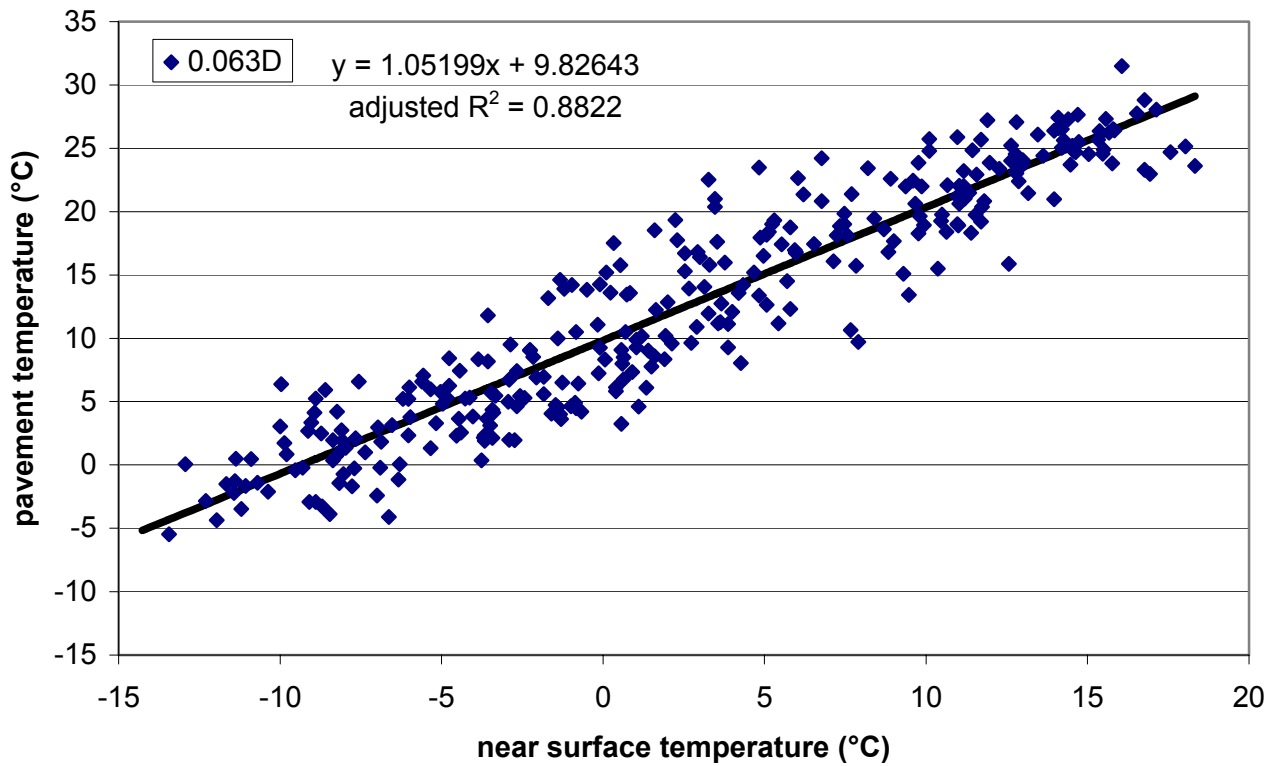


Figure I.35. Section D – daily minimum near surface temperature vs. daily minimum pavement temperature (0.063m depth) with linear model.

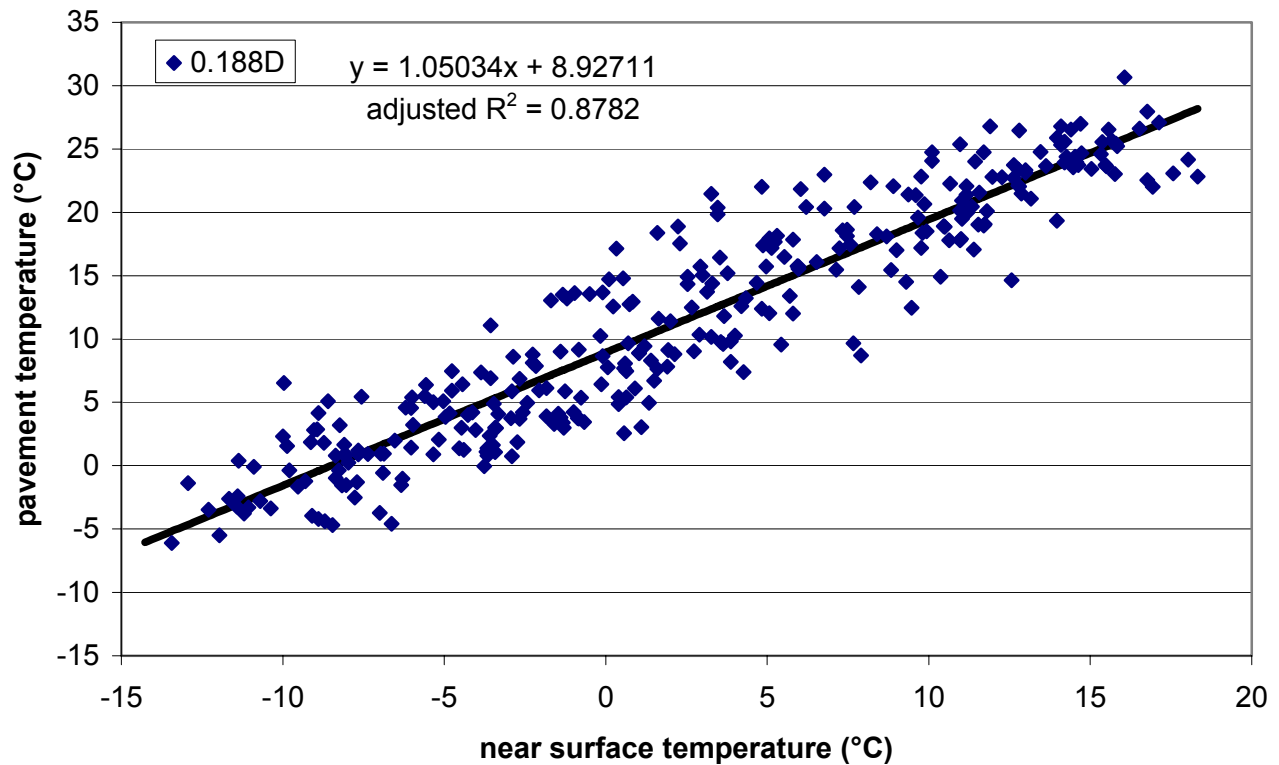


Figure I.36. Section D – daily minimum near surface temperature vs. daily minimum pavement temperature (0.188m depth) with linear model.

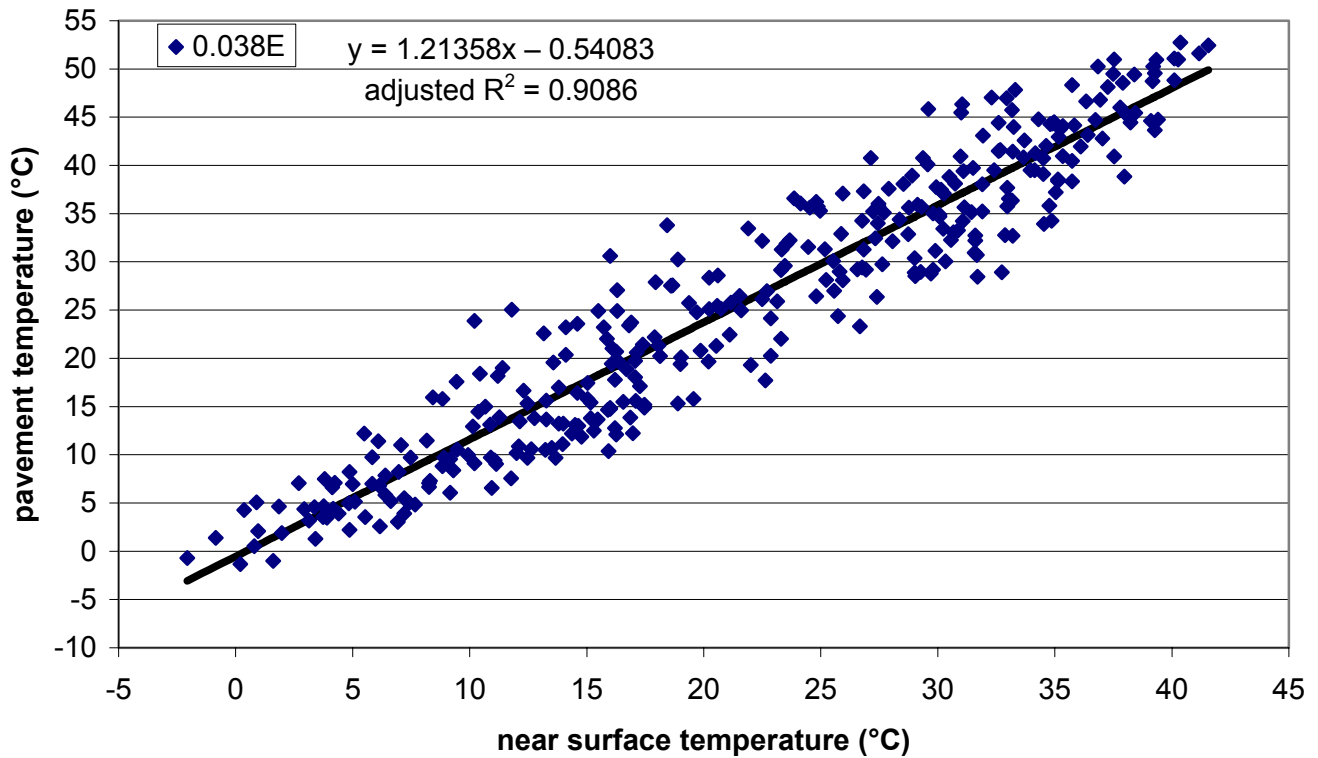


Figure I.37. Section E – daily maximum near surface temperature vs. daily maximum pavement temperature (0.038m depth) with linear model.

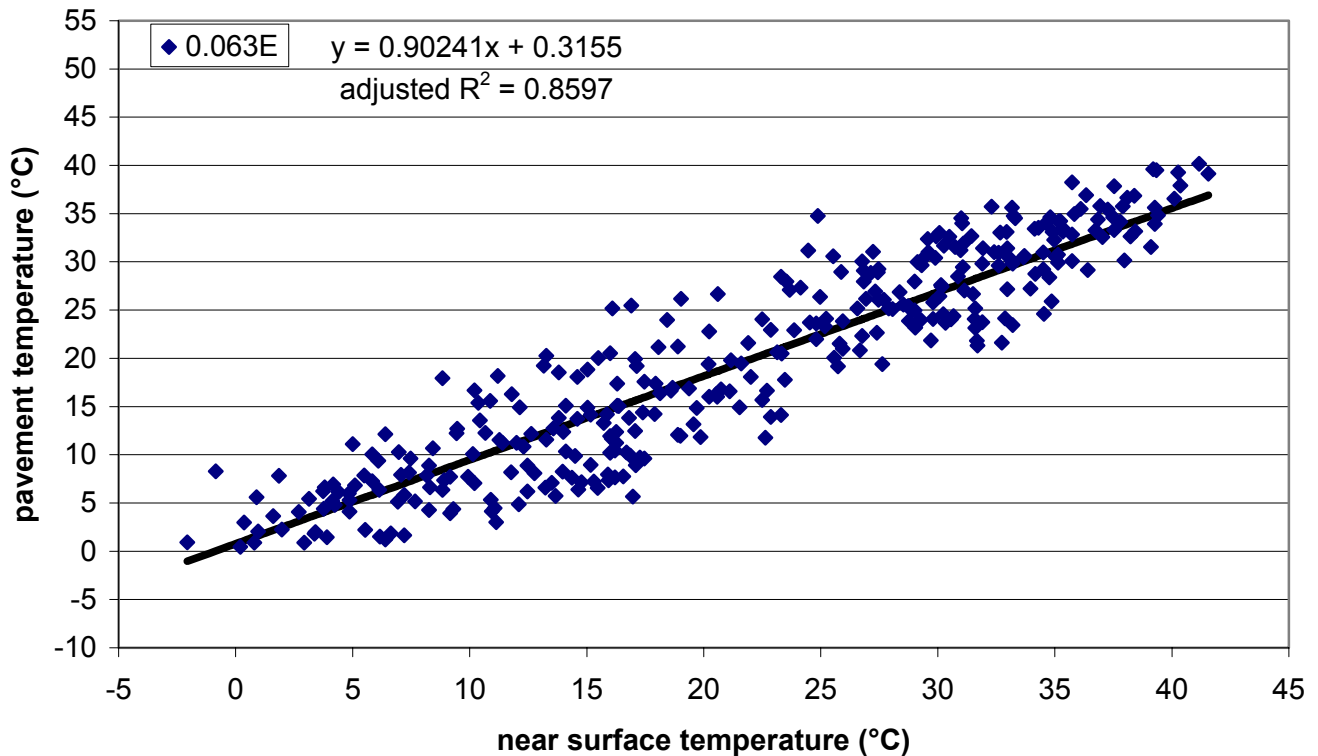


Figure I.38. Section E – daily maximum near surface temperature vs. daily maximum pavement temperature (0.063m depth) with linear model.

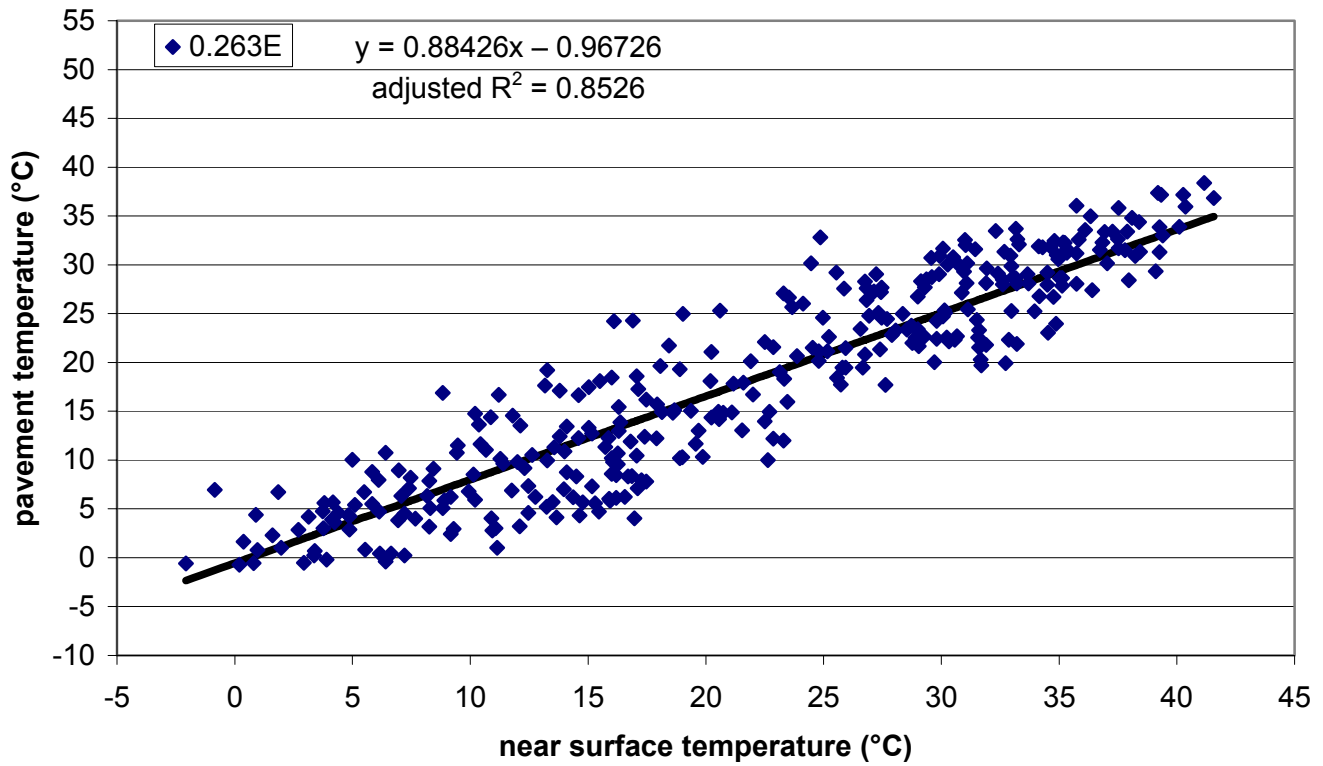


Figure I.39. Section E – daily maximum near surface temperature vs. daily maximum pavement temperature (0.263m depth) with linear model.

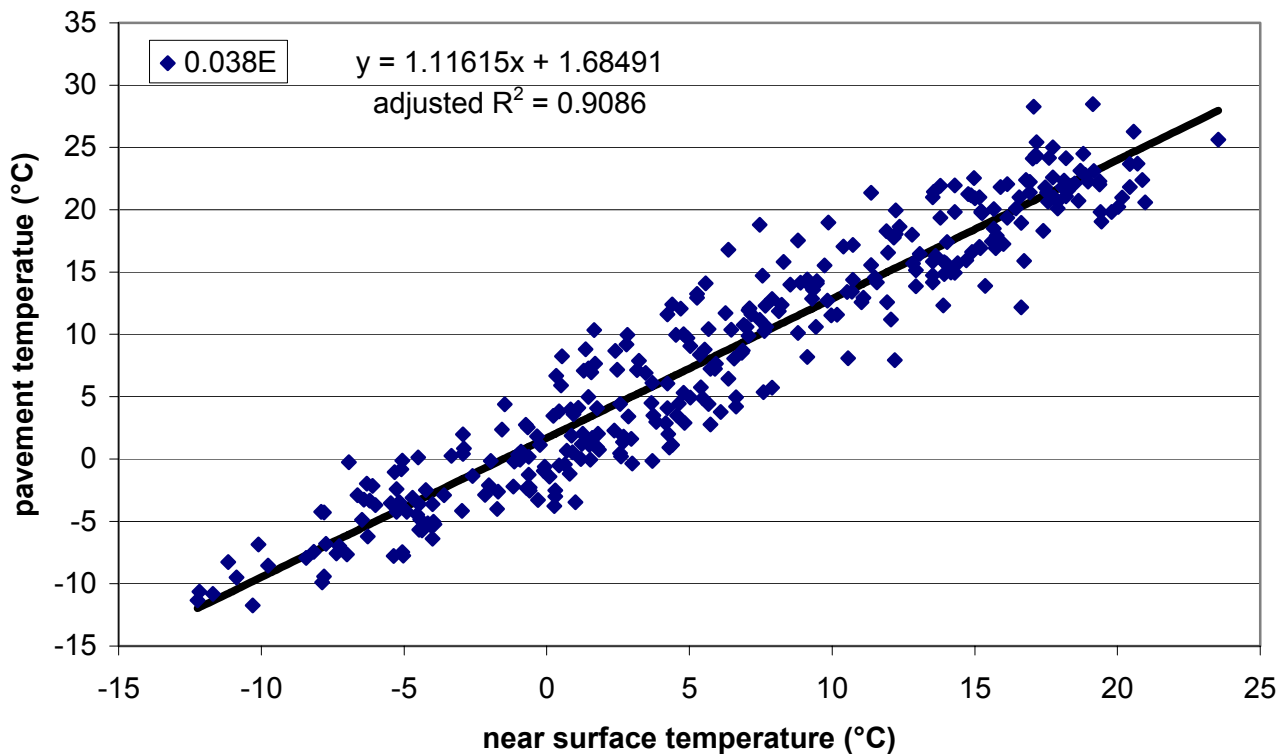


Figure I.40. Section E – daily minimum near surface temperature vs. daily minimum pavement temperature (0.038m depth) with linear model.

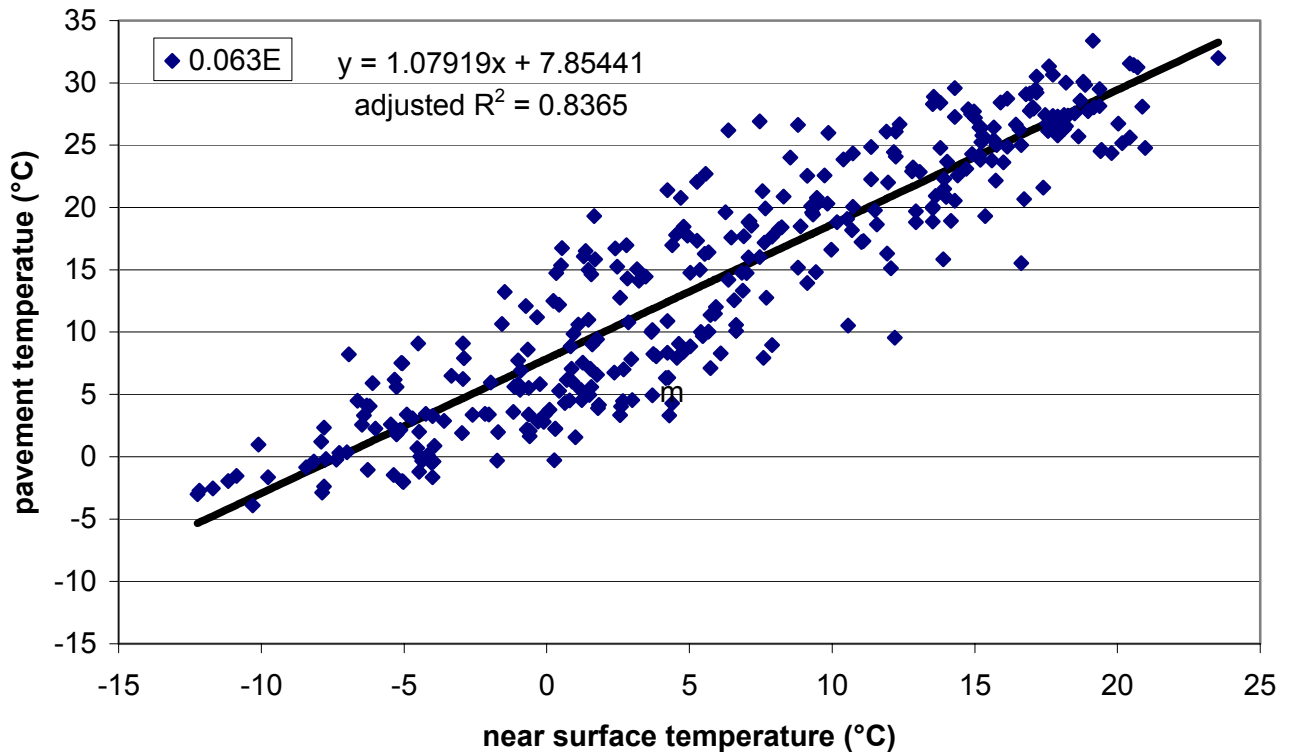


Figure I.41. Section E – daily minimum near surface temperature vs. daily minimum pavement temperature (0.063m depth) with linear model.

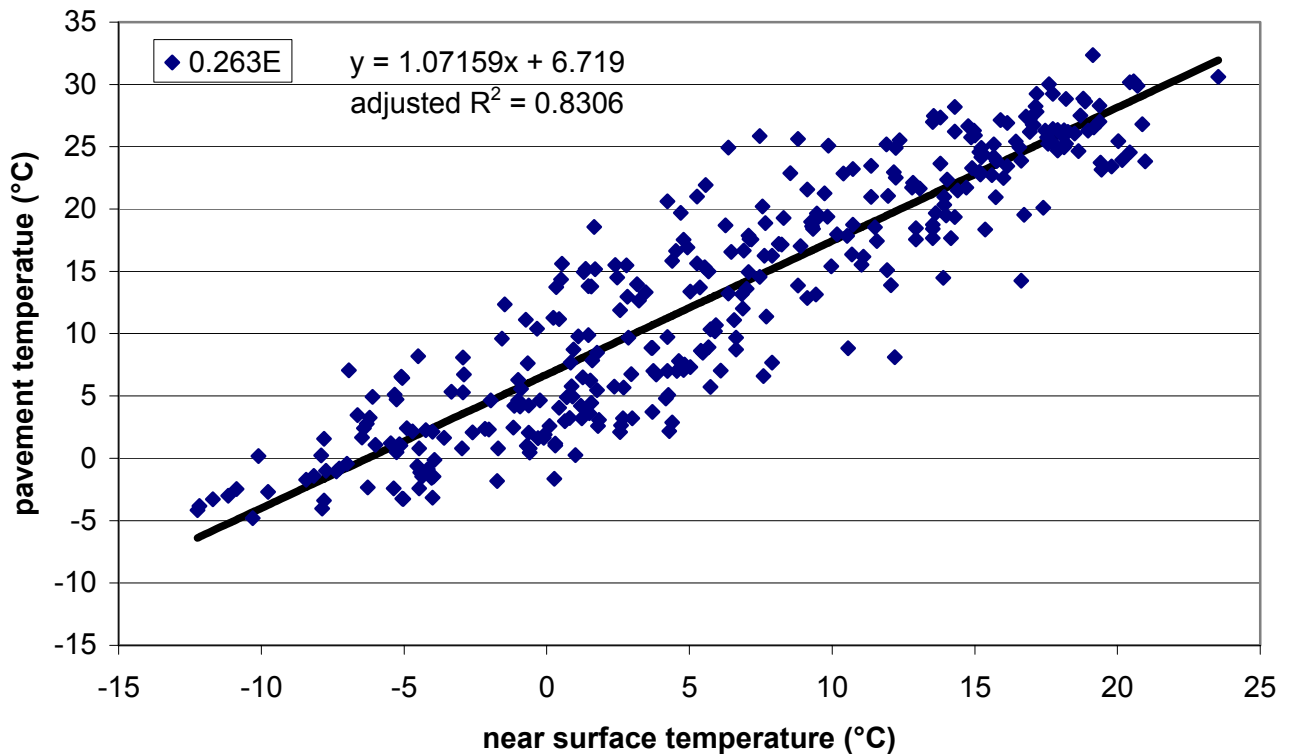


Figure I.42. Section E – daily minimum near surface temperature vs. daily minimum pavement temperature (0.263m depth) with linear model.

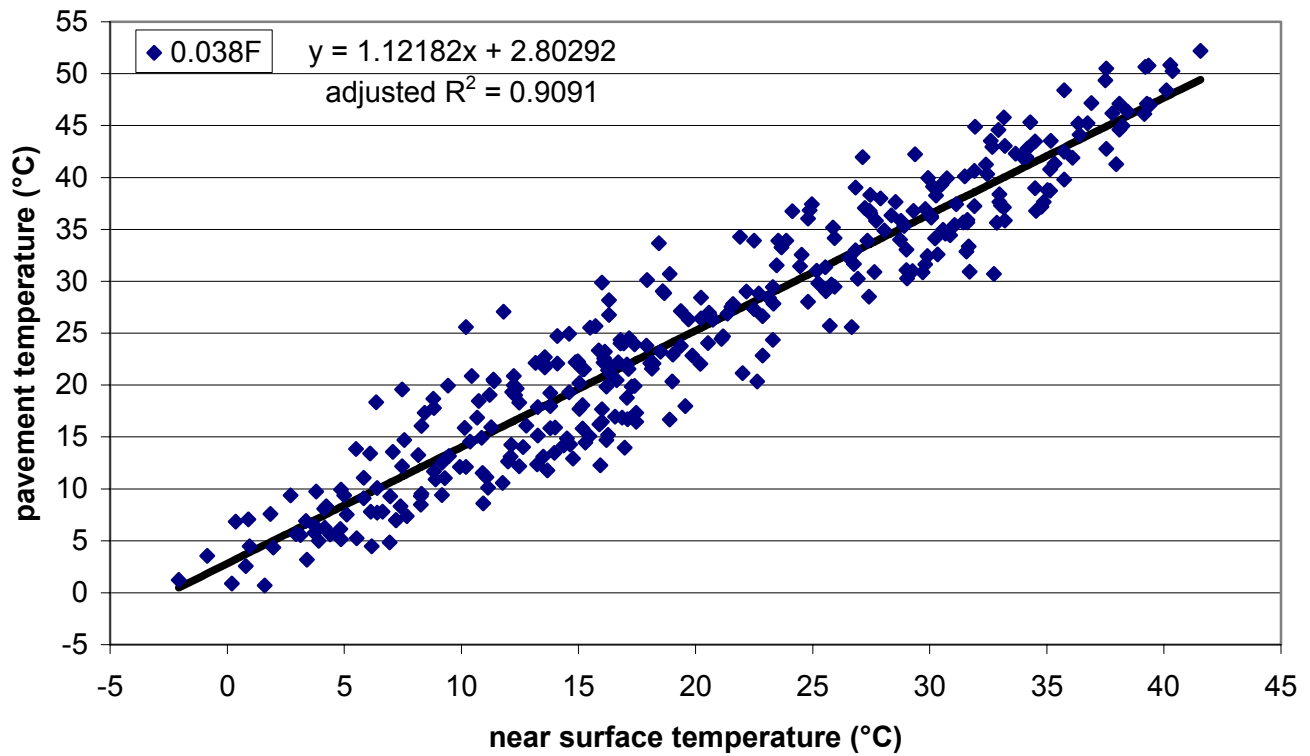


Figure I.43. Section F – daily maximum near surface temperature vs. daily maximum pavement temperature (0.038m depth) with linear model.

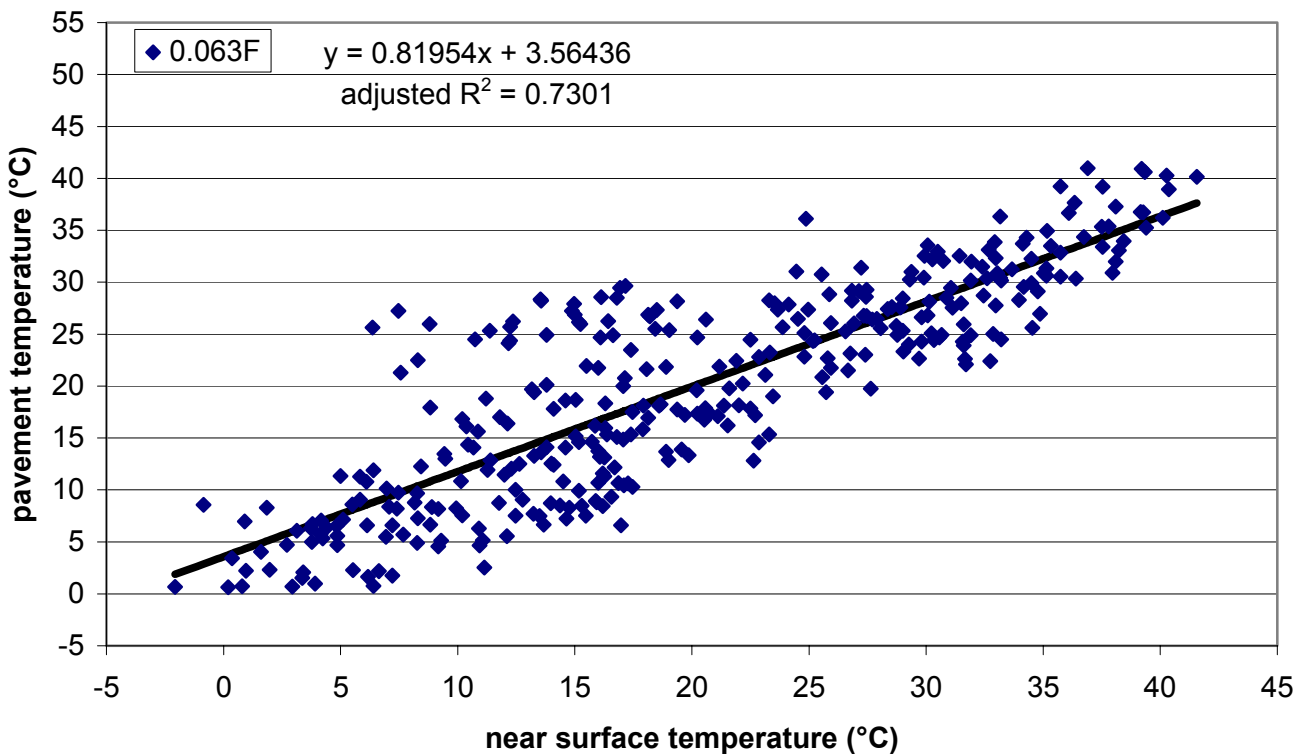


Figure I.44. Section F – daily maximum near surface temperature vs. daily maximum pavement temperature (0.063m depth) with linear model.

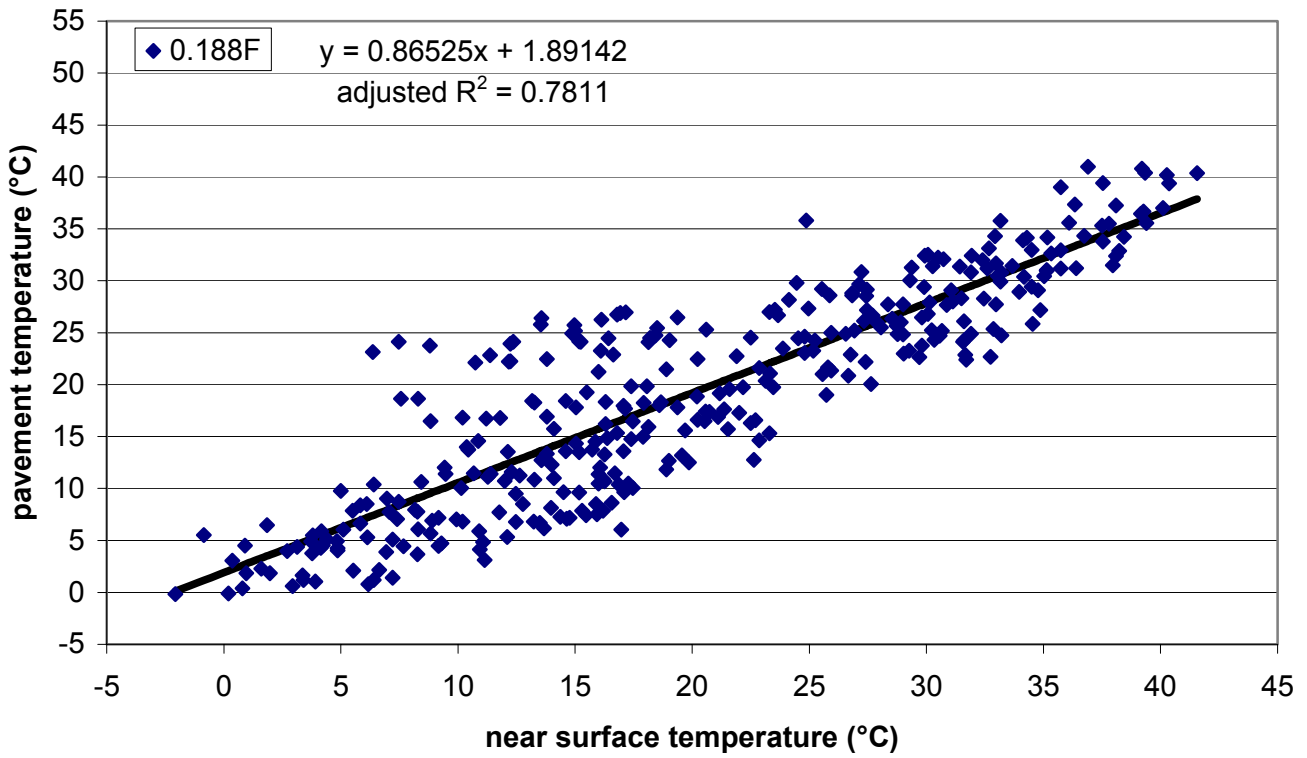


Figure I.45. Section F – daily maximum near surface temperature vs. daily maximum pavement temperature (0.188m depth) with linear model.

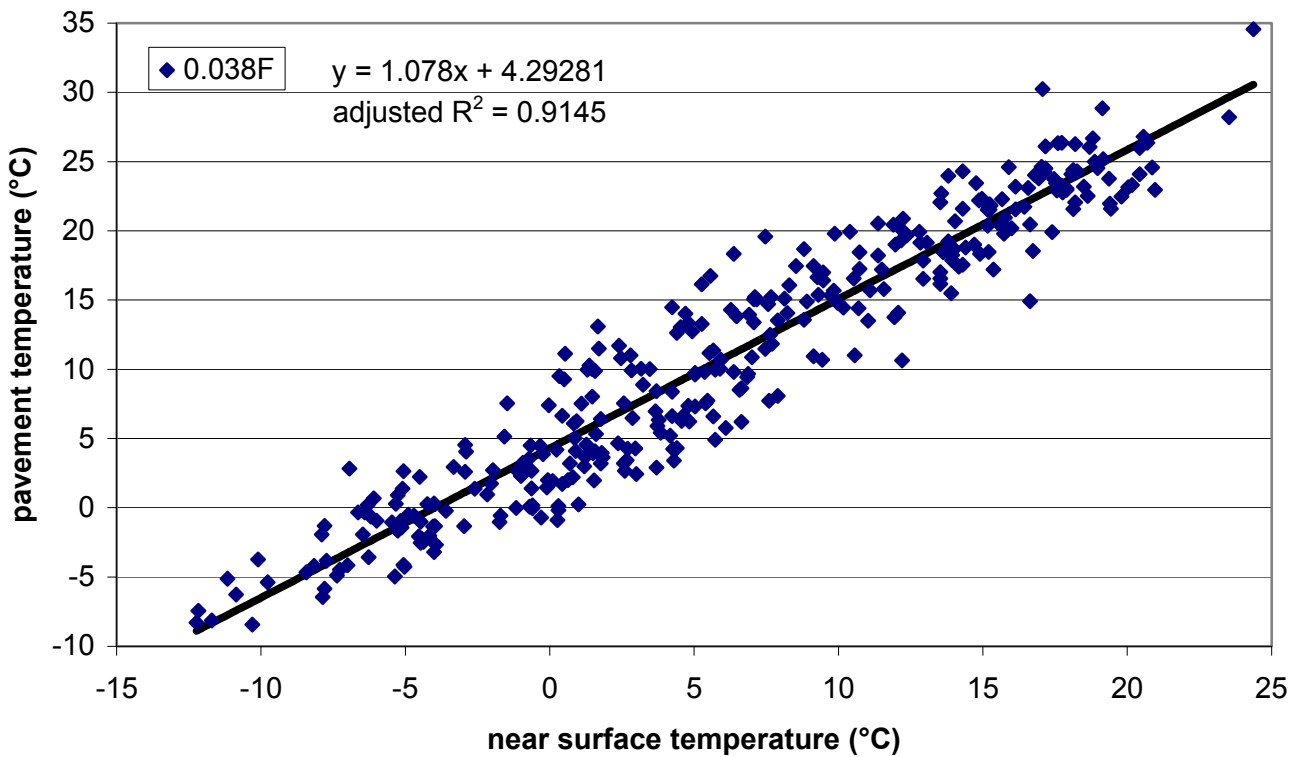


Figure I.46. Section F – daily minimum near surface temperature vs. daily minimum pavement temperature (0.038m depth) with linear model.

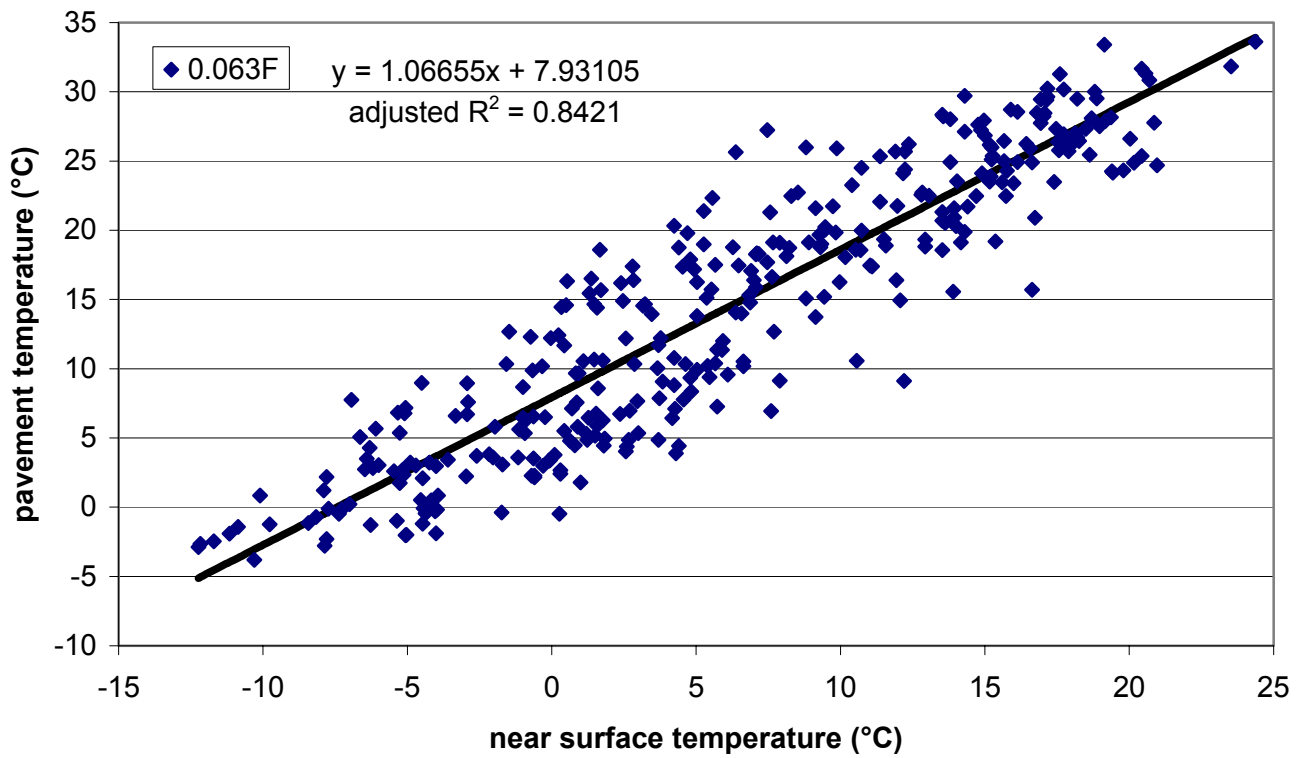


Figure I.47. Section F – daily minimum near surface temperature vs. daily minimum pavement temperature (0.063m depth) with linear model.

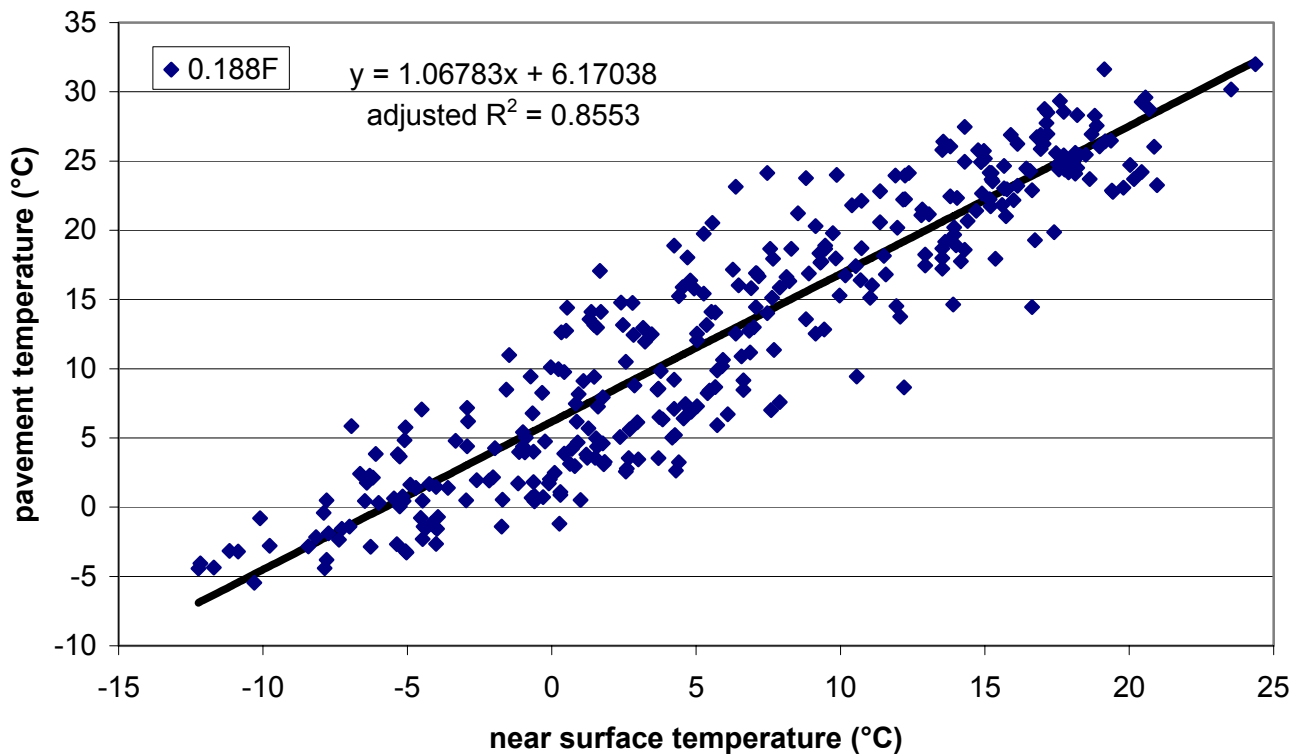


Figure I.48. Section F – daily minimum near surface temperature vs. daily minimum pavement temperature (0.188m depth) with linear model.

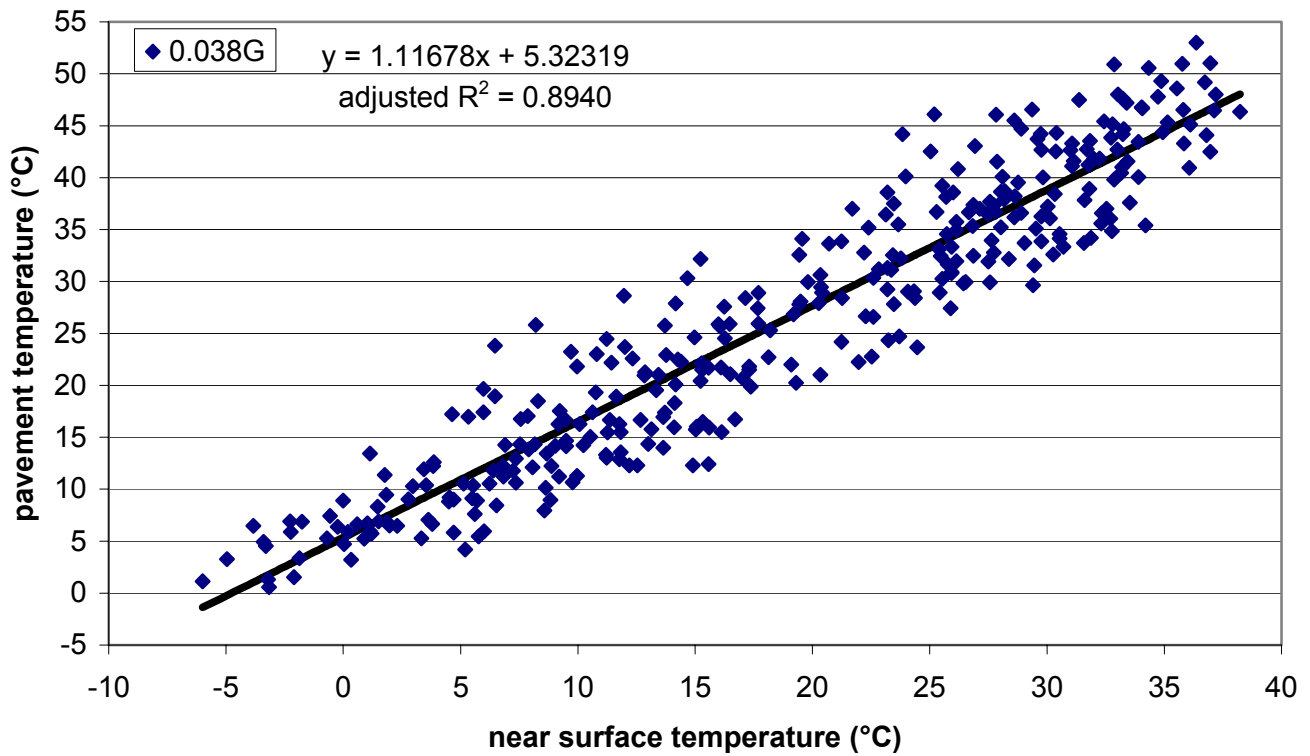


Figure I.49. Section G – daily maximum near surface temperature vs. daily maximum pavement temperature (0.038m depth) with linear model.

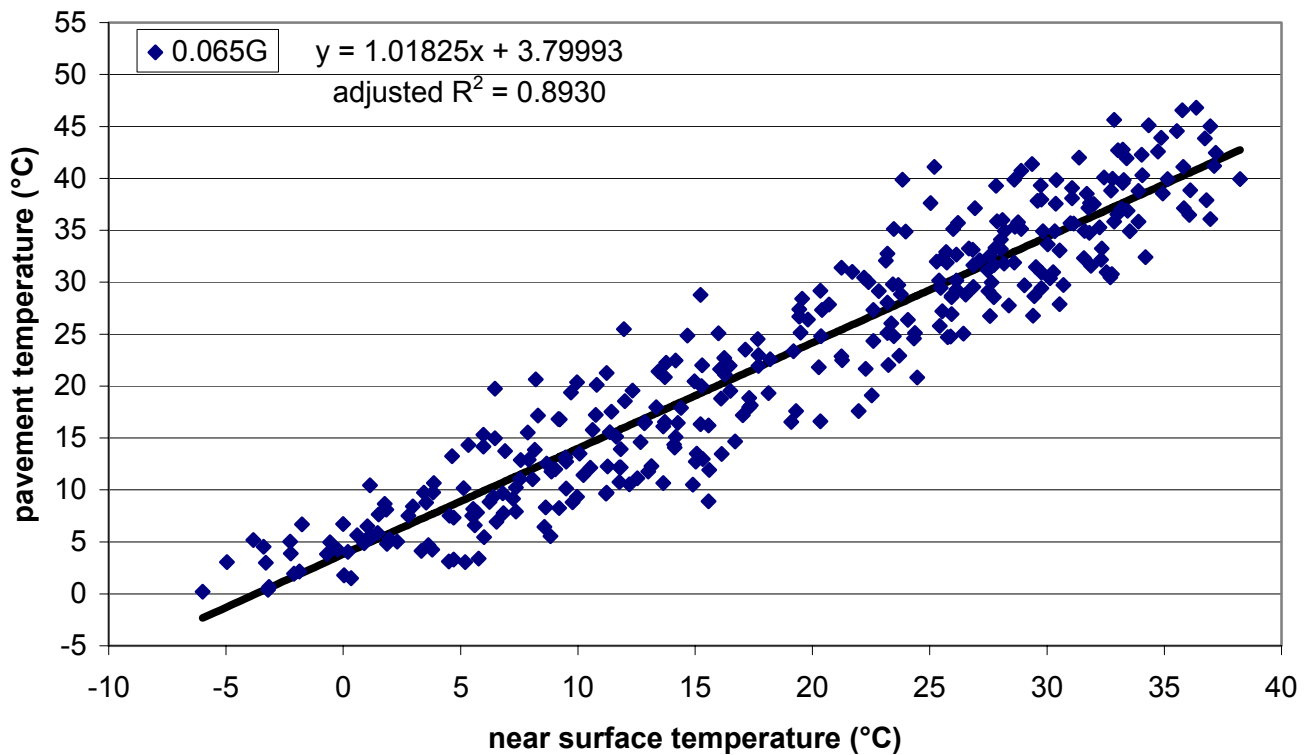


Figure I.50. Section G– daily maximum near surface temperature vs. daily maximum pavement temperature (0.065m depth) with linear model.

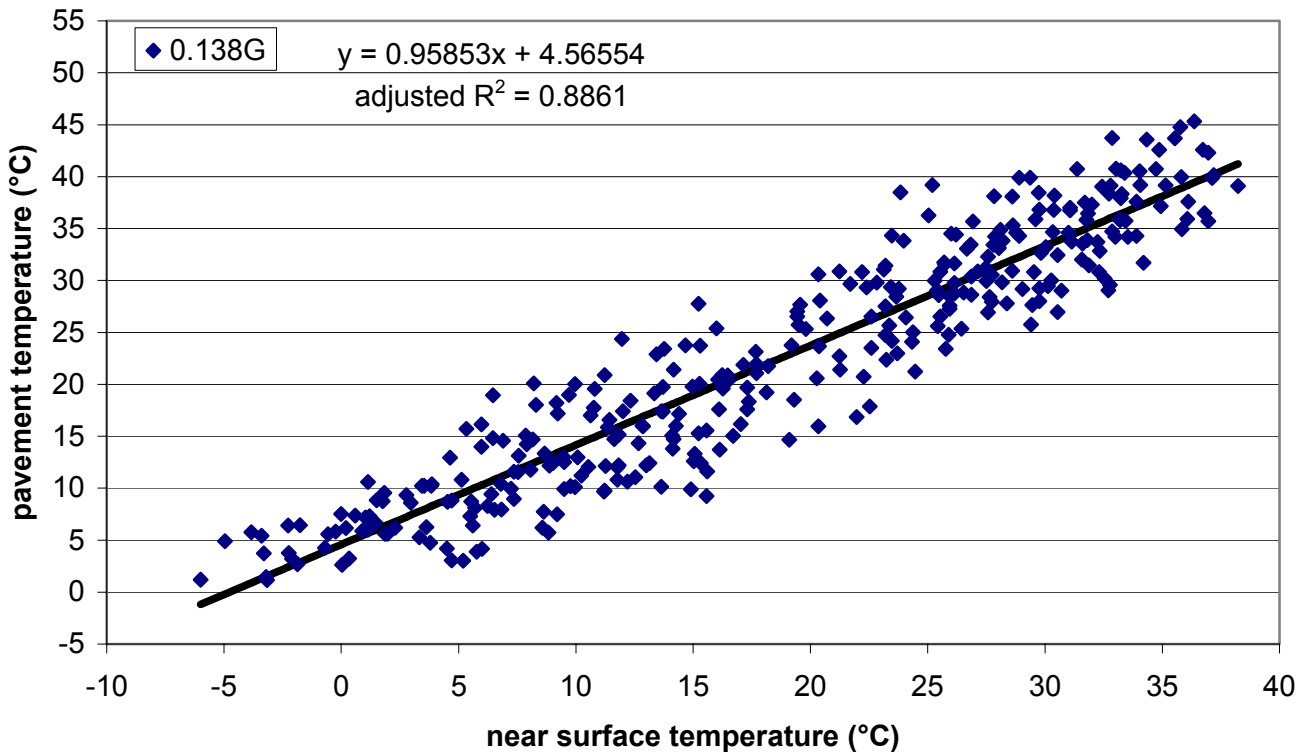


Figure I.51. Section G – daily maximum near surface temperature vs. daily maximum pavement temperature (0.138m depth) with linear model.

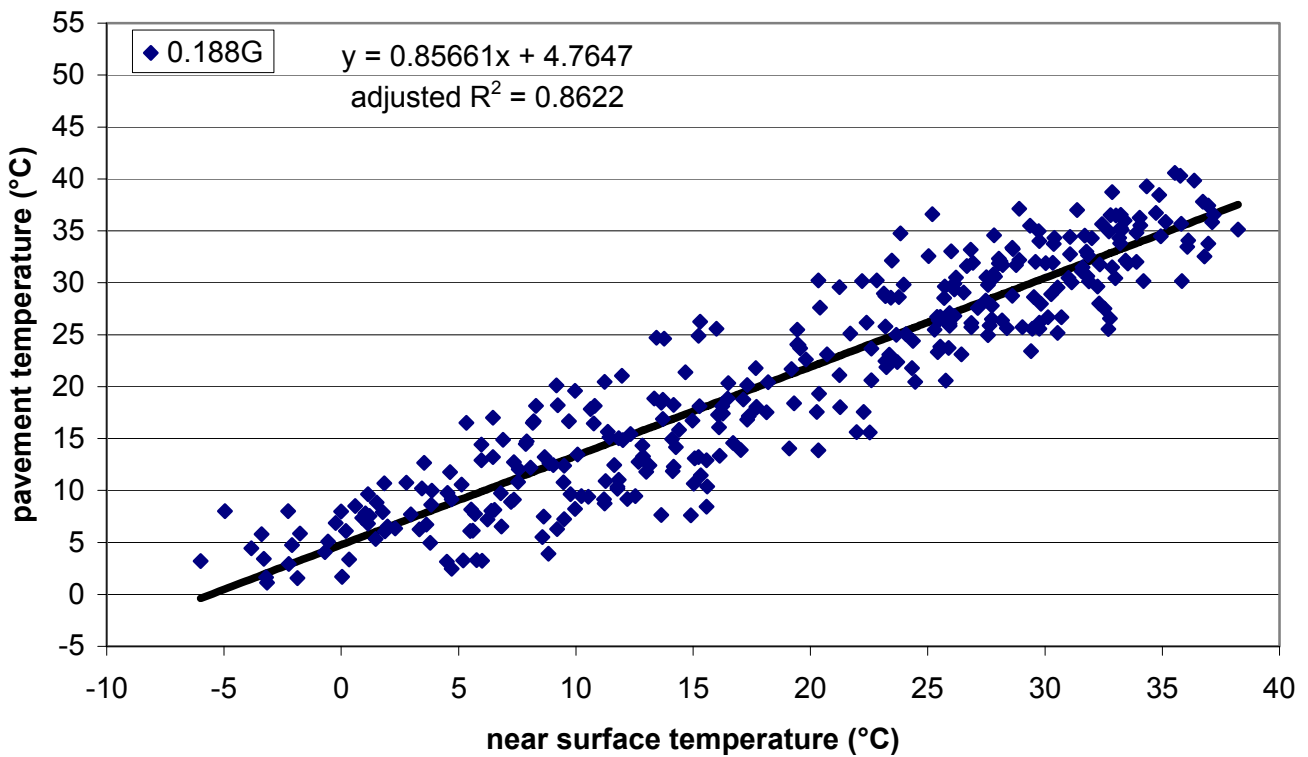


Figure I.52. Section G – daily maximum near surface temperature vs. daily maximum pavement temperature (0.188m depth) with linear model.

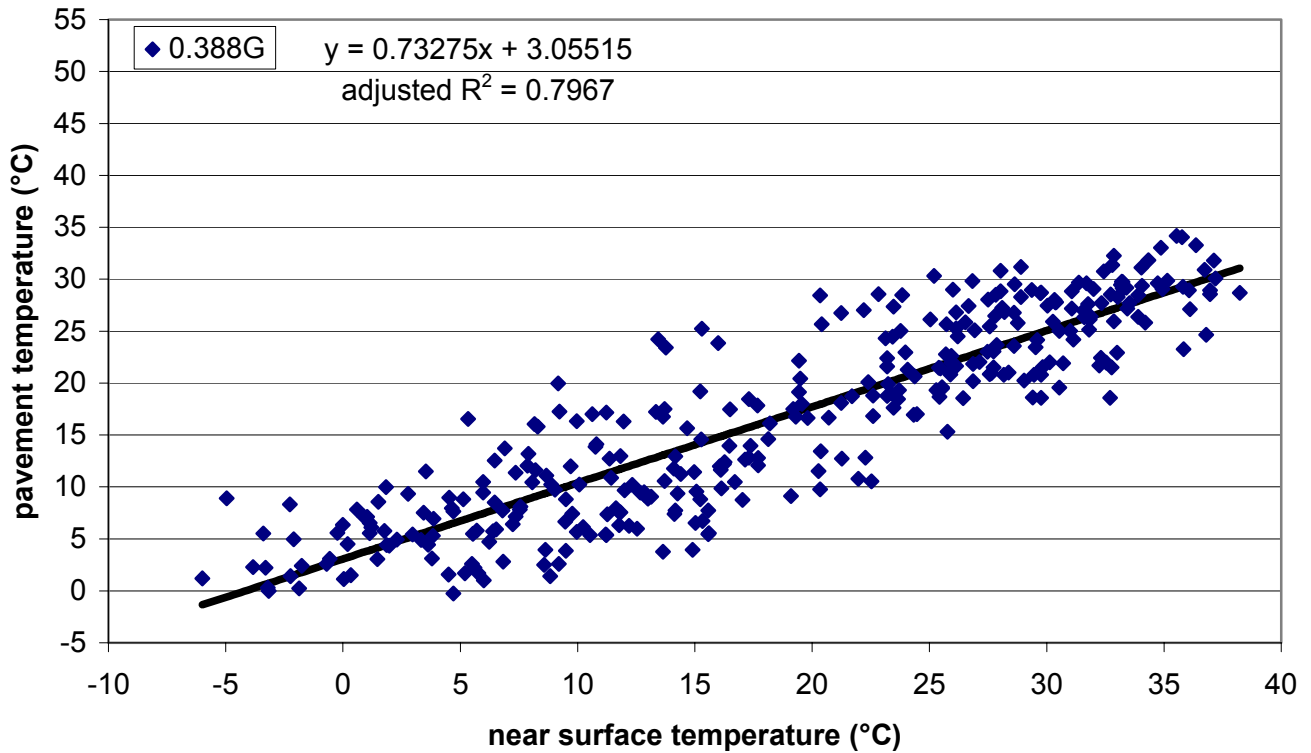


Figure I.53. Section G – daily maximum near surface temperature vs. daily maximum pavement temperature (0.388m depth) with linear model.

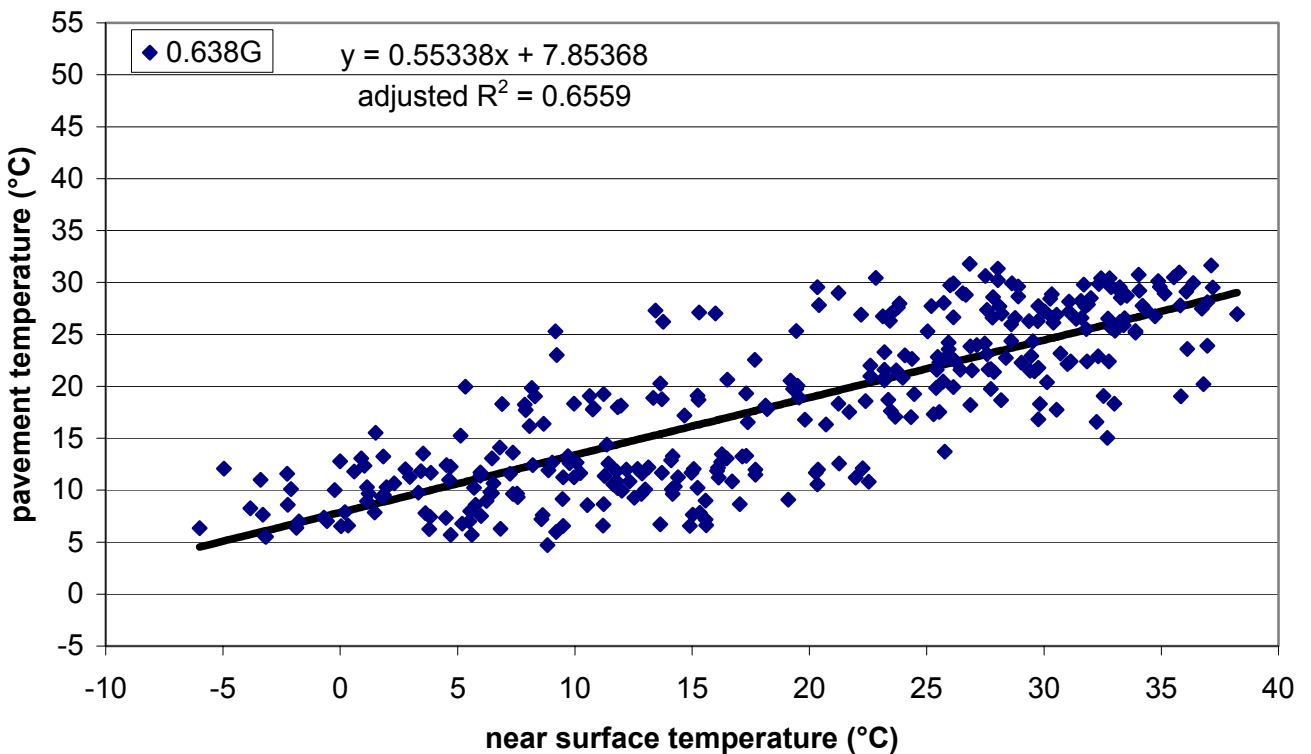


Figure I.54. Section G – daily maximum near surface temperature vs. daily maximum pavement temperature (0.638m depth) with linear model.

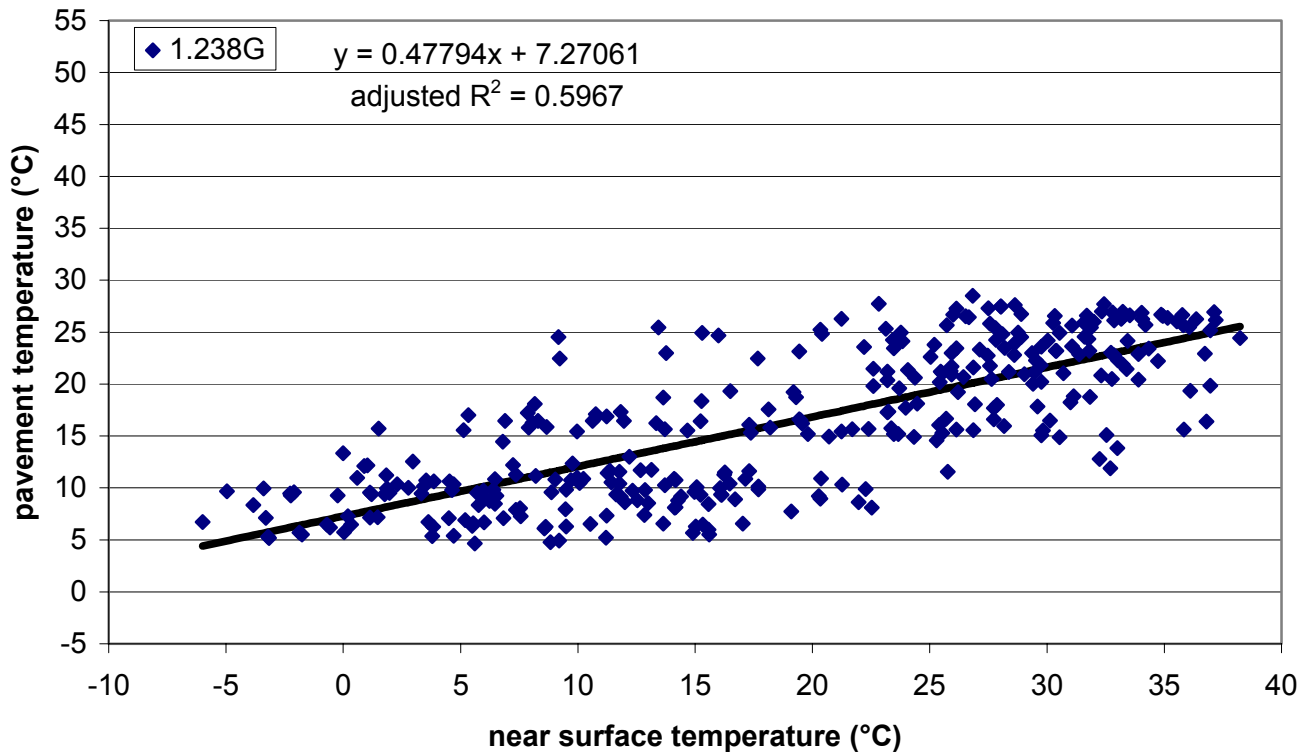


Figure I.55. Section G – daily maximum near surface temperature vs. daily maximum pavement temperature (1.238m depth) with linear model.

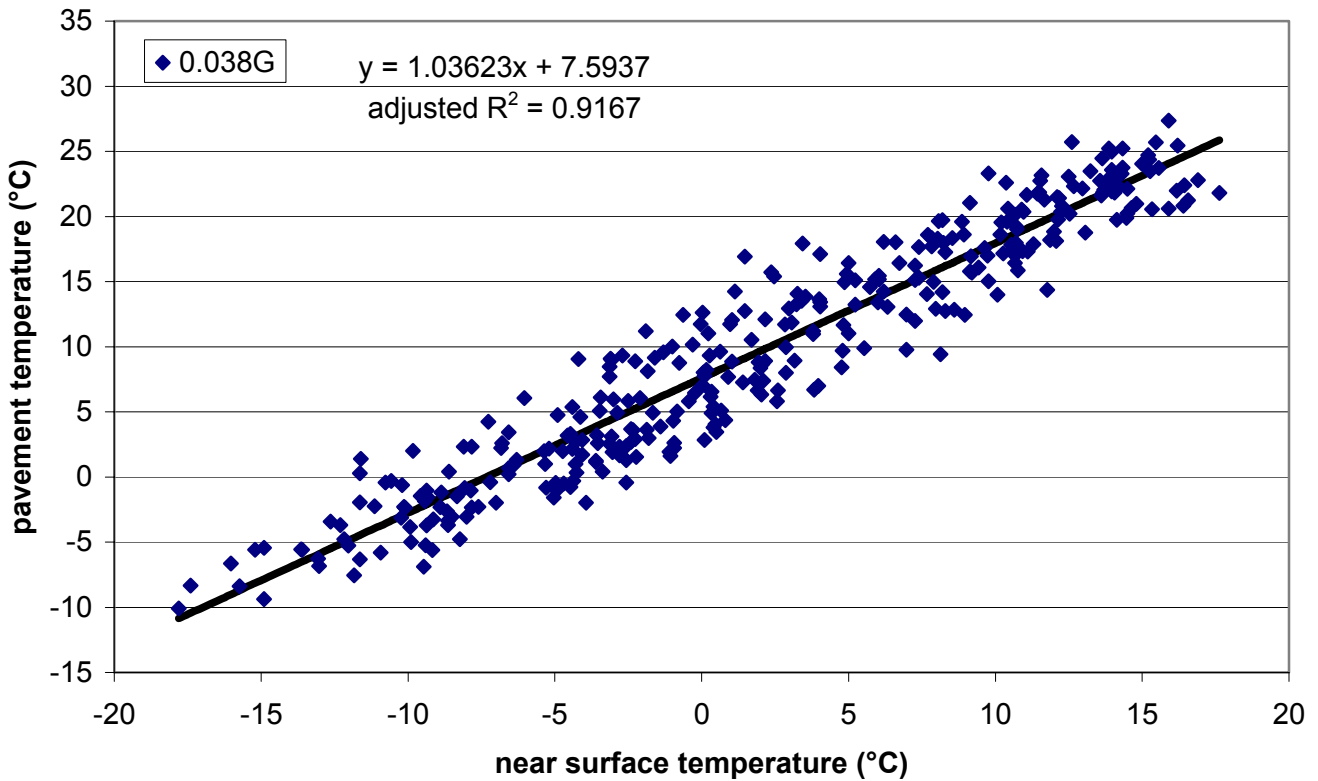


Figure I.56. Section G – daily minimum near surface temperature vs. daily minimum pavement temperature (0.038m depth) with linear model.

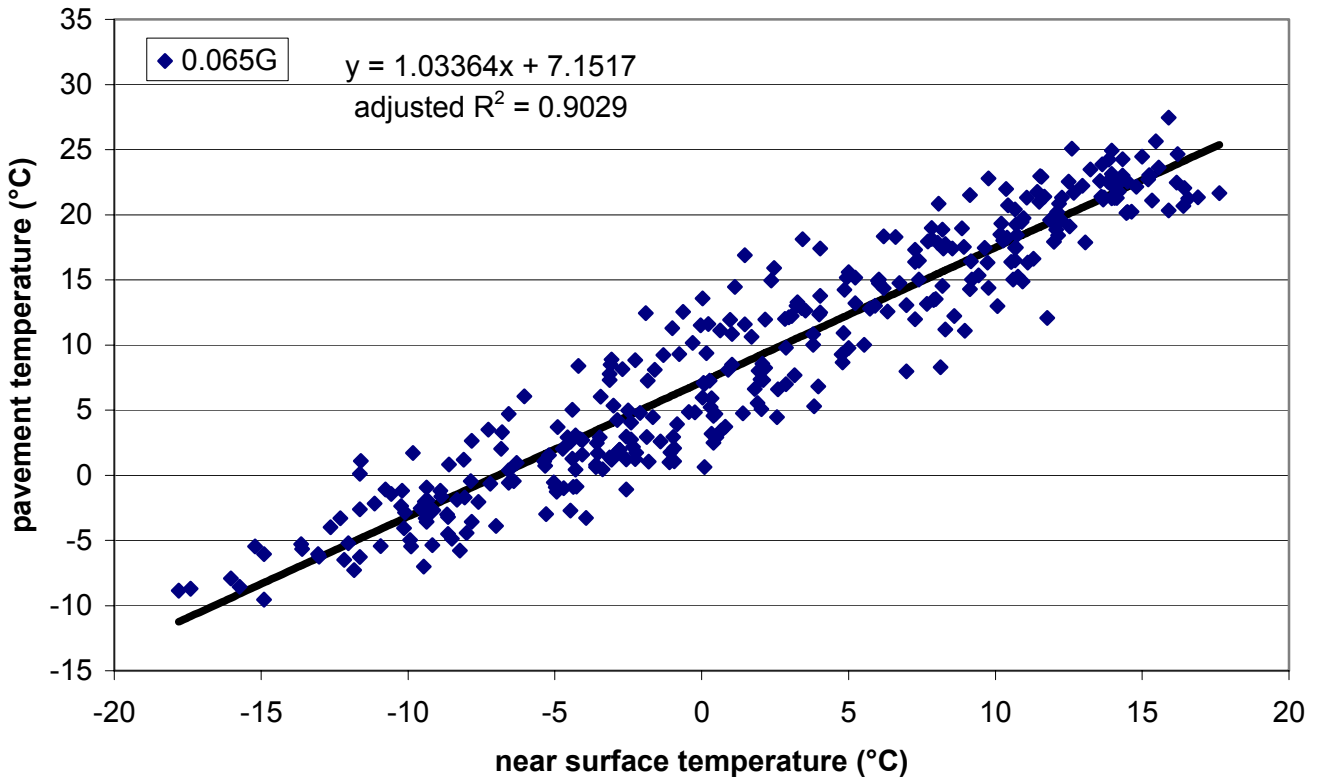


Figure I.57. Section G – daily minimum near surface temperature vs. daily minimum pavement temperature (0.065m depth) with linear model.

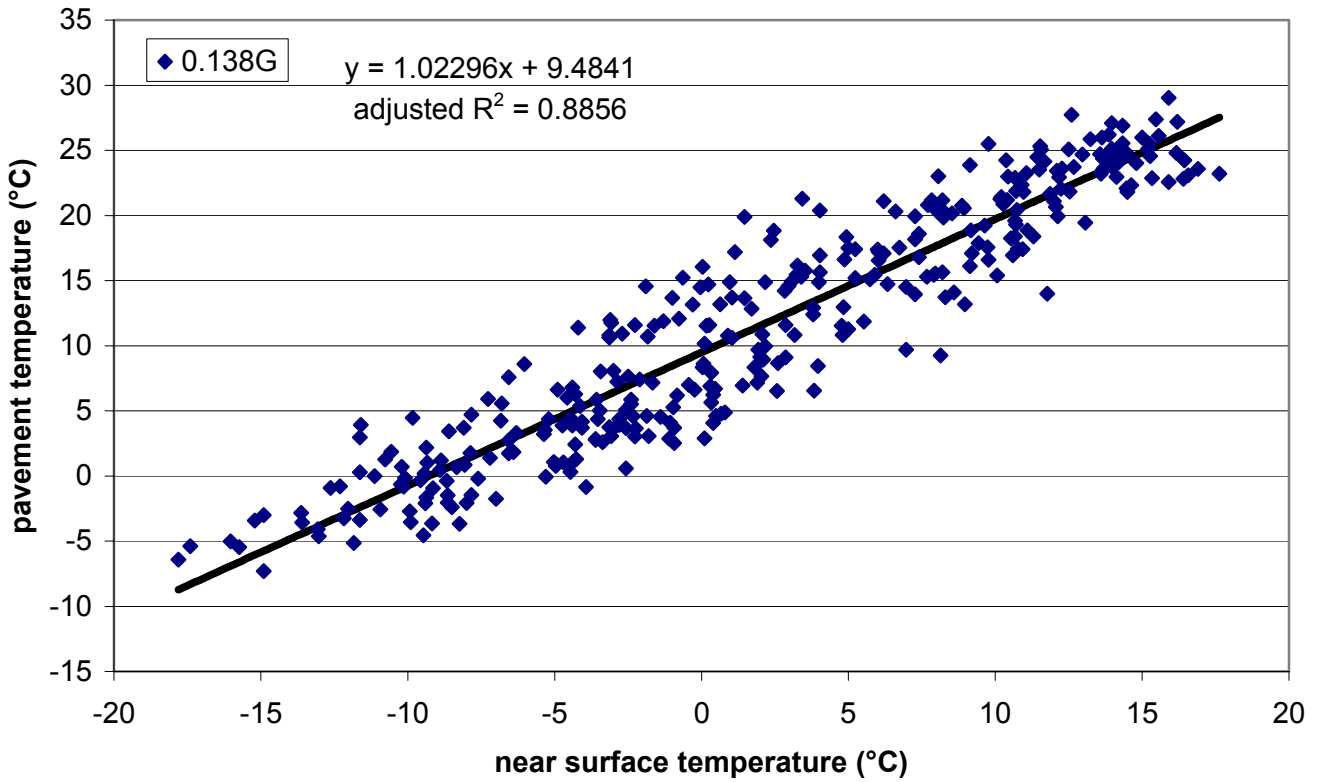


Figure I.58. Section G – daily minimum near surface temperature vs. daily minimum pavement temperature (0.138m depth) with linear model.

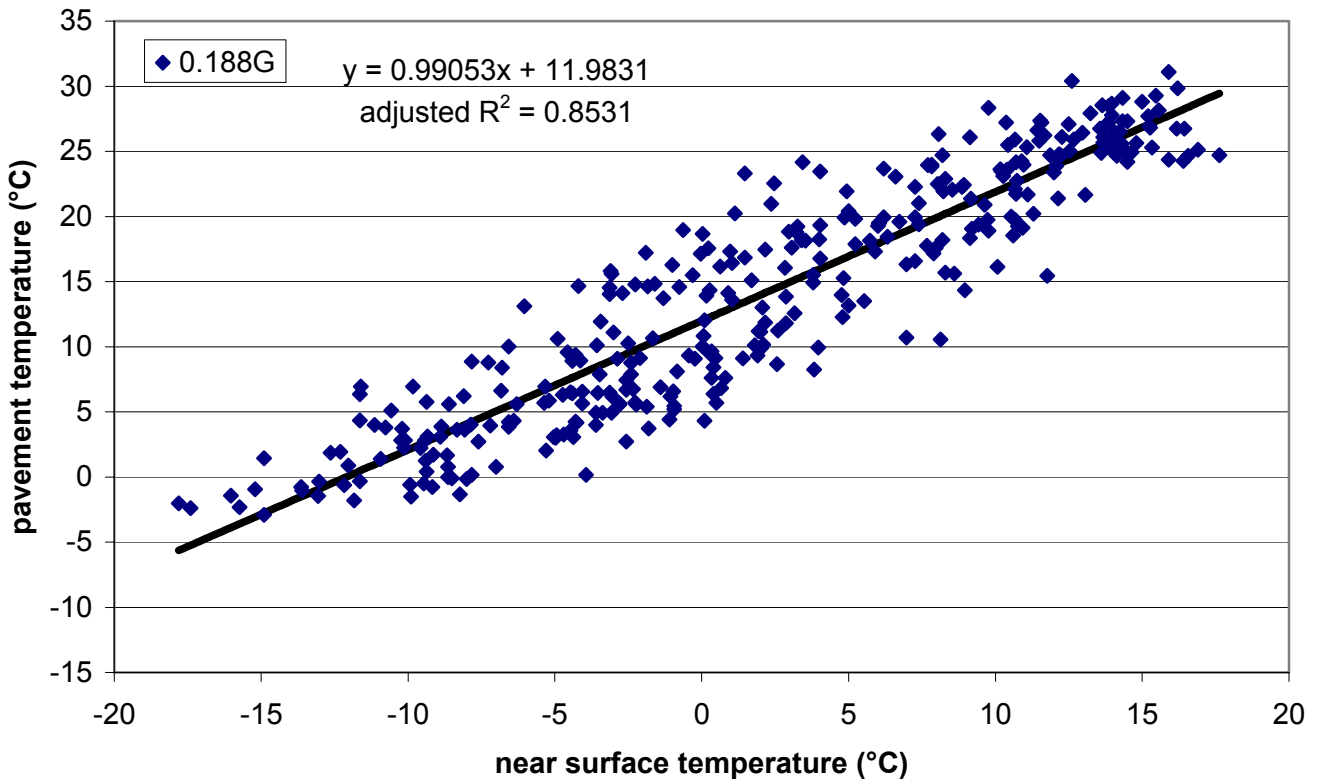


Figure I.59. Section G – daily minimum near surface temperature vs. daily minimum pavement temperature (0.188m depth) with linear model.

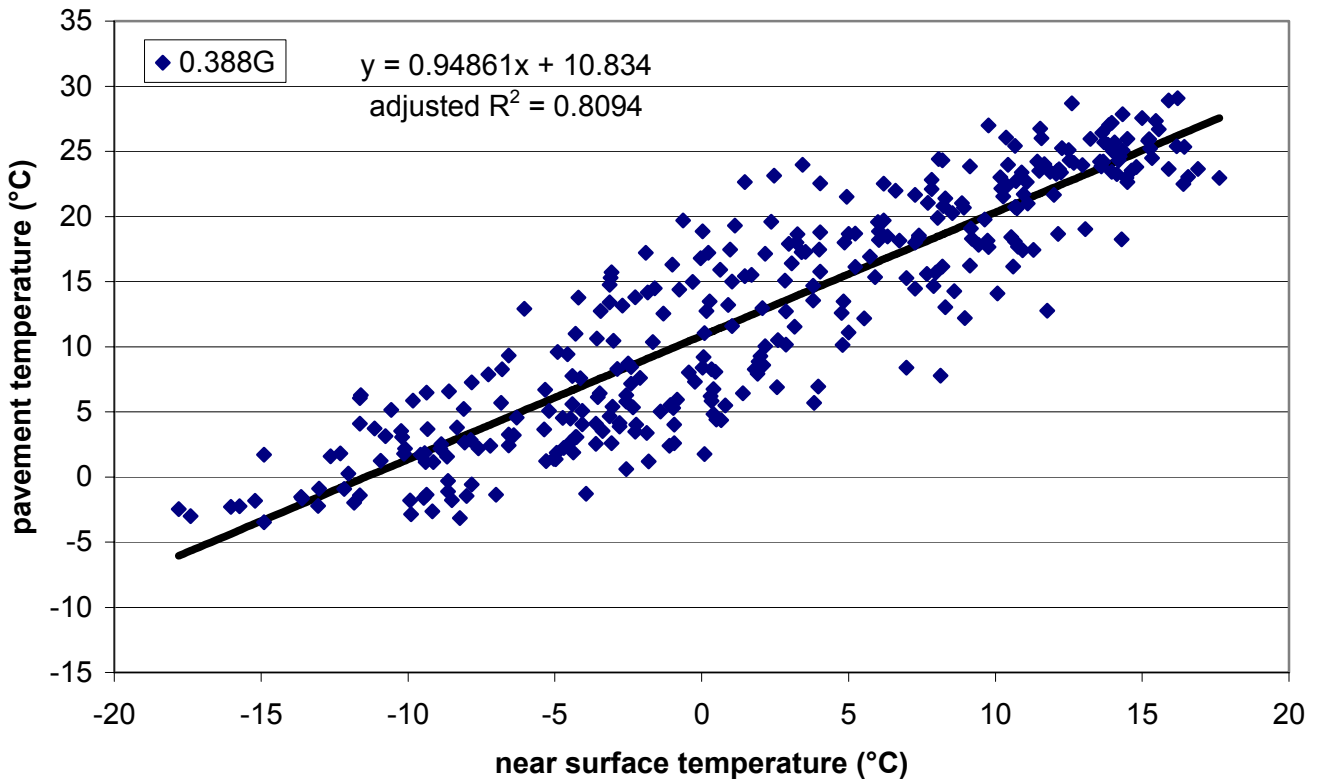


Figure I.60. Section G – daily minimum near surface temperature vs. daily minimum pavement temperature (0.388m depth) with linear model.

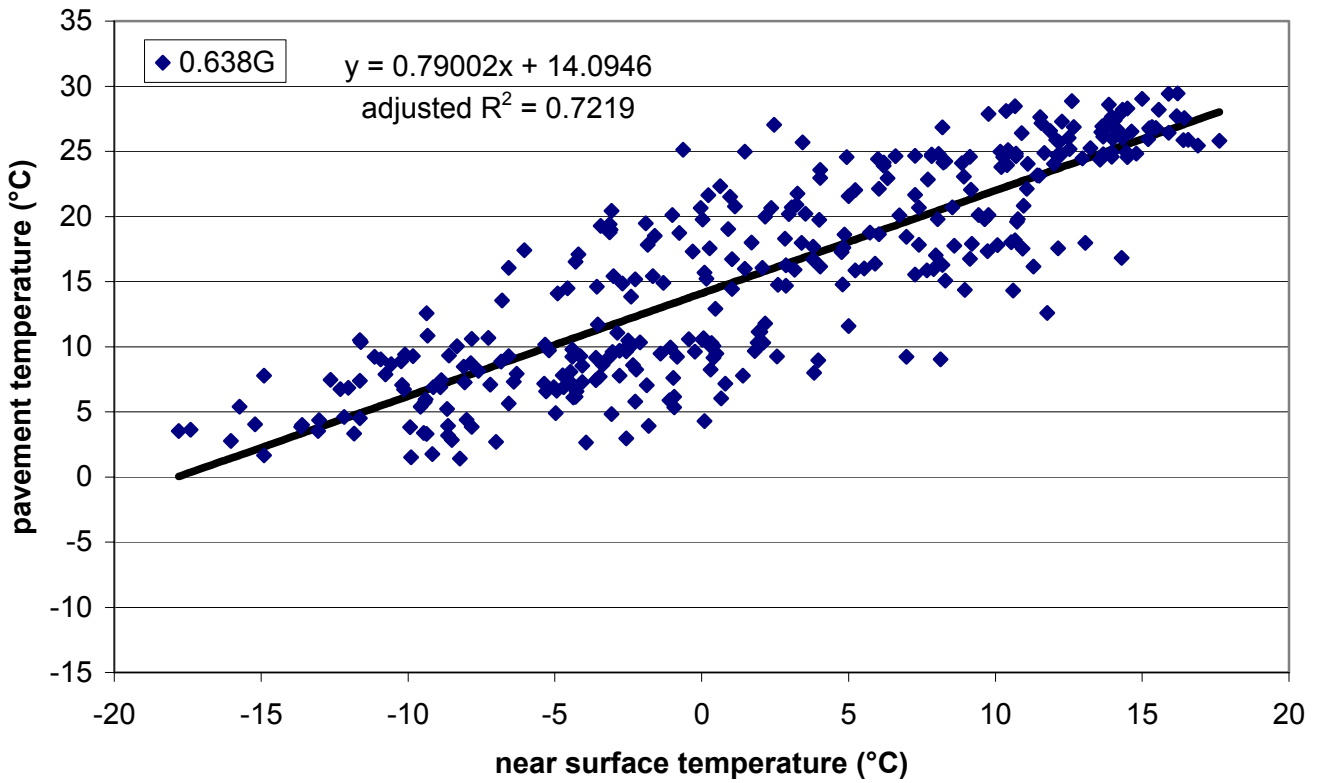


Figure I.61. Section G – daily minimum near surface temperature vs. daily minimum pavement temperature (0.638m depth) with linear model.

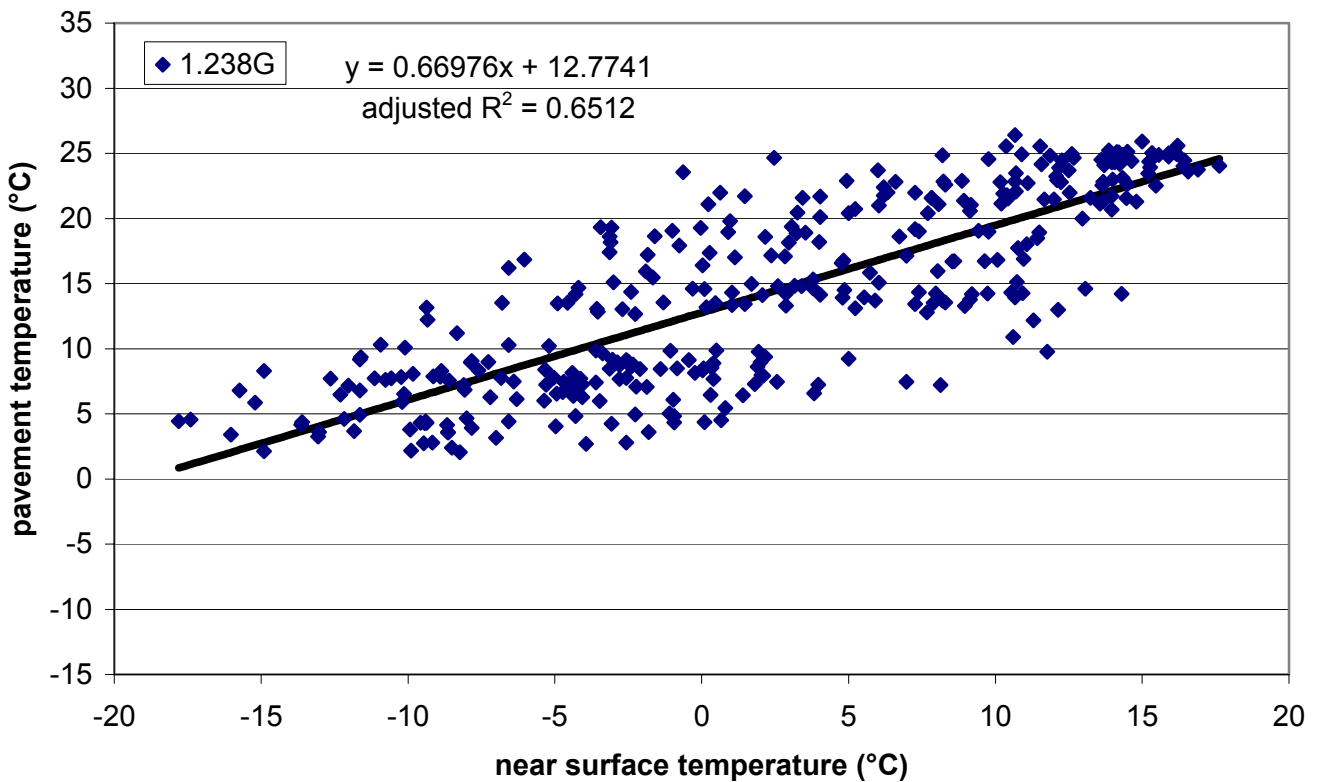


Figure I.62. Section G – daily minimum near surface temperature vs. daily minimum pavement temperature (1.238m depth) with linear model.

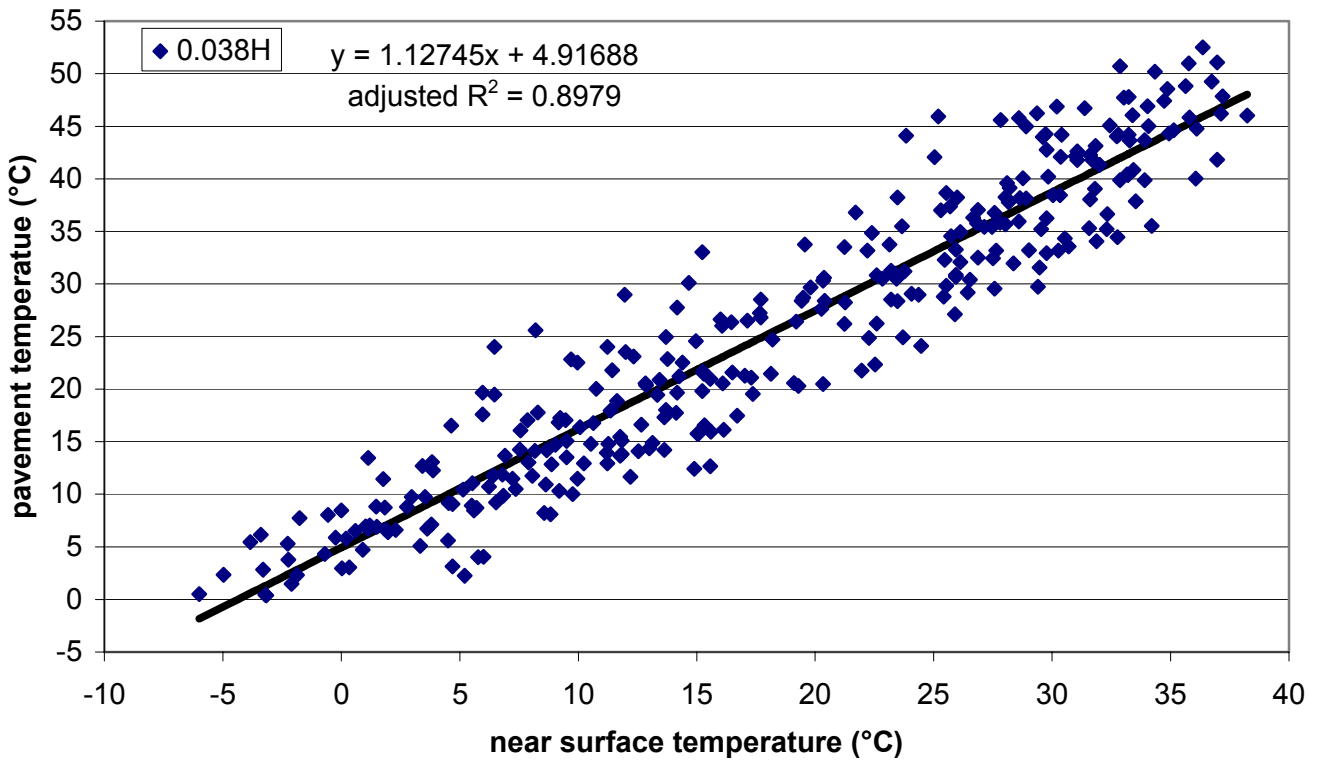


Figure I.63. Section H – daily maximum near surface temperature vs. daily maximum pavement temperature (0.038m depth) with linear model.

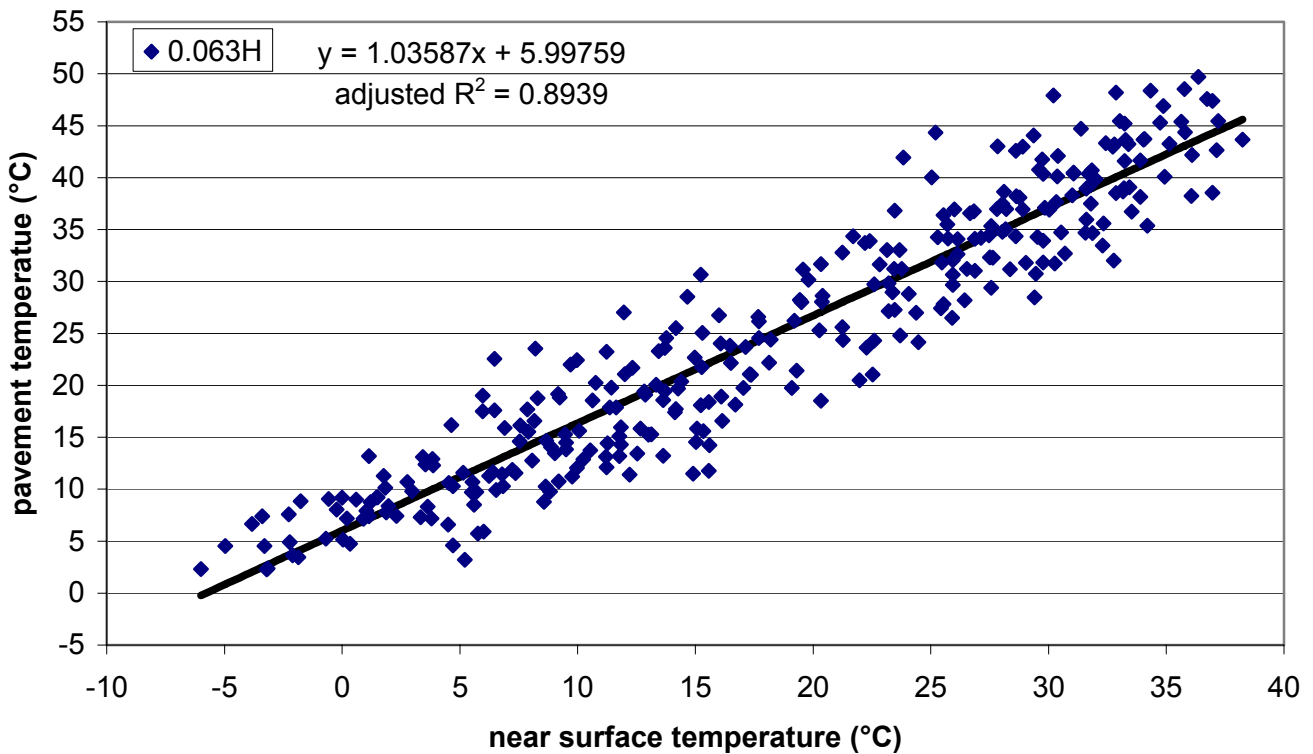


Figure I.64. Section H – daily maximum near surface temperature vs. daily maximum pavement temperature (0.063m depth) with linear model.

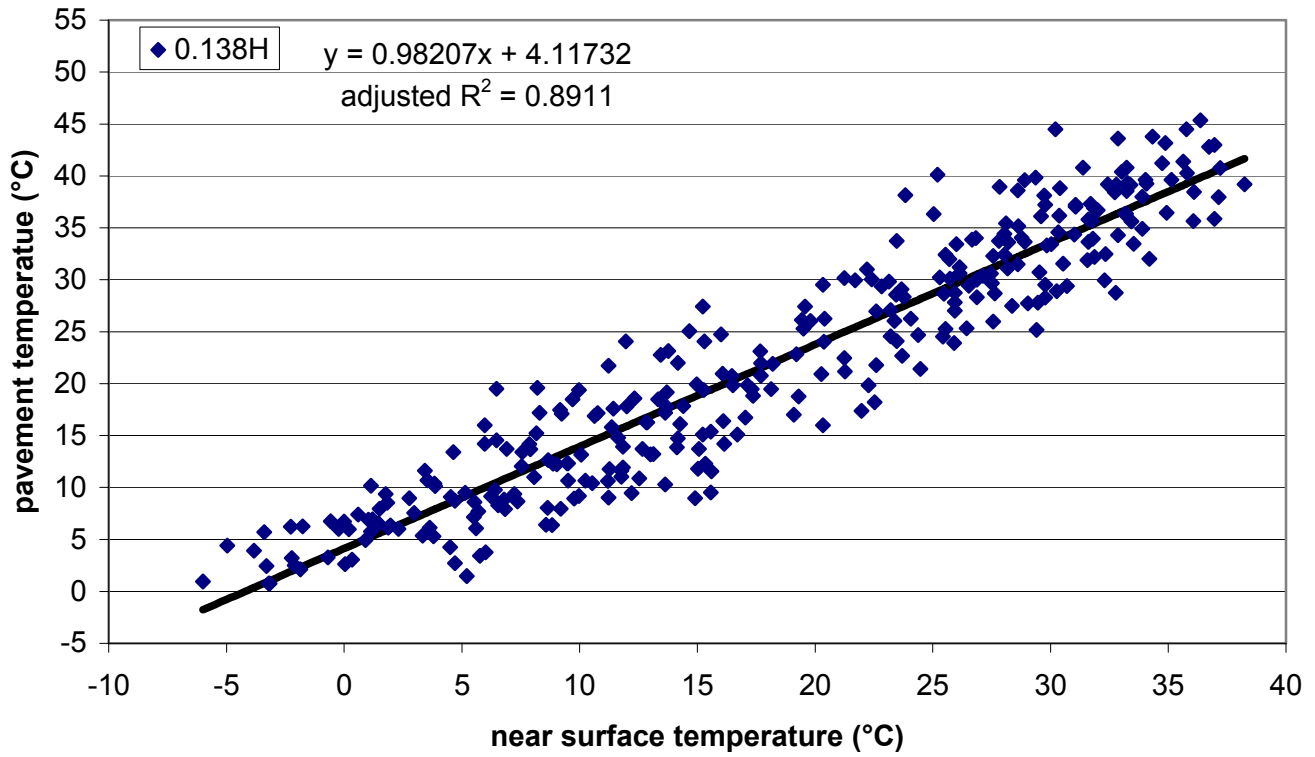


Figure I.65. Section H – daily maximum near surface temperature vs. daily maximum pavement temperature (0.138m depth) with linear model.

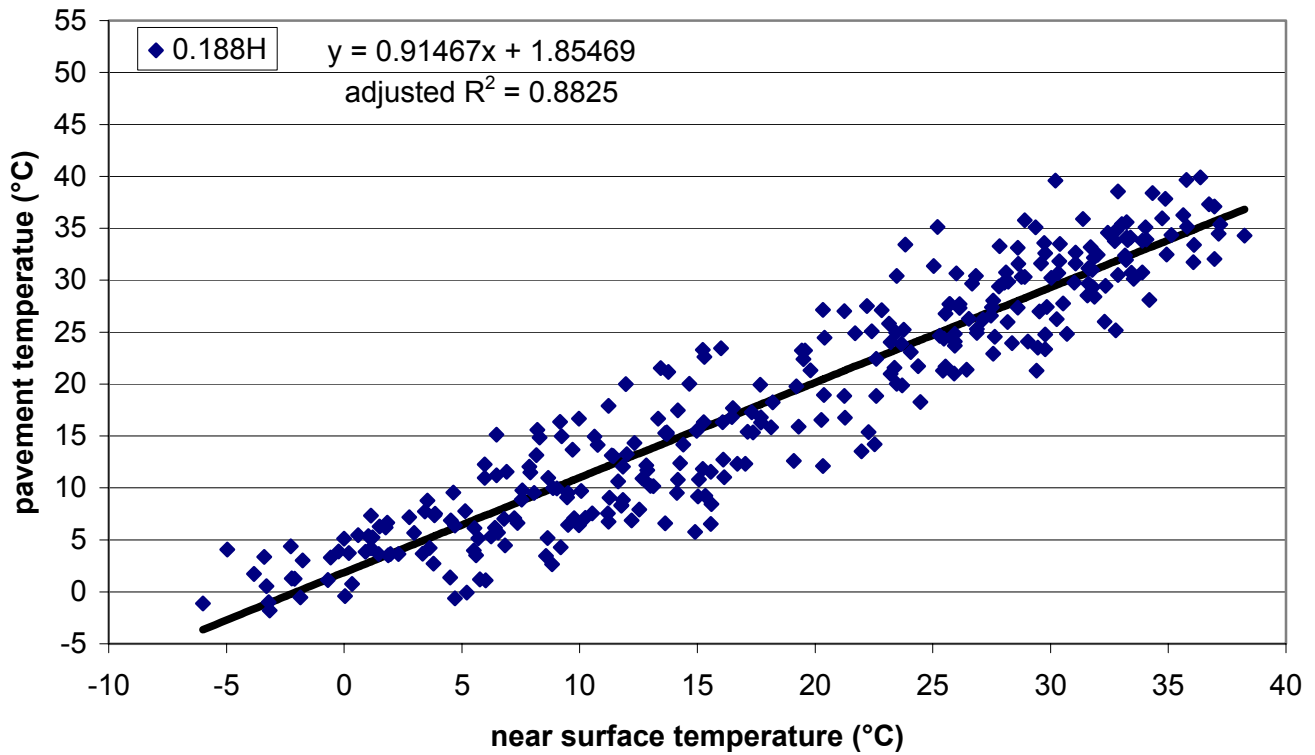


Figure I.66. Section H – daily maximum near surface temperature vs. daily maximum pavement temperature (0.188m depth) with linear model.

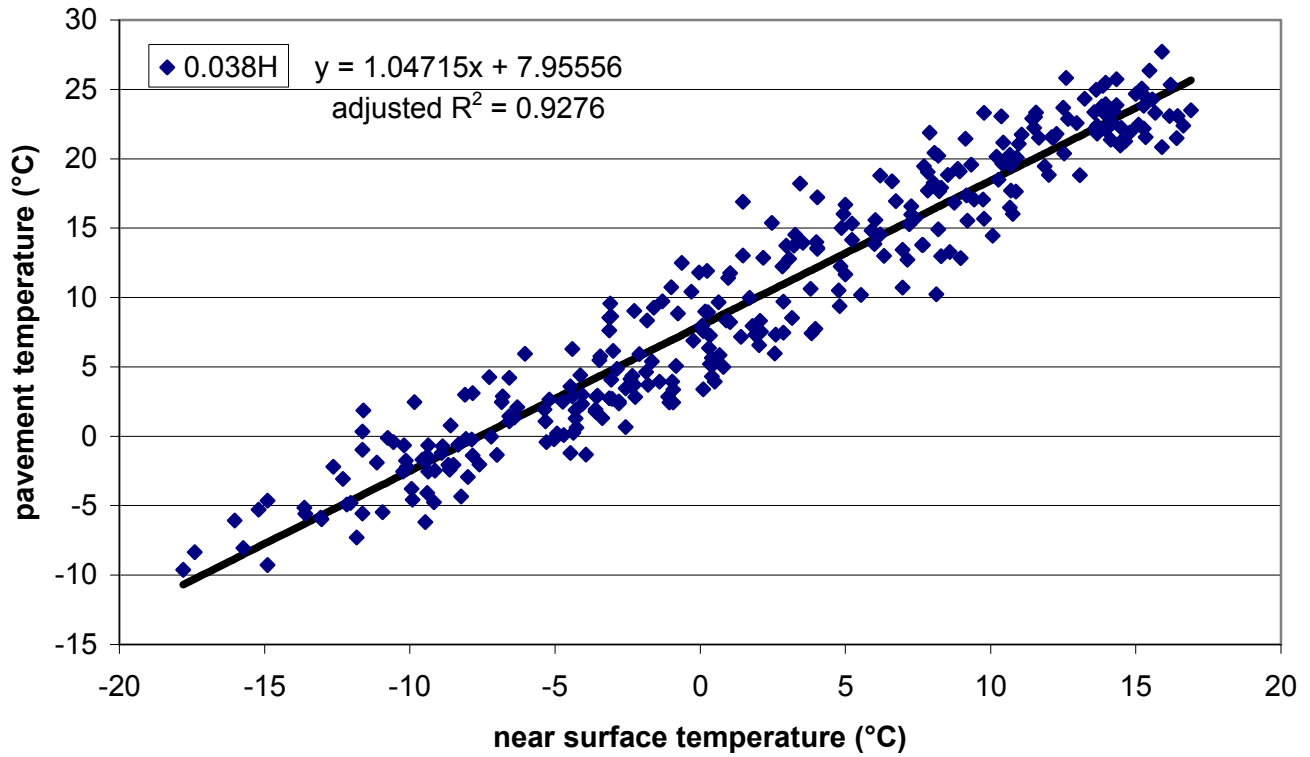


Figure I.67. Section H – daily minimum near surface temperature vs. daily minimum pavement temperature (0.038m depth) with linear model.

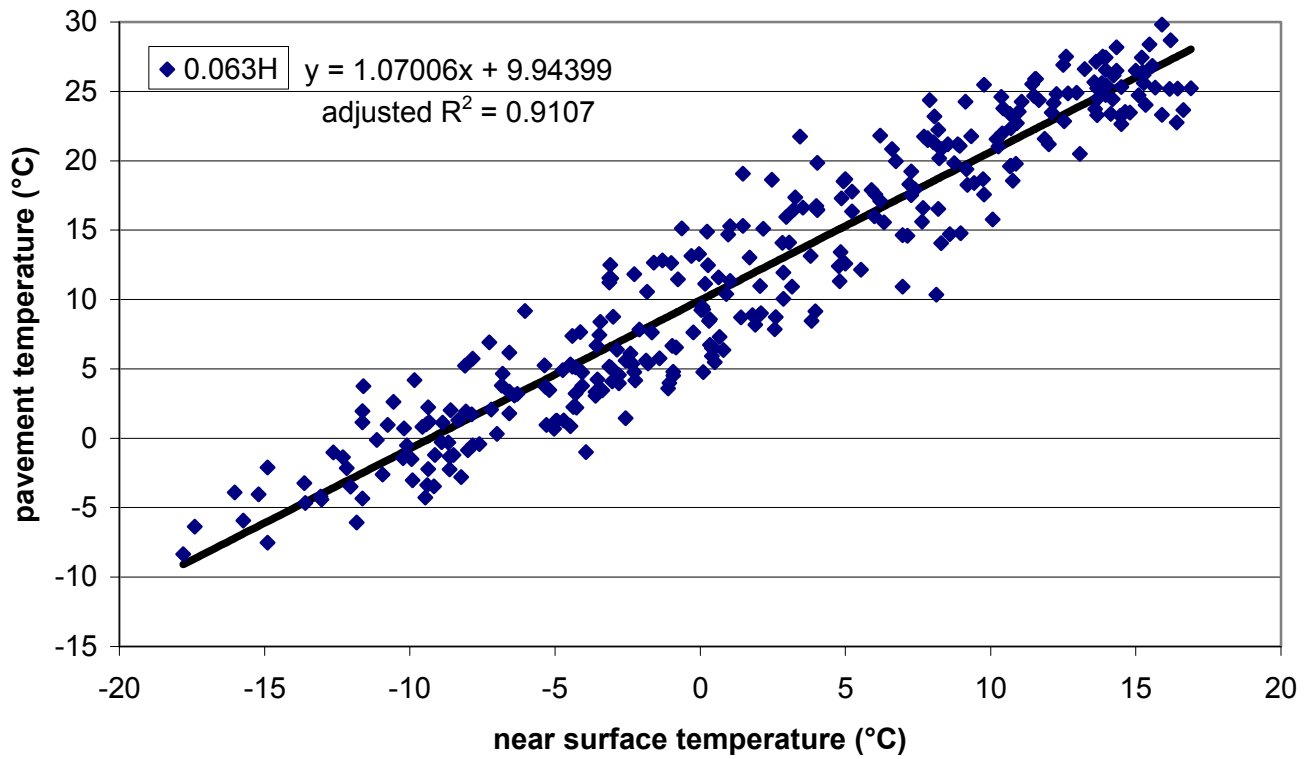


Figure I.68. Section H – daily minimum near surface temperature vs. daily minimum pavement temperature (0.063m depth) with linear model.

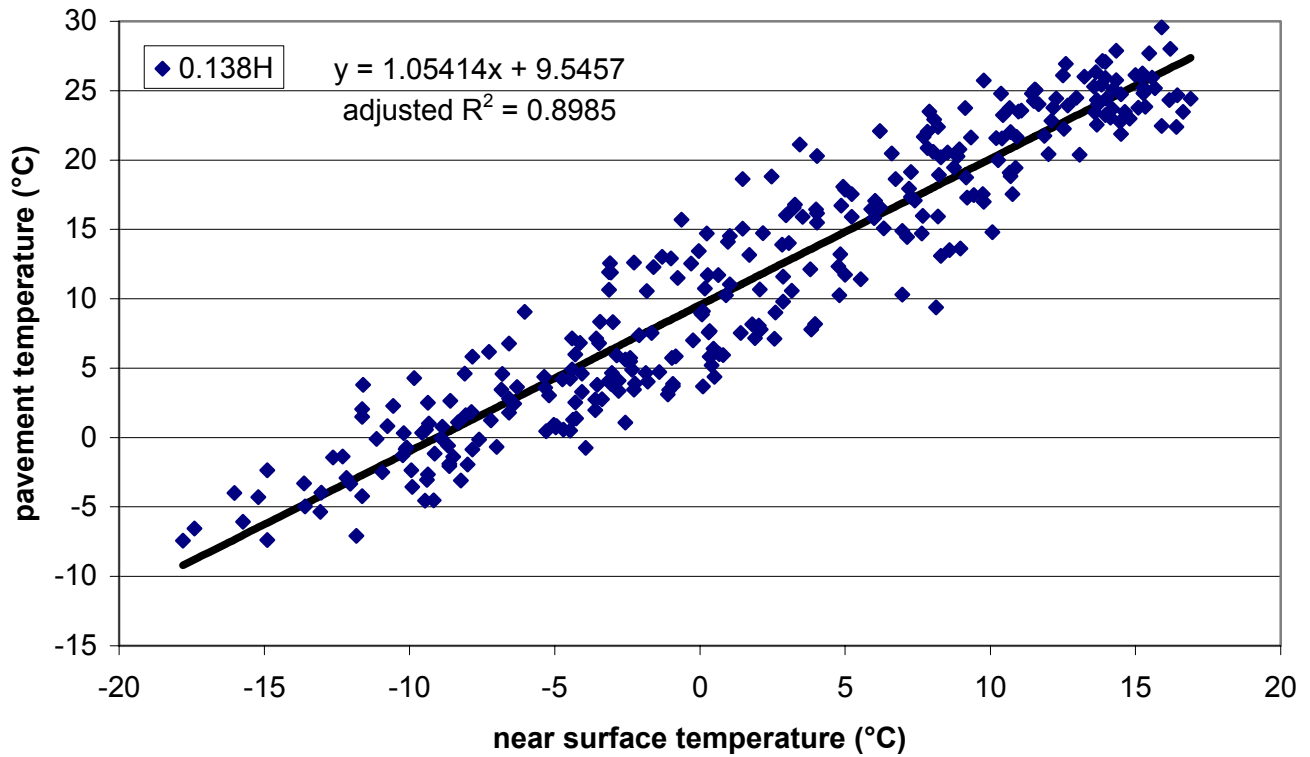


Figure I.69. Section H – daily minimum near surface temperature vs. daily minimum pavement temperature (0.138m depth) with linear model.

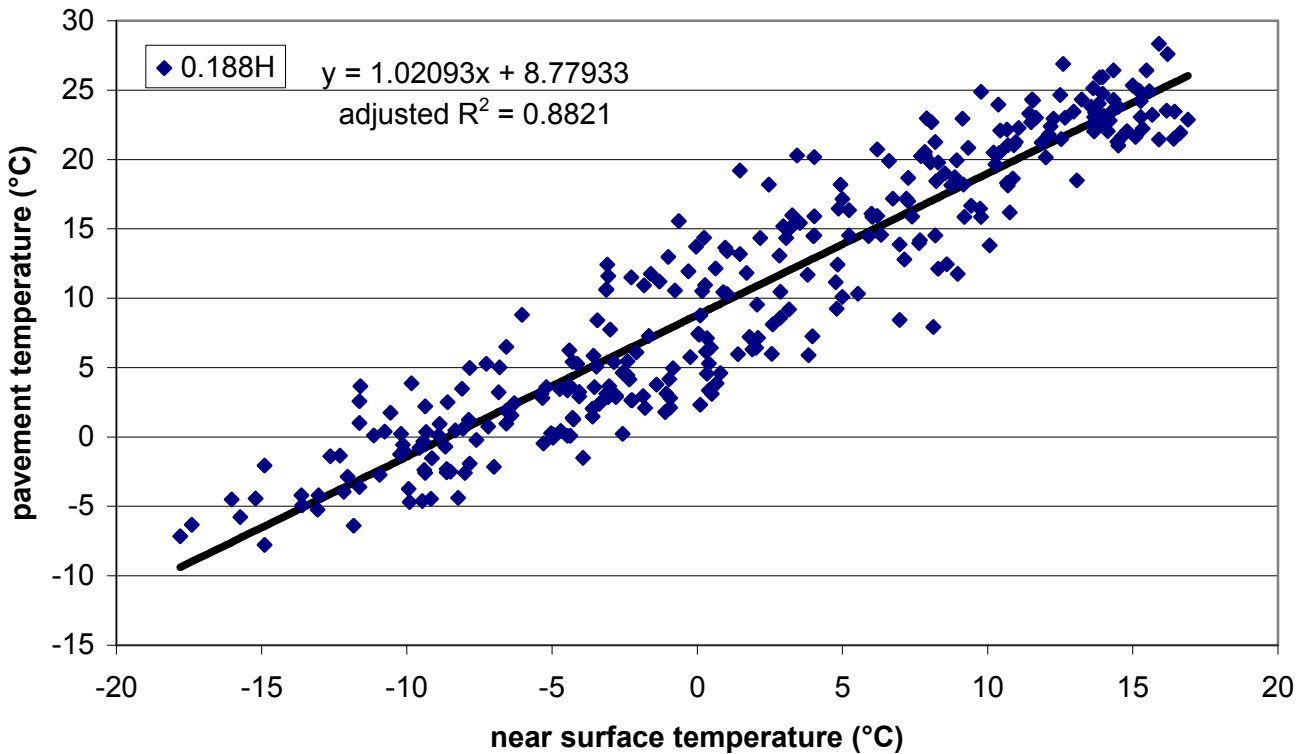


Figure I.70. Section H – daily minimum near surface temperature vs. daily minimum pavement temperature (0.188m depth) with linear model.

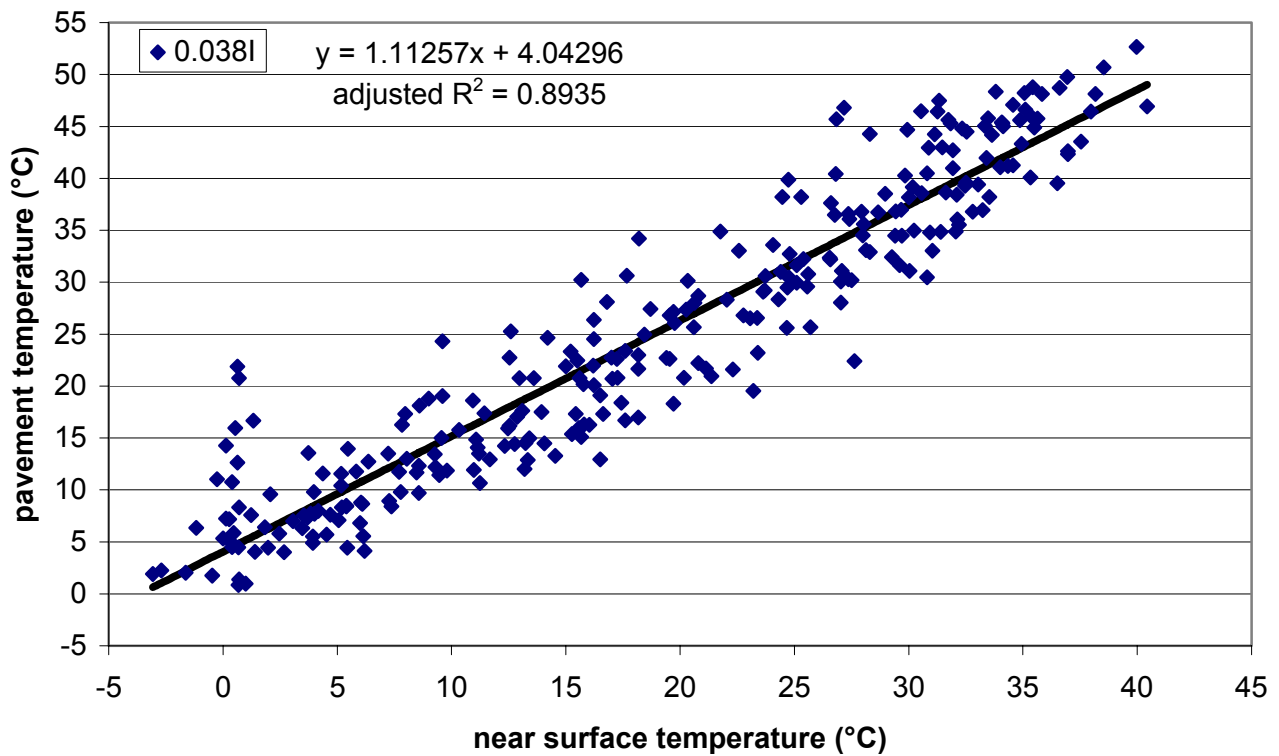


Figure I.71. Section I – daily maximum near surface temperature vs. daily maximum pavement temperature (0.038m depth) with linear model.

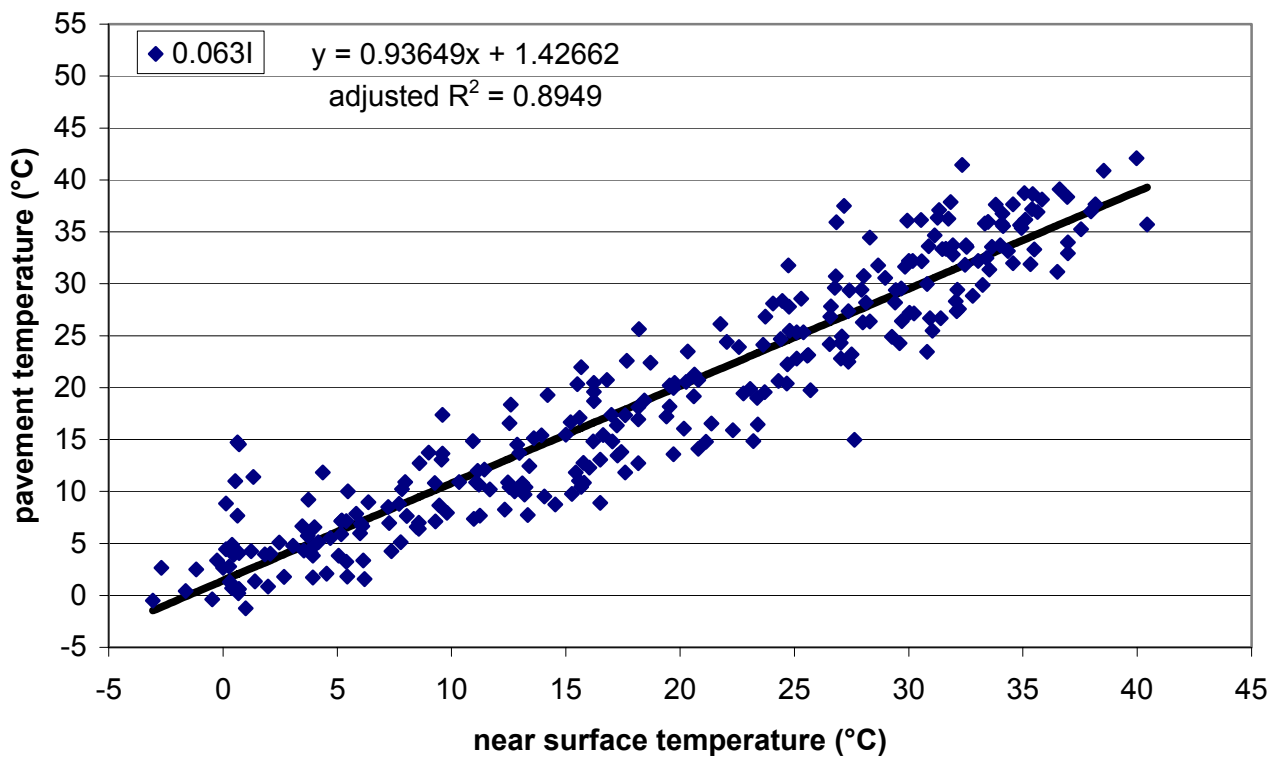


Figure I.72. Section I – daily maximum near surface temperature vs. daily maximum pavement temperature (0.063m depth) with linear model.

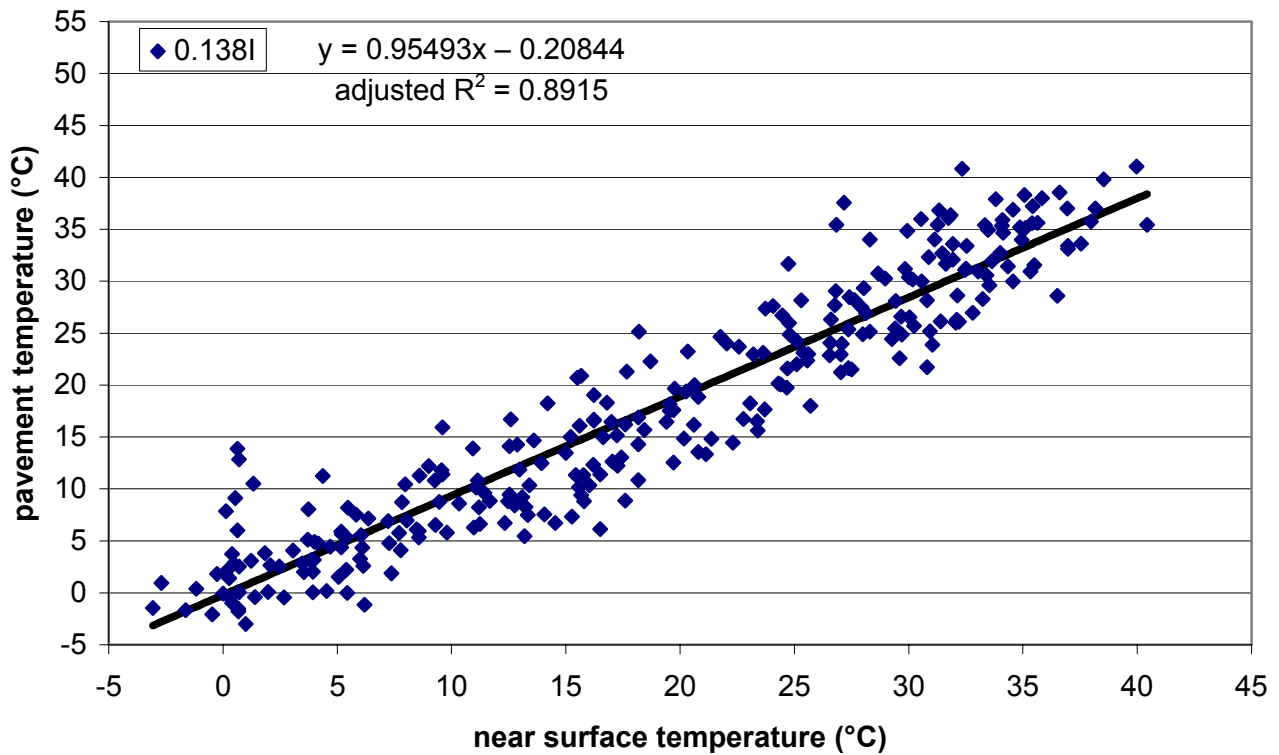


Figure I.73. Section I – daily maximum near surface temperature vs. daily maximum pavement temperature (0.138m depth) with linear model.

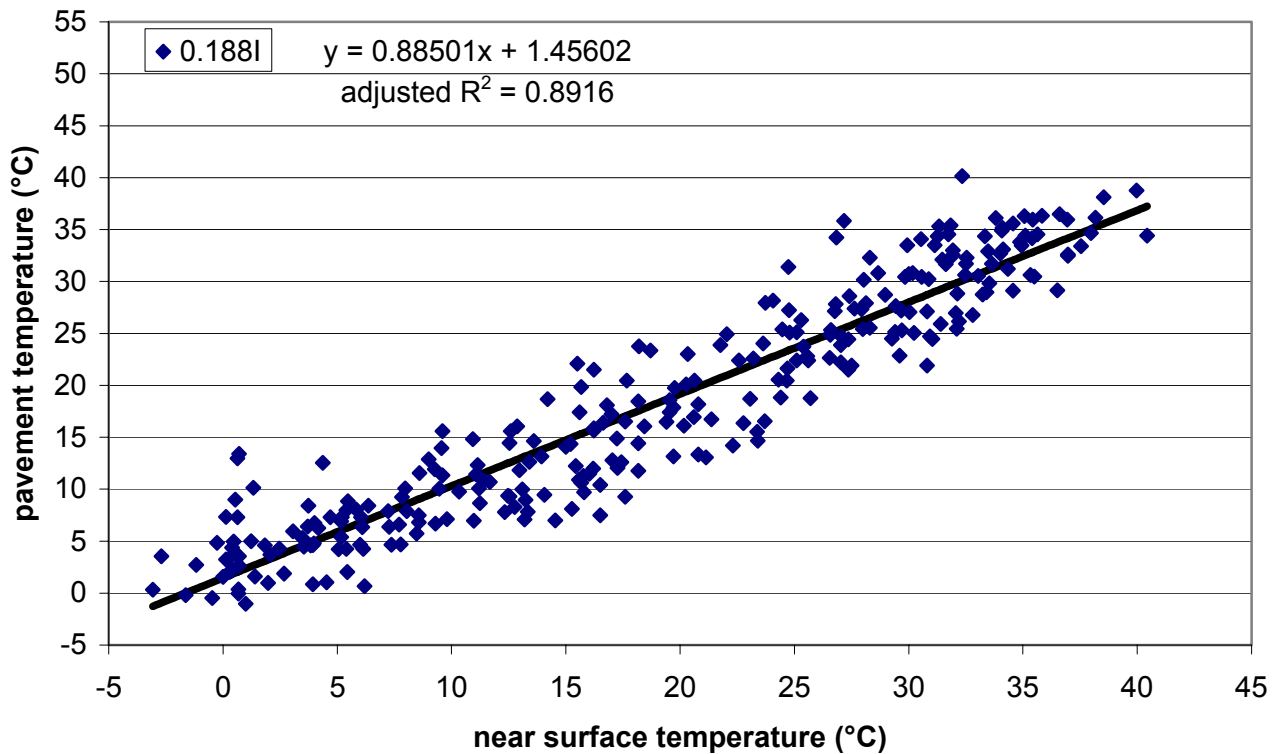


Figure I.74. Section I – daily maximum near surface temperature vs. daily maximum pavement temperature (0.188m depth) with linear model.

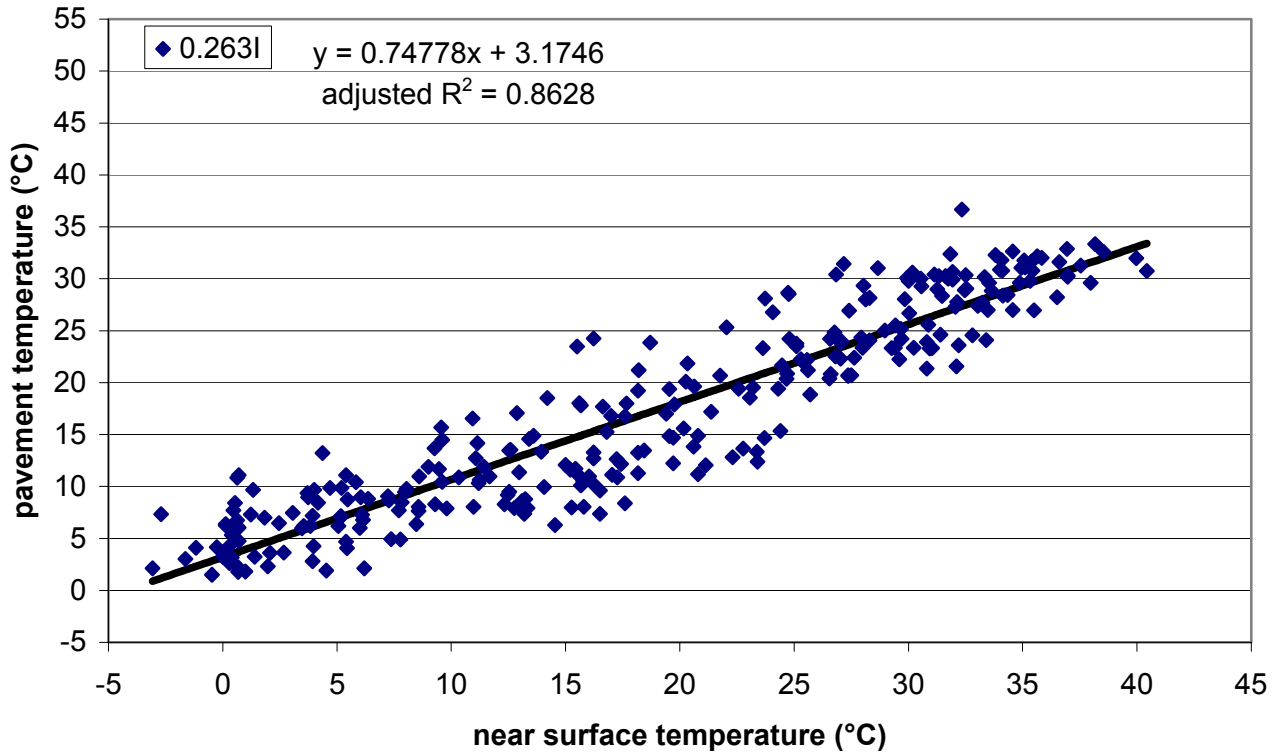


Figure I.75. Section I – daily maximum near surface temperature vs. daily maximum pavement temperature (0.263m depth) with linear model.

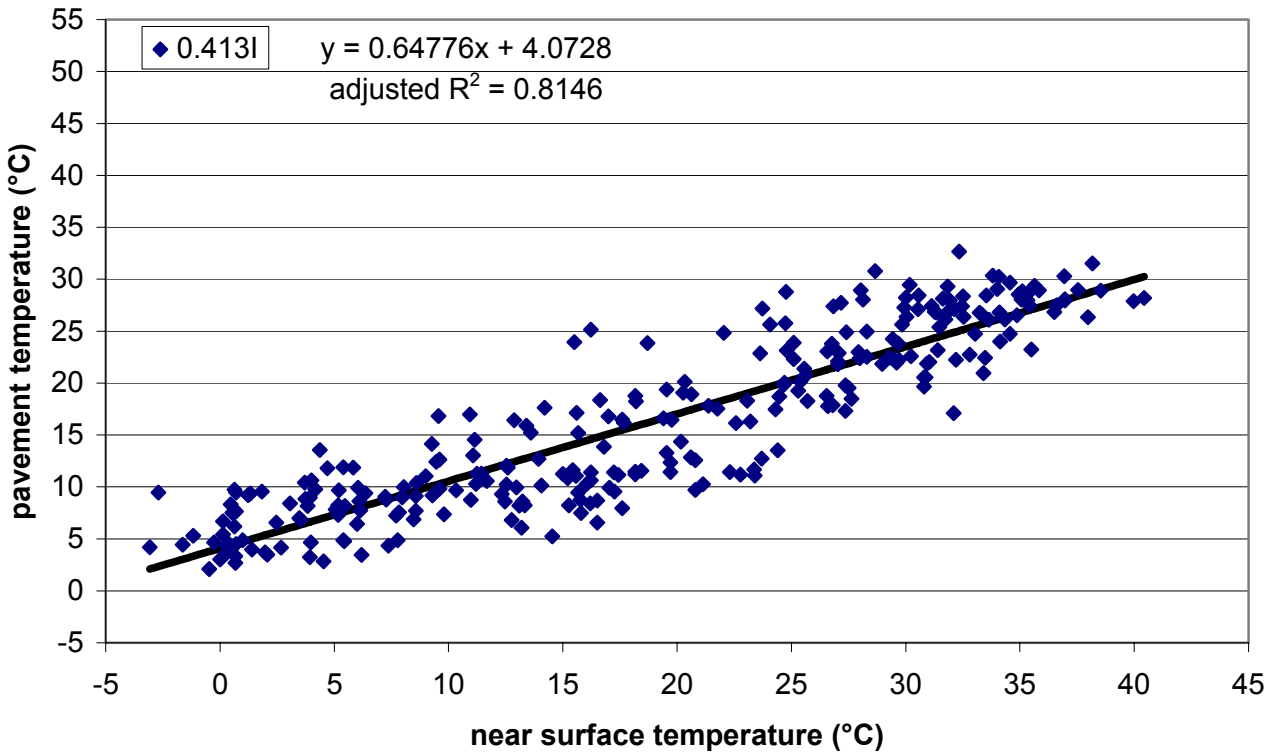


Figure I.76. Section I – daily maximum near surface temperature vs. daily maximum pavement temperature (0.413m depth) with linear model.

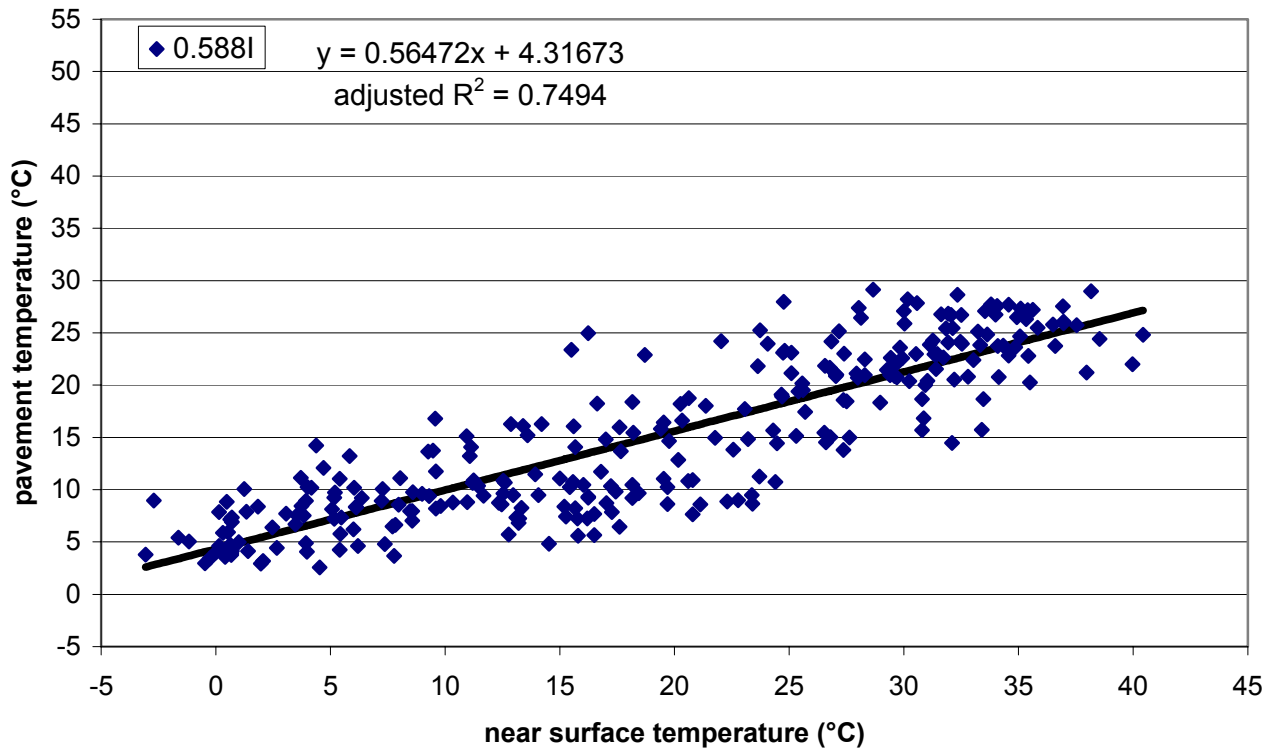


Figure I.77. Section I – daily maximum near surface temperature vs. daily maximum pavement temperature (0.588m depth) with linear model.

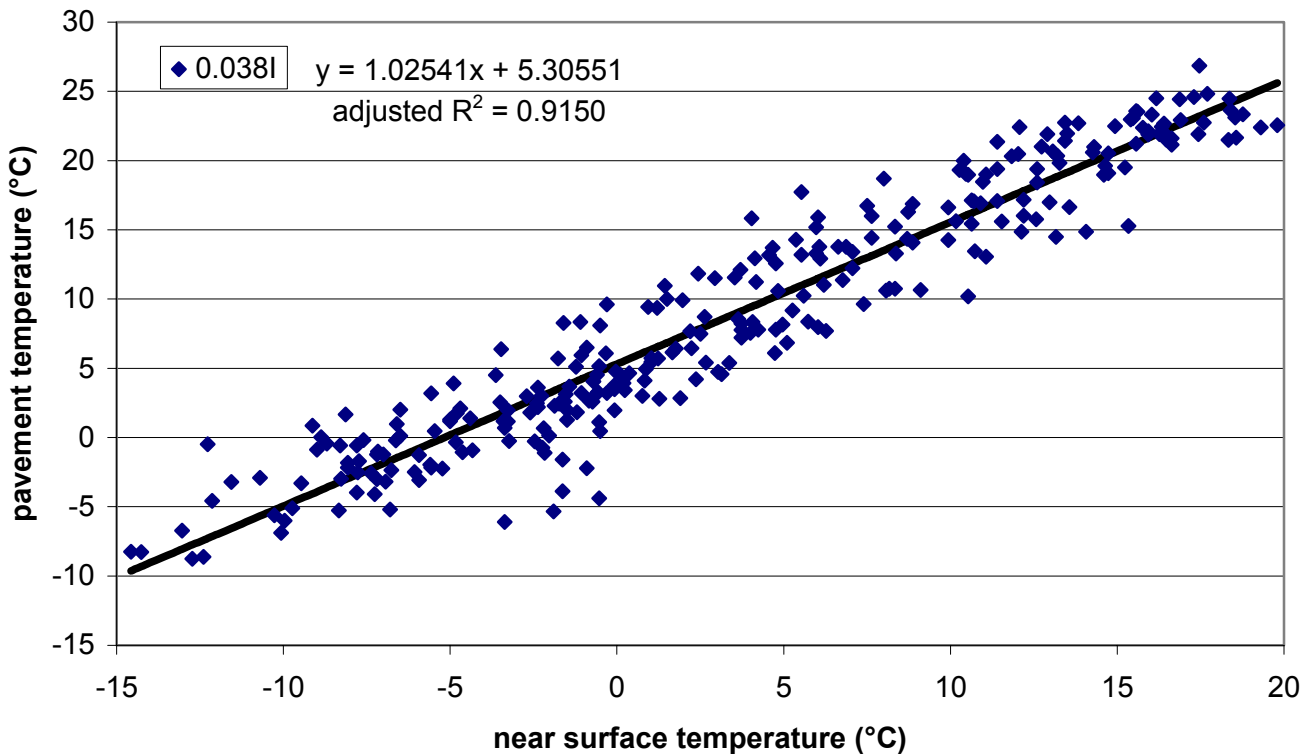


Figure I.78. Section I – daily minimum near surface temperature vs. daily minimum pavement temperature (0.038m depth) with linear model.

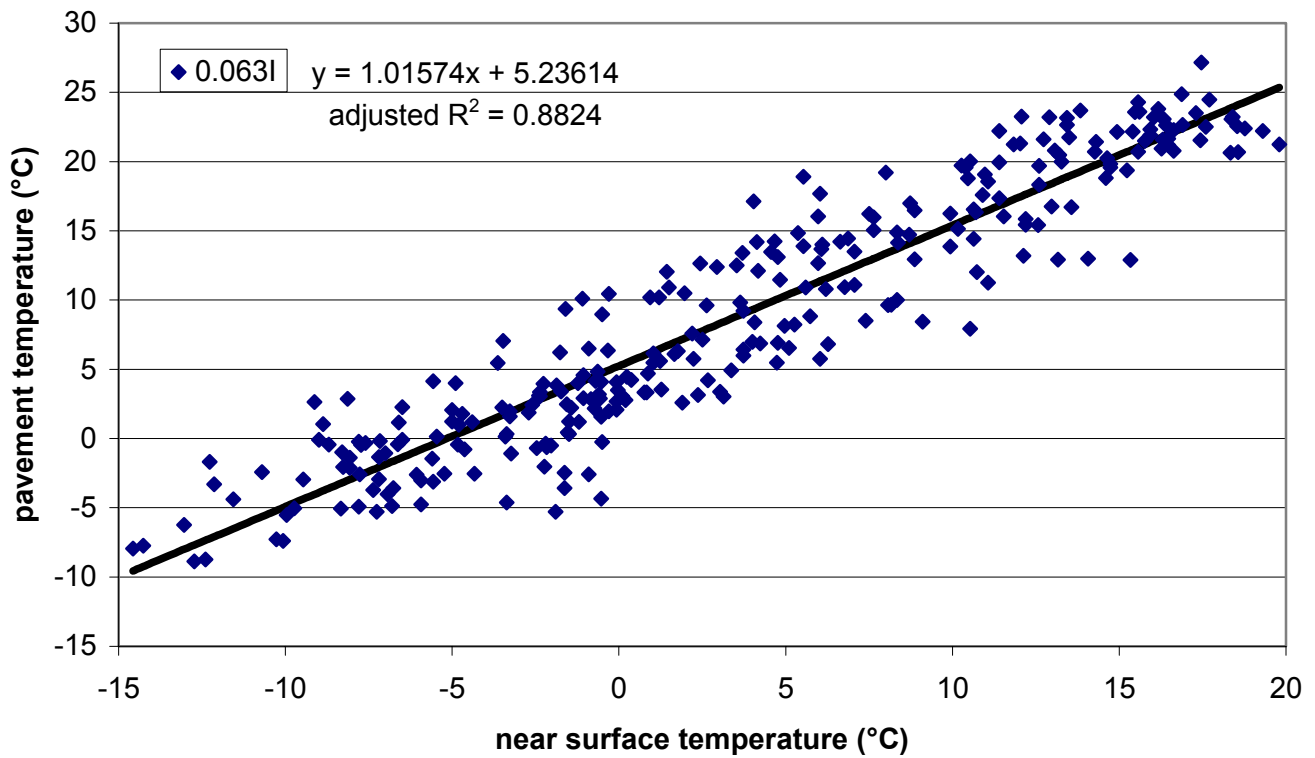


Figure I.79. Section I – daily minimum near surface temperature vs. daily minimum pavement temperature (0.063m depth) with linear model.

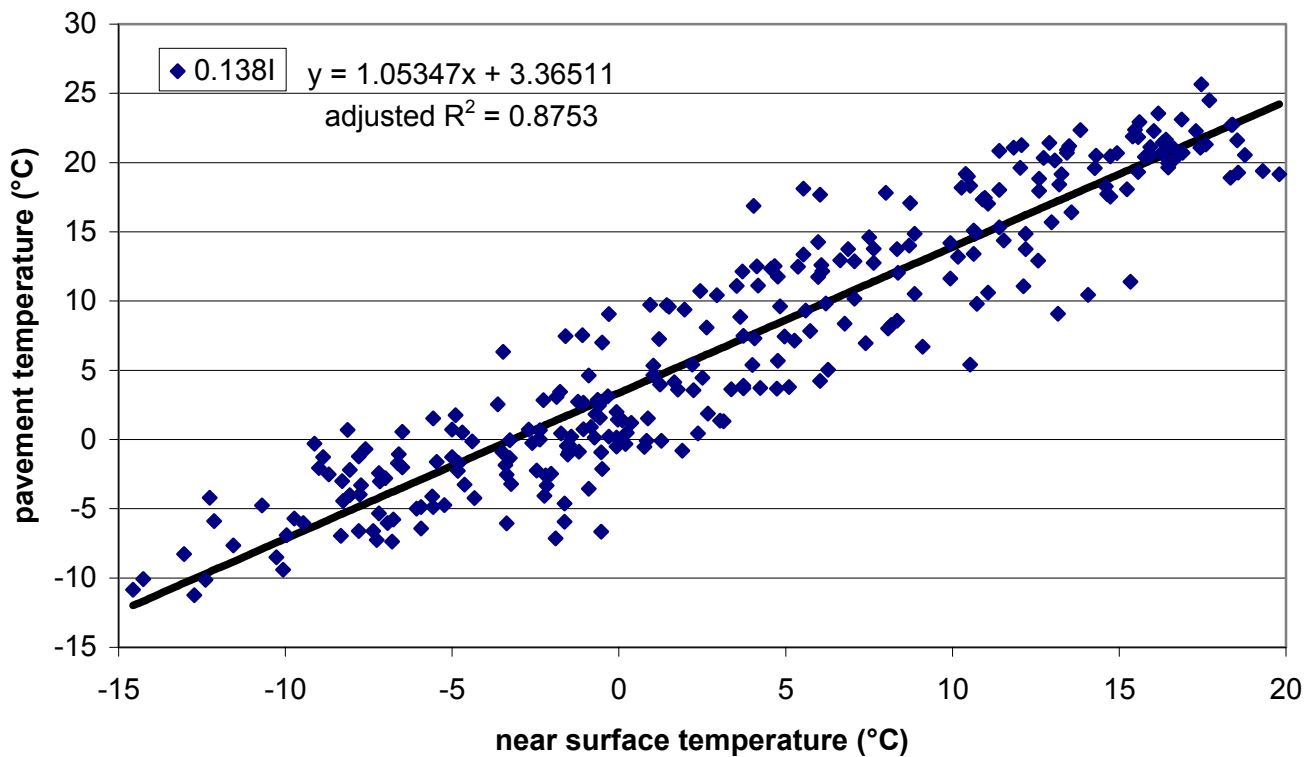


Figure I.80. Section I – daily minimum near surface temperature vs. daily minimum pavement temperature (0.138m depth) with linear model.

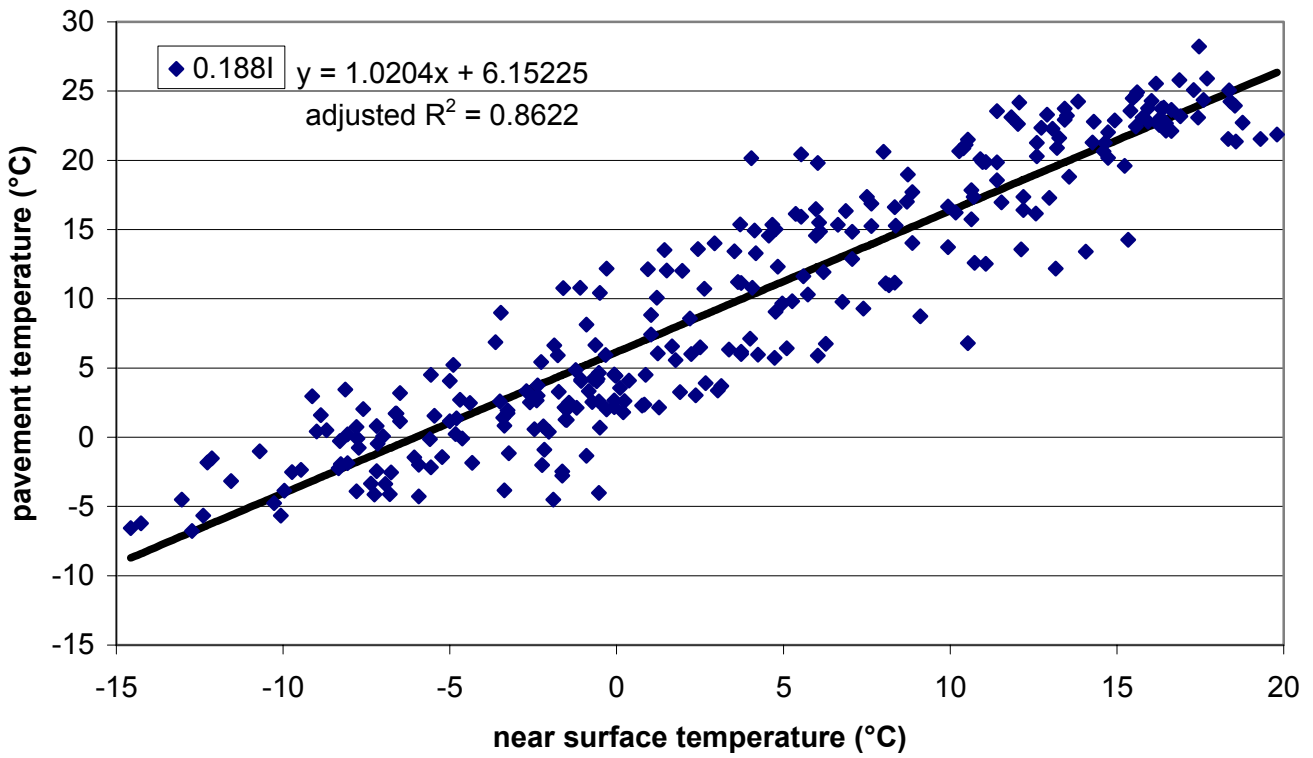


Figure I.81. Section I – daily minimum near surface temperature vs. daily minimum pavement temperature (0.188m depth) with linear model.

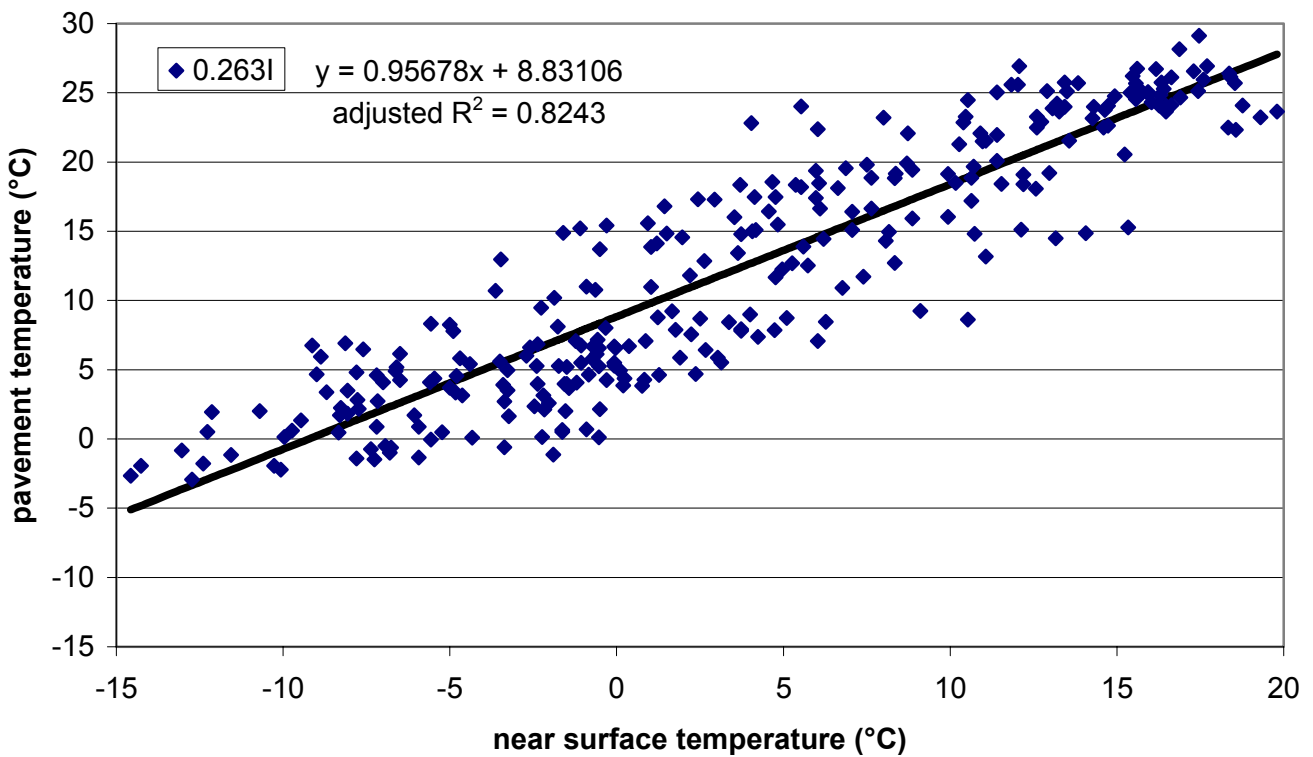


Figure I.82. Section I – daily minimum near surface temperature vs. daily minimum pavement temperature (0.263m depth) with linear model.

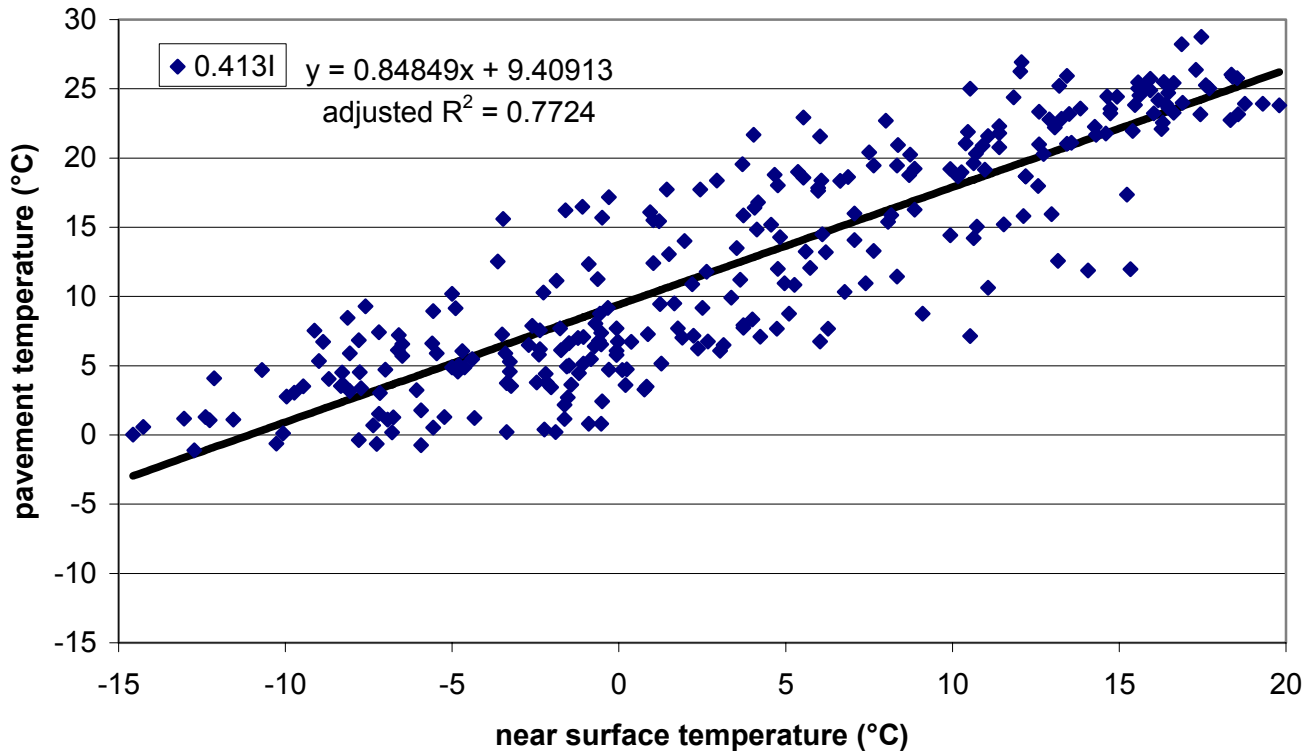


Figure I.83. Section I – daily minimum near surface temperature vs. daily minimum pavement temperature (0.413m depth) with linear model.

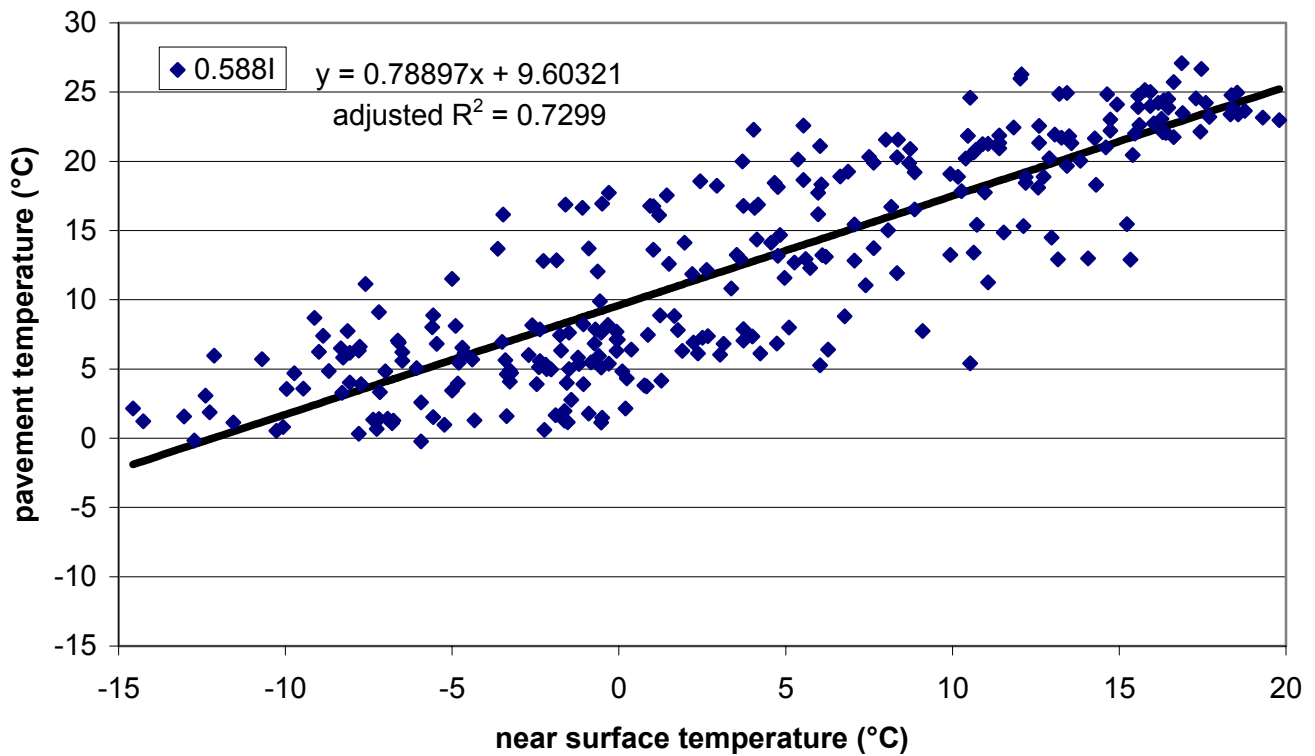


Figure I.84. Section I – daily minimum near surface temperature vs. daily minimum pavement temperature (0.588m depth) with linear model.

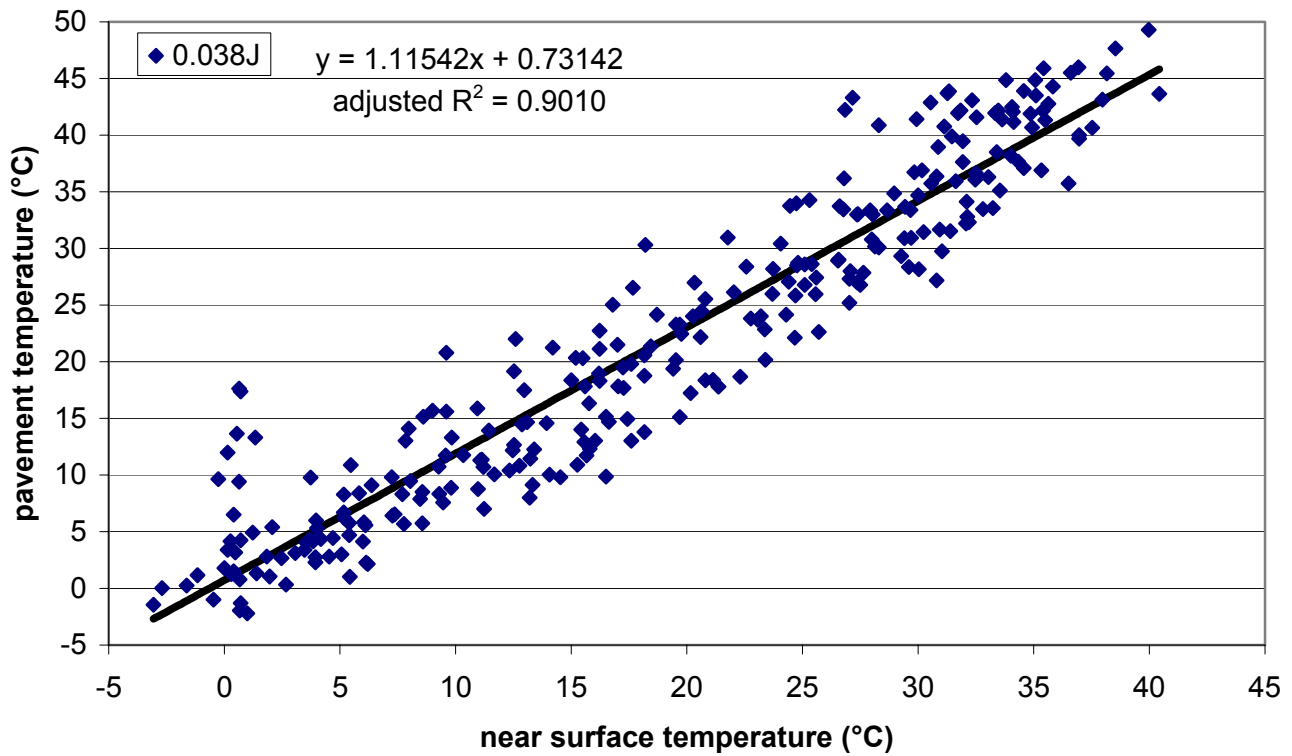


Figure I.85. Section J – daily maximum near surface temperature vs. daily maximum pavement temperature (0.038m depth) with linear model.

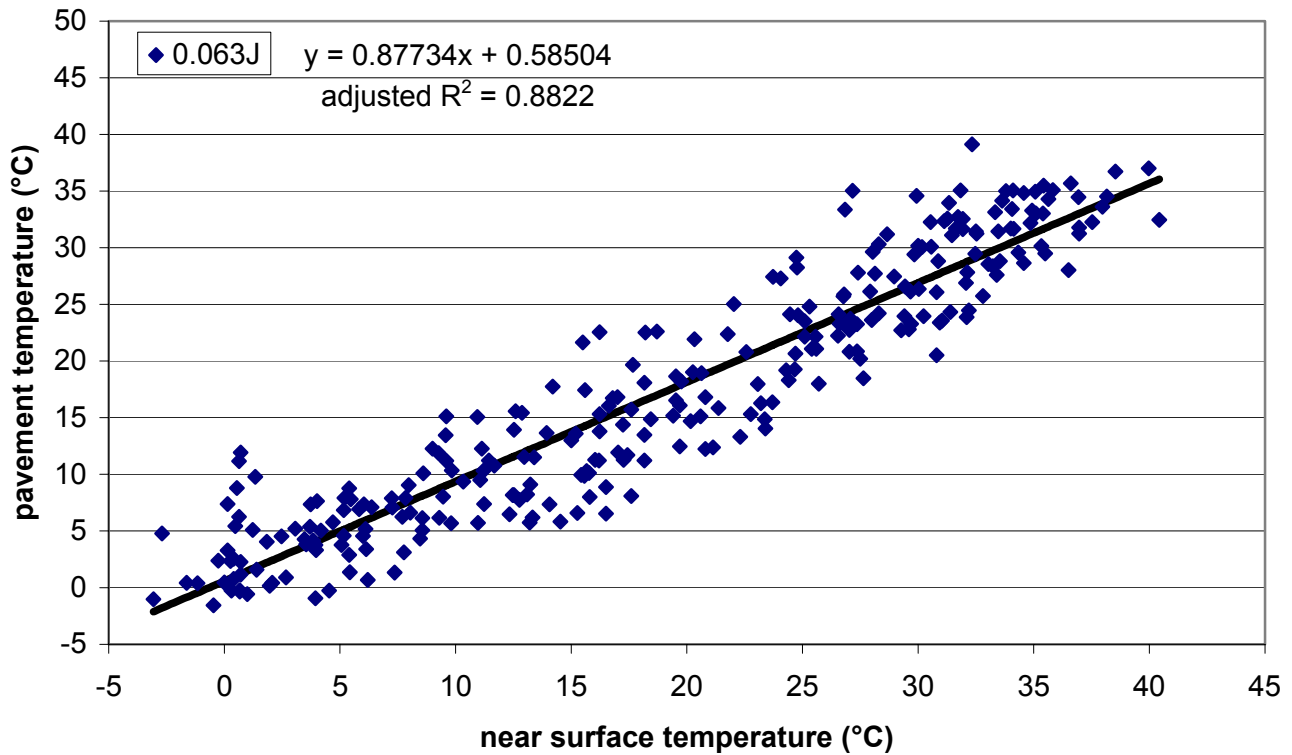


Figure I.86. Section J – daily maximum near surface temperature vs. daily maximum pavement temperature (0.063m depth) with linear model.

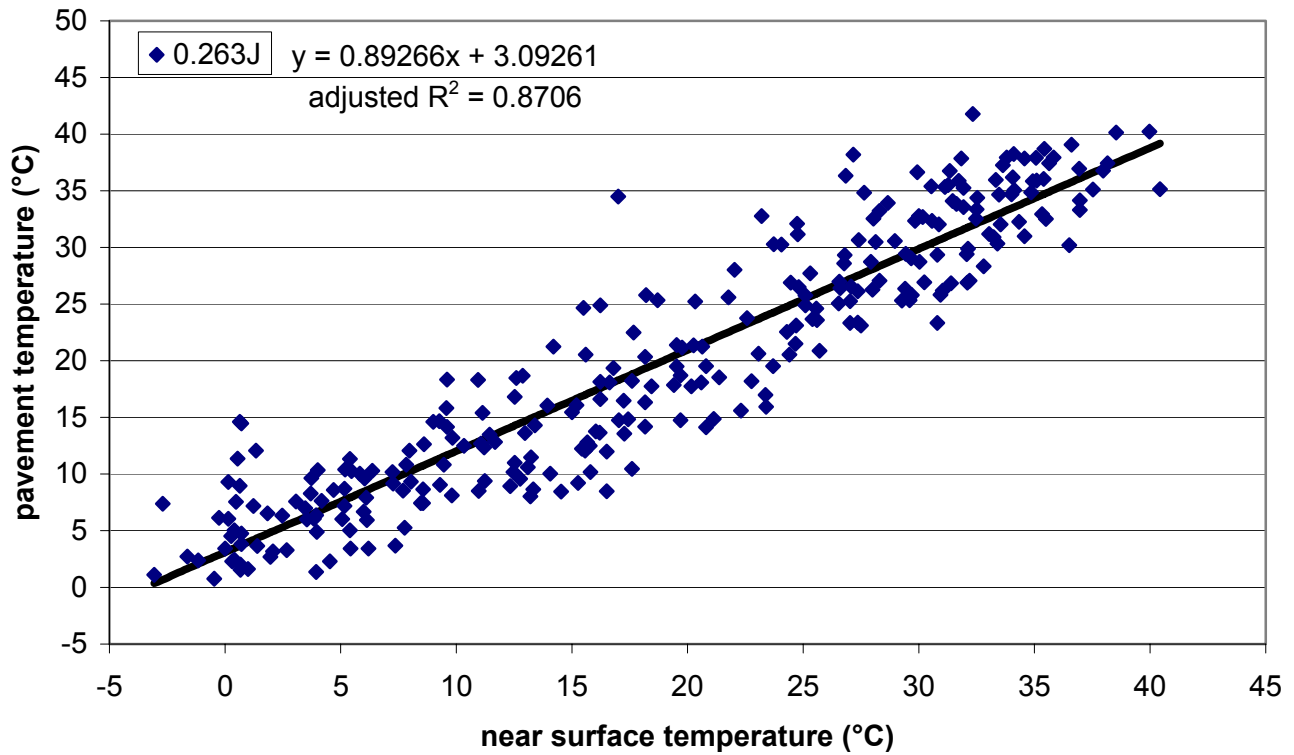


Figure I.87. Section J – daily maximum near surface temperature vs. daily maximum pavement temperature (0.263m depth) with linear model.

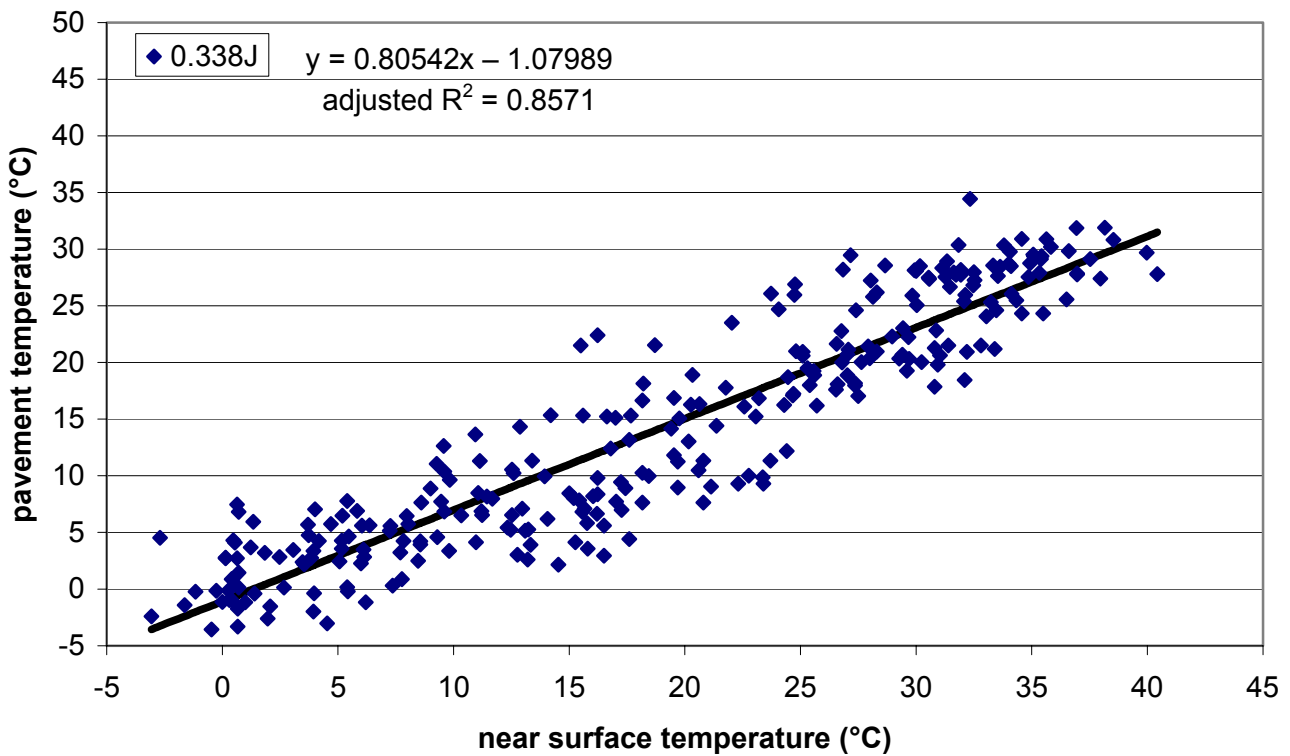


Figure I.88. Section J – daily maximum near surface temperature vs. daily maximum pavement temperature (0.338m depth) with linear model.

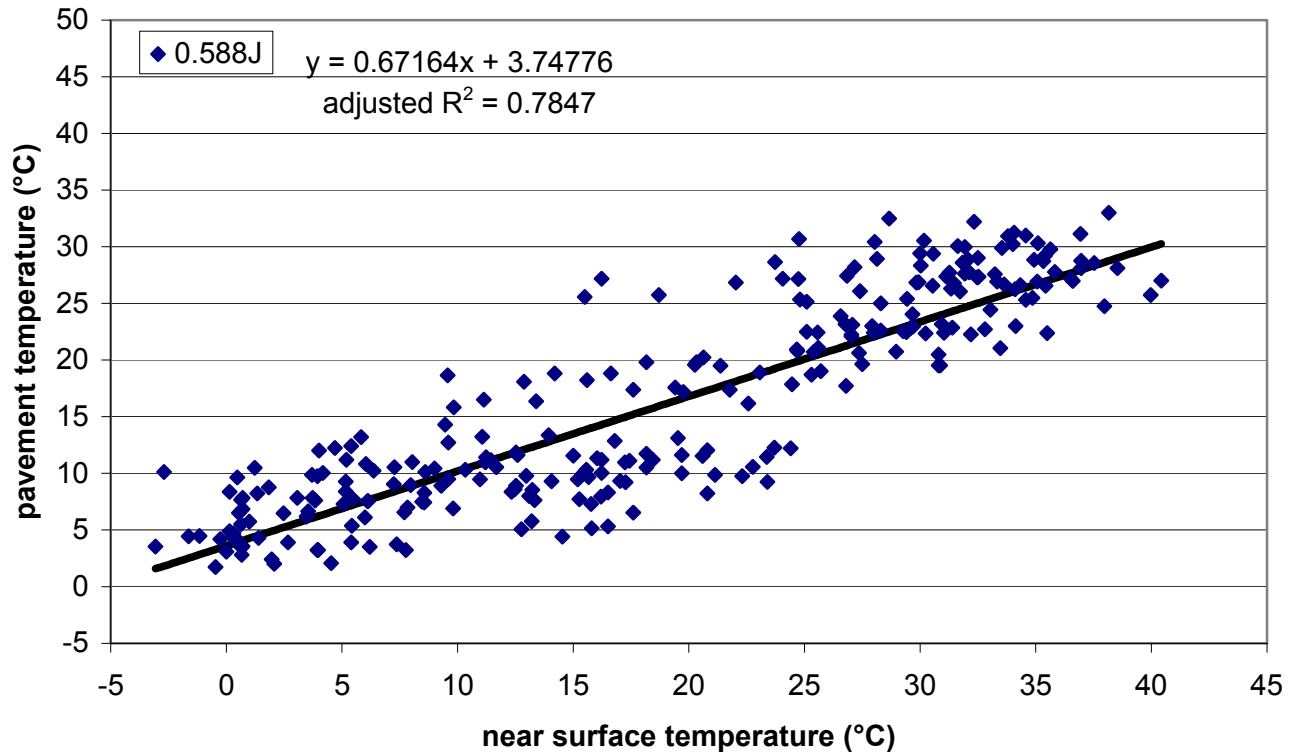


Figure I.89. Section J – daily maximum near surface temperature vs. daily maximum pavement temperature (0.588m depth) with linear model.

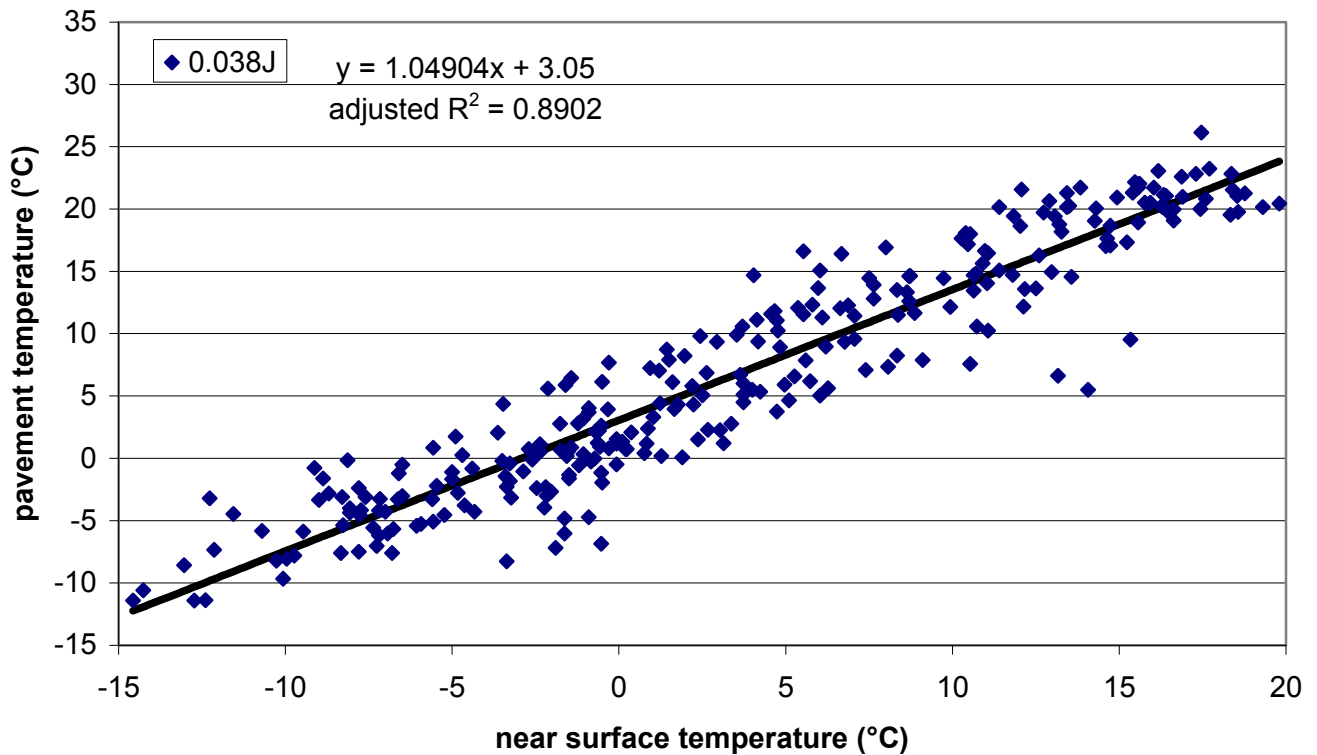


Figure I.90. Section J – daily minimum near surface temperature vs. daily minimum pavement temperature (0.038m depth) with linear model.

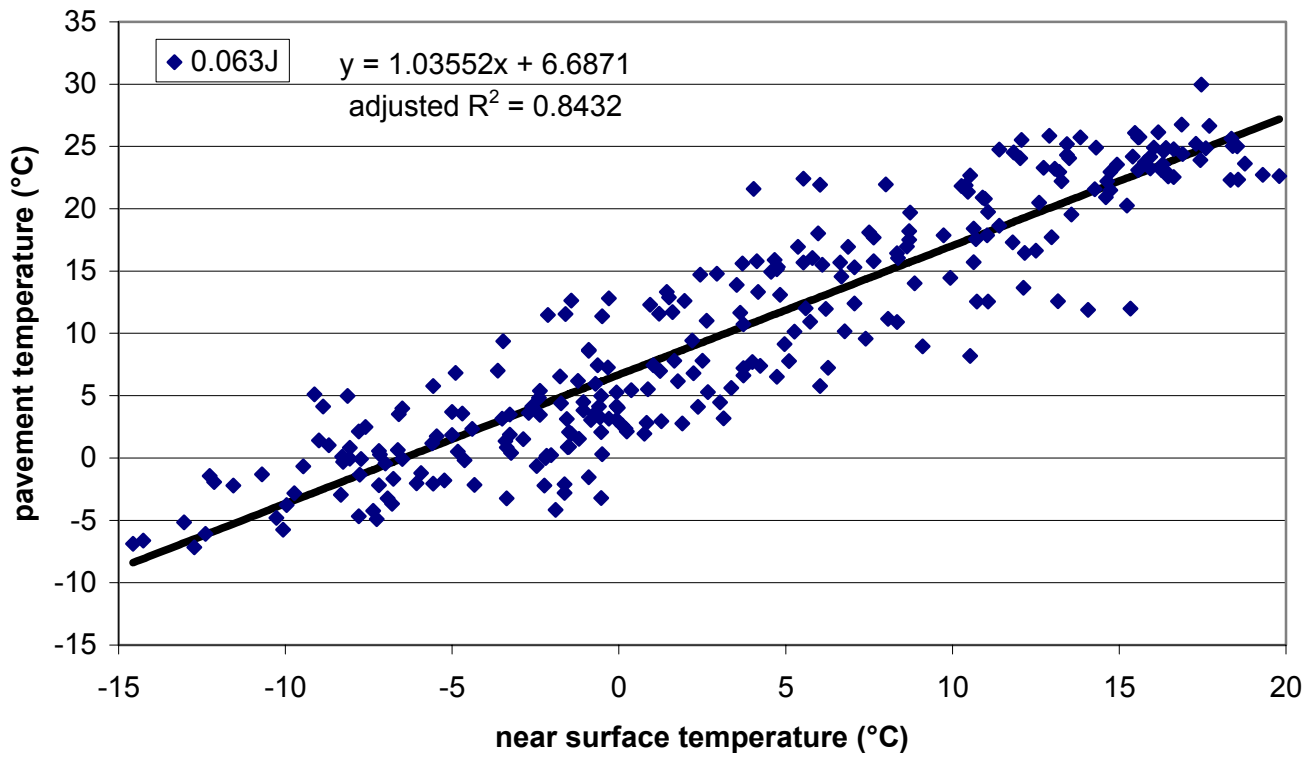


Figure I.91. Section J – daily minimum near surface temperature vs. daily minimum pavement temperature (0.063m depth) with linear model.

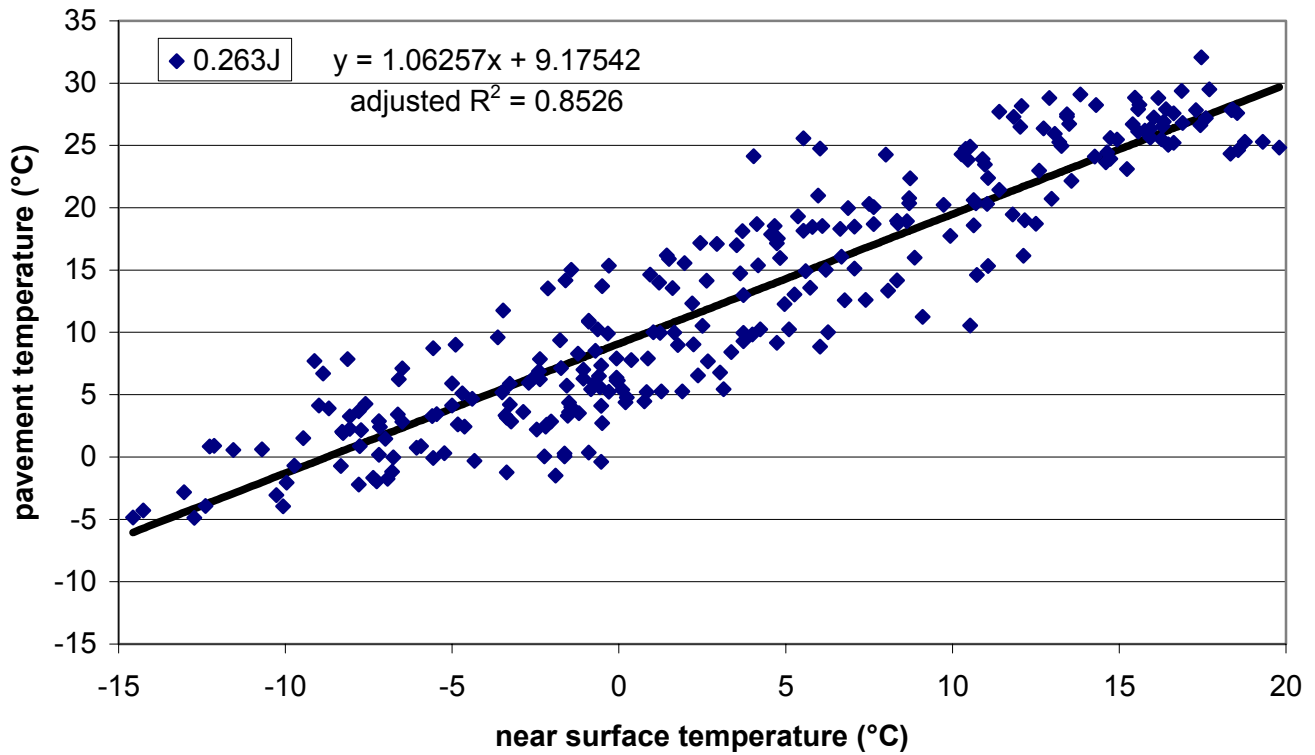


Figure I.92. Section J – daily minimum near surface temperature vs. daily minimum pavement temperature (0.263m depth) with linear model.

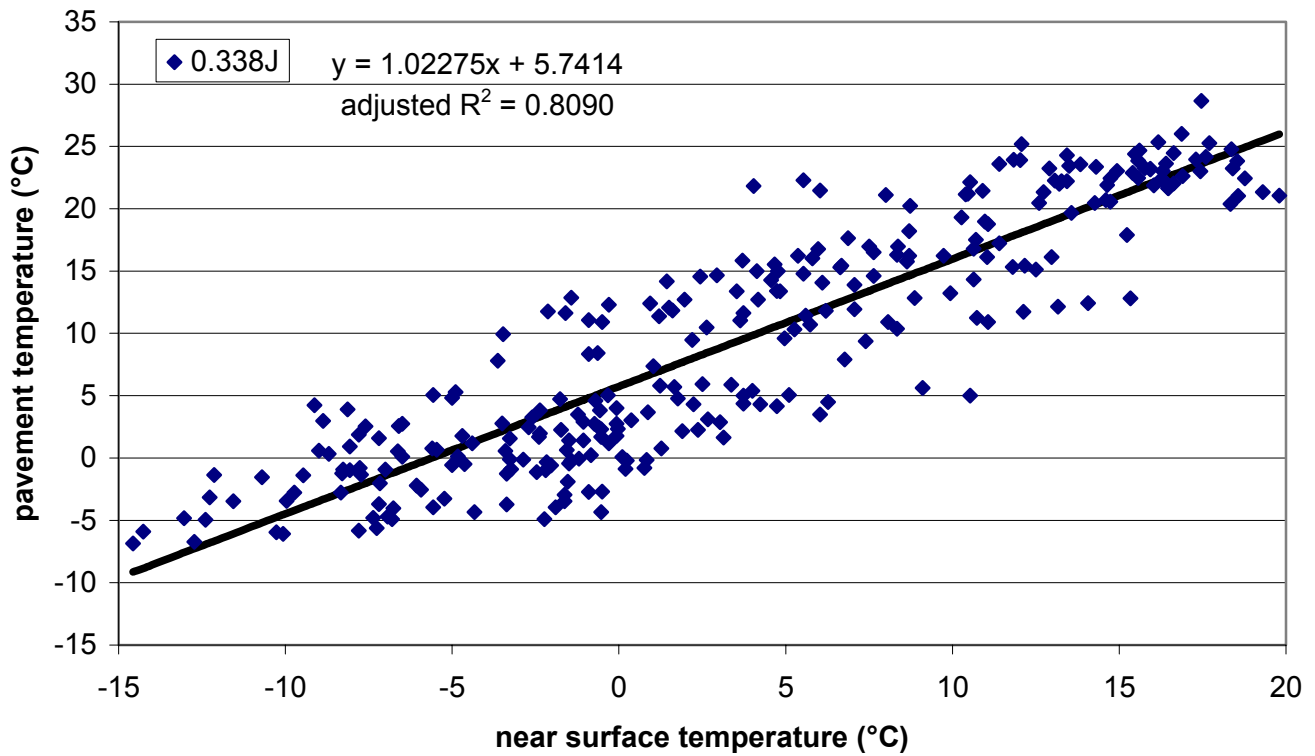


Figure I.93. Section J – daily minimum near surface temperature vs. daily minimum pavement temperature (0.338m depth) with linear model.

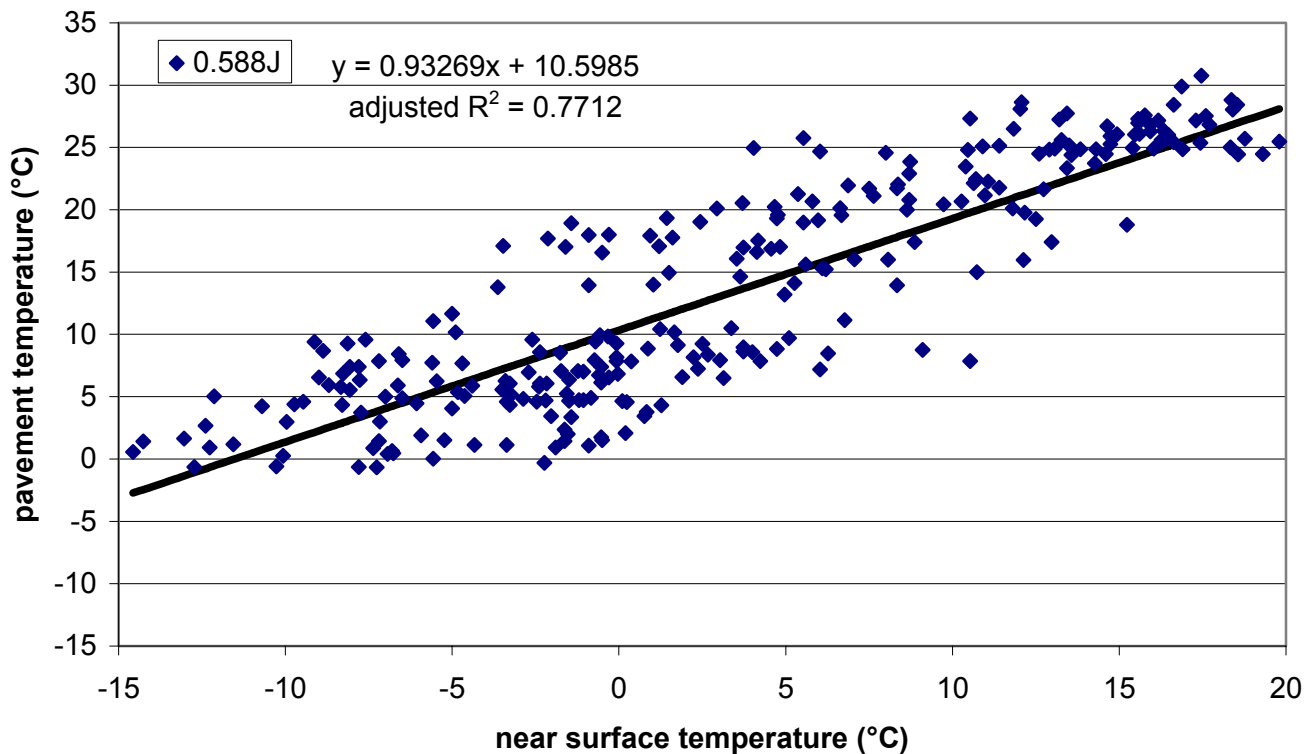


Figure I.94. Section J – daily minimum near surface temperature vs. daily minimum pavement temperature (0.588m depth) with linear model.

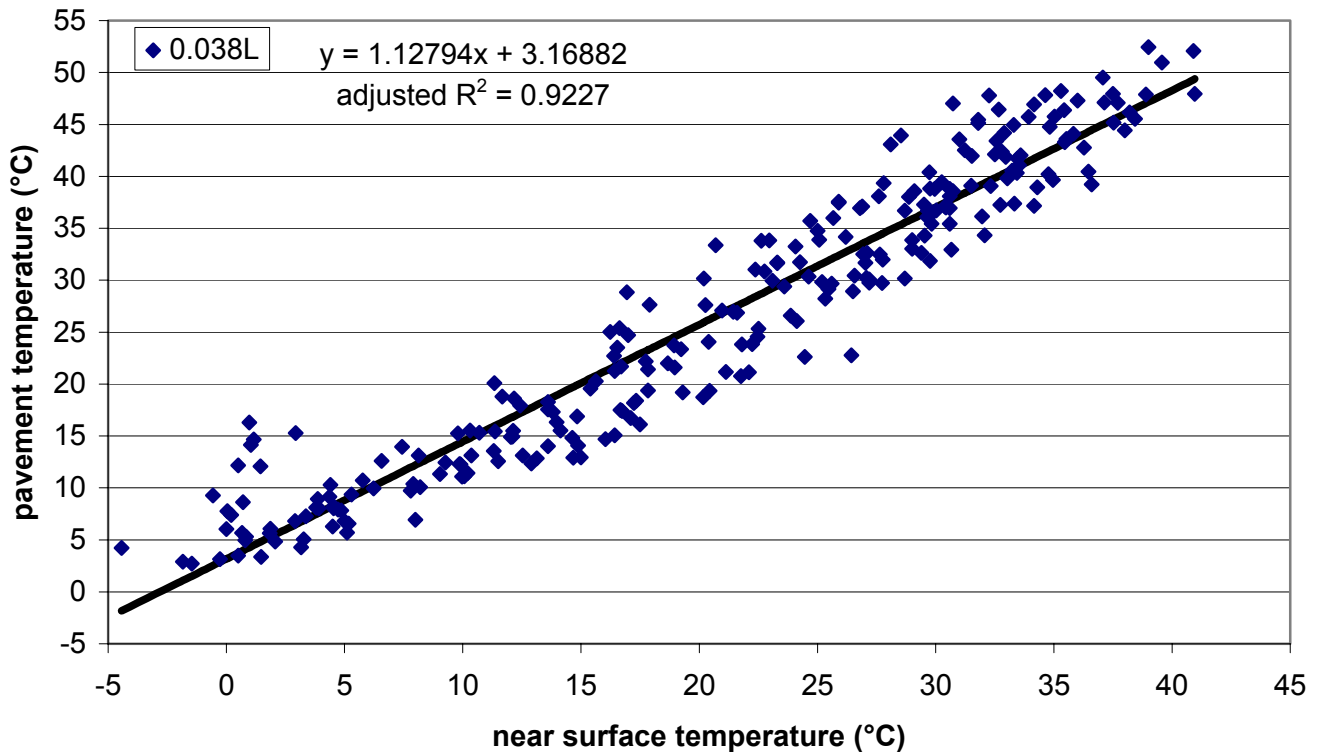


Figure I.95. Section L – daily maximum near surface temperature vs. daily maximum pavement temperature (0.038m depth) with linear model.

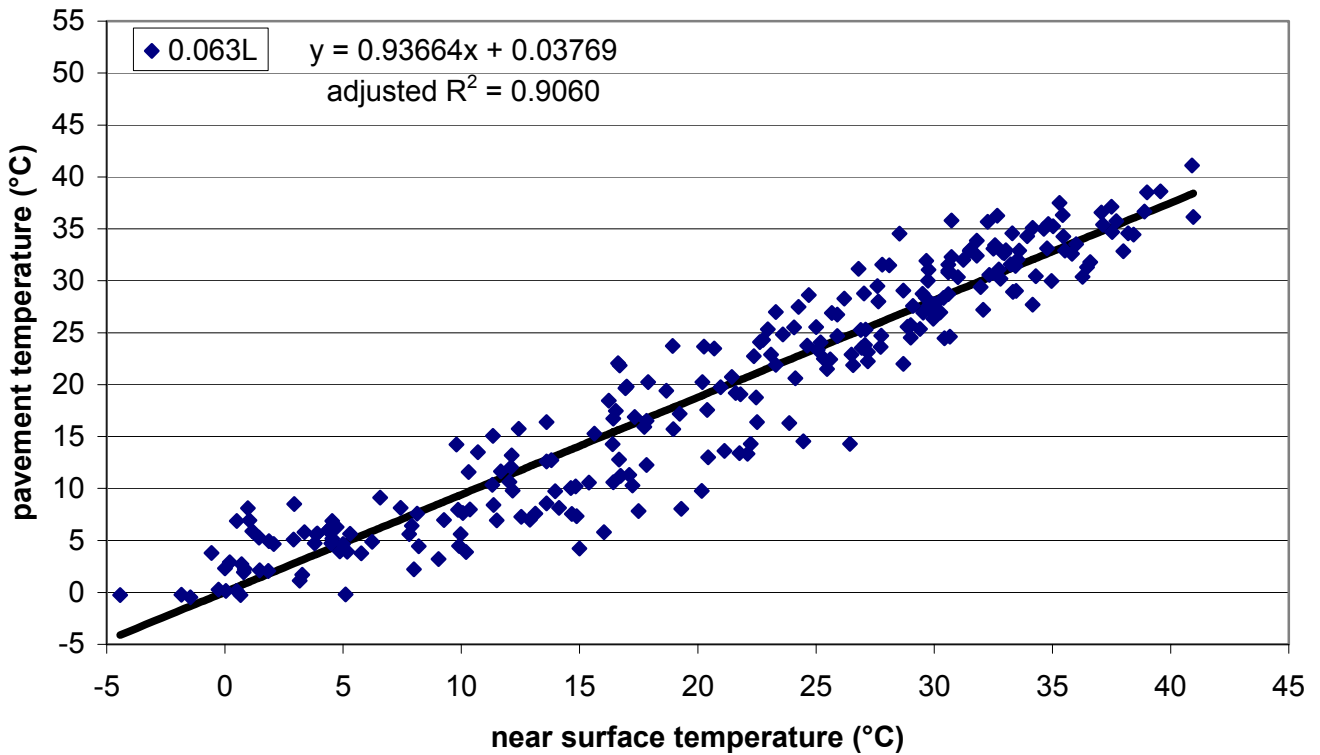


Figure I.96. Section L – daily maximum near surface temperature vs. daily maximum pavement temperature (0.063m depth) with linear model.

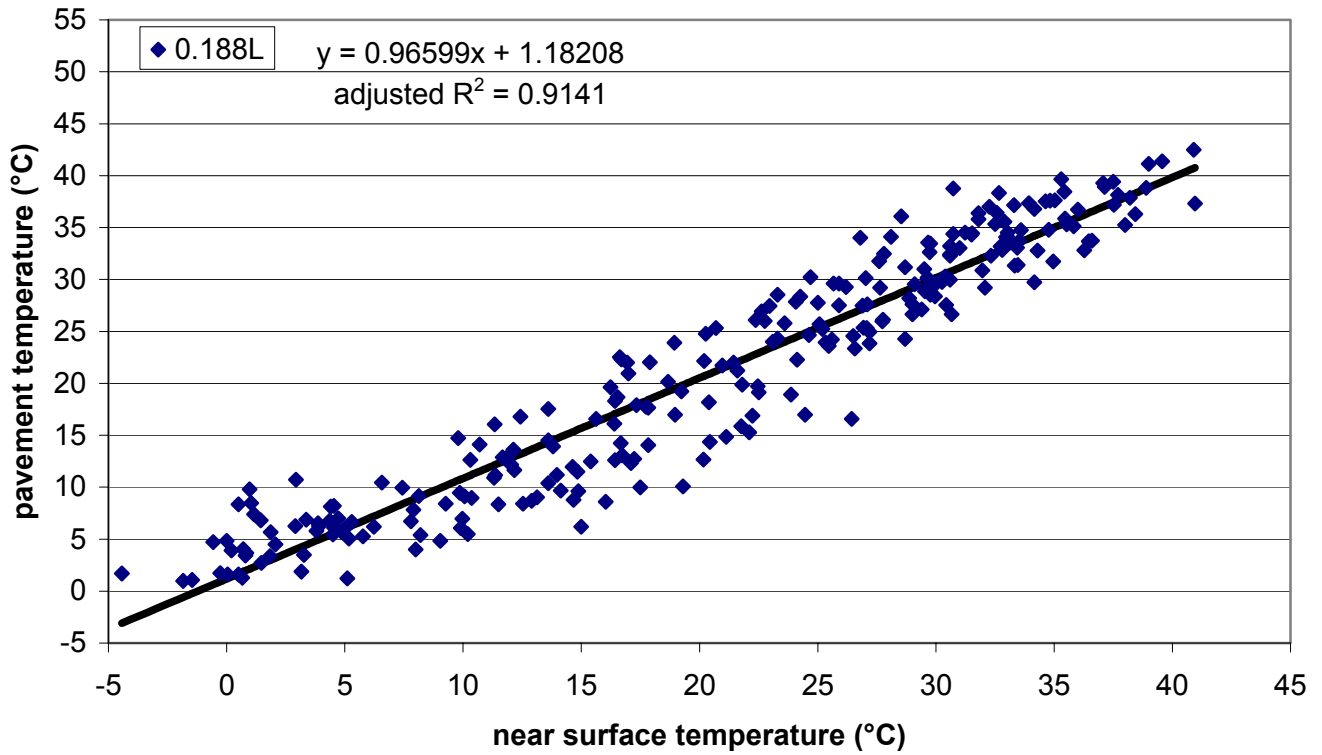


Figure I.97. Section L – daily maximum near surface temperature vs. daily maximum pavement temperature (0.188m depth) with linear model.

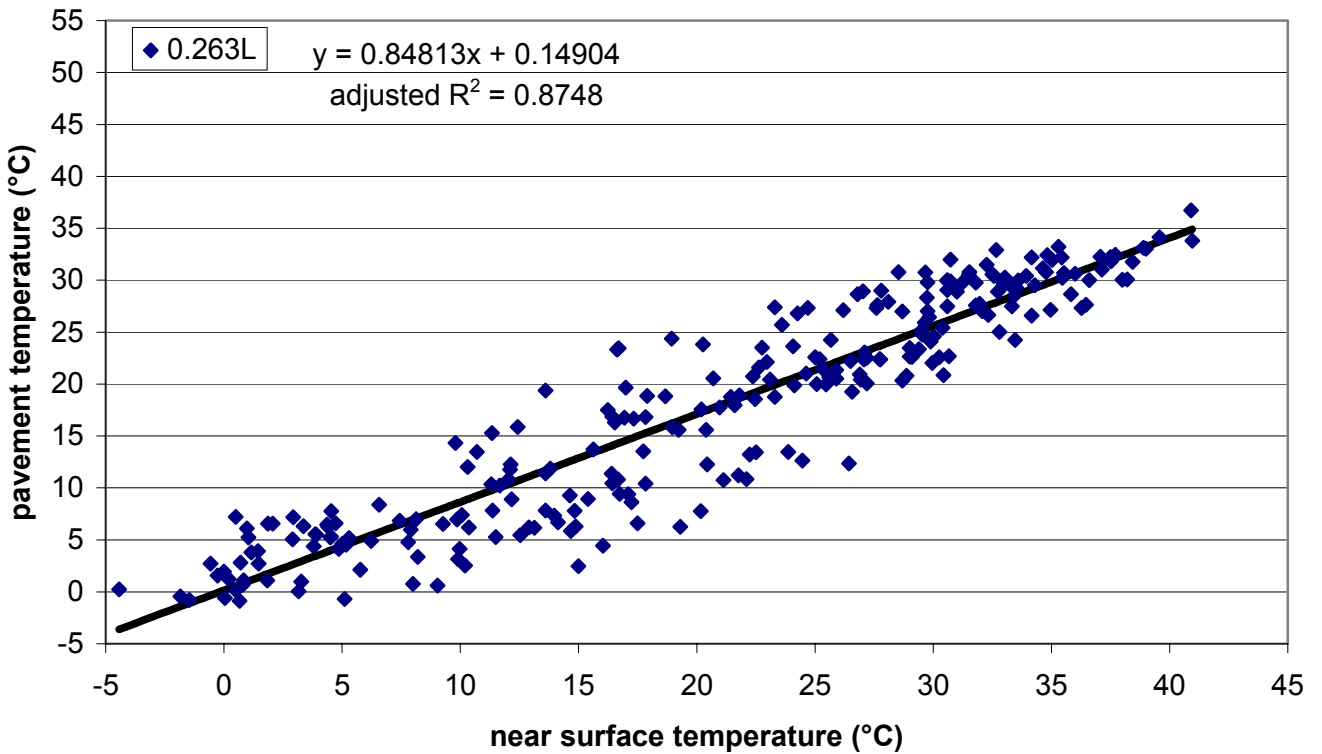


Figure I.98. Section L – daily maximum near surface temperature vs. daily maximum pavement temperature (0.263m depth) with linear model.

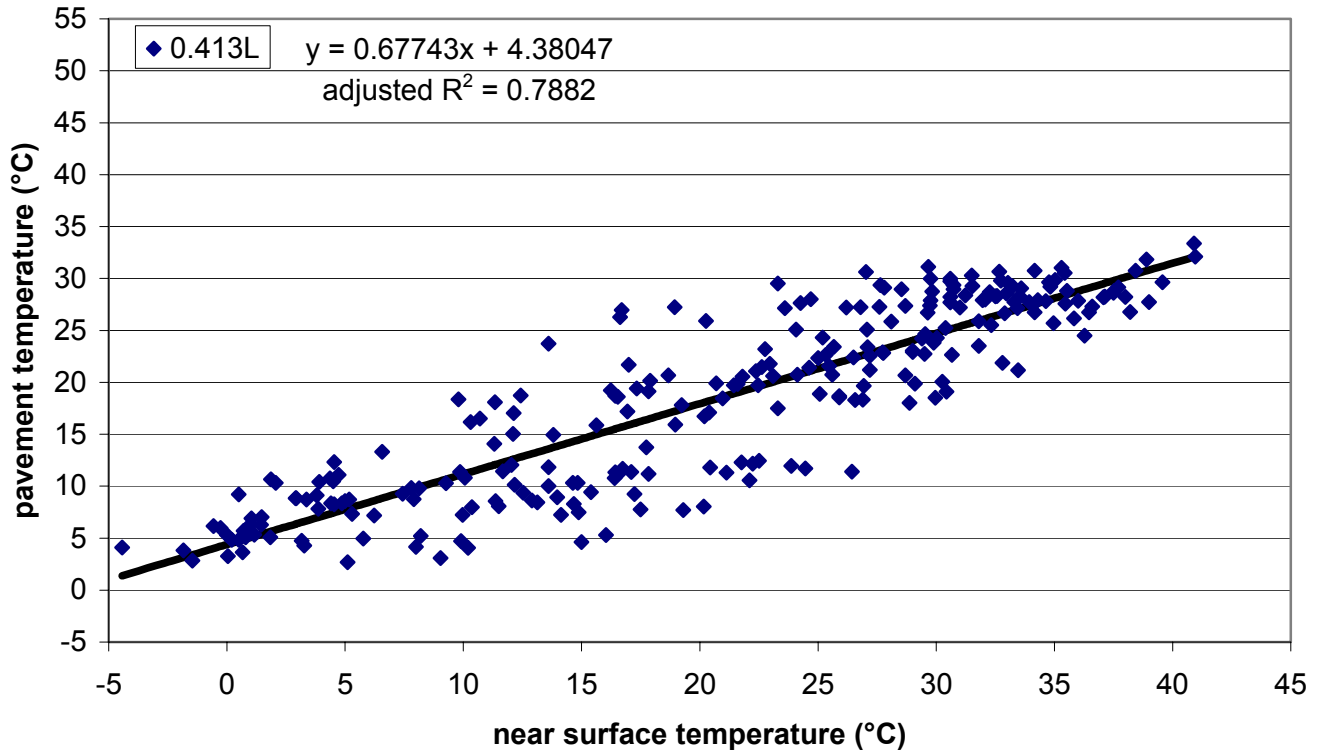


Figure I.99. Section L – daily maximum near surface temperature vs. daily maximum pavement temperature (0.413m depth) with linear model.

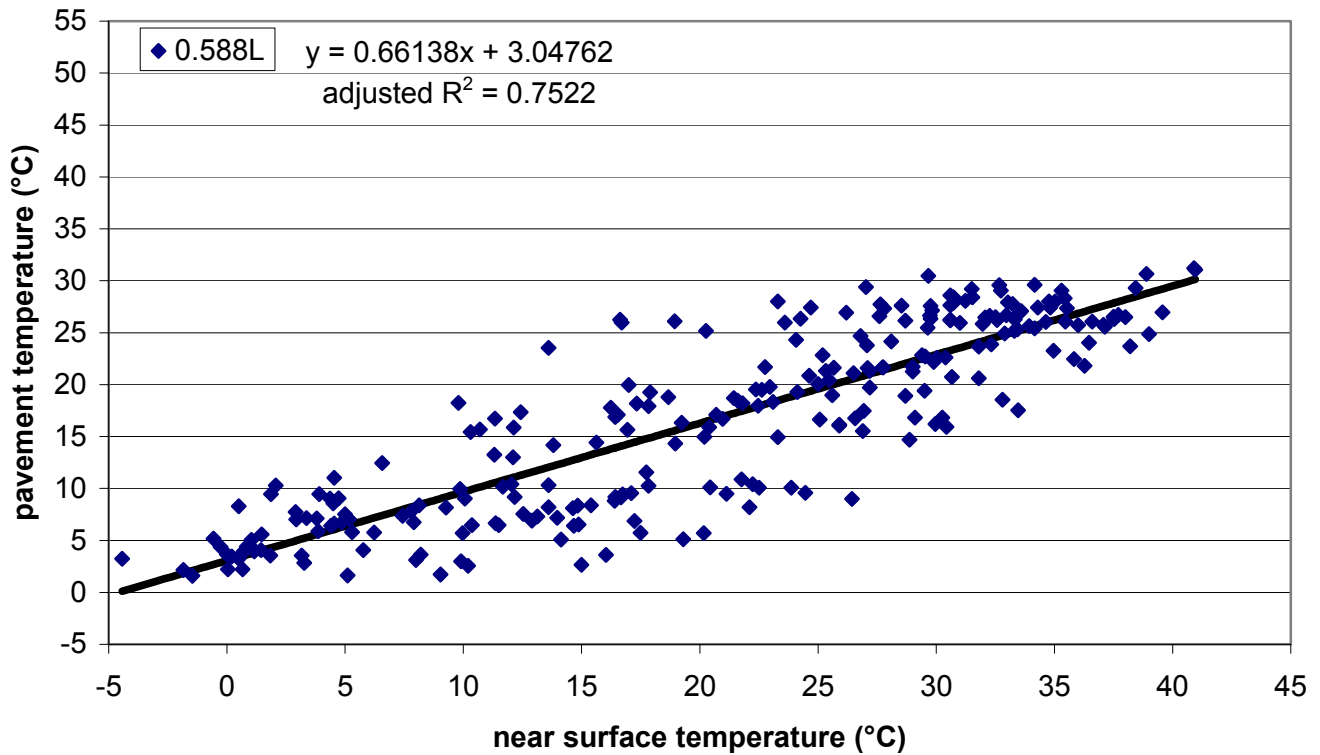


Figure I.100. Section L – daily maximum near surface temperature vs. daily maximum pavement temperature (0.588m depth) with linear model.

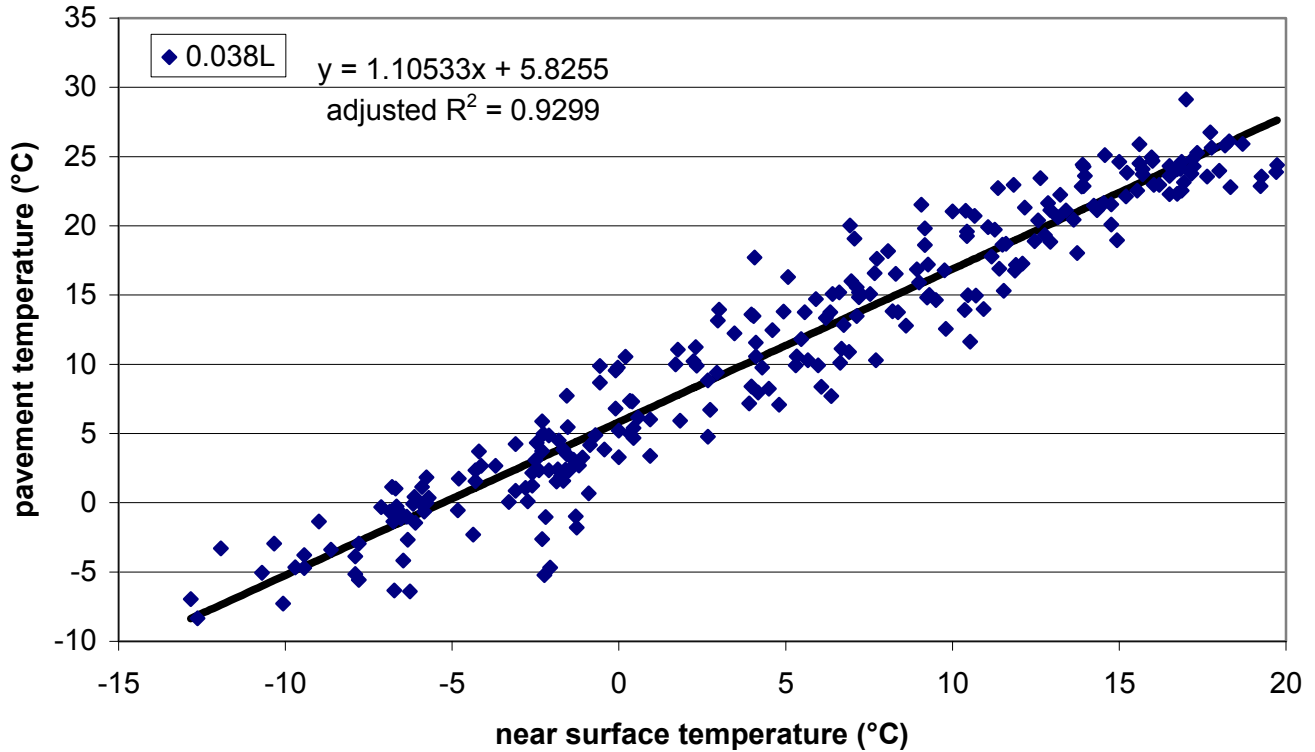


Figure I.101. Section L – daily minimum near surface temperature vs. daily minimum pavement temperature (0.038m depth) with linear model.

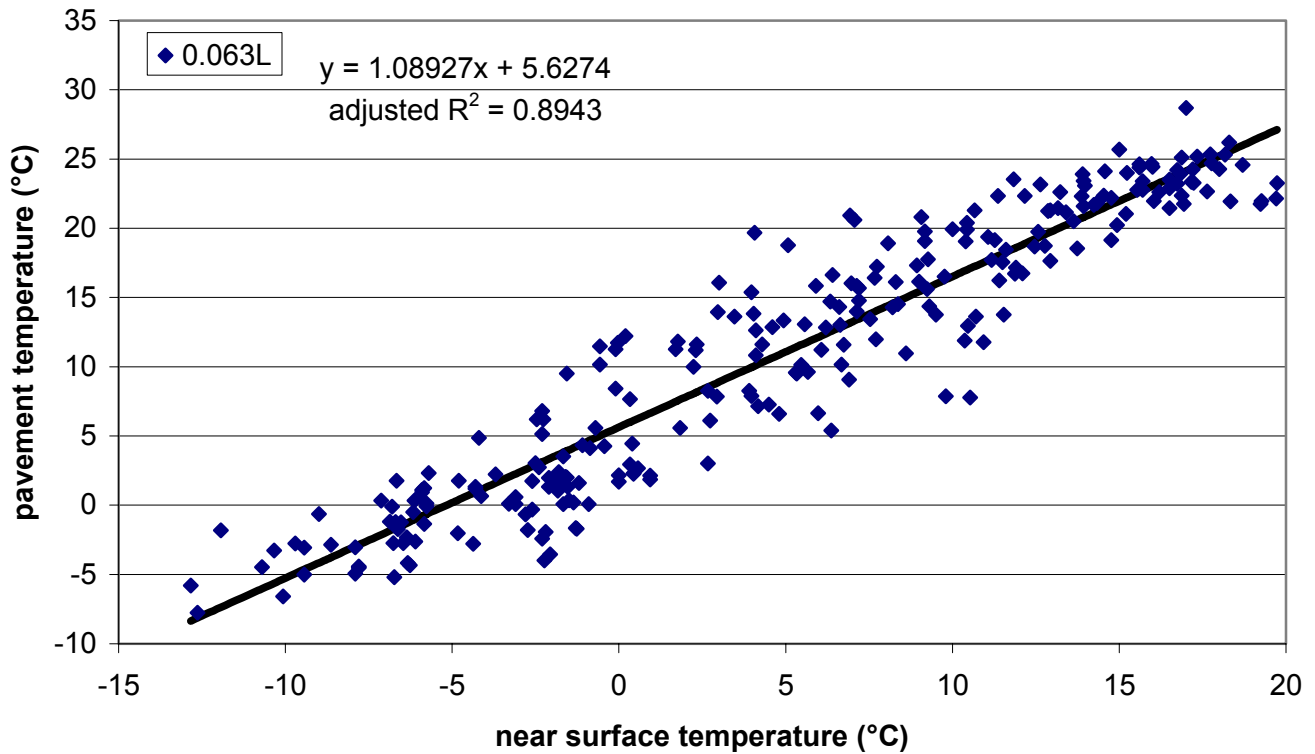


Figure I.102. Section L – daily minimum near surface temperature vs. daily minimum pavement temperature (0.063m depth) with linear model.

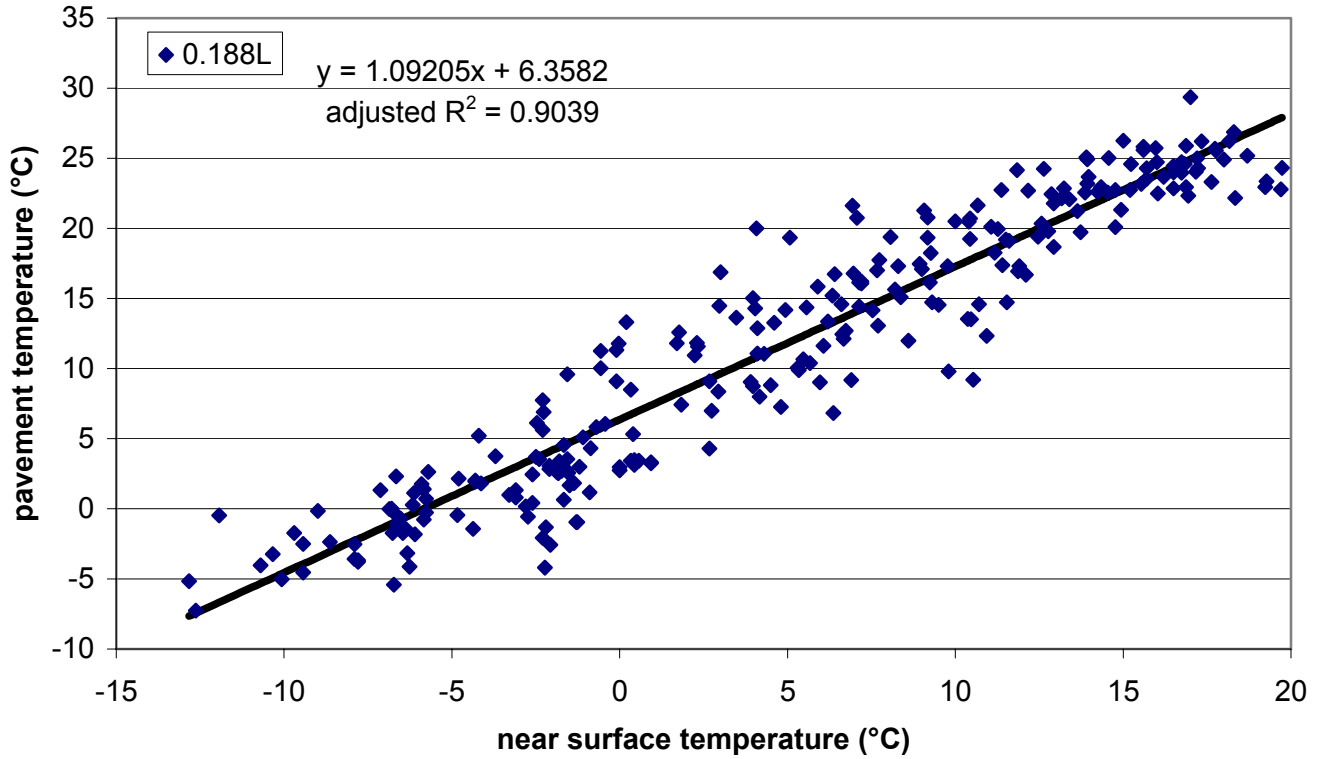


Figure I.103. Section L – daily minimum near surface temperature vs. daily minimum pavement temperature (0.188m depth) with linear model.

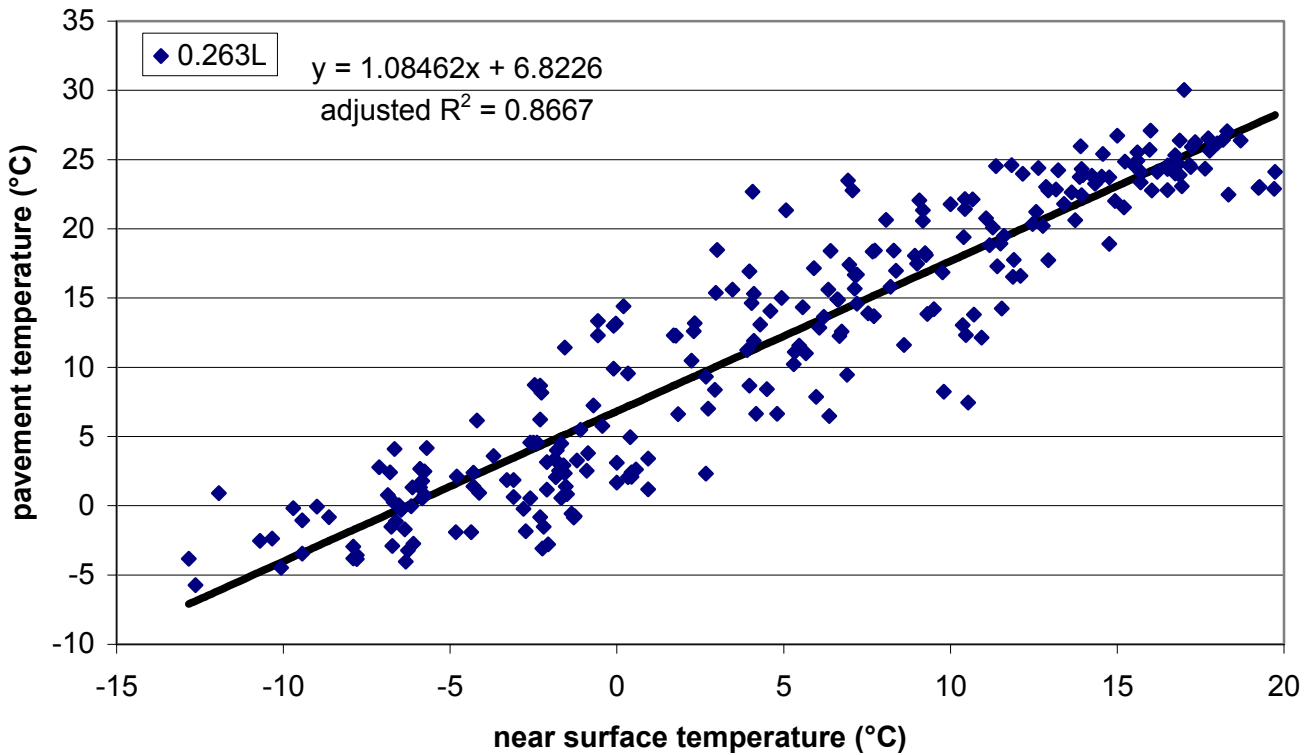


Figure I.104. Section L – daily minimum near surface temperature vs. daily minimum pavement temperature (0.263m depth) with linear model.

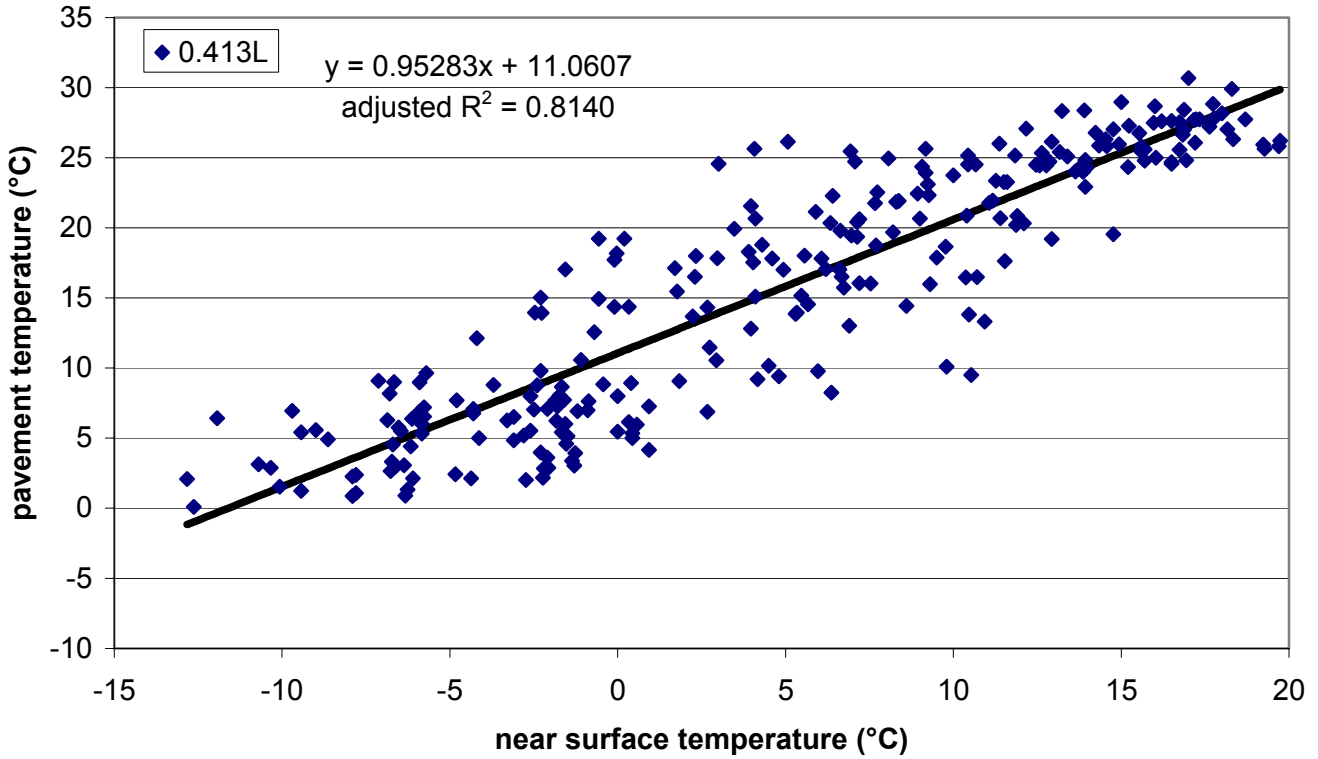


Figure I.105. Section L – daily minimum near surface temperature vs. daily minimum pavement temperature (0.413m depth) with linear model.

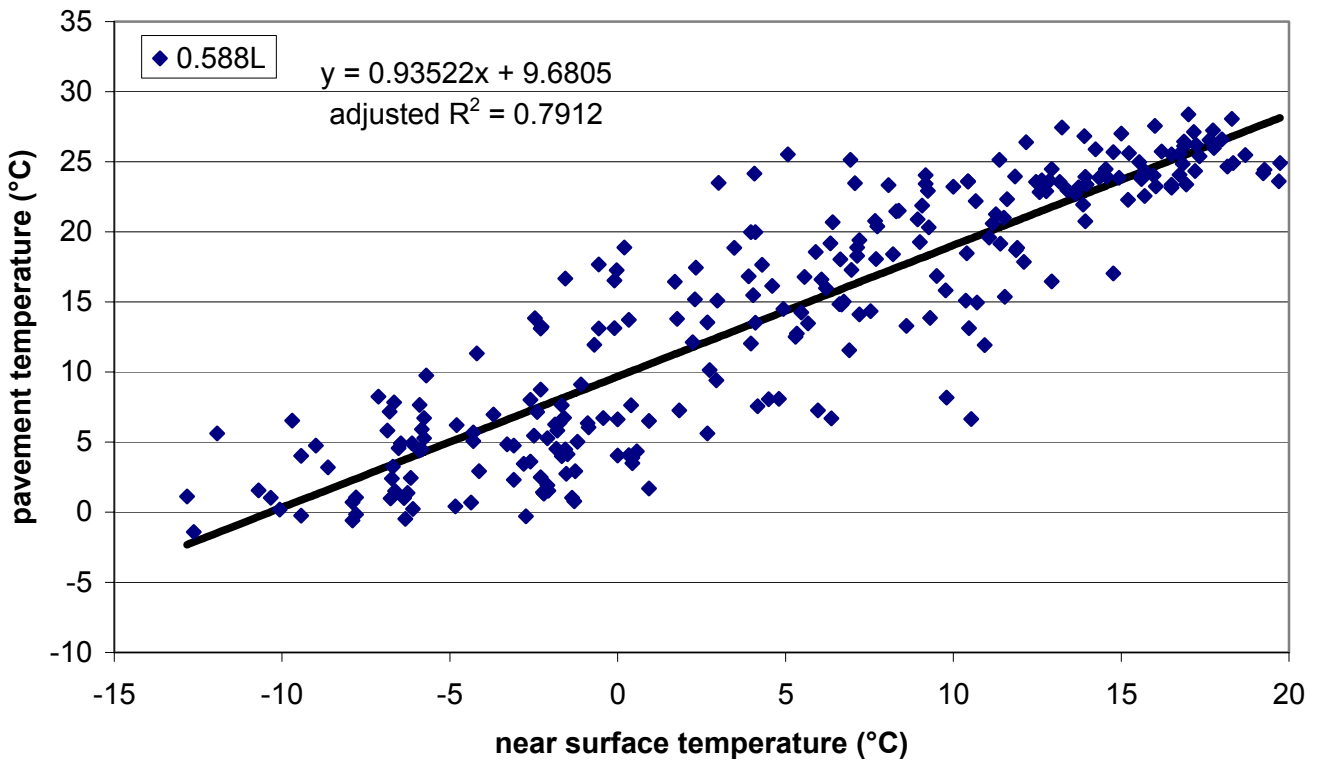


Figure I.106. Section L – daily minimum near surface temperature vs. daily minimum pavement temperature (0.588m depth) with linear model.

VITAE

Brian K. Diefenderfer was born on April 10, 1973 in Washington, DC to Norris and Barbara Diefenderfer. He graduated from North Hagerstown High School in Hagerstown, Maryland in June 1991. The authors' undergraduate studies were completed at Virginia Polytechnic Institute and State University in Blacksburg, Virginia. He received a Bachelor of Science degree in Civil Engineering in May 1996. The author received a Master of Science degree with a major in Civil Engineering from Virginia Tech in 1998. His thesis was entitled "Development and Testing of a Capacitor Probe to Detect Deterioration in Portland Cement Concrete." The author anticipates completing his PhD dissertation "Moisture Content Determination and Temperature Profile Modeling of Flexible Pavement Structures" at Virginia Tech in Spring 2002.